DANMARKS OG GRØNLANDS GEOLOGISKE UNDERSØGELSE RAPPORT 2003/15

EFP-01 Rock Physics of Impure Chalks
Final Report

ENS J. nr. 1313/01-0006

Peter Japsen, Anders Bruun, Ida L. Fabricius, Christian Høier,
Gary Mavko, Christian Mogensen, Jacob Mørch Pedersen,
Rasmus Rasmussen and Ole V. Vejbæk

GEUS Report included in this volume: 2002/23

GEOLOGICAL SURVEY OF DENMARK AND GREENLAND
MINISTRY OF THE ENVIRONMENT

G E U S

DANMARKS OG GRØNLANDS GEOLOGISKE UNDERSØGELSE RAPPORT 2003/15

EFP-01 Rock Physics of Impure Chalks
Final Report

ENS J. nr. 1313/01-0006

Peter Japsen[1], Anders Bruun[2], Ida L. Fabricius[3], Christian Høier[1],
Gary Mavko[4], Christian Mogensen[2], Jacob Mørch Pedersen[2],
Klaus Bolding Rasmussen[2], Rasmus Rasmussen[1]
and Ole V. Vejbæk[1]

Released 01.10.2005

[1] Geological Survey of Denmark and Greenland (GEUS)
[2] Ødegaard A/S
[3] Technical University of Denmark (DTU)
[4] Stanford University

GEUS Report included in this volume:
Danmarks og Grønlands Geologiske Undersøgelse Rapport 2002/23:
Speciel Core Analysis for the Rock Physics Project (EFP-2001)
ENS J. nr. 1313/01-006
Ultrasonic velocity measured on plugs from the Ekofisk and Tor Formation. Samples taken from the wells: Rigs-1, Rigs-2 and SA-1, the South Arne Field.

GEUS Core Laboratory
Christian Høier

GEOLOGICAL SURVEY OF DENMARK AND GREENLAND
MINISTRY OF THE ENVIRONMENT

G E U S

GEUS

DTU

LELAND STANFORD JUNIOR UNIVERSITY

ORGANIZED 1891

Summary

We have estimated the elastic properties of chalk at three different scales on the South Arne field, North Sea, by analysing ultrasonic core data, downhole log-readings and results of AVO-inversion based on near- and far-offset stack seismic data (Amplitude Versus Offset). Here we present main results from papers and reports enclosed in this volume.

Fluid substitution in chalks: Effects of saturation scales

We investigated some aspects of ultrasonic fluid substitution in chalks, and we found that Gassmann's relations can be used to understand the variations of velocity with saturation in our samples, even though the velocity data are ultrasonic (high frequency). This suggests that in these samples there are no significant high frequency dispersion effects from the squirt-flow or Biot mechanisms that would invalidate the use of the Gassmann's relations. There is, however, evidence for patchy saturation in the ultrasonic data with a characteristic patch size less than 1/10 mm. This is observed in limited V_p and V_s versus water saturation data (Fig. 1). We also find that fluid substituting to full brine saturation using a modified patchy mixing rule gives velocities more consistent with empirical trends than assuming a fine-scaling mixing rule. It is likely that fine-scale mixing is dominant at logging frequencies in chalks. Another finding is that the dry-rock ultrasonic data tend to be inconsistent, in a Gassmann sense, with data from the water-bearing samples (Japsen et al. 2002). Specifically, the dry-rock velocities are "too fast."
(Mavko & Japsen *this report*)

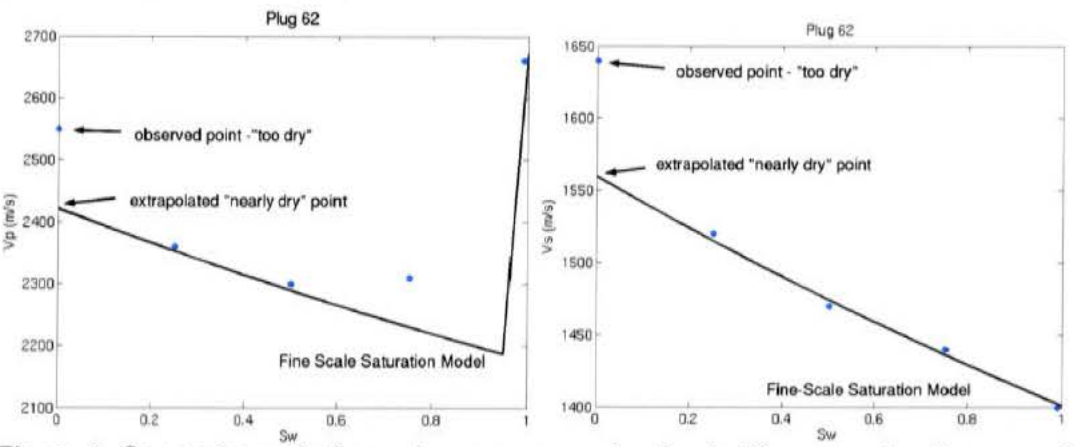

Figure 1. Comparison of ultrasonic measurements of velocities vs. saturation on a South Arne chalk sample, compared with the fine-scale mixing model. Note the departure in V_p *from the fine-scale mixing curve at high saturations. But the characteristic patch size for this sample is only 0,04 mm, and this suggests that fine-scale mixing will be dominant at the lower frequencies used in sonic logging. Core plug 62,* ϕ*=40%, permeability = 1.4 mDarcy.*

Modeling elastic moduli of impure chalk

In impure chalk the elastic moduli are not only controlled by porosity, but also by cementation resulting in relatively large moduli and by admixtures of clay and fine silica which results in relatively small moduli. Based on a concept of framebuilding contra suspended solids (iso-frame values, IF), we model P-wave moduli, *M*, and S-wave moduli, *G*, of dry and wet plug samples by an effective medium model using chemical, mineralogical and textural input ($M = \rho V_p^2, G = \rho V_s^2$ where ρ is bulk density; Fig. 2). We use a modified upper Hashin Shtrikman mixing-model assuming a critical porosity of 70%. The textural and mineralogical data may potentially be assessed from logging data on spectral gamma radiation, density, acoustic velocity and water saturations in a hydrocarbon zone.

In chalk of reservoir quality, elastic moduli are predictable (Fig. 3): The solid phase has roughly uniform composition, and as porosity decreases from 45% to 25%, the IF-value increases from 0.5 to 0.6. At intermediate porosity (25%–18%) IF-values vary between 0.5 and 0.9: Samples with high IF-values have pore-filling cementation, whereas samples with low IF-values have high amounts of suspended submicron-size quartz in the pore space. Low-porosity samples (13%–16%) have relatively low IF-values (around 0.6) and are packed with pore-filling smectite.
(Fabricius et al. *this report*)

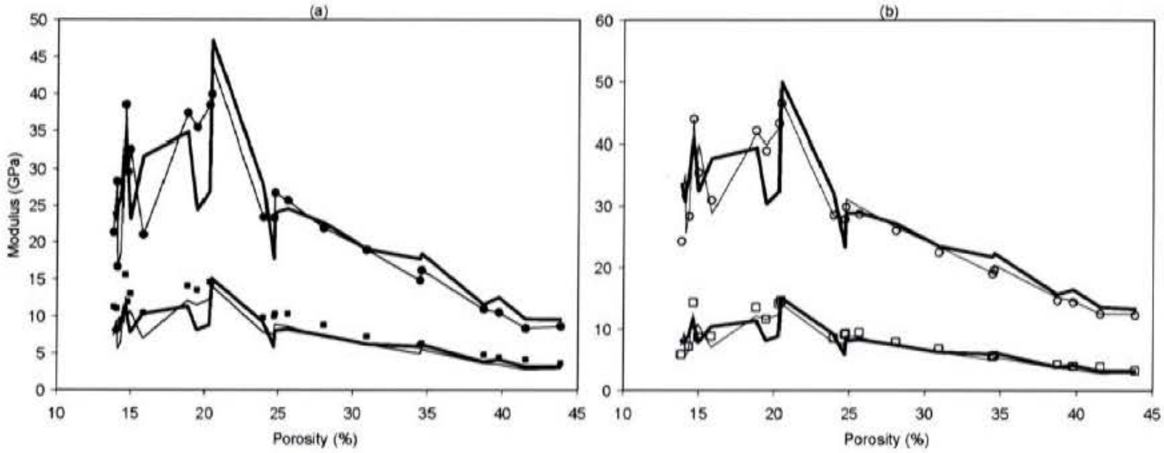

Figure 2. Elastic modulus data and elastic models versus porosity.
a. Dry samples. b. Water saturated samples.
The models fit the wet P-wave modulus data, whereas especially the dry S-wave moduli tend to be higher than predicted. The model based on image analysis has the advantage of being based on petrographic data.
Circles: P-wave modulus data. Squares: S-wave modulus data.
Thin lines: model based on dry P-wave and density data.
Thick lines: model based on image-analysis data calibrated to dry P-wave data.

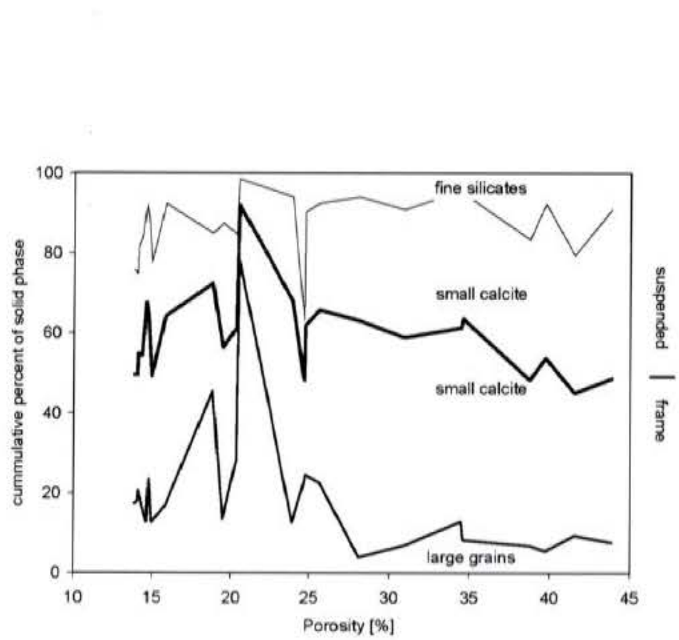

Figure 3. Composition of solid phase of chalk samples versus porosity. The thick line denotes the IF-value of each sample. The area below the thick line represents the solid phase modeled as solid frame with spherical pores, whereas the area above the line represents the solid modeled as being in suspension. Large grains include calcitic microfossils, porfilling carbonate cement, as well as clasts of quartz, feldspar and kaolinite. Fine silicates include smectite, kaolinite and quartz.

Influence of porosity and pore fluid on acoustic properties of chalk: AVO-response from oil

We find that the velocity-porosity relation of the plug data are in agreement with the empirical, modified upper Hashin-Shtrikman (MUHS) model established by Walls et al. (1998) for chalk from the Ekofisk field for porosities between 10% and 40%. In pure chalk intervals, this model furthermore, matches log-estimated values of the shear modulus which are unaffected by fluid content according to Gassmann's relations.

Due to higher porosities in the South Arne field we extend the range of the model to 45% porosity based on the ultrasonic data (Fig. 4). The model predicts the shear modulus to be smaller than observed from logging data for porosities above c. 40%. Erroneous log-determination of Vs may be the cause of this difference when S-wave traveltimes becomes very long.

Variations of the bulk modulus, K, as a function of water saturation are predicted by the model combined with Gassmann's equations, and we find that the sonic log data represent chalk where the oil has been partly flushed by invasion of mud filtrate; $K = \rho(V_p^2 - 4/3 \cdot V_s^2)$. We use the difference between logging data- and model-estimates of the shear modulus to correct the model by scaling it according to clay content as estimated by the water saturation. The water saturation in e.g. the Rigs-2 well can be regarded as a measure of the impurities in the chalk because the chalk is water-wet and the water saturation is close to irreducible saturation (Fabricius et al. 2002).

A characteristic depth-wise pattern of the Poisson ratio, ν, with pronounced peaks at top Ekofisk and top Tor and low values in the high-porous Tor reservoir is derived for the Rigs-2 well from the forward modeling of the acoustic properties of the virgin zone based

on the corrected, modified upper Hashin-Shtrikman model (Fig. 5; $\nu = (V_p^2 / V_s^2 - 2)/(V_p^2 / V_s^2 - 1)/2$). This pattern agrees with the inverted seismic data, whereas these features are not captured if the acoustic properties of the virgin zone are derived from the sonic logs and estimates of residual oil in the flushed zone because of almost complete invasion where porosity is high (Fig. 6). We have thus found AVO-inversion to provide direct evidence for presence of light oil in the high-porous chalk of the South Arne field.
(Japsen et al. *this report*)

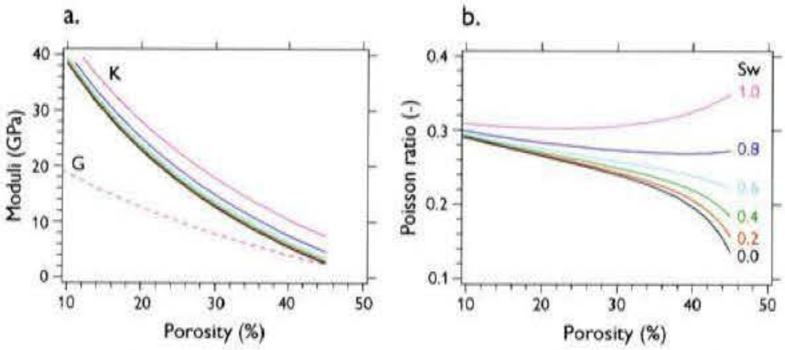

Fig. 4. Acoustic properties of chalk as a function of porosity and water saturation, Sw, predicted from the MUHS model and Gassmann's relations assuming fine-scaled Reuss mixing of the fluids.

a. Bulk and shear modulus, K and G. b. Poisson ratio.

Note the pronounced variation in Poisson ratio for porosities above c. 35% between pure brine and pure oil (density 1.035 and 0.633 g/cm^3). MUHS: Modified Upper Hashin-Shtrikman.

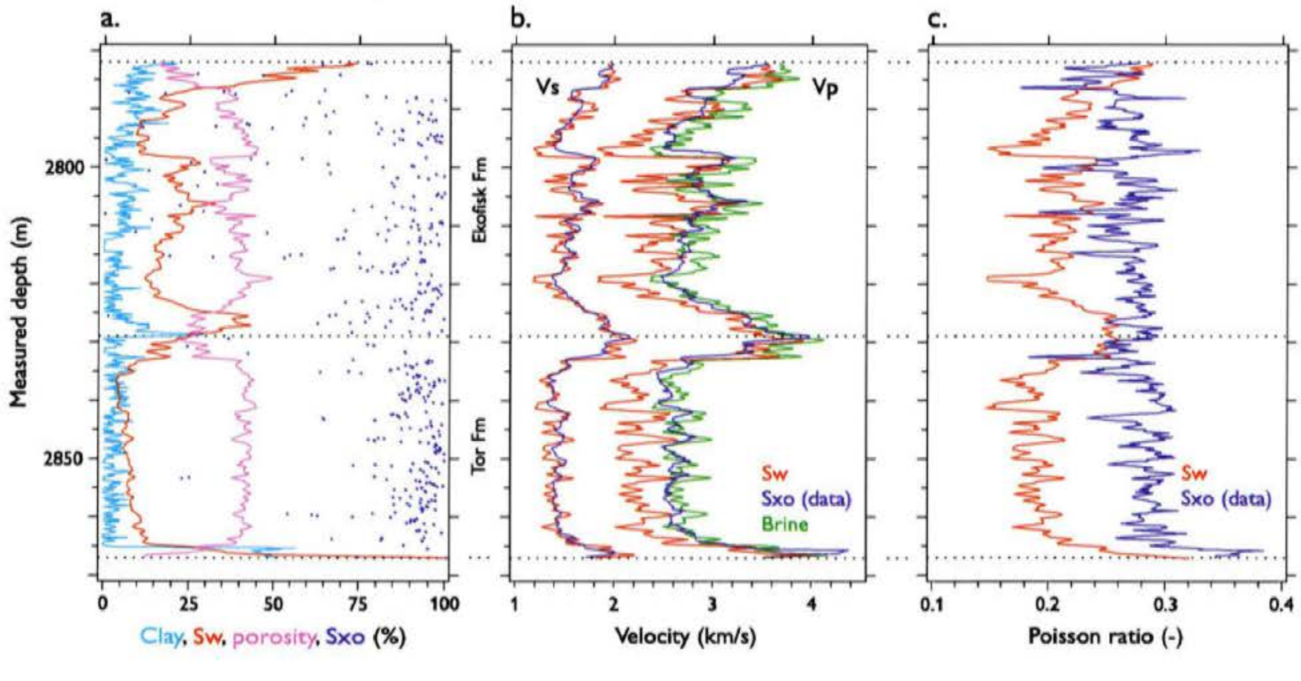

Fig. 5. Log data and predictions based on the corrected MUHS model for the chalk section in the Rigs-2 well.

a. Clay content (from gamma log), porosity and water saturation, Sw and Sxo. Sxo (dots) is estimated from the relation between the measured sonic data and the corrected MUHS model.

b. V_P and V_S. Data and predictions of the corrected MUHS model based on porosity and Sw. Brine-estimate for Vs not shown.

c. Poisson ratio. Data and predictions of the corrected MUHS model. Brine-estimate not shown.

In the high-porosity oil zone of the Tor Formation, the oil is predicted to be almost completely flushed as indicated by the closeness of the measured Vp(Sxo) (blue curve) and the predicted Vp(brine) (green curve) whereas Vp(virgin zone, Sw) is predicted to be low. MUHS: Modified Upper Hashin-Shtrikman.

AVO-inversion of seismic data

AVO attributes were calculated from inverted 2D seismic lines (near- and far-offset data) extracted from the South Arne 3D survey. The inversion was carried out for the two-way time window 1.9–3.6 s and was targeted on the chalk interval. Log data from the I-1x, Rigs-1, -2 and SA-1 wells were used in the inversion process. These data comprise V_p- and V_s-logs based on the corrected, modified upper Hashin-Shtrikman model described above plus density logs, check shot and deviation data. Using a least-squares wavelet estimation method with constrain on the phase, wavelets were estimated for each offset stack and for each of the wells. The wavelet estimated from the I-1x well was preferred based on inversion tests.

Low-frequency components of the acoustic impedance variations with depth are not present in seismic data. Since this information is essential to the interpretation, it should be accounted for in the seismic inversion. Simple low-frequency impedance models were constructed by extrapolation of the angle-dependent impedance well logs through the 3D volume tied to seismic horizons, followed by low-pass filtering. The inversion results are good in terms of match with the angle-dependent impedance well logs.

AVO-attributes were computed from the angle-dependent impedance inversions combined with low-frequency information: Acoustic impedance, shear impedance and Poisson's ratio were extracted at the location of the I-1x, Rigs-1, -2 and SA-1 wells. The AVO-results are good in terms of match with the well log data. Low values of Poisson's ratio at the location of Rigs-2 is in agreement with the presence of light oil in the high-porous chalk of the South Arne field (Fig. 6).
(Bruun *this report*)

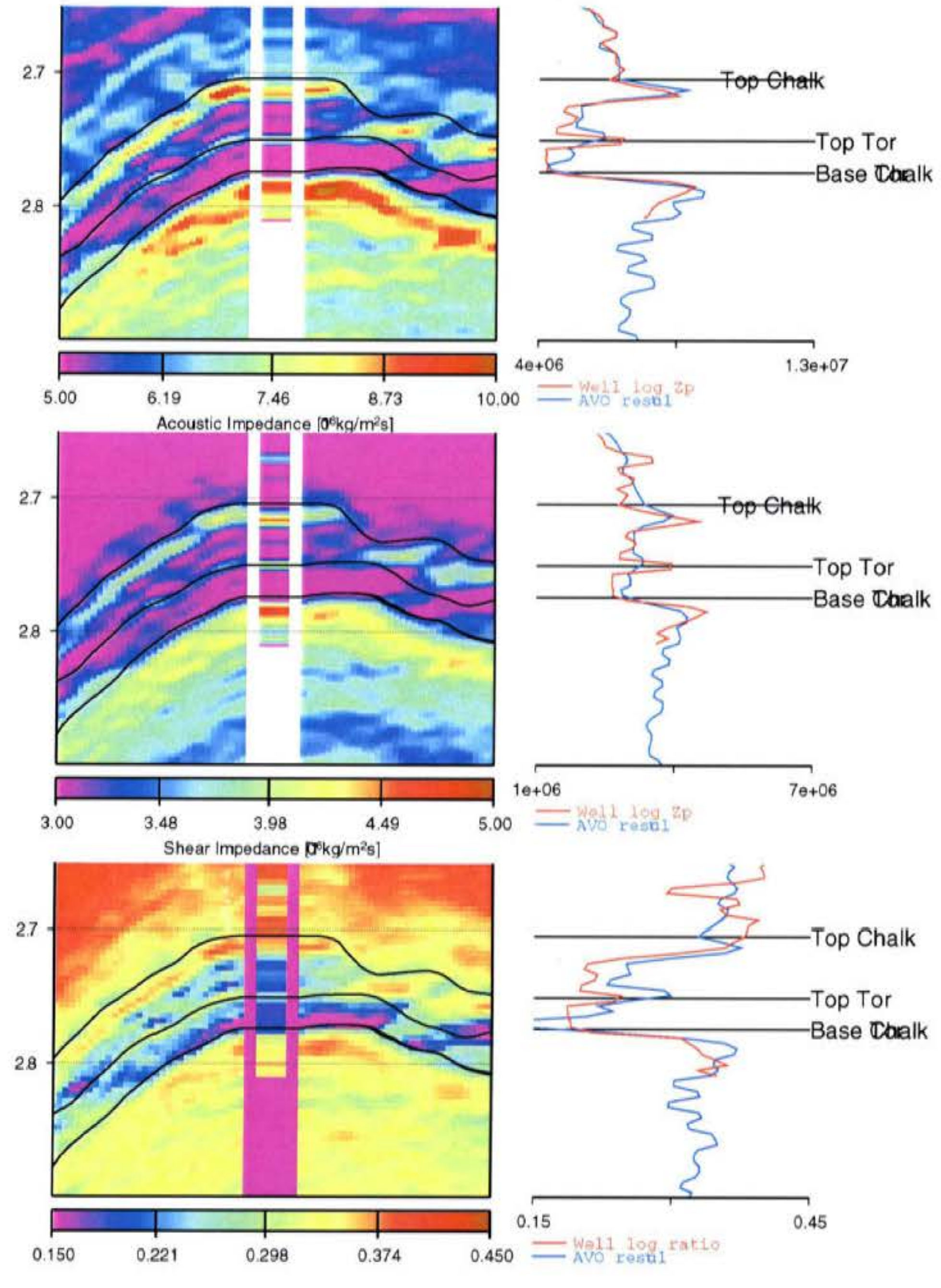

Figure 6. Two-way time section with AVO-inversion of seismic data and inserted log response for the Rigs-2 well computed from forward modeling of the corrected, modified upper Hashin-Shtrikman model NE-SW orented cross section.

a. Acoustic impedance, b. shear impedance, c. Poisson ratio.

Very good agreement is observed for both acoustic and shear impedance. Note the peaks in the tight zones near top chalk and top Tor, There is good agreement between the log- and AVO-pattern of Poisson's ratio, e.g. the peak at top Tor and the low values within the Tor Formation. This pattern cannot be resolved by the log if the acoustic properties are estimated from the sonic log because the water saturation near the well bore is unkown.

Modelling seismic response from chalk reservoirs resulting from changes in burial depth and fluid saturation

We have investigated changes in seismic response caused by changes in degree of compaction and fluid content in North Sea Chalk reservoirs away from a well bore by forward modelling. The investigated seismic response encompasses reflectivity changes, AVO and acoustic impedance based on well data from the South Arne and Dan fields, Danish North Sea and these results are compared to seimic field records. Depth of burial (changes in effective stress) and changes in hydrocarbon saturation are the two main variables to use for seismic response prediction away from the well bore (Fig. <ov-0<). The three main modelling tools used for the modelling are 1) rock physics, 2) saturation modelling and 3) compaction/de-compaction modelling.

1) Rock physics theory is applied to obtain all necessary elastic parameters for the application of the Zoeppritz equations. The challenge is not only to predict the shear velocity, but also to account for the changes in fluid content via application of Gassmann's equations. An approach akin to the one suggested for the Ekofisk Field by Walls et al. (1998) is applied for the prediction of changes in degree of compaction.
2) Hydrocarbon saturation in North Sea Chalk is strongly affected by capillary forces due to the small scale of the pores and transition zones in the order of 50 m are not uncommon. We use the EQR and similar saturation models, which have proved robust for the prediction of saturation profiles in Danish Chalk reservoirs.
3) Compaction modelling relies on a new exponential porosity-depth trend, where abnormal fluid pressures are accounted for. This trend is based on a normal velocity-depth trend established for the North Sea Chalk. The porosity-depth trend appears to be sufficiently fine-tuned to allow fairly precise predictions of abnormal fluid pressures from observed average porosity. Based on this, the relative contribution to porosity preservation by abnormal fluid pressure and early hydrocarbon invasion may be estimated.

Based on these assumptions we find that reflectivity is correlating with porosity, acoustic impedance is more susceptible to porosity variation than to hydrocarbon saturation, and the poisson ratio may be rather sensitive to hydrocarbon saturation.
(Vejbæk et al. *this report*)

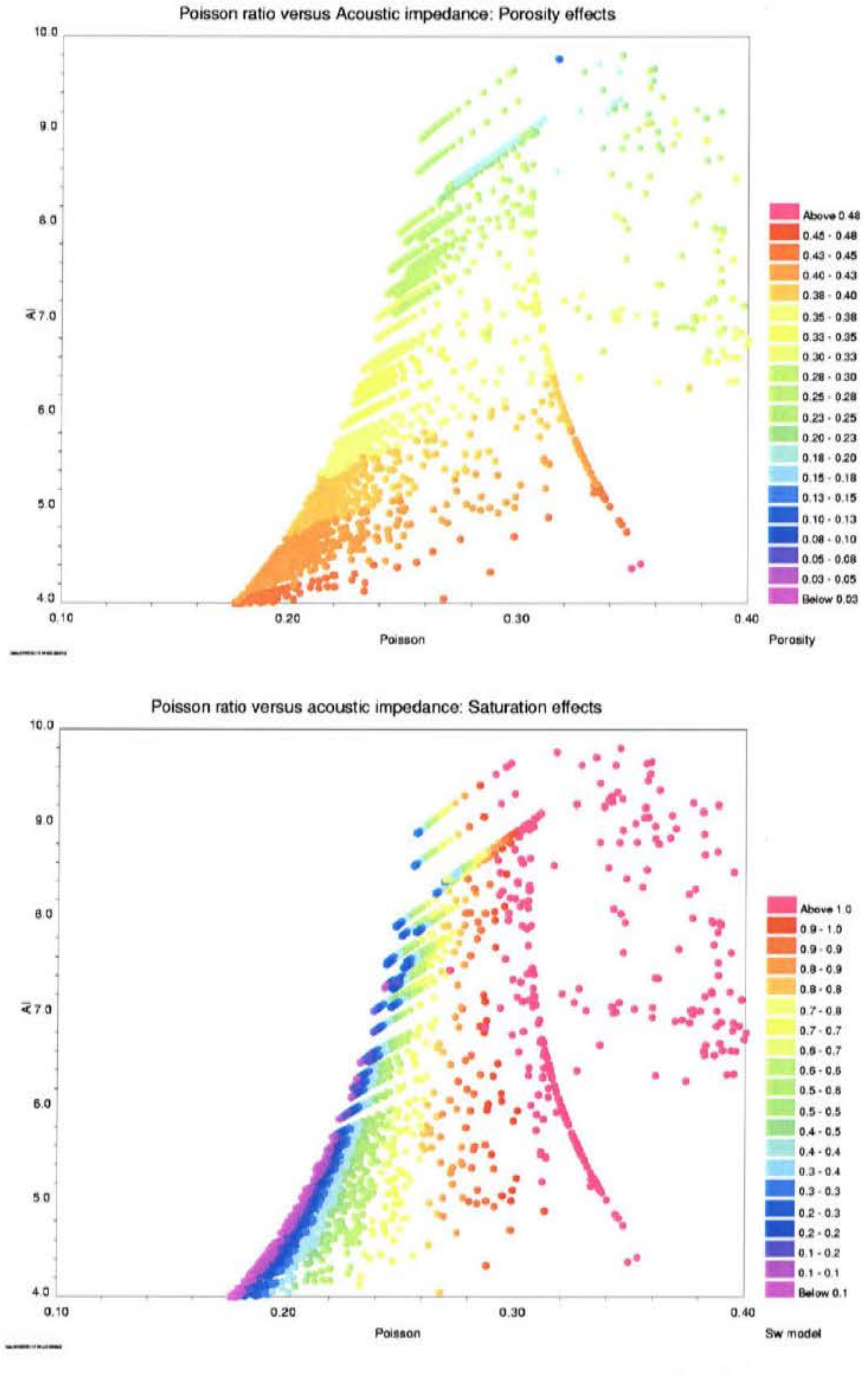

Figure 7. Poisson ratio versus acoustic impedance caused by modelled Sw changes (several free water level positions) in the Rigs-2 well. X- and Y-axis are identical in plot a and b, but colours show porosity and Sw. Points in the upper right are from outside the chalk. Note that acoustic impedance is more sensitive to porosity changes, than to saturation changes whereas the Poisson ratio is more susceptible to saturation changes.

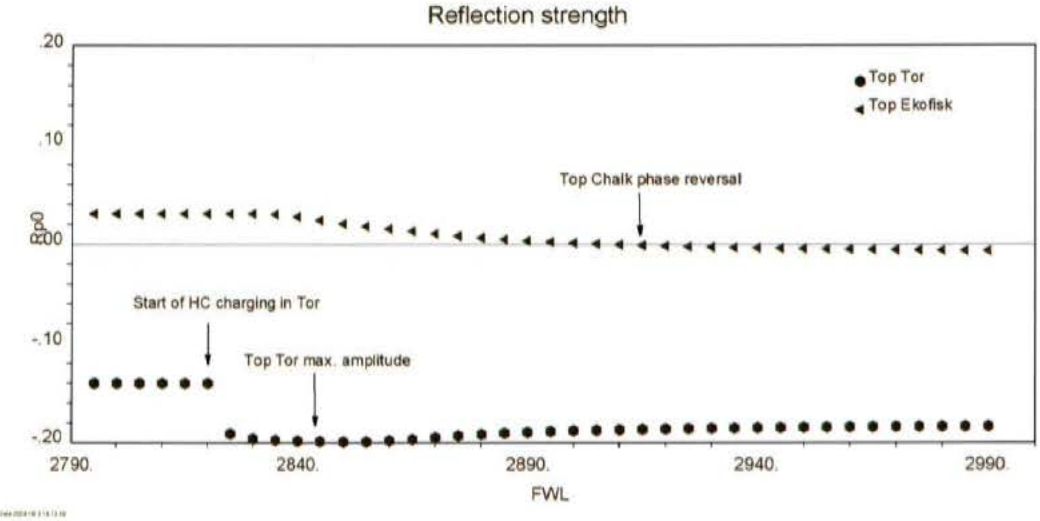

Figure 8. Reflection strength and sign of the Top Chalk and Top Tor reflectors as a function of free water level (or modelled saturation distribution). It is seen that the amplitude of this reflector increases abruptly (more negative) as oil enters the formation. As FWL deepens (saturations increases) it gains amplitude until low to moderate oil saturations. From moderate to high oil saturation it slowly decrease again. The Top Chalk reflector is also affected by increasing oil saturation. It is seen to loose amplitude with increasing oil saturation, and at saturations slightly higher than observed in the well, a reversal is predicted.

References

Bruun, A. *this report*: Seismic AVO inversion of 2D seismic data for use in the EFP 2001 Rock Physics Of Impure Chalk project using the ISIS Software Package. Ødegaard Report 02.24017.01. March 2003. 69 pp.

Fabricius, I. L., Mavko, G., Mogensen, C., & Japsen, P. 2002: Elastic moduli of chalk as a reflection of porosity, sorting, and irreducible water saturation. SEG 2002 Annual Meeting. 4 pp.

Fabricius, I. L, Høier, C., Japsen, P. & Korsbech, U. *this report*: Modeling elastic moduli of impure chalk. *To be submitted to Geophysics.*

Japsen, P., Høier, C., Rasmussen, K. B., Fabricius, I., Mavko, G., & Pedersen, J. M. 2002: Effect of fluid substitution on ultrasonic velocities in chalk plugs, South Arne field, North Sea. SEG 2002 Annual Meeting. 4 pp.

Japsen, P., A. Bruun, I. L. Fabricius, Rasmussen, R., Vejbæk, O.V., Pedersen, J. M., Mavko, G. & Mogensen, C. *this report*: Influence of porosity and pore fluid on acoustic properties of chalk: AVO-response from oil, South Arne field, North Sea. *To be submitted to Petroleum Geoscience.*

Mavko, G. & Japsen, P. *this report*: Fluid substitution in chalks: Effects of saturation scales. *To be submitted to Geophysical Prospecting.*

Vejbæk, O. V., Rasmussen, R., Japsen, P., Pedersen, J. M., Fabricius, I. L., & Marsden, M. *this report*: Modelling seismic response from North Sea Chalk reservoirs resulting from changes in burial depth and fluid saturation. *To be submitted to the Petroleum Geology Conference, London, October 2003.*

Walls, J. D., Dvorkin, J. & Smith, B. A. 1998. Modeling seismic velocity in Ekofisk Chalk. *SEG 68th annual conference*. 1016-1019.

Papers and reports enclosed

Papers

Fabricius, I. L, Høier, C., Japsen, P. & Korsbech, U. *this report*: Modeling elastic moduli of impure chalk. *To be submitted to Geophysics.*

Japsen, P., A. Bruun, I. L. Fabricius, Rasmussen, R., Vejbæk, O.V., Pedersen, J. M., Mavko, G. & Mogensen, C. *this report*: Influence of porosity and pore fluid on acoustic properties of chalk: AVO-response from oil, South Arne field, North Sea. *To be submitted to Petroleum Geoscience.*

Mavko, G. & Japsen, P. *this report*: Fluid substitution in chalks: Effects of saturation scales. *To be submitted to Geophysical Prospecting.*

Vejbæk, O. V., Rasmussen, R., Japsen, P., Pedersen, J. M., Fabricius, I. L., & Marsden, M. *this report*: Modelling seismic response from North Sea Chalk reservoirs resulting from changes in burial depth and fluid saturation. *To be submitted to the Petroleum Geology Conference, London, October 2003.*

Abstracts

Fabricius, I. L., Mavko, G., Mogensen, C., & Japsen, P. 2002: Elastic moduli of chalk as a reflection of porosity, sorting, and irreducible water saturation. SEG 2002 Annual Meeting. 4 pp.

Fabricius, I.L., Høier, C. & Korsbech, U. accepted: Modeling elastic moduli of Danian North Sea chalk from petrographic data. EAGE 65th conference, Stavanger June 2003, 4 pp.

Japsen, P., Høier, C., Rasmussen, K. B., Fabricius, I., Mavko, G., & Pedersen, J. M. 2002: Effect of fluid substitution on ultrasonic velocities in chalk plugs, South Arne field, North Sea. SEG 2002 Annual Meeting. 4 pp.

Vejbæk, O.V., Rasmussen, R., Japsen, P., Pedersen, J.M. & Marsden, G. accepted: Modelling seismic response from North Sea Chalk reservoirs resulting from changes in burial depth and fluid saturation. Petroleum Geology Conference, London, October 2003. 1 p.

Reports and technical notes

DTU E&R report - Fabricius, I. & Høier, C. 2002: Selection of samples. EFP-01 Rock Physics of Impure Chalk, revised January 2002, 12 pp.

DTU E&R report - Fabricius, I. L. in prep: Sample characterization report, EFP-01 Rock Physics of Impure Chalk.

GEUS rapport 2002/23 - Høier, C. 2002: Special core analysis for the rock physics project (EFP-2001), 26 pp.

Ødegaard Report 02.24017.01 - Bruun, A. 2003: Seismic AVO inversion of 2D seismic data for use in the EFP 2001 Rock Physics Of Impure Chalk project using the ISIS Software Package. March 2003, 69 pp.

Ødegaard Report 01.1031 - Mogensen, C. & Fabricius, I. 2002: EFP 2001: Quality control of well log data from the South Arne field. January 2002, 18 pp.

TN 2003/1 - Mavko, G. 2003: Some Comments on upscaling rock physics relations in North Sea chalks. EFP-01 Rock Physics of Impure Chalk – Technical Note, March 2003, 7 pp.

TN 2002/4 - Japsen, P. 2002: Extrapolation of the modified upper Hashin-Shtrikman model of Walls et al. (1998). EFP-01 Rock Physics of Impure Chalk – Technical Note, November 2002, 3 pp.

TN 2002/3 - Japsen, P. & Rasmussen, R. 2002: Compilation ultrasonic data for chalk plugs from the South Arne field, Tor And Ekofisk formations. EFP-01 Rock Physics of Impure Chalk – Technical Note, November 2002, 23 pp.

TN 2002/2 - Rasmussen, K. B., Japsen, P. Mavko, G. 2002: Discussion on the elastic properties of wet and dry chalk samples. EFP-01 Rock Physics of Impure Chalk – Technical Note, January 2002, 8 pp.

TN 2002/1 - Japsen, P. 2002: Analysis of acoustic well log data from the South Arne field. EFP-01 Rock Physics of Impure Chalk – Technical Note, December 2002, March 2003, 29 pp.

TN 2001/2 - Mavko, G. 2001: Some thoughts on upscaling rock physics relations. EFP-01 Rock Physics of Impure Chalk – Technical Note, October 2001, 1 p.

TN 2001/1 - Japsen, P. 2001: Well data summary, South Arne field. EFP-01 Rock Physics of Impure Chalk – Technical Note, May 2001, 25 pp.

Intended for submission to Geophysics

MODELING ELASTIC MODULI OF IMPURE CHALK

by Ida L. Fabricius*, Christian Høier**, Peter Japsen**, and Uffe Korsbech*

*DTU, **GEUS

ABSTRACT

In impure chalk the elastic moduli are not only controlled by porosity, but also by cementation resulting in relatively large moduli and by admixtures of clay and fine silica which results in relatively small moduli. Based on a concept of framebuilding contra suspended solids, we model P-wave and S-wave moduli of dry and wet plug samples by an effective medium model using chemical, mineralogical and textural input. We use a Modified Upper Hashin Shtrikman model assuming a critical porosity of 70%. The textural and mineralogical data may potentially be assessed from logging data on spectral gamma radiation, density, acoustic velocity and water saturations in a hydrocarbon zone.

The studied chalk was interpreted as follows: In chalk of reservoir quality, elastic moduli are predictable. The solid phase has roughly uniform composition, and as porosity decreases from 45% to 25%, IF-value increases from 0.5 to 0.6. At intermediate porosity (25% - 18%) IF-value varies between 0.5 and 0.9. Samples with high IF have pore-filling cementation, whereas samples with low IF-value have high amounts of suspended submicron-size quartz in the pore space. The samples with low porosity (13% - 16%) have relatively low IF-value (around 0.6) and are packed with pore-filling smectite.

INTRODUCTION

We have succeeded in building an effective medium model for impure chalk based on petrographic data. This is not a straightforward task, because the relationship between porosity and elastic moduli of carbonates depends on several factors. According to Marion and Jizba (1997) these factors are mineralogy, pore-shape and fluid type.

The problem of fluid type is in our case probably minor because Gassmanns relations apparently may be used even for ultrasonic data on chalk (Røgen at al. in rev.). The problem of pore shape is related to porosity type. In chalk the porosity is predominantly intergranular. In high-porosity chalk, pores are ill-defined, and may be best described as the irregular continuous space around the irregular but well defined particles. When chalk is subjected to cementation, pores become more and more regular and well defined, while particles fuse to a progressively stiffer frame. During cementation the chalk will thus approach the spherical pore model of an Upper Hashin Shtrikman Bound (Hashin and Shtrikman, 1963).

The question of mineralogy may in our case be simplified to a question of proportion between the dominant low-Mg calcite, quartz, kaolinite, and smectite.

This does not solve the problem, however. Even small amounts of clay may significantly reduce elastic moduli of sandstone (Han et al., 1986), so that the texture (the spatial organization of mineral particles) has significant influence. In a recent study, Avseth et al. (2000) have shown how texture and degree of cementation both control the elastic moduli of sandstone.

In the case of impure chalk we must then find out how the impurities are arranged, are they floating freely in the pore-space or are they part of the solid frame? As we will show below, they may be either. We also need a means of assessing degree of cementation, and thus stiffness of the chalk frame. In order to solve the problem we apply the concept of iso-frame (IF-value), (Fabricius, 2002) which defines to which extent the chalk has achieved a stiff structure with spherical pores as defined by a modified Upper Hashin Shtrikman model (Nur et al., 1998).

We study of the relationship between chalk composition and elastic moduli in 24 plug samples of Danian chalk from the South Arne field in the Danish North Sea (Mackertich and Goulding, 1999). We furthermore demonstrate the use of wire-line logging data to assess composition and degree of cementation.

METHODS

Velocity data

P- and S-wave moduli were measured on dry and water saturated 1½ inch plug samples (Table 1, Figure 1). Samples were dried at 110°C and left to equilibrate at room conditions to constant humidity before dry data were recorded; for smectite bearing samples this resulted in up to 34% water saturation. In order to obtain wet data, smectite poor samples were saturated with calcite-equilibrated tap water. Smectite rich samples were saturated with synthetic formation brine, but contains up to 8% atmospheric air, due to low permeability (Table 1). The ultrasonic measurements were done at a hydrostatic confining pressure of 75 bar in accordance with the procedure described in Røgen et al. (in rev.).

Other physical core data

For all plugs, He-porosity and gas permeability, along with grain density were measured by standard methods.

In order to correlate core data to gamma ray-logs, the concentrations of U, Th and K were measured on powdered samples by a NaI-crystal gamma spectrometer; and in order to interpret the water saturation data, the specific surface of the samples were measured by N_2 adsorption (BET).

Textural and mineralogical data

We estimated the mineralogical and textural composition of each sample. The mineralogical composition was derived from X-ray diffractograms of bulk sample and insoluble residue, carbonate content by titration, Mg, Al, Si, K, Ca, Fe, and Ba by Atomic Adsorption Spectrophotometric analysis of filtrate as well as remanence, P by spectrophotometry (Dr. Lange), and S by combustion in LECO-oven.

Mineralogical and textural data were derived from thin section petrography, backscatter electron microscopy, qualitative energy dispersive microprobe analysis, and petrographic image analysis of electron micrographs at two magnifications (Figure 2). Large grains (more than 2 microns in cross section), and large pores (more than 0.5 microns in cross section) were determined by filtering based on the method of Borre (1998). Specific perimeter of the calcite-pore interface was determined according to the method of Borre et al. (1997). Image analysis included assessment of the amount of silicates in suspension in the pores, as well as assessment of the amount of silicate grains in the solid frame.

Effective medium model

We constructed an effective medium model for the elastic moduli of the samples based on mineralogical and textural data. Large silicate grains, as well as large calcite grains and calcite cement were considered part of the solid frame, whereas small silicate-particles were considered to be suspended in the pore fluid. We modeled the porosity to be spherical holes with part of the solid phase suspended in the pore fluid (air and water), and calculated to which extent the small calcite particles may be modeled as being a part of the solid frame (IF-value for the fine-grained calcite), and to which extent they may be modeled as being in suspension in order to fit dry P-wave modulus data (model (1)). Together with the fraction of large particles this will define the total fraction of solid in the frame or iso-frame (IF) value of a sample (Fabricius, 2002). In order to obtain an IF-value based on petrographic data alone, we correlated the IF-value for the fine-grained calcite to the specific perimeter of the fine-grained calcite as measured by petrographic image analysis. We may now turn around and assess the IF value of the fine-grained calcite from image analysis data and calculate the IF for the total sample from mineralogical and petrographic data alone (model (2), Figure 3, 4).

In order to asses to which extend the IF value applies more generally, the IF-s of model (1) and (2) were used to calculate wet P-wave moduli, as well as S-wave moduli. These predictions fit reasonably well to the measured data (Figure 1).

Model (2) thus involves the following steps when porosity is known: 1) from mineralogical and petrographic analysis assessing amount of large calcite (microfossils and carbonate cement), large silicates (quartz, kaolinite, and feldspar clasts), suspended silicates (quartz, kaolinite, and smectite), as well as specific interface between fine-grained calcite and pores; 2) calculate IF for fine-grained calcite from specific interface, together with large grains this will also define IF for the total sample; 3) calculate elastic modulus for the suspension. For dry samples air, water and suspended solids were mixed according to a homogenous Reuss model. For wet samples, water and suspended solids were mixed according to Reuss model, whereas the air should be mixed with the fluid in accordance with a patchy Voigt model (Figure 5); 4) mixing this suspension with the frame building minerals according to an Upper Hashin Shtrikman bound (Hashin and Shtrikman, 1963) as generalized by Berryman, and by modifying the bound under assumption of a critical porosity (Nur et al., 1998, citations in Mavko et al., 1998). A critical porosity of 70% was in the present case chosen in accordance with ODP data (Fabricius, 2002).

Log-interpretation

The concept of IF-value allows us to model degree of cementation from logging data, alongside a more conventional interpretation of bulk composition (Figure 6).

Solid composition was estimated from spectral gamma-ray Th data and from water saturation data. The Th-log was chosen because it correlates well with core-sample Th-data. We did not use the K and U signal of the spectral gamma-ray log as well as the natural gamma ray log because these logs in the present case have little character and do not correlate with gamma-spectral core-data. The core-sample Th-data correlates roughly to total clay content and to non-carbonate fraction of the core samples.

Fluid saturations were determined by the Archie method by assuming default petrophysical constants for carbonate: a = 1, m = 2, and n = 1. Hydrocarbon density 0.633 g/cm^3, brine density: 1.054 g/cm^3, and brine resistivity of 0.0225 Ohmm and 0.0260 Ohmm respectively for Rigs-1 and Rigs-2 (J. Jensenius pers. comm.). In the presence of more detailed knowledge of the relationship between chalk composition and petrophysical parameters, these may be adjusted accordingly.

For the studied wells, the water saturation gives information on chalk texture because almost the entire logged chalk interval is in the zone of irreducible water saturation. In this case we may assume that in the water wet chalk, the water covers the particle surfaces and rests at particle contacts (Fabricius et al. 2002). The water saturation was recalculated to water volume pr. solid volume, and correlated to specific surface by BET (also recalculated to surface area pr. solid volume). BET correlates to the content of smectite in core samples.

We may thus estimate content of oil, water, smectite, total clay and insoluble residue. In accordance with the petrographic data we assume that smectite is totally in suspension, whereas the remaining clay and insoluble residue are 50% in suspension and 50% in the frame. We may now determine the IF value via adjusting the proportion of calcite in the frame to fit P-wave modulus calculated from density and sonic logging data.

In Rigs-1 water saturations are relatively high, and we may use the logging data directly. In Rigs-2 water saturations are low and invasion may severely affect the sonic signal (Gommesen et al. 2002). Therefore, the sonic velocity of the virgin zone was modeled from porosity and fluid saturation data together with a relationship between porosity and elastic moduli based on core data and in accordance with the relationship for logging data of Walls et al. (1998).

RESULTS

Core data

Elastic moduli calculated from ultrasonic velocities in the chalk core samples may now be given a textural interpretation (Figure 1, 4, Table 1).

In the porosity interval from 45% to 25% elastic moduli show a steady increase. The solid phase does not vary much in composition, but the IF-value increases gradually from around 0.5 to around 0.6. The frame building part of the solid contains a low to moderate amount of large grains of silicates and partially cemented calcitic microfossils (Figure 2a); the suspended part of the solid includes apparently authigenic submicron-size quartz, smectite-illite, and kaolinite.

In the porosity interval from 25% to 18% elastic moduli are more variable but tend to be high. IF value varies between 0.5 and 0.9 with an average around 0.7. Samples with high elastic moduli (and high IF) are characterized by a microfossil-rich texture (Figure 2b) and pore-filling cementation (Figure 2c). Samples with low elastic moduli (and low IF) in this porosity interval are characterized by high amounts of suspended apparently authigenic submicron-size quartz in the pore space (Figure 2f).

For low porosity (13% - 16%), elastic moduli tend to be lower than would be expected by extrapolating the trend from high-porosity chalk; IF is around 0.6. These samples all contain pore-filling, possibly allochtoneous smectite (Figure 2d), accompanied by large kaolinite clasts (Figure 2e). Smectite rich samples have high specific surface as measured by BET.

Logging data

We may now apply the IF model to log interpretation of the chalk interval of Rigs-1 and Rigs-2 (Figure 6).

In both wells the porosity varies considerably, but in general porosity is higher in Rigs-2 than in Rigs 1. The lower porosities in Rigs 1 are accompanied by higher proportions of calcite in the solid frame. The proportion of calcite in the solid frame may be interpreted as degree of cementation, so that Rigs 1 in general appear more cemented than Rigs 2. In clay rich intervals the porosity may be low without the proportion of calcite in frame (i.e. degree of cementation) is correspondingly high.

DISCUSSION AND CONCLUSIONS

We found that elastic P-wave and S-wave moduli calculated from ultrasonic core samples of impure chalk can be modeled from the mineralogical and textural composition of the solid phase as well as the pore fluid composition. The model is the same for S- and P-waves for dry as well as wet samples (Figure 1).

In accordance with petrographic data, a part of the solid is modeled as suspended in the pore fluids. This suspension is then modeled as the soft component in a stiff frame composed of the remaining solid according to a Modified Upper Hashin Shtrikman bound under assumption of a critical porosity of 70%.

Core data

In order to do this, we applied the concept of IF-value which describes to which extent the solid of the sample may be regarded as a frame with spherical pores. In line with this concept, Anselmetti and Eberli (1997) found that carbonate samples with vuggy porosity tend to be stiffer than carbonate samples with other types of porosity. We see IF as a measure of degree of cementation and in accordance with this concept, samples with high IF indeed were seen to be heavily cemented and to have high elastic moduli.

In the studied samples, part of the calcite is modeled as being in suspension although it physically is attached to other particles. A link between the actual pore-shape and the IF model is the specific perimeter of the calcite-pore interface as measured by petrographic image analysis of electron micrographs.

The impurities of the chalk include quartz, kaolinte, and smectite. Quartz and kaolinite occur partly as solid clasts which we consider as part of the frame, partly as suspended pore-filling sub-micron-size particles. The ultra fine-grained quartz is apparently authigenic and may be sourced from dissolved opaline fossils. That these fossils have existed is indicated by the presence of molds. Smectite also occur in two textural ways. High-porosity samples may contain apparently authigenic smectite-illite, whereas low-porosity samples may be packed with apparently allochtoneous smectite. These low porosity smectite rich samples have relatively low IF and relatively low elastic moduli.

Logging data

Sonic logging data have been widely used as an indicator of porosity type, e.g. the velocity–deviation log of Anselmett and Eberli (1999). In the studied chalk the porosity is mainly of intergranular type, although intrafossil porosity and moldic porosity occur frequently but in minor amounts.

Via the IF concept we suggest that the sonic log may be used as an indicator of cementation. This requires that we first assess the mineralogical composition and fluid saturations of the chalk, then estimate to which extent the non-carbonates are in the solid frame and to which extend in suspension (in the present case this was done from studies of core samples), and finally that we by iteration find which IF's fit the elastic modulus-log.

The mineralogical composition was in this case assessed from the spectral gamma Th-log and from the water saturation. The Th log was used for a rough estimate of total clay as well as for total non-carbonate fraction. In the present case the integral gamma and spectral U and K-logs proved of little use, but this may depend logging equipment and on choice of drilling mud. The use of water-saturation log as a smectite indicator is only valid because we could assume that the water saturation is irreducible. In the absence of these specific smectite data, we might have overcome the problem by adjusting the proportion of the total clay that we assume are in suspension.

ACKNOWLEDGEMENTS

Financial support for this study is acknowledged from a Danish Energy Research Program EFP-2001 grant, as well as from Amerada Hess A/S and DONG A/S. For technical support Sinh Hy Nguyen and Hector Diaz, DTU are acknowledged.

REFERENCES

Anselmetti, F. S., and Eberli, G. P., 1997, Sonic velocity in carbonate sediments and rocks, *in* Palaz, I., and Marfurt, K. J., Eds., Carbonate Seismology: Society of Exploration Geophysicists, 53-74.

Anselmetti, F. S., and Eberli, G. P., 1999, The velocity-deviation log: a tool to predict pore type and permeability trends in carbonate drill holes from sonic and porosity or density logs: AAPG Bulletin, **83**, No. 3, 450-466.

Avseth, P., Dvorkin, J., Mavko, G., and Rykkje, J., 2000, Rock physics diagnostic of North Sea sands: link between microstructure and seismic properties: Geophysical Research Letters, **27**, No. 17, 2761-2764.

Borre, M., 1998, Ultrasonic velocity of North Sea Chalk – predicting saturated data from dry, *in* Middleton, M. F., Ed., Nordic Petroleum Series IV, Research in Petroleum Technology: Nordisk Energi Forskningsprogram, 71-98.

Borre, M., Lind, I., and Mortensen, J., 1997, Specific surface as a measure of Burial Diagenesis of Chalk: Zbl. Geol. Paläont. Teil 1, **1995**, 1071-1078.

Fabricius, I. L., 2002, Porosity Loss in Chalk Facies Sediments by Physical Compaction or by Cementation – Consequences for P-wave Modulus: AAPG Ann. Mtg, 2002, Extended Abstracts CD-ROM.

Fabricius, I. L., Mavko, G., Mogensen, C., and Japsen, P., 2002, Elastic Moduli of Chalk as a reflection of porosity, sorting and irreducible water saturation: Soc. Expl. Geophys. Int. Exp. and 72th Ann. Mtg., Paper 445, CD-ROM.

Gommesen, L., Mavko, G., Mukerji, T., Fabricius, I. L. 2002, Fluid Substitution for North Sea Chalk Logging Data: Soc. Expl. Geophys. Int. Exp. and 72th Ann. Mtg., Paper 410, CD-ROM.

Han, D.-h., Nur, A., and Morgan, D., 1986, Effects of porosity and clay content on wave velocities in sandstone: Geophysics, **51**, No. 11, 2093-2107.

Hashin, Z., and Shtrikman, S., 1963, A variational approach to the elastic behavior of multiphase materials: J. Mech. Phys. Solids, **11**, No. 2, 127-140.

Mackertich, D. S., and Goulding, D. R. G., 1999, Exploration and appraisal of the South Arne field, Danish North Sea, *in* Fleet, A. J., and Boldy, S. A. R., Eds., Petroleum Geology of Northwest Europe: Proc. 5th Conf. Geological Society, London, 959-974.

Marion, D., and Jizba, D., 1997, Acoustic properties of carbonate rocks: use in quantitative interpretation of sonic and seismic measurements, *in* Palaz, I., and Marfurt, K. J., Eds., Carbonate Seismology: Society of Exploration Geophysicists, 75-93.

Mavko, G., Mukerji, T., and Dvorkin, J., 1998, The Rock Physics Handbook: Cambridge University Press.

Nur, A., Mavko, G., Dvorkin, J., and Galmudi, D., 1998, Critical porosity: A Key to relating Physical Properties to Porosity in Rocks: The Leading Edge **17**, No. 3, 357-362.

Røgen, B., Fabricius, I. L., Japsen, P., Høier, C., Mavko, G., and Pedersen, J. M., in rev, Ultrasonic velocities of North Sea chalk samples – influence of porosity, fluid content and texture.

Walls, J. D., Dvorkin, J., and Smith, B. A., 1998, Modeling seismic velocity in Ekofisk chalk.: Proc. Soc. Expl. Geophys. Ann. Conf. and Exh., 1016-1019.

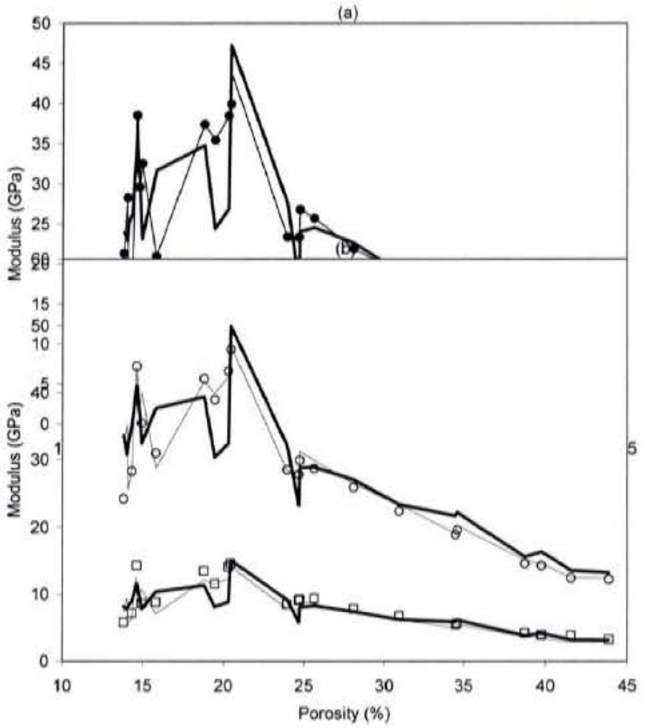

FIG. 1. Elastic modulus data and elastic models. Circles denote P-wave modulus data, squares denote S-wave modulus data. Thin lines: model (1) based on dry P-wave and density data. Thick lines: model (2) based on image analysis data calibrated to model (1). (a) Dry samples (b) Water saturated samples. Model (1) fits the wet P-wave modulus data, whereas especially the dry S-wave moduli tend to be higher than predicted. Model (2) fits less well but has the advantage of being based on petrographic data.

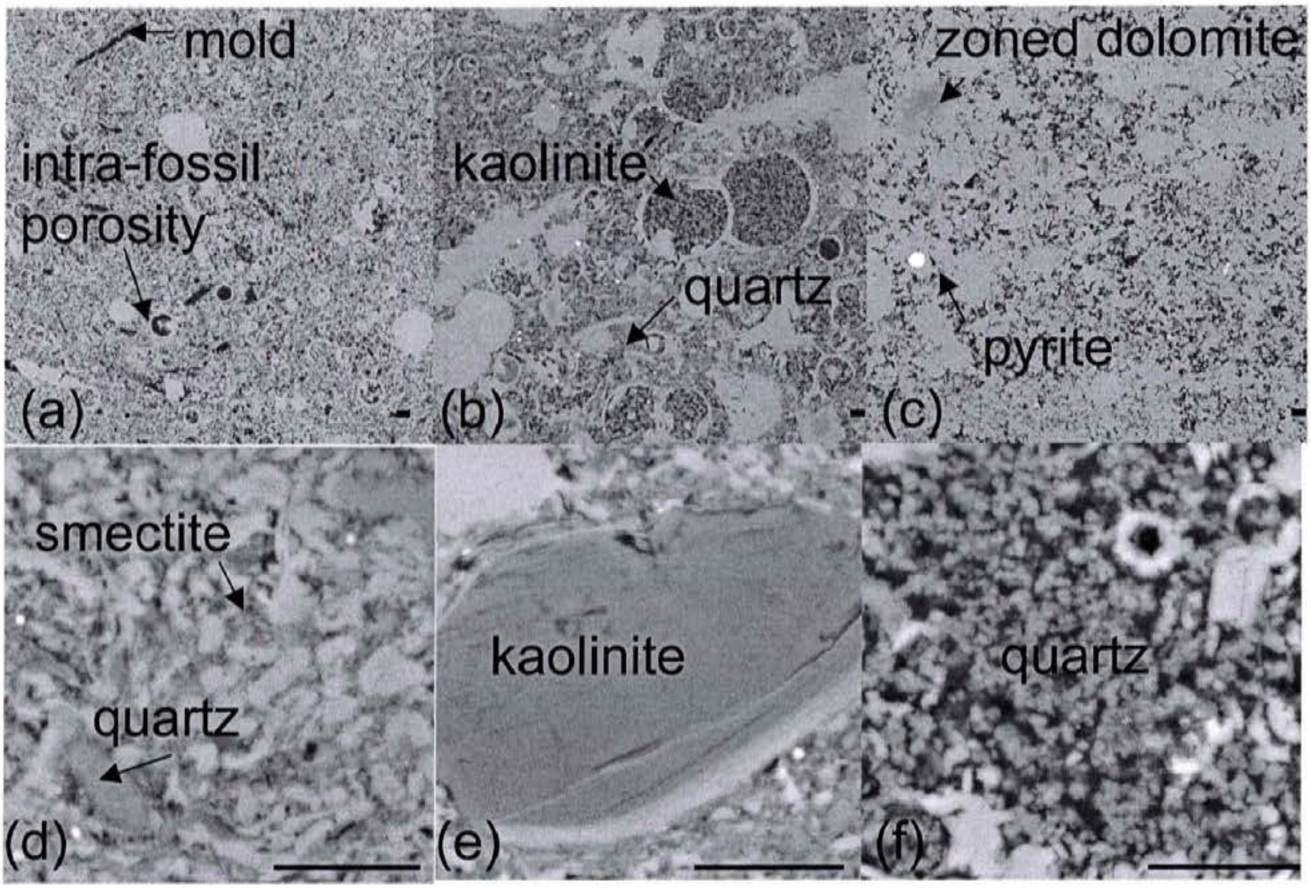

FIG. 2. Backscatter electron micrographs of epoxy-impregnated and polished samples. Black indicates pore-space, various shades of grey reflect densities of the minerals. The black bars measure 10 microns. (a) Rigs 1, 9250.39 ft MD, chalk mudstone with 30.9% porosity. Of the bulk volume 4.8% is large calcite, 4.4% is large intra-fossil porosity and molds. Model (1) and (2) both indicate an IF value of 0.6. (b) Rigs 2, 2824.00 m MD, chalk wackestone with 24.7% porosity. Of the bulk volume 16.2% is large calcite grains and cement, 4.4% is large intra-fossil porosity, 26.2% is disperse sub-micron size pore-filling quartz, and 1.1% is disperse sub-micron size pore-filling kaolinite. Model (1) indicates an IF value of 0.6, model (2) an IF value of 0.5. (c) Rigs 1, 9287.32 ft MD, white chalk wackestone with 20.4% porosity. Of the bulk volume 53.9% is large calcite grains and cement, 9.3% is large intergranular pore space. The calcite cement covers zoned dolomite/ankerite crystals. Model (1) and (2) both indicate an IF value of 0.9. (d) Rigs 1, 9111 ft MD, chalk mudstone with 13.8% porosity. Of the bulk volume 6.1% is clasts of quartz and albite, 5.6% is pore filling smectite. Model (1) indicates an IF value of 0.5, model (2) an IF value of 0.6. (e) Rigs 1, 9114 ft MD. Kaolinite clasts constitute 6.9% of the bulk volume in the chalk mudstone with 14.1% porosity. (f) Rigs 1, 9153.20 ft MD. Disperse sub-micron size pore-filling quartz constitute 9.2% of the bulk volume in the chalk mudstone with 19.5% porosity.

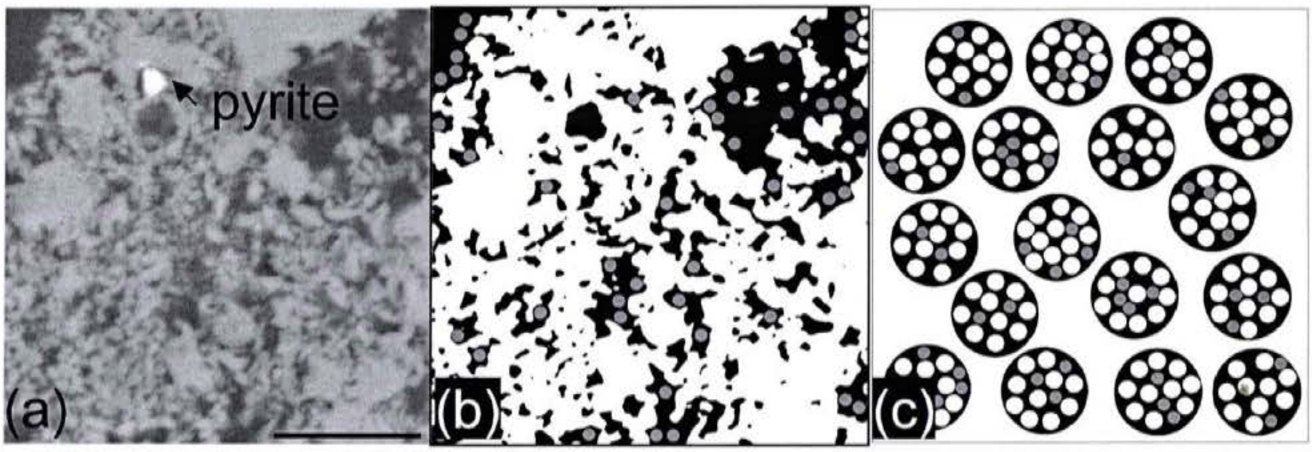

FIG. 3. Iso-frame (IF) model for chalk. (a) Backscatter electron micrograph of the epoxy-impregnated and polished sample Rigs 1, 9210.0 ft MD, chalk mudstone with 28.1% porosity. The black bar measures 10 microns. Of the bulk volume 5.9% is fine grained silicates. (b) By petrographic image analysis the fine-grained calcite (including a pyrite crystal) is marked as white and the pore space as black. The fine grained silicates are symbolized by grey circles. The specific perimeter of the white phase is calculated to be 2.9 micron^{-1}. From correlation with elastic data, this specific perimeter corresponds to an IF value of 0.65 for the fine-grained calcite. When taking large pores and grains (not visible at this magnification) and fine-grained silicates into account, we obtain an IF value of 0.6 for the sample. (c) Model: of the solid phase 70% is forming a frame with spherical pores. The remaining solids are suspended in the fluid within the pores.

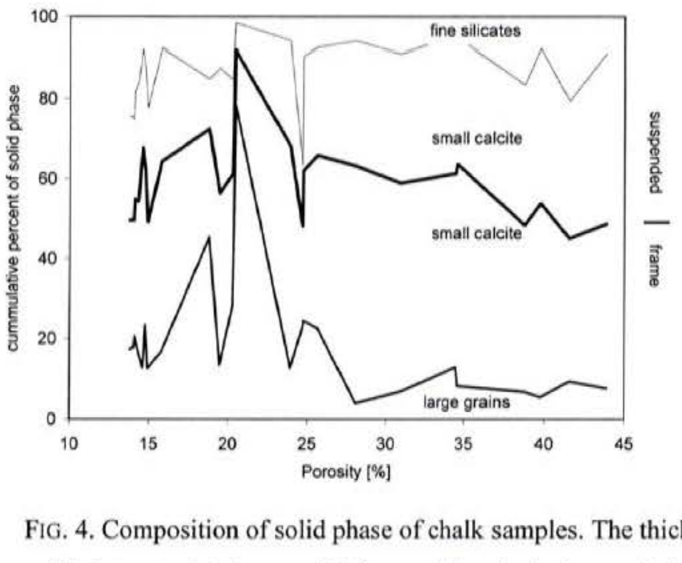

FIG. 4. Composition of solid phase of chalk samples. The thick line denotes the IF value of each sample. The part of the solid phase modeled as a solid frame with spherical pores is below the thick line. The part of the solid modeled as being in suspension is above the thick line. Large grains include calcitic microfossils, as well as clasts of quartz, feldspar and kaolinite. Fine silicates include (apparently athigenic) smectite, kaolinite and quartz.

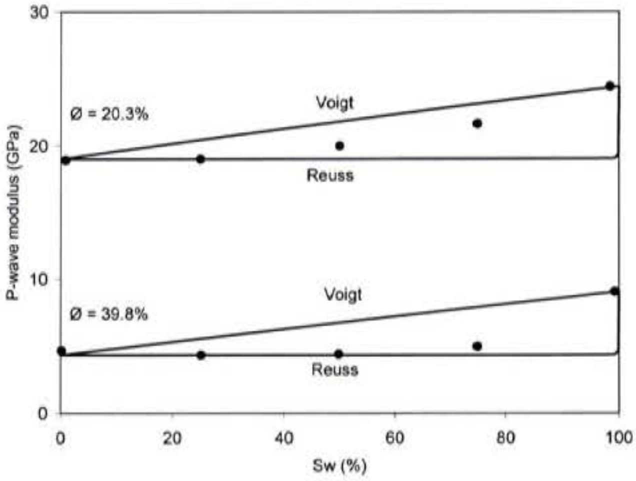

FIG. 5. P-wave modulus of partially water saturated samples compared to modeled moduli. The two models assume water and air to be mixed patchily according to an iso-strain (Voigt) respectively a homogeneous iso-stress (Reuss) model. The modeled data were calculated using Gassmanns equations. The low Sw end point was chosen as a "nearly dry rock" based on extrapolation of data from Sw = 25%. The low Sw end point matches the data for the dry 20.3% porosity sample, whereas the 39.8% porosity sample may stiffen due to superdry-effect at Sw near 0.

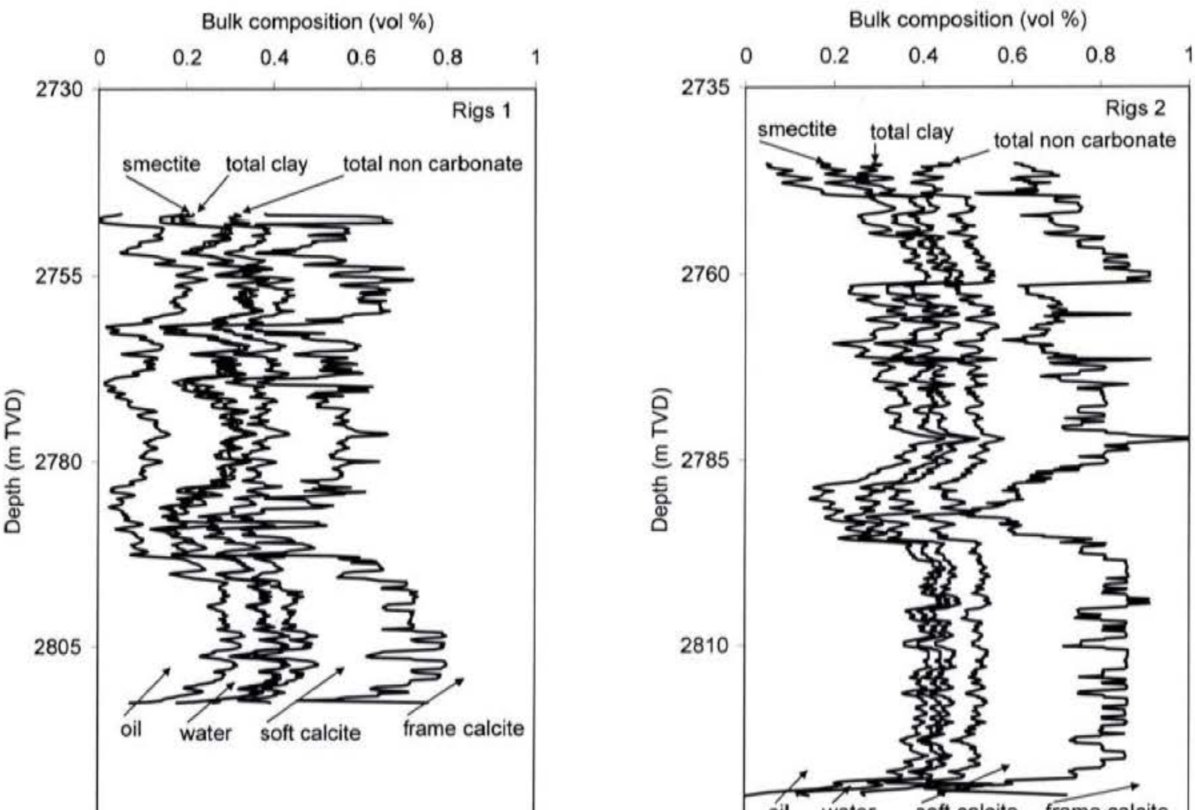

FIG. 6. Bulk composition of chalk interval as interpreted from logging data. The well Rigs 1 has higher water content and smectite content than Rigs 2, where the smectite log disappears in the curve separating water and total clay. Rigs 1 apparently is more cemented as indicated by a higher proportion of the calcite being part of the solid frame.

						Dry samples			Wet samples			Composition of solid phase							(1)	(2)
Core depth	Ø %	k mD	BET m^2/g	ρ_{grain} g/cm^3	ρ_{fluid} g/ml	S_w %	v_P m/s	v_S m/s	S_w %	v_P m/s	v_S m/s	Non-carb. %	Total clay %	Smec-tite %	Susp. Quartz %	Susp. Kaol. %	Silica-te gr. %	Large Calcite %	IF	IF
Rigs 1 ft																				
9111	13.8	0.7	12.2	2.71	1.073	6.8	3020	2192	92.2	3132	1536	35.3	16.0	7.2	8.7	6.9	6.2	10.2	0.5	0.5
9114	14.1	0.5	11.6	2.71	0.998	30.4	2659	1868				34.7	15.9	6.7	11.1	0.0	11.0	8.2	0.4	0.5
9114-h	14.0	3.1	12.9	2.71	0.998	34.1	3452	2155				41.4	21.2	8.5	9.2	6.4	9.3	7.2	0.6	0.5
9116-h	14.9	15.0	10.2	2.70	1.073	11.8	3746	2375	102.6	3791	1871	32.6	13.5	5.8	9.6	5.8	5.2	6.8	0.6	0.5
9117	14.3	0.4	10.2	2.71	1.073	12.3		2004	103.0	3378	1702	30.8	14.4	6.0	4.5	5.5	9.3	6.4	0.4	0.5
9117-h	14.8	0.7	10.9	2.73	1.073	11.8	3556	2256				31.7	14.6	6.0	5.6	0.4	12.6	8.8	0.6	0.6
9138	15.8	0.1	7.5	2.70	0.998	7.7	3029	2137	102.4	3565	1904	20.0	9.3	3.3*	3.2	1.4	7.0	9.1	0.5	0.6
9153-h	19.5	0.4	5.8	2.71	0.998	3.6	4024	2486	99.0	4051	2210	23.2	4.1	1.4*	10.6	0.0	6.0	6.9	0.7	0.6
9154	24.7	0.2	3.2	2.71	0.998	1.9	3620	2250	97.9	3619	2015	19.8	2.3	0.8*	8.5	0.0	6.4	17.7	0.7	0.6
9176	34.5	0.8	2.5	2.71	0.998	0.5	2893	1844	98.8	2993	1615	8.8	1.5	0.4*	3.3	0.5	2.5	10.3	0.5	0.6
9193	14.6	0.0	3.3	2.71	0.998	5.0	4070	2590	95.2	4230	2412	21.2	3.7	0.7*	7.1	0.0	9.0	3.0	0.7	0.7
9210	28.1	0.3	4.0	2.71	0.998	1.7	3350	2124	98.3	3413	1879	9.2	3.0	0.6*	3.7	1.6	1.0	2.9	0.6	0.6
9216	23.9	0.2	4.5	2.72	0.998	2.0	3361	2176	97.4	3521	1925	17.5	3.2	0.8*	5.1	0.0	8.2	3.9	0.6	0.7
9230	34.6	0.6	2.7	2.69	0.998	0.3	3035	1890	99.6	3051	1640	12.3	1.6	0.4*	4.0	0.7	4.8	3.2	0.6	0.6
9250	30.9	0.6	2.6	2.70	0.998	0.6	3187	1972	97.8	3213	1765	11.0	1.6	0.6*	7.5	0.6	0.0	6.9	0.6	0.6
9274	18.8	0.1	2.5	2.71	0.998	2.0	4117	2529	99.8	4197	2378	26.2	4.2	1.6*	13.0	0.0	7.2	37.8	0.8	0.7
9287	20.4	0.3	2.5	2.72	0.998	0.9	4296	2597	97.7	4437	2486	14.1	4.7	1.7*	0.0	0.0	10.1	67.7	0.9	0.9
Rigs 2 m																				
2800	41.6	1.9	3.2	2.70	0.998	0.5	2304	1622	98.8	2506	1394	23.6	5.1	0.6*	15.3	3.6	0.0	9.3	0.4	0.5
2802	25.6	0.1	4.0	2.70	0.998	0.9	3576	2264	93.4	3574	2045	23.9	5.6	0.7*	6.5	0.0	12.0	9.7	0.7	0.7
2806	38.7	1.3	3.0	2.69	0.998	0.4	2578	1702	99.4	2680	1447	19.7	2.7	0.4*	13.8	1.6	0.2	6.6	0.5	0.5
2814	39.8	1.4	2.9	2.70	0.998	0.2	2546	1645	99.3	2662	1396	10.8	2.5	0.3*	5.9	1.2	1.1	4.3	0.5	0.5
2818	43.9	3.2	2.7	2.71	0.998	0.2	2386	1541	98.4	2506	1293	11.7	2.3	0.3*	7.1	1.2	0.5	7.2	0.4	0.5
2824	24.7	0.2	3.7	2.67	0.998	0.3	3408	2232	99.8	3509	2010	42.1	4.1	0.7*	30.9	1.3	1.0	21.5	0.6	0.5
2826	20.3	0.2	1.7	2.70	0.998	0.8	4230	2611	98.5	4291	2452	21.7	1.1	0.2*	14.5	0.0	3.3	24.8	0.8	0.6

TABLE. 1. Core plug data. –h indicates a horizontal sample, Ø is He-porosity, k is gas permeability, BET specific surface by N_2 adsorption, ρ is density, S_w is water saturation, v_P and v_S are *P*- and *S*-wave ultrasonic (700 kHz) velocities measured at a hydrostatic confining stress of 75 bar. Experimental errors for v_P is c. ± 25 m/s for v_S c. ±15 m/s. Composition of solid phase is interpreted from X-ray diffraction, chemical analysis, image analysis of backscatter electron micrographs and qualitative energy-dispersive microprobe analysis. IF's are from model (1) and (2). *smectite-illite.

Intended for submission to Petroleum Geoscience

Influence of porosity and pore fluid on acoustic properties of chalk: AVO-response from oil, South Arne field, North Sea

Peter Japsen[1], Anders Bruun[2], Ida L. Fabricius[3], Rasmus Rasmussen[1], Ole V. Vejbæk[1], Jacob Mørch Pedersen[2], Gary Mavko [4] & Christian Mogensen[2]

[1] Geological Survey of Denmark and Greenland (GEUS), [2] Ødegaard A/S, [3] Technical University of Denmark (DTU), [4] Stanford University

Abstract

We have found AVO-inversion to provide direct evidence for presence of light oil in the high-porous chalk of the South Arne field. We estimated the elastic properties of chalk at three different scales on the South Arne field, North Sea, by analysing ultrasonic core data, downhole log-readings and results of AVO-inversion based on near- and far-offset stack seismic data (Amplitude Versus Offset). We find that the velocity-porosity relation of the plug data are in agreement with a modified upper Hashin-Shtrikman model established for chalk from the Ekofisk field and due to higher porosities in the South Arne field we extend the range of the model to 45% porosity. In pure chalk intervals, this model furthermore, matches log-estimated values of the shear modulus which are unaffected by fluid content according to Gassmann's relations. The model thus predicts the variations of the bulk modulus as a function of water saturation. We find that the sonic logging data represent chalk where the oil has been partly flushed by invasion of mud filtrate. We use the difference between logging data- and model-estimates of the shear modulus to correct the model by scaling it according to clay content as estimated by the water saturation that is controlled by silicate content and particle sorting in the zone of irreducible water saturation in water-wet chalk. Forward modeling of the acoustic properties of the virgin zone thus results in a characteristic depth-wise pattern of the Poisson ratio with low values in the high-porosity intervals. This pattern agrees with the inverted seismic data, whereas these features are not captured if the acoustic properties of the virgin zone are derived from the sonic logs and

estimates of residual oil in the flushed zone because of almost complete invasion where porosity is high.

Introduction

Understanding the influence of pore fluids on acoustic properties of sediments is a central issue for evaluating seismic data; e.g. in amplitude versus offset techniques which depend on the discrimination of fluid content from variations in P- and S-velocities (e.g. Castagna & Backus 1993). Much research has been focused on describing such effects in sandstone, whereas few studies have been published on the rock physics of chalk (e.g. Walls *et al.* 1998; Japsen *et al.* 2000; 2002; Fabricius *et al.* 2002; Gommesen *et al.* 2002; Røgen 2002; Gommesen 2003). In the North Sea, chalk is an important reservoir rock and more information could be extracted from seismic data if fundamental physical properties of chalk were better understood. A phase-reversal due to the presence of gas in chalk was documented by Megson (1992), but so far, presence of oil in chalk has not been demonstrated to have effect on surface seismic data. The need for a better link between chalk reservoir parameters and geophysical observables has only increased since the discovery of the Halfdan field proved major reserves outside four-way dip closures (Jacobsen *et al.* 1999, Vejbæk & Kristensen 2000).

We have investigated the acoustic properties of chalk of the Danian Ekofisk Formation and the Maastrichtian Tor Formation in the Danish South Arne field where porosities up to 45% are found in the Tor reservoir at c. 3 km depth due to overpressure caused by compaction disequilibrium (Mackertich & Goulding 1999; Scholle 1978; Japsen 1998). We find that it is possible to describe the velocity-porosity relation for relatively pure chalk in terms of a modified upper Hashin-Shtrikman bound and Gassmann's (1951) relations as suggested by Walls et al. (1998). The model predicts a pronounced change in the relation between P- and S-velocities (and thus a drop in the Poisson ratio) for oil-bearing chalk with porosities above c. 35%. This span in Poisson ratio makes it probable that the light oil in the high-porous chalk of the South Arne field may be detected through AVO-inversion of surface seismic data. But the link between the surface seismic data and the reservoir is hampered by invasion of mud filtrate into the zone where the sonic log is registered (Gommesen et al. 2002). We find that the acoustic properties of the reservoir agree with those estimated from AVO-inversion if we compute a synthetic sonic log from the modified upper Hashin-Shtrikman model with porosity and water saturation of the virgin zone as input.

Data

Measurements on core plugs

Ultrasonic measurements (700 kHz) were carried out on 34 chalk samples from the South Arne field under both dry and saturated conditions; wells SA-1, Rigs-1 and Rigs-2 (Fig. 1; see also Røgen *et al.* 2002; Japsen *et al.* 2002). In order to prevent over-dry conditions, the samples were kept at room-moisture for two months after being dried at 110°C. The water saturation in the saturated plugs was generally between 97% and 103% (related to minor weight errors), but low permeability prevented total saturation in three samples (Sw=92%–95%). Three samples regained high water content after drying, as reflected in high smectite content (Sw=7%–12%; smectite content 3%–7%).

P- and S-wave velocities were determined from measured sample lengths and readings of travel times. The plugs were measured at 75 bar hydrostatic confining pressure corresponding to the magnitude of the effective stress at reservoir conditions. Density, ρ [g/cm^3], grain density, ρ_{gr}, porosity, ϕ [fractions] and permeability, k [Darcy] were also determined. Mineralogical composition of the samples was modelled on the basis of X-ray diffraction data, chemical analysis of insoluble residue and of filtrate after treatment with hydrochloric acid, backscatter electron microscopy of epoxy-impregnated polished samples, as well as qualitative energy dispersive microprobe analysis.

Very good correlation is observed between P- and S-velocity and porosity for saturated samples. Three samples with high clay content have outlying values relative to these trends.

Log data

Well log data from six wells in the South Arne field were quality controlled and for the chalk sections we calculated porosity and shale volume, as well as water saturation and density of the virgin zone. Four wells have readings of compressional and shear velocities, Vp and Vs, and out of these wells data for the near-vertical Rigs-2 well was selected for further analysis because we have good core data for this well and because it is situated outside the "gas cloud" on seismic sections.

Porosity, ϕ, was estimated from log-readings of the bulk density, ρ_{bulk}, assuming full invasion of the mud filtrate and thus we converted density to porosity based on mud filtrate densities rather than of mixtures of brine and hydrocarbons (Fig. 2). These estimates of porosity were found to match porosity measured on core samples from the Rigs-1 and -2 wells.

Water saturation, Sw, was estimated for the virgin zone from a range of pore water resistivity values based on the LLS and LLD logs. A shallow resistivity log was however not available and the saturation, Sxo, in the zone invaded by mud filtrate could thus not be estimated directly.

Shale volume was calculated from the gamma log based on a calibration to the measured gamma ray level in the sealing shale sequence relative to the purest chalk interval in each well. However, the relation between the gamma response and the clay content in the chalk may be rather arbitrary and the presence of e.g. smectite and silica are not recorded by the gamma log.

Bulk density, ρ, of chalk for a given water saturation was calculated as a function porosity:

$$\rho = \rho_{oil}(1-S_w)\phi + \rho_{brine} \cdot S_w \cdot \phi + \rho_{matrix}(1-\phi)$$

for the density of oil, brine and chalk matrix in the reservoir of the South Arne field (Table 1).

Seismic data

Near- and far-offset data were available from a 3D survey covering the South Arne field. The two sub-cubes are generated as partial stacks offset defined.

Theory

Fluid substitution using Gassmann's equations

The bulk and the shear moduli, K and G [GPa], of a rock are related to Vp and Vs [km/s] and density [g/cm^3] by the following expressions:

$$K = \rho(V_p^{\,2} - 4/3 \cdot V_s^{\,2}),\ G = \rho V_s^{\,2}.$$

We can transform the moduli of the rock for the initial fluid saturation (fluid 1) to moduli of the rock saturated with a new fluid (fluid 2) using Gassmann's (1951) relations (see Mavko *et al.* 1998):

$$K_{\mathrm{sat}2} = K_{\mathrm{m}} \cdot A/(1+A), \quad G_{\mathrm{sat}1} = G_{\mathrm{sat}2} \quad \text{where}$$
$$A = \frac{K_{\mathrm{sat}1}}{(K_{\mathrm{m}} - K_{\mathrm{sat}1})} - \frac{K_{\mathrm{fl}1}}{\phi(K_{\mathrm{m}} - K_{\mathrm{fl}1})} + \frac{K_{\mathrm{fl}2}}{\phi(K_{\mathrm{m}} - K_{\mathrm{fl}2})} \tag{1}$$

K_{sat1}, K_{sat2} are the bulk modulus of rock with the original and new pore fluid; K_{m} is the bulk modulus of mineral material making up rock; K_{fl1}, K_{fl2} are the bulk modulus of the original and the new pore fluid; G_{sat1}, G_{sat2} are the shear modulus of rock with the original and the new pore fluid. In particular we see that the shear modulus is predicted to be unaffected by fluid content. Gassmann's equations are established for homogenous mineral modulus and statistical isotropy. The equations are valid at sufficiently low frequencies such that the pore pressures induced by the sonic wave are equilibrated throughout the pore space. Gommesen et al. (2002) found that Gassmann's theory may be applied to chalk at logging frequencies
and Mavko & Japsen (this report) concluded that Gassmann's relations can be used to understand ultrasonic velocity-variations in chalk samples (cf. Japsen *et al.* 2002). We therefore apply Gassmann's relations to calculate the effects on the acoustic properties of chalk estimated from logging data when one pore fluid is substituted by another.

Properties of mixed fluids and materials

We can calculate the exact bulk modulus, K_{fl}, of mixtures of fluids, $K_{\mathrm{fl}\,1}$, $K_{\mathrm{fl}\,2}$ (brine/hydrocarbons or brine/air) as a Reuss average if the fluids form a homogenous mixture (Fig. 3):

$$1/K_{fl} = S_{fl1}/K_{fl1} + (1-S_{fl1})/K_{fl2} \tag{2}$$

where $S_{\mathrm{fl}\,1}$ is the relative saturation of fluid 1 (e.g. brine, S_{w}). Even small amounts of the light component (e.g. hydrocarbon or air) reduce the bulk modulus of the mixed fluid significantly because the average modulus is calculated from the inverse values of the individual moduli.

The properties of mixtures can be estimated as a Voigt average as an approximation to the patchy saturation "upper bound" where the fluids are not evenly distributed:

$$K_{fl} = S_{fl1} \cdot K_{fl1} + (1-S_{fl1}) \cdot K_{fl2}. \tag{3}$$

Here the average modulus is more dependent on the denser constituents. We assume Reuss mixing to be the best approximation based on the conclusion of Mavko & Japsen (this report) that fine-scale mixing is dominant at logging frequencies in chalk.

Modified upper Hashin-Shtrikman (MUHS) model

Walls et al. (1998) found that a modified upper Hashin-Shtrikman model predicts the velocity-porosity behaviour of chalk estimated from well logs from the Ekofisk field (porosities from 10% to 40%). The model describes how the dry bulk and shear moduli, K and G increase as porosity is reduced from a maximum value, ϕ_{max}, to zero porosity. The upper and lower Hashin-Shtrikman bounds give the narrowest possible range on the modulus of a mixture of grains and pores without specifying anything about the geometries of the constituents (Hashin & Shtrikman 1963). The upper bound represents the stiffest possible pore shapes for porosity ranging from 0% to 100%, whereas the modified upper bound is defined for porosity up to a maximum value less than 100%. Here we refer the high-porosity end member as the maximum porosity rather than as the critical porosity which is defined as the porosity limit above which a sedimentary rock can only exist as a suspension (Nur *et al.* 1998). The low-porosity end-members, K_s and G_s, are the moduli of the solid at zero porosity found by extrapolation of the data trend at non-zero porosities. The modified upper Hashin-Shtrikman model, MUHS, is given by the dry-rock bulk and shear modulus, K^{MUHS} and G^{MUHS}:

$$
\begin{aligned}
K^{MUHS} &= \left[\frac{\phi/\phi_{\max}}{K_{\phi\max} + \frac{4}{3}G_s} + \frac{1-\phi/\phi_{\max}}{K_s + \frac{4}{3}G_s} \right]^{-1} - \tfrac{4}{3}G_s \\
G^{MUHS} &= \left[\frac{\phi/\phi_{\max}}{G_{\phi\max} + Z_s} + \frac{1-\phi/\phi_{\max}}{G_s + Z_s} \right]^{-1} - Z_s, \quad \text{where } Z_s = \frac{G_s}{6}\cdot\frac{9K_s+8G_s}{K_s+2G_s}
\end{aligned}
\tag{4}
$$

The end-member moduli of the dry rock found by Walls et al. (1998) were

$$
\begin{aligned}
&K_{\phi\max} = 4\text{ GPa},\ G_{\phi\max}\ 4\text{ GPa for } \phi_{\max} = 40\%, \text{ and} \\
&K_s\text{=65 GPa and } G_s\text{=27 GPa for } \phi = 0\%
\end{aligned}
\tag{5}
$$

Once these end-member parameters are estimated we can calculate the moduli of the dry rock from the MUHS model and given porosity and estimate moduli for the saturated rock using Gassmann's relations and the appropriate fluid properties, and finally calculate V_P and V_S.

Extended MUHS model based on ultrasonic V-ϕ data

Ultrasonic data from core samples from the South Arne field are in good agreement with the model of Walls et al. (1998), which is defined for porosities less than 40% (Fig. 1). However, chalk porosities between 40% and 45% occur on the South Arne field as estimated from both log data and core samples. For this reason we extrapolated the range of the MUHS model from 40% to 45% by estimating the high-porosity end-member at 45% porosity while keeping the low-porosity end-member unchanged (equations 4, 5):

$$K_{\phi max} = 1.5 \text{ GPa}, \mu_{\phi max} = 2.5 \text{ GPa for } \phi_{max} = 45\% \qquad (6)$$

This extrapolated model is in agreement with the acoustic properties of the south Arne plug samples with porosities between 40% and 45% (Fig. 1). We tried to extrapolate the MUHS model to 50% porosity, but even with $K_{\phi max}$ as low as 0.2 GPa the V_P-prediction was above that of the Walls et al. model and the measured values for the plug samples. The upper Hashin-Shtrikman formalism that reflects stiff pores shapes does thus not apply to the high porosity (45%-70%) pelagic carbonate deposits for which the increase of velocity with porosity reduction is limited (e.g. Urmos & Wilkens 1993).

We can apply the MUHS model to compute elastic moduli and Poisson's ratio for chalk as a function of porosity for the range of water saturations encountered on the South Arne field (Fig. 4), where the Poisson ratio, ν [-], is defined as:

$$\nu = \frac{3K - 2G}{2(3K + G)} = \frac{V_p^2 / V_s^2 - 2}{2(V_p^2 / V_s^2 - 1)}.$$

We see that even minor amounts of oil shift the bulk modulus down as expected from the assumed fine-scale Reuss mixing of the fluids (Fig. 3). The shear modulus is, however, unaffected by fluid properties as predicted by Gassmann's relations and consequently we predict pronounced variations in the Poisson ratio at high porosities. For pure brine, the Poisson ratio is almost constant $\approx$0.31 for $10\% < \phi < 36\%$, but increases along a banana shaped curve to 0.35 for ϕ=45% (cf. Gommesen 2003). For pure oil, the Poisson ratio decreases to 0.14 for ϕ=45% and we thus get a pronounced span in Poisson's ratio for porosities above c. 35% between heavy brine and light oil (density 1.035 and 0.633 g/cm^3). This span in Poisson ratio predicted by the MUHS model makes it probable that the light oil in the high-porous chalk on the South Arne field might be detected through AVO inversion of surface seismic data.

Sonic measurements in chalk affected by mud invasion

The acoustic properties of high-porosity chalk depend critically on fluid content, and we expect that the acoustic signal travels in the zone close to the well bore. Because there is no shallow resistivity log available, we cannot follow the procedure of Gommesen et al. (2002) and compare the acoustic signal to a model based on the saturation in the invaded zone. We do, however, not know if invasion was significant, and thus whether the acoustic waves registered by the sonic logs in the Rigs-2 well travelled through the invaded zone where the water saturation, Sw, is known from the deep resistivity log. We will examine the sonic data by comparing them to the MUHS model for brine at reservoir conditions using Gassmann's relations (eq. 6; Table 1). The MUHS model is in agreement with both ultrasonic data from the South Arne field and with the log data from the near-by Ekofisk field.

We find that the logging data are influenced by the presence of hydrocarbons (Fig. 5A): Bulk modulus and Poisson's ratio are low compared to the MUHS model due to presence of low-density oil. The shear modulus (which is unaffected by fluid content according to Gassmann theory) plots close the MUHS trend for $\phi < $ c. 40% (see below). Note that the high-porosity chalk appears to be almost completely flushed as the bulk moduli are close to the MUHS model for $\phi > 40\%$.

If the sonic log data are transformed from water saturation as estimated by S_w to brine conditions assuming no invasion, the result appears to be overcorrected (Fig. 5C): The bulk modulus plots above the MUHS model for high porosities. We therefore find that the sonic logs in the Rigs-2 well are measured in chalk where oil is present but in smaller amounts than indicated by Sw due to invasion of mud filtrate (cf. Gommesen *et al.* 2002).

Erroneous S-velocities from log data for porosities above c. 40%

The S-velocities measured by the dipole log in the Rigs-2 well are almost constant and increasingly higher than those predicted by the extended MUHS model for porosities above c. 40% (Vs less than 1.3 km/s) - and thus higher than Vs measured on the chalk samples (see plot of G versus ϕ, Fig. 5). At 45% porosity, the shear velocity based on lab data is only 1.1 km/s whereas the value from the log data remains c. 1.3 km/s (G=2.4 and 3.5 GPa, respectively). We suggest that this difference is due to erroneous log-determination of Vs when S-wave traveltimes becomes so long that the S-arrivals are masked by minor P-waves or by direct arrivals in the borehole mud.

Acoustic properties of the virgin zone

We want to estimate the acoustic properties of the virgin zone with water saturation Sw to compare with the seismic data that reflect rock properties unaffected by invasion of mud filtrate. We are, however, confronted with two obstacles: First and most importantly, that the sonic log is measured in the mud-invaded zone where we do not know the water saturation, Sxo. Second, that the recording of the shear velocities appear to be erroneous for porosities above c. 40%. Two approaches may be followed:

- Either to estimate Sxo from empirical relations of irreducible water saturation in chalk and transform the sonic data to Sw-conditions using Gassmann's relations (Fig. 6)
- or to estimate the acoustic properties from forward modeling using the MUHS model and Gassmann's relations with ϕ and Sw as input. The bulk moduli estimated from the model and from the data may be used to quantify Sxo using Gassmann's relations (Fig. 7).

Virgin zone properties estimated from sonic data and Land's equation for residual oil

The water saturation of the flushed zone, Sxo (equivalent to the residual oil content) may be estimated from Land's formula (Land 1968):

$$S_{xo} = 1 - \frac{1 - S_{wi}}{1 + C(1 - S_{wir})} \qquad (7)$$

where S_{wi} is the initial water saturation (=Sw, the saturation of the virgin zone), S_{wir} is the irreducible water saturation and C=2.5 for the South Arne field (Flemming Iff, pers. comm.). We can calculate S_{wir} from the normalised capillary pressure curve method developed for the tight chalk in the North Sea (the equivalent radius method, EQR; Engstrøm 1995):

$$S_{wir} = \left(\frac{A}{\phi}\right)^{B}$$

where A and B are constants. We compute Sxo for the Rigs-2 well based on these two equations where we distinguish between the Ekofisk and Tor formations where S_{wir} is higher for the Ekofisk Formation (Fig. 6); A=0.12641, B=2.45422 (Ekofisk Fm) and

A=0.06596, B=2.19565 (Tor Fm) (P. Frykman, pers. comm.). The mean water saturation is predicted to increase from 17% to 76% in the flushed zone of the Tor Formation and Sxo is seen to mirror Sw so that relatively more oil is removed from the more oil-saturated intervals. Based on this estimate of Sxo we can do fluid substitution to any saturation using Gassmann's relations and Reuss fluid mixing law (eqs 1, 2).

Resulting acoustic response

We assume that the measured Vp- and Vs logging-data (blue curves) reflect the conditions of the flushed zone with Sxo estimated by Land's equation, and do fluid substitution to compute the acoustic properties of the chalk saturated with the fluids of the virgin zone (red curve) and with pure brine (green curve) (Fig. 6b). The P-velocity of the invaded zone and of the virgin zone are not predicted to differ much because the fluid properties are rather identical for medium saturations due to the assumed Reuss mixing of the fluids (Fig. 3). A bigger change in Vp is predicted from the data curve to the brine curve (green). This is to be expected from the assumed Reuss fluid mixing because minor amounts of light fluids reduce the bulk modulus of the brine notably.

Virgin zone properties estimated from the MUHS model with ϕ and Sw as input

Forward modeling may be used to calculate the acoustic response corresponding to the measured porosity and the water saturation, Sw, in the virgin zone (Fig. 7). The modeling is done in three steps where step 2 may be included to correct the moduli of the most shaley intervals:

1. Calculate the properties of the dry rock from the MUHS model with the porosity log as input (eq. 6).
2. Correct the moduli in the intervals with impure chalk as estimated by Sw by scaling the low-porosity end-member of the MUHS model (see below; eq. 8).
3. Calculate the properties of the virgin zone where the water saturation is given by Sw using Gassmann's relations and the Reuss mixing law (eqs 1, 2).

Corrected MUHS model

In Fig. 8 we see the result of the uncorrected MUHS model (steps 1 and 3) and the corrected MUHS model (steps 1 to 3) compared with the measured data. The big difference in the bulk modulus between the model (of the virgin zone) and data (from the flushed zone) is caused by removal of oil by mud invasion. However, the shear modulus is unaffected by fluid content and the model-estimate of G is close to the data-estimate. We compute the difference in the estimates of the shear modulus as $\Delta G = G_{MUHS} - G_{data}$ for the uncorrected MUHS model (Fig. 9). We get large differences expressed as ΔG up to 10 GPa where porosity is low (and moduli large) and where water saturation is high. The clay content estimated from the gamma log reveals, however, no correlation with the mismatch between model and data. Furthermore, we get minor differences expressed as ΔG down to –2 GPa for porosities above 40%.

The too low S-velocities (ΔG<0) modelled at high porosities may be explained by erroneous log-measurements of shear velocities as discussed above. Our interpretation of the too high S-velocities (ΔG>0) modelled at low porosities is that velocity is reduced due to a content of clay, which causes the assumption of a calcite mineral matrix to be too inaccurate. The clay content estimated from the gamma log does however not correlate with ΔG, partly because this log may be erroneous, e.g. due to use of oil-based drilling mud and partly because non-carbonate constituents as quarts and smectite have no or insignificant gamma response. We thus assume that the water saturation can be regarded as a measure of the impurities in the chalk which in this well where the water is irreducible (Fig. 7).

The water saturation may be regarded as irreducible because the water saturation does not increase with depth (apart from the deepest 10 m of the Tor Formation), so that the water saturation reflects the size of the particle-pore interface and amount of particle contacts (Fabricius *et al.* 2002). The controlling factor for the degree of water saturation in the chalk thus becomes clay content and particle sorting. A clear distinction between the Ekofisk and the Tor formations is revealed by Sw but not by the gamma log (Fig. 7). The distinction between these formations is also evident from the well-known lower permeability of the Ekofisk Formation that may be attributed to the higher content of silicates in the Ekofisk formation (Røgen 2003). The relatively low moduli for chalk with high shale content is also evident from the plug data with values of ΔG and ΔK up to –10.5 and -10.0 GPa around 15% porosity (Fig. 1).

In order to correct the MUHS model (eq. 6) for the effect of clay-softening we have chosen a simplistic, but apparently effective approach (Figs 9a2, b2): We have scaled the low-porosity end-members, M_s, of the MUHS model (eq. 5) by the 'clay' content, cl, taken as cl = Sw – 0.2. For a given value of Sw, we calculated M_s as a kind of Hill average by computing the arithmetic average of the upper and lower Hashin-Shtrikman bounds, HS_U and HS_L (see Mavko et al., 1998):

$$M_s = (HS_U + HS_L)/2 \tag{8}$$

where the bounds are calculated as a mixture defined by cl between the 'no-clay' end-member moduli for pure chalk given by Walls et al. (1998): M_{chalk}=(65 GPa, 27 GPa) and the end-member moduli for pure 'clay' equals those for clay given by Table 1: M_{clay}=(25 GPa, 9 GPa). This procedure effectively scales M_s between M_{chalk} for Sw<0.2 and (30 GPa, 11 GPa) for Sw=1. The correction reduces the too high predictions of G to match the data values in the low-porosity zones where Sw reaches maximum values (cf. Figs 7, 8).

Water saturation estimated from sonic data

The bulk modulus, K_{sat}, of the flushed zone is known from the sonic data whereas the dry-rock modulus, K_{dry}, of the chalk can be estimated from the corrected MUHS model (eq. 8; fig. 8). To avoid erroneous Vs-data we use Vs from the corrected MUHS model to compute K_{sat} for ϕ>40%. We can thus rearrange Gassmann's relations expressed in terms of K_{sat} and K_{dry} to give us the effective bulk modulus, k_{fl}, of the pore fluid in the flushed zone (eq. 1; see Mavko et al. 1998):

$$k_{fl} = \phi K_m \frac{A-B}{1+\phi(A-B)}, \text{ where } A = \frac{K_{sat}}{K_m - K_{sat}}, \ B = \frac{K_{dry}}{K_m - K_{dry}}$$

Substituting this result into the Reuss equation for fine-scaled fluid mixing in the reservoir (eq. 2), we get the saturation of the flushed zone, Sxo:

$$S_{xo} = \frac{k_{brine}(k_{oil} - k_{fl})}{k_{fl}(k_{oil} - k_{brine})} \tag{9}$$

where k_{oil} and k_{brine} are the bulk moduli of the oil and the brine of the reservoir (Table 1). Only values of Sxo in the interval from 0 to 1 are valid (234 out of 306 data points for the Rigs-2 well). Sxo is predicted to be 81% in the Tor Formation which is in very good agreement with the 76% obtained by Land's equation (eq. 7). However, Sxo has a large scatter and the indicated mean value includes values above 90% water saturation over much of the Tor reservoir where porosity exceeds 40% (Fig. 7).

Resulting acoustic response

Also in this case we assume that the measured Vp- and Vs-data (blue curve) reflect the conditions of the flushed zone with water saturation given by Sxo, which may be estimated over part of the reservoir by the above equation (Fig. 7). However, we estimate the acoustic properties of the chalk in the virgin zone (red curve) from the corrected MUHS model based on the porosity log and Sw (Fig. 7b). The P-velocity of the flushed zone does not differ much from that predicted for brine (green curve) because of the almost complete mud invasion. A significant difference in Vp is now predicted between the virgin zone and the flushed zone.

AVO-inversion based on logs from the MUHS model

AVO attributes were calculated from inverted 2D seismic lines (near- and far-offset data) extracted from the South Arne 3D survey. The inversion was carried out for the two-way time window 1.9–3.6 s and was targeted on the chalk interval (cf. Cooke & Schneider 2003). Log data from the I-1x, Rigs-1, -2 and SA-1 wells were used in the inversion process. These data comprise Vp- and Vs-data based on the corrected MUHS model described above plus density logs, check shot and deviation data. Using a least-squares wavelet estimation method with constrain on the phase, wavelets were estimated for each offset stack. The wavelet estimations was carried for each of the wells (Fig. 10). The I-1x well has no shear log data so Vp/Vs=2 was used in the calculations. The wavelet estimated from the I-1x well was preferred based on inversion tests.

Low-frequency components of the acoustic impedance variations with depth are not present in seismic data. Since this information is essential to the interpretation, it should be accounted for in the seismic inversion. Low-frequency near- and far-angle impedance models were constructed by extrapolation of the angle-dependent impedance well logs through the 3D volume tied to seismic horizons, followed by low-pass filtering (cf. Castagna & Backus 1993). The final inversion results models 93.7% of the seismic energy for the near-offset stack and 93.4% for the far-offset stack. The inversion results are good in terms of match with the angle impedance well logs.

AVO-attributes were computed from the angle-dependent impedance inversions combined with low-frequency information (Bach *et al.* 2003): Acoustic impedance, shear impedance and Poisson's ratio were extracted at the location of the Rigs-2 well.

The AVO-results are good in terms of match with the well log data. Low values of Poisson's ratio at the location of Rigs-2 is in agreement with the presence of light oil in the high-porous chalk of the South Arne field (Fig. 11).

Discussion and conclusions

We have extended the Modified Upper Hashin-Shtrikman trend established by Walls et al. (1998) for chalk on the Ekofisk field based on log data. This trend describes an empirical relation between porosity and the dry-rock moduli of chalk and hence velocity of saturated chalk through application of Gassmann's relations. Ultrasonic data for relatively pure chalk samples of the Ekofisk and Tor formations from the South Arne field match the trend and due to the higher porosities on the South Arne field we can extend the range of the MUHS model from 10%–40% to 10%–45% (eq. 6). Shaley chalk samples, e.g. with a smectite content of 3%–7% have significantly smaller moduli and a higher Poisson ratio than the general data trend. Modeling of the acoustic properties of chalk as a function of water saturation predicts a pronounced drop in Poisson ratio for oil-bearing chalk with porosities above c. 35%.

Comparison of the MUHS model with sonic data from the South Arne field clearly show that the data records the conditions of a zone close to the well bore where drilling-mud has flushed the reservoir and the water saturation, Sxo, thus is higher than the saturation, Sw, in the virgin zone as estimated from the deep resistivity log. Lacking shallow resistivity data to assess the water saturation in the flushed zone we have investigated two approaches to estimate the acoustic properties of the virgin zone in order to compare the result with inversion of surface seismic data:

1. Estimation of Sxo from Land's (1968) prediction of the irreducible water saturation in chalk followed by transformation of the sonic data to Sw-conditions using Gassmann's relations (eq. 7).
2. Estimation of the acoustic properties from forward modeling using the MUHS model and Gassmann's relations with ϕ and Sw as input. The bulk modulus depend on fluid content and we use differences between the sonic data and the MUHS model to quantify Sxo using Gassmann's relations and Reuss' fine-scale fluid-mixing law. The shear modulus, G, is unaffected by fluid content and we observe good agreement between MUHS model and data in pure chalk. We use the differences between data- and model-estimates of G to establish a corrected

MUHS model where we scale the low-porosity end-member of the MUHS trend according to shale content as estimated by Sw. We do so because the MUHS model predicts too high shear moduli where porosity is low and water saturation is high, whereas we see no correlation with clay content estimated from the gamma log. The water saturation can thus be regarded as a measure of the impurities in the chalk in this well where the chalk is water-wet and the water saturation is irreducible. The controlling factor for the degree of water saturation thus becomes clay content and particle sorting. The MUHS model predicts the shear modulus to be smaller than observed from logging data for porosities above c. 40%. We suggest that this difference is due to erroneous log-determination of Vs when S-wave traveltimes becomes very long.

A characteristic depth-wise pattern of the Poisson ratio with pronounced peaks at top Ekofisk and top Tor and low values in the high-porous Tor reservoir results from forward modeling of the acoustic properties of the virgin zone (Fig. 12). This pattern is in good agreement with the inverted seismic data (Fig. 11), but these features are not captured in the approach based on Land's (1968) equation. We therefore find that Land's equation underestimates the mud-invasion of the high-porous part of the reservoir. We find that the best way to estimate the acoustic properties of the virgin zone is to use the extended Modified Upper Hashin-Shtrikman velocity-porosity relation for chalk presented here. AVO-inversion of the seismic data based on such synthetic sonic logs reveals a zone of very low Poisson ratio that correlates with the oil reservoir in the Tor Formation. AVO-inversion thus provides direct evidence for presence of oil in high-porous chalk saturated with the light oil of the South Arne field.

Acknowledgements

These results are part of the outcome of the energy research project Rock Physics of Impure Chalk which was sponsored by the Danish Energy Research Program (EFP-2001), Amerada Hess A/S and Dong E&P.

References

Bach, T., Espersen, T. B., Pedersen, J. M., Hinkley, R., Pillet, R. P. & Rasmussen, K. B. 2003. Seismic inversion of AVO data. In press for *Inverse methods II, Springer Verlag.*

Castagna, J. P. & Backus, M. M. 1993. *Offset-dependent reflectivity – Theory and practice of AVO analysis.* Society of Exploration Geophysicists, Tulsa.

Cooke, D. A. & Schneider, W. A. 2003. Generalised linear inversion of reflection seismic data. *Geophysics,* **48**, 665-676.

Engstrøm, F. 1995. A new method to normalise capilary pressure curves. *Proceedings from the International Symposium of the Society of Core Analysis.* 12 pp.

Fabricius, I. L., Mavko, G., Mogensen, C. & Japsen, P. 2002. Elastic moduli of chalk as a reflection of porosity, sorting, and irreducible water saturation. *SEG 72nd annual meeting, Salt Lake City, USA.* 4 pp.

Gassmann, F. 1951. Über die Elastizität poröser Medien. *Vier. der Natur. Gesellschaft in Zürich,* **96**, 1-23.

Gommesen, L. 2003. Prediction of porosity and fluid in chalk from acoustic measurements. Technichal University of Denmark (DTU). PhD Thesis.

Gommesen, L., Mavko, G., Mukerji, T. & Fabricius, I. L. 2002. Fluid substitution studies for North Sea chalk logging data. *72nd SEG annual meeting, Salt Lake City, USA.* 4 pp.

Hashin, Z. & Shtrikman, S. 1963. A variational approach to the elastic behavior of multiphase materials. *J. Mech. Phys. Solids,* **11**, 127-140.

Jacobsen, N. L., Engstrøm, F., Uldall, A. & Petersen, N. W. 1999. Delineation of hydrodynamic/geodynamic trapped oil in low permeability chalk (SPE 56514). *SPE annual technical conference.* 10-1.

Japsen, P. 1998. Regional velocity-depth anomalies, North Sea Chalk: a record of overpressure and Neogene uplift and erosion. *AAPG Bulletin,* **82**, 2031-2074.

Japsen, P., Høier, C., Rasmussen, K. B., Fabricius, I. L., Mavko, G. & Pedersen, J. M. 2002. Effect of fluid substitution on ultrasonic velocities in chalk plugs, South Arne field, North Sea. *SEG 72nd annual meeting, Salt Lake City, USA.* 4 pp.

Japsen, P., Wagner, H., Gommesen, L. & Mavko, G. 2000. Rock physics of Chalk: modeling the sonic velocity of the Tor Formation, Danish North Sea. *EAGE 62nd conference, Glasgow, Scotland.* 1-4.

Land, C. S. 1968. Calculation of imbibition relative permeability for two- and three-phase flow from rock properties. *Society of Petroleum Engineers Journal,* **1968**, 149-156.

Mackertich, D. S. & Goulding, D. R. G. 1999. Exploration and appraisal of the South Arne field, Danish North Sea. *In:* Fleet,A.J. & Boldy,S.A.R. (eds) *Petroleum Geology of Northwest Europe: Proceedings of the 5th Conference.* Geological Society, London. 959-974.

Mavko,G. and Japsen,P. *submitted.* Fluid substitution in chalks: Effects of saturation scales. Submitted to Geophysical Prospecting.

Mavko, G., Mukerji, T. & Dvorkin, J. 1998. *The rock physics handbook.* Cambridge University Press, Cambridge.

Megson, J. B. 1992. The North Sea chalk play; examples from the Danish Central Graben. *In:* Hardman,R.F.P. (ed.) *Exploration Britain: Geological insights for the next decade.* Geological Society Special Publication, **67**, 247-25.

Nur, A., Mavko, G., Dvorkin, J. & Galmundi, D. 1998. Critical porosity; a key to relating physical properties to porosity in rocks. *Leading Edge,* **17**, 357-362.

Røgen, B. 2002. North Sea chalk - textural, petrophysical and acoustic properties. Technichal University of Denmark (DTU). PhD Thesis.

----- 2003. Influence of clay and silica on permeability and capillary entry pressure of chalk reservoirs in the North Sea. *Petroleum Geoscience,* **8**, 293.

Røgen, B., Fabricius, I. L., Japsen, P., Høier, C., Mavko, G. & Pedersen, J. M. 2002. Ultrasonic velocities of chalk samples - influence of porosity, fluid content and texture. *In:* Røgen,B. (ed.) *North Sea chalk - textural, petrophysical and acoustic properties.* Technical University of Denmark (DTU), Lyngby.

Scholle, P. 1978. Diagenesis hydrocarbon potential of Upper Cretaceous chalks of Western Interior. 892-892.

Urmos, J. & Wilkens, R. H. 1993. In situ velocities in pelagic carbonates: New insights from Ocean Drilling Program Leg 130, Ontong Java Plateau. *Journal of Geophysical Research,* **98**, 7903-7920.

Vejbæk, O. V. & Kristensen, L. 2000. Downflank hydrocarbon potential identified using seismic inbersion and geostatistics: Upper Maastrichtian reservoir unit, Dan Field, Danish Central Graben. *Petroleum Geoscience,* **6**, 1-13.

Walls, J. D., Dvorkin, J. & Smith, B. A. 1998. Modeling seismic velocity in Ekofisk Chalk. *SEG 68th annual conference.* 1016-1019.

Table 1. Elastic properties. Bulk and shear modulus, K and G, and density, ρ.

	K [GPa]	G [GPa]	ρ [g/cm^3]
Calcite	71	30	2.71
Clay	25	9	2.70
Brine	2.96**	0	1.035*
Hydrocarbon	0.52**	0	0.633*

Mineral properties after Mavko et al. (1998). Fluid properties estimated for the Rigs-2 well.

* Densities estimated at reservoir level at the South Arne field (J. Jensenius pers.comm.)

** Values for fluids at the crest of the South Arne field estimated with Batzle-Wang algorithm FOR T=100°, P=44 MPa, Oil gravity=33 API, Gas gravity=0.815 (Alister Colby pers.comm.). GOR=1685 scf/BBL in order to match the hydrocarbon density.

Figures

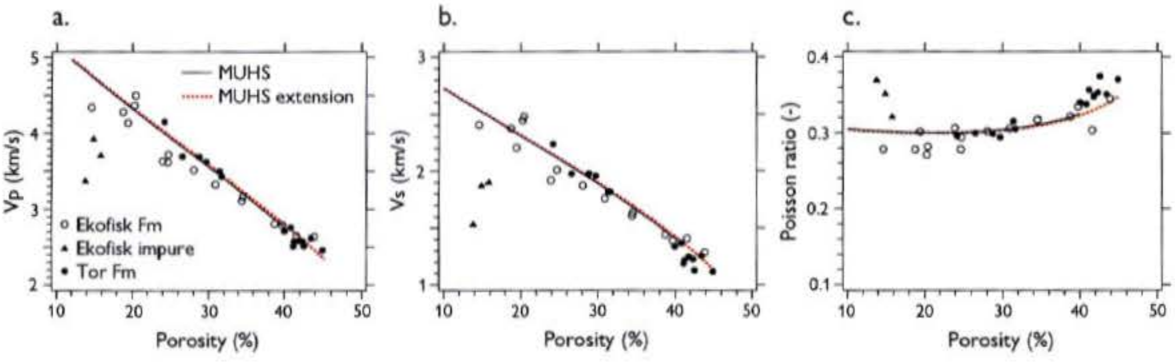

Fig. 1. Acoustic properties of 34 saturated chalk samples versus porosity.

a. P-velocity, V_P.

b. S-velocity, V_S.

c. Poisson's ratio.

Good agreement is observed between the South Arne core data and the MUHS model based on log data from the Ekofisk field (full line; eq. 5; Walls et al. 1998;). We suggest an extrapolation of the model from 40% to 45% porosity that agrees with the plug data (dashed line; eq 6). Both lines for brine at reservoir conditions. Acoustic properties measured on core samples saturated with tap water at 75 bar confining pressure and transformed to the brine properties at reservoir conditions in the South Arne field using Gassmann's relations (Table 1). MUHS: Modified Upper Hashin-Shtrikman.

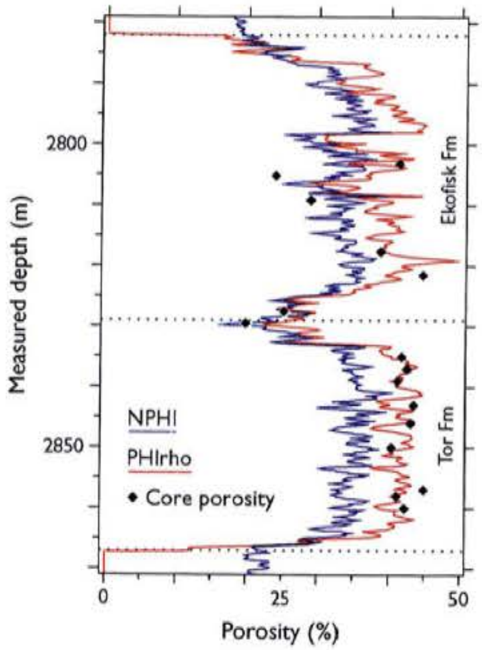

Figure 2. Porosity logs for the Rigs-2 well and data points for core porosity. Note the agreement between core porosity and the density log, PHIrho, which was estimated from log-readings of the bulk density, ρ_{bulk}, assuming full invasion of the mud filtrate. This indicates that ρ_{bulk} measures in the zone fully invaded by mud filtrate. The neutron porosity log, NPHI, underestimates porosity due to the presence of hydrocarbons.

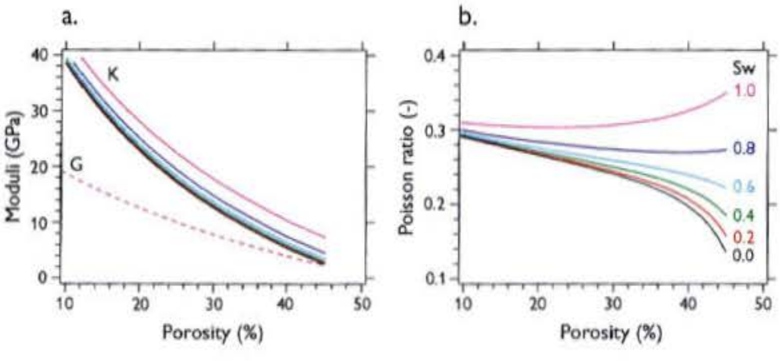

Fig. 4. Acoustic properties of chalk as a function of porosity and water saturation, Sw, predicted from the MUHS model and Gassmann's relations assuming fine-scaled Reuss mixing of the fluids (eqs 6, 1, 2).

a. Bulk and shear modulus, K and G.

b. Poisson ratio.

Note the pronounced variation in Poisson ratio for porosities above c. 35% between pure brine and pure oil (density 1.035 and 0.633 g/cm^3; Table 1). MUHS: Modified Upper Hashin-Shtrikman.

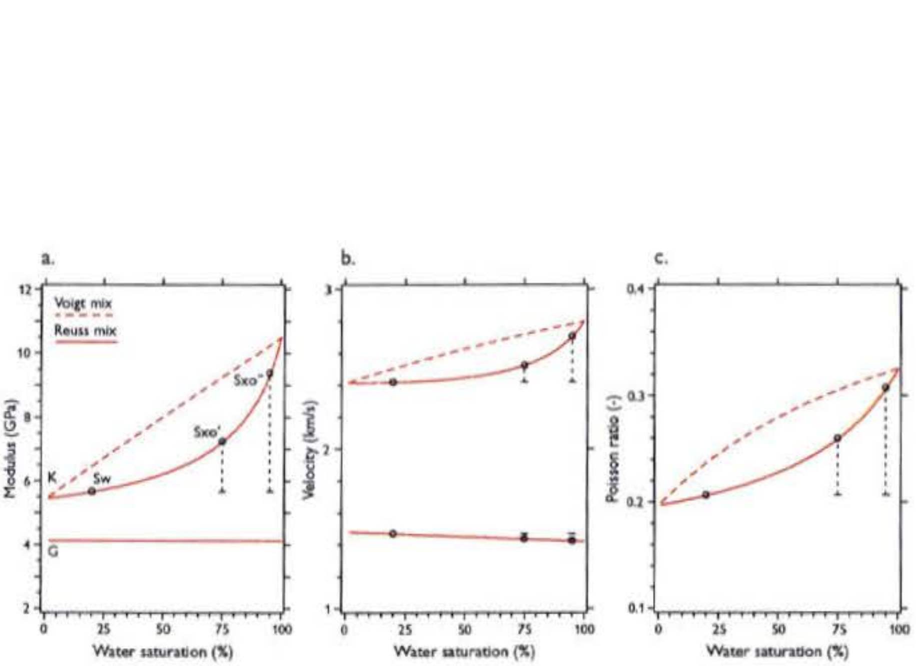

Fig. 3. Acoustic properties as a function of water saturation for chalk with 40% porosity.

a. Bulk and shear modulus, K and G.

b. P- and S- velocities, Vp and Vs,

c. Poisson ratio.

Flushing of the reservoir increases the bulk modulus of the oil-brine mixture along a Reuss curve .

Minor variations in the estimation of Sxo result in major changes in the acoustic properties as indicated by the dashed lines. Dry-rock properties from MUHS model and fluid properties for the South Arne field (eq. 6; Table 1)

Legend:

Sw: Water saturation of the virgin zone.

Sxo': Saturation of the mud-invaded reservoir according to Lands equation for residual oil (eq. 7; Fig. 6).

Sxo'': Saturation of the mud-invaded reservoir estimated from sonic data and the MUHS model (eq. 9; Fig. 7).

Upper bound: Voigt fluid mixture (eq. 3).

Lowert bound: Reuss fluid mixture (eq. 2).

MUHS: Modified Upper Hashin-Shtrikman.

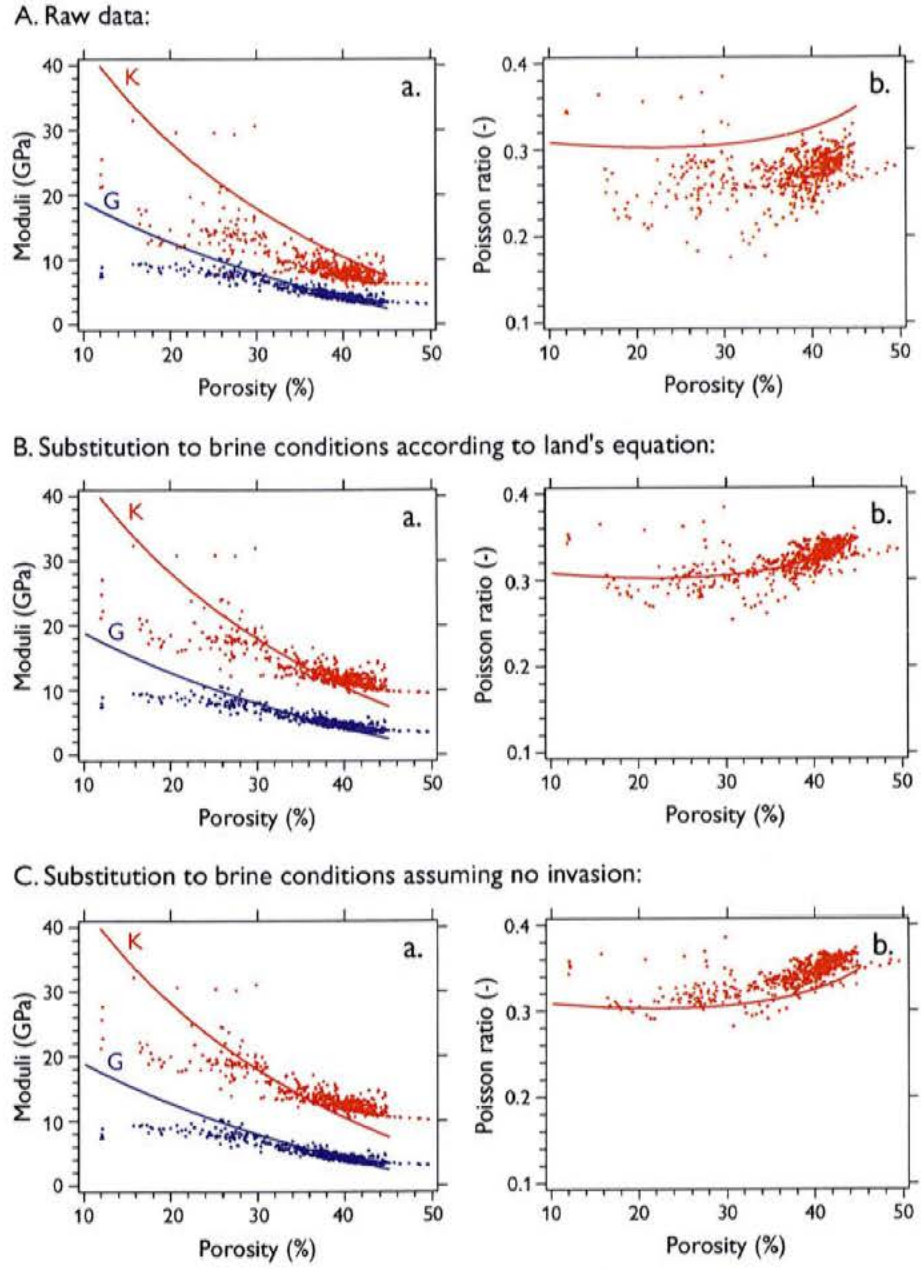

Fig. 5. Acoustic properties of the chalk in the Rigs-2 well versus porosity.

a. Bulk and shear modulus, K and G.

b. Poisson's ratio.

Note that the estimated shear moduli – that are unaffected by fluid content – plot on the MUHS trend for ϕ>40%. This suggests that the MUHS model is valid for log data for the South Arne chalk and that the shear velocity log data probably are erroneous for ϕ>40% where Vs is predicted to be less than 1.4 km/s.

A. Original data. Bulk moduli plot below the MUHS model due to presence of hydrocarbons whereas shear moduli plot on the trend. Note that for ϕ>40% the bulk moduli are close to the MUHS model for brine conditions and this indicates that the high-porosity chalk is almost completely flushed.

B. Substitution to brine conditions assuming invasion according to Land's equation (eq. 7). Bulk moduli plot close to the MUHS model for ϕ up to 40% indicating that Land's equation works well at medium porosities.

C. Substitution to brine conditions assuming no invasion. Bulk moduli plot above the MUHS model indicating that Sw overestimates the oil-content in the flushed zone.

Legend:

Full lines: MUHS model for brine at reservoir conditions (equations 1, 6; Table 1).

MUHS: Modified Upper Hashin-Shtrikman.

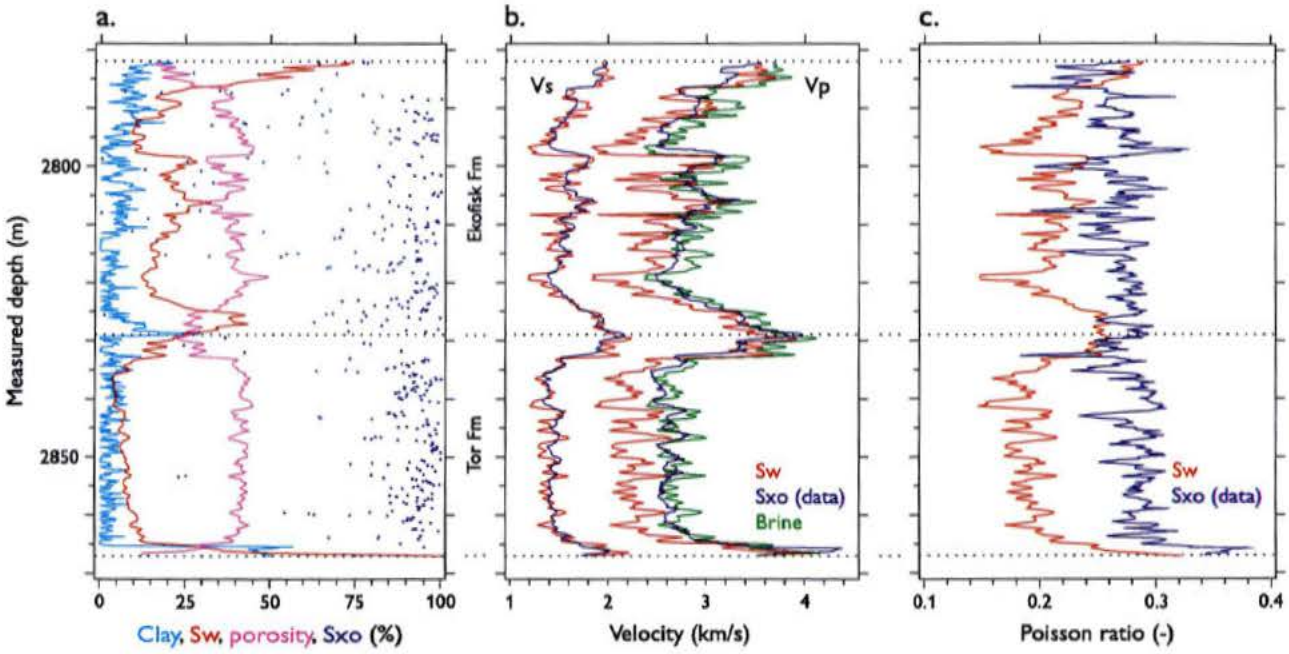

Fig. 7. Log data and predictions based on the corrected MUHS model for the chalk section in the Rigs-2 well (eqs 6, 8; Fig. 8).

a. Clay content (from gamma log), porosity and water saturation, Sw and Sxo. Sxo (dots) is estimated from the relation between the measured sonic data and the corrected MUHS model (eq 9).

b. V_P and V_S. Data and predictions of the corrected MUHS model based on porosity and Sw. Brine-estimate for Vs not shown.

c. Poisson ratio. Data and predictions of the corrected MUHS model. Brine-estimate not shown.

In the high-porosity oil zone of the Tor Formation, the oil is predicted to be almost completely flushed as indicated by the closeness of the measured Vp(Sxo) (blue curve) and the predicted Vp(brine) (green curve) whereas Vp(virgin zone, Sw) is predicted to be low (cf. Fig. 3). MUHS: Modified Upper Hashin-Shtrikman.

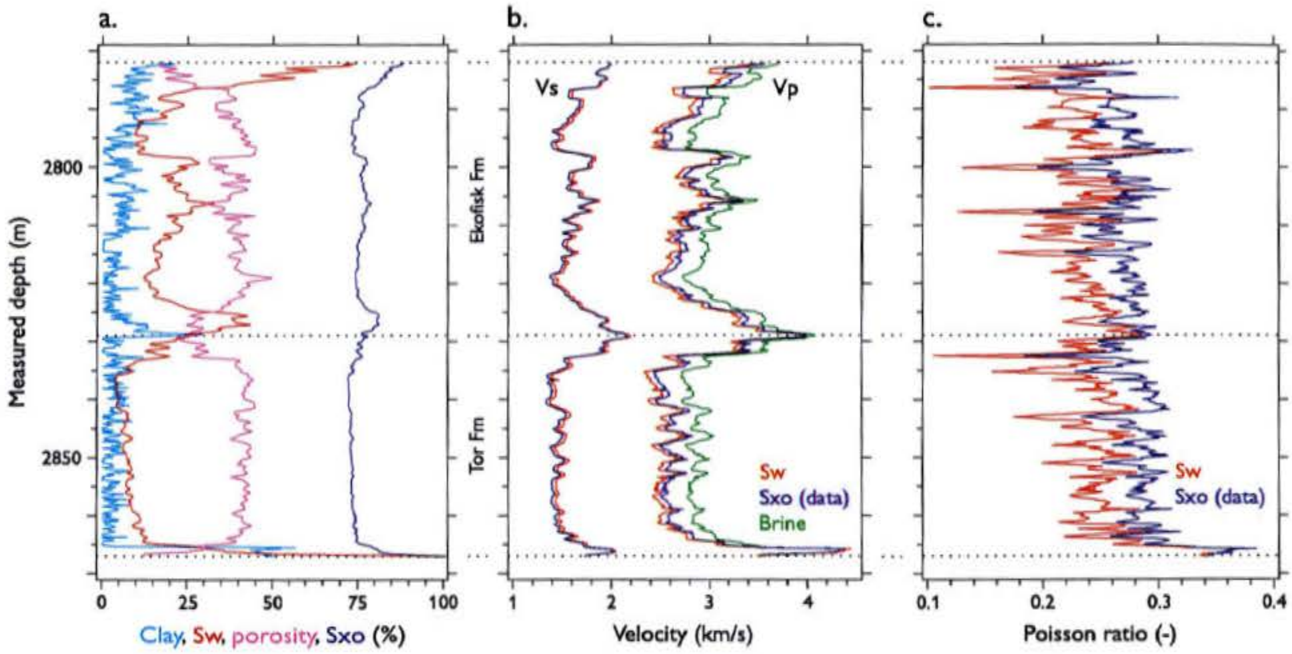

Fig. 6. Log data and predictions based on Land's estimate of residual oil for the chalk section in the Rigs-2 well (eqs 6, 8; Fig. 8).

a. Clay content, porosity and water saturation, Sw and Sxo. Sxo is estimated from Land's equation (eq 7).

b. V_P and V_S. Data and predictions based on fluid substitution from Sxo. Brine-estimate for Vs not shown

c. Poisson ratio. Data and predictions of the Land model. Brine-estimate not shown.

In the high-porosity oil zone of the Tor Formation, Sxo is predicted to be reduced to c. 75% and due to the Reuss mixing of the fluids the acoustic properties of invaded zone and of the virgin zone do not differ much. This is indicated by the closeness of the measured Vp(Sxo) (blue curve) and the predicted Vp(virgin zone) (red curve) whereas Vp(brine) (green curve) is predicted to be significantly higher (cf. Fig. 3).

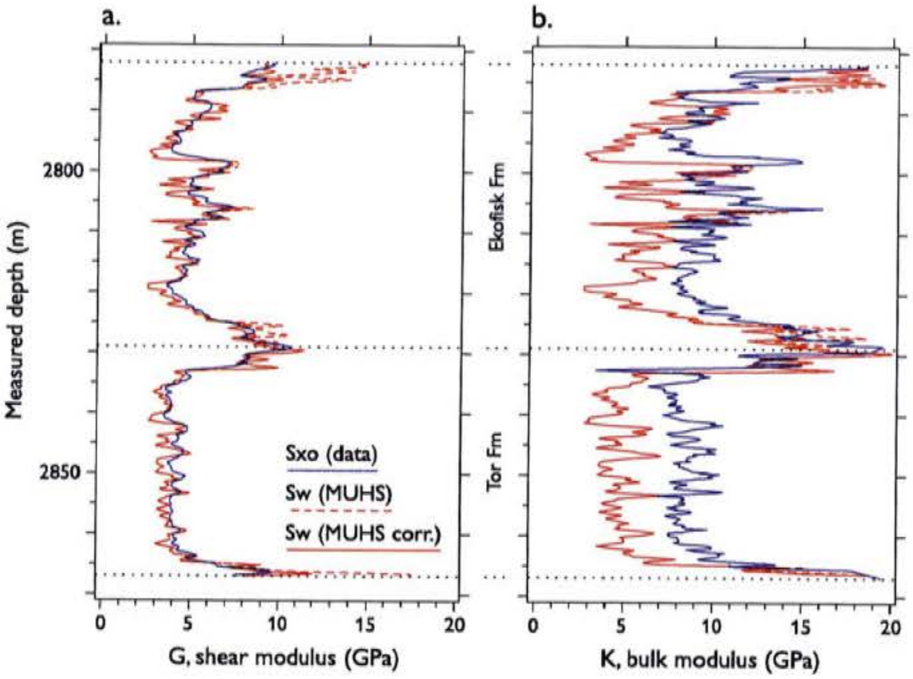

Fig. 8. Log response predicted for the virgin zone from the corrected and the uncorrected MUHS-model compared with data from the invaded zone (eqs 6, 8).

a. Shear modulus.

b. Bulk modulus.

Note the good agreement between the shear modulus estimated from data and from the corrected MUHS model. Poor sorting and clay content may explain the difference between the estimated shear modulus from uncorrected MUHS model and from the data in the tight zones (Figs 7, 9). The difference between the two estimates of the bulk modulus is caused by removal of oil by mud invasion in the zone investigated by the sonic log. MUHS: Modified Upper Hashin-Shtrikman.

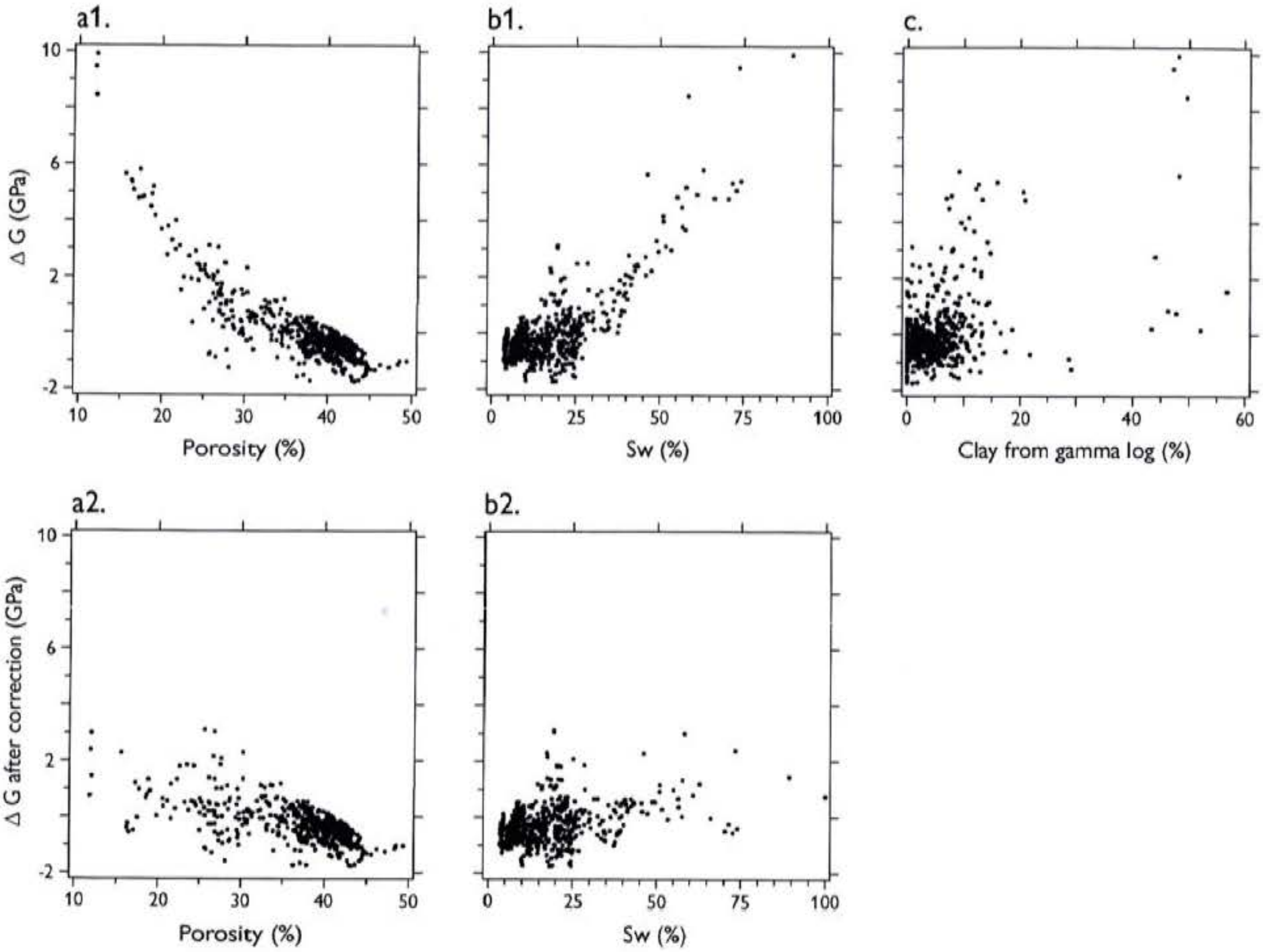

Fig. 9. Error in prediction of the shear modulus, $\Delta G = G_{MUHS} - G_{data}$ and $\Delta G_c = G_{MUHS\_c} - G_{data}$ where G_{MUHS} and G_{MUHS_c} are estimated from the MUHS model and the corrected MUHS model (eqs 6, 8).

a1–c1. ΔG versus porosity, water saturation and clay content estimated from the gamma log.

a2–b2. ΔG_c versus porosity and water saturation.

The error in the MUHS model correlates with Sw and this indicates that the water saturation reflects the degree of impurity of the chalk in this reservoir where the chalk is water wet and the water saturation irreducible (see Fig. 7). The clay content estimated from the gamma log does not correlate with ΔG. MUHS: Modified Upper Hashin-Shtrikman.

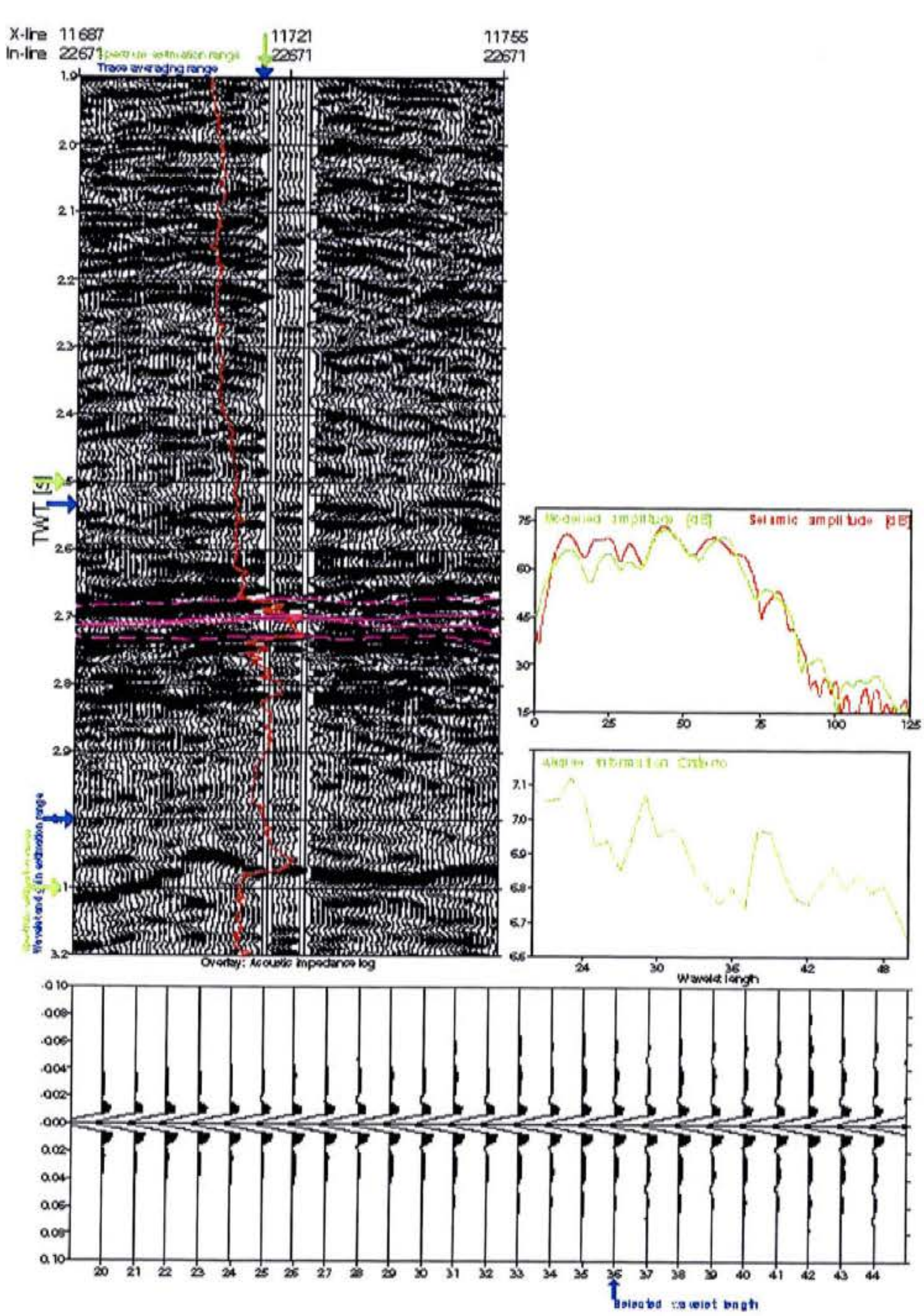

Fig. 10. Near offset stack: Least squares wavelet estimation in well I-1x.

Left: Synthetic seismic trace obtained by convolution of the optimum wavelet (length 36 samples) with the near offset angle reflectivity log from the well inserted into the seismic data.

Top right: Amplitude spectra in the wavelet estimation window of the seismic trace at the well location and the synthetic seismic trace.

Bottom right: Relative misfit energy, Akaike's FPE, cross-correlation and relative number of parameters for the wavelet suite. Left-hand axis refers to the curves of relative misfit energy and Akaike's FPE. Right-hand axis refers to the curves of cross-correlation and relative number of parameters.

Bottom: Wavelet suite. The lengths of the predicted wavelets range from 20 samples to 44 samples (80 ms to 176 ms, horizontal axis).

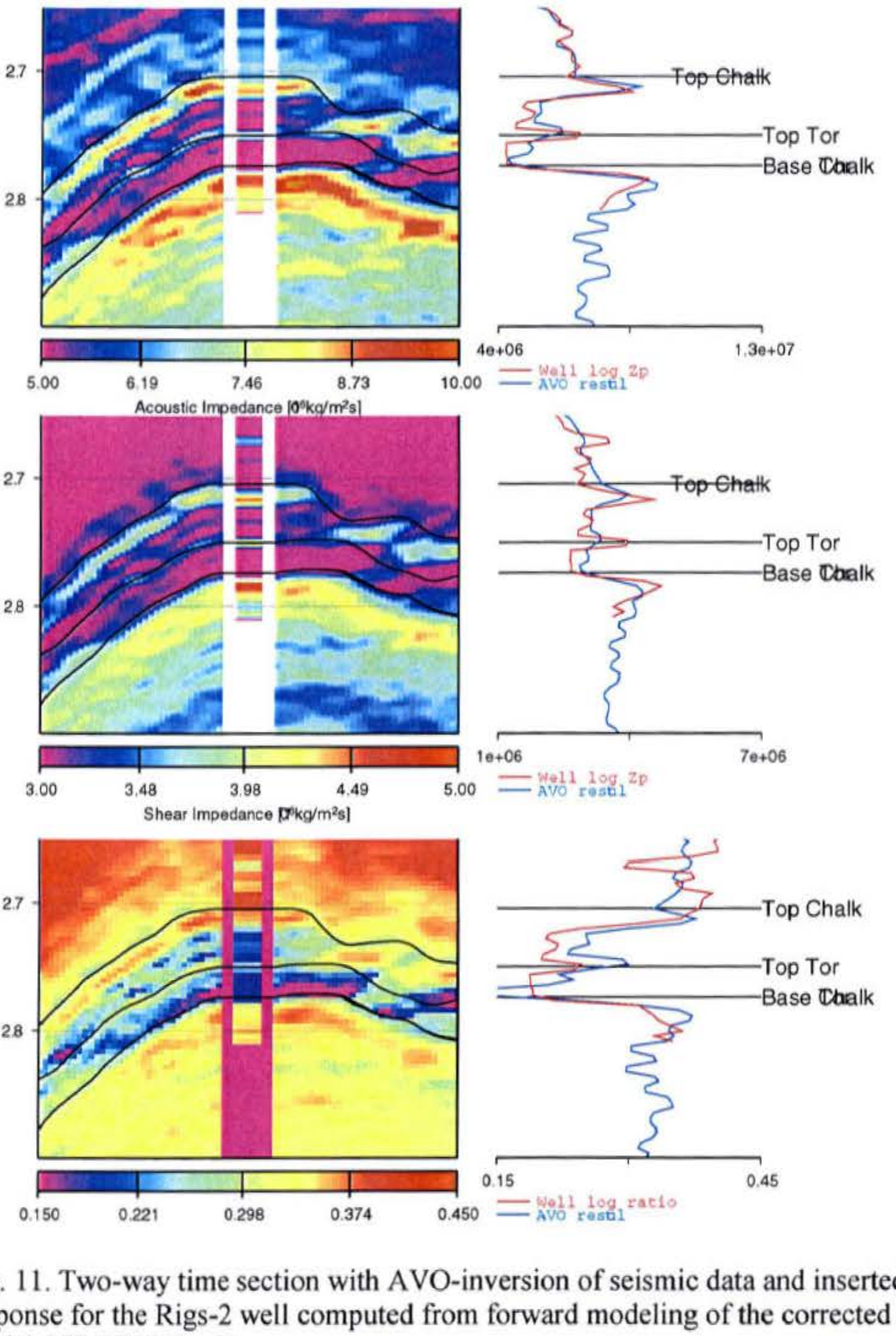

Fig. 11. Two-way time section with AVO-inversion of seismic data and inserted log response for the Rigs-2 well computed from forward modeling of the corrected MUHS model, NE-SW (Fig. 7).

a. Acoustic impedance, b. shear impedance, c. Poisson ratio.

Very good agreement is observed for both acoustic and shear impedance. Note the peaks in the tight zones near top chalk and top Tor, There is good agreement between the log- and AVO-pattern of Poisson's ratio, e.g. the peak at top Tor and the low values within the Tor Formation. This pattern cannot be resolved by the log if the acoustic properties are estimated from the sonic log because the water saturation near the well bore is unkown (Figs 6, 12).

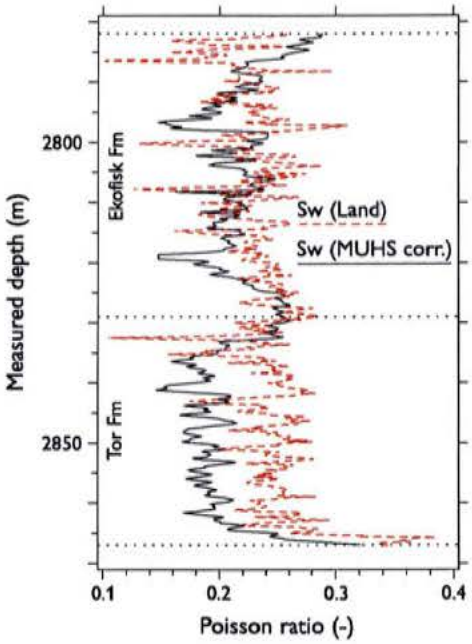

Fig. 12. Poisson's ratio versus measured depth estimated for the virgin zone based on Land's equation and on the corrected MUHS model (eqs. 7, 8). Forward modeling based on the MUHS model results in a low ratio in the high-porous Tor reservoir and pronounced peaks at top Ekofisk and top Tor in agreement with the inverted seismic data (Fig. 11). These features are not captured in the approach based on Land's equation because this model underestimates the flushing of the reservoir.

Intended for submission to Geophysical Prospecting

FLUID SUBSTITUTION IN CHALKS: EFFECTS OF SATURATION SCALES

Gary Mavko and Peter Japsen

ABSTRACT

In this paper we discuss some aspects of ultrasonic fluid substitution in chalks. We find that Gassmann's relations can be used to understand the variations of velocity with saturation in our samples, even though the velocity data are ultrasonic (high frequency). This suggests that in these samples there are no significant high frequency dispersion effects from the squirt-flow or Biot mechanisms that would invalidate the use of the Gassmann's relations. There is, however, evidence for patchy saturation in the ultrasonic data with a characteristic patch size less than 1/10 mm. This is observed in limited Vp and Vs versus Sw data. We also find that fluid substituting to full brine saturation using a modified patchy mixing rule gives velocities more consistent with empirical trends than assuming a fine-scaling mixing rule. It is likely that fine-scale mixing is dominant at logging frequencies in chalks. Another finding is that the dry-rock ultrasonic data tend to be inconsistent, in a Gassmann sense, with data from the water-bearing samples. Specifically, the dry rock velocities are "too fast."

INTRODUCTION

In this paper we discuss some aspects of ultrasonic fluid substitution in chalks. One important finding is that Gassmann's (1951) relations can be used to understand the variations of velocity with saturation in our samples, even though the velocity data are ultrasonic (high frequency). This suggests that in these samples there are no significant high frequency dispersion effects from the squirt-flow (Mavko and Jizba, 1991) or Biot (1956) mechanisms that would invalidate the use of the Gassmann's relations. There is, however, evidence for patchy saturation in the ultrasonic data (Domenico, 1975; Dutta and Odé, 1979; Knight and

Nolen-Hoeksema, 1990; Mavko and Nolen-Hoeksema, 1994; Mavko and Mukerji, 1998). Patchy saturation is another form of velocity dispersion, and its presence means that care must be taken to choose an appropriate mixing law for the air-water mix in the rocks, before applying Gassmann's relations.

Another finding is that the dry-rock ultrasonic data tend to be inconsistent, in a Gassmann sense, with data from the water-bearing samples. Specifically, the dry rock velocities are "too fast," an observation reported by other workers for limestones (Cadoret, 1993) and sandstones (Murphy, 1982; Knight and Dvorkin, 1992; Tutuncu, 1992). Third, we find evidence of patchy saturation during drainage of chalk samples at water saturation above c. 70% and ultrasonic frequencies. This corresponds to a characteristic patch size of much less than 1 mm for the chalk and it is thus likely that fine-scale mixing is dominant at logging frequencies in chalks.

We will begin with short discussions of previous observations of patchy saturation and anomalous dry-rock data. Then, we present evidence for saturation effects in our chalk data.

PREVIOUS OBSERVATIONS OF PATCHY SATURATION BEHAVIOR IN SANDSTONES AND LIMESTONES

It is now well-recognised (e.g. Mavko and Mukerji, 1998) that in rocks with mixed fluid phases, velocities depend not only on saturations but also on the spatial distributions of the phases within the rock. When the gas, oil, and brine phases are mixed uniformly at a very small scale in a rock, the different wave-induced increments of pore pressure in each phase will have time to diffuse and equilibrate during a seismic period. In this case we can replace the mixture of fluids with an average fluid whose bulk modulus, K_{fluid}, is given by the Reuss (1929) iso-stress average:

$$\frac{1}{K_{fluid}} = \frac{S_{water}}{K_{water}} + \frac{S_{oil}}{K_{oil}} + \frac{S_{gas}}{K_{gas}} \tag{1}$$

where $K_{fluid}, K_{oil}, K_{gas}$ are the bulk moduli of the individual phases and $S_{fluid}, S_{oil}, S_{gas}$ are the saturations. This K_{fluid} can, in turn, be substituted into Gassmann's relations to describe the effect of the fluid mix on the overall rock bulk modulus:

$$\frac{K_{sat}}{K_{mineral}-K_{sat}}=\frac{K_{dry}}{K_{mineral}-K_{dry}}+\frac{K_{fluid}}{\phi\left(K_{mineral}-K_{fluid}\right)};\quad \mu_{sat}=\mu_{dry}$$

where K_{dry}, K_{sat}, and $K_{mineral}$ are the bulk moduli of the saturated rock, the dry rock and the mineral; μ_{dry} and μ_{sat} are dry and saturated rock shear moduli; and ϕ is the porosity.

Mavko and Mukerji (1998) showed that equation (1) represents a lower bound; i.e., a fine scale mix of pore fluids gives the lowest possible rock bulk modulus (or P-velocity) for a given rock and given set of saturations. An important assumption of equation (1) is that the pore pressure increments are equal in the gas, oil, and water phases – hence, the name "iso-stress" average.

An approximate upper bound (Mavko and Mukerji, 1998) on velocity (neglecting very high frequency effects such as squirt-flow) can be approximated using a Voigt average fluid mix:

$$K_{fluid}=S_{water}K_{water}+S_{oil}K_{oil}+S_{gas}K_{gas} \tag{2}$$

and putting the resulting K_{fluid} into Gassmann's relations. The Voigt average is sometimes called the "iso-strain" average, which in a pure mixture of fluids is not particularly relevant. However in a porous medium, widely segregated fluid phases can be shown to mimic isostrain behaviour (Mavko and Mukerji, 1998).

What do we mean by a "fine-scale" mix of the fluid phases? A simple diffusion analysis suggests that during a seismic period, pore pressures can equilibrate over spatial scales smaller than $L_c \approx \sqrt{\kappa K_{fluid} / f\eta}$, where f is the seismic frequency, κ is the permeability, and η *and* K_{fluid} are the viscosity and bulk modulus of the most viscous fluid phase (Mavko and Mukerji, 1998; Sengupta, 2000). If the saturation scales are finer than $\sim L_C$, then diffusion allows the pore pressures in the various phases to be equilibrated, and equation (1) should be valid. In contrast, saturations that are heterogeneous over scales larger than $\sim L_C$ will have wave-induced pore pressure gradients that cannot equilibrate, and equation (1) will fail. We refer to this latter state as "patchy saturation." Table 1 illustrates a few examples of this scaling.

Table 1. Diffusion length or patch size for some values of permeability and seismic frequency (viscosity, η= 1 cPoise ; bulk modulus, K_{fluid} = 2.2 GPa).

Frequency, f	Permeability, κ	L_c
700 kHz	1 mD	0.0004 m
100 Hz	1000 mD	0.3 m
100 Hz	100 mD	0.1 m
100 Hz	1 mD	0.01 m
10 Hz	1000 mD	1.0 m

Examples of Patchy Behaviour

Figure 1 shows low frequency P- and S-wave velocities versus water saturation for Massilon sandstone, measured by Murphy (1982) using the resonant bar technique. The shear velocity V_S was measured in torsional mode at frequencies of 385-653 Hz, and extensional wave velocity V_E was measured at 599-997 Hz. P-wave velocity V_P was calculated from V_S and V_E . Saturations were achieved through drying, beginning with a fully saturated state. These data agree quite well with the fine-scale mixing model, i.e., K_{fluid} from equation (1) into Gassmann's equation, which is shown plotted. Exceptions are the data very close to Sw=0, which we discuss below. Some estimates of the velocities for patchy saturation are plotted for comparison, including the method based on the Voigt average fluid modulus, described above. The curve labelled as the "patchy upper bound" is another approximation, based on the Hill average, and discussed in detail in Mavko and Mukerji (1998) and Sengupta (2000).

Figure 2 shows low frequency P- and S-wave velocities versus water saturation for Estaillades limestone, measured by Cadoret (1993), also using the resonant bar technique, near 1 kHz. The closed circles show data measured during increasing water saturation via an imbibition process combined with pressurisation and depressurisation cycles designed to desolve trapped air. As with Murphy's Massilon sandstone data, these imbibition data fit the fine-scaling mixing (lower bound) model very well, except for the few data points near Sw=0.

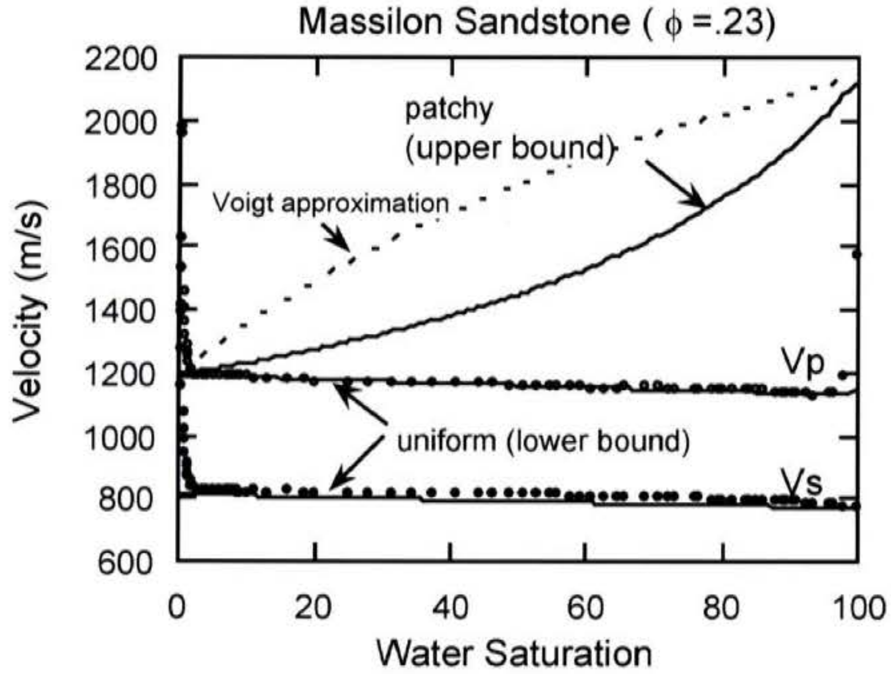

Figure 1. Low frequency data from Murphy (1982), showing excellent agreement with the uniform effective fluid model (lower bound).

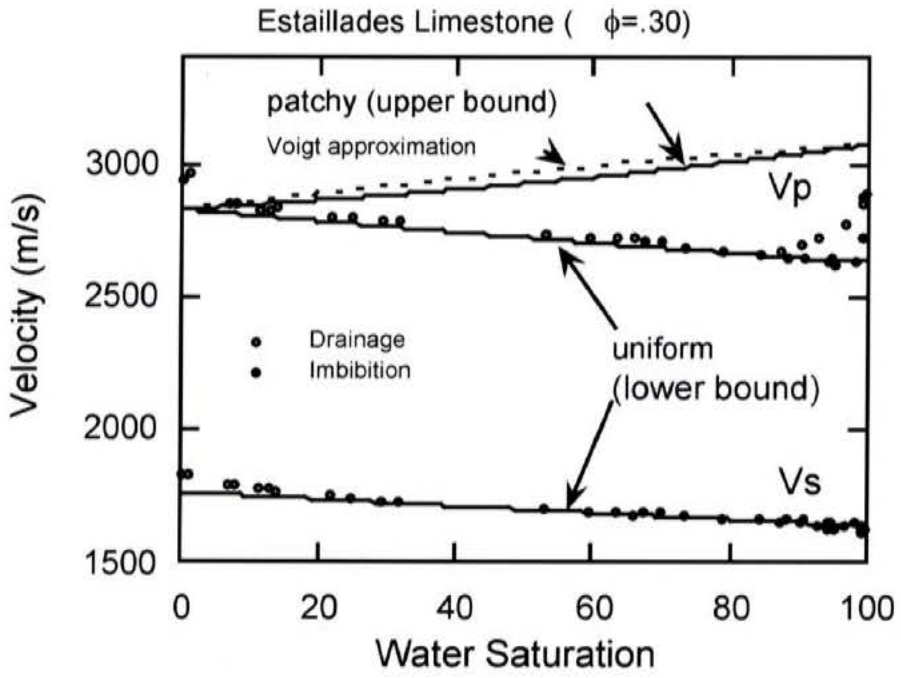

Figure 2. Low frequency data from Cadoret (1993). Closed circles show data during imbibition and are in excellent agreement with the uniform effective fluid model (lower bound). Open circles show data during drainage, indicating heterogeneous or patchy fluid distributions for saturation greater than about 80%. The Voigt approximation does a good job of estimating the patchy upper bound.

The open circles (Figure 2) show data measured during drainage. At saturations greater than 80%, the V_P fall above the uniform saturation line but below the patchy upper bound, indicating a heterogeneous or somewhat patchy fluid distribution. The V_S data fall again on the uniform fluid line, as expected, since patchy saturation is predicted to have no effect on V_S. On the other hand, other sources of dispersion, such as the Biot and squirt mechanisms (Mavko and Jizba, 1991) would cause both V_P and V_S to lie above the uniform saturation lines. Cadoret (1993) used X-ray CAT scans to confirm that, indeed, the imbibition process created saturations uniformly distributed at a fine, sub-millimetre scale, while the drainage process created saturation patches at the several centimetre scale. Using the measured permeability of ~250 mD, we estimate a critical diffusion length $L_c \approx 2$ cm. Thus we believe that during initial drainage, large centimetre-scale patches appeared, causing V_P to fall near the upper bound. With decreasing saturation, the characteristic patch size quickly decreased to less than $L_c \approx 2$ cm, causing V_P to fall near the lower bound at saturations less than 80%.

Figure 3 shows the velocities for Estaillades limestone from Figure 2, with an additional set of velocities measured at 50 kHz. Because the frequency is much higher, we expect the 50 kHz velocities to be contaminated by the ultrasonic dispersion mechanisms; as a result, they exceed the low frequency bounds at saturations > 80%. At 100% saturation, the distinction between patchy and uniform disappears. Hence, using the method of Winkler (1986), we take the difference between the measured V_P and the Gassmann predicted V_P at full saturation as an estimate of the high frequency dispersion, $\Delta V_P \approx 150\ m/s$. Subtracting this 150 *m/s* (~5%) from each of the data leaves a rough estimate of the patchy effect, replotted as the "corrected" values.

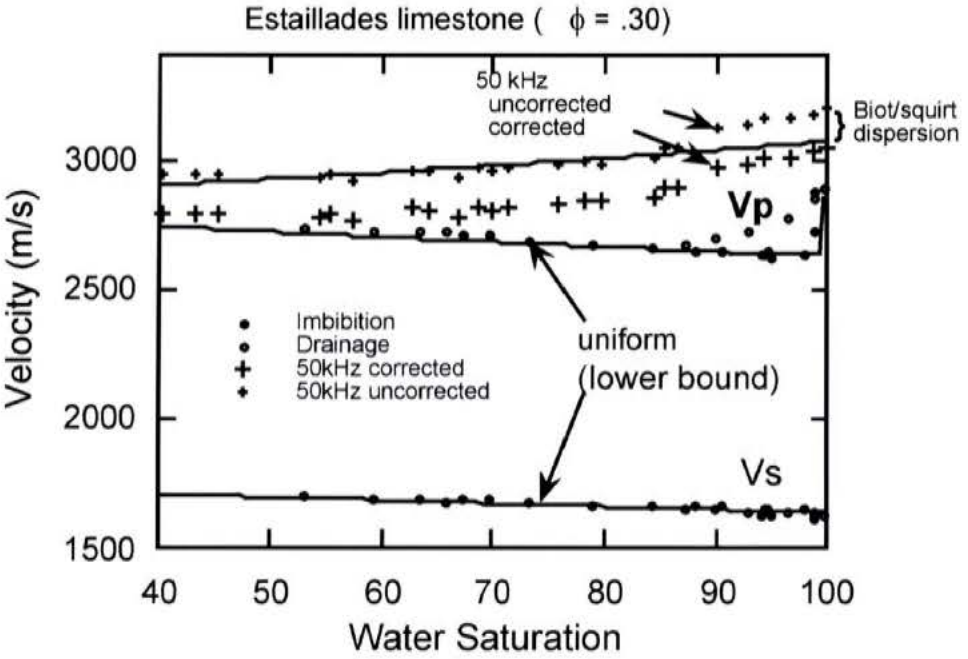

Figure 3. Data from Cadoret (1993). "+" symbols show high frequency data at 50 kHz. The corrected velocities are obtained by removing high frequency dispersion effects estimated from the measured and Gassmann predicted velocities at 100% saturation. Open and closed circles are resonant bar data, near 1 kHz.

In summary, we interpret the three sets of data in Figure 3 as follows: the low frequency imbibition data, falling along the lower bound are consistent with saturations always uniform at scales smaller than $L_c \approx 2$ cm; the low frequency drainage data are consistent with patches comparable to $L_c \approx 2$ cm at water saturations above 80% and smaller than $L_c \approx 2$ cm at lower water saturations; the ultrasonic data are consistent with patches larger than $L_c \approx 0.3$ cm at saturations greater than 60%; furthermore, the ultrasonic data show evidence of high frequency dispersion of the type that might be caused by the squirt-flow or Biot mechanisms.

The Problem With Very Dry Data

Figure 4 illustrates other features of the saturation problem. The data are from the same limestones as in Figures 2 and 3, measured by Cadoret (1993) using the resonant bar technique at 1 kHz. The very dry (dried in a vacuum) rock velocity is approximately 2.95 km/s. Upon initial introduction of moisture (water), the velocity drops by about 4%. This apparent softening of the rock occurs at tiny volumes of pore fluid, equivalent to a few mono-layers of liquid if distributed uniformly over the internal surfaces of the pore space. These amounts are hardly sufficient for a fluid dynamic description as in the Biot-Gassmann theories. Similar behaviour has been reported in sandstones by Murphy (1982), Knight and Dvorkin (1992), and Tutuncu (1992).

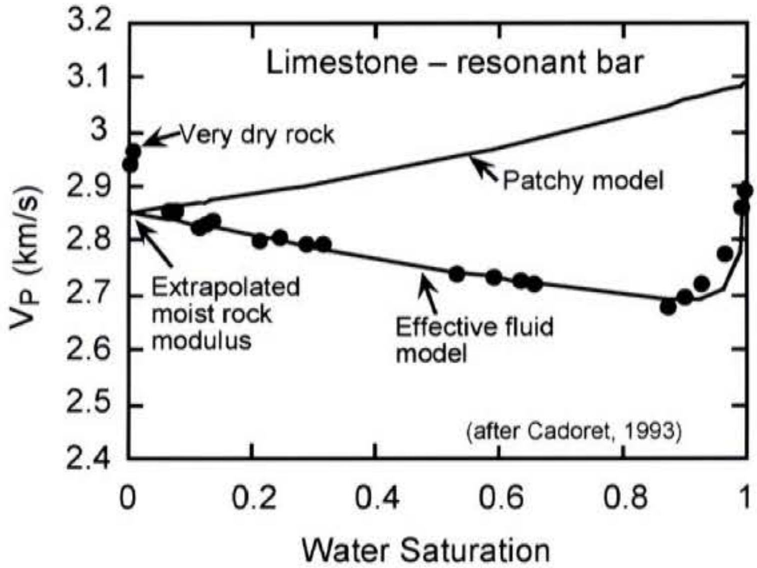

Figure 4. Velocity versus water saturation for a limestone measured at resonant bar frequencies (~1 kHz), from Cadoret (1993). The abrupt change of velocity at very low saturations has been attributed to the disruption of surface forces with the first few monolayers of water.

This velocity drop has been attributed to softening of cements (sometimes called "chemical weakening"), to clay swelling, and to surface effects. In the latter model, very dry surfaces attract each other via cohesive forces, giving a mechanical effect resembling an increase in effective stress. Water or other pore fluids disrupt these forces. A fairly thorough treatment of the subject is found in the papers of Sharma and Tutuncu (Sharma and Tutuncu, 1992; Tutuncu, 1992; Tutuncu and Sharma, 1992; Sharma et al., 1994).

After the first few percent of water saturation, additional fluid effects are primarily elastic and fluid dynamic and are amenable to analysis, for example, by the Biot-Gassmann and squirt models.

A number of authors (Cadoret, 1993; Murphy et al., 1991) have pointed out that classical fluid mechanical models such as the Biot-Gassmann theories perform poorly when the measured very dry rock values are used for the "dry rock" or "dry frame." These models can, however, be fairly accurate if the extrapolated "moist" or "wet" rock modulus (Figures 4 and 5) is used instead. For this reason, and to avoid the artefacts of ultra-dry rocks, it is often recommended to use samples that are at room conditions or that have been prepared in a constant humidity environment as estimates of the Gassmann "dry frame" data, and to not use the vacuum dry data.

Figure 5 shows a similar example for a clean sandstone, from Murphy (1982). Here the jump in velocity at very dry conditions is enormous. Again, using the very dry data in fluid substitution calculations would give nonsense results. However, using the "wet intercept", or measured data at ~ 1% water saturation gives Gassmann-consistent results.

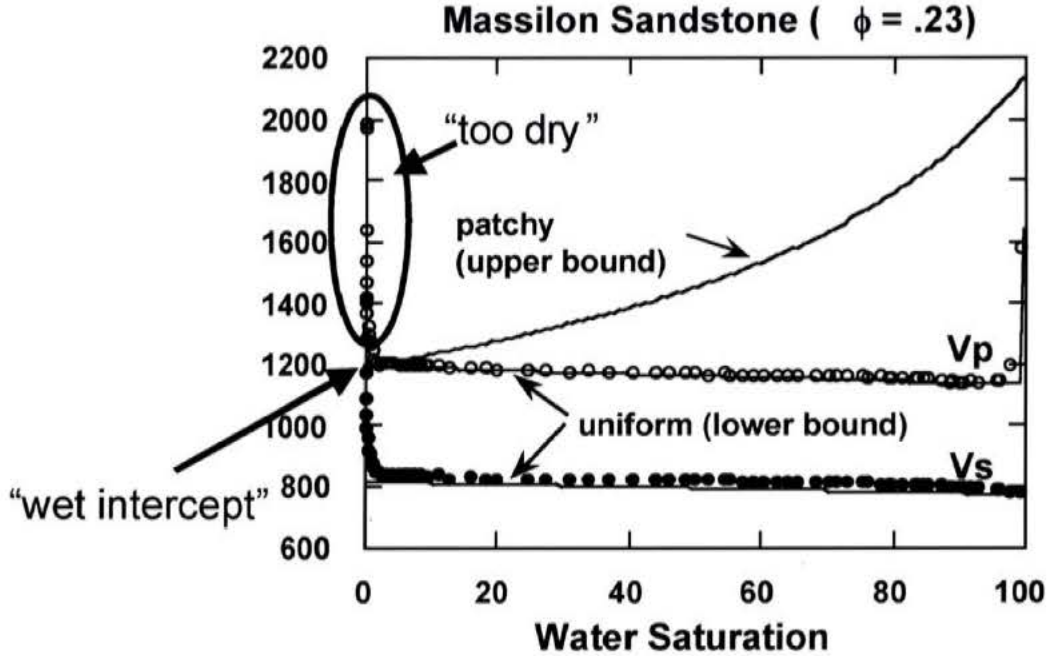

Figure 5. Velocity versus water saturation for a sandstone measured at resonant bar frequencies (~1 kHz), from Cadoret (1982). The abrupt change of velocity at very low saturations has been attributed to the disruption of surface forces with the first few monolayers of water.

Chalk Data

Ultrasonic measurements (700 kHz) were carried out on 77 dry chalk samples and 54 samples saturated with water; out of these 51 samples were investigated under both dry and saturated conditions. The chalk samples were from the Dan and South Arne fields in the Danish North Sea (22 from Danian Ekofisk Formation and 55 from the Maastrichtian Tor Formation. To prevent over-dry conditions, the samples were kept at room-moisture for two months after being dried at 110°C. The water saturation in the saturated plugs was generally between 97% and 103% (related to minor weight errors), but low permeability prevented total saturation in three Ekofisk and one Tor samples (Sw=92%–95%; plug numbers B003, B102, C022). Six Ekofisk samples were characterised by having regained high water content after drying, and this may be indicative of high clay content (Sw=7%–12%, plug numbers B003, B0010, B012 B0036; Sw=30%–34%, plug numbers B007, B008 but these samples fell apart when they were saturated). The remaining 71 dry samples had a mean water saturation of 0.3%. Measurements were also carried out under partially saturated conditions during drainage on two samples (Sw=25%, 50%, 75%; plug numbers C062, C100).

P- and S-wave velocities were determined from measured sample lengths (c. 2 cm) and automated readings of travel times for the maximum amplitude in the first major loop of first arrival events. The maximum amplitude was used rather than the first break because it is less affected by noise. Part of the plugs were measured at 25, 50 and 75 bar hydrostatic confining pressure where 75 bar corresponds to the magnitude of the effective stress at reservoir conditions. The increase of velocity with pressure was found to be limited (*c.* 4% when going from 25 to 75 bar) and velocities were thus only measured at 75 bar for the remaining part of the samples. Values of density, ρ [g/cm^3], grain density, ρ_{gr}, porosity, ϕ [-] and permeability, k [Darcy] were also determined.

Evidence for patchiness On Ultrasonic Chalk Data

Figure 6 shows an example of ultrasonic P- and S-wave velocities vs. water saturation for one of our core plugs. The dots are the ultrasonic measurements, and the solid curves are the predicted velocities assuming fine-scale mixing, equation (1).

For both the P- and S-wave velocities in Figure 6, the measured zero saturation values are "too dry" and "too fast" relative to the other saturation points, similar to what we discussed in for the limestone in Figure 4 and the sandstone in Figure 5. Hence, for our calculations we followed the procedure of Cadoret (1993) and inferred values for "nearly dry" Vp and Vs by extrapolating the data points back to zero saturation. The resulting points are used as the dry frame velocities in Gassmann's relations. We predict the velocities at higher water saturation values relative to the nearly dry values using the fine-scale mixing assumption, using equation (1) to get a K_{fluid} for the air-water mix, and then put K_{fluid} into Gassmann's relations. The results are shown by the solid black curves. Similar to Figure 3 for limestones, we see here that the S-wave velocities are modelled very well using the fine-scale mixing law; the P-wave velocities agree with fine-scale mixing at low saturations, but show evidence of patchiness for Sw greater than about 70%. The characteristic patch size for this sample becomes only 0,04 mm (Table 1), and this suggests that fine-scale mixing will be dominant at the lower frequencies used in sonic logging.

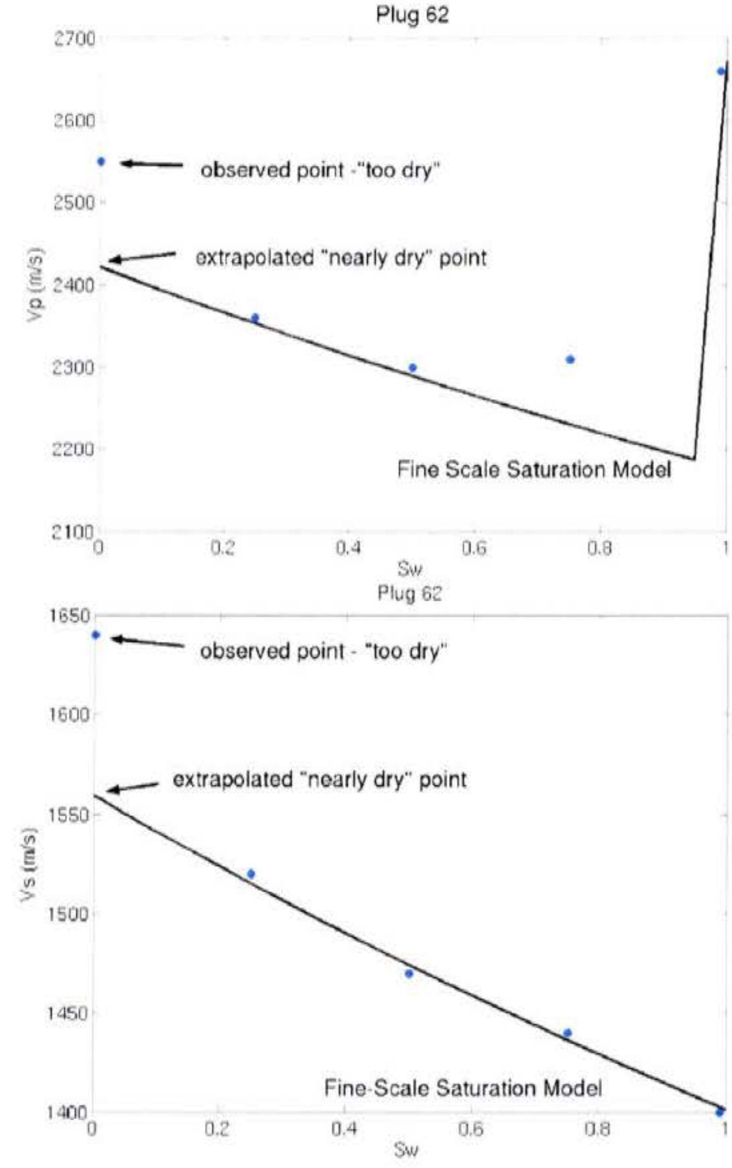

Figure 6. Comparison of ultrasonic measurements of velocities vs. saturation on a North Sea chalk sample, compared with the fine-scale mixing model, for core plug 62. ϕ=40%, permeability = 1.4 mDarcy.

Fluid Substitution to Full Water Saturation

In total, we had ultrasonic data on 77 chalk core plugs. In most cases only two saturations were available, typically Sw near zero or near one, but seldom completely dry or completely saturated. In order to look for systematics in Vp vs. porosity, Vs versus porosity, and Vp versus

Vs, it is desirable to take all measured velocities to a common fluid saturation. In our case, we prefer complete water saturation, since the dry rock velocities are problematic.

Since we have evidence of patchiness in the velocity vs. saturation data (Figure 6), the question is, what fluid mixing law is appropriate for the fluid substitution to full saturation? In this section, we compare the results using the Reuss average fine-scale mixing rule, equation (1), and a "modified patchy" mixing rule, published by Brie et al (1995):

$$K_{fluid} = \left(K_{water} - K_{gas}\right) S^{e}_{water} + K_{gas} \tag{3}$$

where K_{fluid} is the bulk modulus of the gas-water mix, K_{water} and K_{gas} are the moduli of the water and gas phases, and S_{water} is the water saturation. The exponent e is an empirical parameter. When $e=1$, equation (3) reduces to the Voigt model, equation (2) for a patchy gas-water mix. When e becomes very large, $K_{fluid} \rightarrow K_{gas}$, somewhat resembling the behaviour of a Reuss average, equation (1), for a fine-scale gas-water mix. Hence, equation (3) is an interpolation between fine-scale and patchy mixing behaviour. The Brie mixing rule, with a typical value of $e=3$, is plotted in Figure 7, compared with the Voigt and Reuss curves. The Brie mixing model captures some of the behaviour observed in Figures 3 and 6 – essentially fine-scale mixing behaviour at low water saturations, and patchiness at high water saturations.

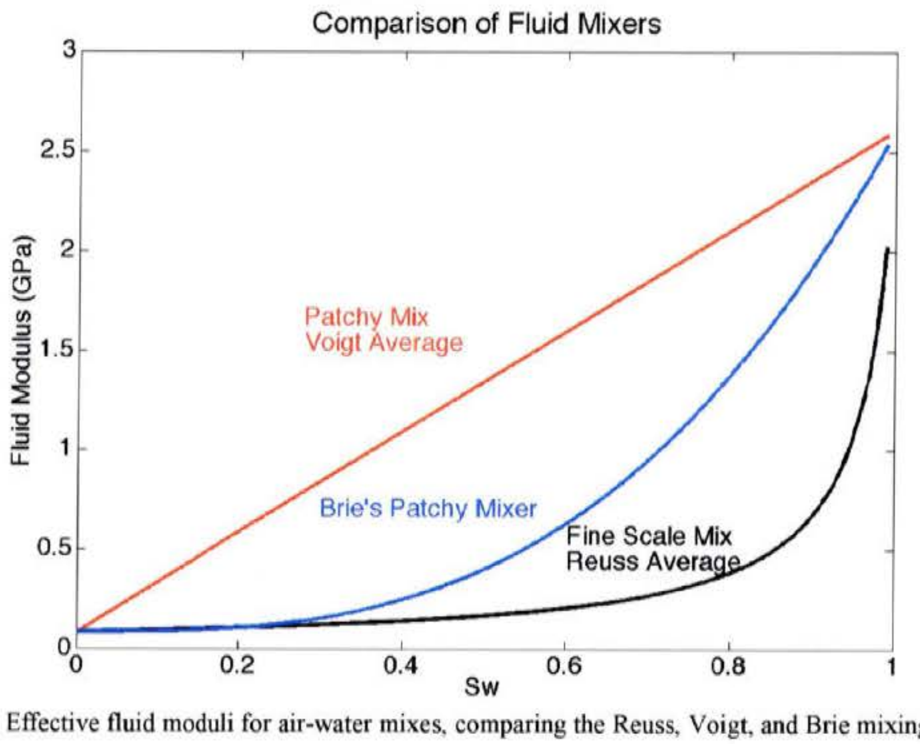

Figure 7. Effective fluid moduli for air-water mixes, comparing the Reuss, Voigt, and Brie mixing laws.

Figure 8 shows results of the fluid substitution calculations. At the top, are the measured ultrasonic Vp vs. Vs relative to Greenberg-Castagna (GC) empirical lines (Greenberg and Castagna, 1992), with the original mixed saturations. The solid green line is the GC empirical trend for water-saturated limestone,, and the dashed green line is for dry carbonates, computed from the GC water-saturated line using the Gassmann relations. The measurements cluster into two trends, mimicking the empirical lines, though at systematically smaller Vp/Vs ratios. The middle plot of Figure 8 shows the results of fluid substitution to 100% water using the Reuss (fine-scale) mixing assumption. We see that all of the nearly dry data are now falling near (slightly below) the empirical trend, though many of the high-Sw data are now overcorrected, falling well above the empirical trend for water-saturated limestone. Effectively, the data still fall along two trends. Finally, the bottom plot in Figure 8 shows the results of fluid substitution to 100% water using the Brie mixing model, with e=3. We see that almost all of the transformed points are now tightly clustered along a very narrow trend, just below the limestone trend. Similar results would have been achieved if had applied Voigt mixing-law to the high-Sw data,

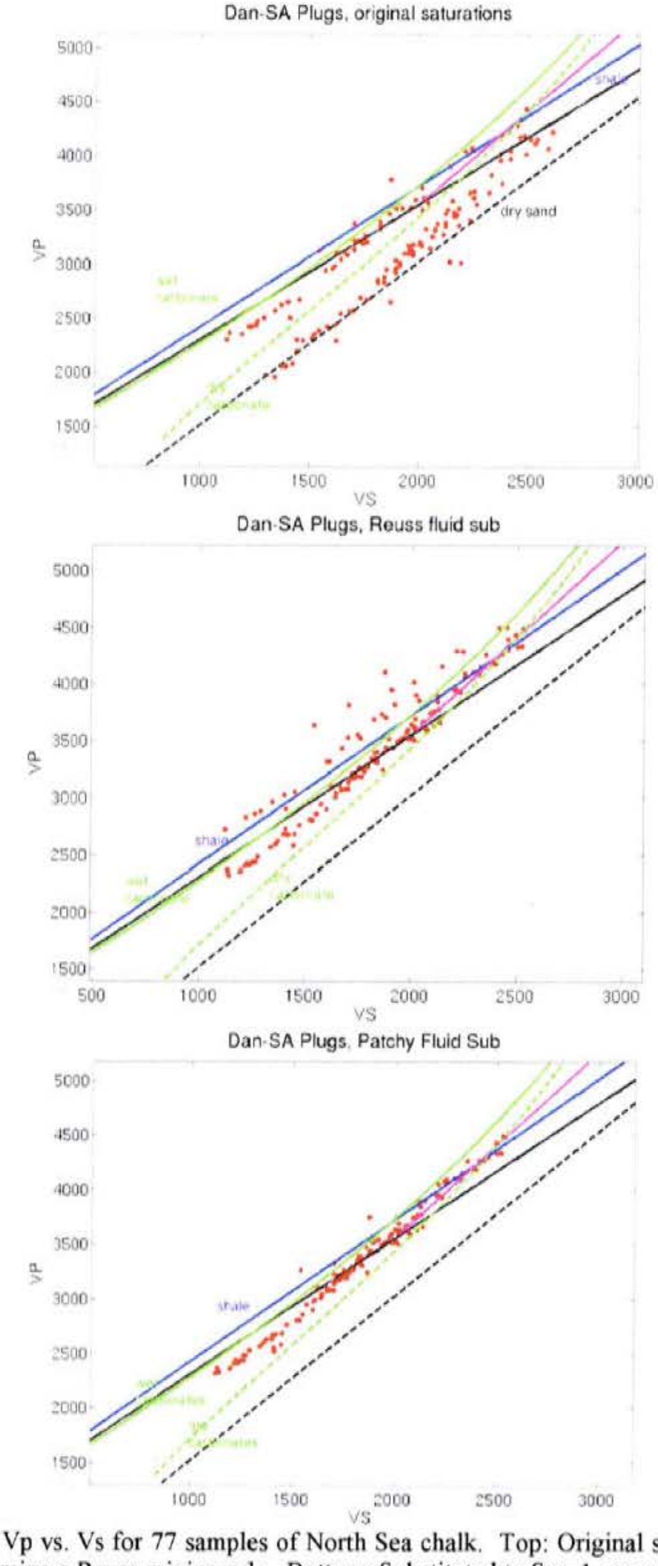

Figure 8. Ultrasonic Vp vs. Vs for 77 samples of North Sea chalk. Top: Original saturations. Middle: Fluid Substituted to Sw=1, assuming a Reuss mixing rule. Bottom: Substituted to Sw=1, assuming a patchy Brie mixing rule with e=3. Empirical relations for unspecified limestone from Greenberg and Castagna (1992). The trend for dry limestone is derived from the Castagna line using Gassmann's relations..

Figure 9 again shows the results of fluid substitution to 100% water using the Brie mixing model, but now comparing two salinities. The red dots are the same as in Figure 8 where the water is assumed to have very low salinity, essentially fresh water. The black dots correspond to reservoir fluids (Kfluid = 2.96 GPa and Rhofluid = 1.35 g/cc). Now we see that the velocities with the representative reservoir fluids fall very close to the GC empirical trend for limestone. The brine salinity and the lithology of the samples studied by Greenberg-Castagna is, however, not known, and the lithology may well be different from the pelagic chalk of the North Sea samples.

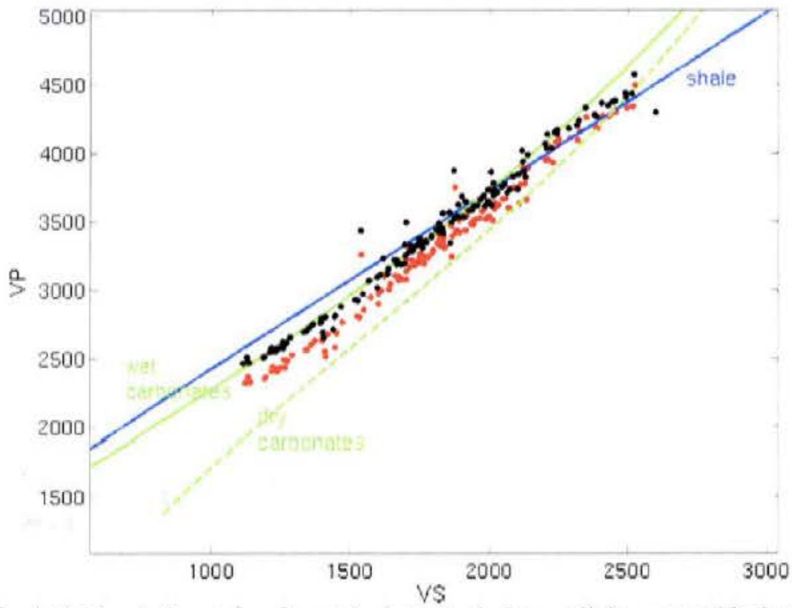

Figure 9. Fluid substitution to Sw=1 for ultrasonic data. Red: Low salinity water; Black: high salinity.

Figure 10 shows results of the same fluid substitution calculations as in Figure 8, but now plotted as Vp/Vs vs. 1/Vp, a typical display for detecting fluids. At the top are the data at original mixed saturations, again relative to Greenberg-Castagna empirical lines. The solid green line is the empirical trend for water-saturated carbonates and the dashed green line is for dry carbonates. Again, the measurements cluster into two trends, corresponding to high and low water saturations. The middle plot of Figure 10 shows the results of fluid substitution to 100% water using the Reuss (fine-scale) mixing assumption. Again, we see that the high-Sw data are overcorrected, falling well above the empirical trend for water. Finally, the bottom plot in Figure 8 shows the results of fluid substitution to 100% water using the Brie mixing model, with e=3. We see that nearly all of the transformed points are tightly clustered along a very narrow trend, below Castagna's limestone trend.

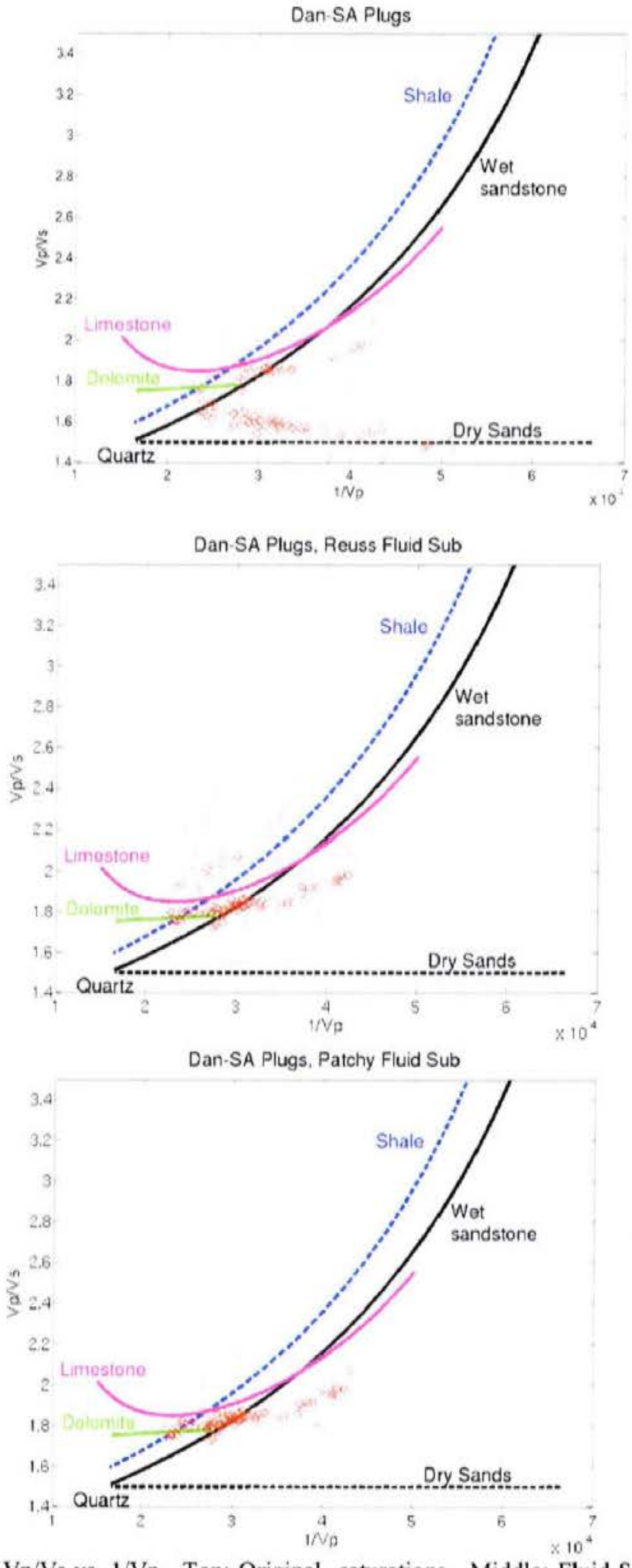

Figure 10. Ultrasonic Vp/Vs vs. 1/Vp. Top: Original saturations. Middle: Fluid Substituted to Sw=1, assuming Reuss mixing. Bottom: Substituted to Sw=1, assuming patchy Brie mixing rule.

SUMMARY

In this paper we discussed some aspects of ultrasonic fluid substitution in chalks. We found that Gassmann's (1951) relations can be used to understand the variations of velocity with saturation in our samples, even though the velocity data are ultrasonic (high frequency). This suggests that in these samples there are no significant high frequency dispersion effects from the squirt-flow or Biot (1956) mechanisms that would invalidate the use of the Gassmann's relations. There is, however, evidence for patchy saturation in the ultrasonic data with a characteristic patch size less than 1/10 mm. This is observed in limited Vp and Vs versus Sw data. We also find that fluid substituting to full brine saturation using a modified patchy mixing rule gives velocities more consistent with empirical trends than assuming a fine-scaling mixing rule. It is likely that fine-scale mixing is dominant at logging frequencies in chalks.

Another finding is that the dry-rock ultrasonic data tend to be inconsistent, in a Gassmann sense, with data from the water-bearing samples. Specifically, the dry rock velocities are "too fast."

ACKNOWLEDGEMENT

These results are part of the outcome of the energy research project Rock Physics of Impure Chalk which was sponsored by the Danish Energy Program (EFP-2001), Amerada Hess A/S and Dong E&P.

REFERENCES

Batzle, M. and Wang, Z., 1992, Seismic properties of pore fluids, *Geophysics*, 57, 1396-1408.

Biot, M. A., 1956, Theory of propagation of elastic waves in a fluid saturated porous solid I. Low-frequency range, *J. Acoust. Soc. Amer.*, 28, 168-178.

Cadoret, T., 1993, *Effet de la Saturation Eau/Gaz sur les Propriétés Acoustiques des Roches*, Ph.D. dissertation, University of Paris, VII.

Domenico, S.N., 1976, Effect of brine-gas mixture on velocity in an unconsolidated sand reservoir, *Geophysics*, 41, 882-894.

Dutta, N. C., and Odé, H., 1979, Attenuation and dispersion of compressional waves in fluid-filled porous rocks with partial gas saturation (White model) – Part 1: Biot theory, Part II: Results, *Geophysics*, 44, 1777-1805.

Gassmann, F., 1951, Über die elastizität poröser medien, *Vier. der Natur Gesellschaft:* 96, 1-23.

Greenberg, M.L. and Castagna, J.P., 1992, Shear-wave velocity estimation in porous rocks: theoretical formulation, preliminary verification and applications, *Geophysical Prospecting*, 40, 195-209.

Knight, R., and Nolen-Hoeksema, R., 1990, A laboratory study of the dependence of elastic wave velocities on pore scale fluid distribution, *Geophys. Res. Lett.*, 17, 1529-1532.

Knight, R., and Dvorkin, J., 1992, Seismic and electrical properties of sandstones at low saturations, *J. Geophys. Res.*, 97, 17425-17432.

Mavko, G., and Jizba, D., 1991, Estimating grain-scale fluid effects on velocity dispersion in rocks, *Geophysics*, 56, 1940-1949.

Mavko, G., and Nolen-Hoeksema, R., 1994, Estimating seismic velocities in partially saturated rocks, *Geophysics*, 59, 252-258.

Mavko, G. and Mukerji, T., 1998, Bounds on low frequency seismic velocity in partially saturated rocks, Geophysics, vol 63., no. 3, pp 918-924.

Murphy, W.F. III, 1982, *Effects of microstructure and pore fluids on the acoustic properties of granular sedimentary materials*, Ph.D. dissertations, Stanford University.

Reuss, A., 1929, Berechnung der Fliessgrense von Mischkristallen, *Zeitschrift fur Angewandte Mathematik und Mechanik*, 9, 49-58.

Sengupta, M. 2000, Integrated rock physics and flow simulation to reduce uncertainties in seismic reservoir characterisation, Ph.D. Dissertation, Stanford University.

Sharma, M.M., and Tutuncu, A.N., 1994, Grain contact adhesion hysteresis: a mechanism for attenuation of seismic waves, *Geophys. Res. Lett.*, 21, 2323-2326.

Sharma, M.M., Tutuncu, A.N., and Podia, A.L., 1994, Grain contact adhesion hysteresis: a mechanism for attenuation of seismic waves in sedimentary granular media, *Extended Abstracts SEG 64th Annual Meeting*, Los Angeles, 1077-1080.

Tutuncu, A.N., 1992, *Velocity Dispersion and Attenuation of Acoustic Waves in Granular Sedimentary Media*, Ph.D. Dissertation, The University of Texas at Austin.

Tutuncu, A.N., and Sharma, M.M., 1992, The influence of grain contact stiffness and frame moduli in sedimentary rocks, *Geophysics*, 57, 1571-1582.

White, J. E., 1975, Computed seismic speeds and attenuation in rocks with partial gas saturation, *Geophysics*, 40, 224-232.

Winkler, K., 1986, Estimates of velocity dispersion between seismic and ultrasonic frequencies, *Geophysics*, 51, 183-189.

Modelling seismic response from North Sea Chalk reservoirs resulting from changes in burial depth and fluid saturation

O. V. Vejbæk[1], R. Rasmussen[1], P. Japsen[1],
J. M. Pedersen[2], I. L. Fabricius[3] and G. Marsden[4]

March 17, 2003

Intended for submission to Petroleum Geology conference, London, 2003.
[1] Geological Survey of Denmark and Greenland, Ministry of the Environment (GEUS), Østervoldgade 10, DK-1350 Copenhagen, Denmark
[2] Ødegaard A/S, Titangade 15, DK-2200 Copenhagen N, Denmark
[3] Technical university of Denmark, (DTU)
[4] Amerada Hess Aps, Østergade 26B, DK-1100 Copenhagen K, Denmark

Abstract

Changes in seismic response caused by changes in degree of compaction and fluid content in North Sea Chalk reservoirs away from a well bore are investigated by forward modelling. The investigated seismic response encompasses reflectivity changes, AVO and acoustic impedance. Synthetic seismic sections, impedance cross sections and AVO response are presented as calculated on the basis of selected wells from the South Arne and Dan Fields, Danish North Sea and compared to field records.

The two main variables to use for seismic response prediction away from the well bore is depth of burial (changes in effective stress) and changes in hydrocarbon saturation (Fig. 0). Three main modelling tools are used for the modelling: 1) Rock physics, 2) Saturation modelling and 3) Compaction/de-compaction modelling.

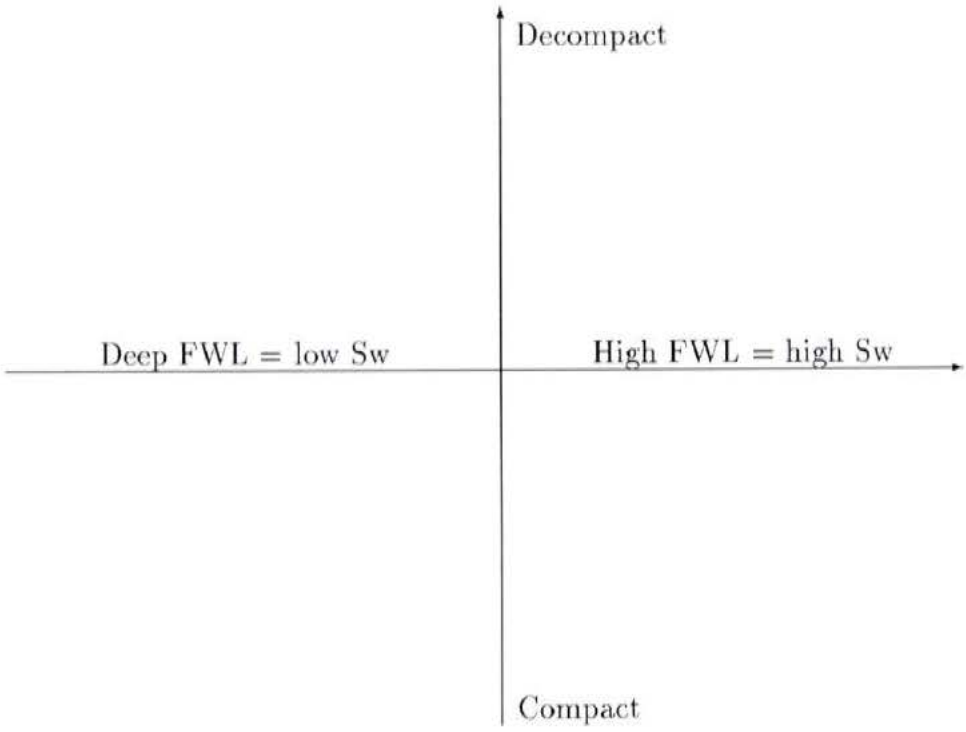

Figure 0: Main variables to investigate away from a well bore are changes in degree of compaction, and changes in HC saturation. The latter is obtained through saturation height modelling via the free water level (FWL)

Rock physics theory is applied to obtain all necessary parameters for the complete set of elastic parameters for the application of the Zoeppritz equations. The challenge is not only to predict the shear velocity, but also to account for the changes in fluid content via application of the Gassmann equation. An approach akin to the one suggested for the Ekofisk Field by Walls et al. (1998) is applied for the prediction of changes in degree of compaction.

Hydrocarbon saturation in North Sea Chalk is strongly affected by capillary forces due to the small scale of the pores and transition zones in the order of 50 m are not uncommon. For this reason, potent saturation modelling is needed in order create realistic input for the seismic modelling. We use saturation height models similar to the EQR model (Engstrøm 1995), which have proved robust for the prediction of

saturation profiles in Danish Chalk reservoirs.

Compaction modelling relies on simple exponential decay of porosity with depth, where abnormal fluid pressures are accounted for. A new set of compaction parameters is presented. These parameters are based on a study on the North Sea Chalk based on some 850 wells. The parameters appear to be sufficiently fine-tuned to allow fairly precise predictions of abnormal fluid pressures from observed average porosity. Based on this, the relative contribution to porosity preservation by abnormal fluid pressure and early hydrocarbon invasion may be estimated.

Some conclusions based on modelling results include: Reflectivity is correlating with porosity, acoustic impedance is more susceptible to porosity variation than to hydrocarbon saturation, and the poisson ratio may be rather sensitive to hydrocarbon saturation.

Introduction

Zero offset seismic response at a well site may be readily modelled provided reliable calibrated sonic and density logs are available. If shear velocity logs are available amplitude versus offset (AVO) response may also be modelled. However, questions may arise as to what cause changes in the response away from the well site. This paper develop methods for creating forward models of the seismic response away from the well site. The models are developed for North Sea Chalk and applied to two wells: Rigs-2 and M-10x drilled in the South - Arne and Dan fields respectively (Fig. 1). The models are aimed at studying effects of hypothetical changes in degree of compaction and hydrocarbon saturation away from a well bore. We aim to use realistic saturation models, which makes it impossible to study changes in compaction without concurrent changes in hydrocarbon saturation. This is because chalk reservoirs are usually strongly affected by capillary forces which vary with porosity. However, this allows us to study more realistic scenarios.

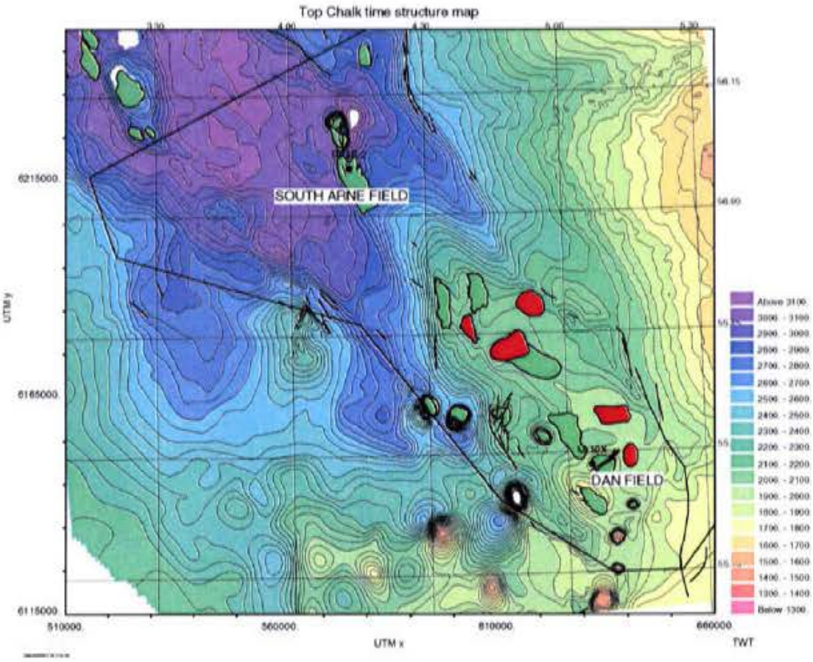

Figure 1: Top Chalk time structure map with locations of wells and fields referred to in this paper.

Compaction modelling

Compaction modelling is done by applying empirical compaction laws where excess fluid pressure is accounted for in a simplistic way. This approach is favoured over deterministic modelling, because pressure development is very hard to model due to inherent uncertainties in the geological development of basinwide hydraulic connectivity.

The goal of the compaction modelling is to calculate porosity logs as a function of changes in burial depth and/or changes in effective stress caused by changes in excess fluid pressure.

Basic assumptions are:

- In the absence of over-pressuring and early diagenesis, porosity decay follows a simple exponential law according to depth.
- Depth is considered a proxy for effective stress in the absence of overpressure.
- Deviations in porosity from the average function are due to very early diagenesis or later over-pressuring for too tight and too porous intervals respectively.
- The overpressure as of today has not dissipated significantly since onset: Overpressure "arrests" porosity as it is at the time of onset.
- Very tight chalk has been cemented shortly after burial, and follows a lower porosity decay curve than standard (This has however proved to be irrelevant for the cases studied here).

The basic approach follows the original proposition by Athy (1930) and is detailed in e.g. Sclater and Christie (1980) and Jensen et al. (1984):

$$\phi = \phi_0 \cdot e^{-a \cdot z} \tag{1}$$

where ϕ_0 is the surface porosity in fractions, z is depth of burial and a is the decay parameter. Some relevant parameters are listed in table 1. This equation can be developed to allow correction of the layer thickness as a function of burial or change in effective stress and thereby preserve rock mass (e.g. Sclater and Christie 1980; Jensen et al. 1984). However, since we are interested in changes away from a well site, and not in what has happened to the succession at the well site, we chose not to change thickness during our compaction/ de-compaction calculations except for the sample subsidence and porosity development curves shown in Figs 3, 4, 5 and 6.

In the case of chalk Sclater and Christie (1980) suggest values of 0.7 for ϕ_0 and $0.00071m^-1$ for a. The reciprocal of the decay parameter, the decay length (reduction to 37% of surface porosity) is equal to 1408.5 m. These values correspond to average normal pressured chalk, but are not consistent with velocity data (Japsen 2000). A compaction trend for North Sea chalk was constructed by transforming the revised normal velocity – depth trend of Japsen (1998, 2000) into a porosity-depth trend. The normal velocity – depth trend for chalk was based on an analysis of data from 845 wells throughout the North Sea Basin and ODP data and burial anomalies relative to the trend were found to agree with estimates of erosion along the basin margins and with measured overpressure in the centre of the basin. The trend was transformed into a porosity – depth trend by converting velocity to porosity via a constructed velocity – porosity trend for chalk (Fig. 2). The velocity – porosity trend was established as a second order polynomial fit to two segments:

a. The modified Hashin – Shtrikman model for chalk with porosities in the range from 10% to 43% suggested by Japsen et al. (2000) and

b. A straight line connecting the endpoint of segment a. at 43% (velocity 2720 m/s) to the parameters corresponding to the critical porosity of chalk at 70% (velocity 1550 m/s).

	ϕ_0	a	$1/a$	source
Neogene	0.56	3.91E-04	2560.2	
Palaeogene	0.71	5.10E-04	1960.0	
Chalk $z < 768.2$	0.70	5.50E-04	1818.2	
Chalk $z > 768.2$	0.97	9.72E-04	1029.3	

Table 1: Compaction constants.

The normal pressure chalk porosity – depth trend derived this way is approximated with a bi-segment exponential model as listed in Table 1.

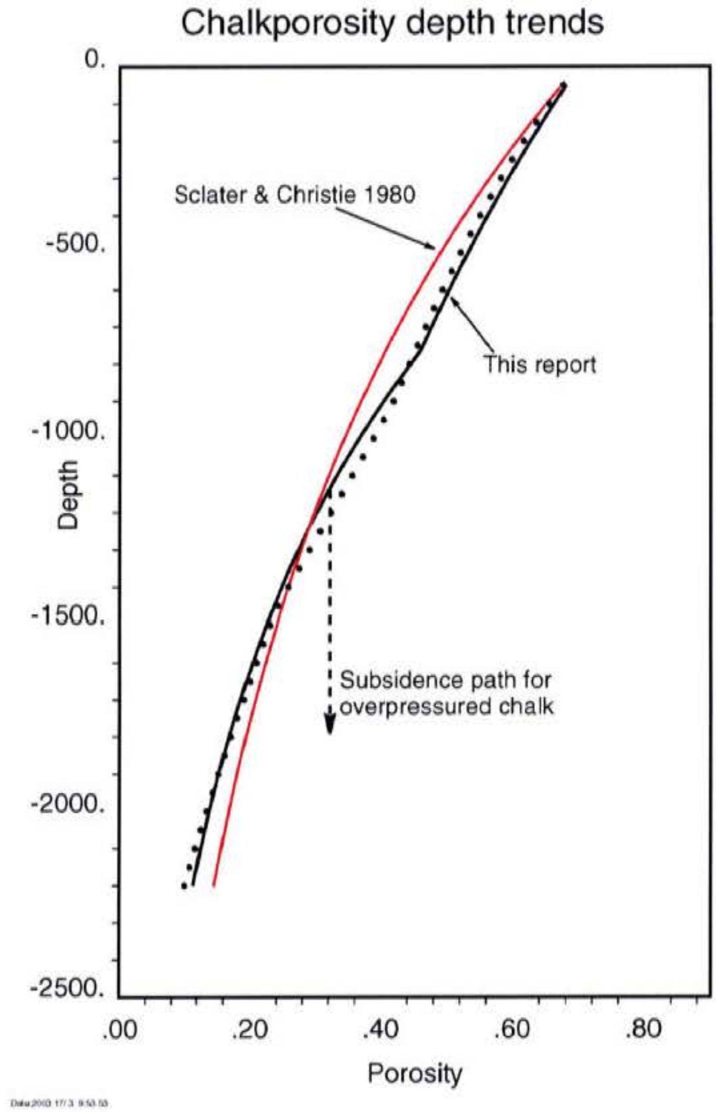

Figure 2: Normal compaction trends for the Chalk. Porosity depth values derived from velocity model is shown as dots, and the fit to this as a black line. Dashed line shows an example porosity – depth path for overpressured chalk.

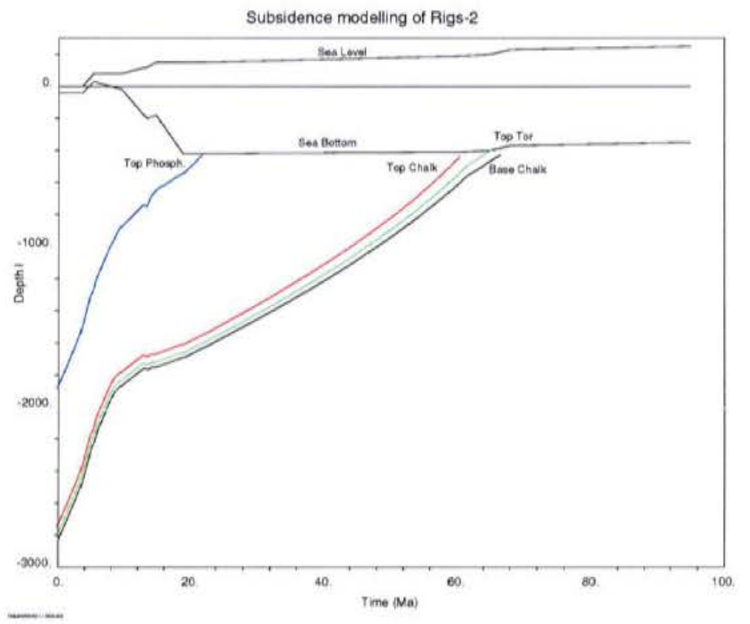

Figure 3: Modelled subsidence at the Rigs-2 well, South Arne Field (see Fig. 1 for location).

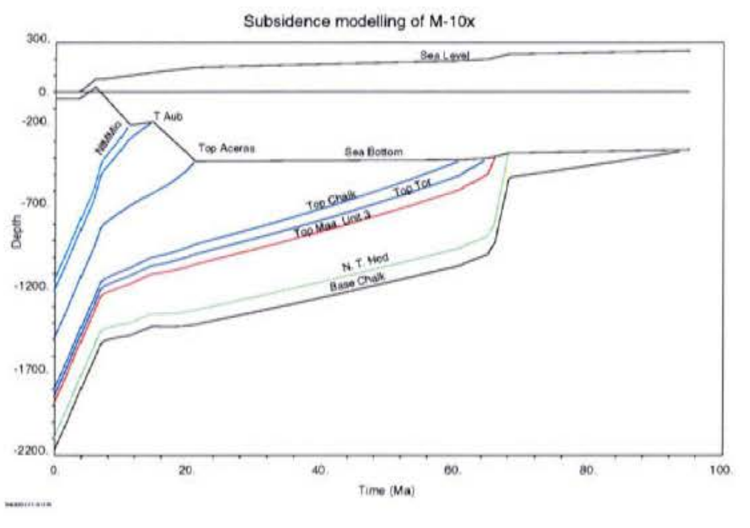

Figure 4: Modelled subsidence at the M-10x well, Dan Field.

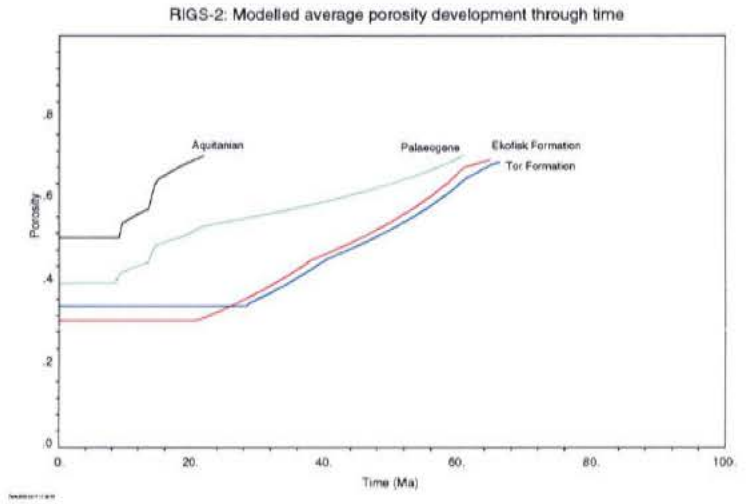

Figure 5: Simplistic porosity development model for the Rigs-2 site. Overpressuring arrests porosity decay in the Palaeogene at $\sim$ 10 Ma, but modelling suggests that HC effects arrest porosity decay in the Chalk much earlier.

Over-pressuring is assumed in depth intervals where the porosity exceeds the porosity expected at the present depth according to the normal compaction trend. It is assumed that excess pore pressure has not dissipated at all since onset. The duration of over-pressuring is the shortest possible with this assumption. This method is hereafter called "pressure preserving de-compaction". An alternative approach would be to assume that overpressure, and thus abnormal porosity, has been building up gradually since deposition, hereafter referred to as "gradual pressure build-up decompaction". The two assumptions may be considered as end-members of possible actual scenarios, but neither handles the case where higher overpressure in the past has dissipated to some extent.

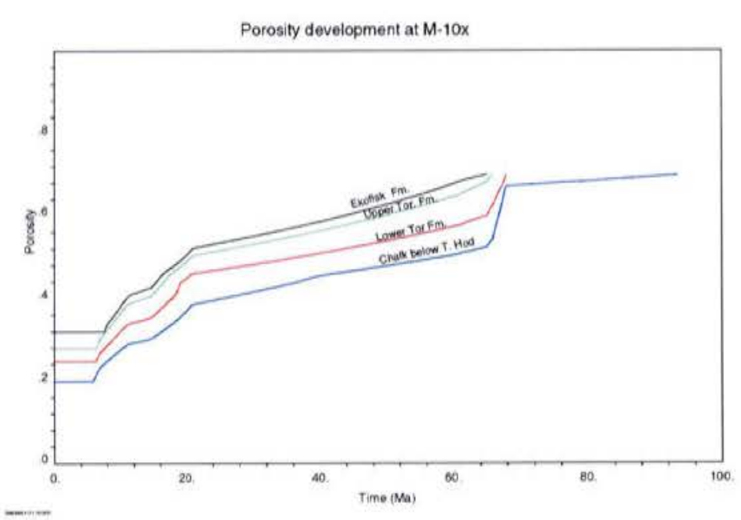

Figure 6: Simplistic porosity development model for the M-10x site. Overpressuring arrests porosity decay at ~ 8 Ma, and HC effects are apparently not important for Chalk porosity preservation.

Burial graphs show rapid burial rates only in the Neogene and very modest burial rates in Cretaceous – Palaeogene times (Figs. 3 and 4). Relative tranquility in Palaeogene times makes it likely that possible earlier over-pressure may have dissipated and present over-pressure to be primarily caused by rapid Neogene deposition. The observed excess pore pressure is therefore assumed to have initiated very late, and only few million years before present. This is further supported by the apparent correspondence between thickness of Neogene deposits and magnitude of overpressure (Japsen 2000). The pressure preserving de-compaction approximation therefore seems to be the best choice as the short time available reduces the problem of modelling pressure dissipation.

In the case of over-pressuring, the average presently observable porosity (ϕ_{obs}) in the interval is higher than predicted by the standard porosity decay function (equation 1). The porosity is assumed to be preserved since onset of over-pressuring. The exact depth where ϕ_{obs} is on the normal compaction curve is given by:

$$z_{obs} = \frac{1}{-a} Log \left(\frac{\phi_{obs}}{\phi_0} \right) \tag{2}$$

where z_{obs} is the depth where the unit left the normal compaction trend. On the basis of the following equation, average burial anomalies (z_{ano}) are computed for each stratigraphic unit where effects of minor lithological is minimized by averaging:

$$z_{ano} = \frac{1}{n} \sum_{n}^{1} \left[z - \frac{1}{-a} Log \left(\frac{\phi_{obs}}{\phi_0} \right) \right] \tag{3}$$

where z is present observation depth and n is the number of porosity log samples in the interval.

During compaction or decompaction a depth shift (Δz) is imposed. The logged porosity is then changed under the assumption that each sample has each their porosity – depth trends. For each sample in the porosity log an individual surface porosity ($\phi_{0'}$)is calculated according to:

$$Log(\phi_{0'}) = a(z - z'_{ano}) + Log(\phi_{obs}) \tag{4}$$

where $z'_{ano} = z_{ano} + \Delta z$ is the depth shift and Δz is the compaction/de-compaction value expressed as a depth shift. It is noted that the surface porosity is corrected according to the depth where the average porosity is on the normally pressured depth trend, and not the present depth. This approach implies that porosity deviations on the log are inherited from surface condition and reflect primary lithological and depositional differences. Diagenetic processes that may add material of cause local redistribution of material are thus neglected.

An example of such depth shifts is discussed below and shown in Fig. 12.

The burial anomalies may be directly converted into an estimated excess pressure as this is the main cause for the porosity anomaly (Japsen 1998). If the overpressure (Δp) is assumed to be caused by Neogene rapid deposition (the burial anomaly), then it is equivalent to the effective stress (σ) exerted by this column:

$$\sigma = \Delta p = (\rho_r - \rho_{br}) \cdot g \cdot z_{ano} \tag{5}$$

where g is the gravity constant. If densities of the rock (ρ_r) and brine (ρ_{br}) are equal to 2000 and $1000 Kg/m^3$, then a burial anomaly of 100 m is roughly equivalent to 1 MPa.

Burial modelling of the Rigs-2 well site

In order to elucidate the conditions at the Rigs-2 well backstripping has been performed. Depths and compaction parameters for this well are listed in table 3. The well encountered excess pressures at 1300 m increasing to app. 7.4 MPa at 1600 m, 12MPa at 2600 m, and 14.8 MPa in the Chalk section (Table 2). In our cases the burial anomalies are calculated as given in table 2 with parameters given in table 3.

Rigs-2	Burial anomaly (m)	Approximate Pressure (MPa)	Observations (MPa)
Below near base Tortonian	381	3.8	-
Below top Aub	730	7.3	-
Below top Aceras	1180	11.8	12
Chalk	1654	16.5	14.8

Table 2: Burial anomalies and excess fluid pressure for the Rigs-2 well. Calculated burial anomalies are converted to over-pressure as described in the text.

The subsidence graph calculated this way (Fig. 3) displays moderate burial rates until approximately 15 Ma b.p., where a considerable increase is noted. At approximately 10 Ma b.p. porosity is arrested in the Palaeogene due to over-pressuring (Fig. 5). Porosity in the Chalk is modelled to be arrested much earlier which reflect early hydrocarbon invasion rather than over-pressuring. A similar modelled porosity development for the M-10x shows no earlier cessation of porosity decay in the chalk reflecting later hydrocarbon charging of the Dan Field as compared to the South Arne Field (Fig. 6).

Rock unit	Base unit TWT Sec.	Base unit m. b.m.s.l.	Surface porosity ϕ_0	Decay length m. $1/a$
Quaternary	na	453.5	0.56	2560.16
Piacenzian	na	794.0	0.56	2560.16
Zanclean	na	809.4	0.56	2560.16
Messinian	na	902.4	0.56	2560.16
Tortonian	1.430	1411.63	0.56	2560.16
Aub	1.805	1772.4	0.71	1960.02
Aceras	2.705	2745.6	0.71	1960.02
Ekofisk Fm.	2.741	2796.1	0.968	1029.34
Tor Fm.	2.766	2829.1	0.968	1029.34

Table 3: Depths and compaction constants for the Rigs-2 well. Note that this listing mode means that for instance Top Chalk is at 2.705 sec.

The observed pressure in the Rigs-2 well is, however, about 10% lower than the estimate based on porosity observations. If the anomalous high porosity in the well is attributed to other factors than over-pressuring, then this other effect may be contributing with 10 % compared to pressures. This other effect may be early hydrocarbon invasion, which frequently has been suggested as a cause for porosity preservation above normal (e.g. Bramwell et al. 1998).

In the Central Graben in general there seem to be roughly the same excess pressure in the water zones of the lower Palaeogene section and the Chalk. As seen in table 2, the calculated excess pressure for the chalk is exceeding the Lower Palaeogene pressure by 3.7 MPa and observed pressure difference is 2.8 MPa. Only 0.74 MPa of this difference is attributable to a direct pressure effect from the hydrocarbons, so the pressure increase in the chalk suggests lateral support from deeper levels.

Within the chalk a difference of 0.9 MPa is seen between observed and calculated excess pressure. It is therefore estimated that the abnormally high porosity is due to a combination of overpressure and preserving effects of the invaded hydrocarbons. It may be estimated that rapid Neogene deposition contributes with 12 MPa, the hydrocarbon column constributes with 0.74 MPa and lateral pressure support contributes 2 MPa to the observed pressures and porosity preservation. The porosity preservation owing to the presence of hydrocarbons could have been replaced by only a further ~ 2 MPa.

Saturation modelling

In order to model the saturation realistically, the strong capillary effects in the chalk must be taken into account. We apply the saturation height model developed by Hess (2001). In this method the saturation is calculated directly from the capillary pressure (P_c) and the capillary entry pressure (P_{ce}):

$$Sw = \left(\frac{P_{ce}}{A \cdot P_c - A \cdot P_{ce} + P_{ce}} \right)^{1/B} \tag{6}$$

where A and B are given by:

$$A = 10^{c_1 + c_2 \cdot \phi} \tag{7}$$

$$B = 0.10 + 1.95 \cdot \phi$$

where ϕ is the porosity (in fractions). Constants c_1 and c_2 differs for the Tor and Ekofisk formations as given in table 4.

The capillary entry pressure is given by an equation of the form:

$$P_{ce} = c_3 \cdot \phi^{c_4} \tag{8}$$

where constants c_3 and c_4 are different for the Tor and Ekofisk Formations as given in table 4.

Formation	c_1	c_2	c_3	c_4
Ekofisk	-0.75	2.70	7.5	-1.2
Tor	-1.10	4.35	7.0	-0.7

Table 4: Constants for the saturation height model.

The capillary pressure is obtained from the height above free water level (FWL):

$$Pc = (FWL - z) \cdot \Delta p \cdot Cap \tag{9}$$

where z is the depth, Δp is the pressure gradient difference between oil and water, and Cap is the conversion factor of interfacial tension in the Hg/air system to the oil/water system at reservoir conditions. In the case of the Rigs-2 well the following values for the parameters are assumed:

$$\Delta p = 0.182psi/ft = 0.0413bar/m \tag{10}$$

$$Cap = \frac{\sigma Cos\theta_{ow}}{\sigma Cos\theta_{Hg/air}} = \frac{28}{367} = 0.076 \tag{11}$$

These parameters produce an acceptable fit to observed Sw, if a FWL at 2900 m (b.m.s.l.) is assumed (Fig. 7). During modelling of seismic response to changes in hydrocarbon saturation (Sw), the above saturation height model is applied. Changes in Sw can occur in the model by imposing changes in FWL, such that realistic vertical differences in Sw are calculated. If alternatively the model is aimed at studying changes in compaction the above saturation height model will automatically impose Sw changes due to the porosity dependency.

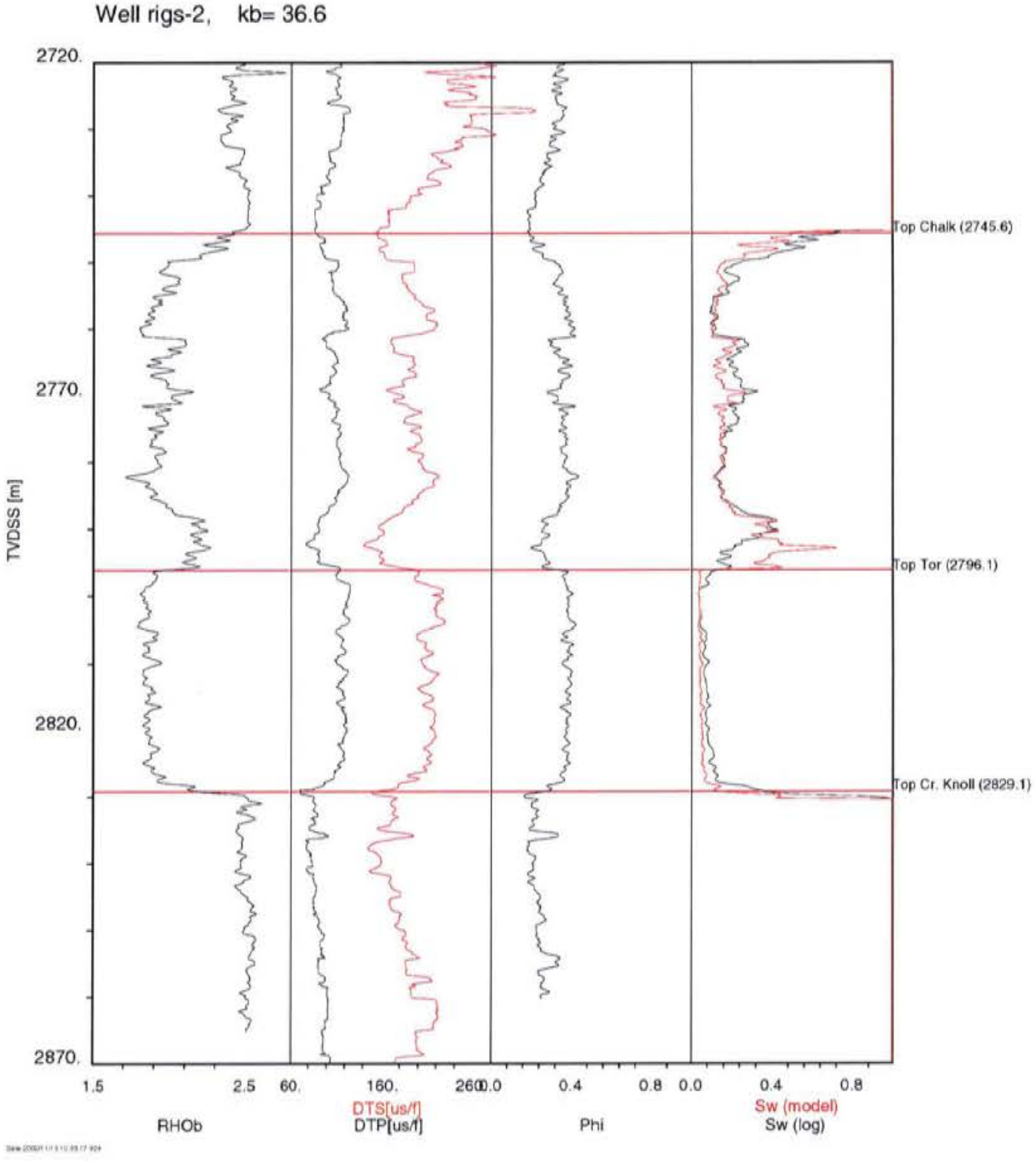

Figure 7: Rigs-2 Log data.

Rock Physics and Fluid substitution

We estimate elastic properties and changes thereof in the chalk as a consequence of changes in hydrocarbon saturation and degree of compaction. The relationships for elastic moduli and velocity versus porosity are described using modified Hashin – Shtrikman bounds and Gassmann's relations in an approach similar to the one suggested by Walls et al (1998).

Fluid substitution

We assume the low-frequency theory for fluid substitution by Gassmann (1951) to be fulfilled for elastic measurements with log tools. It is thus assumed that the chalk is sufficiently permeable to allow pore fluid pressures to equilibrate instantaneously when sound waves propagates through the rock. This is not fulfilled for isolates pores and low permeability rocks at high frequency, but will automatically be fulfilled for seismic data if Gassmann's theory applies to log data. The Gassmann theory gives the following relationship between rock moduli:

$$\frac{K_{sat}}{K_0 - K_{sat}} = \frac{K_{dry}}{K_0 - K_{dry}} + \frac{K_{fl}}{\phi(K_0 - K_{fl})}) \tag{12}$$

and $G_{sat} = G_{dry}$ where K_{dry} ,K_{sat} , K_0 and K_{fl} are bulk moduli of the dry rock, the saturated rock, the mineral components and the pore fluid respectively, G_{sat} and G_{dry} are shear moduli of the saturated and dry rock respectively and ϕ is the porosity. Bulk and shear moduli are related to recorded compressional velocity (V_p), shear velocity (V_s) and density (ρ) according to:

$$K = \rho(V_p^2 - \frac{4}{3}V_s^2) \tag{13}$$

and

$$G = \rho V_s^2$$

We apply this theory for substituting one fluid with another, in which case the Gassmann formula can be develop to:

$$K_{sat2} = \frac{K_0 \cdot A}{1 + A} \tag{14}$$

where

$$A = \frac{K_{sat1}}{K_0 - K_{sat1}} - \frac{K_{fl1}}{\phi(K_0 - K_{fl1})} + \frac{K_{fl2}}{\phi(K_0 - K_{fl2})}$$

and

$$G_{sat1} = G_{sat2}$$

where subscripts $sat1$ and $sat2$ refer to the saturated rock before and after substitution.

Fluid properties (subscripts $fl1$ and $fl2$) are calculated from the properties of formation water and hydrocarbons using Reuss type fluid mixtures:

$$K_{fl} = \frac{1}{Sw/K_w + (1 - Sw)/K_{hc}} \tag{15}$$

where Sw is the water saturation, and subscripts w and hc refer to water and hydrocarbon components respectively. This formula assumes that the two fluids are perfectly mixed considering the influence on wave propagation, which depend on frequency. Laboratory experiments show that this assumption first begin to fail at ultrasonic frequencies (Fabricius et al., this report; Mavco and Japsen, this report). The consequence of the Reuss formulation is that the weak/softer fluid component will dominate the overall acoustic response such that small hydrocarbon saturations will have a large effect.

Effects of compaction/decompation

Changes in rock moduli resulting from changes in porosity are calculated on the basis of a modified Hashin – Shtrikman model similar to the one proposed by Walls et al. (1998) for Ekofisk Field data. The model describes how bulk and shear moduli change with porosity in an interval between zero porosity and a maximum porosity (ϕ_{max}) encompassing the variation in the available data set. Data are allowed to vary between the modified upper Hashin – Shtrikman (MUHS) according to:

$$K_{eff}^{UHS} = \left[\frac{\phi/\phi_{max}}{K_{lim} + \frac{4}{3}G_0} + \frac{1 - \phi/\phi_{max}}{K_0 + \frac{4}{3}G_0}\right]^{-1} - \frac{4}{3}G_0 \tag{16}$$

$$G_{eff}^{UHS} = \left[\frac{\phi/\phi_{max}}{G_{lim} + Z_0} + \frac{1 - \phi/\phi_{max}}{G_0 + Z_0}\right]^{-1} - Z_0$$

where

$$Z_0 = \frac{G_0}{6}\frac{9K_0 + 8G_0}{K_0 + 2G_0}$$

corresponding to the presumably stiffest possible variety, where the subscript lim refer to moduli at the selected maximum porosity. This set of equations can also be developed for the lower bound which, however, is equivalent to the simpler Reuss average as may be developed from:

$$\frac{K_{sat}}{K_0 - K_{sat}} = \frac{K_{dry}}{K_0 - K_{dry}} + \frac{K_R}{K_0 - K_R} \tag{17}$$

where

$$K_R = \left(\frac{\phi_{max} - \phi}{\phi_{max} \cdot K_{lim}} + \frac{1 - (\phi_{max} - \phi)}{\phi_{max} \cdot K_0}\right)^{-1}$$

The upper bound description is applied during changes in porosity, where stratigraphical property differences are accommodated through adjustments of the end members (K_0 and K_{lim}). During decompaction the porosity may exceed ϕ_{max} in which case the further change is set to follow the lower (Reuss) bound.

Seismic model

We obtain zero offset seismic sections and AVO gathers based on the modelled logs as described above. Zero offset synthetic data are obtained from the reflectivity series that are calculated from the P-wave velocity (V_p) and density (ρ) logs as given by equation 22. This reflectivity series is convolved with a Ricker wavelet. A Ricker wavelet with a dominating frequency of 50 Hz was found to produce an acceptable match to field data. P-wave reflectivity for offset gathers ($R(\Theta)$) is calculated on the basis of first order reflectivity equations from the Zoeppritz equations as given by Spratt et al. (1993):

$$R(\Theta) = R_{pp0} + (R_{pp0} - 2'R_{ss0})Sin^2\Theta + 0' \cdot \frac{\Delta\rho}{\rho_a}Sin^2\Theta \tag{18}$$

where

$$2' = 8\left(\frac{V_s}{V_p}\right)^2$$

and

$$0' = 2\left(\frac{V_s}{V_p}\right)^2 - \frac{1}{2}$$

and R_{pp0} and R_{ss0} are zero offset reflection coefficients for P and S-waves as given by equation 22. ρ_a is average density and $\Delta\rho = \rho_2 - \rho_1$; the density difference across the interface.

Offset calculations are based on an assumed 2500m streamer, which with fairly constant overburden velocities around 2000 m/sec will produce incidence angles (Θ) below 22.5° at top chalk level. Refraction in the chalk overburden is considered negligible due to rather homogeneous velocities and is consequently disregarded.

For standard analyses of amplitude versus offset (AVO) we apply the Shuey (1985 in Castangna 1993) approximation:

$$R_{pp}(\Theta_1) \sim R_{pp0} + \left(A_0 R_{pp0} + \frac{\Delta\sigma}{(1-\sigma^2)^2}\right) Sin^2\Theta_1 + \frac{1}{2}\frac{\Delta V_p}{V_{pa}}(Tan^2\Theta_1 - Sin^2\Theta_1) \tag{19}$$

where

$$A_0 = B_0 - 2(1 + B_0)\left(\frac{1-2\sigma}{1-\sigma}\right) \tag{20}$$

and

$$B_0 = \frac{\frac{\Delta V_p}{V_{pa}}}{\frac{\Delta V_p}{\Delta V_{pa}} + \frac{\Delta \rho}{\Delta \rho_a}} \tag{21}$$

and the zero offset P-wave reflectivity (R_{pp0}) is:

$$R_{pp0} = \frac{I_{p2} - I_{p1}}{I_{p2} + I_{p2}} \tag{22}$$

where the impedance is given by $I_p = V_p \cdot \rho$. Substituting V_p with V_s gives the S-wave reflectivity R_{ss0}. σ is the poisson ratio as given by:

$$\sigma = \frac{\frac{1}{2}(\frac{V_p}{V_s})^2 - 1}{(\frac{V_p}{V_s})^2 - 1} \tag{23}$$

The last term in equation 19 is dropped as it is insignificant for moderate angles of incidence (Θ_1). We use the first two term in equation 19 for the intercept versus slope plots given in Figs xx and xx. We also use the poisson ratio (σ, equation 23) to crossplot with acoustic impedance to illustrate effects of porosity and saturation changes.

Seismic model examples

We exemplify modelling of compaction and saturation changes with data from the Rigs-2 well, South Arne Field (Table 4). Seismic examples are given in the appendix. Input data to the modelling are logs, where key logs like V_p, V_s, and density are restored to virgin conditions. Due to a missing shallow resistivity log, this restoration proved to be most reliably performed using rock physical calculations as described in Japsen et al. (*this report*). This results in an implicid self-consistency that causes modelled property changes calculated in this report to perform somewhat better than if restoration was based on shallow resistivity data (see discussion in Japsen et al. *this report*).

Moduli of the formation components have been estimated during laboratory measurements (Fabricius et al. *this report*) and are listed in Table 4.

Component	Bulk Modulus K	Shear Modulus G	Density ρ
Calcite	71.0	30.0	2.71
Silicates	25.0	9.0	2.70
$lim : \phi = 45$	1.5	2.5	
Brine	2.96	0	1.035
Oil	0.52	0	0.633

Table 5: Moduli and densities of formation components

To demonstrate the capabilities of the modelling tools, two scenarios are tested:

a. The free water level is changed from 2795 m b.m.s.l. over the ideal 2900 m to 2990 in steps of 5 m corresponding to 40 cases (or traces).

b. The present effective stress in the chalk is changed corresponding to depth shifts of -900 m to 900 m in steps of 30 m corresponding to 60 cases (or traces).

Change in free water level

A range of synthetic seismograms are modelled by only changing the free water level and via saturation height modelling change the fluid composition. The range is from 2795 m to 2990 m .b.s.l. corresponding to a change from 100% water saturation to approximately irreducible water saturation (Fig. 8. The best fit FWL relative to logged Sw is in the middle of this range, so maximum modelled hydrocarbon saturation far exceeds observed saturations.

A set of plots illustrating poisson ratio versus acoustic impedance shows that Sw changes affects both of these properties (Fig. 10). However, it is clear that acoustic impedance is more sensitive to porosity changes, than to saturation changes whereas the poisson ratio is more susceptible to saturation changes. These tendencies would be more amplified if gas was used rather than oil in the modelling, and acoustic impedance effects from saturation changes would become more significant. Also is the poisson ration becoming more sensitive to saturation with increasing porosity.

Another interesting effect is seen on the Top Chalk and Top Tor reflectors (at 2.741 sec; table 3; Fig. 9). The Top Tor reflector is characterised by downward decreasing impedance. It is seen that the amplitude of this reflector increases abruptly (more negative) as oil enters the formation. As FWL deepens (saturations increases) it gains amplitude until low to moderate oil saturations. From moderate to high oil saturation it slowly decrease again. This is a consequence of the saturation height model, which causes Tor Formation hydrocarbon saturation to increase faster than in the Ekofisk Formation in spite of lower capillary pressures at low overall hydrocarbon saturation. This is a consequence of lower capillary entry pressures in the Tor Formation.

The Top Chalk reflector is also affected by increasing oil saturation (Fig. 9). It is seen to loose amplitude with increasing oil saturation, and at saturations slightly higher than observed in the well, a reversal is predicted.

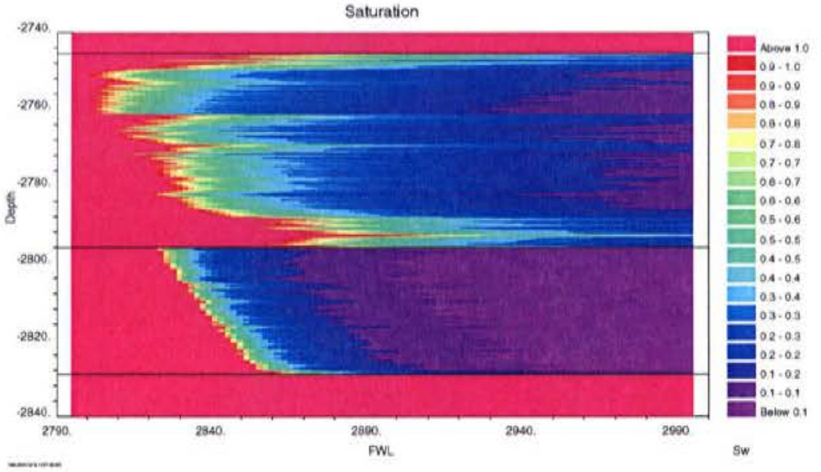

Figure 8: Water saturation profiles calculated by changing the free water level (FWL). Note that different properties in Tor and Ekofisk formations cause the Tor to hold lower saturations for shallow FWL than Ekofisk in spite of lower capillary pressure.

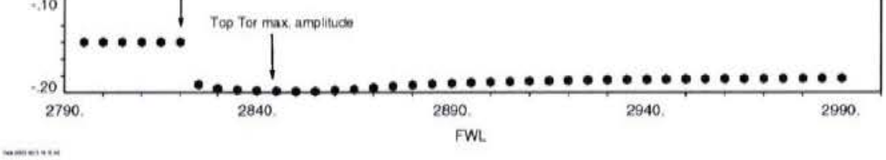

Figure 9: Modelled reflector strength and sign of the Top Chalk and Top Tor reflectors as a function of free water level in the Rigs-2 well(or modelled saturation distribution).

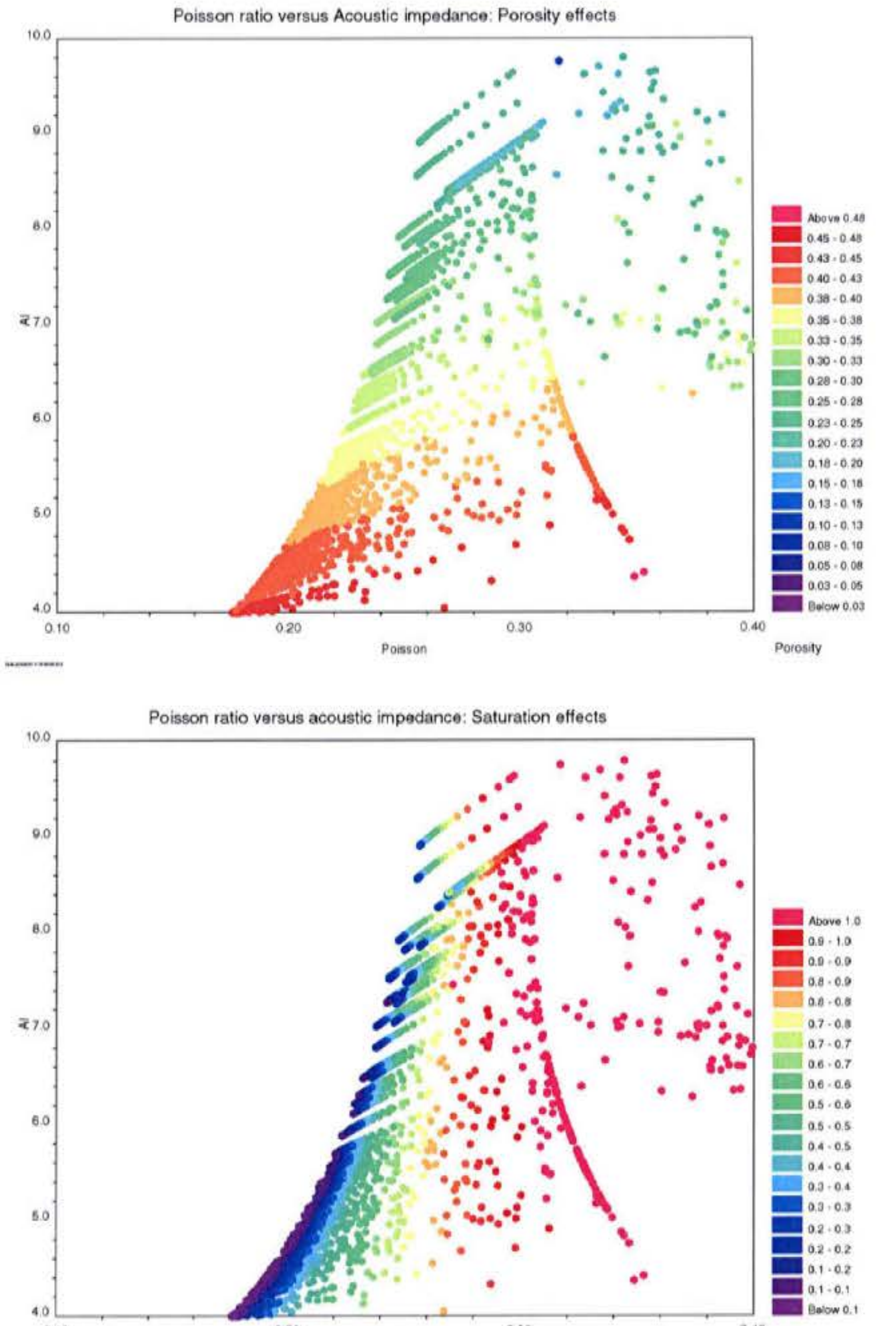

Figure 10: Poisson ratio versus acoustic impedance caused by modelled Sw changes (several free water level positions) in the Rigs-2 well. X and Y are the same, but colours show porosity and Sw. Points in the upper right are from outside the Chalk.

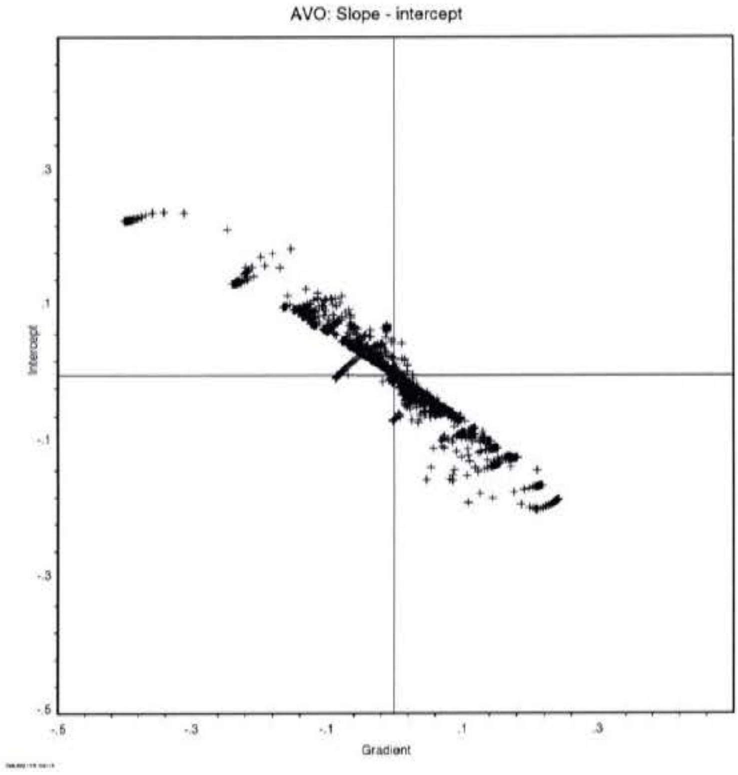

Figure 11: Slope (after Shuey 1985) versus intercept for saturation change models. Chalk interval only.

Change in effective stress

The compaction/de-compaction exercise is illustrated with the porosity logs shown in (Fig. 12). An interesting effect is that the varability in the porosity traces is amplified during de-compaction, and subdued during compaction which is in accordance with observations in seismic data (e.g. Britze et al. 2000). Modelling a change in effective stress inevitably results in saturation changes such that less porosity means higher water saturation. This relationship can be seen to be almost exponential (Fig. 12).

The synthetic porosity and Sw logs also show that the observed Sw is closer to irreducible water saturation in the Tor Formation than in the Ekofisk Formation in spite of lower capillary pressures in Tor. This is seen from the fact that an only negligible reduction in Sw occurs in the Tor although porosity is almost doubled during decompation. The Sw reduction during de-compaction in Ekofisk is more conspicuous. During compaction this diffences, which originates from entry pressure differences, is further amplifed.

Another interesting observation is that amplitudes on the porosity log (as well as the saturation log) are increased during decompation and subdued during compaction. This is a consequence of the design of the compaction/de-compaction model. This effect causes amplitude changes in the seismic model and corresponds to general seismic observations in the Chalk (Britze et al. 2000).

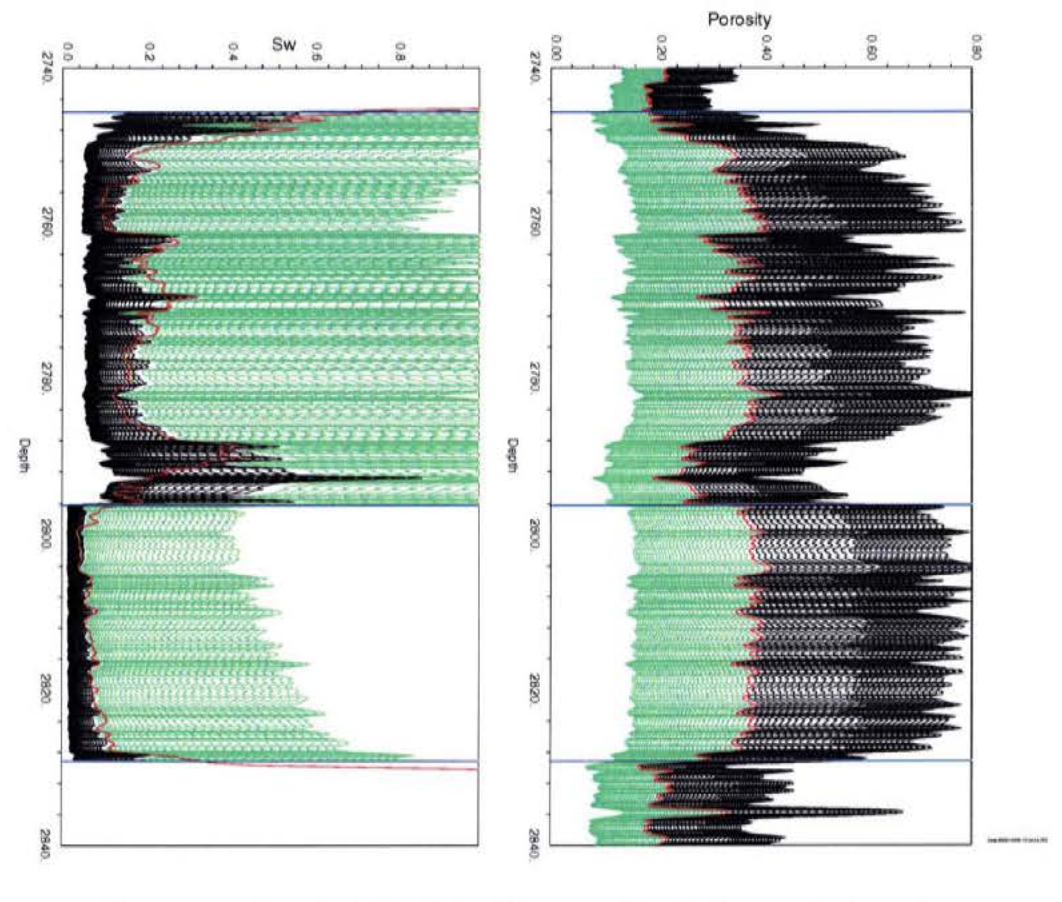

Figure 12: Depth shift of the Rigs-2 well. Right panel shows log traces corresponding to decompaction in black and compaction in green. Corresponding saturation changes resulting from porosity changes are shown to the left in the same colours.

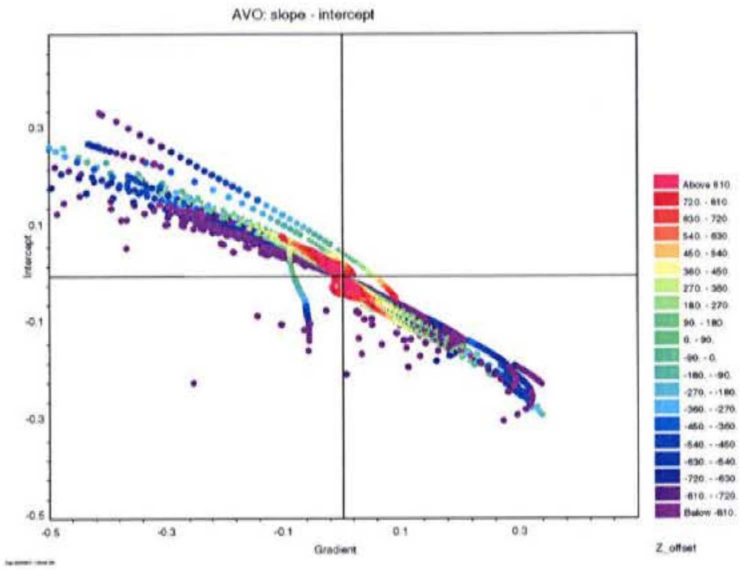

Figure 13: Slope (after Shuey 1985) versus intercept for compaction/de-compaction change models. Chalk interval only. Effective stress changes corresponding to -900 m to +900 m from present position are shown i colour. Very deep burial is seen to subdue reflectivity as well as gradient changes.

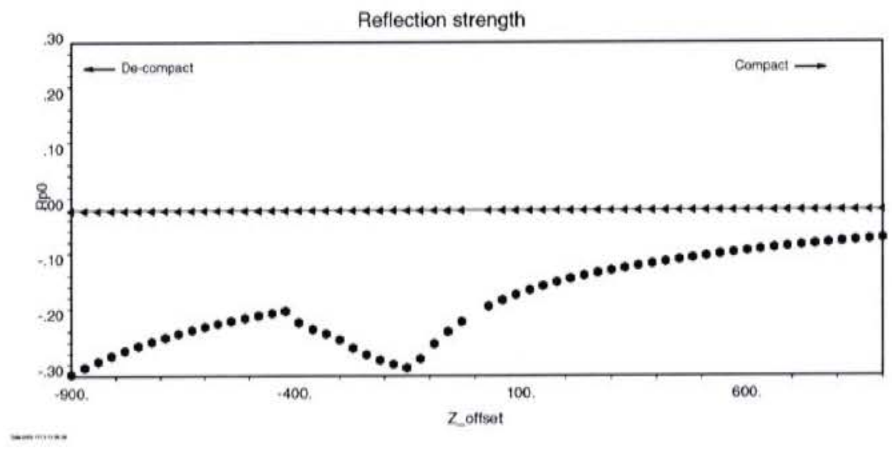

Figure 14: Modelled reflector strength and sign of the Top Chalk and Top Tor reflectors as a function of compaction/decompaction.

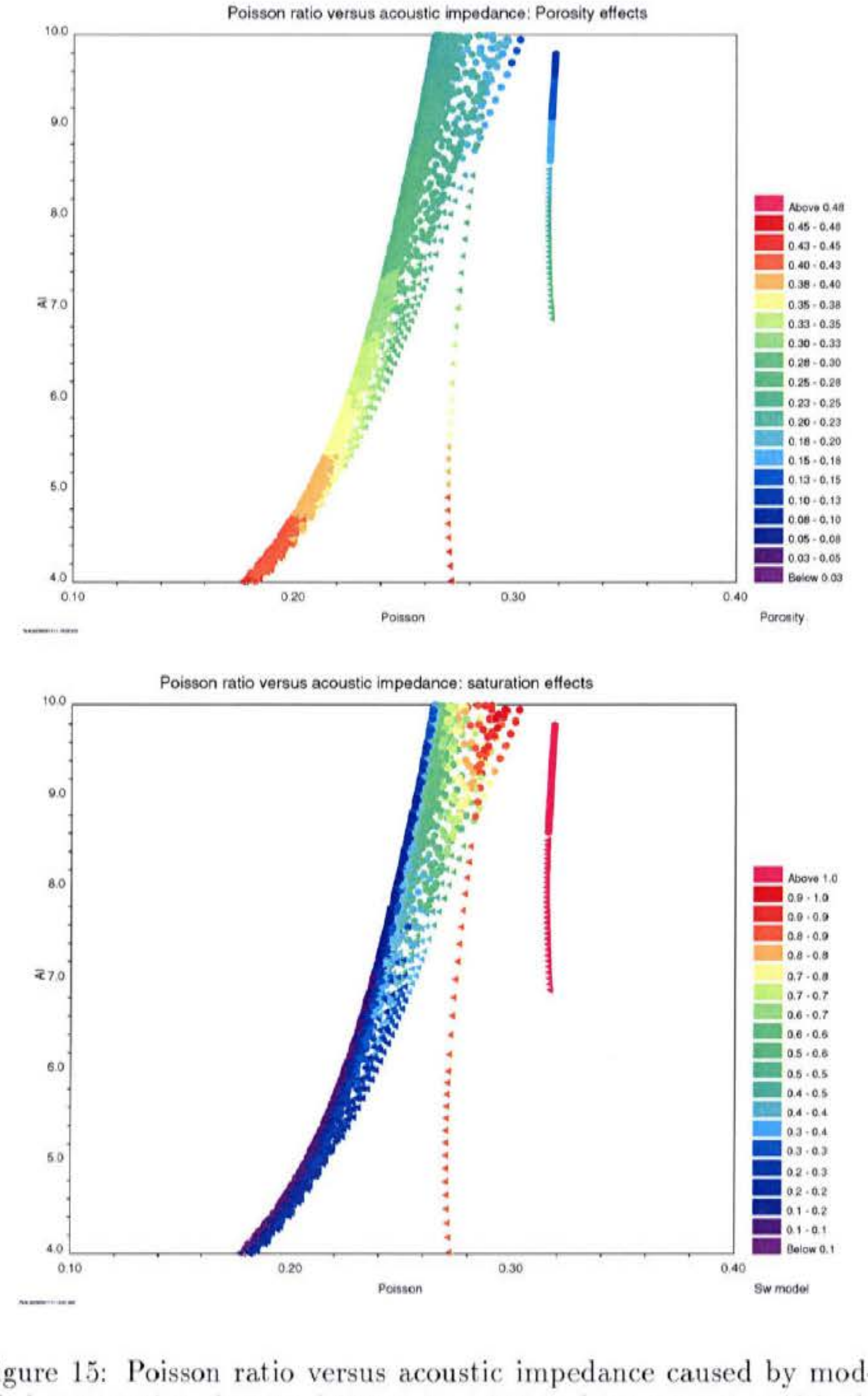

Figure 15: Poisson ratio versus acoustic impedance caused by modelled compaction changes (-900 m to +900 m from present position). Only Chalk from the Rigs-2 well is shown. X and Y are the same, but colours show porosity and Sw.

References

Athy, L. F. 1930: Density, porosity and compaction of sedimentary rocks. Bull. of the American Association of Petroleum Geologists, 14, 1-24.

Bramwell, N. P., Caillet, G., Meciani, L., Judge, N., Green, M. and Adam, P. 1998: Chalk exploration, the search for subtle traps. In Fleet, A. J. & Boldy, S. A. R. (eds.) Petroleum Geology of Northwest Europe: Proceedings of the 5th conference. The Geological society, London, 911-937.

Britze, P., Nielsen, E. B., Dahl, N. and Haug, S., 2000: EAGE, Petrophysics meets Geophysics, Proceedings.

Castagna, J. P. 1993: AVO analysis – Tutorial and review. In J. P. Castagna and M. M. Backus (eds.): Offset-dependent reflectivity – Theory and practice of AVO analysis, Investigations in Geophysics no. 8, Society of Exploration Geophysicists, 3-36.

Engstrøm, F. 1995: A new method to normalize capillary pressure curves. International Symposium of the Society of Core analysts, San Francisco, 1995, SCA no. 9535, 12p.

Fabricius, I. L, Høier, C., Japsen, P. and Korsbech, U. this report: Modeling elastic moduli of impure chalk.

Frederiksen, S., Nielsen, S.B., and Balling, N. 2001: Post-Permian evolution of the Central North Sea: a numerical model. Tectonophysics, 343, 185-203.

Gassmann, F. 1951: Elastic waves through a packing of spheres. Geophysics, 16, 673-685.

Japsen, P. 1998: Regional velocity-depth anomalies, North Sea Chalk; a record of over-pressure and Neogene uplift and erosion. American Association of Petroleum Geologists, Bulletin 82, 2031-2074.

Japsen, P. 1999: Overpressured Cenozoic shale mapped from velocity anomalies relative to a baseline for marine shale, North Sea. Petroleum Geoscience, 5, 321-336.

Japsen, P., 2000: Fra kridthav til Vesterhav, Nordsøbassinets udvikling vurderet ud fra seismiske hastigheder. Geologisk tidskrift, 2, 36 p.

Japsen, P., A. Bruun, I. L. Fabricius, Rasmussen, R., Vejbæk, O.V., Pedersen, J. M., Mavko, G. and Mogensen, C. this report: Influence of porosity and pore fluid on acoustic properties of chalk: AVO-response from oil, South Arne field, North Sea.

Jensen, P. K., Holm, L. and Thomsen, E. 1985: Modelling burial history, temperature and maturation. – In B. M. Thomas et al. (ed.): Petroleum Geochemistry in Exploration of the Norwegian Shelf. Proceedings of a NPF conf. - Graham & Trotman, PP. 145 - 153.

Mavko, G. and Japsen, P. this report: Fluid substitution in chalks: Effects of saturation scales.

Mavko, G., Mukerji, T., and Dvorkin, J. 1998: The rock physics handbook. Tools for seismic analysis in porpus media. Cambridge University Press, 329 p.

Megson, J. and Hardman, R. 2001: Exploration for and development of hydrocarbons in the Chalk of the North Sea: a low permeability system. Petroleum Geoscience, 7, 3-12.

Sclater, J. G. and Christie, P. A. F. 1980: Continental stretching: an explanation of the post-mid-Cretaceous subsidence of the Central North Sea basin. - Jour. of Geoph. Res., vol. 85, no. b7., pp. 3711-3739.

Shuey, R. T. 1985: A simplification of the Zoeppritz equations, Geophysics, 50, 609-614.

Spratt, R. S.m Goins, N. R. and Fitch, T. J. 1993: Pseudo-shear – The analyses of AVO. . In J. P. Castagna and M. M. Backus (eds.): Offset-dependent reflectivity – Theory and practice of AVO analysis, Investigations in Geophysics no. 8, Society of Exploration Geophysicists, 37-56.

Vejbæk, O. V. 2002: Reservoir characterization of the Roar Gas Field, Danish North Sea. Petroleum Geoscience, 2002, 8(1), 71-87.

Walls, J. D., Dvorkin, J., and Smith, B. A. 1998: Modeling SeiSmic Velocity in Ekofisk Chalk. 1998 SEG Expanded abstracts, 4 p.

Appendices

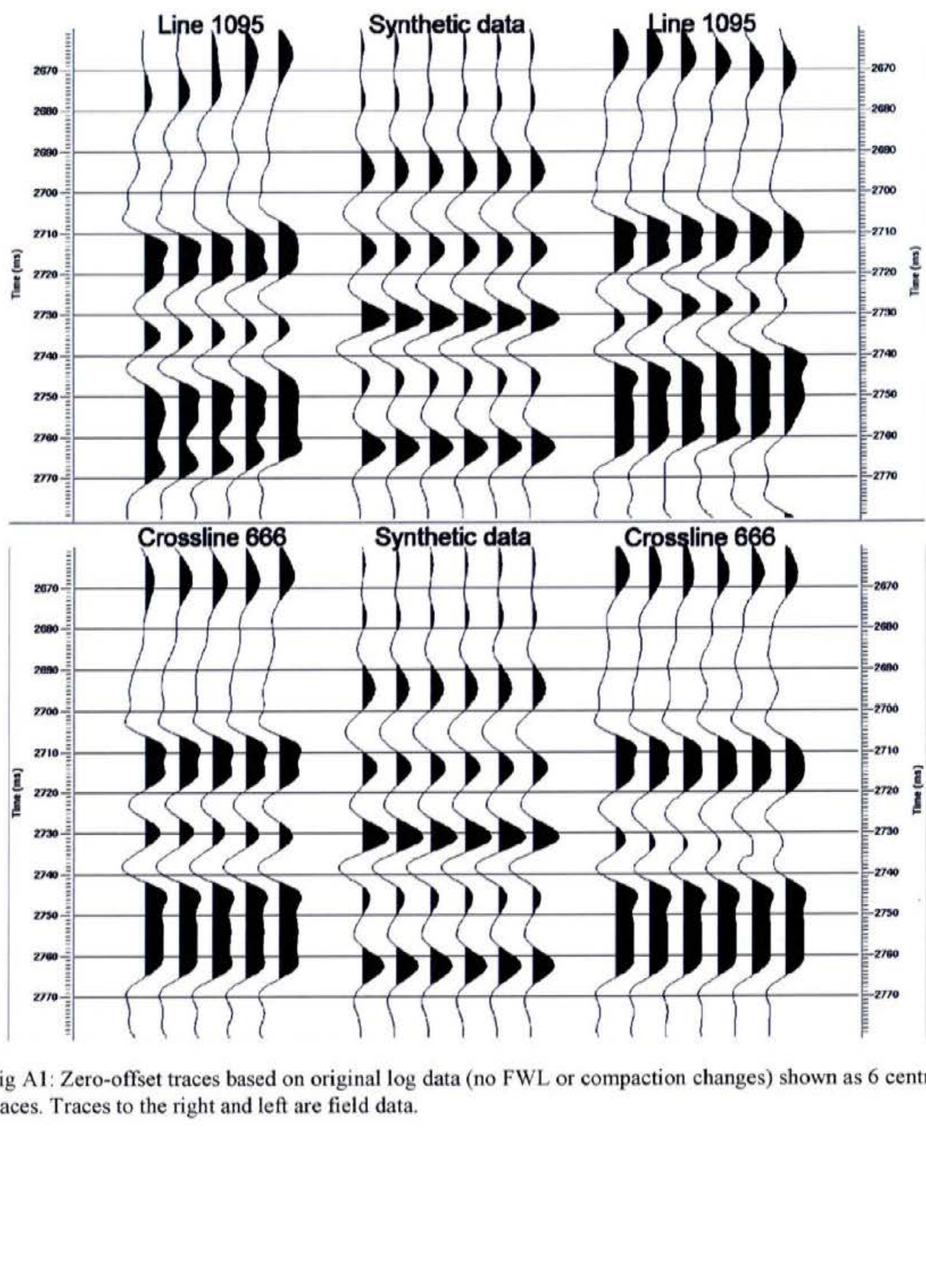

Fig A1: Zero-offset traces based on original log data (no FWL or compaction changes) shown as 6 central traces. Traces to the right and left are field data.

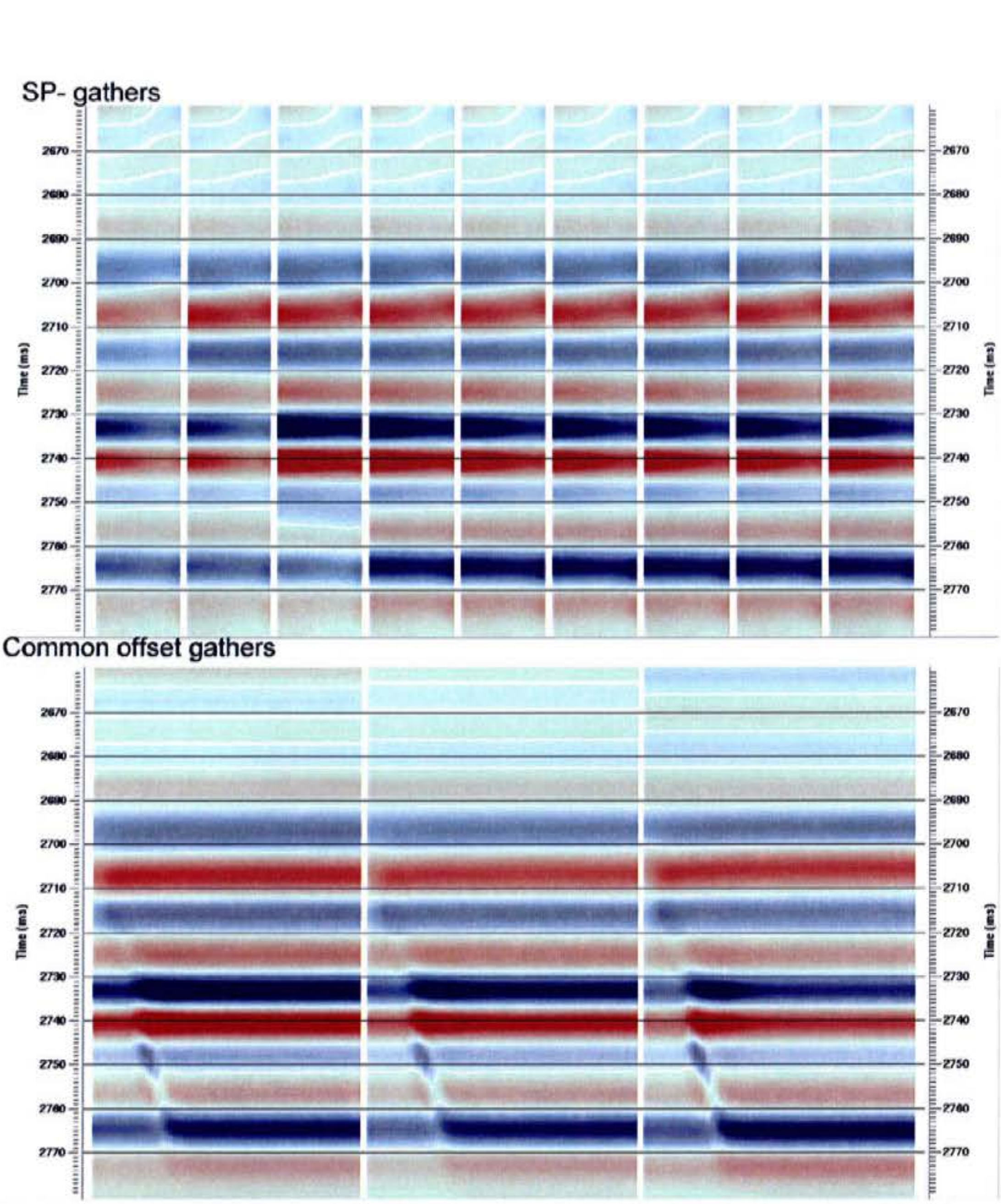

Fig. A2: Synthetic seismic based on modelled changes in saturation. SP-gathers are selected from low saturation models (left) to high saturation models (right). Common offset gathers each display the entire modelled saturation range and represent near offset (left), mid offset and far offset (right). The disturbance in the lower left originates from the modelled oil – water contact.

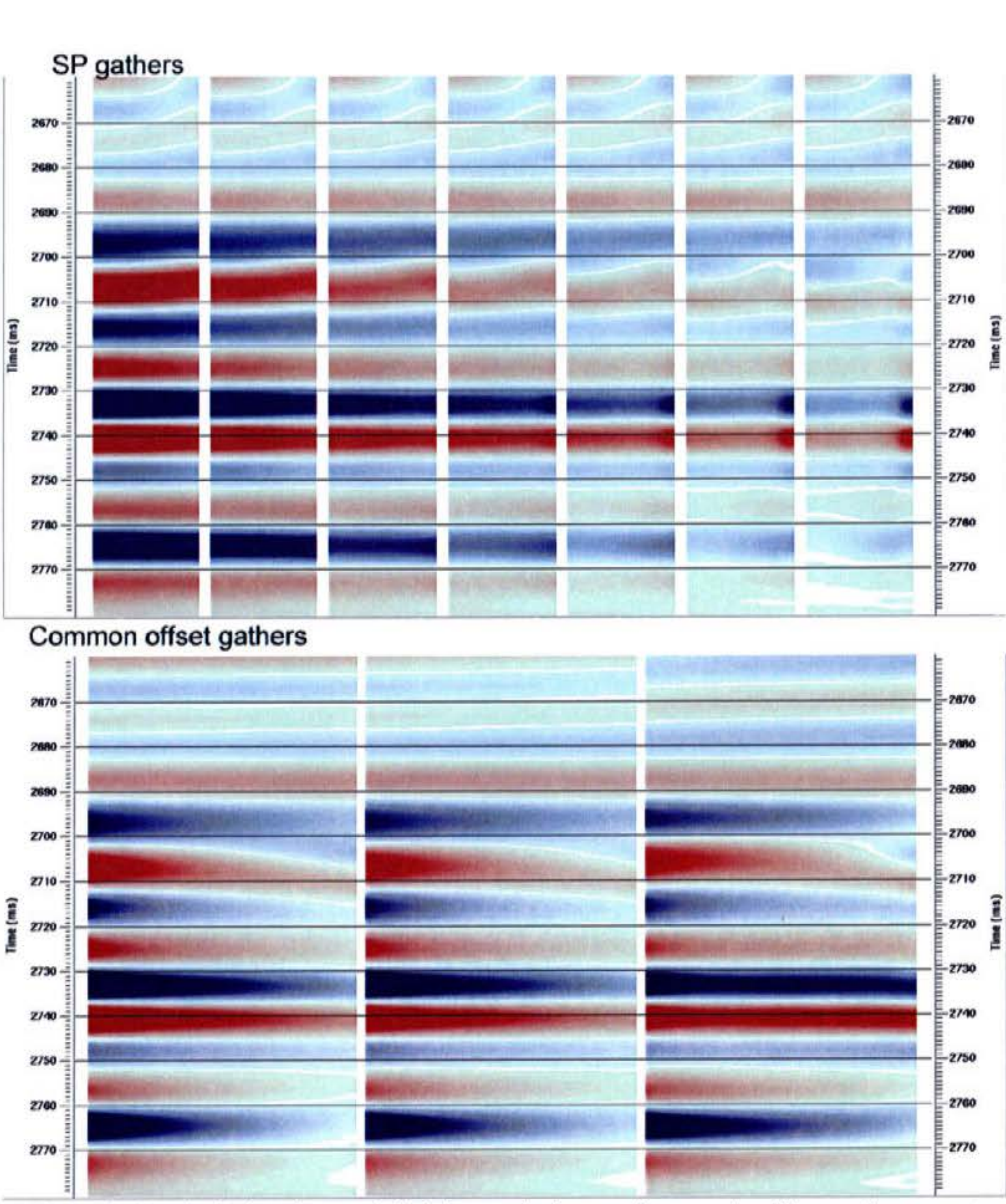

Fig. A3: Synthetic seismic based on modelled changes in degree of compaction. The panels represent increasing compaction with deepest version to the right. The common offset gathers (lower set) shows the entire range, and upper set are selected with 150 m intervals. Note the decreasing reflectivity with increasing compaction. Panels are not scaled similarly to Fig. A4.

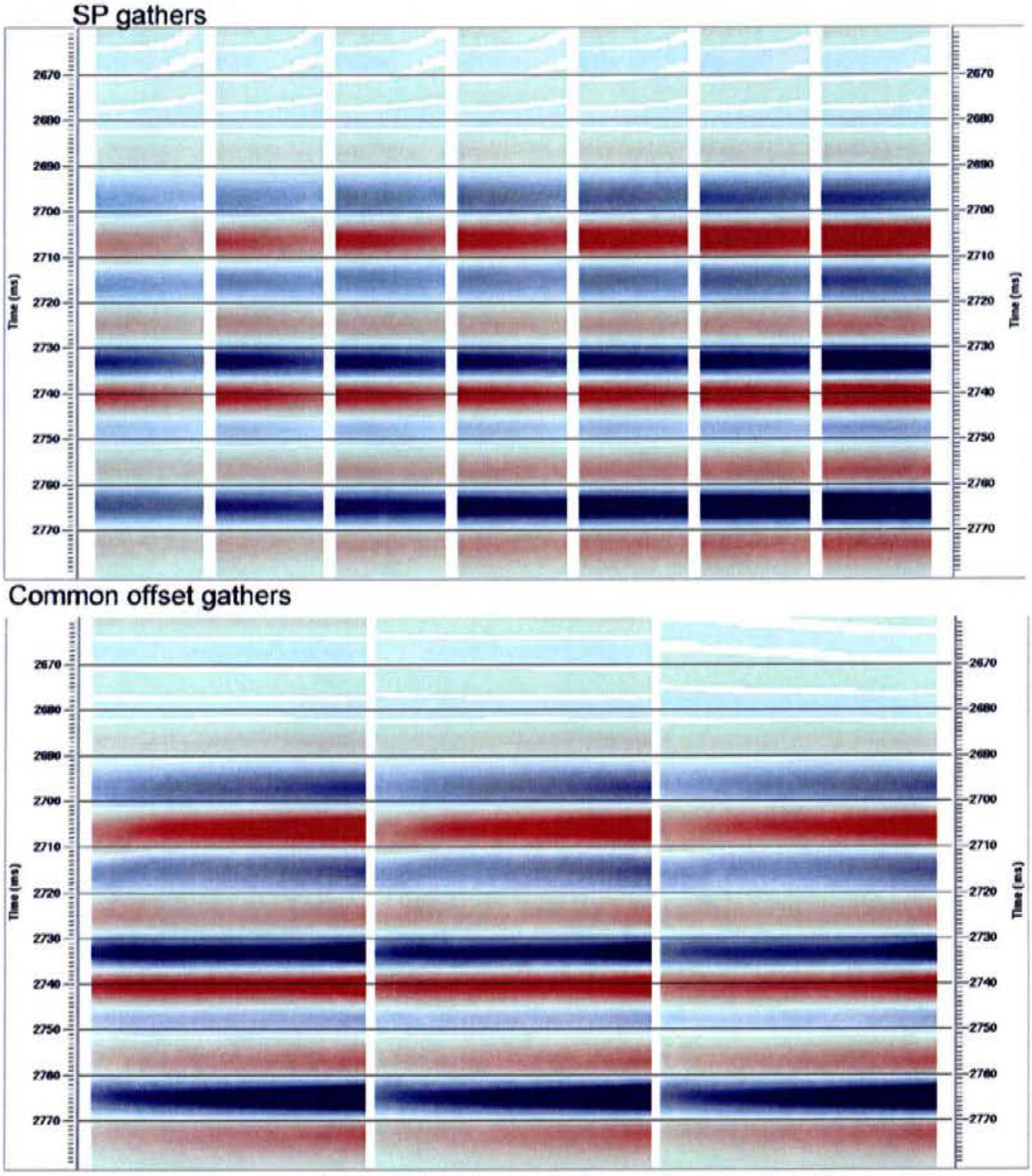

Fig. A4: Synthetic seismic based on modelled changes in degree of compaction. The panels represent decreasing compaction with shallowest version to the right. The common offset gathers (lower set) shows the entire range, and upper set are selected with 150 m intervals. Note the increasing reflectivity with decreasing compaction. Panels are not scaled similarly to Fig. A3.

Modelling seismic response from North Sea Chalk reservoirs resulting from changes in burial depth and fluid saturation

O. V. Vejbæk[1], R. Rasmussen[1], P. Japsen[1],
J. M. Pedersen[2], I. L. Fabricius[3] and G. Marsden[4]

March 17, 2003

Intended for submission to Petroleum Geology conference, London, 2003.
[1] Geological Survey of Denmark and Greenland, Ministry of the Environment (GEUS), Østervoldgade 10, DK-1350 Copenhagen, Denmark
[2] Ødegaard A/S, Titangade 15, DK-2200 Copenhagen N, Denmark
[3] Technical university of Denmark, (DTU)
[4] Amerada Hess Aps, Østergade 26B, DK-1100 Copenhagen K, Denmark

Abstract

Changes in seismic response caused by changes in degree of compaction and fluid content in North Sea Chalk reservoirs away from a well bore are investigated by forward modelling. The investigated seismic response encompasses reflectivity changes, AVO and acoustic impedance. Synthetic seismic sections, impedance cross sections and AVO response are presented as calculated on the basis of selected wells from the South Arne and Dan Fields, Danish North Sea and compared to field records.

The two main variables to use for seismic response prediction away from the well bore is depth of burial (changes in effective stress) and changes in hydrocarbon saturation (Fig. 0). Three main modelling tools are used for the modelling: 1) Rock physics, 2) Saturation modelling and 3) Compaction/de-compaction modelling.

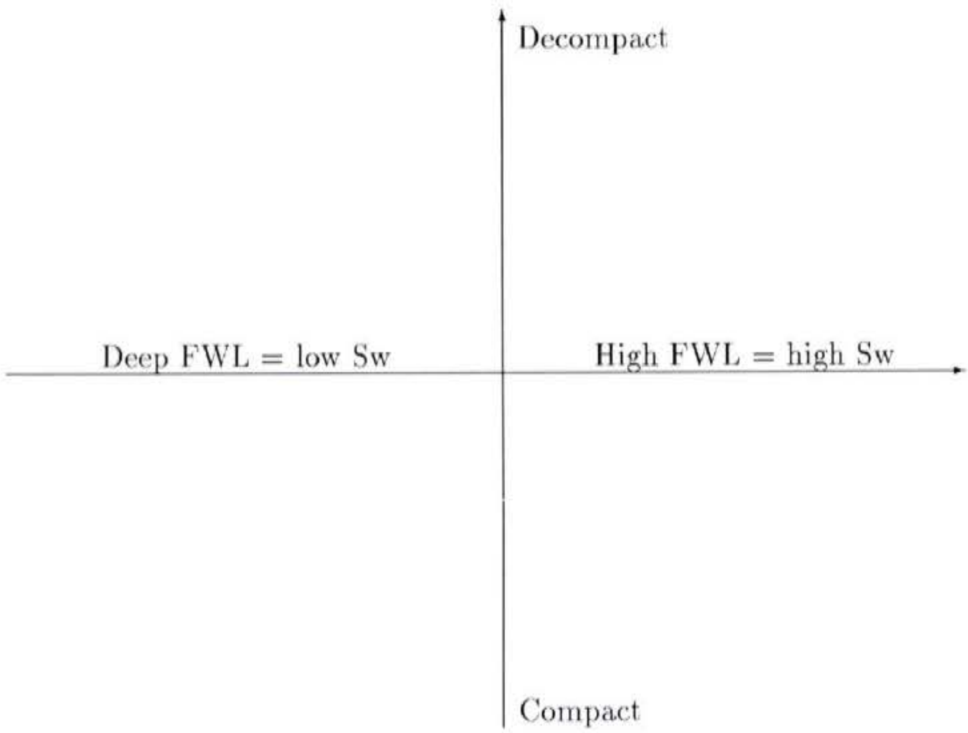

Figure 0: Main variables to investigate away from a well bore are changes in degree of compaction, and changes in HC saturation. The latter is obtained through saturation height modelling via the free water level (FWL)

Rock physics theory is applied to obtain all necessary parameters for the complete set of elastic parameters for the application of the Zoeppritz equations. The challenge is not only to predict the shear velocity, but also to account for the changes in fluid content via application of the Gassmann equation. An approach akin to the one suggested for the Ekofisk Field by Walls et al. (1998) is applied for the prediction of changes in degree of compaction.

Hydrocarbon saturation in North Sea Chalk is strongly affected by capillary forces due to the small scale of the pores and transition zones in the order of 50 m are not uncommon. For this reason, potent saturation modelling is needed in order create realistic input for the seismic modelling. We use saturation height models similar to the EQR model (Engstrøm 1995), which have proved robust for the prediction of

saturation profiles in Danish Chalk reservoirs.

Compaction modelling relies on simple exponential decay of porosity with depth, where abnormal fluid pressures are accounted for. A new set of compaction parameters is presented. These parameters are based on a study on the North Sea Chalk based on some 850 wells. The parameters appear to be sufficiently fine-tuned to allow fairly precise predictions of abnormal fluid pressures from observed average porosity. Based on this, the relative contribution to porosity preservation by abnormal fluid pressure and early hydrocarbon invasion may be estimated.

Some conclusions based on modelling results include: Reflectivity is correlating with porosity, acoustic impedance is more susceptible to porosity variation than to hydrocarbon saturation, and the poisson ratio may be rather sensitive to hydrocarbon saturation.

Introduction

Zero offset seismic response at a well site may be readily modelled provided reliable calibrated sonic and density logs are available. If shear velocity logs are available amplitude versus offset (AVO) response may also be modelled. However, questions may arise as to what cause changes in the response away from the well site. This paper develop methods for creating forward models of the seismic response away from the well site. The models are developed for North Sea Chalk and applied to two wells: Rigs-2 and M-10x drilled in the South - Arne and Dan fields respectively (Fig. 1). The models are aimed at studying effects of hypothetical changes in degree of compaction and hydrocarbon saturation away from a well bore. We aim to use realistic saturation models, which makes it impossible to study changes in compaction without concurrent changes in hydrocarbon saturation. This is because chalk reservoirs are usually strongly affected by capillary forces which vary with porosity. However, this allows us to study more realistic scenarios.

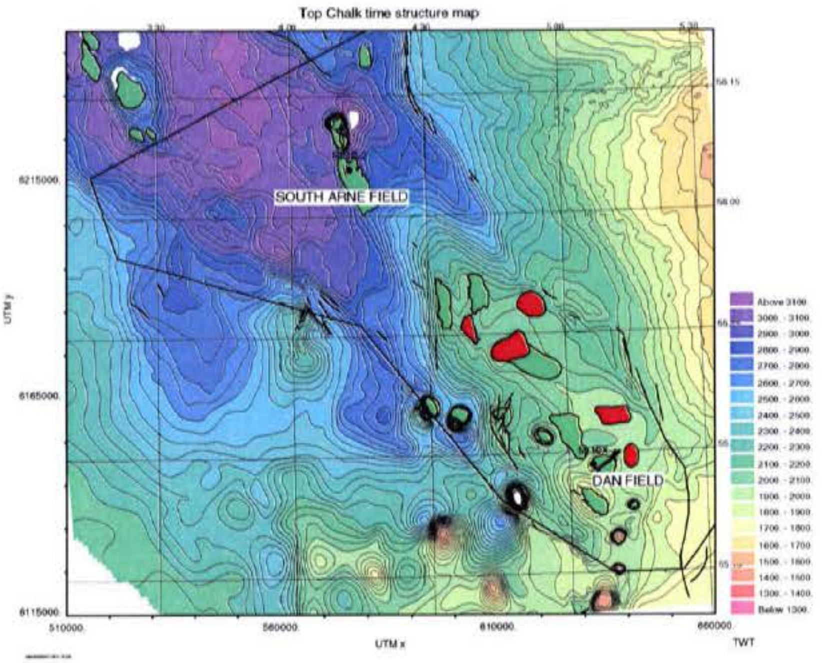

Figure 1: Top Chalk time structure map with locations of wells and fields referred to in this paper.

Compaction modelling

Compaction modelling is done by applying empirical compaction laws where excess fluid pressure is accounted for in a simplistic way. This approach is favoured over deterministic modelling, because pressure development is very hard to model due to inherent uncertainties in the geological development of basinwide hydraulic connectivity.

The goal of the compaction modelling is to calculate porosity logs as a function of changes in burial depth and/or changes in effective stress caused by changes in excess fluid pressure.

Basic assumptions are:

- In the absence of over-pressuring and early diagenesis, porosity decay follows a simple exponential law according to depth.
- Depth is considered a proxy for effective stress in the absence of overpressure.
- Deviations in porosity from the average function are due to very early diagenesis or later over-pressuring for too tight and too porous intervals respectively.
- The overpressure as of today has not dissipated significantly since onset: Overpressure "arrests" porosity as it is at the time of onset.
- Very tight chalk has been cemented shortly after burial, and follows a lower porosity decay curve than standard (This has however proved to be irrelevant for the cases studied here).

The basic approach follows the original proposition by Athy (1930) and is detailed in e.g. Sclater and Christie (1980) and Jensen et al. (1984):

$$\phi = \phi_0 \cdot e^{-a \cdot z} \tag{1}$$

where ϕ_0 is the surface porosity in fractions, z is depth of burial and a is the decay parameter. Some relevant parameters are listed in table 1. This equation can be developed to allow correction of the layer thickness as a function of burial or change in effective stress and thereby preserve rock mass (e.g. Sclater and Christie 1980; Jensen et al. 1984). However, since we are interested in changes away from a well site, and not in what has happened to the succession at the well site, we chose not to change thickness during our compaction/ de-compaction calculations except for the sample subsidence and porosity development curves shown in Figs 3, 4, 5 and 6.

In the case of chalk Sclater and Christie (1980) suggest values of 0.7 for ϕ_0 and $0.00071m^-1$ for a. The reciprocal of the decay parameter, the decay length (reduction to 37% of surface porosity) is equal to 1408.5 m. These values correspond to average normal pressured chalk, but are not consistent with velocity data (Japsen 2000). A compaction trend for North Sea chalk was constructed by transforming the revised normal velocity – depth trend of Japsen (1998, 2000) into a porosity-depth trend. The normal velocity – depth trend for chalk was based on an analysis of data from 845 wells throughout the North Sea Basin and ODP data and burial anomalies relative to the trend were found to agree with estimates of erosion along the basin margins and with measured overpressure in the centre of the basin. The trend was transformed into a porosity – depth trend by converting velocity to porosity via a constructed velocity – porosity trend for chalk (Fig. 2). The velocity – porosity trend was established as a second order polynomial fit to two segments:

a. The modified Hashin – Shtrikman model for chalk with porosities in the range from 10% to 43% suggested by Japsen et al. (2000) and

b. A straight line connecting the endpoint of segment a. at 43% (velocity 2720 m/s) to the parameters corresponding to the critical porosity of chalk at 70% (velocity 1550 m/s).

	ϕ_0	a	$1/a$	source
Neogene	0.56	3.91E-04	2560.2	
Palaeogene	0.71	5.10E-04	1960.0	
Chalk $z < 768.2$	0.70	5.50E-04	1818.2	
Chalk $z > 768.2$	0.97	9.72E-04	1029.3	

Table 1: Compaction constants.

The normal pressure chalk porosity – depth trend derived this way is approximated with a bi-segment exponential model as listed in Table 1.

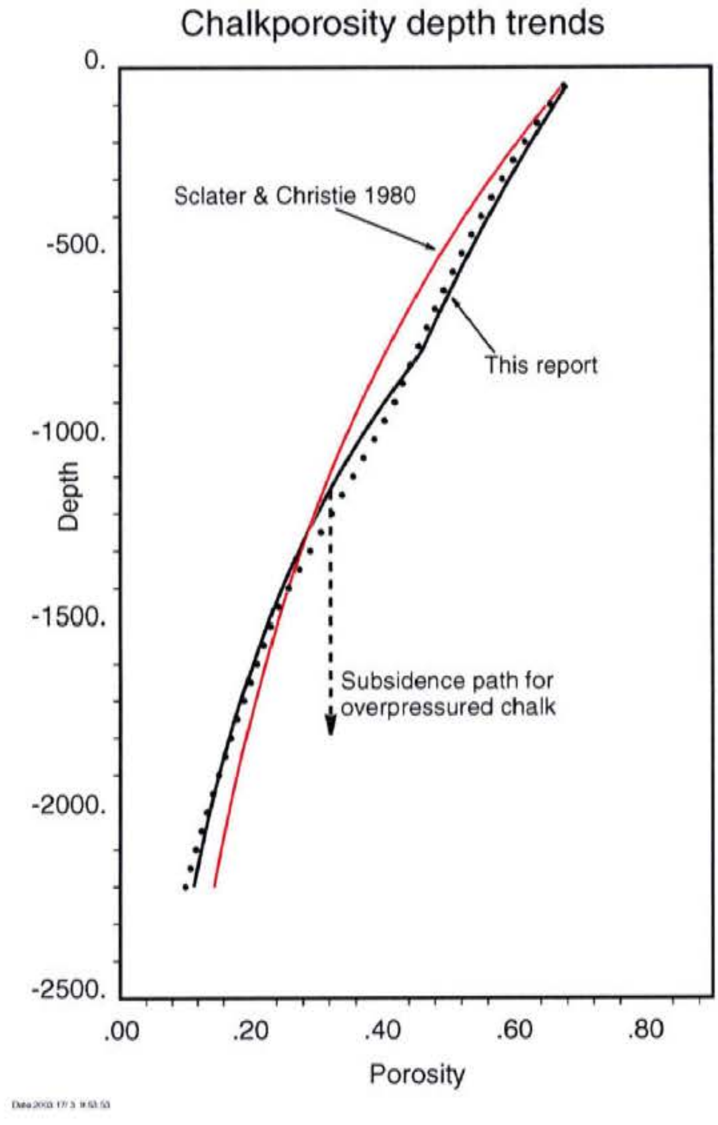

Figure 2: Normal compaction trends for the Chalk. Porosity depth values derived from velocity model is shown as dots, and the fit to this as a black line. Dashed line shows an example porosity – depth path for overpressured chalk.

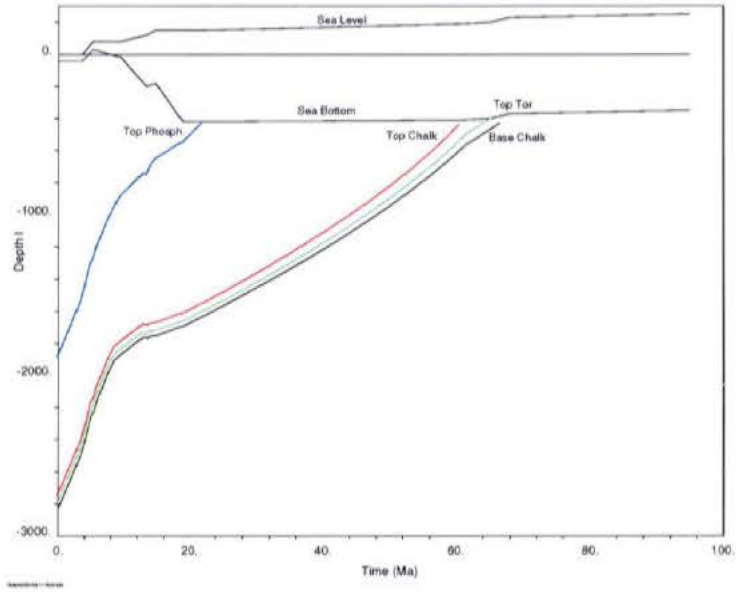

Figure 3: Modelled subsidence at the Rigs-2 well, South Arne Field (see Fig. 1 for location).

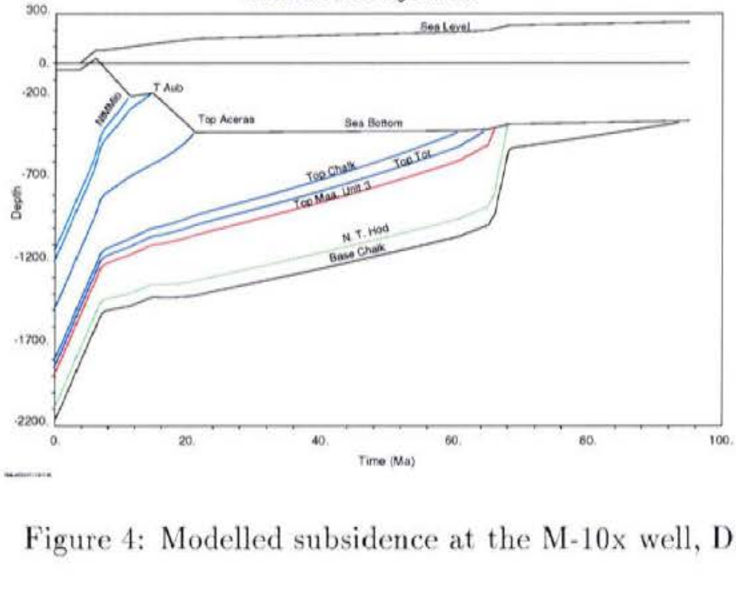

Figure 4: Modelled subsidence at the M-10x well, Dan Field.

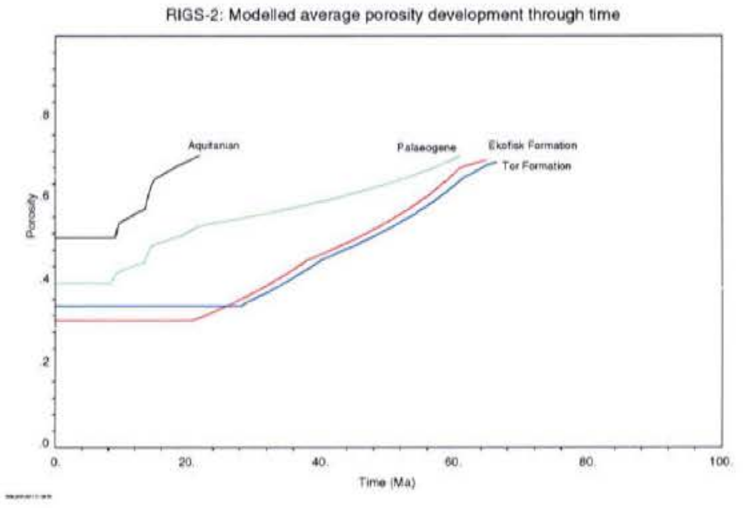

Figure 5: Simplistic porosity development model for the Rigs-2 site. Overpressuring arrests porosity decay in the Palaeogene at $\sim$ 10 Ma, but modelling suggests that HC effects arrest porosity decay in the Chalk much earlier.

Over-pressuring is assumed in depth intervals where the porosity exceeds the porosity expected at the present depth according to the normal compaction trend. It is assumed that excess pore pressure has not dissipated at all since onset. The duration of over-pressuring is the shortest possible with this assumption. This method is hereafter called "pressure preserving de-compaction". An alternative approach would be to assume that overpressure, and thus abnormal porosity, has been building up gradually since deposition, hereafter referred to as "gradual pressure build-up decompaction". The two assumptions may be considered as end-members of possible actual scenarios, but neither handles the case where higher overpressure in the past has dissipated to some extent.

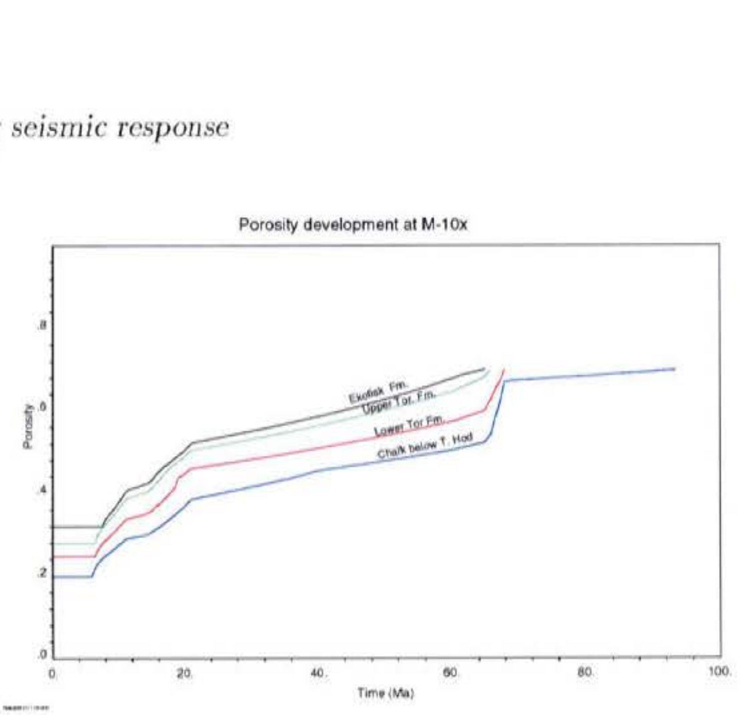

Figure 6: Simplistic porosity development model for the M-10x site. Overpressuring arrests porosity decay at ~ 8 Ma, and HC effects are apparently not important for Chalk porosity preservation.

Burial graphs show rapid burial rates only in the Neogene and very modest burial rates in Cretaceous – Palaeogene times (Figs. 3 and 4). Relative tranquility in Palaeogene times makes it likely that possible earlier over-pressure may have dissipated and present over-pressure to be primarily caused by rapid Neogene deposition. The observed excess pore pressure is therefore assumed to have initiated very late, and only few million years before present. This is further supported by the apparent correspondence between thickness of Neogene deposits and magnitude of overpressure (Japsen 2000). The pressure preserving de-compaction approximation therefore seems to be the best choice as the short time available reduces the problem of modelling pressure dissipation.

In the case of over-pressuring, the average presently observable porosity (ϕ_{obs}) in the interval is higher than predicted by the standard porosity decay function (equation 1). The porosity is assumed to be preserved since onset of over-pressuring. The exact depth where ϕ_{obs} is on the normal compaction curve is given by:

$$z_{obs} = \frac{1}{-a} Log\left(\frac{\phi_{obs}}{\phi_0}\right) \tag{2}$$

where z_{obs} is the depth where the unit left the normal compaction trend. On the basis of the following equation, average burial anomalies (z_{ano}) are computed for each stratigraphic unit where effects of minor lithological is minimized by averaging:

$$z_{ano} = \frac{1}{n}\sum_{n}^{1}\left[z - \frac{1}{-a} Log\left(\frac{\phi_{obs}}{\phi_0}\right)\right] \tag{3}$$

where z is present observation depth and n is the number of porosity log samples in the interval.

During compaction or decompaction a depth shift (Δz) is imposed. The logged porosity is then changed under the assumption that each sample has each their porosity – depth trends. For each sample in the porosity log an individual surface porosity ($\phi_{0'}$)is calculated according to:

$$Log(\phi_{0'}) = a(z - z'_{ano}) + Log(\phi_{obs}) \tag{4}$$

where $z'_{ano} = z_{ano} + \Delta z$ is the depth shift and Δz is the compaction/de-compaction value expressed as a depth shift. It is noted that the surface porosity is corrected according to the depth where the average porosity is on the normally pressured depth trend, and not the present depth. This approach implies that porosity deviations on the log are inherited from surface condition and reflect primary lithological and depositional differences. Diagenetic processes that may add material of cause local redistribution of material are thus neglected.

An example of such depth shifts is discussed below and shown in Fig. 12.

The burial anomalies may be directly converted into an estimated excess pressure as this is the main cause for the porosity anomaly (Japsen 1998). If the overpressure (Δp) is assumed to be caused by Neogene rapid deposition (the burial anomaly), then it is equivalent to the effective stress (σ) exerted by this column:

$$\sigma = \Delta p = (\rho_r - \rho_{br}) \cdot g \cdot z_{ano} \tag{5}$$

where g is the gravity constant. If densities of the rock (ρ_r) and brine (ρ_{br}) are equal to 2000 and $1000 Kg/m^3$, then a burial anomaly of 100 m is roughly equivalent to 1 MPa.

Burial modelling of the Rigs-2 well site

In order to elucidate the conditions at the Rigs-2 well backstripping has been performed. Depths and compaction parameters for this well are listed in table 3. The well encountered excess pressures at 1300 m increasing to app. 7.4 MPa at 1600 m, 12MPa at 2600 m, and 14.8 MPa in the Chalk section (Table 2). In our cases the burial anomalies are calculated as given in table 2 with parameters given in table 3.

Rigs-2	Burial anomaly (m)	Approximate Pressure (MPa)	Observations (MPa)
Below near base Tortonian	381	3.8	-
Below top Aub	730	7.3	-
Below top Aceras	1180	11.8	12
Chalk	1654	16.5	14.8

Table 2: Burial anomalies and excess fluid pressure for the Rigs-2 well. Calculated burial anomalies are converted to over-pressure as described in the text.

The subsidence graph calculated this way (Fig. 3) displays moderate burial rates until approximately 15 Ma b.p., where a considerable increase is noted. At approximately 10 Ma b.p. porosity is arrested in the Palaeogene due to over-pressuring (Fig. 5). Porosity in the Chalk is modelled to be arrested much earlier which reflect early hydrocarbon invasion rather than over-pressuring. A similar modelled porosity development for the M-10x shows no earlier cessation of porosity decay in the chalk reflecting later hydrocarbon charging of the Dan Field as compared to the South Arne Field (Fig. 6).

Rock unit	Base unit TWT Sec.	Base unit m. b.m.s.l.	Surface porosity ϕ_0	Decay length m. $1/a$
Quaternary	na	453.5	0.56	2560.16
Piacenzian	na	794.0	0.56	2560.16
Zanclean	na	809.4	0.56	2560.16
Messinian	na	902.4	0.56	2560.16
Tortonian	1.430	1411.63	0.56	2560.16
Aub	1.805	1772.4	0.71	1960.02
Aceras	2.705	2745.6	0.71	1960.02
Ekofisk Fm.	2.741	2796.1	0.968	1029.34
Tor Fm.	2.766	2829.1	0.968	1029.34

Table 3: Depths and compaction constants for the Rigs-2 well. Note that this listing mode means that for instance Top Chalk is at 2.705 sec.

The observed pressure in the Rigs-2 well is, however, about 10% lower than the estimate based on porosity observations. If the anomalous high porosity in the well is attributed to other factors than over-pressuring, then this other effect may be contributing with 10 % compared to pressures. This other effect may be early hydrocarbon invasion, which frequently has been suggested as a cause for porosity preservation above normal (e.g. Bramwell et al. 1998).

In the Central Graben in general there seem to be roughly the same excess pressure in the water zones of the lower Palaeogene section and the Chalk. As seen in table 2, the calculated excess pressure for the chalk is exceeding the Lower Palaeogene pressure by 3.7 MPa and observed pressure difference is 2.8 MPa. Only 0.74 MPa of this difference is attributable to a direct pressure effect from the hydrocarbons, so the pressure increase in the chalk suggests lateral support from deeper levels.

Within the chalk a difference of 0.9 MPa is seen between observed and calculated excess pressure. It is therefore estimated that the abnormally high porosity is due to a combination of overpressure and preserving effects of the invaded hydrocarbons. It may be estimated that rapid Neogene deposition contributes with 12 MPa, the hydrocarbon column constributes with 0.74 MPa and lateral pressure support contributes 2 MPa to the observed pressures and porosity preservation. The porosity preservation owing to the presence of hydrocarbons could have been replaced by only a further ~ 2 MPa.

Saturation modelling

In order to model the saturation realistically, the strong capillary effects in the chalk must be taken into account. We apply the saturation height model developed by Hess (2001). In this method the saturation is calculated directly from the capillary pressure (P_c) and the capillary entry pressure (P_{ce}):

$$Sw = \left(\frac{P_{ce}}{A \cdot P_c - A \cdot P_{ce} + P_{ce}} \right)^{1/B} \tag{6}$$

where A and B are given by:

$$A = 10^{c_1 + c_2 \cdot \phi} \tag{7}$$

$$B = 0.10 + 1.95 \cdot \phi$$

where ϕ is the porosity (in fractions). Constants c_1 and c_2 differs for the Tor and Ekofisk formations as given in table 4.

The capillary entry pressure is given by an equation of the form:

$$P_{ce} = c_3 \cdot \phi^{c_4} \tag{8}$$

where constants c_3 and c_4 are different for the Tor and Ekofisk Formations as given in table 4.

Formation	c_1	c_2	c_3	c_4
Ekofisk	-0.75	2.70	7.5	-1.2
Tor	-1.10	4.35	7.0	-0.7

Table 4: Constants for the saturation height model.

The capillary pressure is obtained from the height above free water level (FWL):

$$Pc = (FWL - z) \cdot \Delta p \cdot Cap \tag{9}$$

where z is the depth, Δp is the pressure gradient difference between oil and water, and Cap is the conversion factor of interfacial tension in the Hg/air system to the oil/water system at reservoir conditions. In the case of the Rigs-2 well the following values for the parameters are assumed:

$$\Delta p = 0.182 psi/ft = 0.0413 bar/m \tag{10}$$

$$Cap = \frac{\sigma Cos\theta_{ow}}{\sigma Cos\theta_{Hg/air}} = \frac{28}{367} = 0.076 \tag{11}$$

These parameters produce an acceptable fit to observed Sw, if a FWL at 2900 m (b.m.s.l.) is assumed (Fig. 7). During modelling of seismic response to changes in hydrocarbon saturation (Sw), the above saturation height model is applied. Changes in Sw can occur in the model by imposing changes in FWL, such that realistic vertical differences in Sw are calculated. If alternatively the model is aimed at studying changes in compaction the above saturation height model will automatically impose Sw changes due to the porosity dependency.

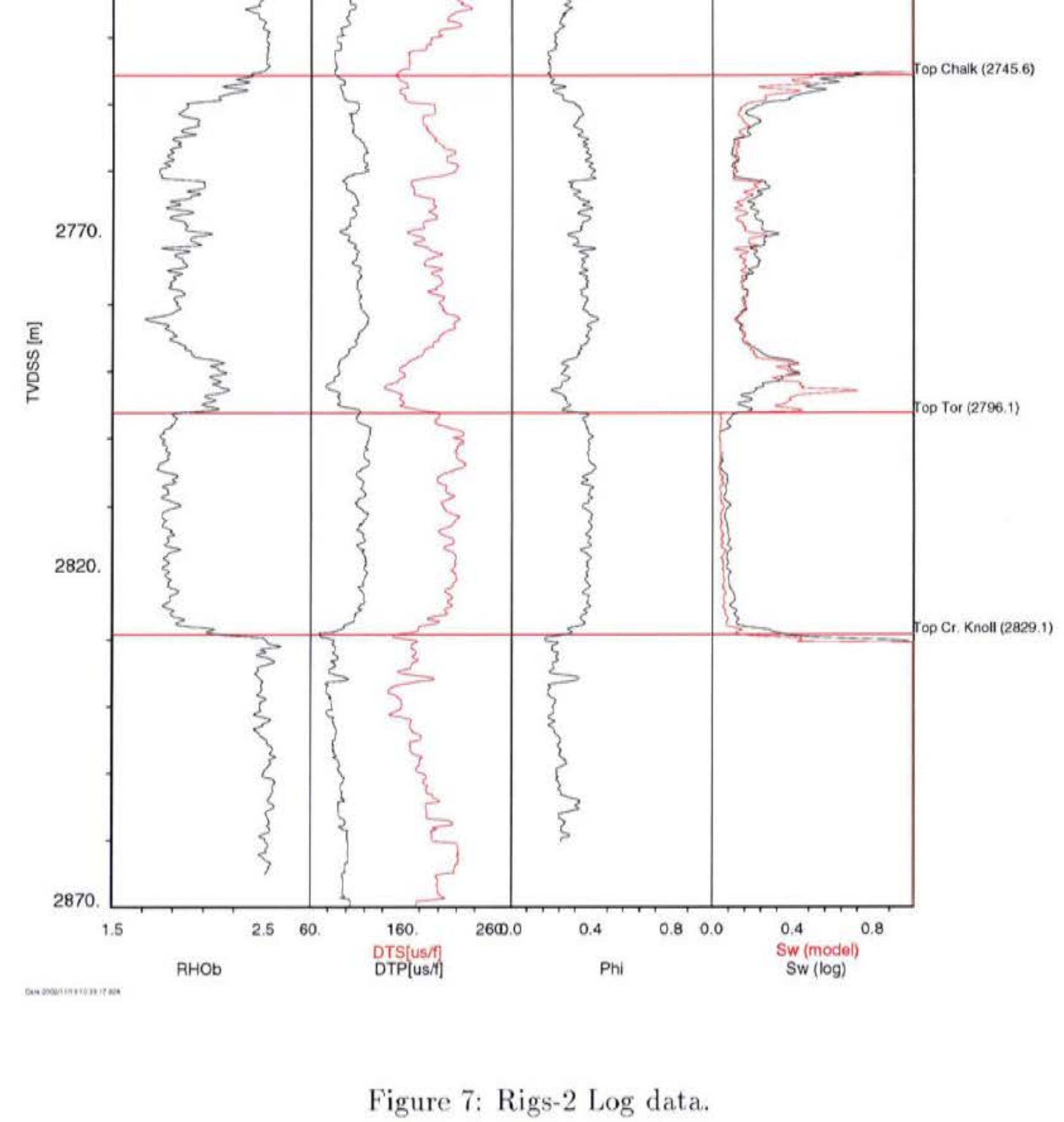

Figure 7: Rigs-2 Log data.

Rock Physics and Fluid substitution

We estimate elastic properties and changes thereof in the chalk as a consequence of changes in hydrocarbon saturation and degree of compaction. The relationships for elastic moduli and velocity versus porosity are described using modified Hashin – Shtrikman bounds and Gassmann's relations in an approach similar to the one suggested by Walls et al (1998).

Fluid substitution

We assume the low-frequency theory for fluid substitution by Gassmann (1951) to be fulfilled for elastic measurements with log tools. It is thus assumed that the chalk is sufficiently permeable to allow pore fluid pressures to equilibrate instantaneously when sound waves propagates through the rock. This is not fulfilled for isolates pores and low permeability rocks at high frequency, but will automatically be fulfilled for seismic data if Gassmann's theory applies to log data. The Gassmann theory gives the following relationship between rock moduli:

$$\frac{K_{sat}}{K_0 - K_{sat}} = \frac{K_{dry}}{K_0 - K_{dry}} + \frac{K_{fl}}{\phi(K_0 - K_{fl}})) \tag{12}$$

and $G_{sat} = G_{dry}$ where K_{dry} ,K_{sat} , K_0 and K_{fl} are bulk moduli of the dry rock, the saturated rock, the mineral components and the pore fluid respectively, G_{sat} and G_{dry} are shear moduli of the saturated and dry rock respectively and ϕ is the porosity. Bulk and shear moduli are related to recorded compressional velocity (V_p), shear velocity (V_s) and density (ρ) according to:

$$K = \rho(V_p^2 - \frac{4}{3}V_s^2) \tag{13}$$

and

$$G = \rho V_s^2$$

We apply this theory for substituting one fluid with another, in which case the Gassmann formula can be develop to:

$$K_{sat2} = \frac{K_0 \cdot A}{1 + A} \tag{14}$$

where

$$A = \frac{K_{sat1}}{K_0 - K_{sat1}} - \frac{K_{fl1}}{\phi(K_0 - K_{fl1})} + \frac{K_{fl2}}{\phi(K_0 - K_{fl2})}$$

and

$$G_{sat1} = G_{sat2}$$

where subscripts $sat1$ and $sat2$ refer to the saturated rock before and after substitution.

Fluid properties (subscripts $fl1$ and $fl2$) are calculated from the properties of formation water and hydrocarbons using Reuss type fluid mixtures:

$$K_{fl} = \frac{1}{Sw/K_w + (1 - Sw)/K_{hc}} \tag{15}$$

where Sw is the water saturation, and subscripts w and hc refer to water and hydrocarbon components respectively. This formula assumes that the two fluids are perfectly mixed considering the influence on wave propagation, which depend on frequency. Laboratory experiments show that this assumption first begin to fail at ultrasonic frequencies (Fabricius et al., this report; Mavco and Japsen, this report). The consequence of the Reuss formulation is that the weak/softer fluid component will dominate the overall acoustic response such that small hydrocarbon saturations will have a large effect.

Effects of compaction/decompation

Changes in rock moduli resulting from changes in porosity are calculated on the basis of a modified Hashin – Shtrikman model similar to the one proposed by Walls et al. (1998) for Ekofisk Field data. The model describes how bulk and shear moduli change with porosity in an interval between zero porosity and a maximum porosity (ϕ_{max}) encompassing the variation in the available data set. Data are allowed to vary between the modified upper Hashin – Shtrikman (MUHS) according to:

$$K_{eff}^{UHS} = \left[\frac{\phi/\phi_{max}}{K_{lim} + \frac{4}{3}G_0} + \frac{1 - \phi/\phi_{max}}{K_0 + \frac{4}{3}G_0}\right]^{-1} - \frac{4}{3}G_0 \tag{16}$$

$$G_{eff}^{UHS} = \left[\frac{\phi/\phi_{max}}{G_{lim} + Z_0} + \frac{1 - \phi/\phi_{max}}{G_0 + Z_0}\right]^{-1} - Z_0$$

where

$$Z_0 = \frac{G_0}{6}\frac{9K_0 + 8G_0}{K_0 + 2G_0}$$

corresponding to the presumably stiffest possible variety, where the subscript lim refer to moduli at the selected maximum porosity. This set of equations can also be developed for the lower bound which, however, is equivalent to the simpler Reuss average as may be developed from:

$$\frac{K_{sat}}{K_0 - K_{sat}} = \frac{K_{dry}}{K_0 - K_{dry}} + \frac{K_R}{K_0 - K_R} \tag{17}$$

where

$$K_R = \left(\frac{\phi_{max} - \phi}{\phi_{max} \cdot K_{lim}} + \frac{1 - (\phi_{max} - \phi)}{\phi_{max} \cdot K_0}\right)^{-1}$$

The upper bound description is applied during changes in porosity, where stratigraphical property differences are accommodated through adjustments of the end members (K_0 and K_{lim}). During decompaction the porosity may exceed ϕ_{max} in which case the further change is set to follow the lower (Reuss) bound.

Seismic model

We obtain zero offset seismic sections and AVO gathers based on the modelled logs as described above. Zero offset synthetic data are obtained from the reflectivity series that are calculated from the P-wave velocity (V_p) and density (ρ) logs as given by equation 22. This reflectivity series is convolved with a Ricker wavelet. A Ricker wavelet with a dominating frequency of 50 Hz was found to produce an acceptable match to field data. P-wave reflectivity for offset gathers ($R(\Theta)$) is calculated on the basis of first order reflectivity equations from the Zoeppritz equations as given by Spratt et al. (1993):

$$R(\Theta) = R_{pp0} + (R_{pp0} - 2' R_{ss0}) Sin^2\Theta + 0' \cdot \frac{\Delta\rho}{\rho_a} Sin^2\Theta \tag{18}$$

where

$$2' = 8\left(\frac{V_s}{V_p}\right)^2$$

and

$$0' = 2\left(\frac{V_s}{V_p}\right)^2 - \frac{1}{2}$$

and R_{pp0} and R_{ss0} are zero offset reflection coefficients for P and S-waves as given by equation 22. ρ_a is average density and $\Delta\rho = \rho_2 - \rho_1$; the density difference across the interface.

Offset calculations are based on an assumed 2500m streamer, which with fairly constant overburden velocities around 2000 m/sec will produce incidence angles (Θ) below 22.5° at top chalk level. Refraction in the chalk overburden is considered negligible due to rather homogeneous velocities and is consequently disregarded.

For standard analyses of amplitude versus offset (AVO) we apply the Shuey (1985 in Castangna 1993) approximation:

$$R_{pp}(\Theta_1) \sim R_{pp0} + \left(A_0 R_{pp0} + \frac{\Delta\sigma}{(1-\sigma^2)^2}\right) Sin^2\Theta_1 + \frac{1}{2}\frac{\Delta V_p}{V_{pa}}(Tan^2\Theta_1 - Sin^2\Theta_1) \tag{19}$$

where

$$A_0 = B_0 - 2(1 + B_0)\left(\frac{1-2\sigma}{1-\sigma}\right) \tag{20}$$

and

$$B_0 = \frac{\frac{\Delta V_p}{V_{pa}}}{\frac{\Delta V_p}{\Delta V_{pa}} + \frac{\Delta \rho}{\Delta \rho_a}} \tag{21}$$

and the zero offset P-wave reflectivity (R_{pp0}) is:

$$R_{pp0} = \frac{I_{p2} - I_{p1}}{I_{p2} + I_{p2}} \tag{22}$$

where the impedance is given by $I_p = V_p \cdot \rho$. Substituting V_p with V_s gives the S-wave reflectivity R_{ss0}. σ is the poisson ratio as given by:

$$\sigma = \frac{\frac{1}{2}(\frac{V_p}{V_s})^2 - 1}{(\frac{V_p}{V_s})^2 - 1} \tag{23}$$

The last term in equation 19 is dropped as it is insignificant for moderate angles of incidence (Θ_1). We use the first two term in equation 19 for the intercept versus slope plots given in Figs xx and xx. We also use the poisson ratio (σ, equation 23) to crossplot with acoustic impedance to illustrate effects of porosity and saturation changes.

Seismic model examples

We exemplify modelling of compaction and saturation changes with data from the Rigs-2 well, South Arne Field (Table 4). Seismic examples are given in the appendix. Input data to the modelling are logs, where key logs like V_p, V_s, and density are restored to virgin conditions. Due to a missing shallow resistivity log, this restoration proved to be most reliably performed using rock physical calculations as described in Japsen et al. (*this report*). This results in an implicid self-consistency that causes modelled property changes calculated in this report to perform somewhat better than if restoration was based on shallow resistivity data (see discussion in Japsen et al. *this report*).

Moduli of the formation components have been estimated during laboratory measurements (Fabricius et al. *this report*) and are listed in Table 4.

Component	Bulk Modulus K	Shear Modulus G	Density ρ
Calcite	71.0	30.0	2.71
Silicates	25.0	9.0	2.70
$lim : \phi = 45$	1.5	2.5	
Brine	2.96	0	1.035
Oil	0.52	0	0.633

Table 5: Moduli and densities of formation components

To demonstrate the capabilities of the modelling tools, two scenarios are tested:

a. The free water level is changed from 2795 m b.m.s.l. over the ideal 2900 m to 2990 in steps of 5 m corresponding to 40 cases (or traces).

b. The present effective stress in the chalk is changed corresponding to depth shifts of -900 m to 900 m in steps of 30 m corresponding to 60 cases (or traces).

Change in free water level

A range of synthetic seismograms are modelled by only changing the free water level and via saturation height modelling change the fluid composition. The range is from 2795 m to 2990 m .b.s.l. corresponding to a change from 100% water saturation to approximately irreducible water saturation (Fig. 8. The best fit FWL relative to logged Sw is in the middle of this range, so maximum modelled hydrocarbon saturation far exceeds observed saturations.

A set of plots illustrating poisson ratio versus acoustic impedance shows that Sw changes affects both of these properties (Fig. 10). However, it is clear that acoustic impedance is more sensitive to porosity changes, than to saturation changes whereas the poisson ratio is more susceptible to saturation changes. These tendencies would be more amplified if gas was used rather than oil in the modelling, and acoustic impedance effects from saturation changes would become more significant. Also is the poisson ration becoming more sensitive to saturation with increasing porosity.

Another interesting effect is seen on the Top Chalk and Top Tor reflectors (at 2.741 sec; table 3; Fig. 9). The Top Tor reflector is characterised by downward decreasing impedance. It is seen that the amplitude of this reflector increases abruptly (more negative) as oil enters the formation. As FWL deepens (saturations increases) it gains amplitude until low to moderate oil saturations. From moderate to high oil saturation it slowly decrease again. This is a consequence of the saturation height model, which causes Tor Formation hydrocarbon saturation to increase faster than in the Ekofisk Formation in spite of lower capillary pressures at low overall hydrocarbon saturation. This is a consequence of lower capillary entry pressures in the Tor Formation.

The Top Chalk reflector is also affected by increasing oil saturation (Fig. 9). It is seen to loose amplitude with increasing oil saturation, and at saturations slightly higher than observed in the well, a reversal is predicted.

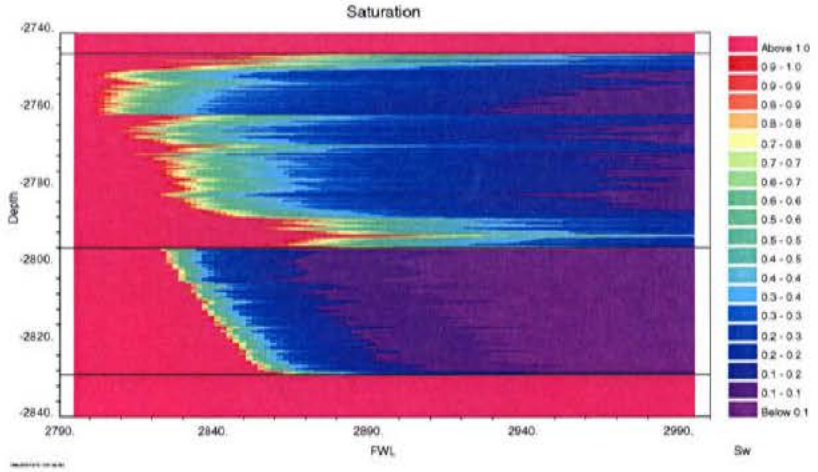

Figure 8: Water saturation profiles calculated by changing the free water level (FWL). Note that different properties in Tor and Ekofisk formations cause the Tor to hold lower saturations for shallow FWL than Ekofisk in spite of lower capillary pressure.

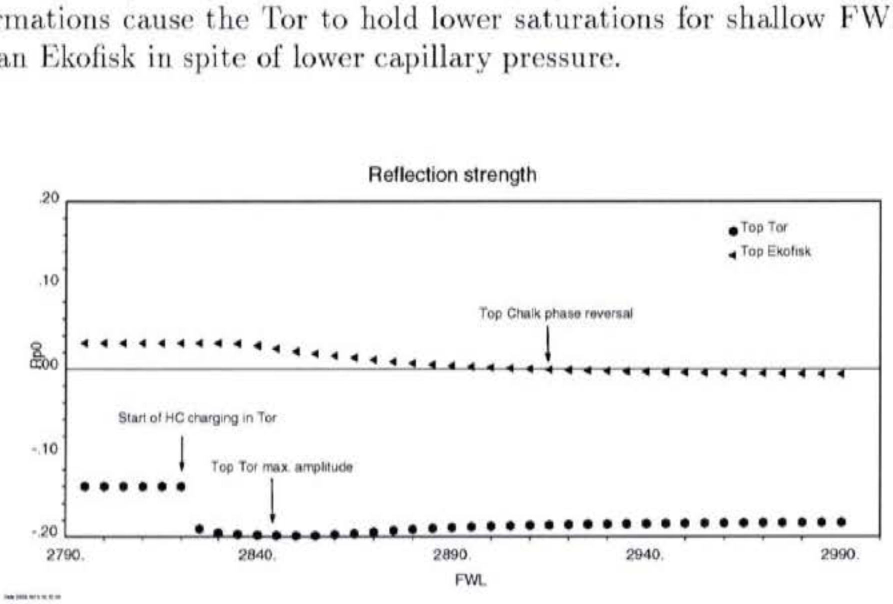

Figure 9: Modelled reflector strength and sign of the Top Chalk and Top Tor reflectors as a function of free water level in the Rigs-2 well(or modelled saturation distribution).

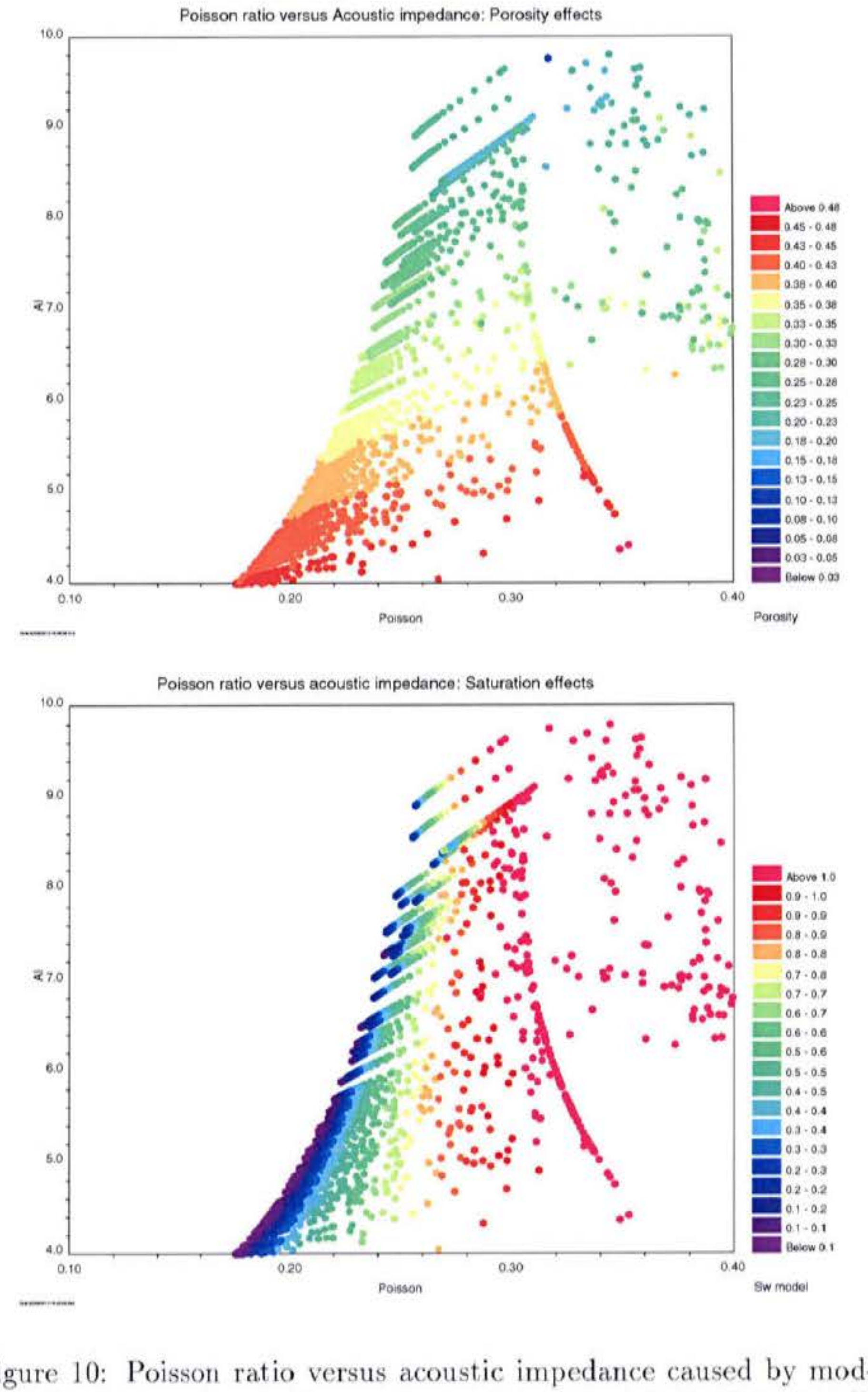

Figure 10: Poisson ratio versus acoustic impedance caused by modelled Sw changes (several free water level positions) in the Rigs-2 well. X and Y are the same, but colours show porosity and Sw. Points in the upper right are from outside the Chalk.

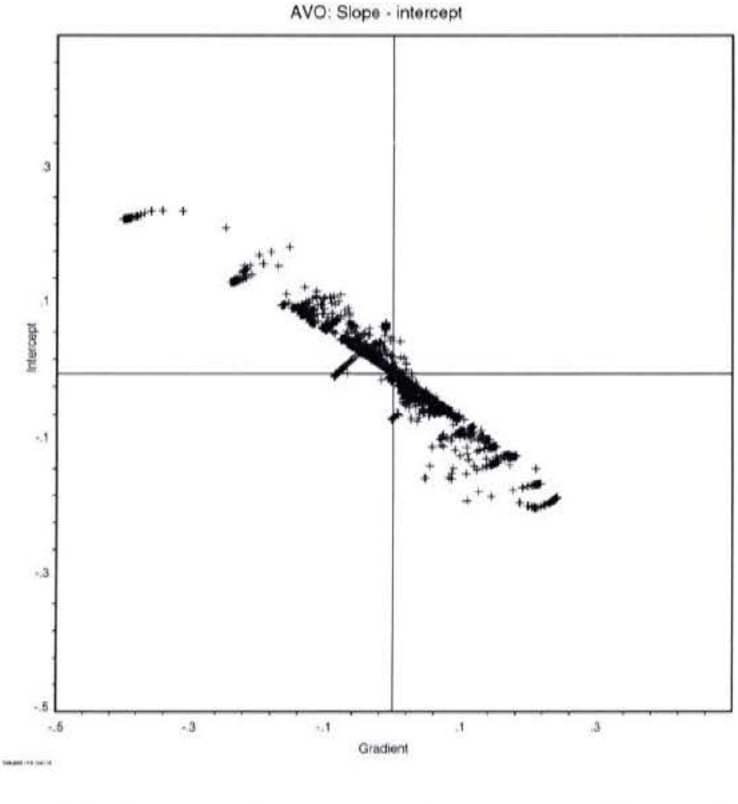

Figure 11: Slope (after Shuey 1985) versus intercept for saturation change models. Chalk interval only.

Change in effective stress

The compaction/de-compaction exercise is illustrated with the porosity logs shown in (Fig. 12). An interesting effect is that the varability in the porosity traces is amplified during de-compaction, and subdued during compaction which is in accordance with observations in seismic data (e.g. Britze et al. 2000). Modelling a change in effective stress inevitably results in saturation changes such that less porosity means higher water saturation. This relationship can be seen to be almost exponential (Fig. 12).

The synthetic porosity and Sw logs also show that the observed Sw is closer to irreducible water saturation in the Tor Formation than in the Ekofisk Formation in spite of lower capillary pressures in Tor. This is seen from the fact that an only negligible reduction in Sw occurs in the Tor although porosity is almost doubled during decompation. The Sw reduction during de-compaction in Ekofisk is more conspicuous. During compaction this diffences, which originates from entry pressure differences, is further amplifed.

Another interesting observation is that amplitudes on the porosity log (as well as the saturation log) are increased during decompation and subdued during compaction. This is a consequence of the design of the compaction/de-compaction model. This effect causes amplitude changes in the seismic model and corresponds to general seismic observations in the Chalk (Britze et al. 2000).

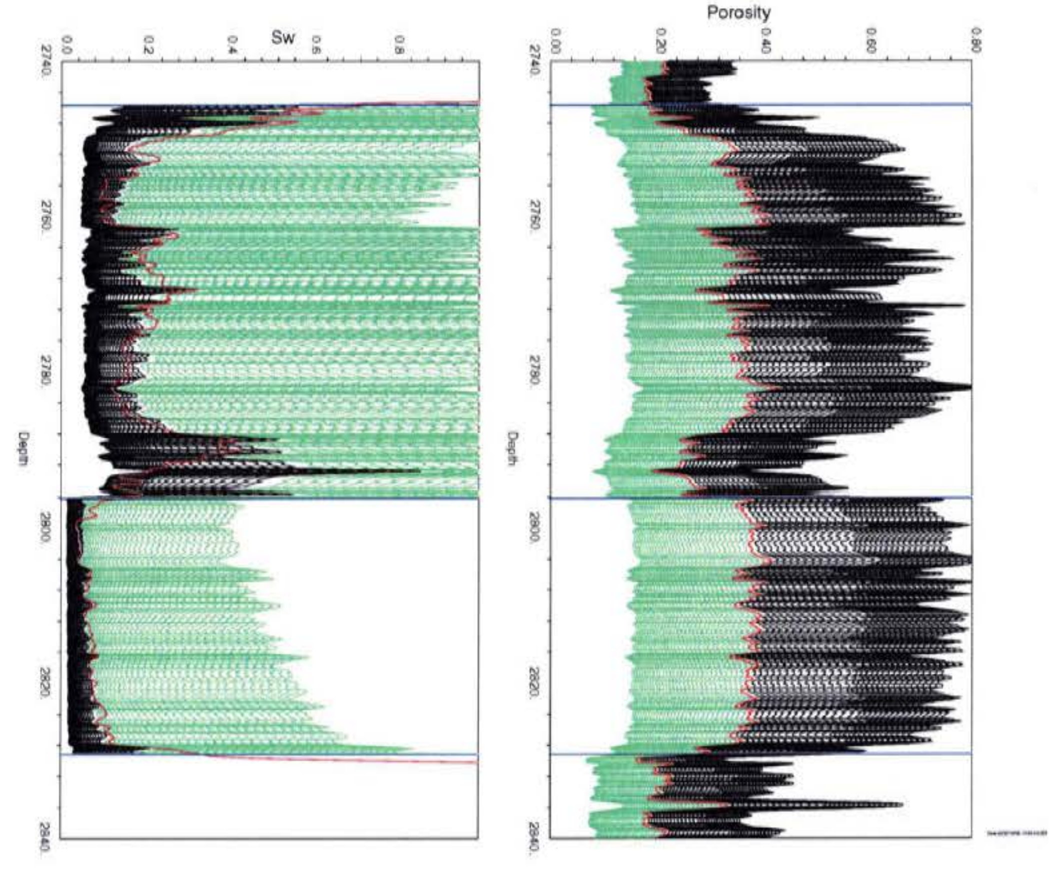

Figure 12: Depth shift of the Rigs-2 well. Right panel shows log traces corresponding to decompaction in black and compaction in green. Corresponding saturation changes resulting from porosity changes are shown to the left in the same colours.

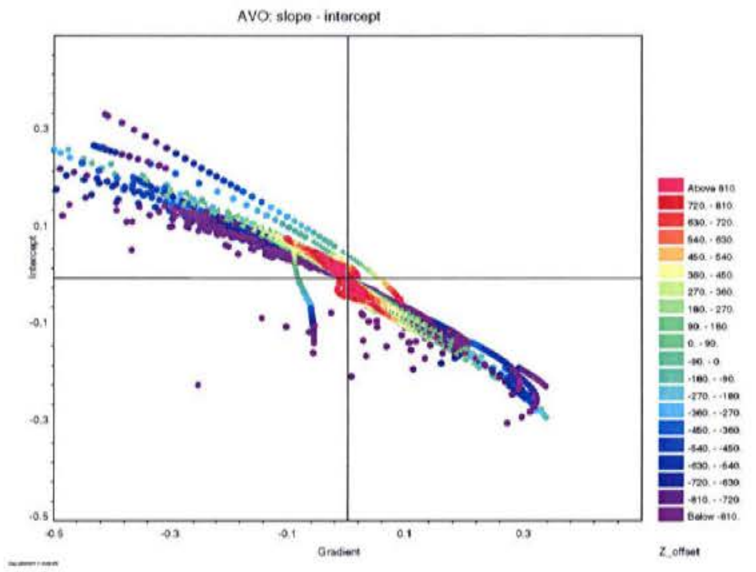

Figure 13: Slope (after Shuey 1985) versus intercept for compaction/de-compaction change models. Chalk interval only. Effective stress changes corresponding to -900 m to +900 m from present position are shown i colour. Very deep burial is seen to subdue reflectivity as well as gradient changes.

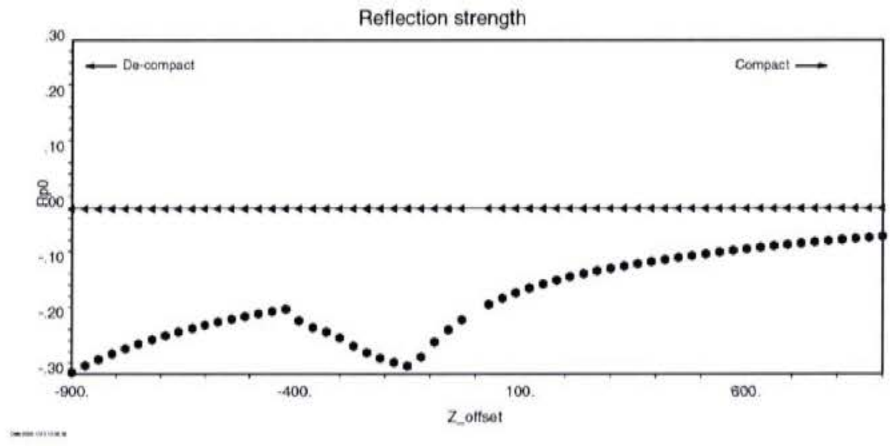

Figure 14: Modelled reflector strength and sign of the Top Chalk and Top Tor reflectors as a function of compaction/decompaction.

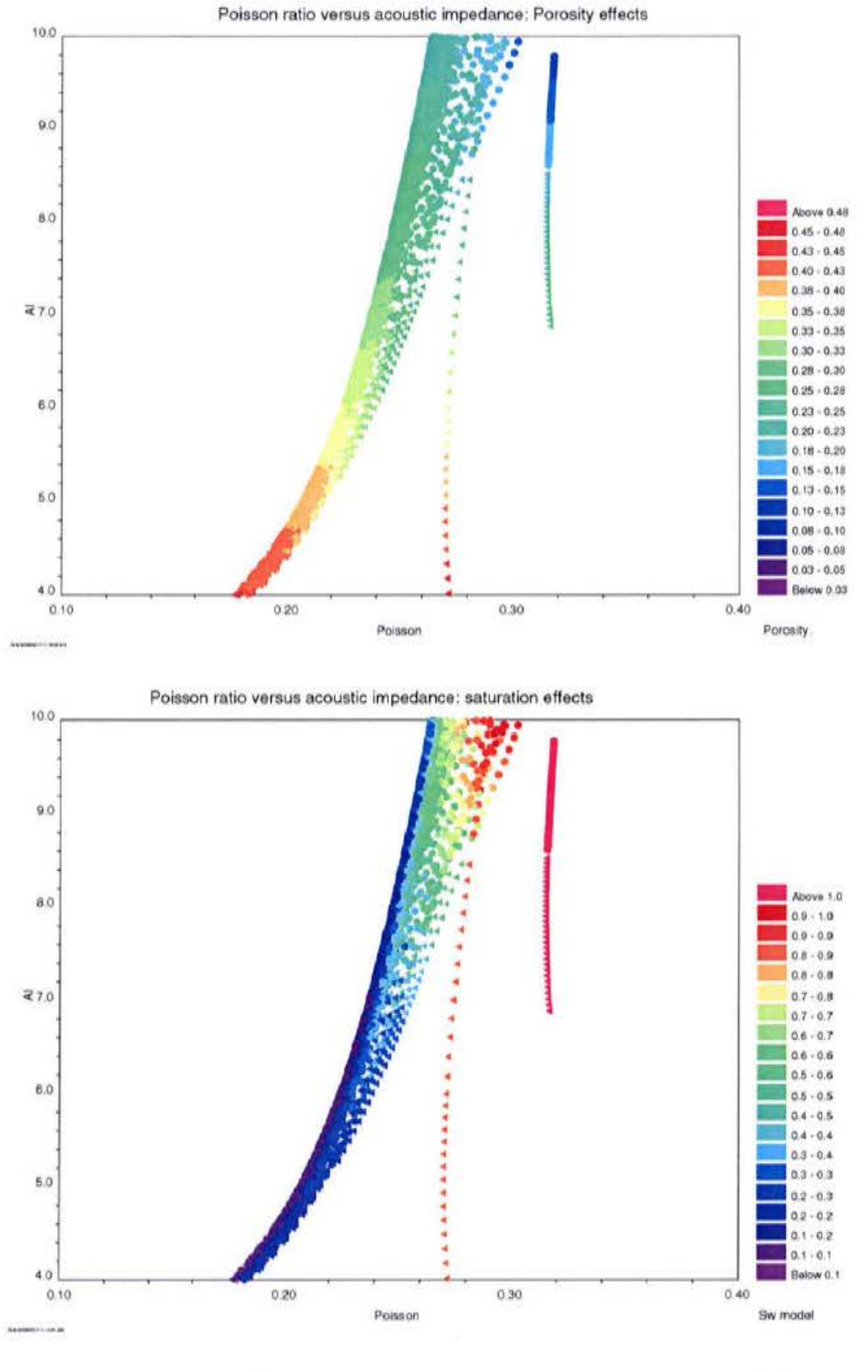

Figure 15: Poisson ratio versus acoustic impedance caused by modelled compaction changes (-900 m to +900 m from present position). Only Chalk from the Rigs-2 well is shown. X and Y are the same, but colours show porosity and Sw.

References

Athy, L. F. 1930: Density, porosity and compaction of sedimentary rocks. Bull. of the American Association of Petroleum Geologists, 14, 1-24.

Bramwell, N. P., Caillet, G., Meciani, L., Judge, N., Green, M. and Adam, P. 1998: Chalk exploration, the search for subtle traps. In Fleet, A. J. & Boldy, S. A. R. (eds.) Petroleum Geology of Northwest Europe: Proceedings of the 5th conference. The Geological society, London, 911-937.

Britze, P., Nielsen, E. B., Dahl, N. and Haug, S., 2000: EAGE, Petrophysics meets Geophysics, Proceedings.

Castagna, J. P. 1993: AVO analysis – Tutorial and review. In J. P. Castagna and M. M. Backus (eds.): Offset-dependent reflectivity – Theory and practice of AVO analysis, Investigations in Geophysics no. 8, Society of Exploration Geophysicists, 3-36.

Engstrøm, F. 1995: A new method to normalize capillary pressure curves. International Symposium of the Society of Core analysts, San Francisco, 1995, SCA no. 9535, 12p.

Fabricius, I. L, Høier, C., Japsen, P. and Korsbech, U. this report: Modeling elastic moduli of impure chalk.

Frederiksen, S., Nielsen, S.B., and Balling, N. 2001: Post-Permian evolution of the Central North Sea: a numerical model. Tectonophysics, 343, 185-203.

Gassmann, F. 1951: Elastic waves through a packing of spheres. Geophysics, 16, 673-685.

Japsen, P. 1998: Regional velocity-depth anomalies, North Sea Chalk; a record of over-pressure and Neogene uplift and erosion. American Association of Petroleum Geologists, Bulletin 82, 2031-2074.

Japsen, P. 1999: Overpressured Cenozoic shale mapped from velocity anomalies relative to a baseline for marine shale, North Sea. Petroleum Geoscience, 5, 321-336.

Japsen, P., 2000: Fra kridthav til Vesterhav, Nordsøbassinets udvikling vurderet ud fra seismiske hastigheder. Geologisk tidskrift, 2, 36 p.

Japsen, P., A. Bruun, I. L. Fabricius, Rasmussen, R., Vejbæk, O.V., Pedersen, J. M., Mavko, G. and Mogensen, C. this report: Influence of porosity and pore fluid on acoustic properties of chalk: AVO-response from oil, South Arne field, North Sea.

Jensen, P. K., Holm, L. and Thomsen, E. 1985: Modelling burial history, temperature and maturation. – In B. M. Thomas et al. (ed.): Petroleum Geochemistry in Exploration of the Norwegian Shelf. Proceedings of a NPF conf. - Graham & Trotman, PP. 145 - 153.

Mavko, G. and Japsen, P. this report: Fluid substitution in chalks: Effects of saturation scales.

Mavko, G., Mukerji, T., and Dvorkin, J. 1998: The rock physics handbook. Tools for seismic analysis in porpus media. Cambridge University Press, 329 p.

Megson, J. and Hardman, R. 2001: Exploration for and development of hydrocarbons in the Chalk of the North Sea: a low permeability system. Petroleum Geoscience, 7, 3-12.

Sclater, J. G. and Christie, P. A. F. 1980: Continental stretching: an explanation of the post-mid-Cretaceous subsidence of the Central North Sea basin. - Jour. of Geoph. Res., vol. 85, no. b7., pp. 3711-3739.

Shuey, R. T. 1985: A simplification of the Zoeppritz equations, Geophysics, 50, 609-614.

Spratt, R. S.m Goins, N. R. and Fitch, T. J. 1993: Pseudo-shear – The analyses of AVO. . In J. P. Castagna and M. M. Backus (eds.): Offset-dependent reflectivity – Theory and practice of AVO analysis, Investigations in Geophysics no. 8, Society of Exploration Geophysicists, 37-56.

Vejbæk, O. V. 2002: Reservoir characterization of the Roar Gas Field, Danish North Sea. Petroleum Geoscience, 2002, 8(1), 71-87.

Walls, J. D., Dvorkin, J., and Smith, B. A. 1998: Modeling SeiSmic Velocity in Ekofisk Chalk. 1998 SEG Expanded abstracts, 4 p.

Appendices

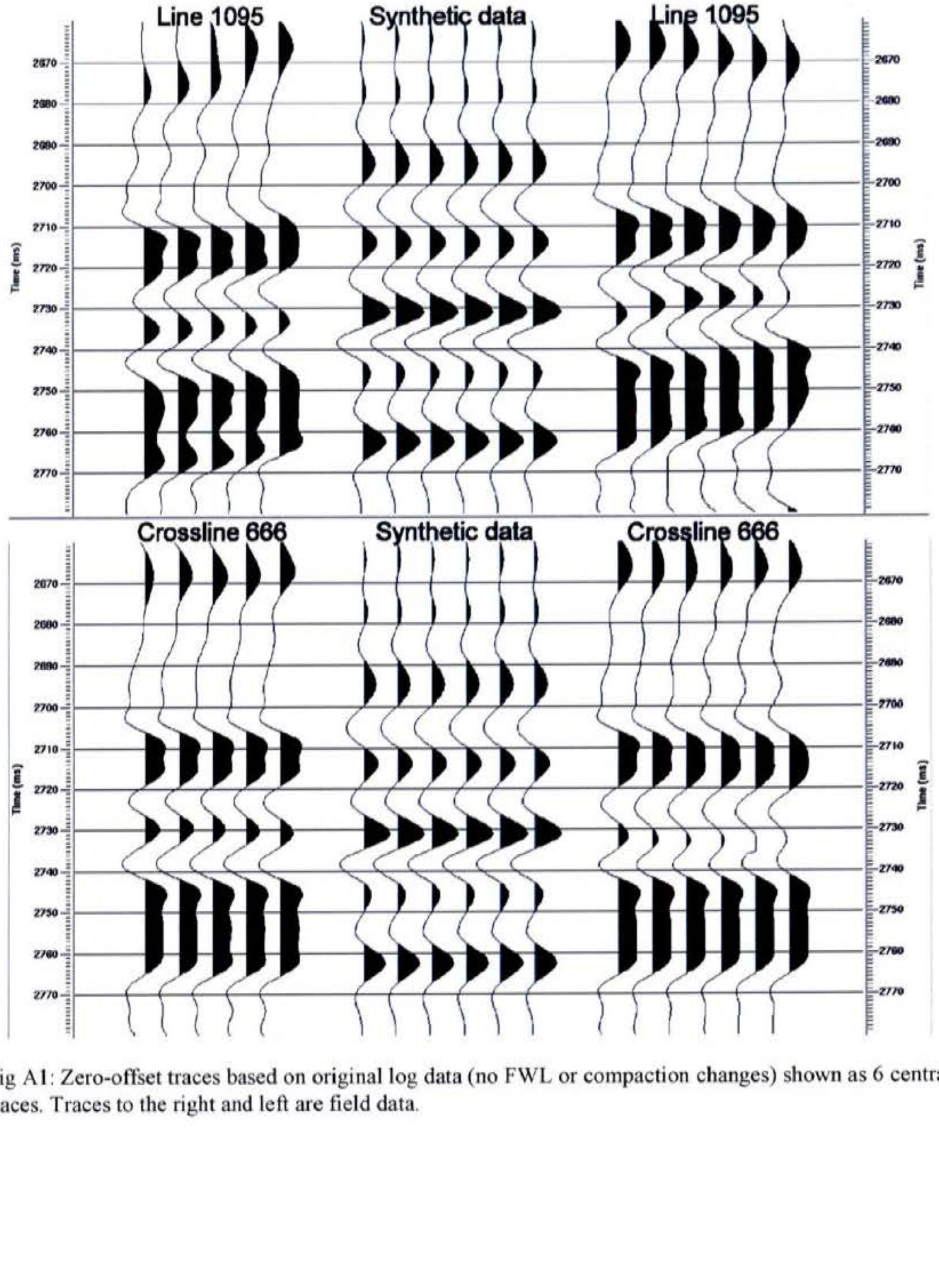

Fig A1: Zero-offset traces based on original log data (no FWL or compaction changes) shown as 6 central traces. Traces to the right and left are field data.

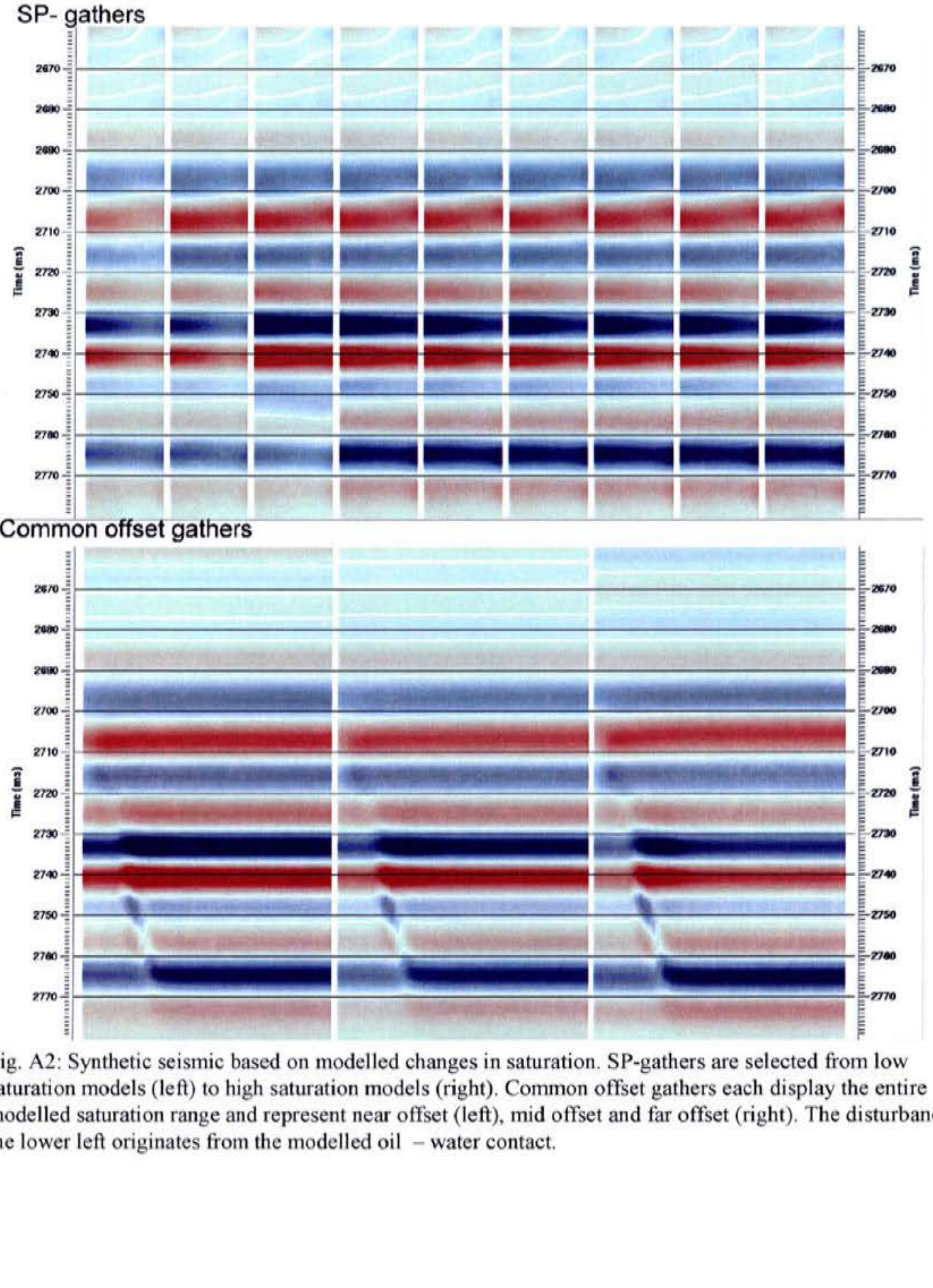

Fig. A2: Synthetic seismic based on modelled changes in saturation. SP-gathers are selected from low saturation models (left) to high saturation models (right). Common offset gathers each display the entire modelled saturation range and represent near offset (left), mid offset and far offset (right). The disturbance in the lower left originates from the modelled oil – water contact.

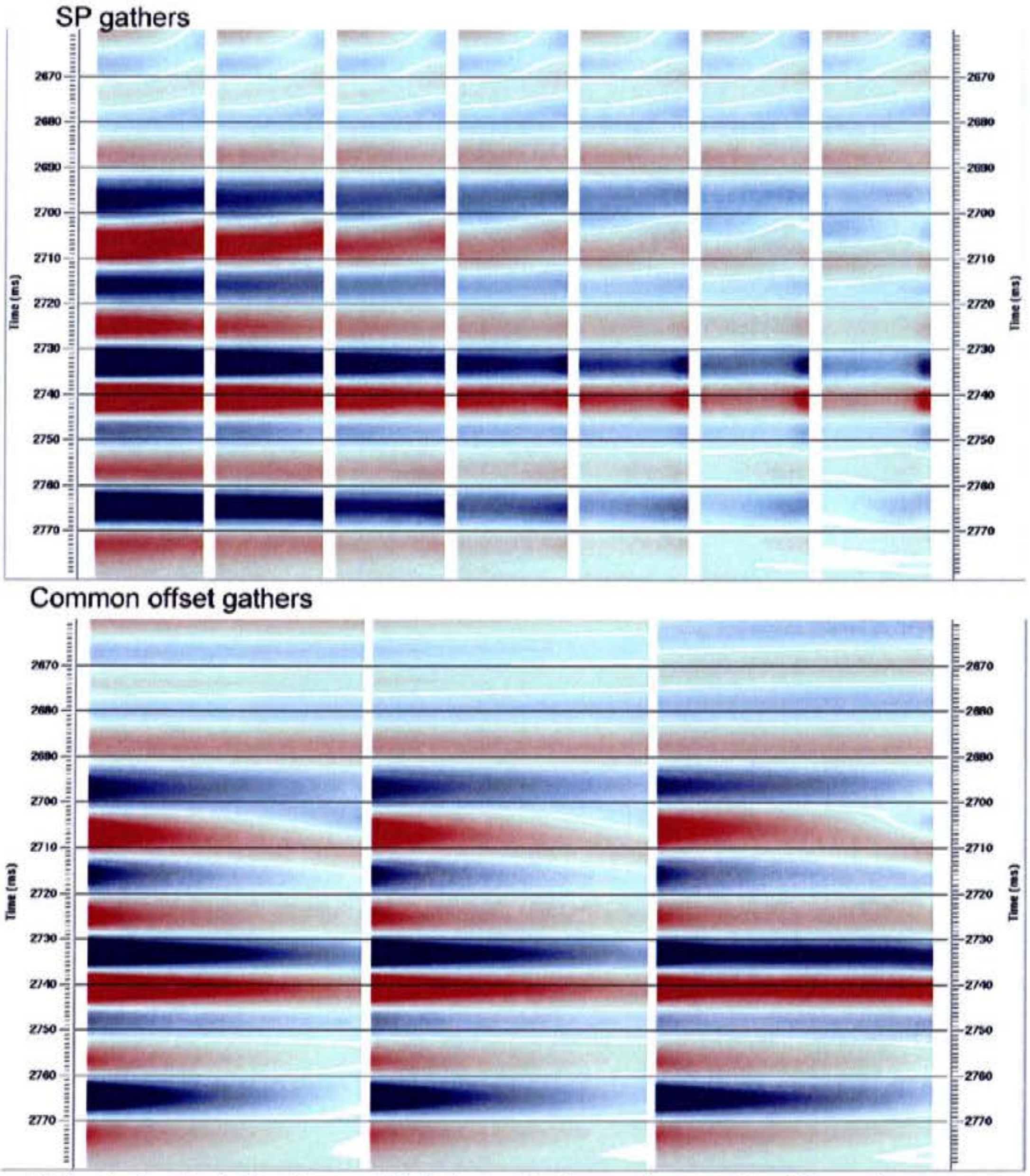

Fig. A3: Synthetic seismic based on modelled changes in degree of compaction. The panels represent increasing compaction with deepest version to the right. The common offset gathers (lower set) shows the entire range, and upper set are selected with 150 m intervals. Note the decreasing reflectivity with increasing compaction. Panels are not scaled similarly to Fig. A4.

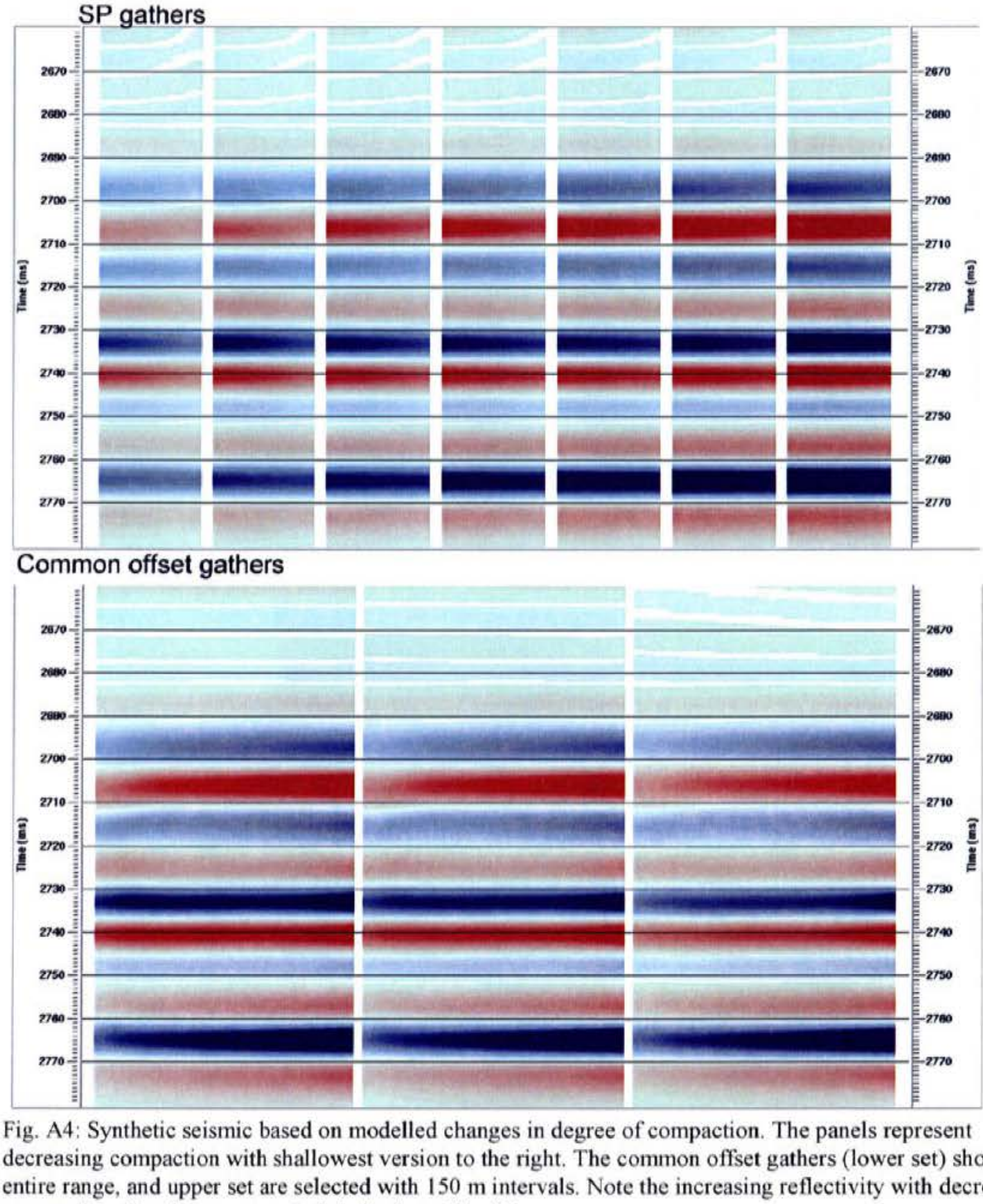

Fig. A4: Synthetic seismic based on modelled changes in degree of compaction. The panels represent decreasing compaction with shallowest version to the right. The common offset gathers (lower set) shows the entire range, and upper set are selected with 150 m intervals. Note the increasing reflectivity with decreasing compaction. Panels are not scaled similarly to Fig. A3.

Elastic moduli of chalk as a reflection of porosity, sorting, and irreducible water saturation

Ida L. Fabricius, Technical University of Denmark, Gary Mavko, Stanford University, Christian Mogensen, Ødegaard A/S, and Peter Japsen, Geological Survey of Denmark and Greenland (GEUS).*

Summary

We studied elastic moduli for oil-bearing chalk by interpreting logging data from three wells in the South Arne field, Danish North Sea. We assumed a water-wet chalk and that water saturation is irreducible because the water saturation does not increase with depth, so that water saturation reflects the size of particle-pore interface and amount of particle contacts. Water saturation may thus be regarded as a measure of clay content and particle sorting. Over a vertical interval of 150 m, compaction causes porosity to decrease with depth and concurrent stiffening causes elastic moduli to increase. Chalk of good sorting compacts and gradually stiffens at high porosities, whereas chalk of poor sorting compacts and stiffens at relatively low porosities.

Introduction

Clay-bearing sandstones tend to have lower elastic moduli for a given porosity than clean sandstone (Dvorkin et al. 2002). We look for equivalent effects of clay in chalk, and studied logging data from three wells each penetrating vertical sections of c. 80 m chalk of Cretaceous and Paleogene age from the South Arne oil field in the Danish North Sea (Mackertich and Goulding, 1999). Kaolinite is a typical clay mineral in this field so we expect that the natural gamma log is a poor indicator of clay. The logged chalk intervals are oil-bearing and because the water saturation does not increase with depth, we assume that the water saturation is irreducible in the entire depth interval, although it varies between less than 5% and more than 90%. Note that high irreducible water saturations are not uncommen in clay-bearing chalk.

In a water-wet chalk, the water phase covers pore walls and pile up in pore corners. The irreducible water saturation is then a reflection of the size of the interface between solid and pores and the number of particle contacts. These properties depend on clay content and sorting. We will thus use the water saturation as a proxy for sorting and study the influence of sorting (clay content) on elastic moduli by comparing the modulus-porosity relationships of chalk with different water saturation.

Method

Porosity and water saturation of the three wells were calculated from logs by standard practice. Acoustic P-wave velocities, v_P, and shear wave velocities, v_S, as well as densities, rho, were assumed to represent the zone near the

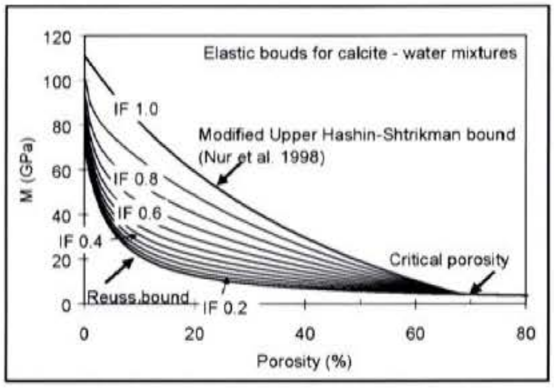

Figure 1: Elastic bounds for P-wave modulus, M, of calcite - water mixtures: A lower, Reuss bound, corresponds to all solid in suspension (Reuss, 1929); a MUHS (Modified Upper Hashin-Shtrikman) bound, corresponds to densest packing of particles, for a critical porosity of 70% (Nur et al. 1998). The space between these bounds contains a series of IF (iso-frame) curves, representing MUHS bounds for mixtures of a constant ratio (IF) of the mineral in the solid frame with the remaining part of the mineral in aqueous suspension (Fabricius, 2002).

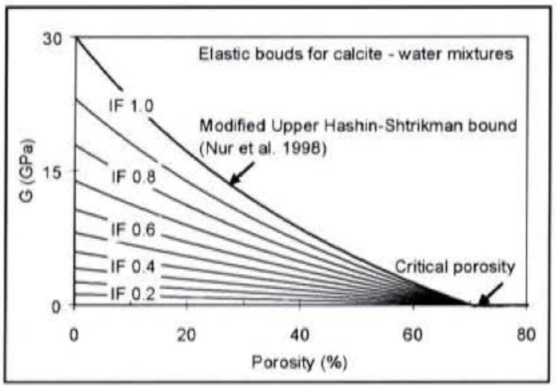

Figure 2: Elastic bounds for shear modulus, G, of calcite - water mixtures versus porosity, equivalent to those shown in Figure 1. The shear modulus bounds give a good separation between IF curves at low porosities.

well bore invaded by mud filtrate. P-wave modulus, M, and shear modulus, G, were calculated accordingly:

$$M = \text{rho} * v_P^2$$

$$G = \text{rho} * v_S^2$$

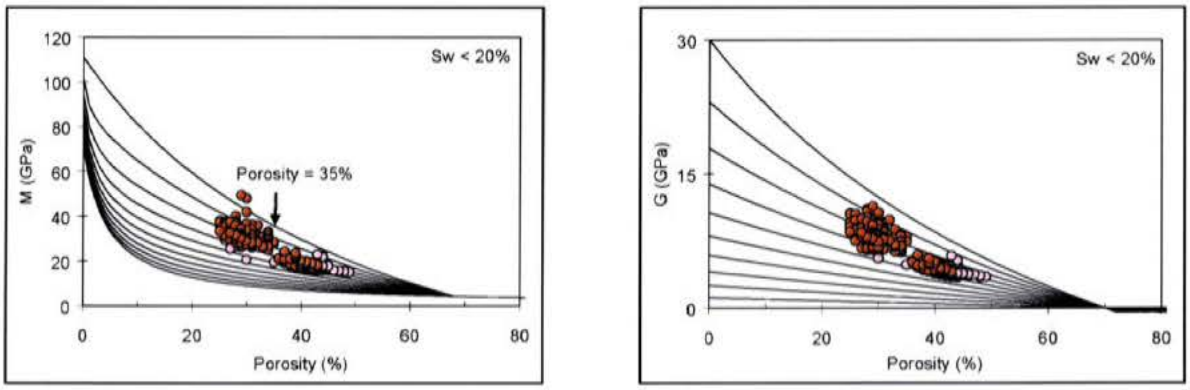

Figure 3: P-wave modulus, M, and shear modulus, G, versus porosity for chalk with less than 20% water saturatiom (Sw). All data are substituted to a reference brine at reservoir conditions using Gassmanns equations. The log data represent a vertical depth interval of 108 m. Light dots are from the upper 54 m of the interval, dark dots from the lower 54 m. Deeper samples tend to have higher IF value than shallower. Data pass from IF 0.7 to IF 0.8 at around 35% porosity.

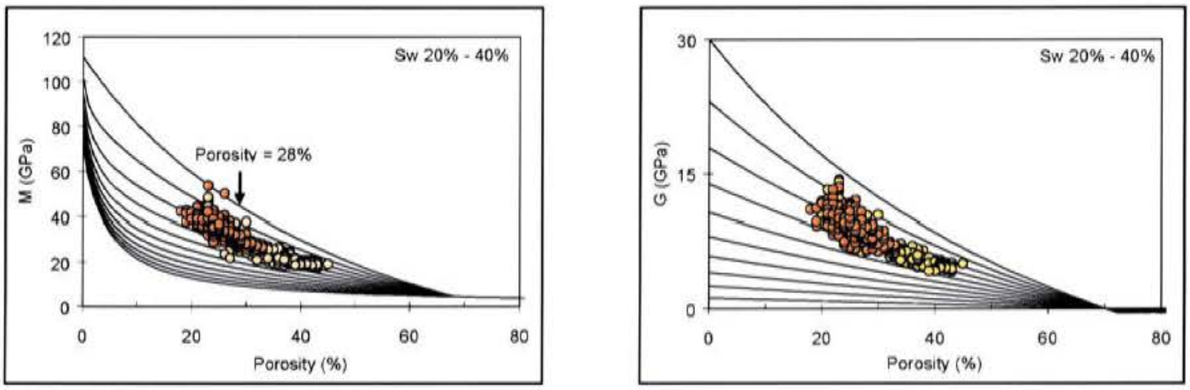

Figure 4: P-wave modulus, M, and shear modulus, G, versus porosity for chalk with 20% -40% water saturatiom (Sw). All data are substituted to a reference brine at reservoir conditions using Gassmanns equations. The log data represent a vertical depth interval of 140 m. Light dots are from the upper 70 m of the interval, dark dots from the lower 70 m. Deep samples tend to have higher IF value than shallower. Data pass from IF 0.7 to IF 0.8 at around 28% porosity.

In order to study how the solid phase controls the elastic moduli, all data were substituted mathematically to represent one pore saturating reference brine by using Gassmanns relations as cited in Mavko et al. (1998).

The resulting M and G data were compared to modeled elastic bounds for mixtures of calcite and brine. The model involves definition of iso-frame (IF) curves of equal induration (Figures 1 and 2). The advantage of using IF values is that they describe high induration even at a high porosity where elastic moduli are modest, and low induration at low porosities and relatively high elastic moduli.

P-wave modulus and shear modulus were chosen rather than bulk modulus for two reasons: 1) v_S and v_P are used to calculate shear modulus respectively P-wave modulus independently, whereas shear and P-wave data are combined when calculating bulk modulus. 2) Bulk modulus tend to have narrower bounds, which may be useful for prediction of modulus from porosity, but is less beneficial when we want to study the effect of lithology by using IF-curves, where a good separation between IF-curves is desirable.

Results and discussion

Data from the three wells were combined into one data set where vertical depth ranges over a 150 m interval. All resulting data were separated into five groups representing

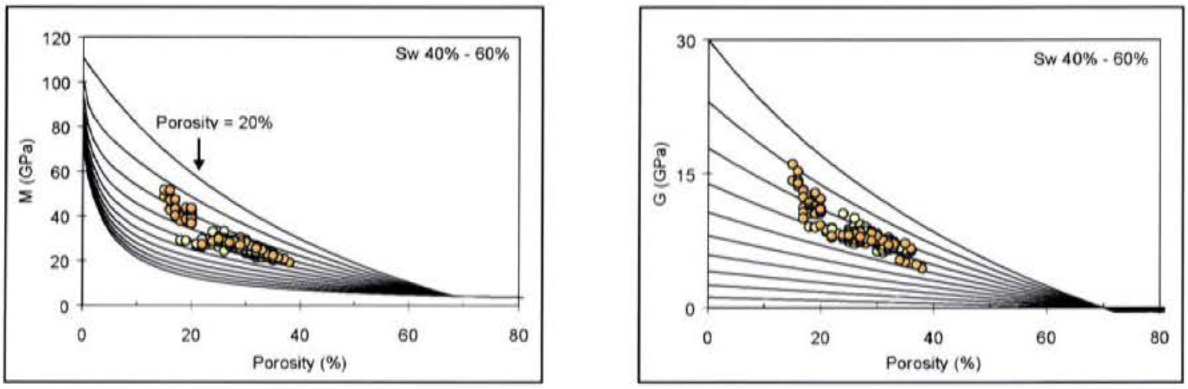

Figure 5: P-wave modulus, M, and shear modulus, G, versus porosity for chalk with 40% - 60% water saturatiom (Sw). All data are substituted to a standard brine at reservoir conditions using Gassmanns equations. The log data represent a vertical depth interval of 66 m. Light dots are from the upper 33 m of the interval, dark dots from the lower 33 m. Deep samples tend to have higher IF value than shallower. Data pass from IF 0.7 to IF 0.8 at around 20% porosity.

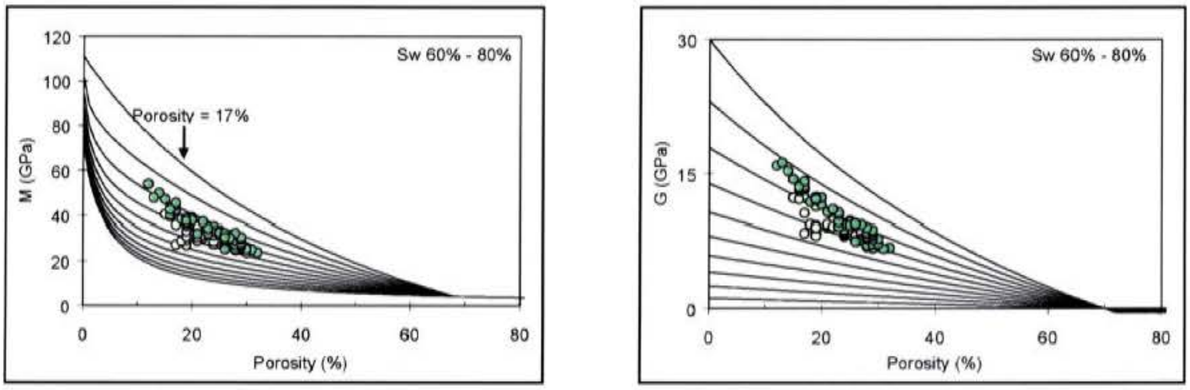

Figure 6: P-wave modulus, M, and shear modulus, G, versus porosity for chalk with 60% - 80% water saturatiom (Sw). All data are substituted to a standard brine at reservoir conditions using Gassmanns equations. The log data represent a vertical depth interval of 42 m. Light dots are from the upper 21 m of the interval, dark dots from the lower 21 m. Deep samples tend to have higher IF value than shallower. Data pass from IF 0.7 to IF 0.8 at around 17% porosity.

20% water saturation intervals (Figures 3 - 7). In each of these groups, samples from the shallowest half of the involved depth interval were compared to data from the deepest half (except for the small group of highly water saturated samples) in order to detect possible effects related to depth-dependent compaction. In all saturation intervals, data from the deepest interval tend to have lower porosities and higher moduli, or rather higher IF-values than data from the shallowest interval. This is probably the effect of compaction.

For high porosities and shallow depths all data tend to fall close to the IF 0.7 curve whereas they increase to around IF 0.8 for low porosities and deeper depth. The data reaches IF 0.8 at different porosities as a reflection of water saturation (sorting or clay content): at c. 35% porosity for the samples with lowest water saturation (low clay content) down to c. 14% porosity for the samples with highest water saturation (high clay content) (Figures 3 - 7).

This result is to be expected because poorly sorted sediments will have lower porosity at a given burial stress than well sorted sediments. Low porosity clay-rich chalk may thus have higher elastic moduli than a well sorted porous chalk The two sediments may still have the same IF value if buried to the same effective depth, so that they are subject to similar burial stress. An opposite effect would have been seen if an increasing water saturation reflected a transition zone with increasing degree of cementation.

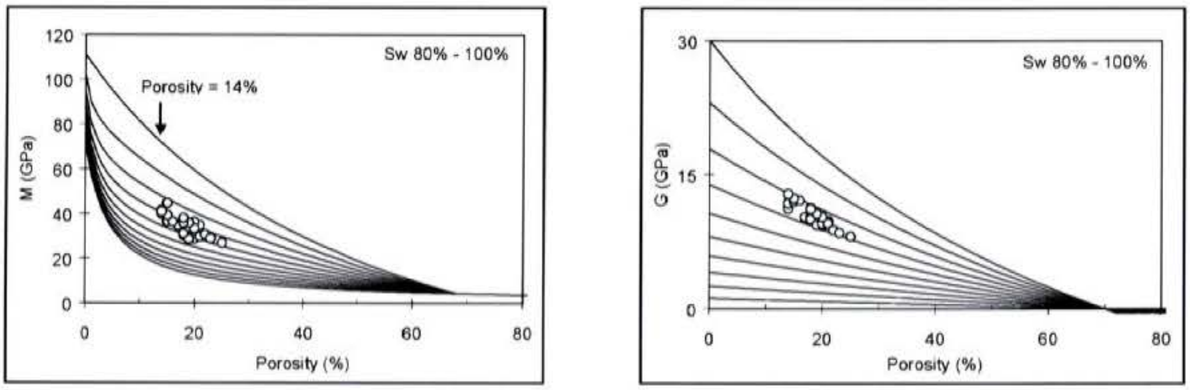

Figure 7: P-wave modulus, M, and shear modulus, G, versus porosity for chalk with 80% - 100% water saturatiom (Sw). All data are substituted to a standard brine at reservoir conditions using Gassmanns equations. The log data represent a vertical depth interval of 26 m. The data approaches IF 0.8 at around 14% porosity.

Conclusions

Elastic moduli for the chalk of three oil wells were compared by using logging data, and by assuming that the acoustic logs and the density log represent the zone invaded by filtrate from the drilling mud. We did mathematical substitution to one pore fluid by using Gassmanns equations. We assume the water saturation in the three wells to be irreducible. Water saturation varies between less than 5% to more than 90%, probably as a reflection of sorting (clay content).

- We can describe the induration of chalk by comparing measured elastic moduli to those predicted from the iso-frame (IF) model of Fabricius (2002) involving modified upper Hashin-Shtrikmann bounds for mixtures of a constant proportion of the calcite in the solid frame and the remaining calcite in aqueous suspension.
- Depth-wise, the elastic moduli of chalk approaches the values of solid frame and obtain higher IF value.
- Chalk with low (irreducible) water saturation is regarded to be well sorted and indurates at relatively high porosity.
- Chalk with high (irreducible) water saturation is regarded to be poorly sorted and indurates at relatively low porosity.
- A trend relating porosity and induration shifts from higher porosities to lower as (irreducible) water saturation increases, and thus in the opposite direction from what should be expected from an effect of pore fluid or of saturation related cementation. The effect thus probably is directly related to sorting and clay content.

References

Dvorkin, J., Gutiérrez, M.A., and Nur, A., 2002, On the universality of diagenetic trends, The Leading Edge, Jan. 2002, 40-43.

Fabricius, I.L., 2002, Porosity Loss in Chalk Facies Sediments by Physical Compaction or by Cementation - Consequences for P-wave Modulus, AAPG Ann. Mtg., March 10-13 2002, Houston, Texas, Ext. Abs., 6pp.

Mackertich, D.S. and Goulding, D.R.G., 1999, Exploration and appraisal of the South Arne field, Danish North sea. In: Fleet, A.J. & Boldy, S.A.R. (eds) Petroleum Geology of Northwest Europe: Proceedings of the 5th Conference. Geological Society, London. 959-974.

Mavko, G., Mukerji, T., and Dvorkin, J., 1998, The Rock Physics Handbook, Cambridge University Press, 329 pp.

Nur, A., Mavko, G., Dvorkin, J., and Galmudi, D., 1998, Critical porosity: A Key to relating Physical Properties to Porosity in Rocks, The Leading Edge 17, 357-362.

Reuss, A., 1929, Berechnung der Fliessgrenze von Mischkristallen auf Grund der Plastizitätsbedingungen für Einkristalle, Zeitschrift für Angewandte Mathematik und Mechanik 9, 49-58.

Acknowledgements

The presented results are from an ongoing research activity: "Rock Physics of Impure Chalk" supported financially by the Danish Energy Research Program, Amerada Hess A/S and DONG A/S. Amerada Hess A/S is thanked for petrophysical logging and fluid data.

Z-99 Modeling elastic moduli of Danian North Sea chalk from petrographic data

IDA LYKKE FABRICIUS*, CHRISTIAN HØIER** AND UFFE KORSBECH***
*E&R, DTU, Kgs Lyngby, Denmark, **GEUS, København, Denmark, ***Ørsted DTU; Kgs Lyngby, Denmark

Abstract

In impure chalk the elastic moduli is not only controlled by porosity, but also by cementation resulting in relatively large moduli and by admixtures of clay and fine silica which results in relatively small moduli. Based on a concept of framebuilding contra suspended solids, we model P-wave and S-wave moduli of dry and wet plug samples by one effective medium model using chemical, mineralogical and textural input. The model is a Modified Upper Hashin Shtrikman model assuming a critical porosity of 70%. The textural and mineralogical data may potentially be assessed from logging data on spectral gamma radiation and water saturations in a hydrocarbon zone.

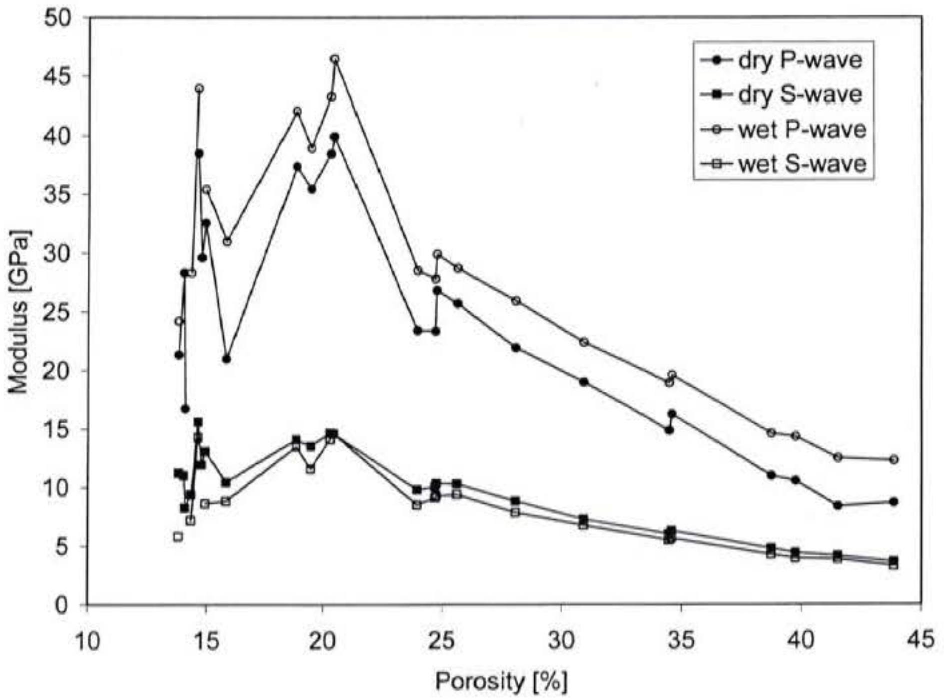

Figure 1. P-wave and S-wave moduli of 1½ inch plug samples. Dry samples were left to equilibrate with atmospheric air at room conditons and contain up to 34% water. Wet samples have salt water saturations down to 92%, where low permeability prevented total saturation.

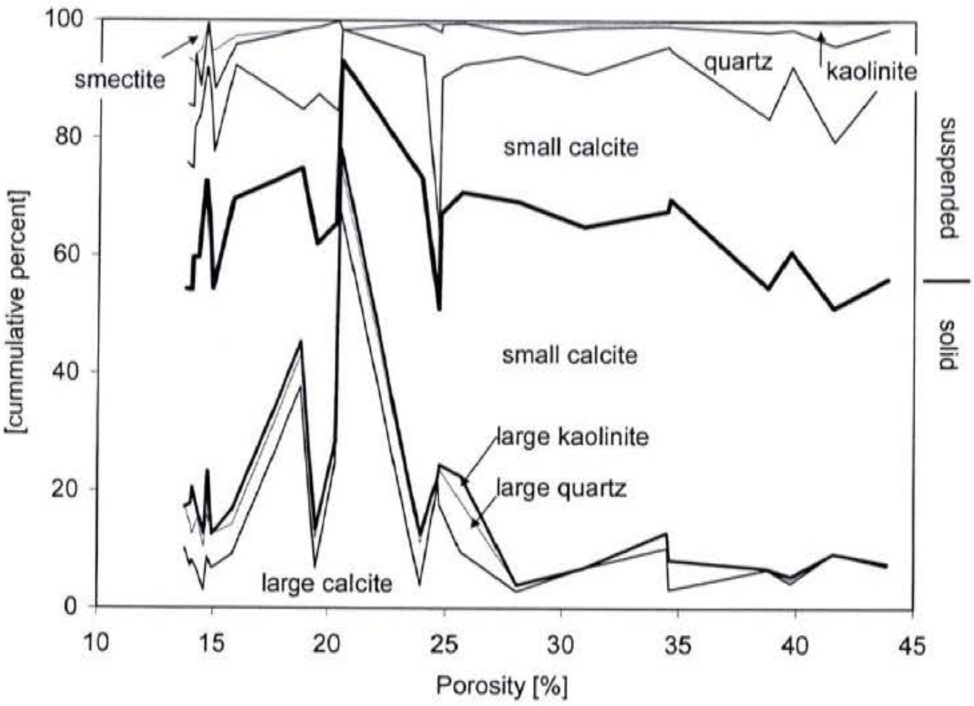

Figure 3. Model of sample composition based on chemical, mineralogical, and petrographic data. Based on image analysis the components are split into solid frame-supporting and loose "suspended" fractions by an IF model (see Fig. 2). Wet chemical analysis was done on carbonate fraction and on residue, X-ray diffractometry on bulk samples and on residue. Petrography was done in light microscope on thin sections and by backscatter electron microscopy of polished sections combined with energy dispersive microprobe analysis of single mineral grains. Petrographic image analysis was done on electron micrographs by the free software UTHSCASA Image Tool. The content of large grains was determined on images measuring 333 by 333 microns. Large grains are here defined as being more than 2 microns in cross section. Large kaolinte and large quartz occur as massive clasts, for simplicity feldspar is counted as quartz. Large calcite is bioclasts or areas fused by cementation, for simplicity zoned dolomite/ankerite crystals are counted as calcite. Pyrite is sporadic and disregarded. Suspended kaolinite, smectite and quartz occur as highly porous pore filling material of submicron size crystals. Small calcite crystals were modeled as solid or suspended on the basis of specific perimeter measured on 33 by 33 micron images according to the procedure of Borre et al. (1997).

Conclusions

Elastic P-wave and S-wave moduli of impure chalk can be modeled from the mineralogical and textural composition of the solid phase as well as the pore fluid composition. In the studied samples, the elastic moduli are increasing smoothly with decreasing porosity in the porosity interval 45% to 25% representing relatively pure chalk with little cement. Calcite cemented samples from the deepest part of the section have porosities around 20% and relatively high elastic moduli, whereas clay and quartz rich samples from the upper part of the section have porosities below 20% and relatively low elastic moduli.

The model is the same for S- and P- waves for dry as well as wet samples.

In accordance with petrographic data, a part of the solid is modeled as suspended in the pore fluids. This suspension is then modeled as the soft component in a stiff frame composed of the remaining solid according to a Modified Upper Hashin Shtrikman bound under assumption of a critical porosity of 70%.

Z-99 Modeling elastic moduli of Danian North Sea chalk from petrographic data

IDA LYKKE FABRICIUS*, CHRISTIAN HØIER** AND UFFE KORSBECH***

*E&R, DTU, Kgs Lyngby, Denmark, **GEUS, København, Denmark, ***Ørsted DTU; Kgs Lyngby, Denmark

Abstract

In impure chalk the elastic moduli is not only controlled by porosity, but also by cementation resulting in relatively large moduli and by admixtures of clay and fine silica which results in relatively small moduli. Based on a concept of framebuilding contra suspended solids, we model P-wave and S-wave moduli of dry and wet plug samples by one effective medium model using chemical, mineralogical and textural input. The model is a Modified Upper Hashin Shtrikman model assuming a critical porosity of 70%. The textural and mineralogical data may potentially be assessed from logging data on spectral gamma radiation and water saturations in a hydrocarbon zone.

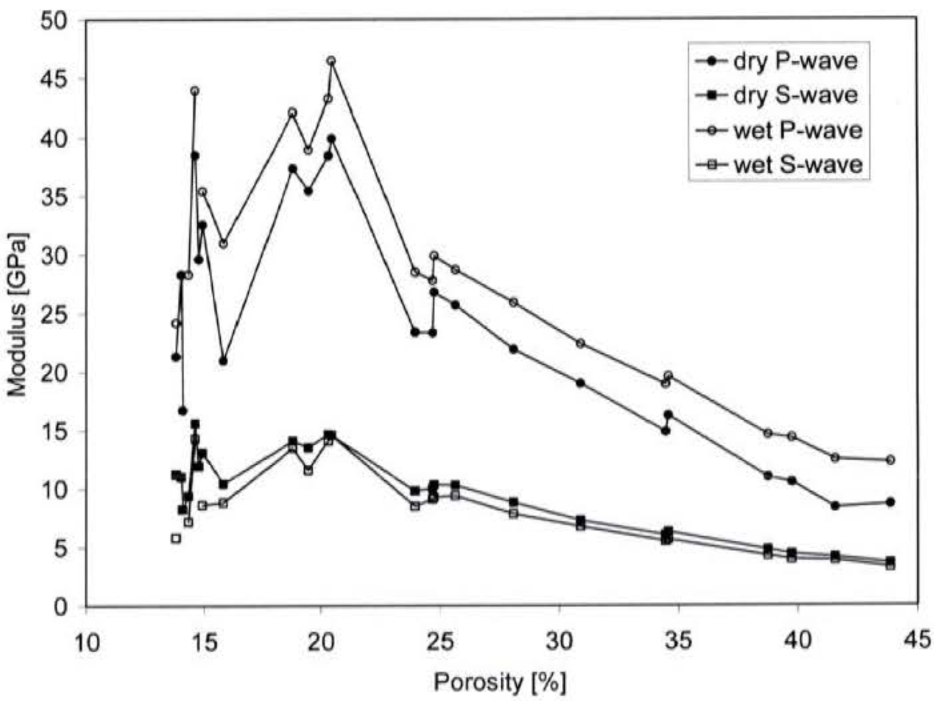

Figure 1. P-wave and S-wave moduli of 1½ inch plug samples. Dry samples were left to equilibrate with atmospheric air at room conditons and contain up to 34% water. Wet samples have salt water saturations down to 92%, where low permeability prevented total saturation.

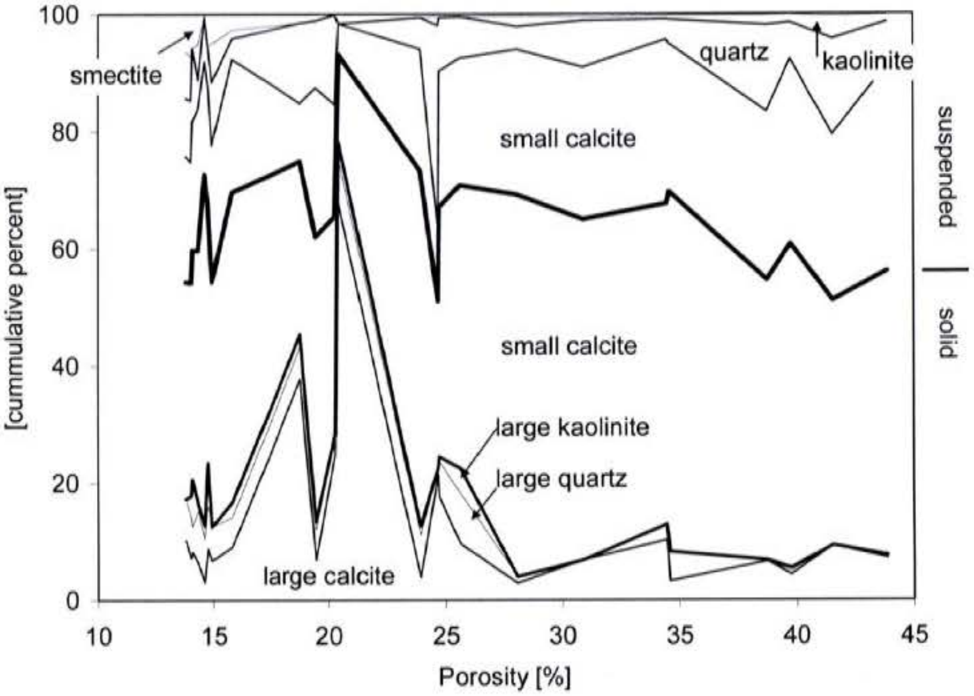

Figure 3. Model of sample composition based on chemical, mineralogical, and petrographic data. Based on image analysis the components are split into solid frame-supporting and loose "suspended" fractions by an IF model (see Fig. 2). Wet chemical analysis was done on carbonate fraction and on residue, X-ray diffractometry on bulk samples and on residue. Petrography was done in light microscope on thin sections and by backscatter electron microscopy of polished sections combined with energy dispersive microprobe analysis of single mineral grains. Petrographic image analysis was done on electron micrographs by the free software UTHSCASA Image Tool. The content of large grains was determined on images measuring 333 by 333 microns. Large grains are here defined as being more than 2 microns in cross section. Large kaolinte and large quartz occur as massive clasts, for simplicity feldspar is counted as quartz. Large calcite is bioclasts or areas fused by cementation, for simplicity zoned dolomite/ankerite crystals are counted as calcite. Pyrite is sporadic and disregarded. Suspended kaolinite, smectite and quartz occur as highly porous pore filling material of submicron size crystals. Small calcite crystals were modeled as solid or suspended on the basis of specific perimeter measured on 33 by 33 micron images according to the procedure of Borre et al. (1997).

Conclusions

Elastic P-wave and S-wave moduli of impure chalk can be modeled from the mineralogical and textural composition of the solid phase as well as the pore fluid composition. In the studied samples, the elastic moduli are increasing smoothly with decreasing porosity in the porosity interval 45% to 25% representing relatively pure chalk with little cement. Calcite cemented samples from the deepest part of the section have porosities around 20% and relatively high elastic moduli, whereas clay and quartz rich samples from the upper part of the section have porosities below 20% and relatively low elastic moduli.

The model is the same for S- and P- waves for dry as well as wet samples.

In accordance with petrographic data, a part of the solid is modeled as suspended in the pore fluids. This suspension is then modeled as the soft component in a stiff frame composed of the remaining solid according to a Modified Upper Hashin Shtrikman bound under assumption of a critical porosity of 70%.

Presented at the SEG 2002 Annual Meeting, Salt Lake City, USA

Effect of fluid substitution on ultrasonic velocities in chalk plugs, South Arne field, North Sea

Peter Japsen[1](pj@geus.dk), Christian Høier[1], Klaus Bolding Rasmussen[2], Ida Fabricius[4], Gary Mavko[3] and Jacob Mørch Pedersen[2].*

[1] Geological Survey of Denmark and Greenland (GEUS), [2] Ødegaard A/S, Copenhagen, [3] Stanford Rock Physics Lab, Stanford University, [4] Technical University of Denmark.

Summary

Ultrasonic P- and S-velocities were measured for 34 chalk samples from the Ekofisk and Tor formations in the South Arne field, North Sea. V_P and V_S correlate strongly with porosity for both dry and saturated samples. Outlying values are found for three samples of the Ekofisk formation that regained a high water content after drying, and this may be indicative of a high clay content.

The mean change in V_P and V_S from saturated to dry samples is a drop of 0.15 km/s and an increase of 0.21 km/s, respectively, for 31 of the samples. These changes correspond to 62% of the drop in V_P predicted by Gassmann's relations, whereas the increase in V_S is 154% of that predicted by Gassmann. The main reason for these deviations from Gassmann-theory is that the shear modulus in average is 0.5 GPa higher for the dry plugs than for the saturated plugs whereas Gassmann-theory predicts the shear modulus to be unchanged by fluid content. However, 94% of the change in the bulk modulus is in average predicted by Gassmann's relations. The shear modulus is found to be constant when measured for two samples at saturated and partly saturated conditions. The factors that cause the increased moduli of the dry samples is not understood, but further laboratory investigations are under way. The acoustic properties of the partly saturated chalk can, however, be estimated by applying Gassmann's relations to data for the saturated samples.

Introduction

Understanding of fluid effects on the acoustic properties of sediments is a central issue for evaluating seismic data; e.g. amplitude versus offset techniques depend on the discrimination of fluid content from variations in P- and S-velocities. Much research has been focused on describing these effects in sandstone, whereas few studies have been published on the rock physics of chalk. In the North Sea, chalk is an important reservoir rock and more information could probably be extracted from seismic data if fundamental physical properties of chalk were better understood. We have thus measured P- and S-velocities on dry and water saturated chalk samples and compared these results to predictions based on Gassmann's theory on the acoustic properties of porous rocks.

Gassmann theory

We can predict the elastic properties of the dry rock from data for the water saturated rock using Gassmann's relations (see Mavko et al. 1998):

$$K_{dry\text{-}G} = \frac{K_{sat}\left(\frac{K_0 \phi}{K_{fl}} + 1 - \phi\right) - K_0}{\frac{K_0 \cdot \phi}{K_{fl}} + \frac{K_{sat}}{K_0} - 1 - \phi}, \quad G_{sat} = G_{dry}$$

$K_{dry\text{-}G}$ = effective bulk modulus of dry rock predicted from Gassmann's relations
K_{sat} = effective bulk modulus of rock with pore fluid
K_0 = bulk modulus of mineral material making up rock
K_{fl} = effective bulk modulus of pore fluid
ϕ = porosity
G_{dry} = effective shear modulus of dry rock
G_{sat} = effective shear modulus of rock with pore fluid

We can thus predict $K_{dry\text{-}G}$ from measured values of K_{sat}, G_{sat} and ϕ with K_0=77 GPa for calcite and K_{fl}=2.25 GPa for water. P- and S-velocities for the dry rock, $V_{P\text{-}dry\text{-}G}$ and $V_{S\text{-}dry\text{-}G}$, are expressed as:

$$V_{P-dry-G} = \sqrt{(K_{dry-G} + G_{sat})/\rho}, \qquad V_{S-dry-G} = \sqrt{G_{sat}/\rho},$$

where $\rho=(1-\phi)\cdot\rho_{gr}$ is dry rock density [g/cm3]; ρ_{gr} is measured grain density for the rock. We can compare the Gassmann predictions for the dry rock with data measured on dry rock samples (K_{dry}, G_{dry}, $V_{P\text{-}dry}$, $V_{S\text{-}dry}$). We can compute the measured difference, ΔP, between the value of any parameter, P, for the dry plug, P_{dry}, and the corresponding value for the saturated plug, P_{sat}:

$$\Delta P = P_{dry} - P_{sat}$$

and the predicted difference, ΔP_G, between the value predicted for the dry plug, $P_{dry\text{-}G}$, and value measured for the saturated plugs:

$$\Delta P_G = P_{dry-G} - P_{sat}\ .$$

The error in the prediction, $E(P_{dry\text{-}G})$, of the dry condition becomes:

$$E(P_{dry-G}) = P_{dry-G} - P_{dry}\ .$$

Finally, we can calculate a 'Gassmann Index', I_G [%] to describe to which degree we observe the change predicted by Gassmann-theory by dividing the measured difference with predicted difference:

$$I_G = \Delta P / \Delta P_G \cdot 100$$

provided that ΔP_G is different from zero. A Gassmann Index may thus only be calculated for V_p, V_s and K.

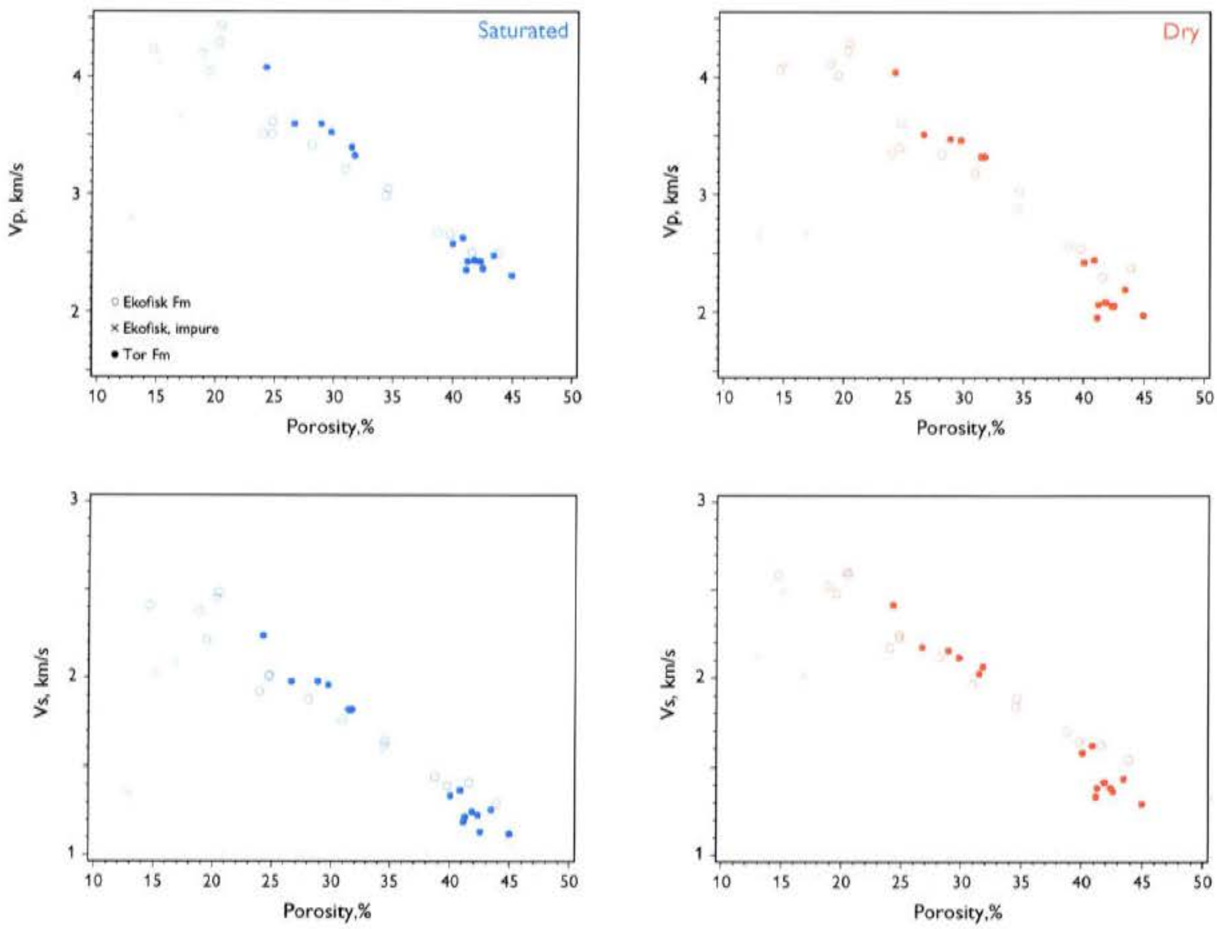

Figure 1: V_p and V_s versus porosity for 34 samples at water saturated and dry conditions (left and right, respectively). Note the good correlation between velocity and porosity, apart from the outlying values for three Ekofisk samples (indicated with crosses).

Data

Ultrasonic measurements were carried out on 19 Ekofisk and 15 Tor Formation samples from three wells on the South Arne field, North Sea (Mackertich & Goulding, 1999). The measurements were made for both dry and water saturated samples, and both P- and S- velocities were determined at an effective confining pressure of 7.5 MPa corresponding to approximate reservoir conditions. To prevent over-dry conditions, the samples were kept at room-moisture for two months after being dryed at 110°C. Accurate readings of travel times were assured by applying an algorithm that identifies the maximum amplitude in the first major loop of first arrival events. The maximum amplitude was used rather than the first break because it is less affected by noise.

Very good correlation is observed between velocity and porosity for both dry and saturated samples (Figure 1). Three samples from the Ekofisk Formation have outlying values relative to these trends. These samples are characterized by having regained high water content after drying, and this may be indicative of high clay content.

To investigate the dependence of acoustic properties of chalk on fluid content, velocities were measured on two samples for water saturations at 0%, 25%, 50%, 75% and 100%. The ultrasonic measurement were carried out on the samples at dry conditions, followed by measurements on the fully saturated and subsequently on the samples during drainage.

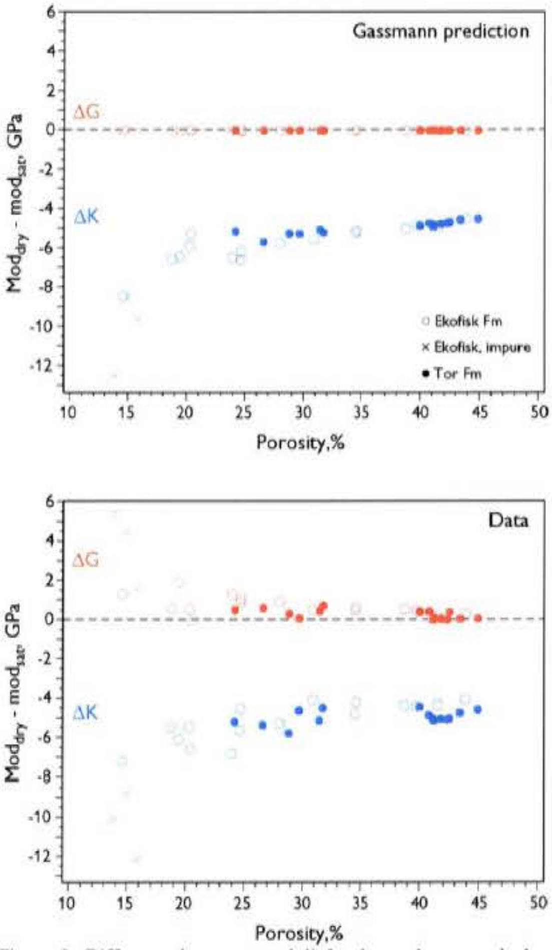

Figure 2: Difference between moduli for dry and saturated plugs versus porosity. Difference between Gassmann-prediction of dry rock moduli (from wet measurement) and measured wet rock moduli, (upper figure). Measured difference between dry and wet rock moduli (lower figure).

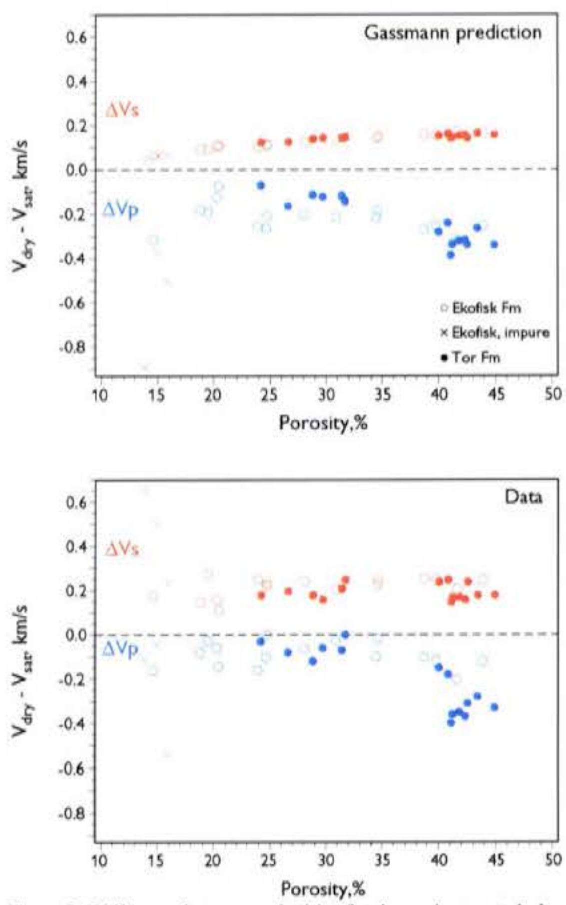

Figure 3: Difference between velocities for dry and saturated plugs versus porosity. Difference between Gassmann-prediction of dry rock velocities (from wet measurement) and measured wet rock velocities, (upper figure). Measured difference between dry and wet rock velocities (lower figure).

Results

Whereas Gassmann's relations predict no difference between the shear moduli for the dry and saturated rock, we observe that the shear modulus is higher for dry plugs than for saturated plugs (Figure 2). In average, the shear modulus for the dry samples is 0.5 GPa higher than those for the saturated samples (Table 1; 31 samples excluding 3 outliers). Moreover, the difference is found to increase as porosity is reduced.

On the contrary, we observe a decrease in the bulk modulus for the dry samples relative to saturated samples that is in the order of the decrease predicted by Gassmann theory.

The mean decrease in the bulk modulus is -5.1 GPa and this is as much as 94% of the predicted decrease. The mean error in predicting dry bulk modulus from saturated rock data is –0.3 GPa.

The difference in V_S between dry and saturated plugs is predicted to be reduced with smaller porosities as the density of the rock approaches the density of the matrix. However, we observe a slightly increasing difference for the smaller porosities due to high values of the dry shear modulus (Figure 3). Correspondingly, the difference in V_P between dry and saturated plugs is less than predicted. This is due to the higher than expected values of both bulk and shear modulus for the dry samples.

We find mean errors of -0.08 and -0.07 km/s in the predictions of V_P and V_S for the dry samples based on data for the saturated samples. So where we expect V_P to decrease with a mean value of -0.23 km/s we observe only a drop of -0.15 km/s, whereas we expect V_S to increase with 0.14 km/s and observe 0.21 km/s. Expressed as the ratio between the measured and the predicted difference we observe only 62% of the drop in V_P predicted by Gassmann, whereas the increase in V_S is 154% of that predicted by Gassmann. The main reason for these deviations from Gassmann-theory is that the shear modulus in average is 0.5 GPa higher for the dry plugs than for the saturated plugs whereas Gassmann predicts these values to be equal. The bulk modulus in average is 0.3 GPa higher for the dry plugs than for the saturated plugs

Velocities were measured on two samples for water saturations at 0, 25, 50, 75 and 100%, and the shear modulus for both samples was found to be about 0.5 GPa higher for the dry measurement than for the almost constant values measured at non-zero saturations (Figure 4). High shear modulus is thus measured for the dry samples even though the samples were left at room-moisture for two months to regain moisture equilibrium.

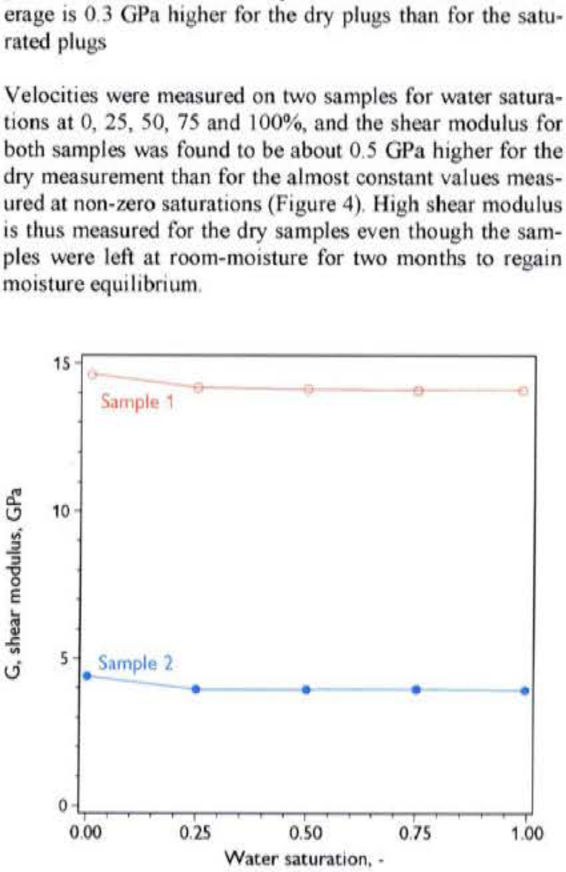

Figure 4: Shear modulus versus water saturation, S_W, for two chalk samples. The shear modulus is almost unaffected by S_W for non-zero saturations, but increases by c. 0.5 GPa for S_W=0 relative to the non-zero saturations for both samples. The factors that cause the increased moduli of the dry samples is not understood, but further laboratory investigations are under way.

Mean values	K	G	V_P	V_S
Predicted diff., ΔP_G	-5.4 GPa	0 GPa	-0.23 km/s	0.14 km/s
Measured diff., ΔP	-5.1 GPa	0.5 GPa	-0.15 km/s	0.21 km/s
Error in prediction ($P_{dry\text{-}G}$)	-0.3 GPa	-0.5 GPa	-0.08 km/s	-0.07 km/s
Meas. diff./ Pred. diff., I_G	94%	-	62%	154%

Table 1: Difference between parameters measured for 31 dry and saturated samples. Comparison between Gassmann prediction of dry rock properties from measurements on saturated samples and measurements on dry samples. Outlying values for three samples are not included (see Figure 1).

Conclusions

Gassmann's relations predict differences in ultrasonic velocities for dry and water saturated chalk samples quite well, and increased values of the dry rock moduli is the main cause of the difference between data and Gassmann theory. The shear modulus is constant for saturated and partly saturated samples. The factors that cause the increased moduli of the dry samples is not understood, but further laboratory investigations are under way.

The fair agreement between ultrasonic measurements on chalk and Gassmann's relations is interesting because these relations are established for low frequencies, and because this agreement is not always found for clastics. It is frequently assumed that Gassmann should not be used for ultrasonics, because of velocity dispersion effects such as squirt dispersion due to microcracks and heterogeneity of pore stiffness. Maybe the relative applicability of Gassmann observed here is related to the homogeneity of the chalk.

References

Mackertich, D.S. & Goulding, D.R.G. 1999: Exploration and appraisal of the South Arne field, Danish North sea. In: Fleet, A.J. & Boldy, S.A.R. (eds) Petroleum Geology of Northwest Europe: Proceedings of the 5th Conference. Geological Society, London. 959-974.

Mavko, G., Mukerji, T. & Dvorkin, J. 1998: The Rock Physics Handbook. Cambridge: Cambridge University Press.

Acknowledgments

These results are part of the outcome of the ongoing energy research project Rock Physics of Impure Chalk which is sponsored by the Danish Energy Program (EFP-2001), Amerada Hess A/S and Dong E&P

To be presented at the Petroleum Geology Conference on NW Europe, QEII, London, October 2003

Modelling seismic response from North Sea Chalk reservoirs resulting from changes in burial depth and fluid saturation

O. V. Vejbæk[1], R. Rasmussen[1], P. Japsen[1], J. M. Pedersen[2], G. Marsden[3]

[1] *Geological Survey of Denmark and Greenland (GEUS), Østervoldgade 10, DK-1350 Copenhagen, Denmark*
[2] *Ødegaard A/S, Titangade 15, DK-2200 Copenhagen N, Denmark*
[3] *Amerada Hess Aps, Østergade 26B, DK-1100 Copenhagen K, Denmark*

Changes in seismic response caused by changes in degree of compaction and fluid content in North Sea Chalk reservoirs away from a well bore are investigated by forward modelling. The investigated seismic response encompasses reflectivity changes, AVO and acoustic impedance. Synthetic seismic sections, impedance cross sections and AVO response are presented as calculated on the basis of selected wells from the South Arne and Dan Fields, Danish North Sea and compared to field records.

The two main variables to use for seismic response prediction away from the well bore is depth of burial (changes in effective stress) and changes in hydrocarbon saturation. Three main modelling tools are used for the modelling: 1) Rock physics, 2) Saturation modelling and 3) Compaction/de-compaction modelling.

Rock physics theory is applied to obtain all necessary parameters for the complete set of elastic parameters for the application of the Zoeppritz equations. The challenge is not only to predict the shear velocity, but also to account for the changes in fluid content via application of the Gassmann equation. An approach akin to the one suggested for the Ekofisk Field by Walls et al. (1998) is applied for the prediction of changes in degree of compaction.

Hydrocarbon saturation in North Sea Chalk is strongly affected by capillary forces due to the small scale of the pores and transition zones in the order of 50 m are not uncommon. For this reason, potent saturation modelling is needed in order create realistic input for the seismic modelling. We use the EQR and similar saturation models, which have proved robust for the prediction of saturation profiles in Danish Chalk reservoirs.

Compaction modelling relies on simple exponential decay of porosity with depth, where abnormal fluid pressures are accounted for. A new set of compaction parameters is presented. These parameters are based on a study on the North Sea Chalk based on some 850 wells. The parameters appear to be sufficiently fine-tuned to allow fairly precise predictions of abnormal fluid pressures from observed average porosity. Based on this, the relative contribution to porosity preservation by abnormal fluid pressure and early hydrocarbon invasion may be estimated.

Modelling results of value in the search for subtle traps include: Reflectivity is correlating with porosity, acoustic impedance is primarily reflecting porosity variation rather than hydrocarbon saturation, and the poisson ratio may be rather sensitive to hydrocarbon saturation.

Walls, J. D., Dvorkin, J., and Smith, B. A. 1998: Modeling Seimic Velocity in Ekofisk Chalk. 1998 SEG Expanded abstracts, 4 p.

DTU

Selection of samples

EFP- 2001 Rock Physics of Impure Chalk, E&R-1

Ida L. Fabricius, DTU
Christian Høier, GEUS

E&R, DTU 2001, revised 17/1 2002 (version 2)

confidential

Selection of samples

EFP- 2001 Rock Physics of Impure Chalk, E&R-1

Ida L. Fabricius, DTU
Christian Høier, GEUS

E&R, DTU 2001, revised 17/1 2002 (version 2)

confidential

Selection of samples

Ida L. Fabricius, DTU and Christian Højer, GEUS

This note contains a brief description of the procedure applied in selecting twentyfour core samples from the Ekofisk Formation of the South Arne field. We also summarise existing data for the sampled material with respect to porosity, permeability, lithology and biostratigraphy.

Selection of wells

Rigs-1 and Rigs-2 were selected for sampling based on comparison of logging data from these wells and from the other possible wells: Baron-2, I-1, and South Arne-1. South Arne-1 has only incomplete logging data and little core from the Ekofisk Formations and was immediately excluded. For the remaining wells, the available core-intervals are shown on Figure 1 and 2. The Ekofisk Formation is well covered with core material in the Baron-2 and Rigs-1 wells. In I-1 the cores have incomplete recovery in the relatively thin Ekofisk Formation, whereas in Rigs-2 only the lower part of the Ekofisk Formation was successfully cored.

Because we could only select relatively few samples, we decided to sample only two wells, which must be well correlatable in order to allow comparison of samples from the same stratigraphic level in the two wells. As a basis for evaluating the correlatability, we used the neutron porosity log, density log, and natural gamma-ray log for each of the four wells (Figures 1 and 2). The neutron porosity log in combination with the density log should give a good measure of porosity, and the natural gamma-ray log should give an indication of the relative amount of clay minerals. On this basis we chose to sample the cores from Rigs-1 and Rigs 2, where the porosity logs show similar overall patterns in the Ekofisk Formation, but different overall levels of porosity (Figure 2).

The log-correlation, though, is not confirmed by the Nanno-plankton ages: The zone NNTp4 *pars.* apparently is represented by a larger depth range in Rigs-2 as compared to Rigs-1, whereas zones NNTp2-3 *pars.* appear to be represented by the larger depth-range in well Rigs-1 (Table 1, Figure 3 and 4, Simon Petroleum Technology ltd. (1995), Network Stratigraphic Consulting ltd. (1999), E. Sheldon, GEUS, pers. com.).

Selection of samples

We selected 24 samples from the chalk cores from the wells Rigs-1 and Rigs-2 in the South Arne field (Table 1). All samples are from the Ekofisk Formation and are selected so as to obtain the largest variation in porosity, clay content and stratigraphic level (Figures 3 and 4). They are 1½" plugs previously used for conventional core analysis, and the conventional core analysis report was used as a basis for selection of samples together with core scanning and logging data.

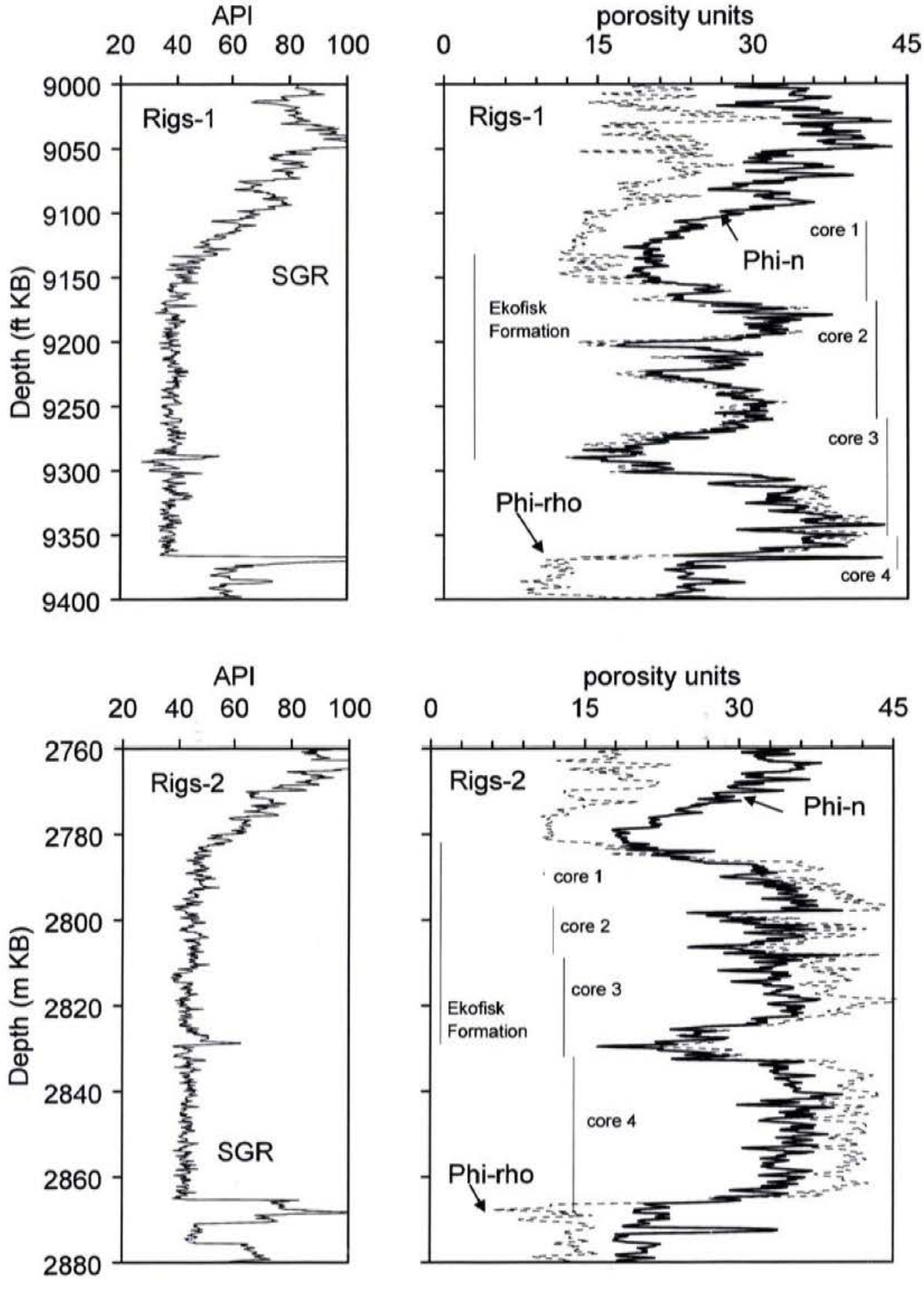

Figure 2. Natural gamma ray (SGR), density-porosity (Phi-rho), and neutron-porosity (Phi-n) for the wells Rigs-1 and Rigs-2. The depth-range of the Ekofisk Formation is indicated, as is the recovered core intervals.

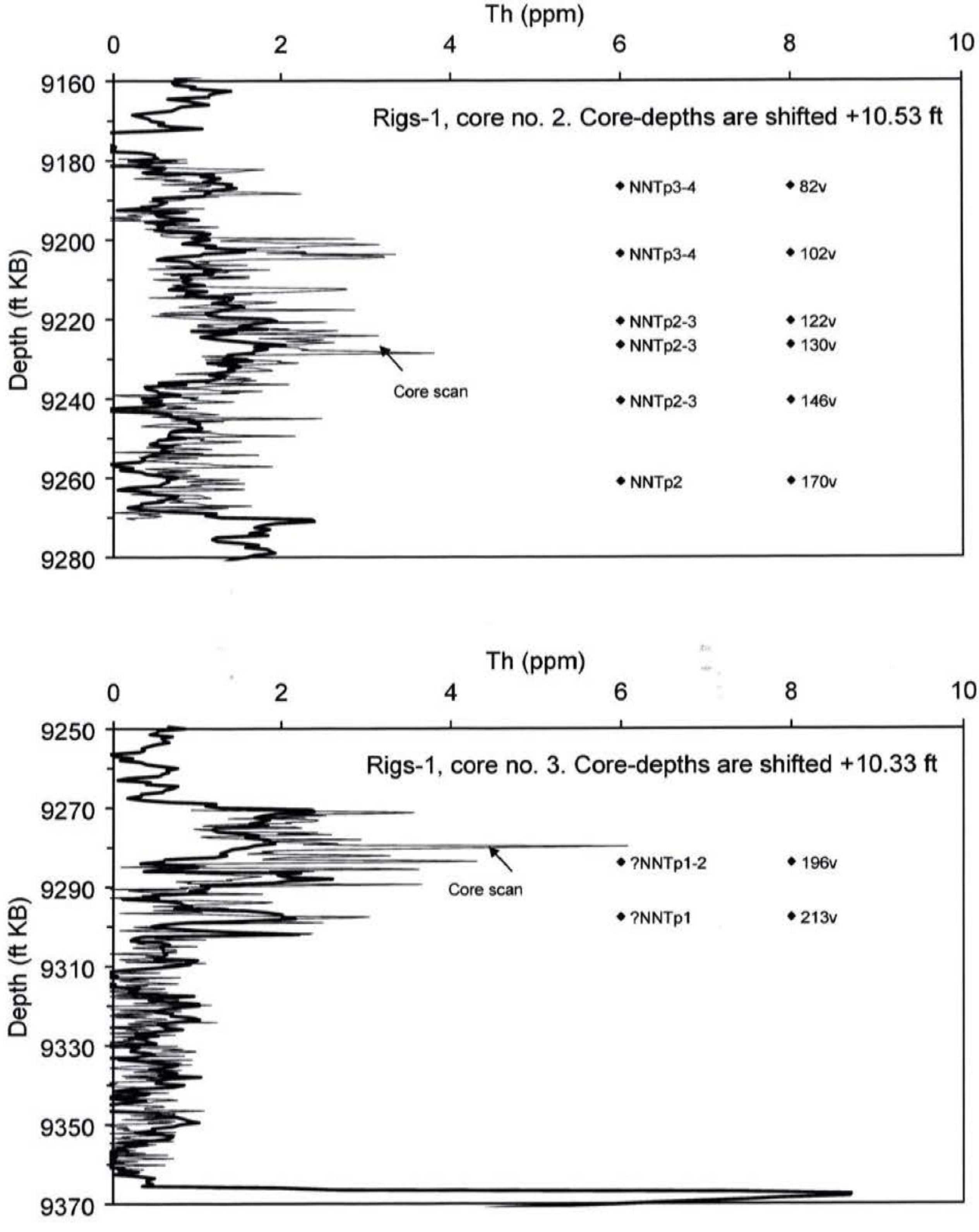

Figure 3 cont. Thorium logs for Rigs-1, core no. 2 and 3. The single core-depths are depth-shifted on the basis of correlation with the Th-core-scan. Nanno-ages and sample numbers are indicated at the corrected depth.

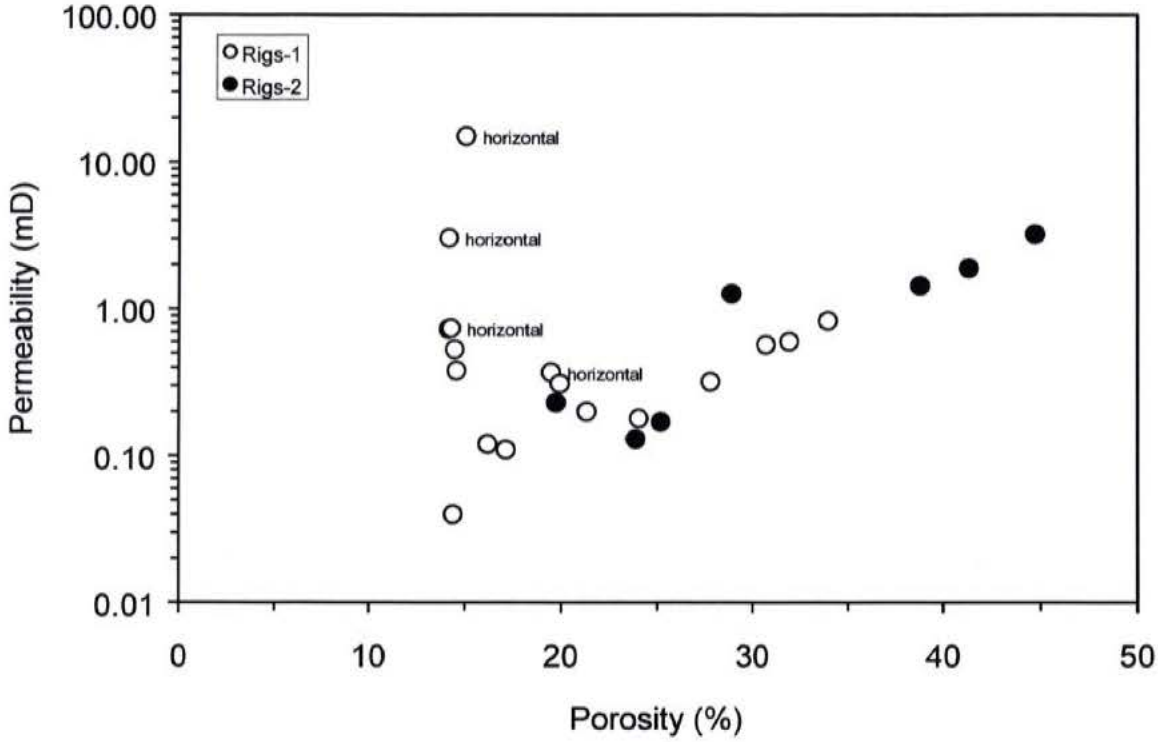

Figure 5. Old core-analyses data. The single horizontal samples are indicated.

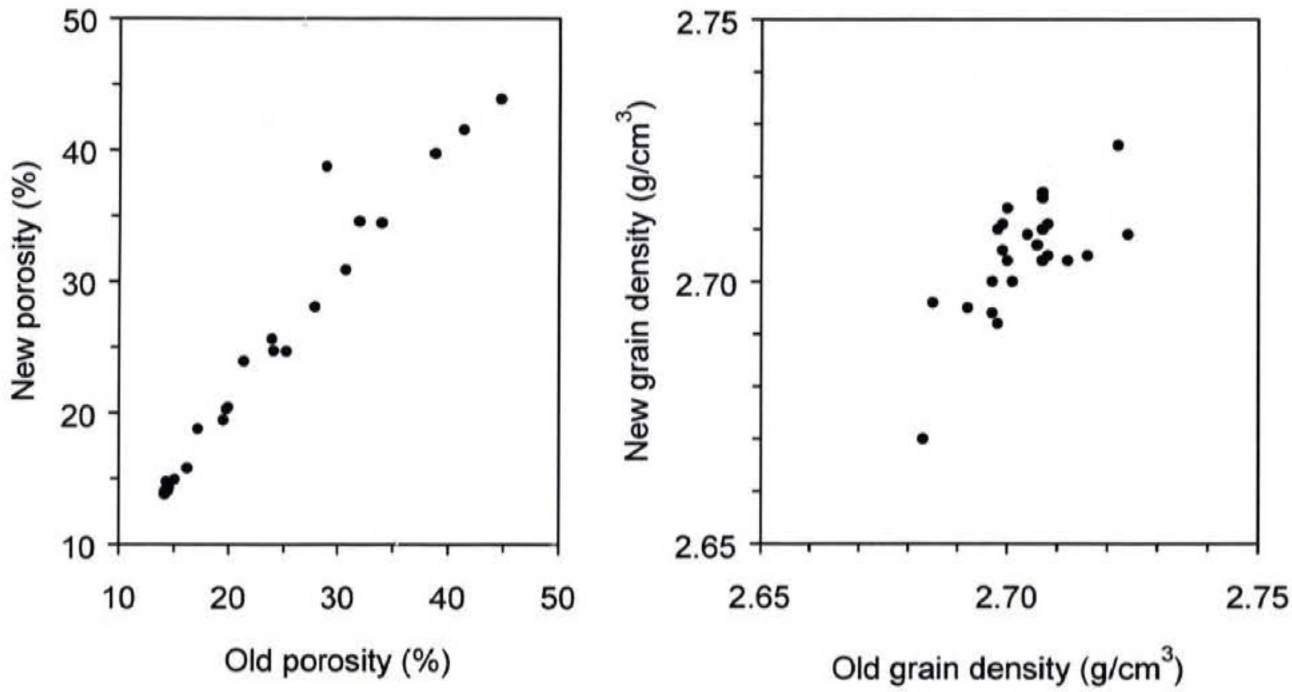

Figure 6. Comparison of old and new core analysis data.

	Rigs-2													
	Core analysis data in file					Remeasurement, this project						Biostratigraphy**	Macroscopic description***	
Plug no.	Depth (m, md, KB)	Inferred log depth (m, KB)	Porosity (%)	Grain Density (g/cm^3)	Permeability (mD)		Porosity (%)	Grain Density (g/cm^3)	Bulk Volume (cm^3)	Pore volume (cm^3)	Nannofossil zones ****	Texture	Comments
C 015+	2800.00	2803.1	41.33	2.685	1.90	vertical	41.55	2.696	15.21	6.32	NNTp4 *pars.*	Mudstone	
C 022	2802.00	2805.1	23.90	2.697	0.13	vertical	25.62	2.700	27.38	7.02	NNTp4 *pars.*	Mudstone	
C 037+	2806.00	2809.1	28.90	2.698	1.27	vertical	38.74	2.692	25.34	9.82	NNTp4 *pars.*	Mudstone	
C 062	2814.15	2817.57	38.79	2.701	1.44	vertical	39.75	2.700	27.15	10.79	NNTp4 *pars.*	Mudstone	
C 074+	2818.04	2821.46	44.73	2.724	3.23	vertical	43.86	2.709	15.21	6.67	NNTp4 *pars.*	Mudstone	
C 093	2824.00	2827.42	25.20	2.683	0.17	vertical	24.69	2.670	27.23	6.72	?NNTp1-2 *pars.*	Mudstone	
C 100	2826.00	2829.42	19.75	2.692	0.23	vertical	20.29	2.695	29.44	5.97	?NNTp1-2 *pars.*	Mudstone	clay layer

\+ The same sample was used for petrography and for sonic measurement.

* Simon Petroleum Technology ltd., 1995: Amarada (Rigs-1) Hess 5604/29-4 well biostratigraphy. Interval 3390'-10130' Danish North Sea.

** Network Stratigraphic Consulting ltd., 1999: Wells Rigs-2 & Rigs-2A. Biostratigraphy of the intervals 2,775m -2,975 m (T.D.) & 2,817m-2,980m.

*** E.B. Nielsen, GEUS,1999.

**** E. Sheldon, GEUS pers. com.

Sample characterization report

Ida Lykke Fabricius, E&R DTU
Sinh Hy Nguyen, E&R DTU
Uffe Korsbech, Ørsted·DTU

Confidential

EFP 2001 Rock physics of impure chalk

Sponsored by the Danish Energy Agency,
Amerada Hess A/S and DONG A/S

E&R DTU, March 2003

Sample characterization report

Ida Lykke Fabricius, E&R DTU
Sinh Hy Nguyen, E&R DTU
Uffe Korsbech, Ørsted·DTU

Confidential

EFP 2001 Rock physics of impure chalk

Sponsored by the Danish Energy Agency,
Amerada Hess A/S and DONG A/S

E&R DTU, March 2003

Contents:

This report contains results from geological characterization of 24 samples from the Ekofisk Formation of Rigs-1 and Rigs-2. The applied methods are described.

1. - 2. Samples

The following samples from the Paleocene of Rigs-1 (B) and Rigs-2 (C) in the South Arne field were selected for analysis in the study of rock physics of impure chalk (Table 1, Fabricius & Høier, 2002).

Table 1

Rigs-1									
				Core data, this project				Biostratigraphy*	Thin section description
Plug no.	Depth (ft, md, KB)	Inferred log depth (ft, KB)		Porosity (%)	Grain Density (g/cm^3)	Bulk Volume (cm^3)	Pore volume (cm^3)	Nannofossil zones ***	
B 003	9111.00	9120.71	Vertical	13.81	2.705	21.22	2.93	NNTp5 *pars.*	mudstone
B 007	9114.00	9123.71	Vertical	14.09	2.705	23.63	3.33	NNTp4-5 *pars.*	mudstone
B 008	9114.32	9124.03	horizontal	14.03	2.707	24.93	4.03	NNTp4-5 *pars.*	mudstone
B 010	9116.30	9126.01	horizontal	14.93	2.704	21.59	3.22	NNTp4-5 *pars.*	mudstone
B 011	9117.00	9126.71	Vertical	14.33	2.711	23.81	3.41	NNTp4-5 *pars.*	mudstone
B 012	9117.32	9127.03	horizontal	14.76	2.726	25.86	3.82	NNTp4-5 *pars.*	mudstone
B 036	9137.51	9147.22	Vertical	15.81	2.704	27.12	4.29	NNTp4-5 *pars.*	mudstone
B 054	9153.20	9162.91	horizontal	19.45	2.709	28.47	5.54	NNTp4 *pars.*	mudstone
B 055	9154.00	9163.71	Vertical	24.73	2.710	27.89	6.90	NNTp4 *pars.*	mudstone
B 082	9176.00	9186.53	Vertical	34.47	2.706	28.30	9.76	NNTp3-4 *pars.*	mudstone
B 102	9193.00	9203.53	Vertical	14.61	2.714	22.12	3.23	NNTp3-4 *pars.*	wackestone
B 122	9210.00	9220.53	Vertical	28.07	2.710	23.45	6.58	NNTp2-3 *pars.*	Mudstone
B 130	9216.00	9226.53	Vertical	23.93	2.717	25.71	6.15	NNTp2-3 *pars.*	mudstone
B 146	9230.00	9240.53	Vertical	34.58	2.694	20.39	7.05	NNTp2-3 *pars.*	mudstone
B 170	9250.39	9260.92	Vertical	30.90	2.704	26.70	8.25	NNTp2 *pars.*	mudstone
B 196	9273.50	9283.83	Vertical	18.79	2.711	26.92	5.06	?NNTp1-2 *pars.*	packstone
B 213	9287.32	9297.65	Vertical	20.43	2.716	27.91	5.70	?NNTp1 *pars.*	wackestone
Rigs-2									
				Core data, this project				Biostratigraphy**	Thin section description
Plug no.	Depth (m, md, KB)	Inferred log depth (m, KB)		Porosity (%)	Grain Density (g/cm^3)	Bulk Volume (cm^3)	Pore volume (cm^3)	Nannofossil zones ***	
C 015+	2800.00	2803.1	Vertical	41.55	2.696	15.21	6.32	NNTp4 *pars.*	mudstone
C 022	2802.00	2805.1	Vertical	25.62	2.700	27.38	7.02	NNTp4 *pars.*	wackestone
C 037+	2806.00	2809.1	Vertical	38.74	2.692	25.34	9.82	NNTp4 *pars.*	mudstone
C 062	2814.15	2817.57	Vertical	39.75	2.700	27.15	10.79	NNTp4 *pars.*	wackestone
C 074+	2818.04	2821.46	Vertical	43.86	2.709	15.21	6.67	NNTp4 *pars.*	mudstone
C 093	2824.00	2827.42	Vertical	24.69	2.670	27.23	6.72	?NNTp1-2 *pars.*	wackestone
C 100	2826.00	2829.42	Vertical	20.29	2.695	29.44	5.97	?NNTp1-2 *pars.*	wackestone

+ The same sample was used for petrography and for sonic measurement.

* Simon Petroleum Technology ltd., 1995: Amarada (Rigs-1) Hess 5604/29-4 well biostratigraphy. Interval 3390'-10130' Danish North Sea.

** Network Stratigraphic Consulting ltd., 1999: Wells Rigs-2 & Rigs-2A. Biostratigraphy of the intervals 2,775m -2,975 m (T.D.) & 2,817m-2,980m.

*** E. Sheldon, GEUS pers. com.

Analytical procedure as preparation for chemistry, X-ray, and BET

Before chemical and physical characterization, each cleaned and dried chalk samples was subjected to the following procedures:

1. Crushing of samples

Coarse crushing: c. 5 g of total chalk sample was crushed in agate mortar to size below 2 mm. Fine grinding: remaining sample was ground in agate ring mortar (SiebTechnik) for 1 min. at 960 rot./min.

BET was measured on coarsely crushed as well as finely ground samples.

The finely ground samples were used for:

- Carbonate content
- insoluble residue
- dissolution by 2 M HCl for chemical analysis (Si, Al, K, Mg, Ca, P, Fe, Ba)
- sulfur and carbon by combustion in total elemental carbon analyzer
- X-ray diffraction (bulk)

2. Carbonate removal by HCl 2 M (insoluble residue)

c. 0.5 g – 20 g (depends on concentration of carbonate) dry, finely ground sample was weighed (to 2 decimals) directly into plastic centrifugal container, and 50 ml distilled water was added, HCl 2 M was gradually added until all carbonate was dissolved and pH reached 2, and the sample rested overnight. Next the sample was centrifuged at 3000 rot./min, clear fluid was removed, the sample was washed in distilled water until no indication of chloride, and the sample finally was dried to constant weight at 50°C.

After removal of all carbonate the insoluble residue was used for:

- dissolution by $LiBO_2$ for chemical analysis (Si, Al, K, Ca, Mg, Fe, Ba)
- sulfur and carbon in total elemental carbon analyzer.
- X-ray diffraction (oriented sample) water-saturated – ethylene-glycol saturated at 60°C- heated to 350°C - and to 550°C
- B.E.T.

3. - 6. Chemical Analysis

Results from the chemical analysis are summarized in Table 2.

3. Carbonate content by titration

c. 0.3 g dry, finely ground sample was weighed (to 4 decimals) directly in a conical flask,

175 ml dist. water and 25.00 ml HCl 0.5000M were added together with c. 10 glass balls. Delicate boiling for 20 minutes to remove carbon dioxide totally. After cooling to room temperature, surplus HCl was titrated back with NaOH 0.5M to faint red color by phenolphthalein indicator.
The concentration of NaOH was checked daily.

4. Dissolution for chemical analysis

4.1 HCl dissolution of total sample
C. 0.5 g finely ground chalk sample was weighed (to 4 decimals) and placed in a 100 ml volumetric flask, moistened with 1 ml dist. water, followed by gradual addition of 10 ml HCl 2M, whereupon the flask was shaken and rested overnight.
Then followed addition of water to fixed volume, and filtering through OOR filter paper. Finally measuring of concentration in filtrate of Si, Al, K, Mg, Ca, Fe, Ba by atomic absorption spectral photometry, Perkin-Elmer model 5000 and P by Dr. Lange spectrophotometer.

4.2 $LiBO_2$ dissolution of insoluble. residue
c 0.15 g dry, finely ground sample was weighed (to 4 decimals) directly into Pt- crucible and mixed with 1g $LiBO_2$ + 0.4g H_3BO_3. The crucible was heated slowly to 800°C and complete melting, and temperature was kept for 40 minutes.
After cooling, the melt was heated and transferred to beaker by a mixture of 20 ml dist. water and 10 ml HNO_3 1:1 until all was dissolved.
The contents of the beaker was moved quantitatively to a 100 ml volumetric flask and distilled water was added to fixed volume.
This solution was used for measurement of Si, Al, K, Mg, Ca, Fe, Ba by atomic absorption spectral photometry, Perkin-Elmer model 5000.

5. Phosphor in chalk sample

Analysis was done directly in 10 mm disposable cuvette. 0.250 ml sample solution from 4.1 above (HCl dissolution of total sample) was diluted by 2.750 ml dist. water.
0.040 ml ascorbic acid- reagent was added – shaken, addition of 0.080 ml acidmolybdate reagent – shaken.
The solution rested 45 min., absorbance measured by Dr. Lange spectrophotometer at a wavelength of 800 nm.
A series of standard solutions with known P-content was prepared from KH_2PO_4, the standard series must be within the measuring interval (0.1 mg P/l – 0.5 mg P/l).

6. Sulphur and carbon by Total elemental carbon analyzer, Leco-CS-225

A suitable amount of sample (normally 0.15g – 0.25g) finely ground and dried, was weighed in Leco-crucible. Then one scoop Lecocel-II- and Tin Alpha AR-076-accerlerator were added. AR-888 was used as standard.

7. X-ray diffractometry

X-ray diffractometry was done on bulk chalk sample as well as on the insoluble residue, and a qualitative interpretation was done (Table 3).

7.1 On finely ground sample (bulk)

c. 0.5 g finely ground total chalk sample was placed in a hole in a brass container, the surface of powder was smoothed by glass plate, and X-ray analysis was done.

7.2 On insoluble residue

c. 0.03 g ins. residue was pulverized and mixed with 1.5 ml dist. water by a pipette. The suspension was placed on object glass and left to dry overnight, and X-ray analysis was done.

7.3 Glycolation

The sample from 8.3 was glycolated at 60°C for two days in desiccator and X-ray analysis was done.

7.4 Heating

The sample was heated to 350°C and X-ray analysis was done. The sample was subsequently heated to 550°C and X-ray analysis was done.

A Philips 1730/10 X-ray diffractometer was used using Cu K-α radiation and automatic divergent slit.

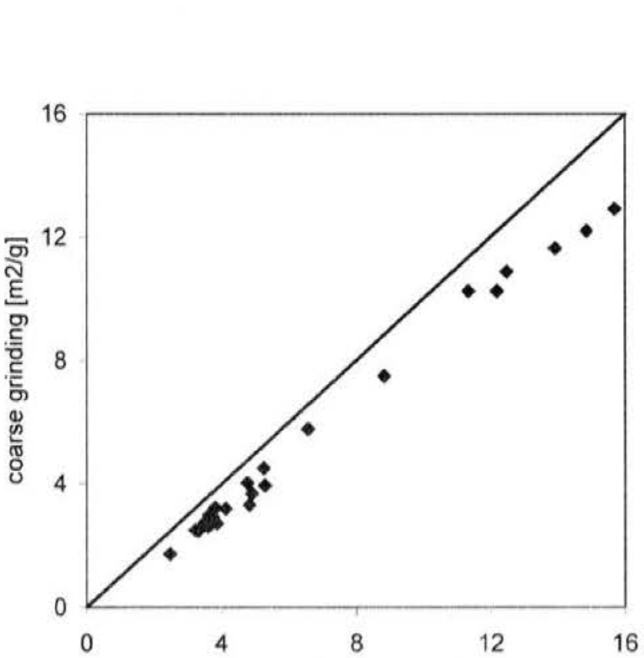

Figure 1. Fine grinding results in too high BET.

8. B.E.T (specific surface)

A suitable amount of sample (for chalk: 1g – 2g) was transferred into a BET-tube, which had been dried and weighed dry already.
The sample was subsequently degassed under nitrogen at 70°C for 5 hrs. The tube with the sample was cooled and weighed.
B.E.T was measured by a Micromeritics Instrument, model Gemini III 2375 by using He gas for measurement of free-space multi pointer with nitrogen as adsorbing gas.

Data are listed in Table 4. We find that grinding in agate ring mortar results in too high specific surface (Figure 1), so data from coarse grinding was used in subsequent analysis. The BET of the total sample is primarily controlled by the BET of the non-carbonate fraction (Figure 2).

Table 2

Plug no.	Wet chemical data. total sample										Wet chemical data. insoluble residue						
	CO_2	SiO_2	MgO	K_2O	Fe	CaO	Al_2O_3	S	P	ins. Res.	SiO_2	MgO	K_2O	Fe	CaO	Al_2O_3	S
	%	%	%	%	%	%	%	%	%	%	%	%	%	%	%	%	%
3	26.26	0.11	0.23	0.06	0.23	34.18	0.14	0.25	0.07	35.29	63.7	1.504	1.602	2.988	0.091	11.74	0.809
7	27.17	0.09	0.26	0.06	0.28	34.73	0.12	0.14	0.07	34.71	64.7	1.480	1.582	2.512	0.100	12.16	0.429
8	24.04	0.36	0.39	0.07	0.51	30.81	0.38	0.21	0.07	41.40	61.3	1.659	1.795	2.666	0.118	13.99	0.538
10	28.49	0.08	0.26	0.03	0.14	36.56	0.10	0.20	0.06	32.56	64.8	1.353	1.483	2.502	0.100	10.89	0.613
11	29.15	0.07	0.29	0.04	0.30	37.54	0.11	0.13	0.08	30.81	62.8	1.478	1.563	2.530	0.119	12.54	0.460
12	28.64	0.07	0.29	0.04	0.29	36.40	0.10	0.66	0.07	31.72	59.1	1.487	1.589	4.000	0.104	12.50	2.250
36	34.14	0.04	0.36	0.04	0.28	43.80	0.07	0.09	0.07	20.00	61.5	1.292	2.020	2.196	0.068	13.45	0.493
54	33.14	0.02	0.23	0.03	0.22	42.51	0.05	0.10	0.05	23.22	74.3	0.528	0.895	1.039	0.046	5.15	0.468
55	34.62	0.02	0.19	0.02	0.21	44.22	0.03	0.05	0.03	19.78	77.1	0.344	0.581	0.686	0.036	3.27	0.317
82	39.13	0.02	0.29	0.01	0.23	49.83	0.02	0.03	0.05	8.83	73.1	0.477	0.804	0.787	0.030	5.07	0.327
102	33.68	0.05	0.19	0.02	0.28	43.11	0.04	0.03	0.05	21.16	74.1	0.342	0.542	0.485	0.033	5.85	0.221
122	39.12	0.07	0.19	0.03	0.21	50.36	0.05	0.03	0.06	9.18	66.8	0.652	1.128	1.027	0.037	10.96	0.509
130	35.54	0.14	0.19	0.04	0.24	45.45	0.09	0.08	0.06	17.50	76.5	0.444	0.826	0.836	0.041	5.88	0.468
146	38.35	0.04	0.18	0.02	0.16	48.78	0.03	0.05	0.05	12.29	77.9	0.323	0.613	0.657	0.037	4.29	0.439
170	38.56	0.05	0.17	0.02	0.17	49.07	0.03	0.04	0.05	11.00	75.1	0.351	0.666	0.713	0.021	3.96	0.041
196	31.92	0.09	0.75	0.03	0.47	39.62	0.06	0.17	0.07	26.22	76.5	0.286	0.553	0.911	0.014	4.51	0.170
213	37.27	0.07	0.87	0.02	0.33	46.72	0.04	0.20	0.08	14.10	68.3	0.500	0.981	1.742	0.041	9.77	0.195
15	33.10	0.04	0.22	0.03	0.24	41.88	0.04	0.08	0.05	23.57	74.8	0.252	0.506	0.636	0.015	7.83	0.471
22	32.51	0.09	0.35	0.04	0.37	41.36	0.06	0.14	0.07	23.86	72.0	0.269	0.530	0.769	0.023	8.43	0.578
37	34.75	0.04	0.20	0.02	0.21	44.25	0.03	0.07	0.04	19.66	76.5	0.185	0.374	0.564	0.017	4.88	0.451
62	38.41	0.03	0.27	0.01	0.23	48.89	0.03	0.09	0.05	10.79	70.9	0.272	0.561	1.021	0.021	8.61	0.924
74	38.17	0.03	0.21	0.02	0.17	48.81	0.03	0.07	0.06	11.73	71.8	0.281	0.594	0.785	0.021	6.89	0.635
93	24.36	0.09	0.41	0.04	0.34	30.57	0.06	0.28	0.08	42.13	79.2	0.211	0.443	0.744	0.021	3.34	0.698
100	33.85	0.02	0.38	0.02	0.19	43.25	0.02	0.08	0.20	21.69	82.7	0.116	0.292	0.478	0.015	1.77	0.453

Table 3

Plug	Calcite	Quartz	Smectite	Smectite-illite	kaolinite	Feldspar	Illite	Ankerite	chlorite?	pyrite
3	xxxx	xxxx	xx 15.2 → 17.0		xx	x	*		*	
7	xxxx	xxxx	xx 15.5 → 17.3		xx	x	x	xxx	*	
8	xxxx	xxxx	xx 15.5 → 17.7		xxx	x	*		*	
10	xxxx	xxx	xx 15.0 → 16.7		xx	*	*		*	
11	xxxx	xxxx	xx 15.0 → 18.0		xx	*	*	xxx	*	
12	xxxx	xxxx	xx 15.5 → 17.0		xx	*	*	xxx	*	xxx
36	xxxx	xxxx		xx 12.3 → 14.0	xx	x	x	xxx	*	
54	xxxx	xxxx		* 11.6 → 9.8,13.0	xx	*				
55	xxxx	xxxx			*	*				
82	xxxx	xxx			xx			xxx		
102	xxxx	xxx			xx	*				
122	xxxx	xxx			xx	*	*			
130	xxxx	xxx		x 11.8 → 10.0,12.8	xx	*	*	xxx		
146	xxxx	xxx			x					
170	xxxx	xxx			x	*				
196	xxxx	xxx			x	*		xxx		
213	xxxx	xxx		*11.8 → 10.0,13.8	x	*	*	xxx		x
15	xxxx	xxx			xxx	*		xxx		
22	xxxx	xxx			xxx			xxx		
37	xxxx	xxx			xx		*			
62	xxxx	xxx								
74	xxxx	xxx			xxx	*	*	xxx		
93	xxxx	xxxx			xx			xxx		
100	xxxx	xxxx			x					

xxxx strong lines in bulk sample
xxx single weaker lines in bulk sample
xx major component in insoluble residue (several strong lines)
x minor component in insoluble residue (several weaker lines)
* Trace in insoluble residue (single weak line)

Table 4

	BET coarse - agat mortar				BET fine - ring mortar				BET insoluble residue					
	single point		multi point		single point		multi point		single point		multi point		micropore area	
chalk sample	average m^2/g	st.dev. m^2/g	average m^2/g	st.dev. m^2/g	average m^2/g	st.dev. m^2/g	average m^2/g	st.dev. m^2/g	average m^2/g	st.dev. m^2/g	average m^2/g	st.dev. m^2/g	average m^2/g	st.dev. m^2/g
3	11.99	0.06	12.20	0.06	14.63	0.06	14.86	0.06	39.51	0.18	40.04	0.20	7.40	0.31
7	11.43	0.03	11.64	0.03	13.70	0.06	13.92	0.06	40.30	0.36	40.86	0.38	7.19	0.15
8	12.68	0.05	12.92	0.05	15.44	0.01	15.70	0.01	43.72	0.35	44.25	0.34	9.37	0.22
10	10.04	0.13	10.24	0.13	11.14	0.66	11.35	0.66	37.14	0.09	37.73	0.09	5.21	0.03
11	10.05	0.07	10.24	0.07	11.99	0.05	12.20	0.05	40.69	0.39	41.31	0.40	6.27	0.21
12	10.68	0.07	10.88	0.06	12.27	0.06	12.48	0.06	39.68	0.38	40.27	0.38	6.39	0.22
36	7.32	0.01	7.49	0.01	8.66	0.00	8.83	0.00	38.23	0.27	39.12	0.26	1.23	0.08
54	5.66	0.12	5.78	0.12	6.44	0.01	6.56	0.01	19.43	0.03	19.89	0.03	0.57	0.00
55	3.13	0.00	3.19	0.00	4.03	0.01	4.11	0.01	12.04	0.04	12.37	0.04		
82	2.39	0.01	2.47	0.01	3.20	0.00	3.31	0.00	11.25	0.08	11.63	0.08		
102	3.25	0.02	3.31	0.02	4.74	0.01	4.82	0.01	14.44	0.02	14.73	0.01		
122	3.96	0.03	4.02	0.03	4.67	0.04	4.76	0.04	19.54	0.07	20.00	0.07		
130	4.43	0.03	4.51	0.03	5.16	0.02	5.24	0.02	18.11	0.00	18.56	0.01		
146	2.66	0.00	2.71	0.00	3.77	0.01	3.85	0.01	9.55	0.07	9.83	0.07		
170	2.54	0.00	2.61	0.00	3.50	0.02	3.59	0.02	9.03	0.02	9.32	0.02		
196	2.44	0.02	2.50	0.02	3.15	0.02	3.22	0.02	7.62	0.06	7.81	0.06		
213	2.42	0.06	2.48	0.06	3.20	0.01	3.28	0.01	13.05	0.01	13.45	0.02		
15	3.09	0.01	3.23	0.01	3.67	0.01	3.81	0.01	7.79	0.04	8.08	0.04		
22	3.87	0.06	3.95	0.06	5.18	0.02	5.27	0.02	11.72	0.03	12.01	0.03		
37	2.85	0.04	2.98	0.04	3.49	0.00	3.62	0.01	7.12	0.01	7.42	0.00		
62	2.85	0.00	2.93	0.00	3.62	0.01	3.72	0.01	8.81	0.03	9.10	0.03		
74	2.62	0.01	2.72	0.01	3.37	0.01	3.47	0.01	8.56	0.01	8.92	0.02		
93	3.59	0.02	3.69	0.02	4.77	0.01	4.89	0.01	8.17	0.03	8.40	0.03		
100	1.67	0.03	1.73	0.03	2.40	0.01	2.47	0.01	5.81	0.07	5.97	0.07	0.00	0.05

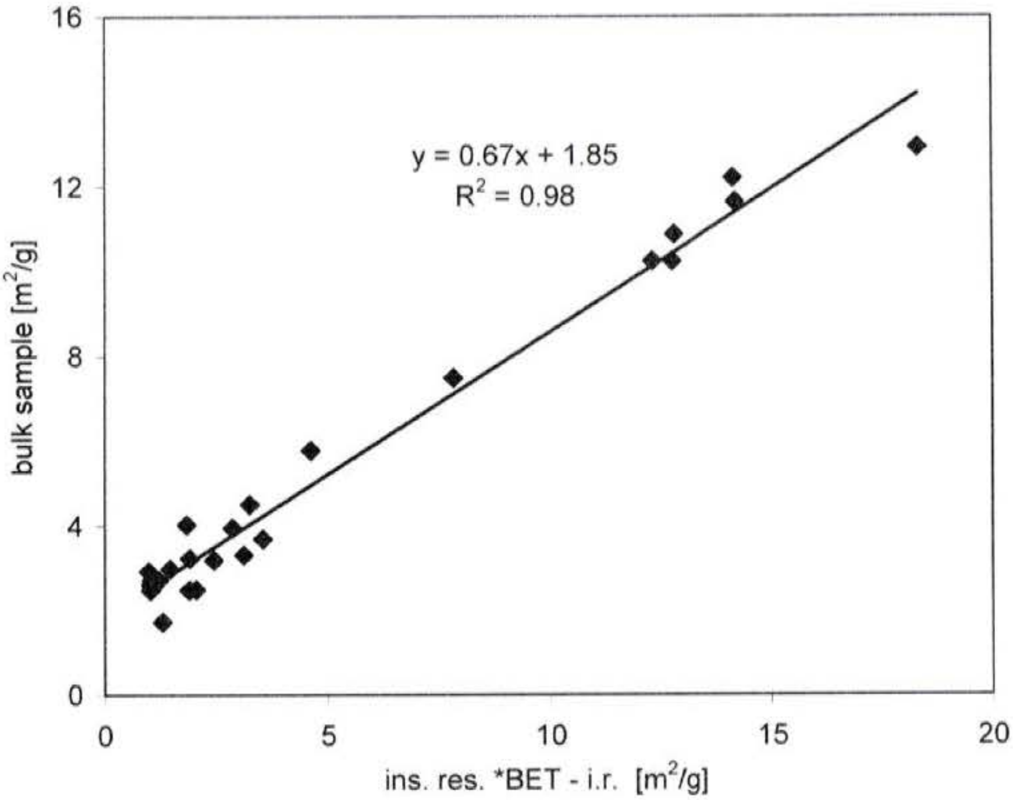

Figure 2. Correlation of BET for bulk sample and insoluble residue becomes obvious when both data sets refer to bulk sample.

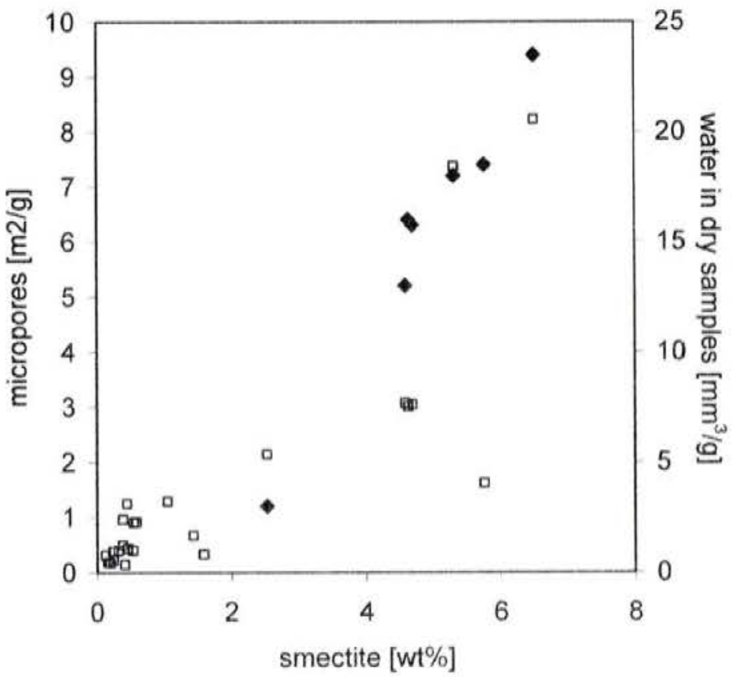

Figure 3. Microporosity as measured by BET (black diamonds) is primarily controlled by smectite. Volume of water in dry samples (open squares) equilibrated to room conditions also largely reflects content of smectite (See 13. Model of composition).

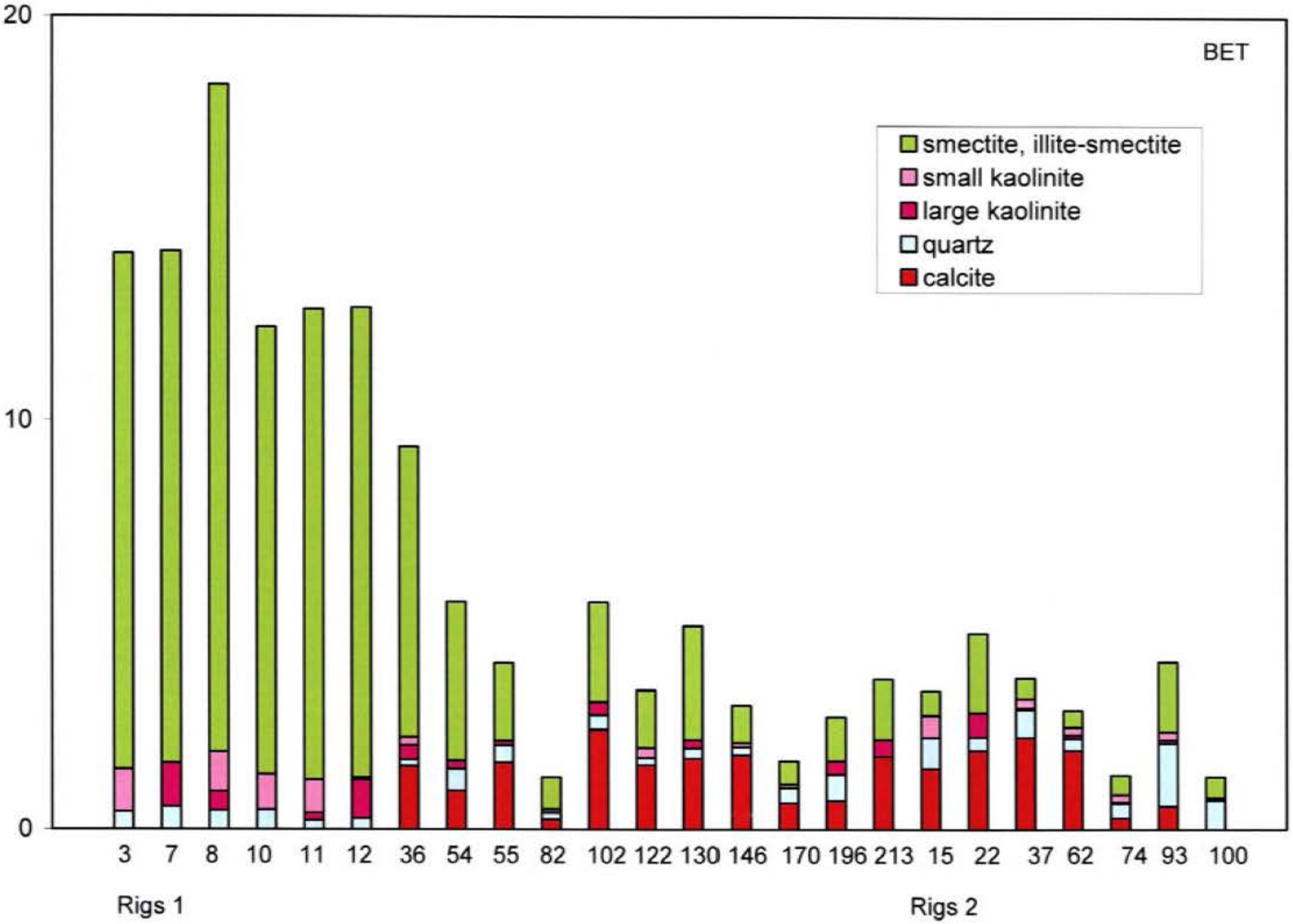

Figure 4. Modeling of BET based on assumed values for each mineral phase.

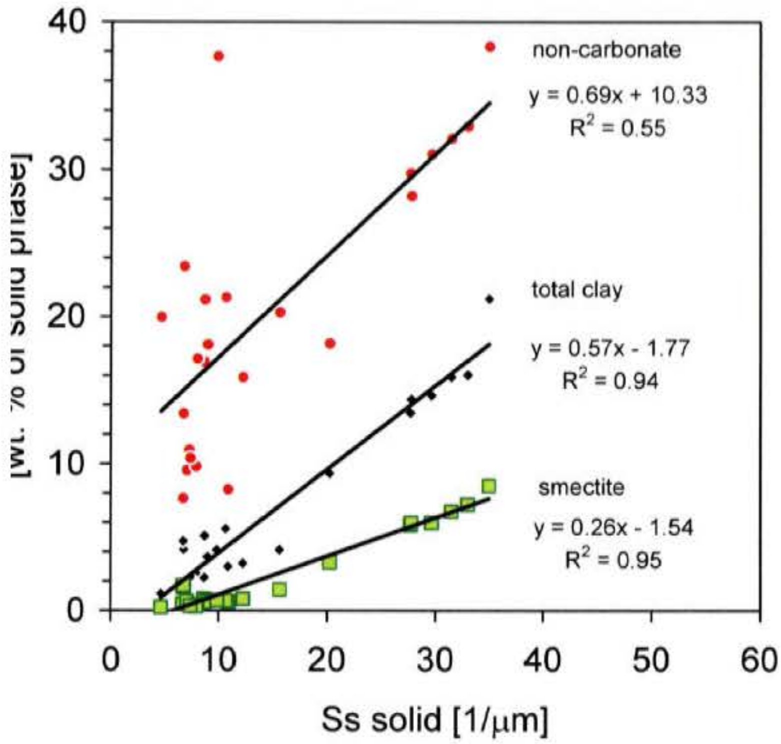

Figure 5. Correlation between specific surface of solid phase and content of selected mineral phases. The specific surface is recalculated to Ss: the surface of the grains relative to the grain volume.

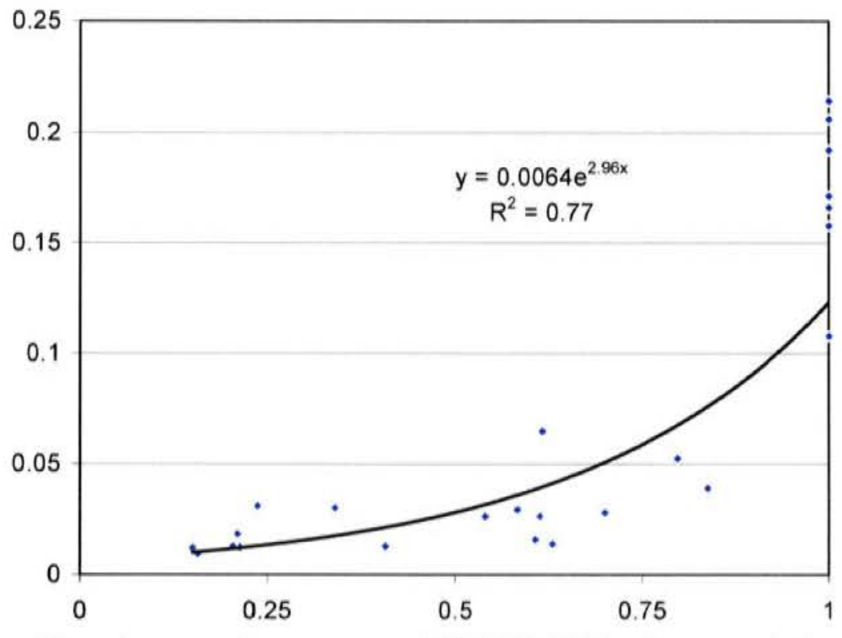

Figure 6. Relationship between specific surface of pores and water saturation from logs. We assume that the water saturation is irreducible.

The microporosity as measured by BET (Table 4) appears to be a reflection of smectite content and closely related to the amount of water a dry sample will adsorb from the atmosphere (Figure 3).

The BET of the total sample may be seen as a combination of the contribution from calcite and a contribution from the insoluble residue. In the smectite rich upper section of Rigs-1, the specific surface of the insoluble residue is larger than what can be accounted for in the BET of the total sample, resulting in apparent negative specific surface of calcite. The specific surface of the non-carbonate fraction must thus have grown during the procedure of removing carbonate. In the remaining samples the calculated specific surface of calcite falls in the range from 0.2 to 2.2 m^2/g.

From the modeled content of mineral phases (see below, section 11) we may model the contribution from each phase to the specific surface (Figure 4). We assumed the following specific surfaces: illite: 65 m^2/g, fine quartz: 5 m^2/g, large quartz and feldspar: 0 m^2/g, kaolinite (large and small): 15 m^2/g. The choice of values is partly based on Røgen and Fabricius (2002). These choices result in a specific surface of smectite of 160 – 215 m^2/g, and of illite-smectite of 6 – 285 m^2/g. The large range of the latter value is probably a reflection of the rather coarse assumptions made in the modeled content of mineral phases.

The specific surface of the bulk sample correlates well with smectite content and total clay content (Figure 5). When the specific surface is recalculated to specific surface of pores we obtain a rather coarse relationship to water saturation from logs (Figure 6). But although we cannot obtain an exact correlation between core and logging data, the result indicates that we may have a possibility of assessing content of smectite (or total clay) from the water saturation in the irreducible zone.

9. Spectral Gamma ray analysis

Th, U, and K in small samples of finely ground chalk were measured in a NaI well crystal gamma detector (Table 5).
Total gamma radiation was calculated as:

$$\text{Total GR} = 0.37 \times \text{Th} + 1.0 \times \text{U} + 1.33 \times \text{K}$$

The corrected gamma radiation (leaving out the uranium signal) was calculated as:

$$\text{CGR} = 0.37 \times \text{Th} + 1.33 \times \text{K}$$

The gamma radiation reflects the composition of the samples as modeled below (section 11). The K signal correlates fairly with non-carbonates and excellently with total clay as well as with smectite (Figure 8). We see no obvious correlation with non-carbonate or clay in the U signal (Figure 8). The Th signal correlates fairly with non-carbonates and total clay (Figure 8), whereas total GR and CGR both correlate well with non-carbonates, smectite, and total clay (Figure 8).

Table 5

	mass g	Th ppm	+/- Th	U ppm	+/- U	K %	+/- K	Total gamma
Rigs 1								
3	15.84	2.7	0.5	0.6	0.2	0.57	0.02	2.36
7	20.61	2.5	0.5	0.6	0.2	0.56	0.02	2.27
8	20.87	3.6	0.5	0.9	0.2	0.69	0.02	3.15
10	22.12	2.6	0.5	0.6	0.2	0.52	0.02	2.25
11	18.68	2.7	0.5	1.1	0.2	0.48	0.02	2.74
12	21.54	2.5	0.4	0.6	0.2	0.51	0.02	2.20
36	15.06	2.4	0.4	0.9	0.1	0.41	0.02	2.33
54	16.96	1.1	0.4	1.1	0.1	0.23	0.02	1.81
55	16.2	0.4	0.4	0.2	0.1	0.12	0.02	0.51
82	13.17	0.5	0.5	0.2	0.2	0.08	0.02	0.49
102	14.41	0.8	0.6	0.3	0.2	0.11	0.02	0.74
122	14.92	1.7	0.5	0.3	0.2	0.13	0.02	1.10
130	16.62	1.5	0.5	0.1	0.2	0.15	0.02	0.85
146	13.3	2	0.4	0.3	0.1	0.04	0.02	1.09
170	13.79	-0.2	0.4	0.6	0.1	0.08	0.02	0.63
196	15.96	1.4	0.4	0.5	0.1	0.14	0.02	1.20
213	16.55	1	0.4	0.5	0.1	0.14	0.02	1.06
Rigs 2								
15	15.54	2.3	0.4	0.2	0.1	0.11	0.02	1.20
22	13.76	1.8	0.4	0.8	0.1	0.14	0.02	1.65
37	14.97	2.1	0.4	0.6	0.1	0.04	0.02	1.43
62	14.47	1.9	0.4	0.1	0.1	0.09	0.02	0.92
74	16.31	1.9	0.5	0.1	0.1	0.08	0.02	0.91
93	11.24	2.9	0.4	2.1	0.1	0.17	0.02	3.40
100	17.48	1.5	0.4	0.6	0.1	0.1	0.02	1.29

The Th-signal of the core samples correlate well with the well logs. So the content of total clay and non-carbonates may be estimated from the Th logs (Figure 9). One has to remember that the sample measurements only concern a volume of 10-18 ml whereas the borehole log results represent 1-2000 times larger volumes.A good correlation between composition and gamma-signal should be expected from the K-log and also for the total GR log and the CGR log, but in the present case K-rich drilling mud was used, so these logs do not correlate well with core data (Figure 10 and 11).

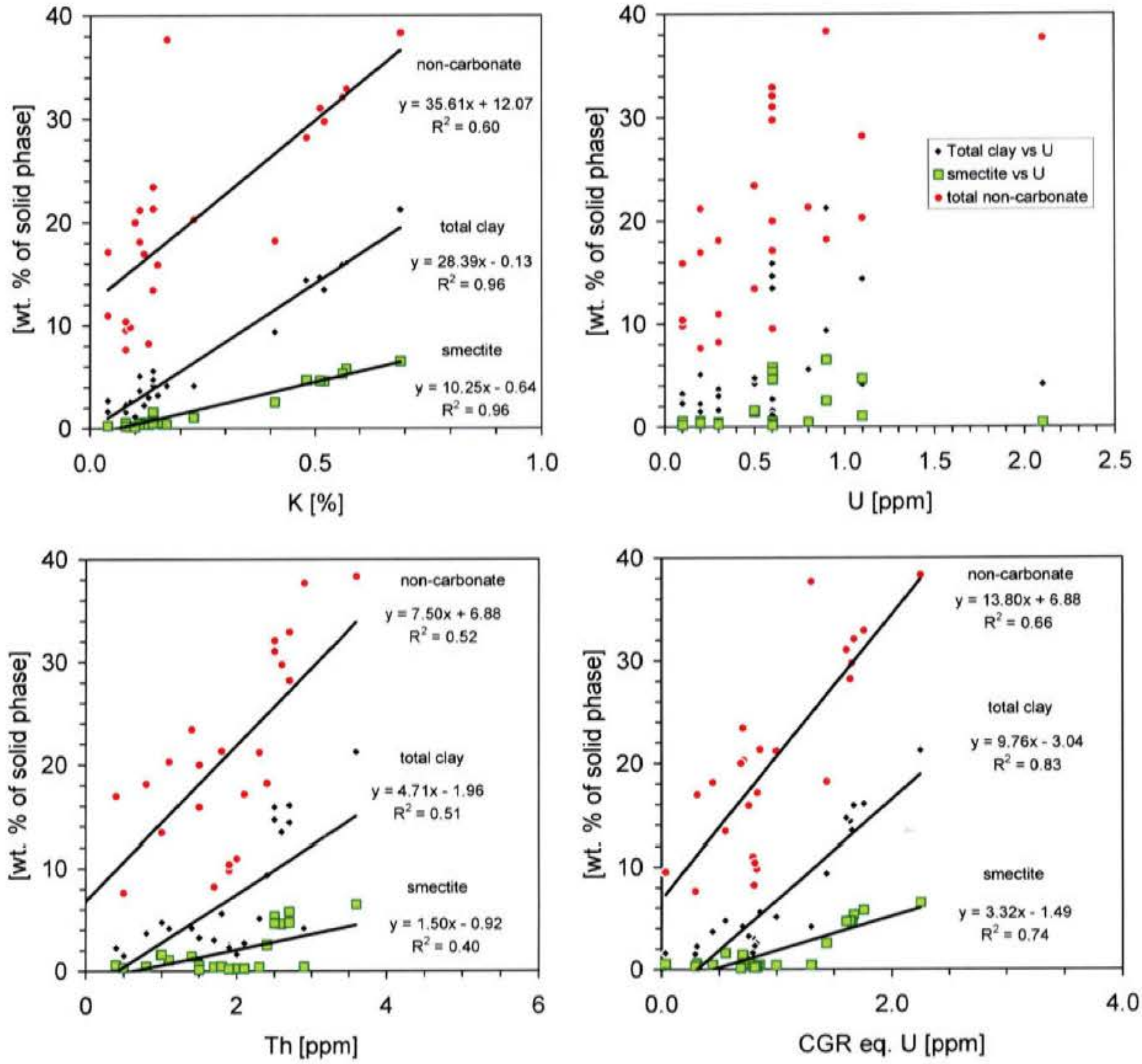

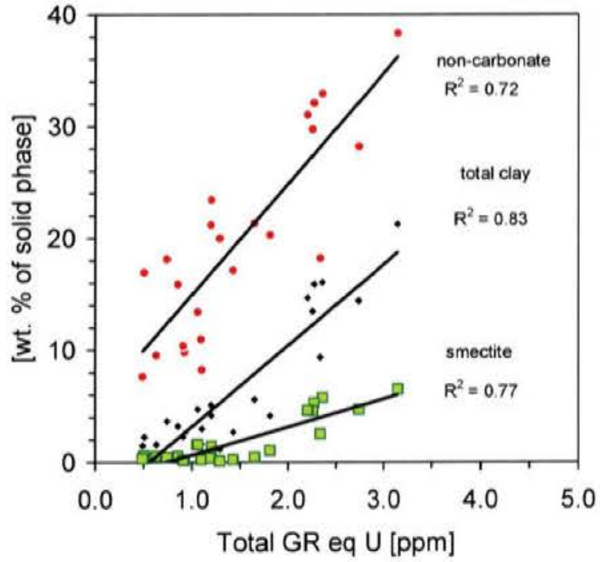

Figure 8. Correlations between natural gamma-radioactivity and composition of samples.

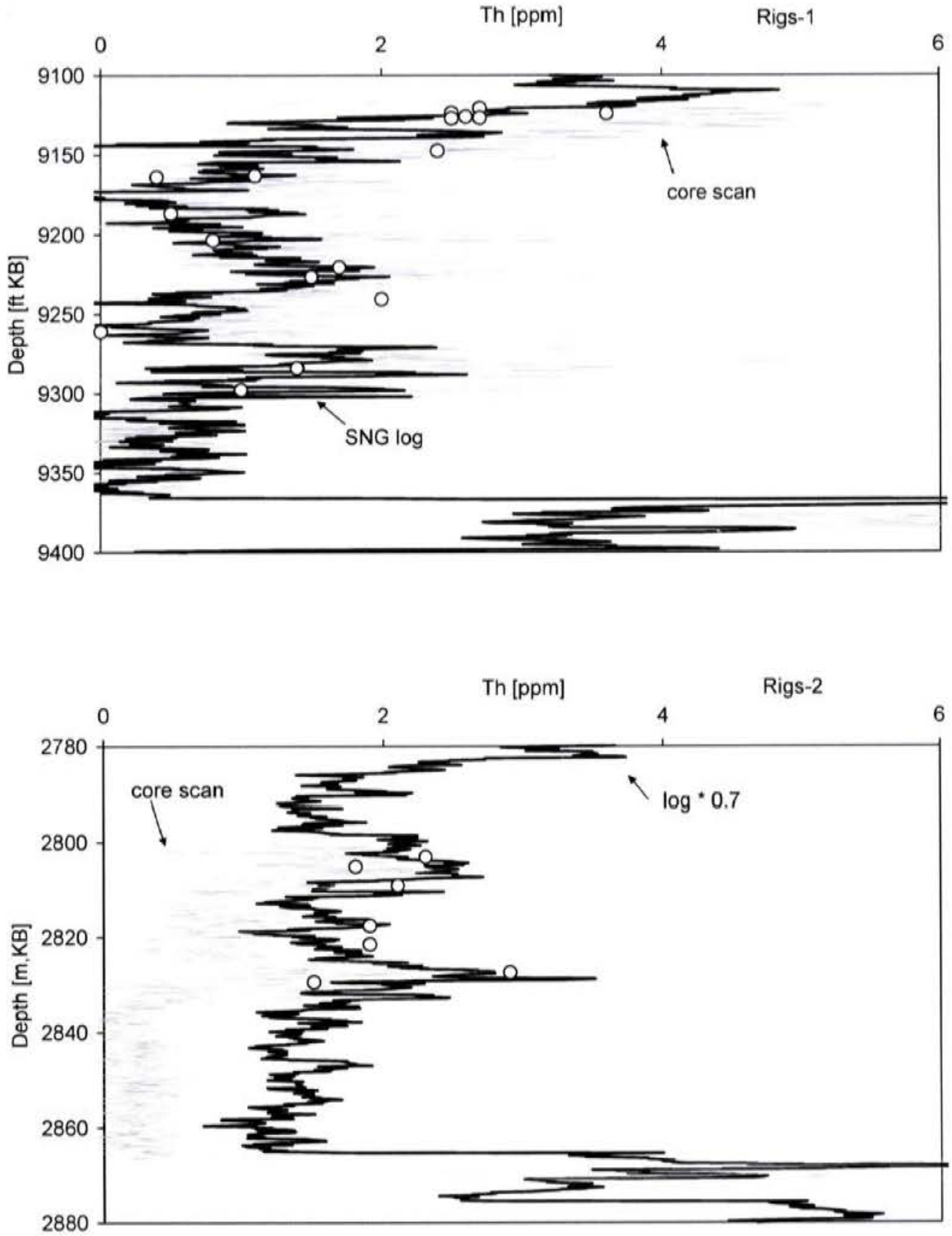

Figure 9. Natural gamma radiation representing Th in Rigs-1 and Rigs-2: Black curves are Th signal from borehole SNG logs, grey curves are Th signal from core scanning (C. Høier, GEUS) and circles represent measurements on powdered core samples. In Rigs-1 the three data sets correlate well, in Rigs-2 the Th-log multiplied by 0.7 correlates well with the core samples.

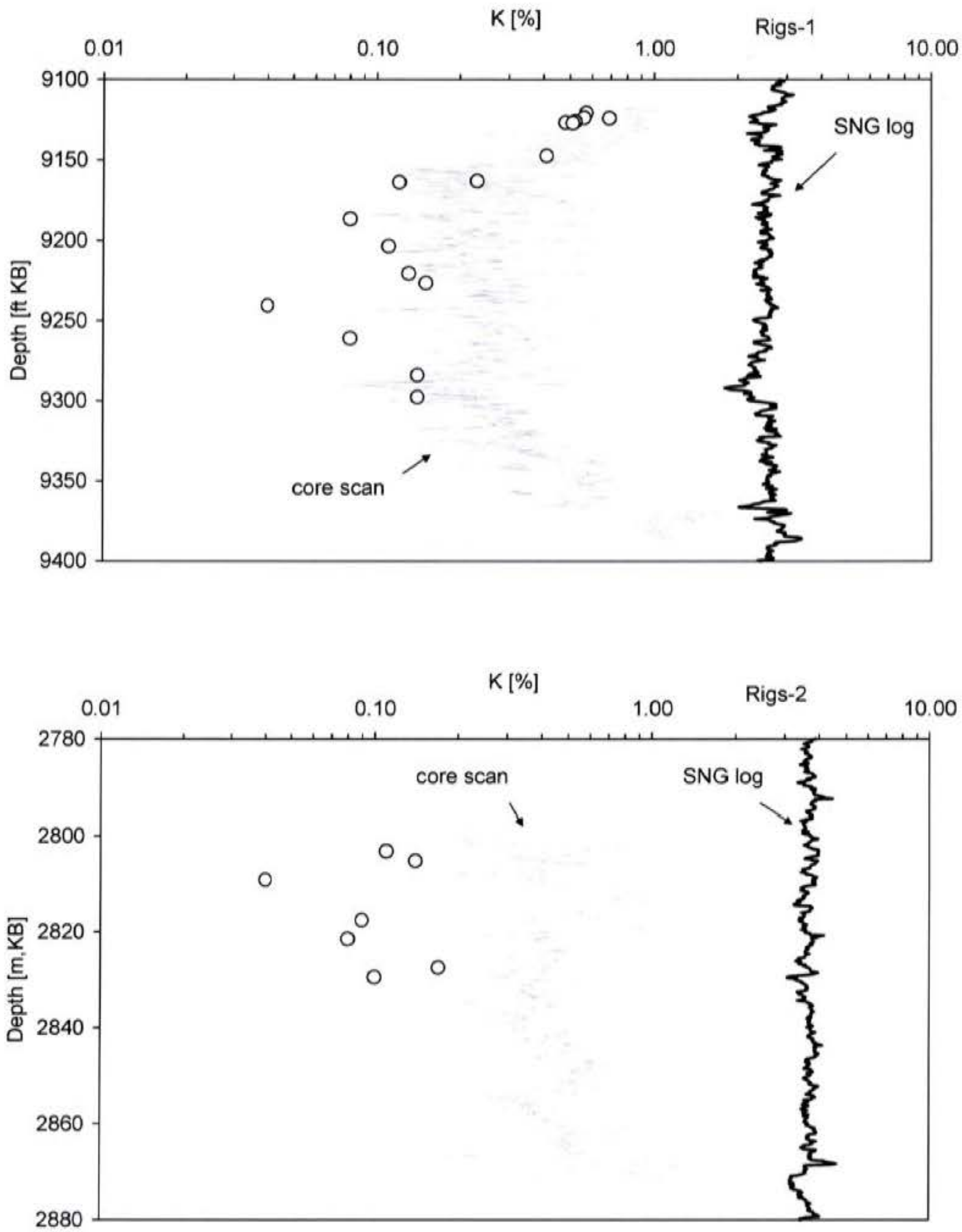

Figure 10. Natural gamma radiation representing K in Rigs-1 and Rigs-2: Black curves are K signal from borehole SNG logs, grey curves are K signal from core scanning (C. Høier, GEUS) and circles represent measurements on powdered core samples. In Rigs-1 the core scan and core data correlate roughly. In neither Rigs-1 nor Rigs-2 do the core data correlate with the logging data.

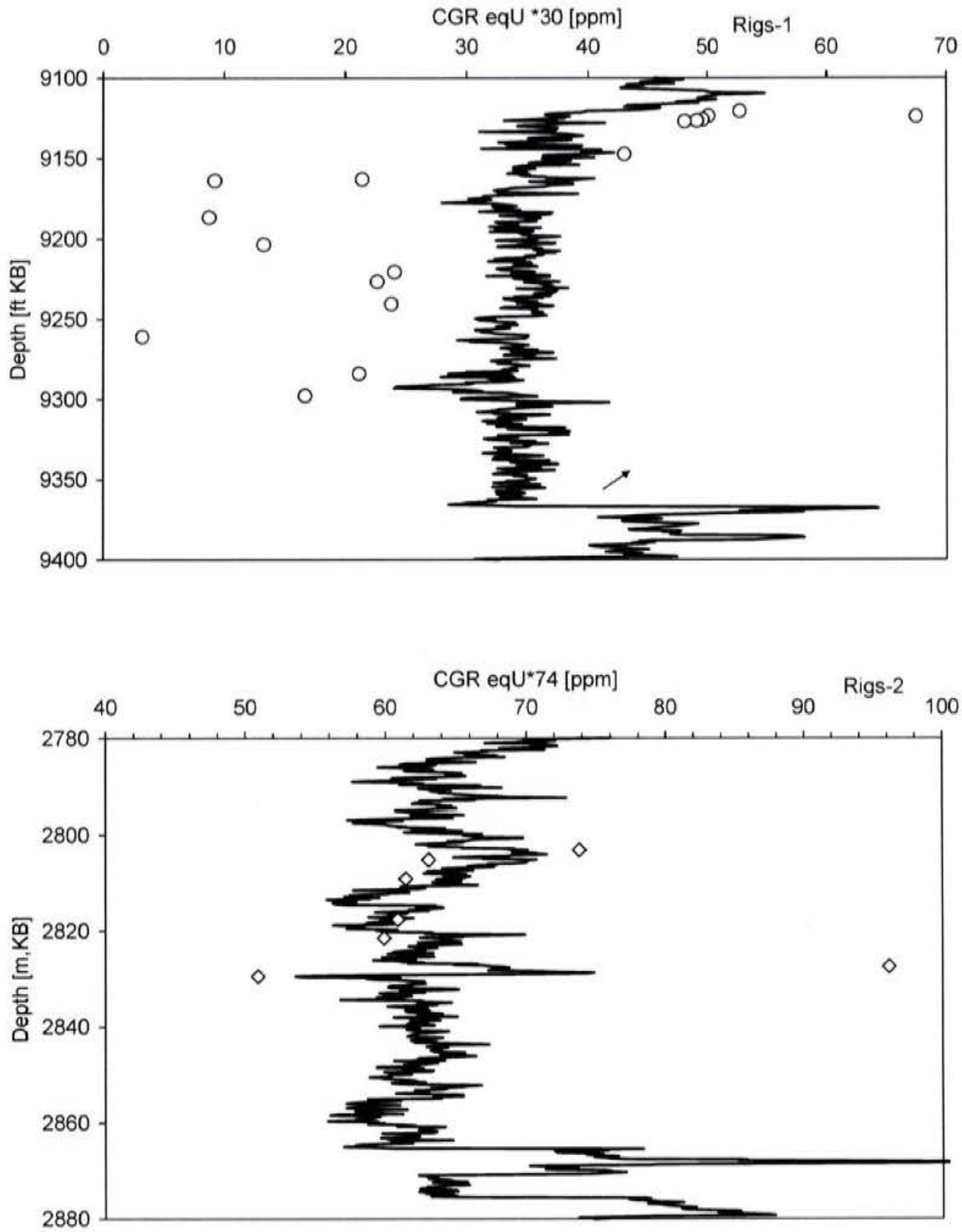

Figure 11. CGR logs and corresponding sample data in Rigs-1 and Rigs-2. A possible correlation between core and log data is only vague.

10. Backscatter electron micrographs and Petrographic image analysis

Backscatter electron micrographs were recorded by the Philips XL-40 Scanning Electron Microscope at GEUS, Copenhagen (see section 13. Backscatter Electron Micrographs) The images were sampled as square images at two magnifications: 333 by 333 microns and 33 by 33 microns. On each sample four sets of images were sampled at regular intervals along a vertical line. The 333 by 333 micron images give information of the bulk composition of the sample, whereas the 33 by 33 micron image give information on the fine grained matrix of the bimodally sorted chalk. Each image is composed of 1024 by 1024 square pixels, so that the pixel dimensions are 0.32 by 0.32 microns at the low magnification and 0.032 by 0.032 microns at the high magnification. Mineral phases were identified from morphology aided by qualitative energy dispersive secondary X-ray spectrometry (EDAX).

Images analysis was done by the free software UTHSCASA Image Tool.
The procedure was as follows: On the 333 by 333 micron images the amounts of large porosity and of pyrite were assessed from the grey level distribution of the raw image. Large porosity is thus pores of a diameter of above c. 0.5 microns in cross section.

In order to asses the amount of larger silicate grains and of larger calcite grains, each image was first smoothed by twice applying a 9 by 9 averaging filter before assessing the amount of silicate grains and calcite grains from the grey level distribution. By the smoothing procedure, grains measuring less than two microns in cross section will obtain a relatively low grey level from averaging with fine pores, and will not be recorded.

The 33 by 33 micron images were used for measuring the composition of the matrix and for measuring the specific circumference of the calcite crystals composing the nannofossils and fossil debris. In order to smooth away the noise at pore-crystal interfaces, the images were first smoothed by applying a 9 by 9 averaging filter one time. On the smoothed image the amount of visible pores (more than 0.1 micron in cross section), the amount of invisible pores and fine silicates (clay and quartz), and the amount of calcite were assessed from grey level distribution. The calcite phase was then selected as one grey level and the remaining image as another grey level. This binary image was then used for measuring the specific circumference of the calcite crystals by applying a 3 by 3 cross filter according the procedure of Borre et al. (1997).

11. Model of composition

The mineralogical composition of the samples was modeled based on X-ray diffraction, wet chemical analysis, thin section microscopy, backscatter electron microscopy, and EDAX-data (Table 6). The strategy was as follows:

1) All Ba goes to barite,
2) remaining S in insoluble residue goes to pyrite,
3) remaining Fe in insoluble residue goes to Fe bearing smectite (glauconite),
4) remaining Mg in insoluble residue goes to smectite (saponite),
5) remaining K in insoluble residue goes to illite (muscovite),
6) remaining Al in insoluble residue goes to kaolinite,
7) remaining Si in insoluble residue goes to quartz,
8) P in filtrate goes to apatite,

Table 6	pyrite	glauconite	Saponite	Illite	kaolinite	quartz	apatite	anhydrite	ankerite	Calcite	sum
Plug no	(%)	(%)	(%)	(%)	(%)	(%)	(%)	(%)	(%)	(%)	(%)
3	0.5	5.8	1.5	1.9	6.9	15.0	0.3	1.0	2.0	59.7	94.6
7	0.3	5.3	1.4	2.0	7.1	15.0	0.3	0.6	2.3	61.1	95.4
8	0.4	6.5	2.0	3.2	9.5	15.5	0.3	0.9	3.7	53.8	95.9
10	0.4	4.6	1.2	1.9	5.8	14.8	0.3	0.8	1.7	64.1	95.6
11	0.3	4.7	1.3	1.8	6.6	12.6	0.3	0.6	2.5	66.1	96.8
12	1.3	4.6	1.3	2.0	6.6	11.9	0.3	2.8	2.4	62.4	95.8
36	0.2	2.5	0.7	2.4	3.7	7.9	0.3	0.4	2.7	77.4	98.3
54	0.2	1.0	0.4	1.4	1.3	15.3	0.2	0.4	1.9	75.1	97.3
55	0.1	0.6	0.2	0.8	0.7	14.2	0.2	0.2	1.7	78.3	96.9
82	0.1	0.3	0.1	0.5	0.5	5.8	0.2	0.1	2.2	88.3	98.2
102	0.1	0.4	0.2	0.9	2.1	14.0	0.2	0.1	2.0	76.3	96.4
122	0.1	0.4	0.2	0.8	1.6	4.7	0.3	0.1	1.7	89.3	99.2
130	0.2	0.5	0.2	1.1	1.3	11.9	0.3	0.3	1.8	80.4	98.0
146	0.1	0.2	0.1	0.6	0.7	8.8	0.2	0.2	1.5	86.4	98.8
170	0.0	0.5	0.1	0.4	0.6	7.5	0.2	0.2	1.4	86.9	97.9
196	0.1	1.4	0.1	0.5	2.1	18.1	0.3	0.7	5.3	69.7	98.3
213	0.1	1.6	0.1	0.4	2.7	7.4	0.4	0.8	5.3	82.2	100.9
15	0.2	0.4	0.2	0.9	3.6	15.3	0.2	0.4	1.9	74.0	97.1
22	0.3	0.5	0.2	1.0	3.9	14.6	0.3	0.6	3.0	72.9	97.2
37	0.2	0.2	0.1	0.6	1.8	13.8	0.2	0.3	1.7	78.3	97.1
62	0.2	0.2	0.1	0.5	1.8	6.5	0.2	0.4	2.1	86.5	98.4
74	0.1	0.2	0.1	0.6	1.4	7.4	0.3	0.3	1.6	86.4	98.4
93	0.6	0.4	0.3	1.6	1.8	31.4	0.4	1.2	3.2	53.2	94.0
100	0.2	0.1	0.1	0.5	0.4	17.4	0.9	0.4	2.4	76.4	98.8

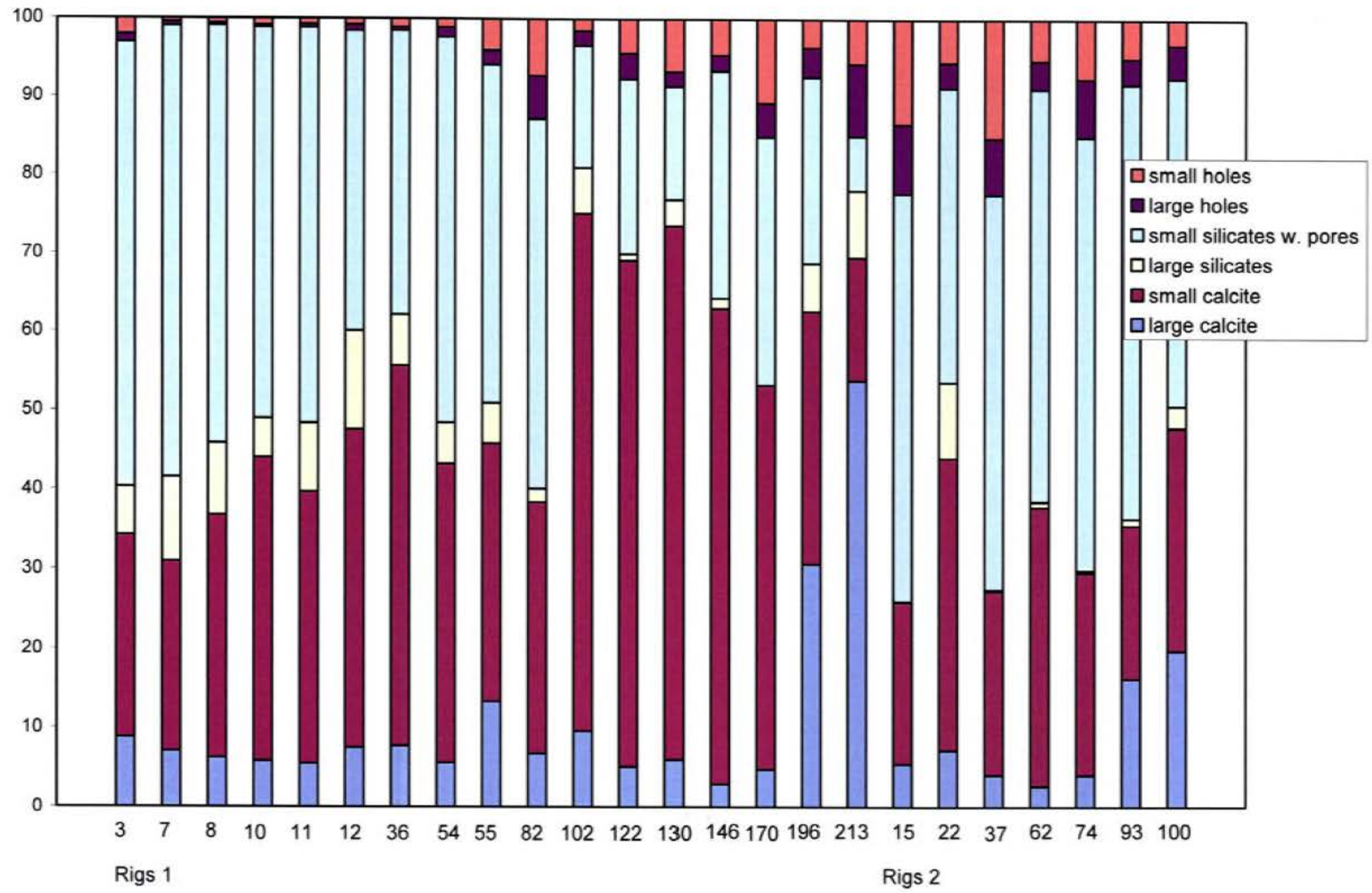

Figure 12. Composition of bulk volume of samples as measured by petrographic image analysis.

9) S in filtrate goes to anhydrite,
10) Mg and Fe in filtrate goes to ankerite,
11) remaining Ca in filtrate goes to calcite.

The model is rather coarse. For instance ideal "glauconite" or "illite" does not exist. Pure saponite is probably not in the samples, but must together with "illite" be seen as a measure of smectite-illite. No allowance is made for feldspars although they are relatively frequent.
The textural composition was modeled from image analysis data (Figure 12), and on the basis of dry P-wave modulus data, the fine grained calcite was modeled as being in suspension or as being part of the solid frame according to an iso-frame or IF model (Fabricius 2002, Table 7). The calculated IF-values were correlated with the specific perimeter of the calcite phase as measured by petrographic image analysis (Figure 13). The resulting total composition of the samples is illustrated in Figure 14.

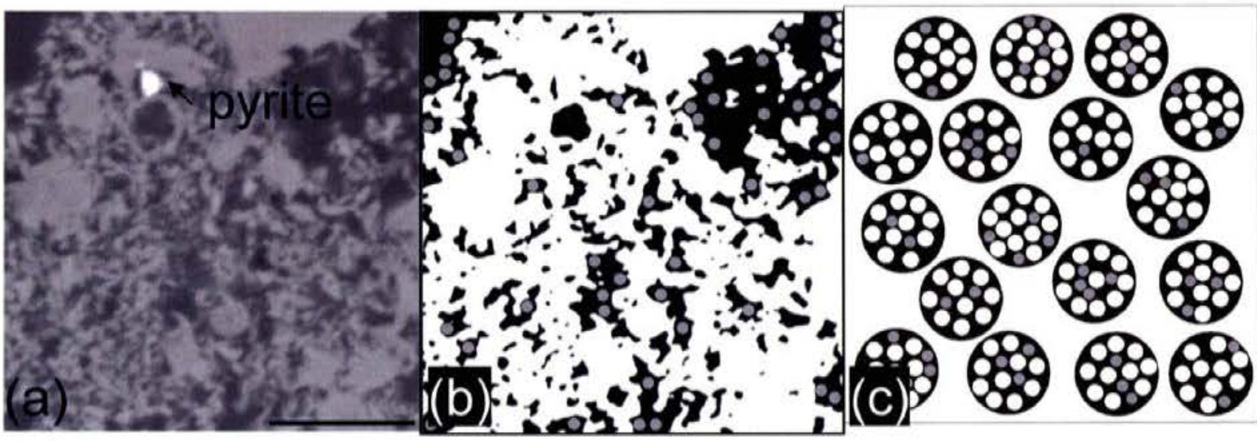

Figure 13. Iso-frame (IF) model for chalk. (a) Backscatter electron micrograph of the epoxy-impregnated and polished sample Rigs 1, 9210.0 ft MD, chalk mudstone with 28.1% porosity. The black bar measures 10 microns. Of the bulk volume 5.9% is fine grained silicates. (b) By petrographic image analysis the fine-grained calcite (including a pyrite crystal) is marked as white and the pore space as black. The fine grained silicates are symbolized by grey circles. The specific perimeter of the white phase is calculated to be 2.9 micron^{-1}. From correlation with elastic data, this specific perimeter corresponds to an IF value of 0.65 for the fine-grained calcite. When taking large pores and grains (not visible at this magnification) and fine-grained silicates into account, we obtain an IF value of 0.6 for the sample. (c) Model: of the solid phase 65% is forming a frame with spherical pores. The remaining solids are suspended in the fluid within the pores.

12. References

Borre, M., Lind, I. L., and Mortensen, J. 1997: "Specific surface as a measure of Burial Diagenesis of Chalk." *Zbl. Geol. Paläont. Teil I* ***1995***, 1071-1078.

Fabricius, I.L., 2002, "Porosity Loss in Chalk Facies Sediments by Physical Compaction or by Cementation – Consequences for P-wave Modulus" *AAPG Annual Meeting, Houston, March 10-13, 2002, Extended Abstracts CD-ROM*, 6 pages.

Fabricius, I. L. and Høier, C. 2002: "Selection of samples, EFP- 2001 Rock Physics of Impure Chalk, E&R-1, E&R, DTU 2001, revised 17/1 2002.

Røgen, B. and Fabricius, I.L., 2002: "Influence of clay and silica on permeability and capillary entry pressure of chalk reservoirs in the North Sea" *Petroleum Geoscience* **8**, 287-293.

Table 7	Bulk volume fraction, model adjusted to dry P-wave modulus data											
	In frame				Suspended				Pores			Specific. perimeter of grains
	large calcite	large quartz	large kaolinite	small calcite	quartz	calcite	kaolinite	smectite	large holes	matrix holes	micropores	
Plug	(%)	(%)	(%)	(%)	(%)	(%)	(%)	(%)	(%)	(%)	(%)	(1/microns)
3	8.8	6.1	0.0	24.2	8.6	26.2	6.8	5.6	1.0	2.0	10.8	5.24
7	7.0	3.8	6.9	17.2	10.7	35.3	0.0	5.0	0.5	0.5	13.1	5.06
8	6.2	6.1	3.0	34.5	9.1	14.4	6.4	6.3	0.3	0.6	13.1	5.13
10	5.8	4.9	0.0	43.3	9.1	12.1	5.5	4.3	0.3	0.8	13.8	5.04
11	5.4	7.7	1.1	21.4	4.2	36.3	5.2	4.3	0.4	0.8	13.1	5.05
12	7.5	6.2	6.2	33.1	5.5	21.9	0.4	4.5	0.8	0.8	13.2	4.03
36	7.7	4.3	2.1	25.7	3.0	37.9	1.2	2.3	0.5	1.1	14.2	3.52
54	5.6	4.1	1.2	48.7	9.2	10.9	0.0	0.9	1.2	1.2	17.1	4.63
55	13.3	4.6	0.6	32.1	6.8	17.4	0.0	0.5	1.9	4.1	18.8	4.88
82	6.8	1.7	0.0	26.2	2.3	28.1	0.4	0.2	5.5	7.3	21.7	4.51
102	2.6	6.3	2.0	50.6	6.5	17.0	0.0	0.4	1.9	1.6	11.1	2.03
122	2.1	0.8	0.0	41.4	2.8	23.3	1.2	0.3	3.3	4.4	20.3	2.86
130	3.0	5.5	1.1	36.0	4.1	26.0	0.0	0.4	1.9	6.8	15.3	2.33
146	2.1	3.3	0.0	32.1	2.7	24.6	0.5	0.2	2.0	4.6	28.0	3.28
170	4.8	0.0	0.0	35.8	5.5	22.2	0.4	0.4	4.4	10.8	15.8	3.73
196	30.7	4.4	1.8	24.9	11.1	7.1	0.0	1.2	3.8	3.7	11.4	2.26
213	53.9	6.1	2.2	7.5	0.0	8.6	0.0	1.3	9.2	5.8	5.4	2.44
15	5.5	0.0	0.0	17.8	9.5	23.2	2.3	0.2	8.9	13.5	19.2	6.21
22	7.2	6.4	3.2	33.8	5.2	18.2	0.0	0.4	3.2	5.6	16.8	3.77
37	4.0	0.0	0.1	24.1	9.0	22.9	1.0	0.2	7.1	15.3	16.3	5.48
62	2.6	0.3	0.3	24.5	3.8	27.8	0.8	0.1	3.5	5.4	30.8	5.16
74	4.0	0.1	0.1	20.8	4.2	26.0	0.7	0.1	7.4	7.6	28.8	6.63
93	16.2	0.4	0.4	28.1	26.2	2.4	1.1	0.3	3.3	5.0	16.4	3.52
100	19.7	2.5	0.3	40.4	12.1	4.6	0.0	0.1	4.3	3.3	12.8	4.53

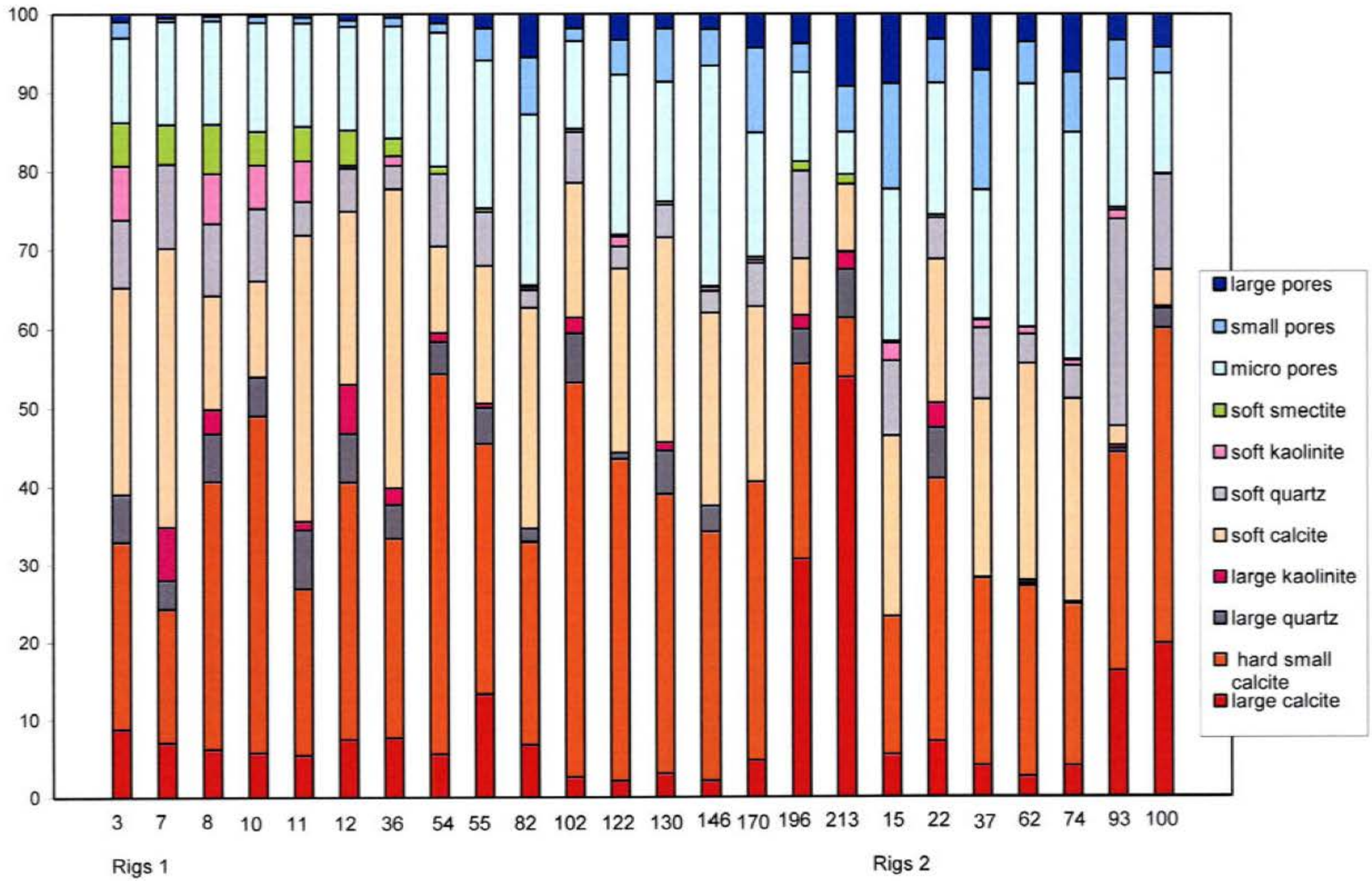

Figure 14. Resulting model for composition of bulk sample.

13. Backscatter Electron Micrographs

This section contains selected backscatter micrographs for each sample. The images to the left measure 333 by 333 microns. The images to the right represent the central 33 by 33 microns of the left images.

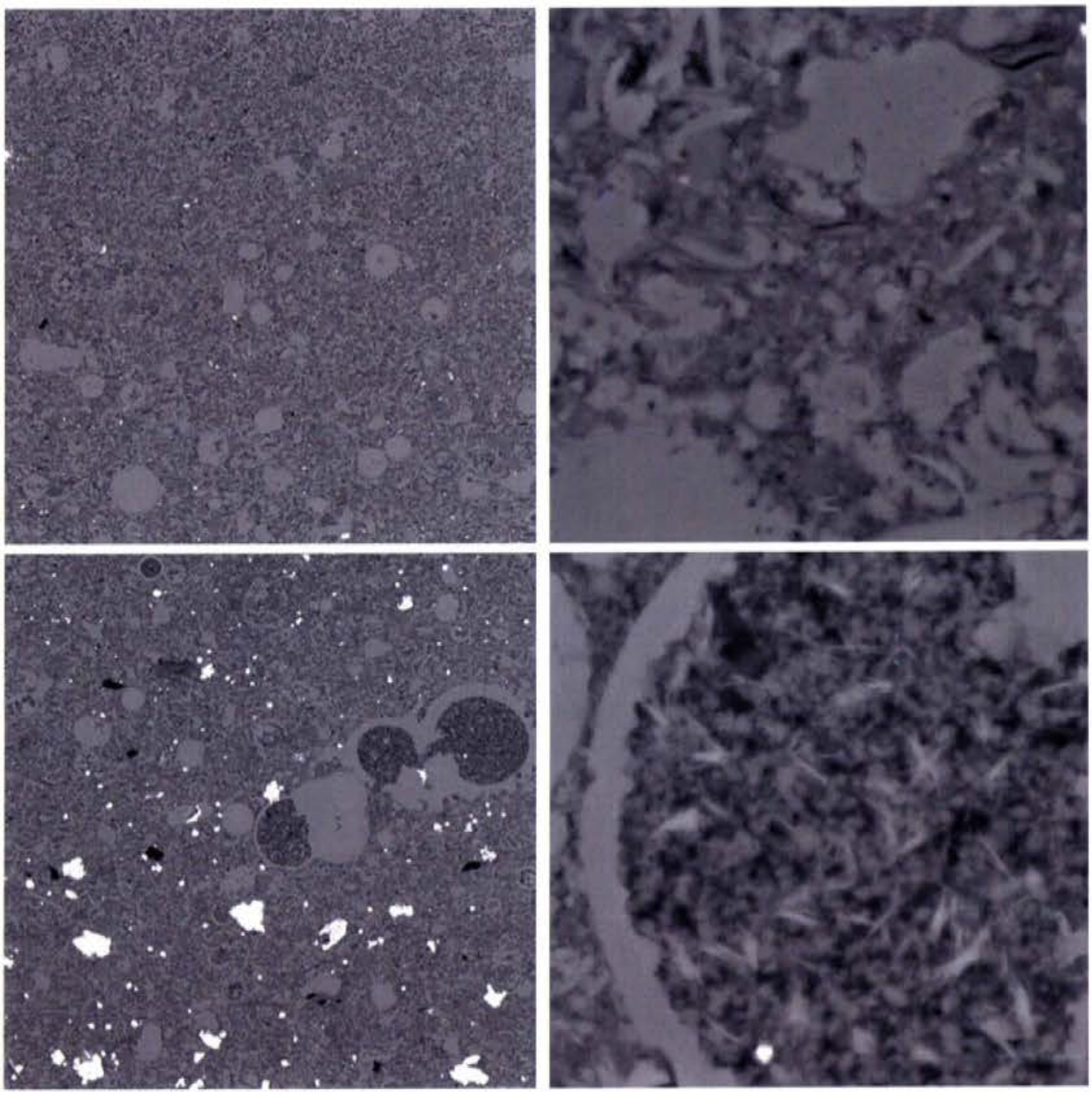

Rigs-1 plug sample 3.

Sample:
Grey, bioturbated mudstone, carbonate microfossils, open and cemented tests, silicic microfossils, pyrite.

BSE:
Intergranular and intrafossil porosity. The space between calcite grains are packed with Fe-bearing clay. Apparently authigenic clay is found in hollow microfossils.
White areas represent pyrite. Black areas in the small magnification images probably represent areas where grains have been plucked out during sample preparation.

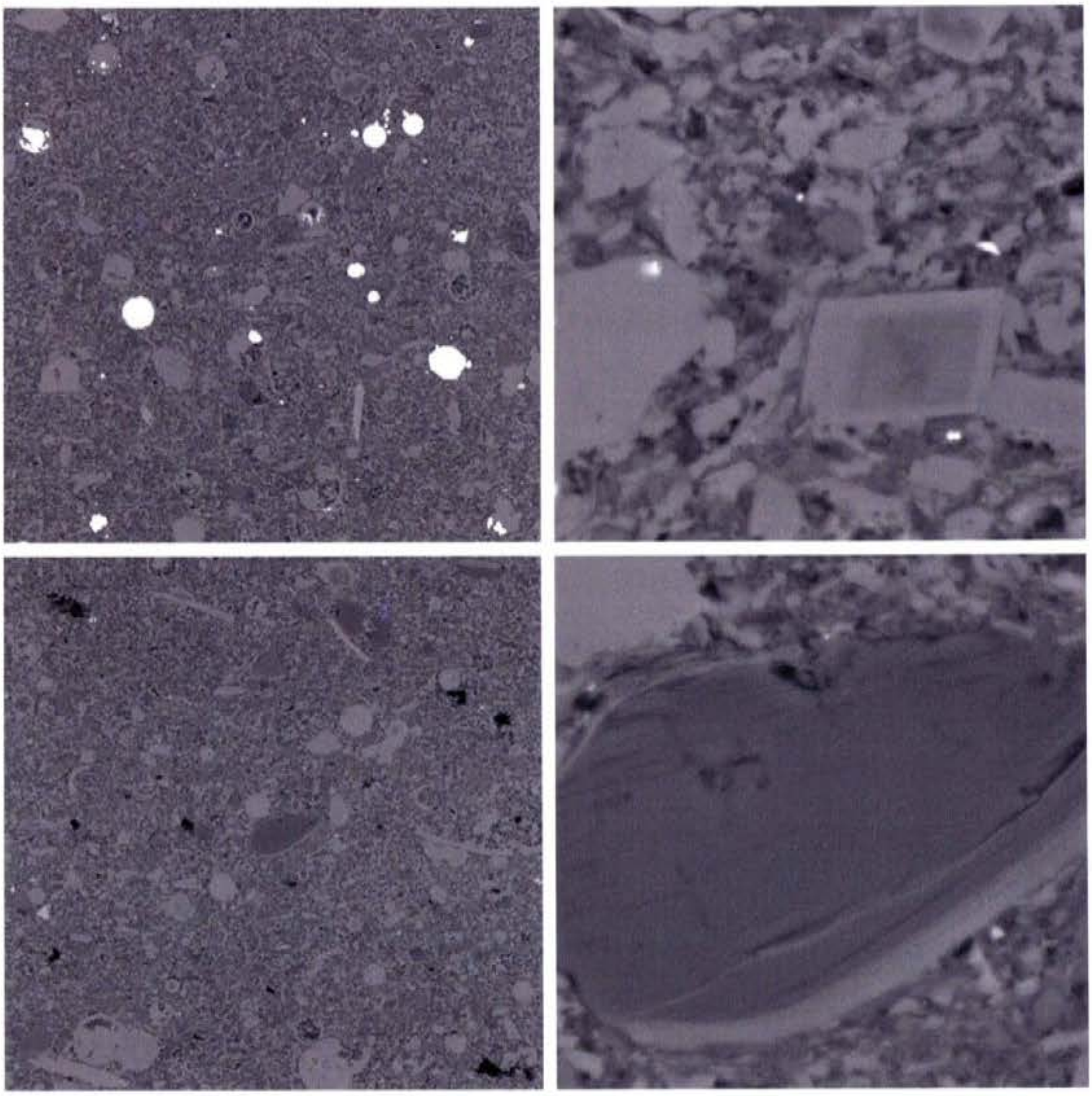

Rigs-1 plug sample 7.

Sample:
Grey, bioturbated mudstone, carbonate microfossils with open and cemented tests, silicic microfossils, pyrite.

BSE:
Intergranular and intrafossil porosity.
The space between calcite grains are packed with Fe-bearing clay.
Clasts of quartz (center of upper right image) and kaolinite (lower right image), as well of feldspar and siderite. Zoned ankerite crystals with varying concentrations of Fe (upper right image).

White areas represent pyrite. Black areas in the small magnification images probably represent areas where grains have been plucked out during sample preparation.

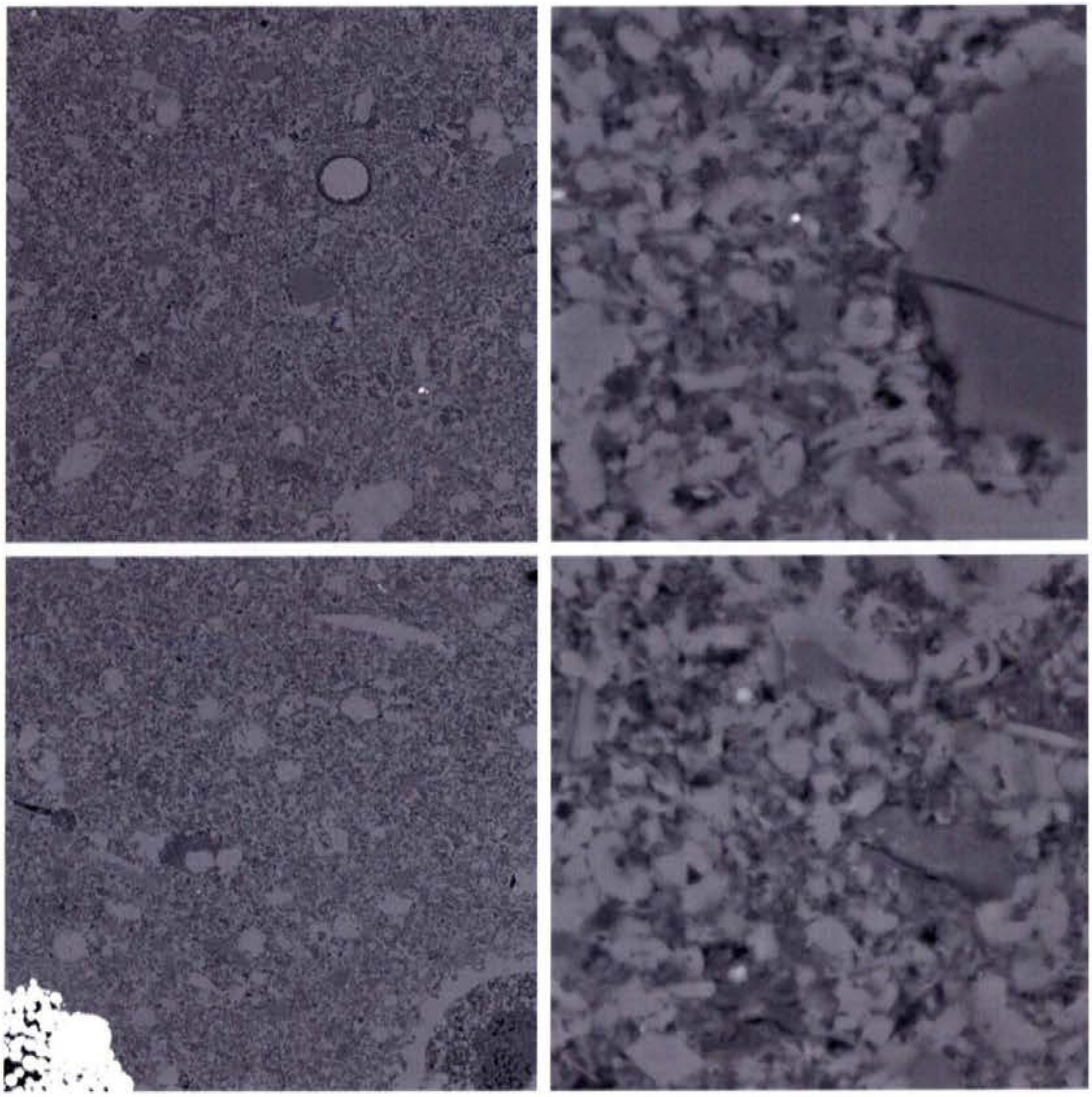

Rigs-1 plug sample 8.

Sample:
Grey, bioturbated, mudstone, carbonate microfossils with open and cemented tests, silicic microfossils, pyrite.

BSE:
Intergranular and intrafossil porosity.
The space between calcite grains are packed with Fe-bearing clay.
Clasts of quartz (right part of upper right image) and feldspar. Apparently authigenic clay is found in hollow microfossils.

White area represents framboidal pyrite.

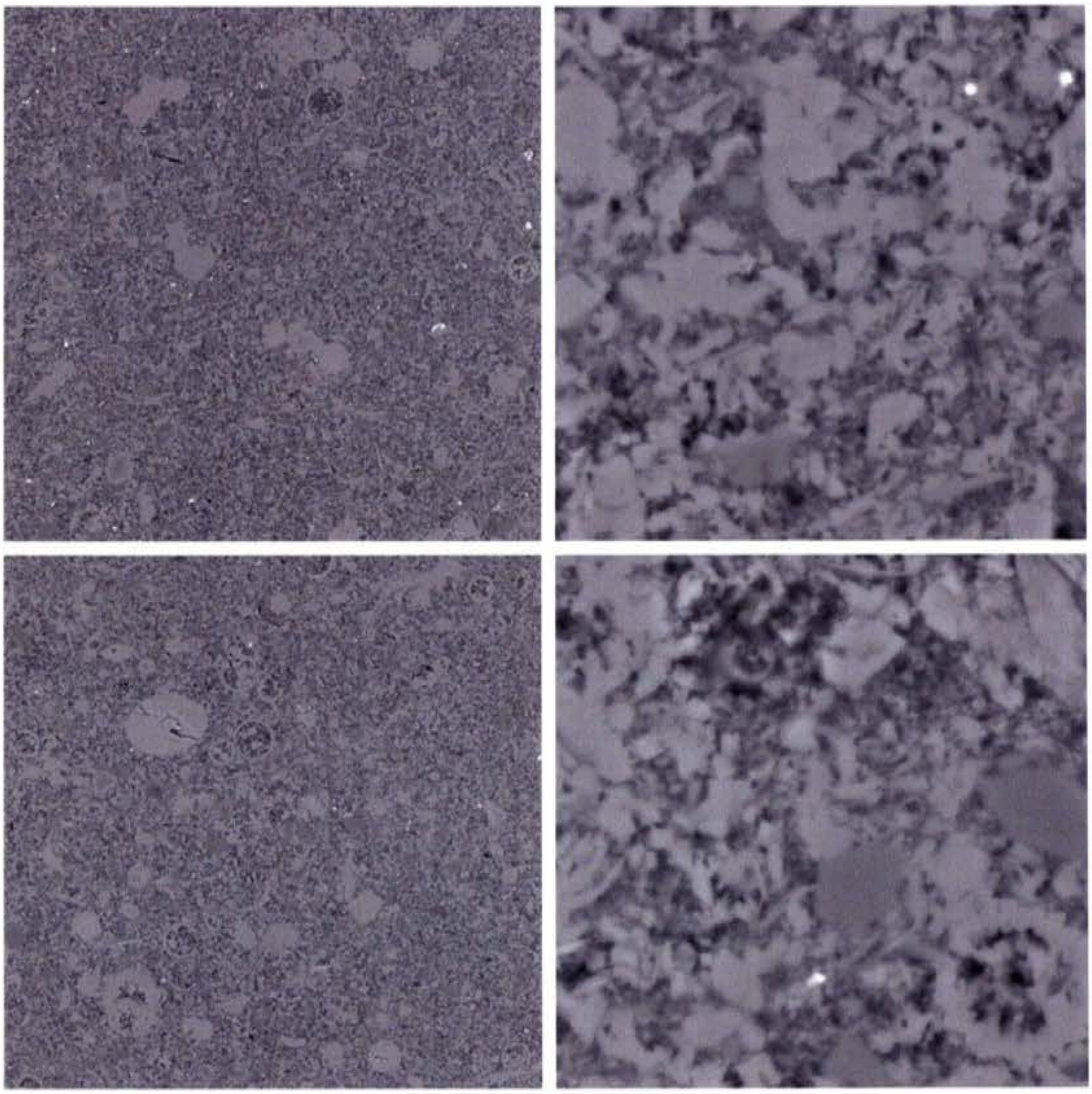

Rigs-1 plug sample 10.

Sample:
Grey, bioturbated, mudstone, carbonate microfossils with open and cemented tests, silicic microfossils, pyrite

BSE:
Intergranular and intrafossil porosity.
The space between calcite grains contains clay. Clasts of quartz and feldspar, single zoned ankerite crystals.

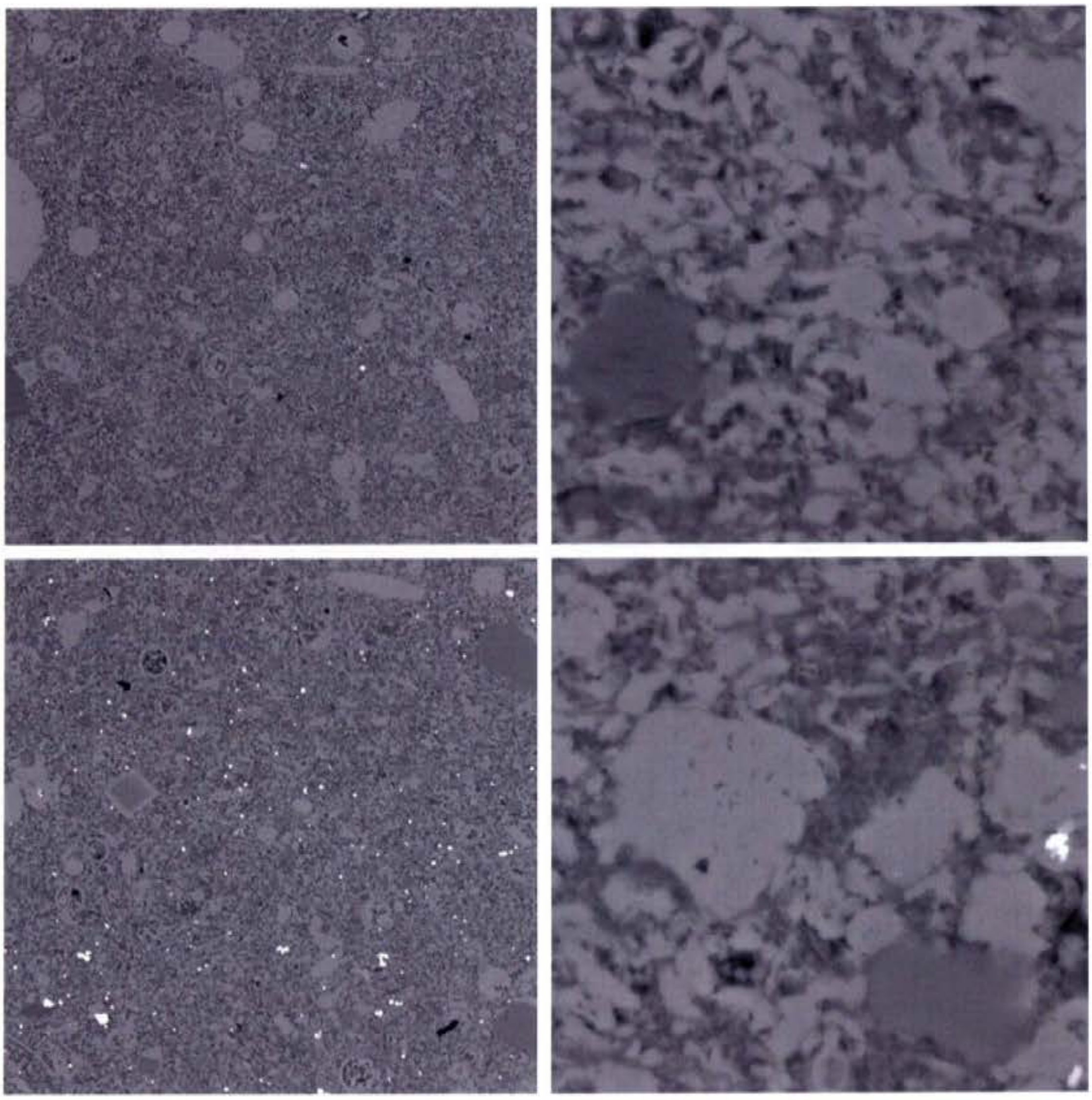

Rigs-1 plug sample 11.

Sample:
Grey, bioturbated, mudstone, carbonate microfossils with cemented tests, single open tests, silicic microfossils, pyrite,

BSE:
Intergranular porosity.
The space between calcite grains contains clay. Clasts of kaolinite and feldspar, single zoned ankerite crystals. White spots are pyrite crystals.

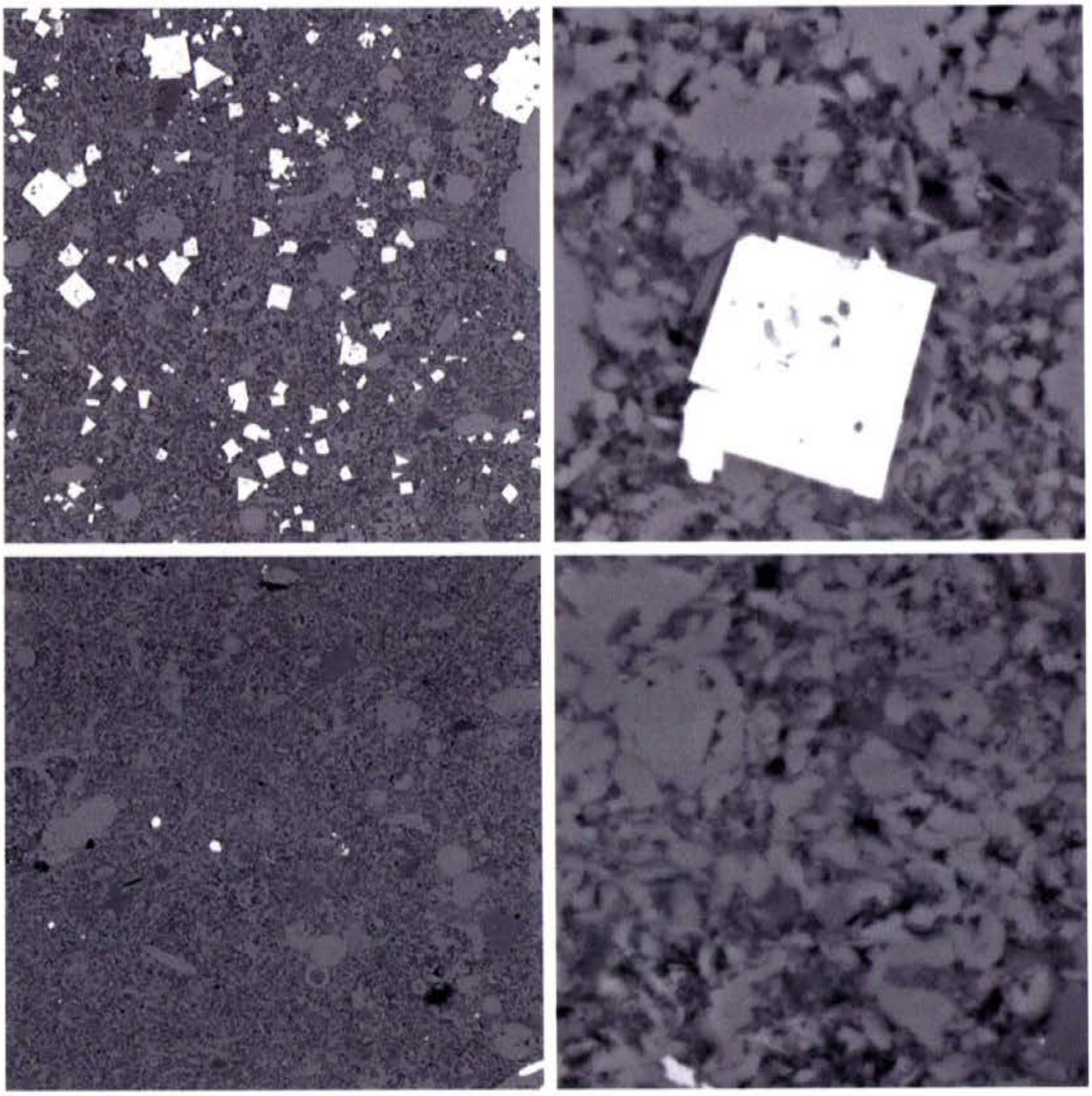

Rigs-1 plug sample 12.

Sample:
Grey, bioturbated, mudstone, carbonate microfossils with cemented tests, single open tests, silicic microfossils, pyrite.

BSE:
Intergranular porosity.
The space between calcite grains contains clay. Clasts of kaolinite, quartz and feldspar. White areas are pyrite crystals.

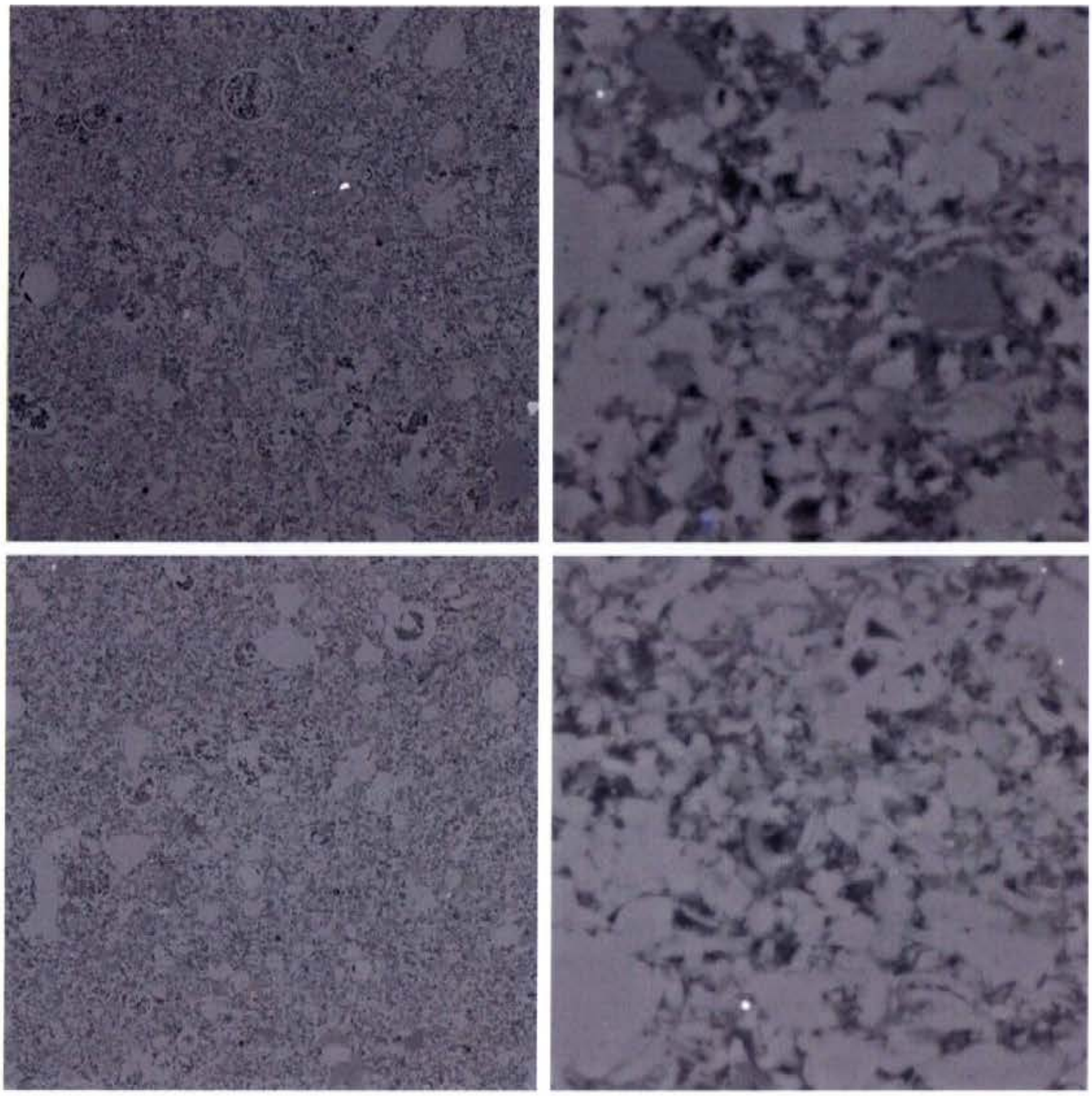

Rigs-1 plug sample 36.

Sample:
Light grey, bioturbated mudstone, carbonate microfossils with cemented tests, single open tests, silicic microfossils, pyrite.

BSE:
Intergranular and intrafossil porosity.
Clasts of kaolinite, quartz and feldspar, zoned ankerite crystal.

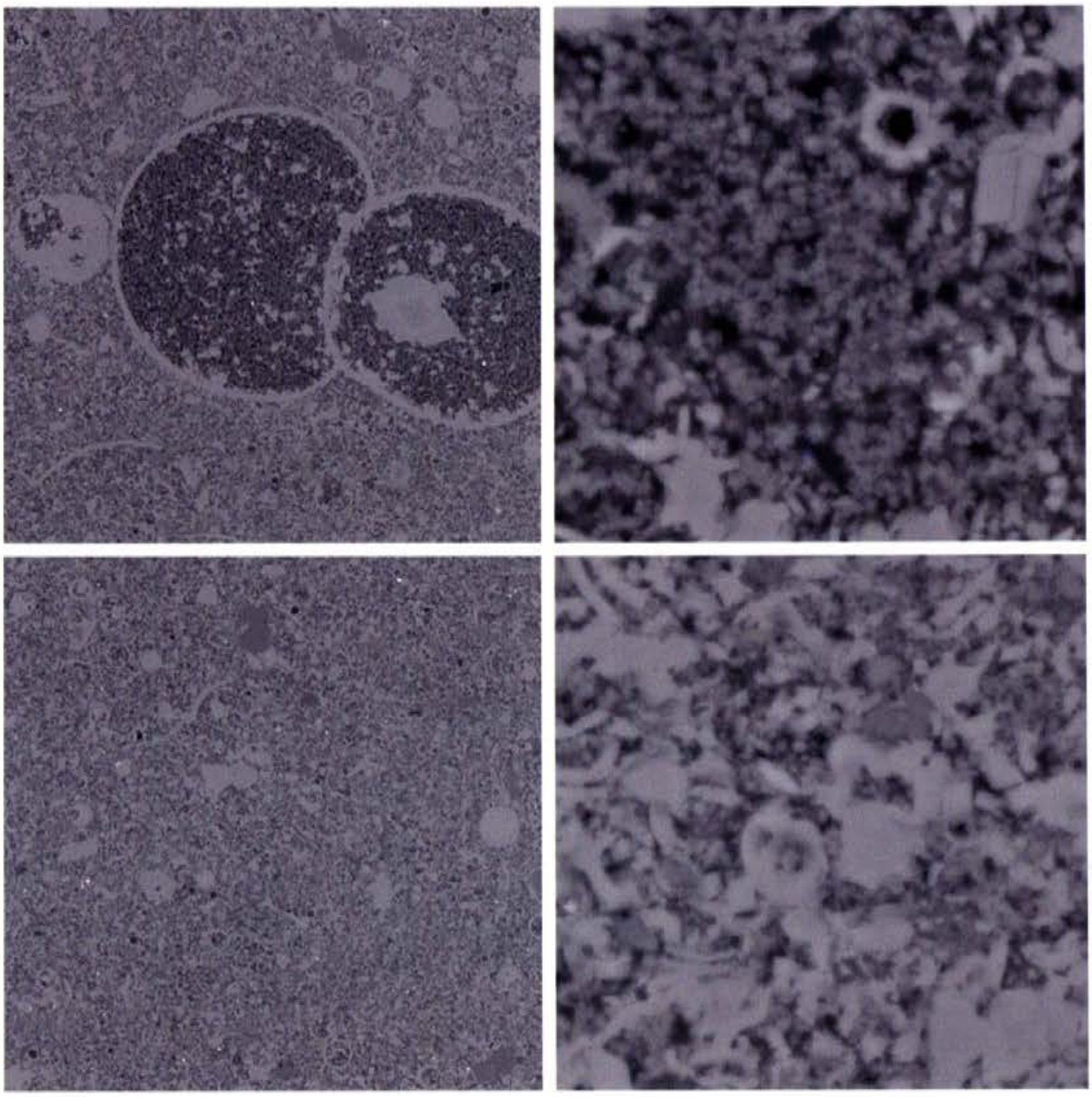

Rigs-1 plug sample 54.

Sample:
Light grey, mudstone, carbonate microfossils with cemented tests, single open tests, stylolite, pyrite.

BSE:
Intergranular and intrafossil porosity.
Clasts of quartz, kaolinite and feldspar. Sub-micronsize quartz in hollow microfossil, large zoned ankerite crystal.

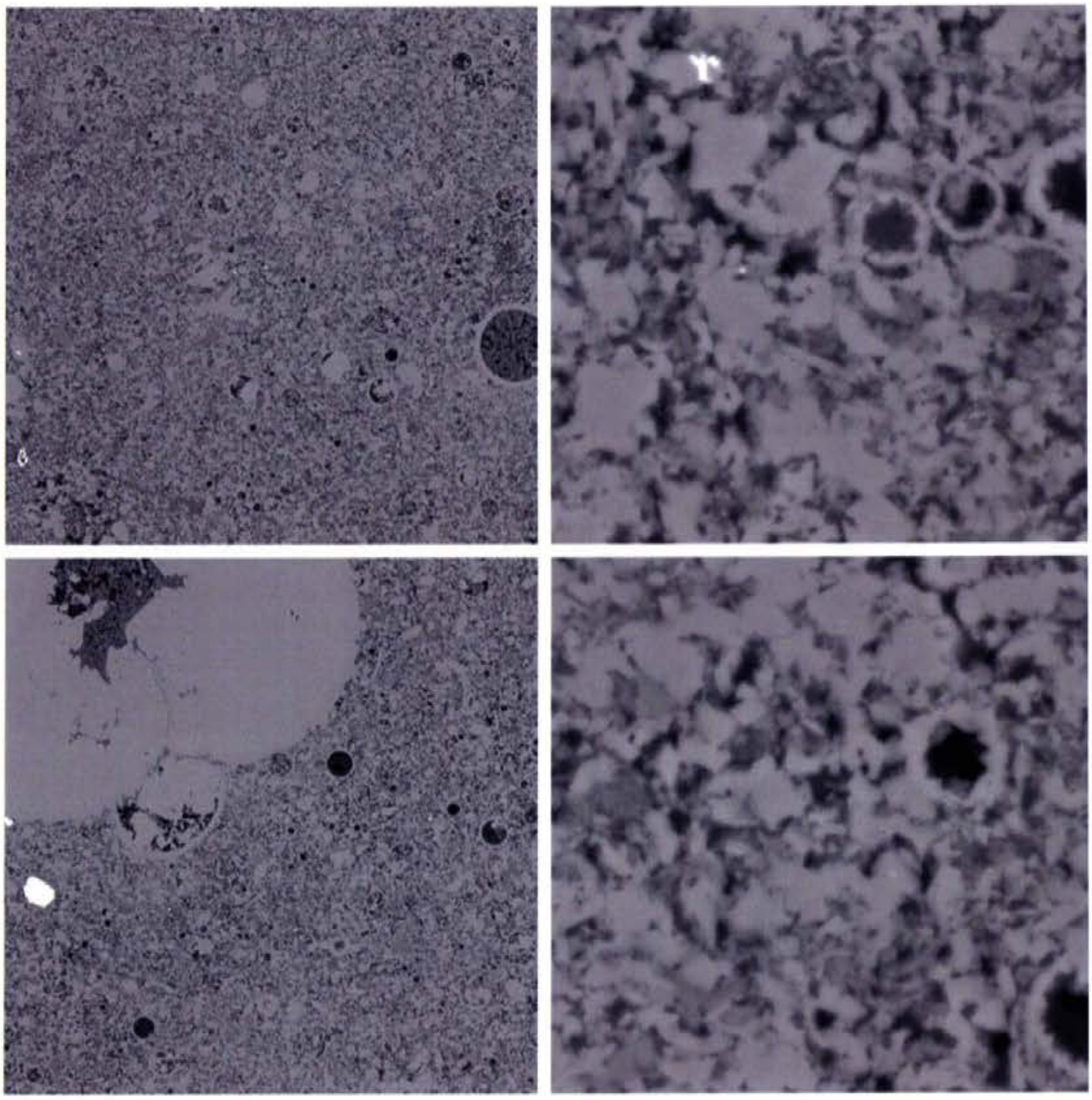

Rigs-1 plug sample 55.

Sample:
White, mudstone, carbonate microfossils with cemented and open tests, floating clay, silicic microfossils.

BSE:
Intergranular and intrafossil porosity.
Submicron size quartz and clay in pore space.

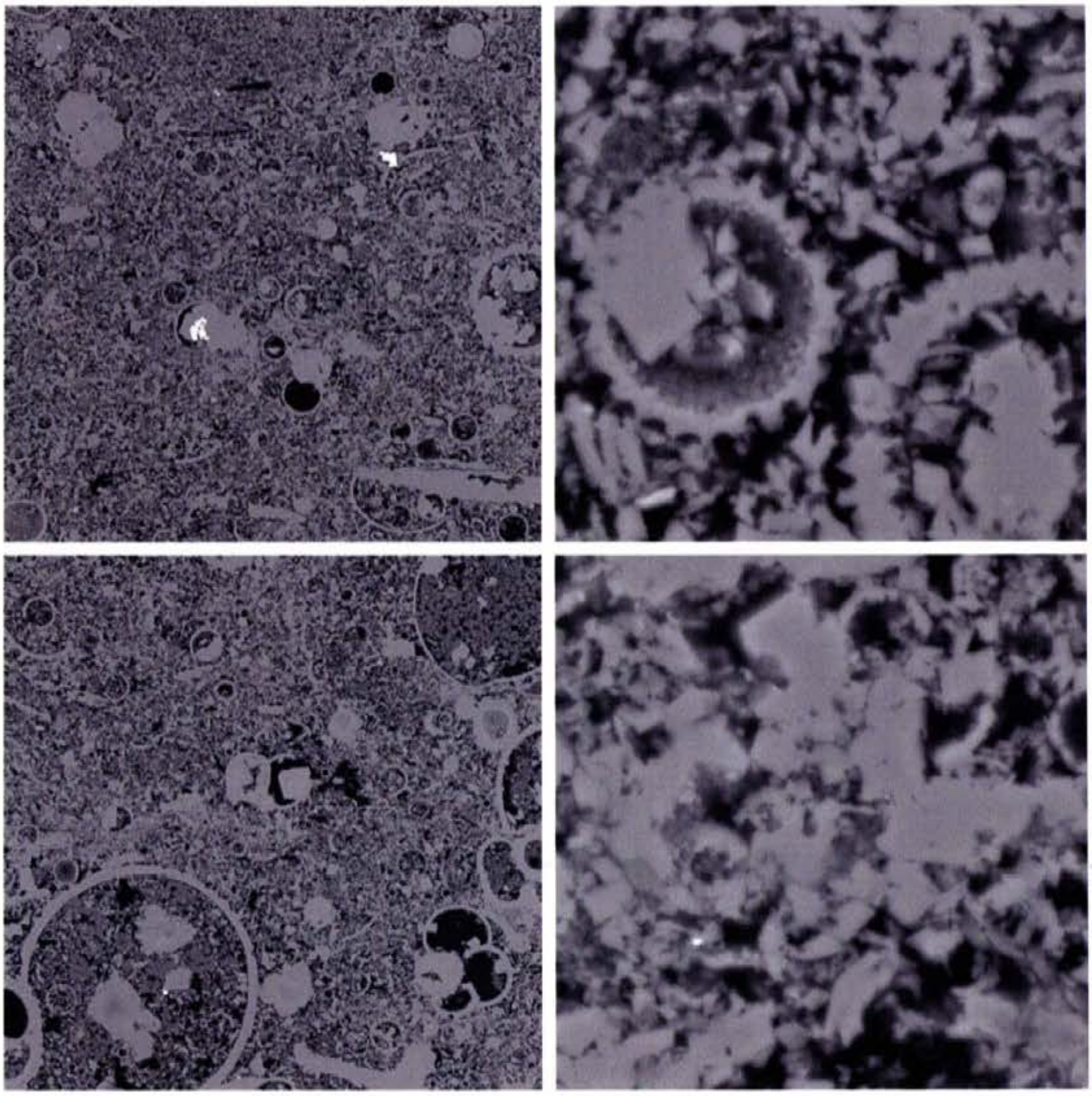

Rigs-1 plug sample 82.

Sample:
White, mudstone, carbonate microfossils, cemented and open tests, floating clay, silicic microfossils.

BSE:
Intergranular, intrafossil and moldic porosity.
In pore-sapce: zoned ankerite, submicron size quartz seemingly partly replaced by larger quartz crystals, apparently authigenic kaolinite.

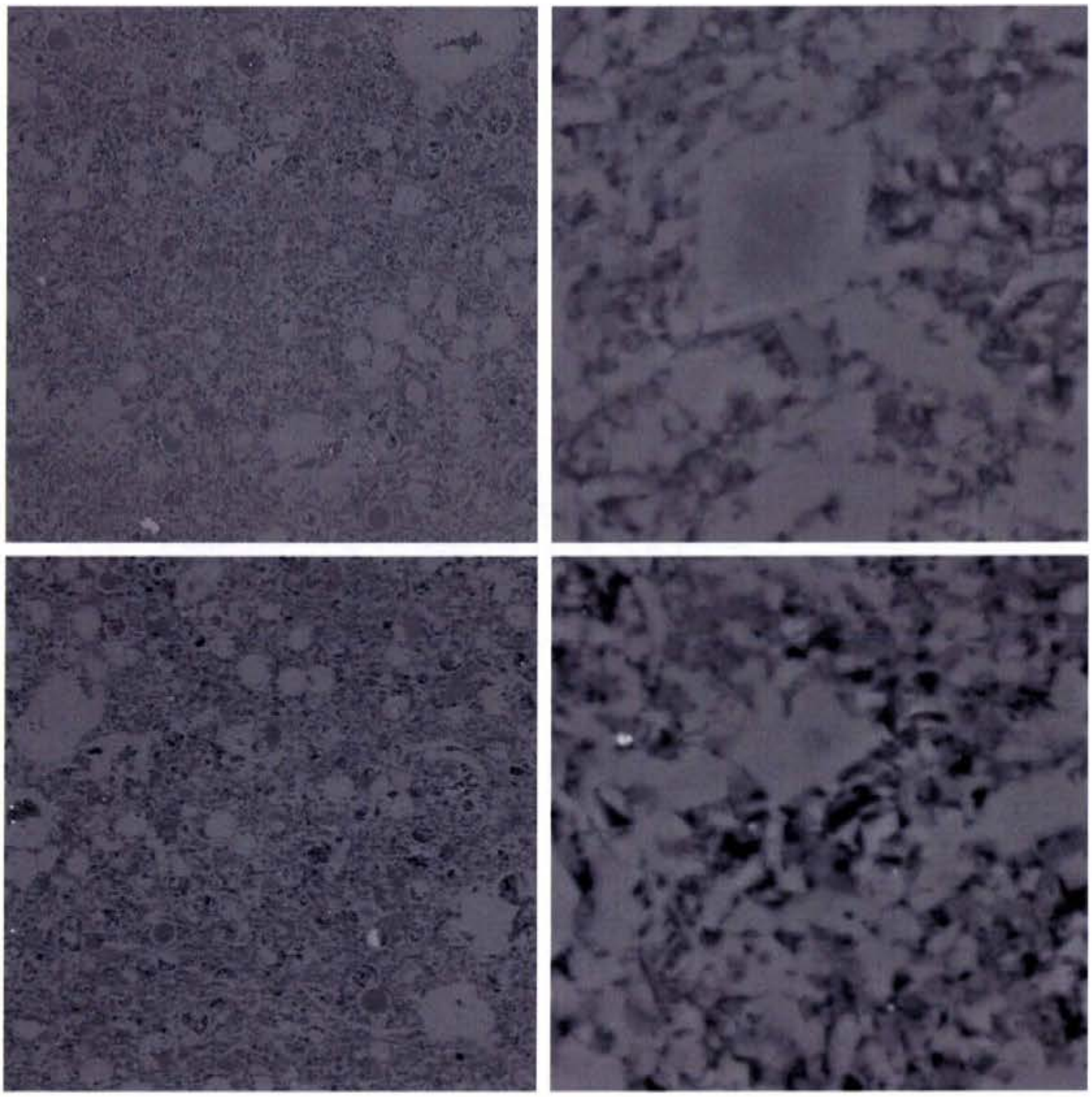

Rigs-1 plug sample 102.

Sample:
White, wackestone, carbonate microfossils w. cemented tests, single open, silicic microfossils.

BSE:
Intergranular and intrafossil porosity
Zoned ankerite crystal, porefilling kaolinite in microfossils. Submicronsize quartz in matrix pores.

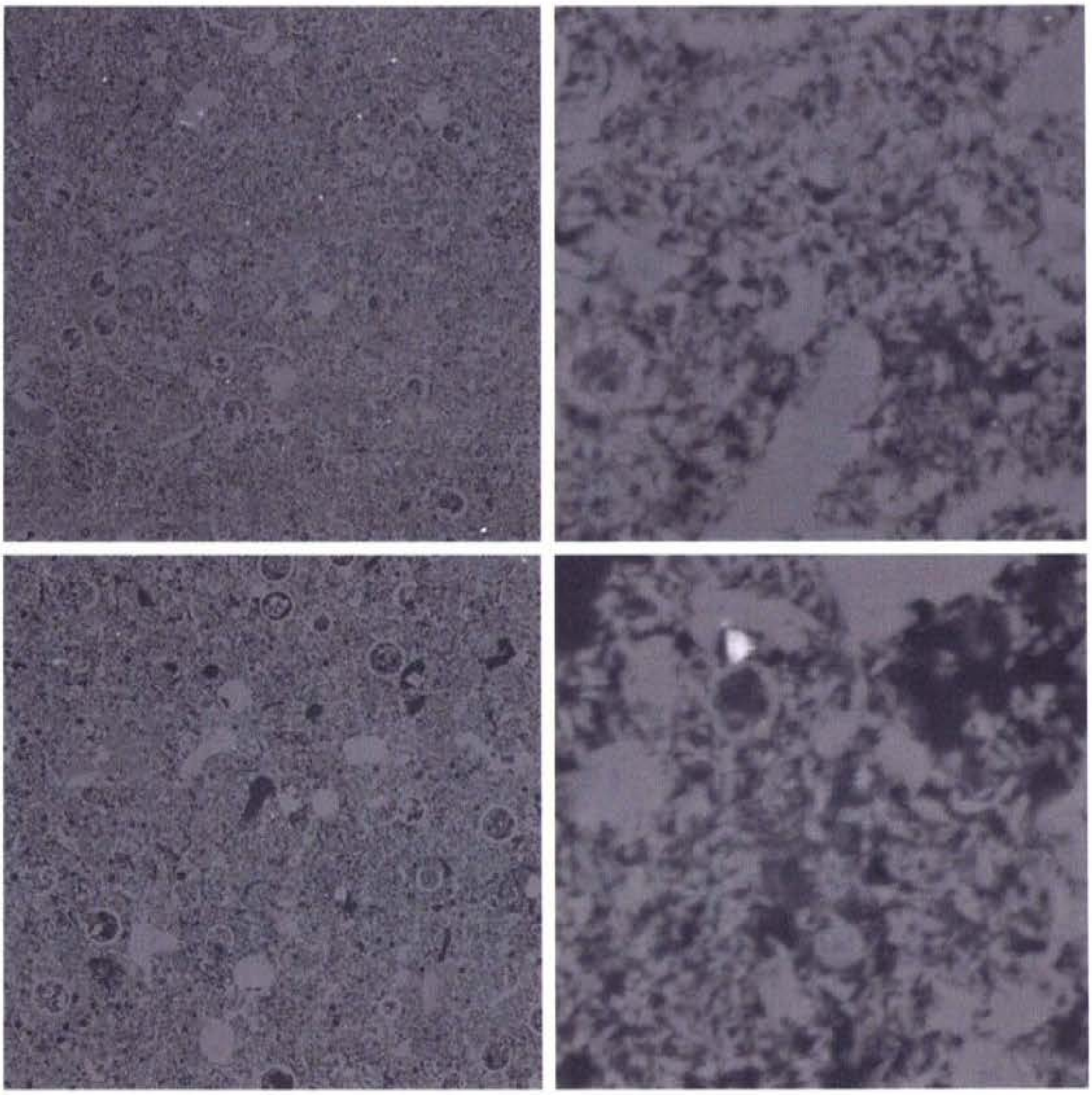

Rigs-1 plug sample 122.

Sample:

White, mudstone, carbonate microfossils with cemented and open tests, silicic microfossils.

BSE;
Intergranular, intrafossil and moldic porosity.

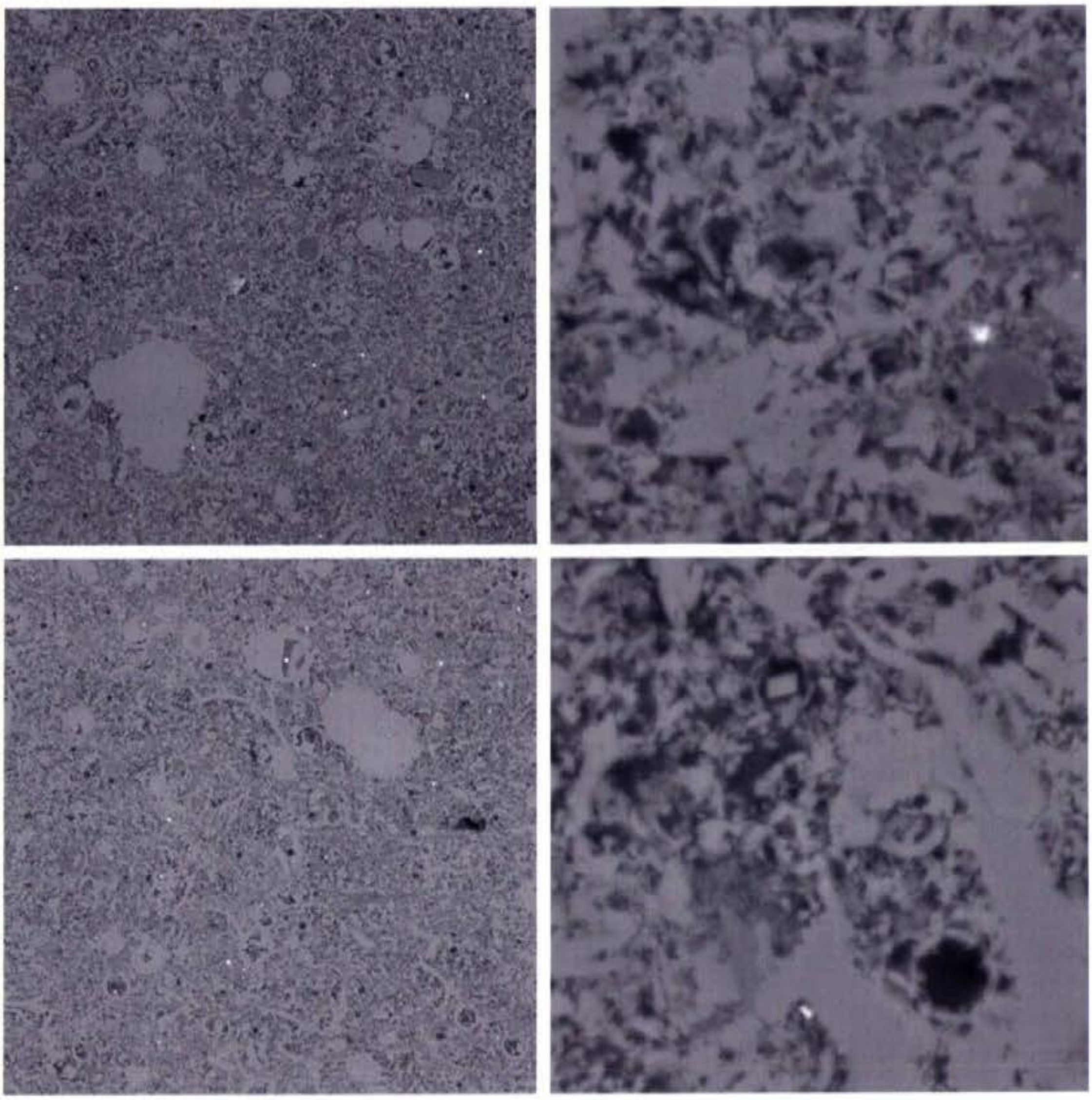

Rigs-1 plug sample 130.

Sample:
white, mudstone, bioturbated, carbonate microfossils with cemented tests, single open tests, silicic microfossils.

BSE
Intergranular and intrafossil porosity.
Clasts of kaolinite and quartz.

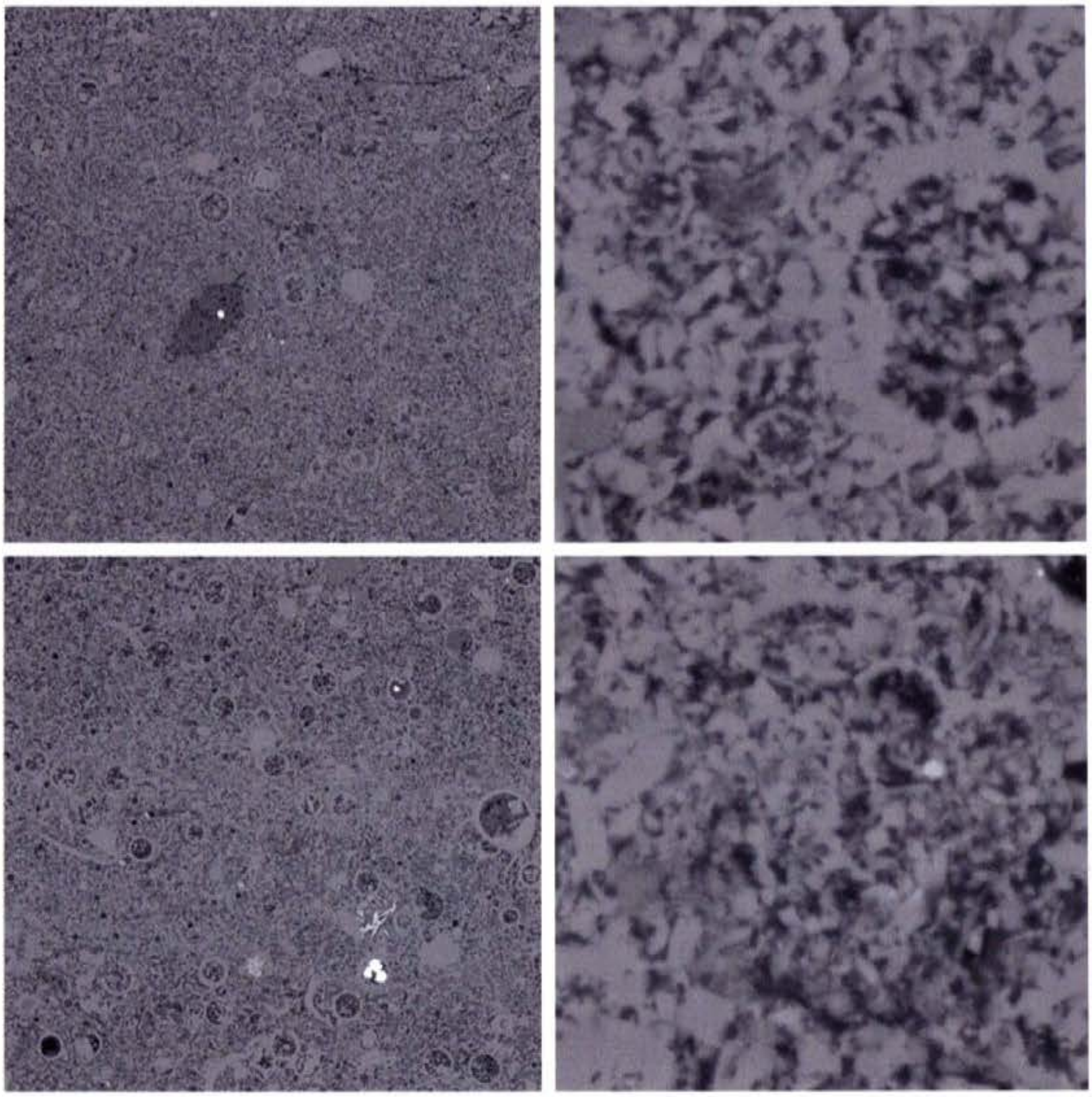

Rigs-1 plug sample 146.

Sample:
White, mudstone, carbonate microfossils with cemented and open tests, floating clay, stylolite, pyrite

BSE:
Intergranular and intrafossil porosity. Clasts of quartz, submicronsize quartz filling moldic pore.

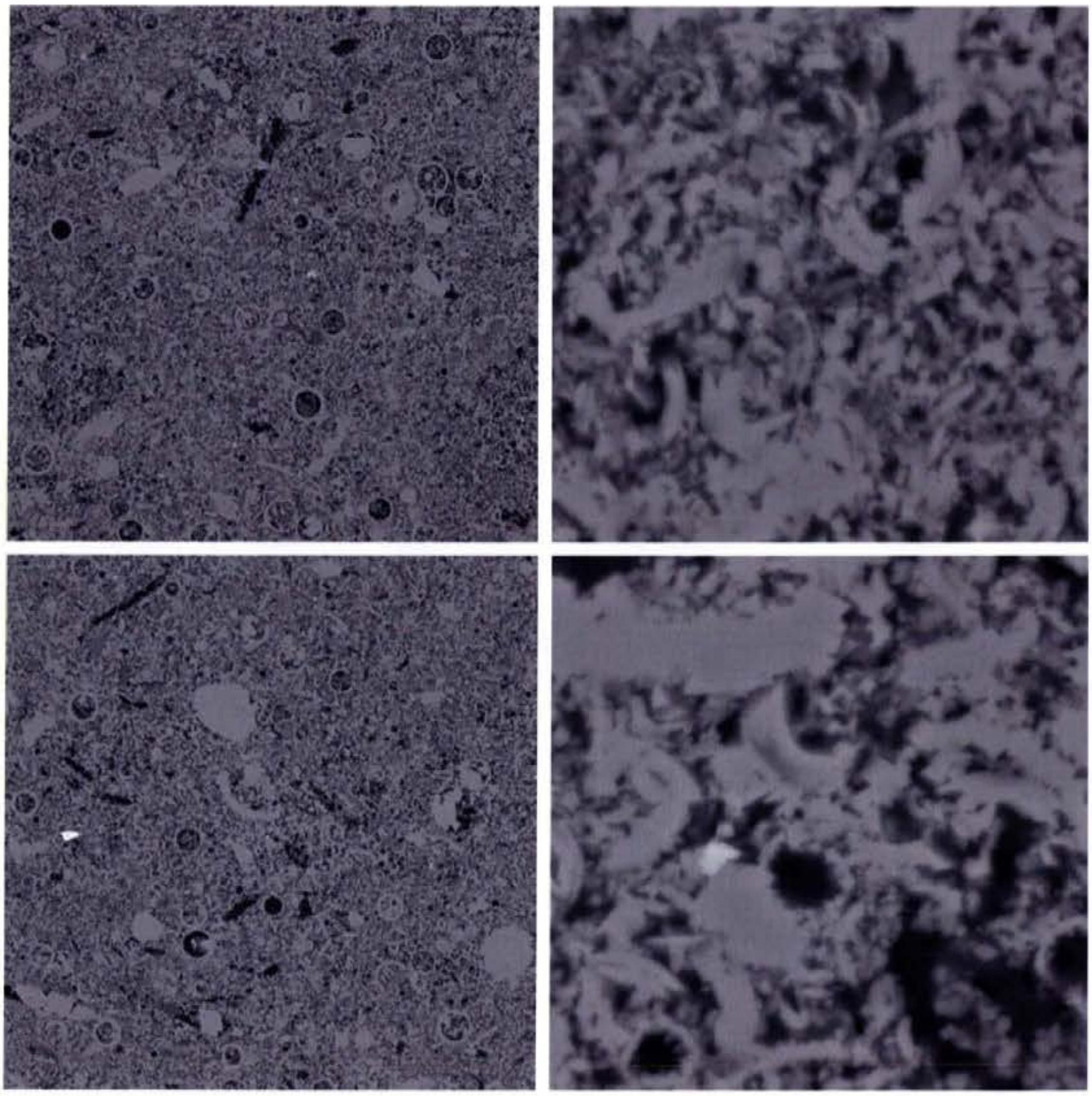

Rigs-1 plug sample 170.

Sample:
White, mudstone, carbonate microfossils with cemented tests, single open tests, silicic microfossils.

BSE;
Intergranular, intrafossil and moldic porosity.
Spotwise pore-filling clay.

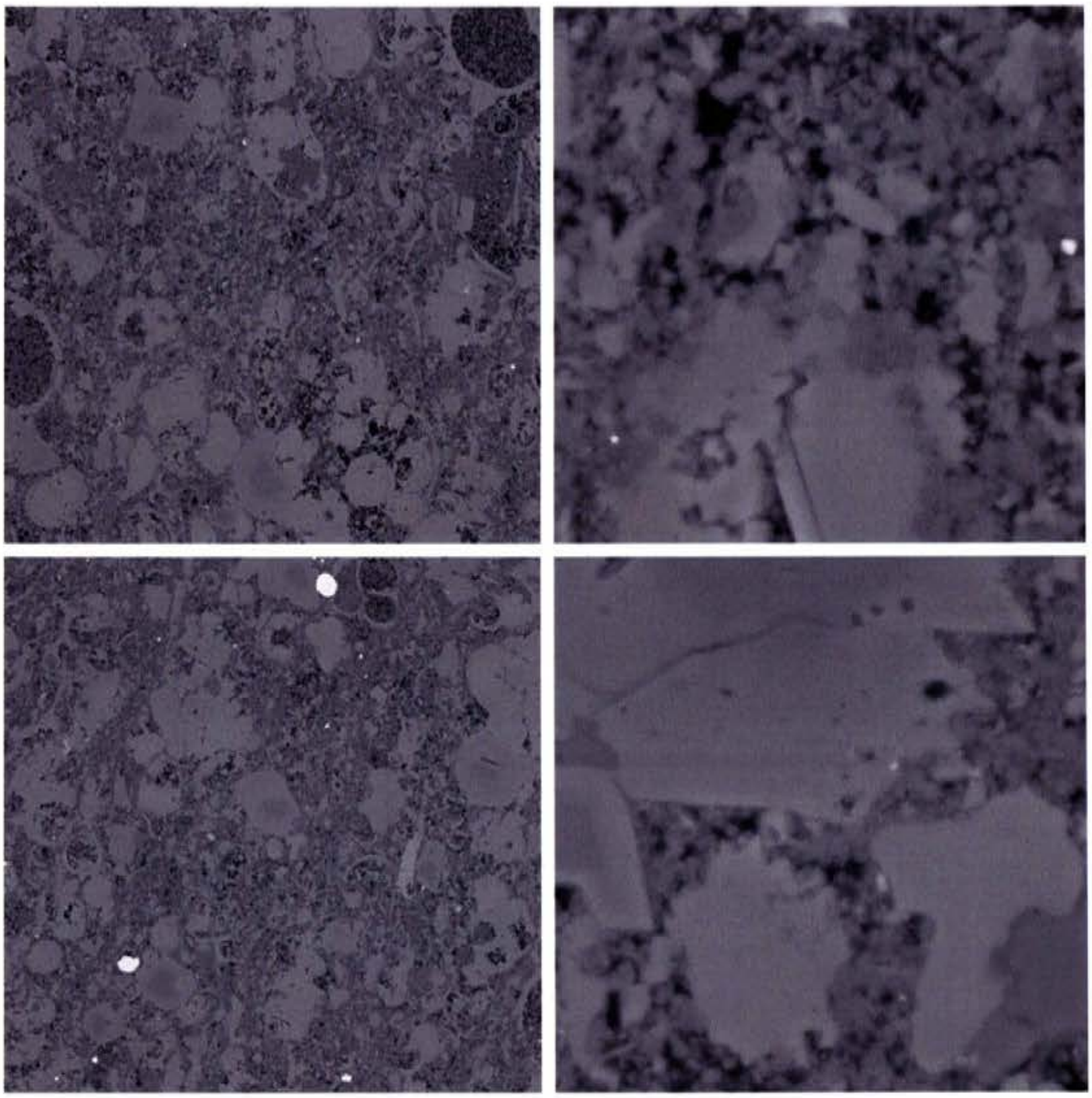

Rigs-1 plug sample 196.

Sample:
Light grey, bioturbated, packstone, carbonate microfossils with cemented tests, single open, pyrite.

BSE:
Intergranular and intrafossil porosity.
Porefilling kaolinite, partly as submicron size particles partly as larger crystals (upper left).
Porefilling quartz, partly as submicron size particles partly as larger crystals (lower left).
Zoned ankerite crystals (lower right).

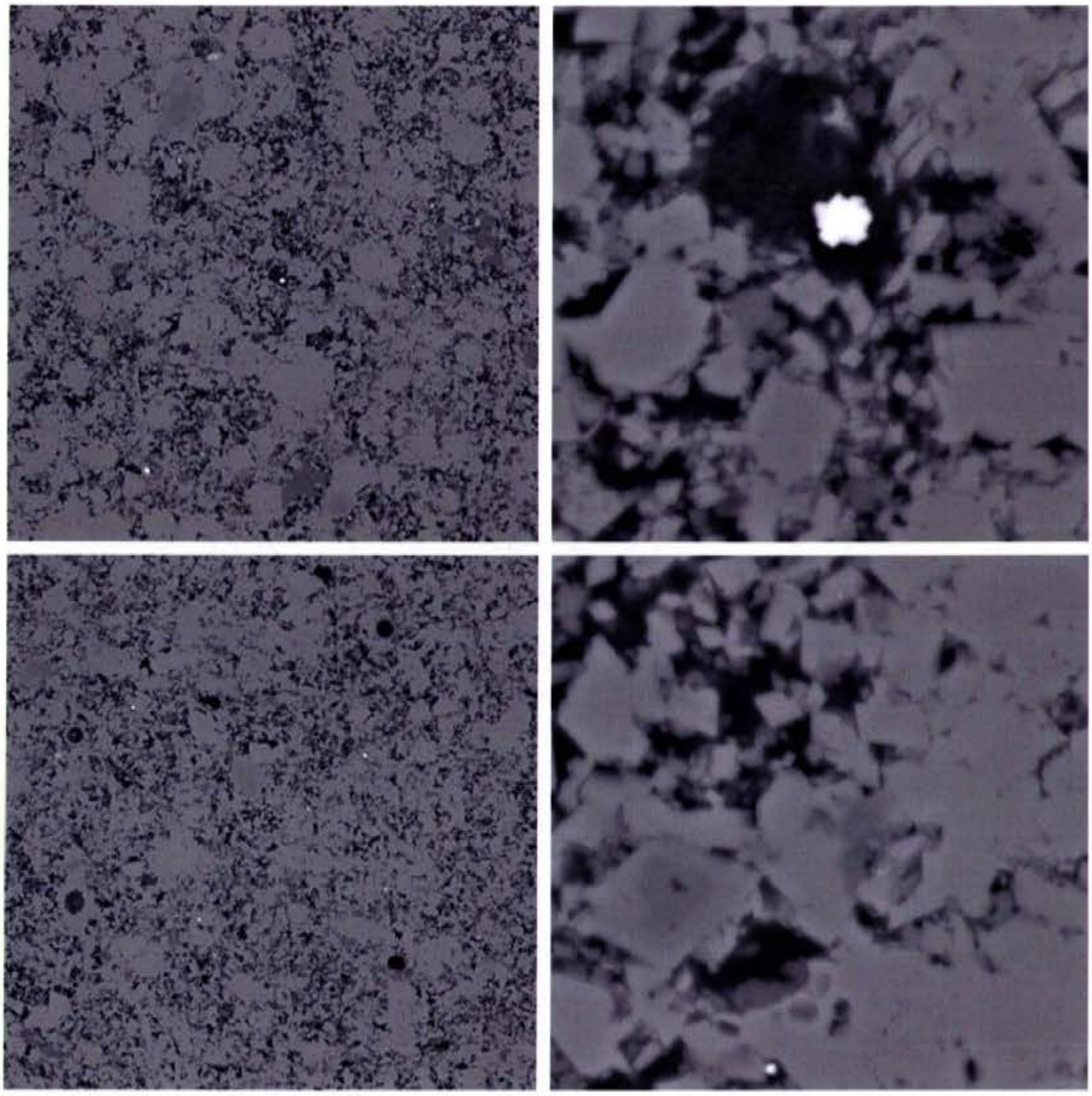

Rigs-1 plug sample 213.

Sample:
White, wackestone, carbonate microfossils with cemented tests, single open tests, silicic microfossils, low-porosity vertical fractures, partly flaser structure.

BSE:
Intergarnular (intercrystal) porosity.
Porefilling carbonate cement, zoned ankerite crystals. Kaolinite as submicronsize free particles and as larger crystals (clasts?). Micronsize quartz and single feldspars.

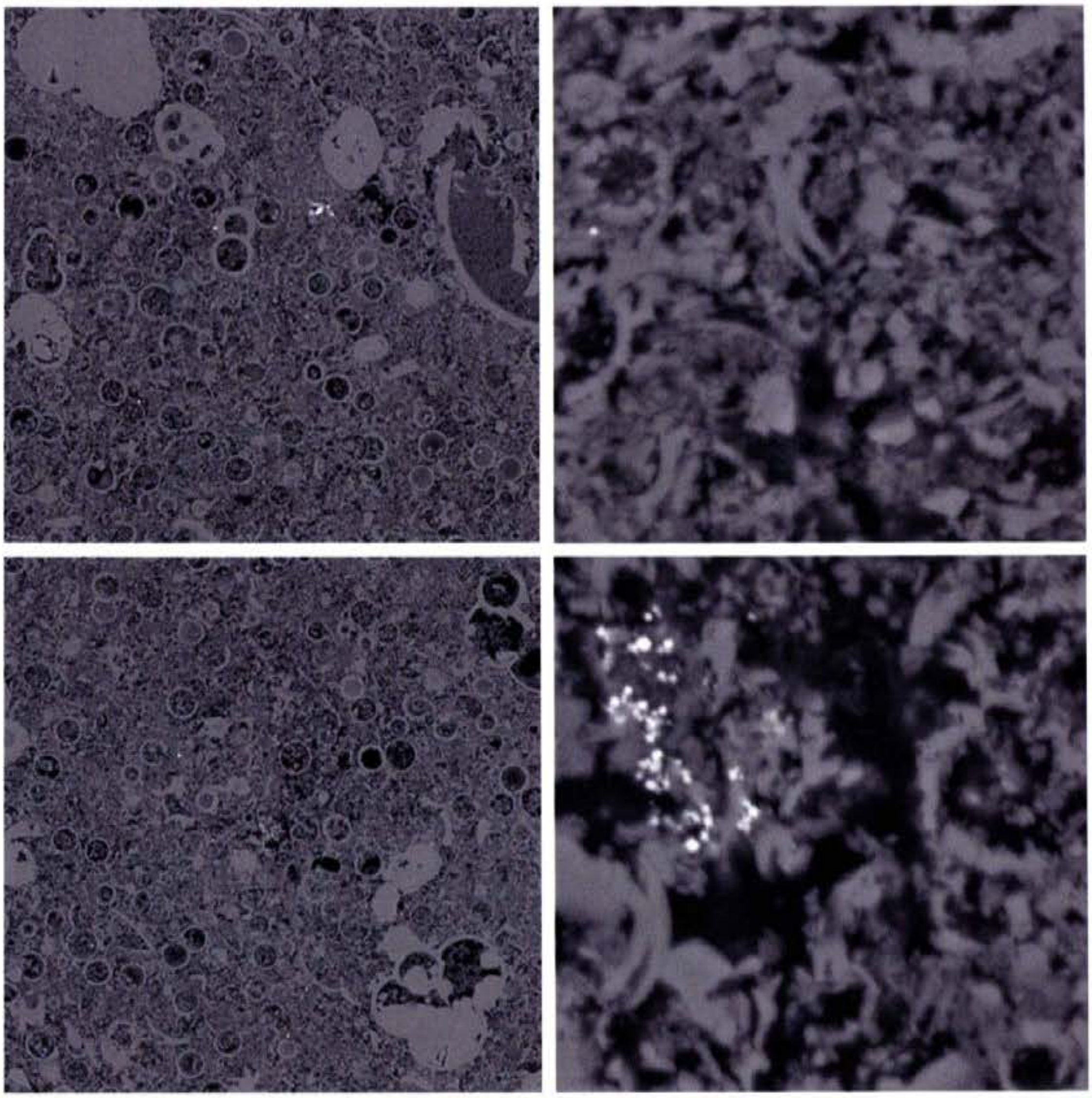

Rigs-2 plug sample 15.

Sample:
White, mudstone, carbonate microfossils with cemented and open tests, silicic microfossils.

BSE:
Intergranular and intrafossil porosity.
Submicron size quartz in pore space.

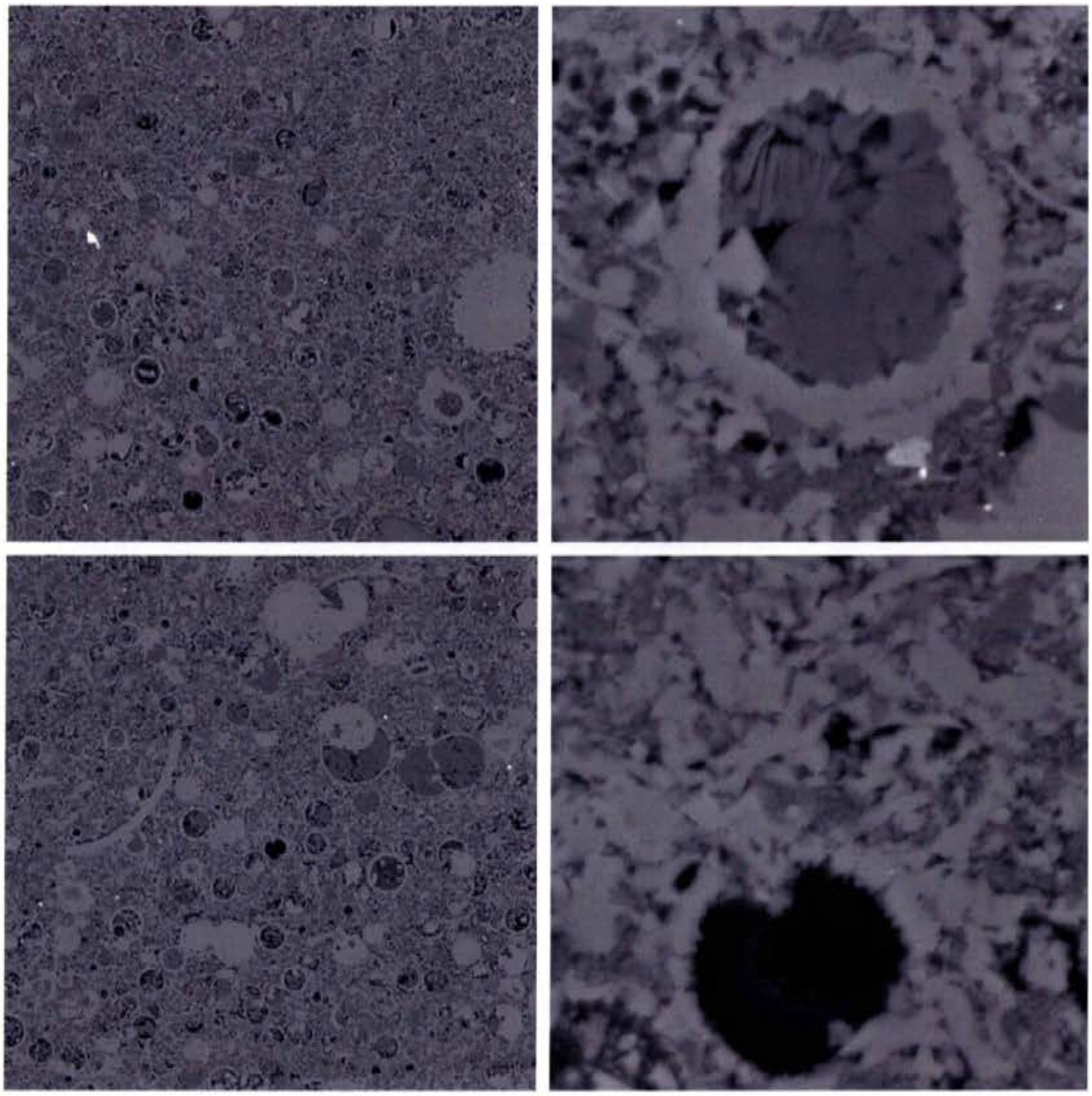

Rigs-2 plug sample 22.

Sample:
White, wackestone, carbonate microfossils with cemented and open tests. Stylolite.

BSE:
Intergranular and intrafossil porosity.
Kaolinite in pore space. Zoned ankerite.

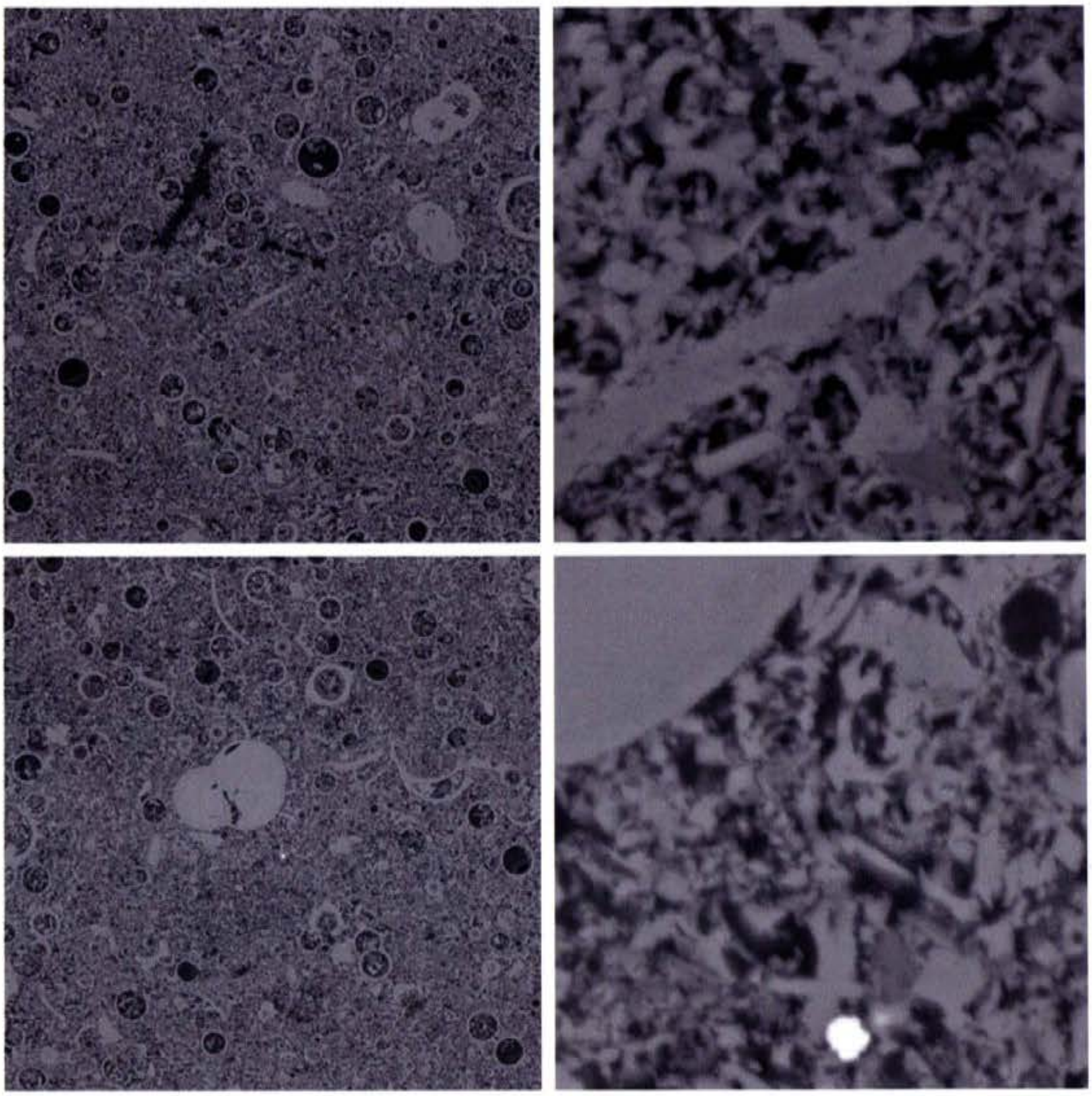

Rigs-2 plug sample 37.

Sample:
Off white (oil stained?), mudstone, calcareous microfossils, cemented and open tests.

BSE:
Intergranular, intrafossil and moldic porosity.
Submicron size quartz and kaolinite in porespace.

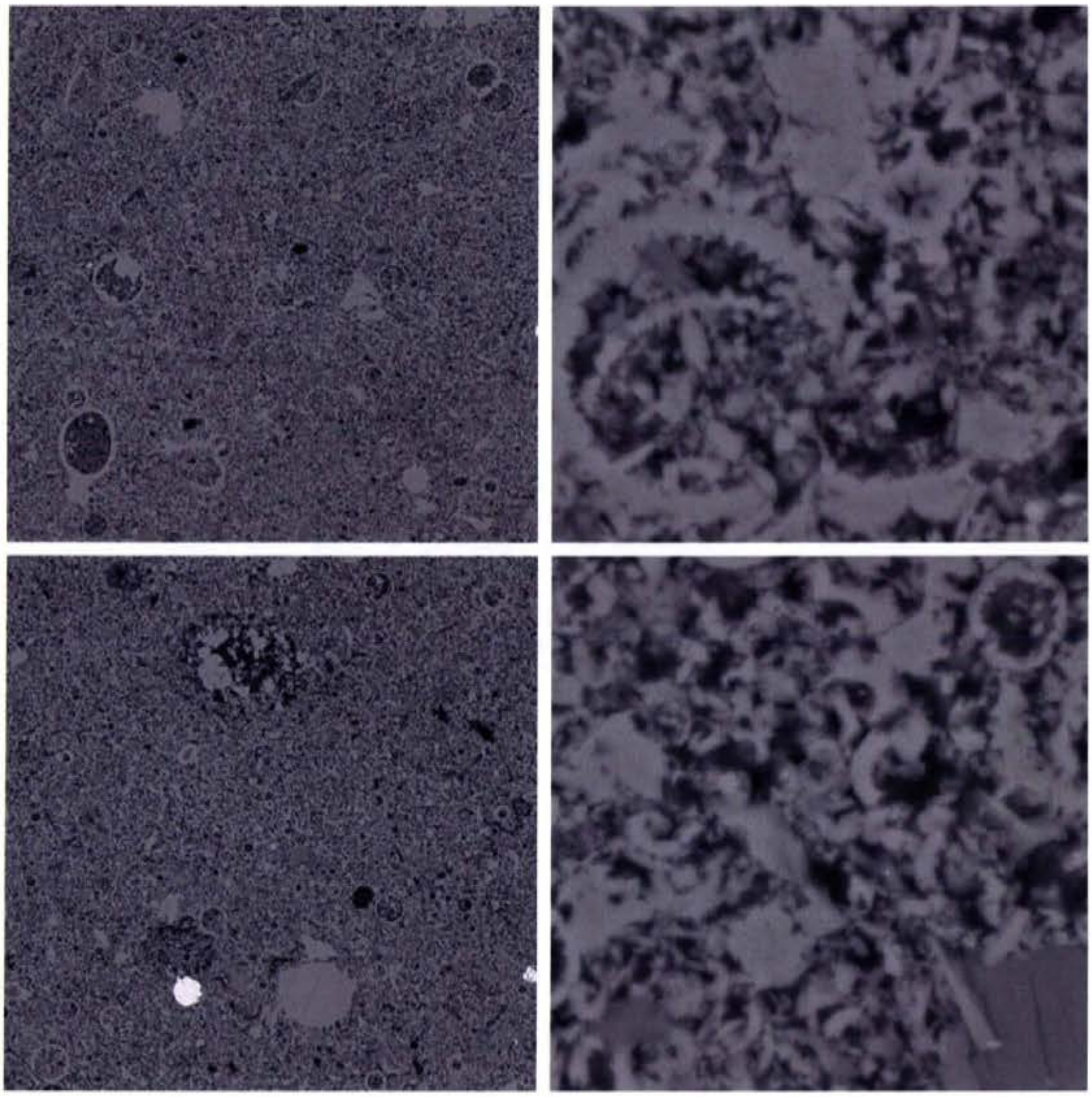

Rigs-2 plug sample 62.

Sample:
Oil stained, wackestone, calcareous microfossils with cemented and open tests, silicic? spines, stylolite.

BSE:
Intergranular, intrafossil and moldic porosity.
Submicronsize quartz in poreapace, micronsize kaolinite.

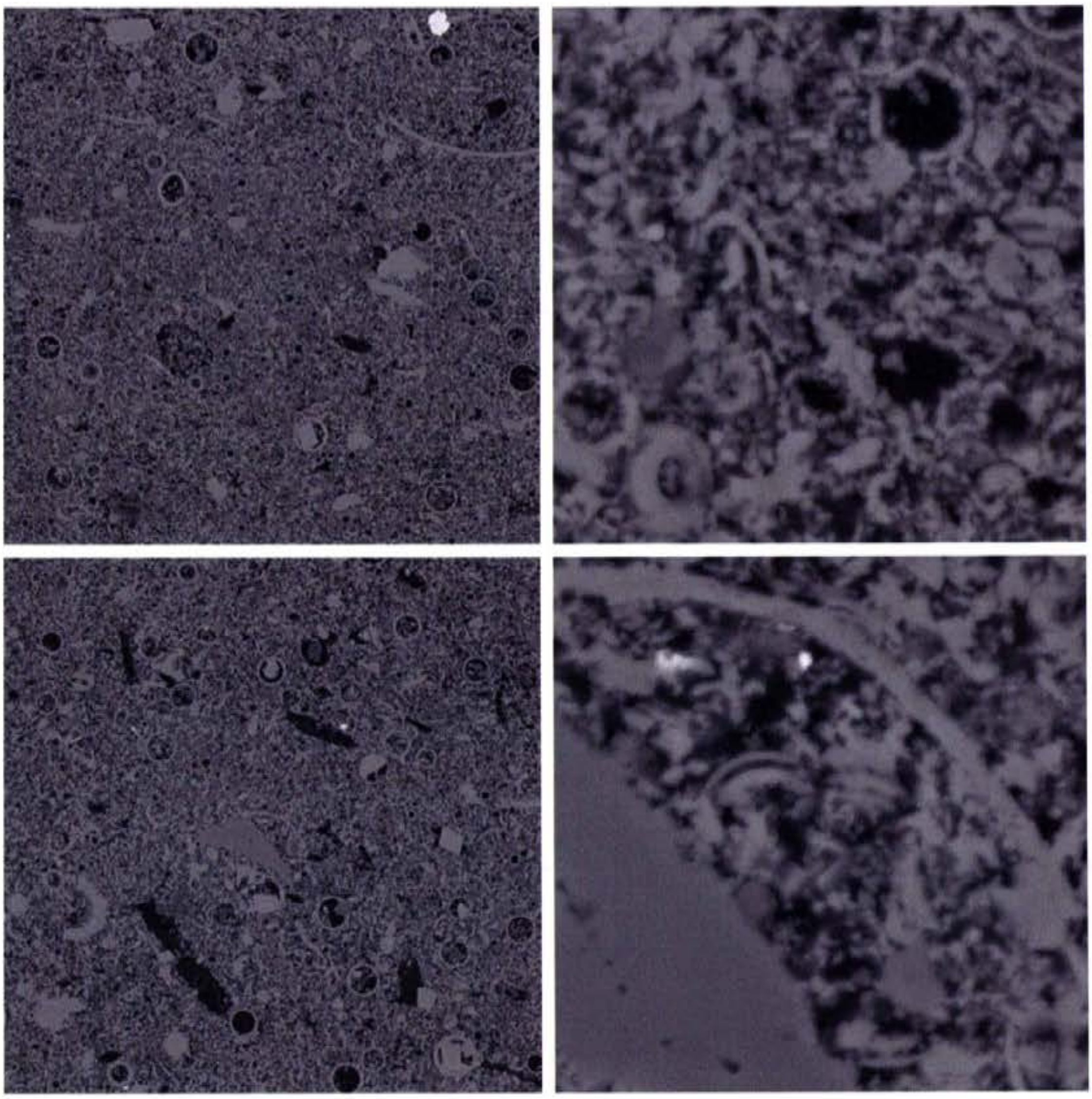

Rigs-2 plug sample 74.

Sample:
Off white (oil stained?), bioturbated, mudstone, calcareous microfossils, cemented and open tests, silic microfossils incl. spines.

BSE:
Intergranular, intrafossil and moldic porosity.
Submicron size in pore space and larger quartz clasts (replaced siliceous fossils, lower images). Micron size kaolinite crystals.

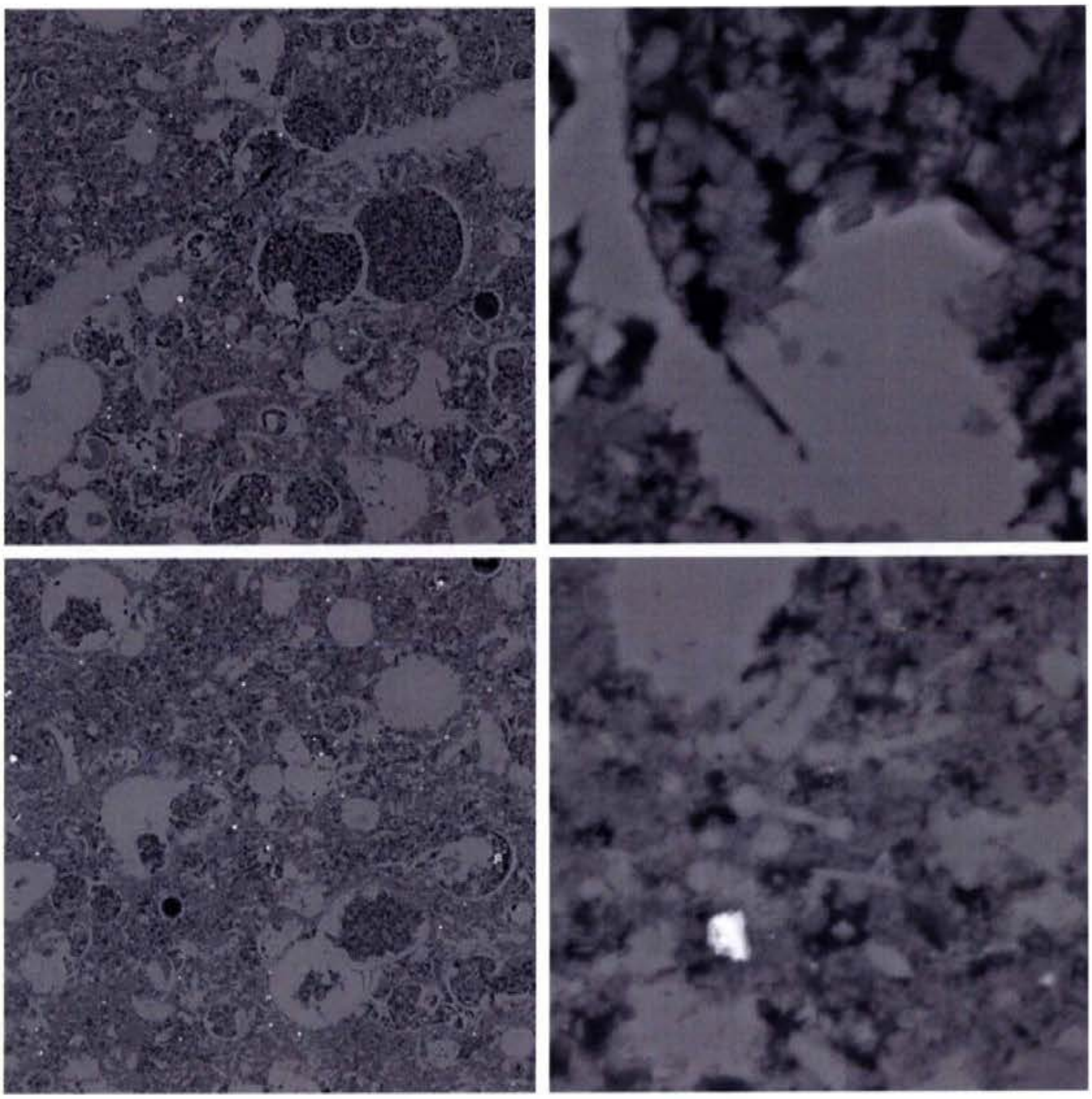

Rigs-2 plug sample 93.

Sample:
Off white (oil stained?), wackestone, calcareous microfossils, cemented tests, silicic microfossils, pyrite.

BSE:
Intergranular and intrafossil porosity.
Submicron – micron size quartz and kaolinite in pore space.

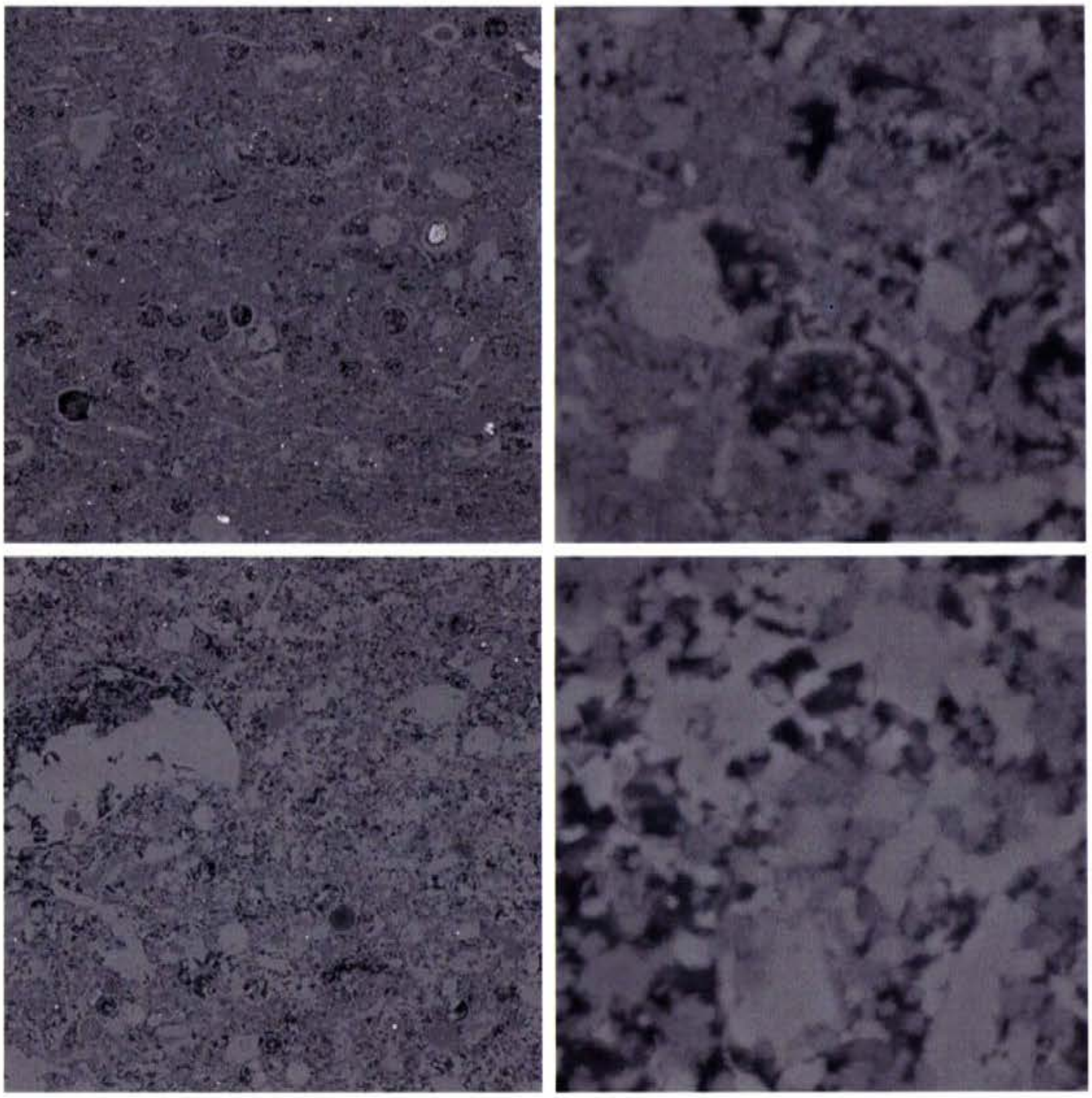

Rigs-2 plug sample 100.

Sample:
white, bioturbated, wackestone, calcareous microfossils, cemented and open, silicic microfossils.

BSE:
Intergranular and intrafossil porosity.
Porefilling quartz.

DANMARKS OG GRØNLANDS GEOLOGISKE UNDERSØGELSE RAPPORT 2002/23

Special Core Analysis for the Rock Physics Project (EFP-2001) ENS J.nr. 1313/01-0006

Ultrasonic velocity measured on plugs from the Ekofisk and Tor formation. Samples taken from the wells: Rigs-1, Rigs-2 and SA-1, the South Arne Field

GEUS Core Laboratory
Christian Høier

CONFIDENTIAL
FORTROLIG

GEOLOGICAL SURVEY OF DENMARK AND GREENLAND
MINISTRY OF THE ENVIRONMENT

GEUS

DANMARKS OG GRØNLANDS GEOLOGISKE UNDERSØGELSE RAPPORT 2002/23

Special Core Analysis for the Rock Physics Project (EFP-2001) ENS J.nr. 1313/01-0006

Ultrasonic velocity measured on plugs from the Ekofisk and Tor formation. Samples taken from the wells: Rigs-1, Rigs-2 and SA-1, the South Arne Field

Confidential report

Copy No.

Not to be released

GEOLOGICAL SURVEY OF DENMARK AND GREENLAND
MINISTRY OF THE ENVIRONMENT

G E U S

Contents

File name: Velocity-Rigs.doc , Velocity-Rigs-table22.doc

1. Introduction

By request of the Rock Physics Project (EFP-2001), GEUS Core Laboratory has carried out special core analysis on plugs from Ekofisk formation in the South Arne field, which include the wells: Rigs-1 and Rigs-2.

The analytical programme was specified by Peter Japsen and included the following services:

- P and S wave measured on dry plugs at reservoir overburden pressure
- P and S wave measured on saturated plugs at reservoir overburden pressure
- P and S wave measured on partly saturated plugs at reservoir overburden pressure
- Re-analysing of P and S wave from "GEUS rapport 2000/19" using the arrival picker

GEUS Core Laboratory received 17 plugs from Rigs-1 and 7 plugs from Rigs-2. Preliminary reports has been forwarded to the Rock Physics Project during year 2001.

2. Sampling and analytical procedure

The laboratory received a total of 24 1.5" diameter plugs from GEUS core Magasin.

2.1 Plug history

The plugs from Rigs 1 and 2 have earlier been hot soxhlet cleaned, dried at 110 °C, and measured for conventional core analysis data by GEUS core laboratory. Data can be seen in table 2.1.

2.2 Conventional core analysis and trimming of plugs

The 1.5" diameter plugs were trimmed to a length of 1.0" and dried at 110 °C. The porosity and grain density were re-measured on the trimmed plugs. Data can be seen in table 2.2.

2.3 Ultrasonic measurements

The transit time for the P- and S-wave was measured by a Tektronix Model TDS3012 2-channel digital phosphor oscilloscope, which was connected to a PAR spike-generator and a modified AutoLab 500 Ultrasonic core holder from New England Research. The P- and S-wave transducer has a centre frequency at 700 kHz.

P- and S-waves were measured on dried and full saturated plugs at 75 bar hydrostatic confining pressure. The confining pressure was increased continually during a time period of 1½ hour using a SP-5400 high pressure pump system from Quizix. The P- and S-waves measurements were saved digitally for later analysis. When unloading the core holder, the confining pressure was decreased continually from 75 to 0 bar during a time period of 1½ hour.

The system delay time was determined by measuring transit time without any plugs and on 3 aluminium plugs with different lengths. The system delay time was found to be $12.685 \cdot 10^{-6}$ sec. for the P wave and $23.714 \cdot 10^{-6}$ sec. for the S wave.

2.4 Dry plugs

The oven dried plugs were left at room conditions for 2 weeks to allow equilibration with the humidity in the air. This was done to prevent the plug from been "over-dry" before measuring. The saturation was monitored by a balance and calculated by mass balance. Data can be seen in table 2.2.

2.5 Saturated plugs

After measuring P and S waves on the dried plugs, the plugs were saturated with chalk saturated tap water by vacuum saturation for one day and then high pressure saturation for 2 days (100 Bar). Data can be seen in table 2.2.

2.5 De-saturation of plugs to 75%, 50% and 25%

A fully saturated plugs were placed on a balance at room condition. In time the water evaporated and mass balance was used for the calculations.

2.6 Analysing of the ultrasonic signal

The first amplitude extrema of the ultrasonic signal has been pick by a program named "first arrival picker" made by Ødegaard. Se section 4.

2.7 Re-analysing of data from "GEUS rapport 2000/19"

The ultrasonic measurements on plugs from South Arne were reanalysed using the first arrival picker. The data is listed in section 5.

2.8 List of tables and figures

Table 2.1 Conventional core analysis from report "GEUS 1996/26" and "GEUS 1996/77"

Well	Plug no.	Plug Type	Depth	Porosity	Gas Perm.	Gr.Dens.
			Feet or meter	%	mD	g/cc
Rigs-1	3	Vertical	9111.00	14.14	0.73	2.716
Rigs-1	7	Vertical	9114.00	14.47	0.53	2.708
Rigs-1	8	Horizontal	9114.32	14.17	3.05	2.706
Rigs-1	10	Horizontal	9116.30	15.07	15.0	2.707
Rigs-1	11	Vertical	9117.00	14.57	0.38	2.708
Rigs-1	12	Horizontal	9117.32	14.29	0.74	2.722
Rigs-1	36	Vertical	9137.51	16.20	0.12	2.712
Rigs-1	54	Horizontal	9153.20	19.48	0.37	2.704
Rigs-1	55	Vertical	9154.00	24.05	0.18	2.698
Rigs-1	82	Vertical	9176.00	33.97	0.83	2.699
Rigs-1	102	Vertical	9193.00	14.39	0.04	2.700
Rigs-1	122	Vertical	9210.00	27.81	0.32	2.707
Rigs-1	130	Vertical	9216.00	21.34	0.20	2.707
Rigs-1	146	Vertical	9230.00	31.94	0.60	2.697
Rigs-1	170	Vertical	9250.39	30.72	0.57	2.700
Rigs-1	196	Vertical	9273.50	17.15	0.11	2.699
Rigs-1	213	Vertical	9287.32	19.93	0.31	2.707
Rigs-2	15	Vertical	2800.00	41.33	1.90	2.685
Rigs-2	22	Vertical	2802.00	23.90	0.13	2.697
Rigs-2	37	Vertical	2806.00	28.90	1.27	2.698
Rigs-2	62	Vertical	2814.15	38.79	1.44	2.701
Rigs-2	74	Vertical	2818.04	44.73	3.23	2.724
Rigs-2	93	Vertical	2824.00	25.20	0.17	2.683
Rigs-2	100	Vertical	2826.00	19.75	0.23	2.692

Table 2.2 Plug data measured at 23 ^{0}C.

Well	Plug no.	Depth feet/meter	Porosity %	Gr.density g/ml	Perm. mD	Bulk vol. ml	Pore vol. ml	Length mm	Weight g	Dry weight g	Saturation %	Sat. weight g	Saturation %	Fluid density g/ml
Rigs-1	3	9111.00	13.81	2.705	0.7	21.22	2.93	18.69	49.47	49.67	7	52.37	92	1.073
Rigs-1	7	9114.00	14.09	2.705	0.5	23.63	3.33	21.00	54.91	55.92	30	-	-	0.998
Rigs-1	8	9114.32	14.03	2.707	3.1	24.93	3.50	22.43	58.02	59.21	34	-	-	0.998
Rigs-1	10	9116.30	14.93	2.704	15.0	21.59	3.22	18.84	49.66	50.04	12	53.21	103	1.073
Rigs-1	11	9117.00	14.33	2.711	0.4	23.81	3.41	20.93	55.29	55.71	12	59.06	103	1.073
Rigs-1	12	9117.32	14.76	2.726	0.7	25.86	3.82	22.98	60.09	60.54	12	-	-	1.073
Rigs-1	36	9137.51	15.81	2.704	0.1	27.12	4.29	23.80	61.75	62.08	8	66.13	102	0.998
Rigs-1	54	9153.20	19.45	2.709	0.4	28.47	5.54	25.50	62.12	62.32	4	67.59	99	0.998
Rigs-1	55	9154.00	24.73	2.710	0.2	27.89	6.90	24.54	56.9	57.03	2	63.64	98	0.998
Rigs-1	82	9176.00	34.47	2.706	0.8	28.30	9.76	24.81	50.19	50.24	1	59.81	99	0.998
Rigs-1	102	9193.00	14.61	2.714	0.0	22.12	3.23	19.45	51.27	51.43	5	54.34	95	0.998
Rigs-1	122	9210.00	28.07	2.710	0.3	23.45	6.58	20.82	45.71	45.82	2	52.17	98	0.998
Rigs-1	130	9216.00	23.93	2.717	0.2	25.71	6.15	22.88	53.14	53.26	2	59.12	97	0.998
Rigs-1	146	9230.00	34.58	2.694	0.6	20.39	7.05	18.08	35.94	35.96	0	42.95	100	0.998
Rigs-1	170	9250.39	30.90	2.704	0.6	26.70	8.25	23.45	49.89	49.94	1	57.94	98	0.998
Rigs-1	196	9273.50	18.79	2.711	0.1	26.92	5.06	23.83	59.27	59.37	2	64.31	100	0.998
Rigs-1	213	9287.32	20.43	2.716	0.3	27.91	5.70	24.73	60.31	60.36	1	65.87	98	0.998
Rigs-2	15	2800.00	41.55	2.696	1.9	15.21	6.32	13.68	23.97	24.00	0	30.20	99	0.998
Rigs-2	22	2802.00	25.62	2.700	0.1	27.38	7.01	24.48	55.13	55.19	1	61.67	93	0.998
Rigs-2	37	2806.00	38.74	2.692	1.3	25.34	9.82	22.50	41.78	41.82	0	51.52	99	0.998
Rigs-2	62	2814.15	39.75	2.700	1.4	27.15	10.79	24.25	44.17	44.19	0	54.87	99	0.998
Rigs-2	74	2818.04	43.86	2.709	3.2	15.21	6.67	13.48	23.13	23.14	0	29.68	98	0.998
Rigs-2	93	2824.00	24.67	2.670	0.2	27.23	6.72	24.14	54.75	54.77	0	61.44	100	0.998
Rigs-2	100	2826.00	20.29	2.695	0.2	29.44	5.97	26.09	63.25	63.30	1	69.12	98	0.998

3. Flow chart of the analytical procedure

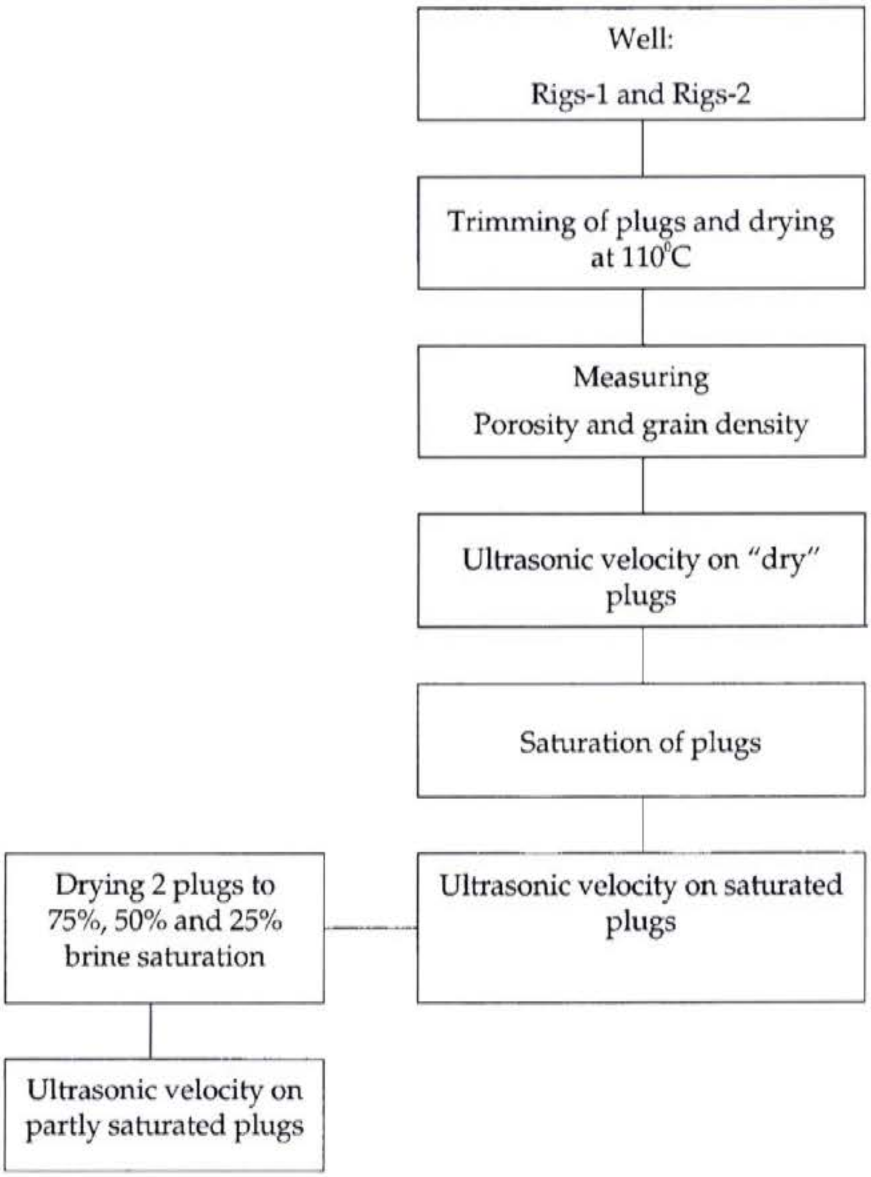

4. Analytical methods

The following is a short description of the methods used by GEUS Core Laboratory. For a more detailed description of methods, instrumentation and principles of calculation the reader is referred to API recommended practice for core analysis procedure (API RP 40, 1998).

4.1 Ultrasonic measurements

The ultrasonic velocity is calculated from the following equation.

$$\text{Ultrasonic velocity}\,[\text{m/s}] = \frac{\text{Sample length[m]}}{\text{Transit time[s]} - \text{system delay[s]}}$$

The transit time of a plug is measured using an oscilloscope, which is connected to a spike-generator and an ultrasonic core holder. The system delay time is the transit time of the system without any plugs. It can be determined by measuring the transit time without any plugs or measuring the transit time for uniform plugs with known length and extrapolate to 0.

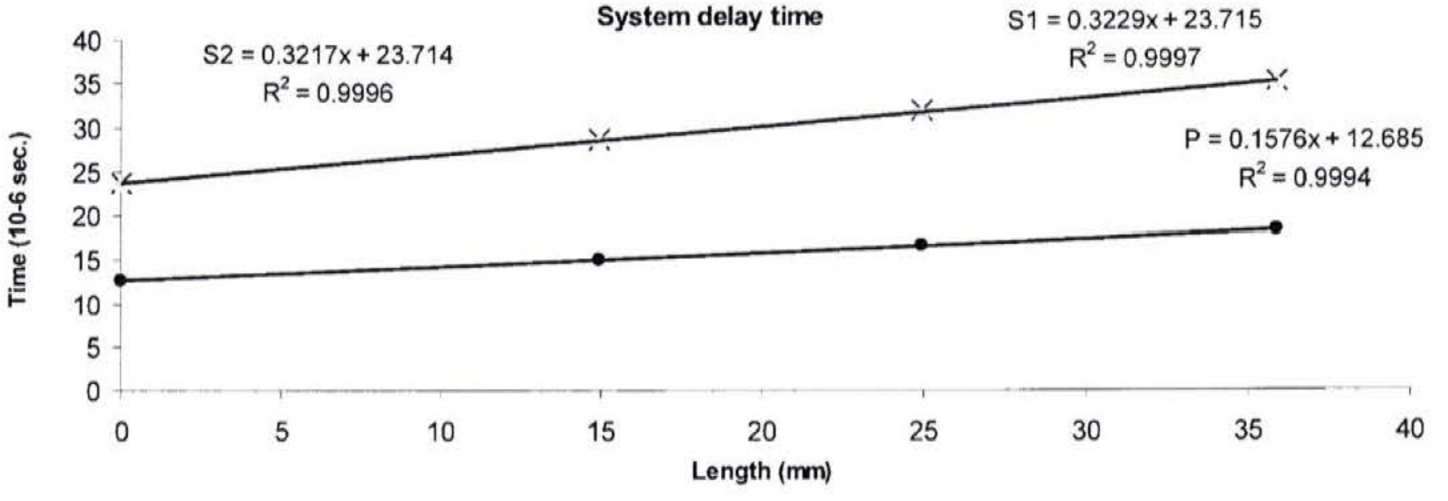

Figure 4.1 Determination of the system delay time.

The system is tested against 2 reference plugs giving the following result.

Aluminium 6061 plug:	P-velocity m/s	S1-velocity m/s	S2-velocity m/s
Measured	6417	3112	3120
Reference	6396	3125	3125
Difference (%)	-0.32	0.42	0.15

Acrylic plug:	P-velocity m/s	S1-velocity m/s	S2-velocity m/s
Measured	2745	1391	1387
Reference	2750	1392	1392
Difference (%)	0.19	0.08	0.35

4.2 The arrival picker

To reduce the inaccuracy and subjectivity of manual picking in the ultrasound signal, a first arrival picker program was develop by Ødegaard A/S. An additional advantage of the proposed approach is that more scientific solid uncertainty information can be obtained.

Picking the signal:

The program looks for two consecutive local extrema with amplitudes of opposite sign. The search can be limited to a given time interval and to a given polarity, i.e. the sign of the first extrama. In a typical ultrasonic signal the desired event will give the maximum output in the following non-linear object function:

$$\frac{|\,\text{FirstExtremaAmplitude} - 2 * \text{SecondExtremaAmplitude}\,|}{\text{HeadAmplitude}}$$

Where the HeadAmplitude denotes the maximum absolute amplitude of the signal in an interval ending just before the onset of the half period containing the first extrema. The length of the interval has been set to 5 mean periods, i.e. 5 divided by the mean frequency. The precise time of the first extrema is found using (Newton-Raphson) local optimisation starting from the solution determined previously and using (sinc) interpolation between the samples.

The global uncertainty:

In order to describe how easy it is to identify the desired event, the global uncertainty is defined as the ratio of the object function between its second largest value and its largest value. The global uncertainty takes values between 0 and 1, where 0 represents a very easy case and 1 means that two or more picks were equally good, in fact equally bad.

The local uncertainty (Error-band):

In order to describe how much the picked time could be wrong due to that additive noise has moved the chosen extrema of the observable signal, the local uncertainty is computed. The chosen HeadAmplitude is used as a noise estimate in that computation.

4.3 Gas permeability

The plug is mounted in a Hassler core holder, and a confining pressure of 400 psi applied to the sleeve. The specific permeability to gas is measured by flowing nitrogen gas through a plug of known dimensions at differential pressures between 0 and 1 bar. No back pressure is applied. The readings of the digital gas permeameter are checked regularly by routine measurement of permeable steel reference plugs.

4.4 He-porosity and grain density

The porosity is measured on cleaned and dried samples. The porosity is determined by subtraction of the measured grain volume and the measured bulk volume. The Helium technique, employing Boyle's Law, is used for grain volume determination, applying a double chambered Helium porosimeter with digital readout, whereas bulk volume is measured by submersion of the plug in a mercury bath using Archimedes principle. Grain density is calculated from the grain volume measurement and the weight of the cleaned and dried sample.

4.5 Precision of analytical data

Conventional core analysis:

The table below gives the precision (= reproducibility) at the 68% level of confidence (+/- 1 standard deviation) for routine core analysis measurements performed at GEUS Core Laboratory.

Measurement	Range, mD	Precision
Grain density		0.003 g/cc
Porosity		0.1 porosity-%
Gas Permeability	0.001-0.01 0.01-0.1 > 0.1	25% 15% 4%

4.6 Precision of ultrasonic data

The uncertainty of the plug length is 0.1 mm and this leads to the error given in the column "Error-length". The precision of picking the right signal is listed in column "Uncertainty" and error due to the noise is listed in column "Error-picking" in both μs and m/s. The column "Error-total" is the error added from "Error-length" and "Error-picking". See the table 4.1 below.

Table 4.1 Precision of ultrasonic data – Ekofisk formation

Well	Plug no.	Wave type	Saturation	Length mm	First arrival 10-6 sec	Velocity m/s	Error-picking 10-6 sec	Error-picking m/s	Error-length m/s	Error-total m/s	Uncertainty Value: 0 -1
Rigs-1	3	P	DRY	18.69	18.87	3020	0.020	10	16	26	0.06
Rigs-1	3	S1	DRY	18.69	32.24	2192	0.012	3	12	15	0.03
Rigs-1	3	S2	DRY	18.69	32.24	2192	0.021	5	12	17	0.06
Rigs-1	3	P	WET	18.69	18.65	3132	0.018	10	17	26	0.06
Rigs-1	3	S1	WET	18.69	35.94	1528	0.092	12	8	20	0.35
Rigs-1	3	S2	WET	18.69	35.83	1543	0.110	14	8	22	0.45
Rigs-1	7	P	DRY	21.00	20.58	2659	0.017	6	13	18	0.06
Rigs-1	7	S1	DRY	21.00	34.99	1863	0.024	4	9	13	0.10
Rigs-1	7	S2	DRY	21.00	34.93	1873	0.022	4	9	13	0.07
Rigs-1	8	P	DRY	22.43	19.18	3452	0.013	7	15	22	0.05
Rigs-1	8	S1	DRY	22.43	33.89	2205	0.163	36	10	46	0.26
Rigs-1	8	S2	DRY	22.43	34.12	2155	0.021	4	10	14	0.04
Rigs-1	10	P	DRY	18.84	17.71	3746	0.018	14	20	34	0.06
Rigs-1	10	S1	DRY	18.84	31.65	2374	0.015	5	13	17	0.06
Rigs-1	10	S2	DRY	18.84	31.64	2376	0.023	7	13	19	0.06
Rigs-1	10	P	WET	18.84	17.65	3791	0.013	10	20	30	0.04
Rigs-1	10	S1	WET	18.84	33.35	1956	0.056	11	10	22	0.15
Rigs-1	10	S2	WET	18.84	34.26	1786	0.115	20	9	29	0.28
Rigs-1	11	P	DRY	20.93	-	-	0.267	-	-	-	-
Rigs-1	11	S1	DRY	20.93	34.23	1991	0.025	5	10	14	0.08
Rigs-1	11	S2	DRY	20.93	34.09	2016	0.025	5	10	14	0.06
Rigs-1	11	P	WET	20.93	18.88	3378	0.031	17	16	33	0.08
Rigs-1	11	S1	WET	20.93	36.04	1698	0.083	12	8	20	0.42
Rigs-1	11	S2	WET	20.93	35.98	1706	0.082	11	8	20	0.36
Rigs-1	12	P	DRY	22.98	19.15	3556	0.119	66	15	82	0.33
Rigs-1	12	S1	DRY	22.98	33.80	2279	0.100	23	10	33	0.94
Rigs-1	12	S2	DRY	22.98	34.00	2234	0.086	19	10	29	0.95

Table 4.1 Precision of ultrasonic data – Ekofisk formation (continued)

Well	Plug no.	Wave type	Saturation	Length mm	First arrival 10-6 sec	Velocity m/s	Error-picking 10-6 sec	Error-picking m/s	Error-length m/s	Error-total m/s	Uncertainty Value: 0 -1
Rigs-1	36	P	DRY	23.80	20.54	3029	0.013	5	13	18	0.04
Rigs-1	36	S1	DRY	23.80	34.84	2138	0.019	4	9	13	0.04
Rigs-1	36	S2	DRY	23.80	34.85	2136	0.031	6	9	15	0.07
Rigs-1	36	P	WET	23.80	19.36	3565	0.022	12	15	27	0.07
Rigs-1	36	S1	WET	23.80	36.19	1908	0.041	6	8	14	0.16
Rigs-1	36	S2	WET	23.80	36.24	1899	0.047	7	8	15	0.12
Rigs-1	54	P	DRY	25.50	19.02	4024	0.012	8	16	23	0.04
Rigs-1	54	S1	DRY	25.50	34.25	2420	0.033	8	9	17	0.14
Rigs-1	54	S2	DRY	25.50	33.97	2486	0.012	3	10	13	0.03
Rigs-1	54	P	WET	25.50	18.98	4051	0.010	7	16	22	0.04
Rigs-1	54	S1	WET	25.50	35.34	2193	0.033	6	9	15	0.07
Rigs-1	54	S2	WET	25.50	35.17	2226	0.031	6	9	15	0.06
Rigs-1	55	P	DRY	24.54	19.46	3620	0.010	5	15	20	0.04
Rigs-1	55	S1	DRY	24.54	34.61	2252	0.017	4	9	13	0.04
Rigs-1	55	S2	DRY	24.54	34.63	2248	0.015	3	9	12	0.03
Rigs-1	55	P	WET	24.54	19.47	3619	0.011	6	15	21	0.04
Rigs-1	55	S1	WET	24.54	35.87	2019	0.021	4	8	12	0.05
Rigs-1	55	S2	WET	24.54	35.92	2011	0.026	4	8	12	0.09
Rigs-1	82	P	DRY	24.81	21.26	2893	0.010	3	12	15	0.03
Rigs-1	82	S1	DRY	24.81	37.22	1837	0.014	2	7	9	0.03
Rigs-1	82	S2	DRY	24.81	37.12	1850	0.032	4	7	12	0.08
Rigs-1	82	P	WET	24.81	20.97	2993	0.010	4	12	16	0.04
Rigs-1	82	S1	WET	24.81	39.20	1602	0.015	2	6	8	0.03
Rigs-1	82	S2	WET	24.81	38.96	1627	0.026	3	7	9	0.06
Rigs-1	102	P	DRY	19.45	17.46	4070	0.013	11	21	32	0.05
Rigs-1	102	S1	DRY	19.45	31.22	2590	0.014	5	13	18	0.04
Rigs-1	102	S2	DRY	19.45	31.22	2590	0.026	9	13	22	0.06
Rigs-1	102	P	WET	19.45	17.28	4230	0.010	9	22	31	0.04
Rigs-1	102	S1	WET	19.45	31.77	2415	0.023	7	12	19	0.08
Rigs-1	102	S2	WET	19.45	31.78	2410	0.019	6	12	18	0.05
Rigs-1	122	P	DRY	20.82	18.90	3350	0.015	8	16	24	0.06
Rigs-1	122	S1	DRY	20.82	33.53	2121	0.030	6	10	17	0.10
Rigs-1	122	S2	DRY	20.82	33.50	2127	0.026	6	10	16	0.06
Rigs-1	122	P	WET	20.82	18.78	3413	0.011	6	16	23	0.04
Rigs-1	122	S1	WET	20.82	34.79	1880	0.021	4	9	13	0.05
Rigs-1	122	S2	WET	20.82	34.81	1877	0.032	5	9	14	0.09
Rigs-1	130	P	DRY	22.88	19.49	3361	0.026	13	15	28	0.08
Rigs-1	130	S1	DRY	22.88	34.25	2171	0.025	5	9	15	0.13
Rigs-1	130	S2	DRY	22.88	34.21	2180	0.019	4	10	13	0.04
Rigs-1	130	P	WET	22.88	19.18	3521	0.010	6	15	21	0.03
Rigs-1	130	S1	WET	22.88	35.61	1923	0.041	7	8	15	0.17
Rigs-1	130	S2	WET	22.88	35.59	1927	0.046	8	8	16	0.17
Rigs-1	146	P	DRY	18.08	18.64	3035	0.022	11	17	28	0.07
Rigs-1	146	S1	DRY	18.08	33.27	1892	0.075	15	10	25	0.61
Rigs-1	146	S2	DRY	18.08	33.29	1888	0.060	12	10	22	0.18
Rigs-1	146	P	WET	18.08	18.61	3051	0.017	9	17	26	0.05
Rigs-1	146	S1	WET	18.08	34.68	1648	0.036	5	9	15	0.15
Rigs-1	146	S2	WET	18.08	34.79	1632	0.040	6	9	15	0.13

Table 4.1 Precision of ultrasonic data – Ekofisk formation (continued)

Well	Plug no.	Wave type	Saturation	Length mm	First arrival 10-6 sec	Velocity m/s	Error-picking 10-6 sec	Error-picking m/s	Error-length m/s	Error-total m/s	Uncertainty Value: 0 -1
Rigs-1	170	P	DRY	23.45	20.04	3187	0.021	9	14	23	0.07
Rigs-1	170	S1	DRY	23.45	35.60	1972	0.060	10	8	18	0.24
Rigs-1	170	S2	DRY	23.45	35.37	2011	0.071	12	9	21	0.21
Rigs-1	170	P	WET	23.45	19.98	3213	0.020	9	14	22	0.06
Rigs-1	170	S1	WET	23.45	36.93	1774	0.062	8	8	16	0.31
Rigs-1	170	S2	WET	23.45	37.07	1755	0.194	26	7	33	0.70
Rigs-1	196	P	DRY	23.83	18.47	4117	0.021	15	17	33	0.08
Rigs-1	196	S1	DRY	23.83	33.15	2525	0.026	7	11	18	0.07
Rigs-1	196	S2	DRY	23.83	33.12	2532	0.032	9	11	19	0.10
Rigs-1	196	P	WET	23.83	18.36	4197	0.017	12	18	30	0.06
Rigs-1	196	S1	WET	23.83	33.77	2371	0.016	4	10	14	0.03
Rigs-1	196	S2	WET	23.83	33.71	2384	0.023	6	10	16	0.05
Rigs-1	213	P	DRY	24.73	18.44	4296	0.036	27	17	45	0.09
Rigs-1	213	S1	DRY	24.73	33.28	2585	0.033	9	10	19	0.09
Rigs-1	213	S2	DRY	24.73	33.19	2609	0.051	14	11	25	0.12
Rigs-1	213	P	WET	24.73	18.26	4437	0.026	21	18	39	0.07
Rigs-1	213	S1	WET	24.73	33.60	2501	0.045	12	10	22	0.21
Rigs-1	213	S2	WET	24.73	33.72	2471	0.046	12	10	21	0.15
Rigs-2	15	P	DRY	13.68	18.62	2304	0.033	13	17	30	0.07
Rigs-2	15	S1	DRY	13.68	32.62	1536	0.044	8	11	19	0.07
Rigs-2	15	S2	DRY	13.68	32.15	1622	0.053	10	12	22	0.09
Rigs-2	15	P	WET	13.68	18.14	2506	0.016	7	18	26	0.04
Rigs-2	15	S1	WET	13.68	33.53	1394	0.130	19	10	29	-
Rigs-2	15	S2	WET	13.68	33.25	1435	0.201	31	10	41	-
Rigs-2	22	P	DRY	24.48	19.53	1253	0.010	1	5	6	0.04
Rigs-2	22	S1	DRY	24.48	34.52	2265	0.019	4	9	13	0.04
Rigs-2	22	S2	DRY	24.48	34.53	2262	0.016	3	9	13	0.03
Rigs-2	22	P	WET	24.48	19.53	3574	0.012	6	15	21	0.04
Rigs-2	22	S1	WET	24.48	35.70	2043	0.019	3	8	12	0.04
Rigs-2	22	S2	WET	24.48	35.67	2047	0.025	4	8	13	0.07
Rigs-2	37	P	DRY	22.50	21.41	2578	0.016	5	11	16	0.05
Rigs-2	37	S1	DRY	22.50	36.99	1695	0.026	3	8	11	0.07
Rigs-2	37	S2	DRY	22.50	36.87	1710	0.034	4	8	12	0.13
Rigs-2	37	P	WET	22.50	21.08	2680	0.012	4	12	16	0.04
Rigs-2	37	S1	WET	22.50	39.28	1445	0.021	2	6	8	0.07
Rigs-2	37	S2	WET	22.50	39.25	1448	0.028	3	6	9	0.08
Rigs-2	62	P	DRY	24.25	22.21	2546	0.014	4	10	14	0.05
Rigs-2	62	S1	DRY	24.25	38.47	1643	0.026	3	7	10	0.06
Rigs-2	62	S2	DRY	24.25	38.44	1646	0.022	2	7	9	0.04
Rigs-2	62	P	0.25	24.25	22.95	2361	0.017	4	10	14	0.04
Rigs-2	62	S1	0.25	24.25	39.64	1523	0.012	1	6	7	0.02
Rigs-2	62	S2	0.25	24.25	39.79	1508	0.018	2	6	8	0.04
Rigs-2	62	P	0.5	24.25	23.21	2304	0.012	3	9	12	0.03
Rigs-2	62	S1	0.5	24.25	40.24	1468	0.025	2	6	8	0.05
Rigs-2	62	S2	0.5	24.25	40.14	1477	0.024	2	6	8	0.05
Rigs-2	62	P	0.75	24.25	23.18	2310	0.018	4	10	14	0.05
Rigs-2	62	S1	0.75	24.25	40.63	1433	0.017	1	6	7	0.05
Rigs-2	62	S2	0.75	24.25	40.57	1438	0.026	2	6	8	0.05
Rigs-2	62	P	WET	24.25	21.79	2662	0.011	3	11	14	0.04
Rigs-2	62	S1	WET	24.25	41.19	1387	0.029	2	6	8	0.07
Rigs-2	62	S2	WET	24.25	40.98	1404	0.033	3	6	8	0.08

Table 4.1 Precision of ultrasonic data – Ekofisk formation (continued)

Well	Plug no.	Wave type	Saturation	Length mm	First arrival 10-6 sec	Velocity m/s	Error-picking 10-6 sec	Error-picking m/s	Error-length m/s	Error-total m/s	Uncertainty Value: 0 -1
Rigs-2	74	P	DRY	13.48	18.33	2386	0.012	5	18	23	0.04
Rigs-2	74	S1	DRY	13.48	32.49	1536	0.021	4	11	15	0.05
Rigs-2	74	S2	DRY	13.48	32.43	1547	0.021	4	11	15	0.05
Rigs-2	74	P	WET	13.48	18.06	2506	0.010	5	19	23	0.03
Rigs-2	74	S1	WET	13.48	34.17	1289	0.027	3	10	13	0.05
Rigs-2	74	S2	WET	13.48	34.10	1297	0.045	6	10	15	0.13
Rigs-2	93	P	DRY	24.14	19.77	3408	0.012	6	14	20	0.04
Rigs-2	93	S1	DRY	24.14	34.52	2234	0.016	3	9	13	0.04
Rigs-2	93	S2	DRY	24.14	34.53	2231	0.020	4	9	13	0.05
Rigs-2	93	P	WET	24.14	19.56	3509	0.060	31	15	45	0.19
Rigs-2	93	S1	WET	24.14	35.74	2007	0.025	4	8	12	0.07
Rigs-2	93	S2	WET	24.14	35.70	2014	0.023	4	8	12	0.04
Rigs-2	100	P	DRY	26.09	18.85	4230	0.016	11	16	27	0.06
Rigs-2	100	S1	DRY	26.09	33.71	2610	0.022	6	10	16	0.09
Rigs-2	100	S2	DRY	26.09	33.70	2612	0.021	5	10	15	0.05
Rigs-2	100	P	0.25	26.09	18.96	4155	0.010	6	16	22	0.03
Rigs-2	100	S1	0.25	26.09	33.98	2541	0.020	5	10	15	0.04
Rigs-2	100	S2	0.25	26.09	33.97	2543	0.017	4	10	14	0.04
Rigs-2	100	P	0.5	26.09	18.96	4157	0.020	13	16	29	0.06
Rigs-2	100	S1	0.5	26.09	34.12	2507	0.014	3	10	13	0.03
Rigs-2	100	S2	0.5	26.09	34.11	2509	0.024	6	10	15	0.08
Rigs-2	100	P	0.75	26.09	18.90	4195	0.010	7	16	23	0.03
Rigs-2	100	S1	0.75	26.09	34.25	2476	0.018	4	9	14	0.07
Rigs-2	100	S2	0.75	26.09	34.24	2478	0.018	4	9	14	0.04
Rigs-2	100	P	WET	26.09	18.76	4291	0.013	9	16	26	0.05
Rigs-2	100	S1	WET	26.09	34.36	2451	0.016	4	9	13	0.03
Rigs-2	100	S2	WET	26.09	34.35	2453	0.023	5	9	15	0.05
System	Alu1	P	DRY	14.94	15.06	6280	0.011	30	42	72	0.04
System	Alu1	S1	DRY	14.94	28.61	3052	0.036	23	20	43	0.14
System	Alu1	S2	DRY	14.94	28.60	3058	0.032	20	20	41	0.14
System	Alu2	P	DRY	24.93	16.69	6232	0.013	20	25	45	0.04
System	Alu2	S1	DRY	24.93	31.84	3067	0.031	12	12	24	0.09
System	Alu2	S2	DRY	24.93	31.81	3079	0.023	9	12	21	0.07
System	Alu3	P	DRY	35.90	18.28	6411	0.012	13	18	31	0.04
System	Alu3	S1	DRY	35.90	35.22	3120	0.042	12	9	20	0.13
System	Alu3	S2	DRY	35.90	35.17	3133	0.076	21	9	30	0.23
System	Transducer	P	DRY	-	12.65	-	0.009	-	-	-	0.04
System	Transducer	S1	DRY	-	23.65	-	0.025	-	-	-	0.06
System	Transducer	S2	DRY	-	23.64	-	0.024	-	-	-	0.06
Ref.	ALU-6061	P	DRY	25.40	16.64	6417	0.011	17	25	43	0.03
Ref.	ALU-6061	S1	DRY	25.40	31.88	3112	0.032	12	12	24	0.09
Ref.	ALU-6061	S2	DRY	25.40	31.85	3120	0.031	12	12	24	0.09
Ref.	Acrylic	P	DRY	25.44	21.95	2745	0.014	4	11	15	0.04
Ref.	Acrylic	S1	DRY	25.44	42.00	1391	0.028	2	5	8	0.08
Ref.	Acrylic	S2	DRY	25.44	42.05	1387	0.050	4	5	9	0.11

Table 4.2 Precision of ultrasonic data – Tor formation

Well	Plug no.	Wave type	Saturation	Length mm	First arrival 10-6 sec	Velocity m/s	Error-picking 10-6 sec	Error-picking m/s	Error-length m/s	Error-total m/s	Uncertainty Value: 0 -1
Rigs-1	216	P	DRY	19.9	17.34	4305	0.047	44	22	66	0.14
Rigs-1	216	S1	DRY	19.9	31.39	2576	0.064	22	13	35	0.12
Rigs-1	216	S2	DRY	19.9	31.27	2629	0.055	19	13	32	0.13
Rigs-1	220	P	DRY	27.9	21.09	3331	0.018	7	12	19	0.06
Rigs-1	220	S1	DRY	27.9	37.13	2072	0.019	3	7	10	0.05
Rigs-1	220	S2	DRY	27.9	37.20	2066	0.018	3	7	10	0.04
Rigs-1	220	P	WET	27.9	21.08	3335	0.021	8	12	20	0.06
Rigs-1	220	S1	WET	27.9	39.00	1820	0.032	4	7	10	0.07
Rigs-1	220	S2	WET	27.9	38.94	1830	0.032	4	7	10	0.06
Rigs-1	236	P	DRY	25.6	20.85	3152	0.081	32	12	44	0.37
Rigs-1	236	S1	DRY	25.6	36.85	1944	0.065	10	8	17	0.26
Rigs-1	236	S2	DRY	25.6	36.23	2045	0.066	11	8	19	0.13
Rigs-1	240	P	DRY	27.9	23.55	2571	0.034	8	9	17	0.11
Rigs-1	240	S1	DRY	27.9	40.31	1674	0.019	2	6	8	0.03
Rigs-1	240	S2	DRY	27.9	40.21	1687	0.022	2	6	8	0.04
Rigs-1	244	P	DRY	25.1	21.48	2865	0.023	7	11	19	0.06
Rigs-1	244	S1	DRY	25.1	37.73	1785	0.029	4	7	11	0.06
Rigs-1	244	S2	DRY	25.1	37.43	1828	0.047	6	7	14	0.08
Rigs-1	260	P	DRY	26	23.35	2448	0.049	11	9	21	0.31
Rigs-1	260	S1	DRY	26	39.90	1604	0.028	3	6	9	0.13
Rigs-1	260	S2	DRY	26	39.62	1635	0.070	7	6	13	0.31
Rigs-1	260	P	WET	26	22.61	2632	0.085	23	10	33	0.12
Rigs-1	260	S1	WET	26	42.62	1373	0.064	5	5	10	0.26
Rigs-1	260	S2	WET	26	44.42	1256	0.124	8	5	12	0.60
Rigs-1	264	P	DRY	26.8	23.74	2433	0.024	5	9	14	0.08
Rigs-1	264	S1	DRY	26.8	40.66	1578	0.029	3	6	9	0.06
Rigs-1	264	S2	DRY	26.8	40.58	1589	0.049	5	6	11	0.12
Rigs-1	264	P	WET	26.8	23.12	2577	0.023	6	10	15	0.07
Rigs-1	264	S1	WET	26.8	43.62	1344	0.052	3	5	9	0.13
Rigs-1	264	S2	WET	26.8	43.72	1340	0.075	5	5	10	0.22
Rigs-1	274	P	DRY	22.8	21.23	2683	0.021	7	12	18	0.06
Rigs-1	274	S1	DRY	22.8	36.66	1759	0.035	5	8	12	0.08
Rigs-1	274	S2	DRY	22.8	36.64	1765	0.041	6	8	13	0.09
Rigs-2	121	P	DRY	26.8	25.55	2086	0.059	10	8	17	0.18
Rigs-2	121	S1	DRY	26.8	42.77	1401	0.043	3	5	8	0.09
Rigs-2	121	S2	DRY	26.8	42.40	1431	0.044	3	5	9	0.07
Rigs-2	121	P	WET	26.8	23.68	2441	0.023	5	9	14	0.07
Rigs-2	121	S1	WET	26.8	45.12	1248	0.049	3	5	8	0.16
Rigs-2	121	S2	WET	26.8	45.11	1250	0.133	8	5	13	0.27
Rigs-2	128	P	DRY	27.2	25.89	2064	0.056	9	8	16	0.27
Rigs-2	128	S1	DRY	27.2	43.59	1365	0.092	6	5	11	0.61
Rigs-2	128	S2	DRY	27.2	43.36	1383	0.064	5	5	10	0.75
Rigs-2	128	P	WET	27.2	24.21	2366	0.053	11	9	20	0.12
Rigs-2	128	S1	WET	27.2	47.64	1134	0.132	6	4	10	0.51
Rigs-2	128	S2	WET	27.2	47.65	1136	0.207	10	4	14	0.39

Table 4.2 Precision of ultrasonic data – Tor formation (continued).

Well	Plug no.	Wave type	Saturation	Length mm	First arrival 10-6 sec	Velocity m/s	Error-picking 10-6 sec	Error-picking m/s	Error-length m/s	Error-total m/s	Uncertainty Value: 0 -1
Rigs-2	136	P	DRY	26.1	25.34	2072	0.033	6	8	13	0.11
Rigs-2	136	S1	DRY	26.1	42.58	1382	0.040	3	5	8	0.09
Rigs-2	136	S2	DRY	26.1	42.51	1390	0.046	3	5	9	0.09
Rigs-2	136	P	WET	26.1	23.48	2429	0.025	6	9	15	0.08
Rigs-2	136	S1	WET	26.1	45.03	1224	0.062	4	5	8	0.22
Rigs-2	136	S2	WET	26.1	45.11	1221	0.111	6	5	11	0.20
Rigs-2	151	P	DRY	25.7	24.42	2198	0.026	5	9	14	0.06
Rigs-2	151	S1	DRY	25.7	41.88	1413	0.035	3	5	8	0.07
Rigs-2	151	S2	DRY	25.7	41.33	1460	0.027	2	6	8	0.04
Rigs-2	151	P	WET	25.7	23.09	2480	0.028	7	10	16	0.07
Rigs-2	151	S1	WET	25.7	44.27	1249	0.056	3	5	8	0.10
Rigs-2	151	S2	WET	25.7	43.84	1278	0.078	5	5	10	0.14
Rigs-2	162	P	DRY	24.7	23.37	2323	0.040	9	9	18	0.11
Rigs-2	162	S1	DRY	24.7	41.27	1405	0.146	12	6	17	0.30
Rigs-2	162	S2	DRY	24.7	40.08	1511	0.040	4	6	10	0.08
Rigs-2	176	P	DRY	25.6	22.20	2704	0.059	17	11	27	0.13
Rigs-2	176	S1	DRY	25.6	38.36	1744	0.072	9	7	15	0.23
Rigs-2	176	S2	DRY	25.6	38.70	1709	0.085	10	7	16	0.37
Rigs-2	200	P	DRY	18.9	22.26	1979	0.042	9	10	19	0.13
Rigs-2	200	S1	DRY	18.9	38.20	1300	0.055	5	7	12	0.54
Rigs-2	200	S2	DRY	18.9	38.28	1296	0.038	3	7	10	0.07
Rigs-2	200	P	WET	18.9	20.89	2311	0.020	6	12	18	0.07
Rigs-2	200	S1	WET	18.9	40.30	1136	0.094	6	6	12	0.50
Rigs-2	200	S2	WET	18.9	40.83	1103	0.085	6	6	11	0.20
Rigs-2	204	P	DRY	26.8	26.42	1959	0.028	4	7	11	0.09
Rigs-2	204	S1	DRY	26.8	43.62	1345	0.030	2	5	7	0.13
Rigs-2	204	S2	DRY	26.8	43.95	1326	0.050	3	5	8	0.11
Rigs-2	204	P	WET	26.8	24.07	2364	0.025	5	9	14	0.08
Rigs-2	204	S1	WET	26.8	46.30	1186	0.073	4	4	8	0.13
Rigs-2	204	S2	WET	26.8	46.24	1191	0.113	6	4	10	0.15
Rigs-2	212	P	DRY	26.5	25.57	2063	0.016	3	8	10	0.05
Rigs-2	212	S1	DRY	26.5	42.64	1397	0.025	2	5	7	0.07
Rigs-2	212	S2	DRY	26.5	42.82	1387	0.031	2	5	8	0.06
Rigs-2	212	P	WET	26.5	23.63	2429	0.019	4	9	13	0.06
Rigs-2	212	S1	WET	26.5	45.24	1229	0.043	2	5	7	0.10
Rigs-2	212	S2	WET	26.5	45.23	1232	0.077	4	5	9	0.14
SA-1	755	P	DRY	25.9	19.11	4048	0.043	28	16	43	0.16
SA-1	755	S1	DRY	25.9	34.32	2428	0.027	6	9	15	0.07
SA-1	755	S2	DRY	25.9	34.41	2415	0.028	6	9	16	0.05
SA-1	755	P	WET	25.9	19.06	4079	0.021	13	16	29	0.08
SA-1	755	S1	WET	25.9	35.20	2242	0.057	11	9	20	0.12
SA-1	755	S2	WET	25.9	35.24	2242	0.034	7	9	15	0.07
SA-1	759	P	DRY	22.9	19.64	3309	0.032	15	14	30	0.10
SA-1	759	S1	DRY	22.9	34.78	2063	0.024	4	9	13	0.06
SA-1	759	S2	DRY	22.9	34.85	2056	0.021	4	9	13	0.04
SA-1	760	P	DRY	26.3	20.27	3485	0.050	23	13	37	0.54
SA-1	760	S1	DRY	26.3	35.85	2160	0.023	4	8	12	0.42
SA-1	760	S2	DRY	26.3	35.87	2162	0.052	9	8	18	0.20
SA-1	760	P	WET	26.3	20.03	3597	0.016	8	14	21	0.06
SA-1	760	S1	WET	26.3	36.95	1981	0.119	18	8	25	0.64
SA-1	760	S2	WET	26.3	36.94	1987	0.106	16	8	24	0.33

Table 4.2 Precision of ultrasonic data – Tor formation (continued).

Well	Plug no.	Wave type	Saturation	Length mm	First arrival 10-6 sec	Velocity m/s	Error-picking 10-6 sec	Error-picking m/s	Error-length m/s	Error-total m/s	Uncertainty Value: 0 -1
SA-1	761	P	DRY	26.2	-	-	-	-	-	-	-
SA-1	761	S1	DRY	26.2	-	-	-	-	-	-	-
SA-1	761	S2	DRY	26.2	36.72	2013	0.109	17	8	25	0.51
SA-1	761	P	DRY	26.2	19.53	1342	0.010	1	5	6	0.04
SA-1	761	P	WET	26.2	20.28	3466	0.023	11	13	24	0.08
SA-1	761	S1	WET	26.2	37.79	1855	0.091	12	7	19	0.45
SA-1	761	S2	WET	26.2	37.80	1859	0.200	27	7	34	0.70
SA-1	763	P	DRY	25.7	20.01	3518	0.040	19	14	33	0.17
SA-1	763	S1	DRY	25.7	35.47	2175	0.030	6	8	14	0.08
SA-1	763	S2	DRY	25.7	35.50	2175	0.057	10	8	19	0.12
SA-1	763	P	WET	25.7	19.85	3598	0.018	9	14	23	0.06
SA-1	763	S1	WET	25.7	36.63	1981	0.100	15	8	23	0.29
SA-1	763	S2	WET	25.7	36.69	1976	0.064	10	8	17	0.14
SA-1	767	P	DRY	24.2	19.70	3466	0.028	14	14	28	0.10
SA-1	767	S1	DRY	24.2	35.09	2121	0.027	5	9	14	0.07
SA-1	767	S2	DRY	24.2	35.14	2118	0.029	5	9	14	0.06
SA-1	767	P	WET	24.2	19.58	3529	0.013	7	15	21	0.04
SA-1	767	S1	WET	24.2	36.02	1961	0.026	4	8	12	0.07
SA-1	767	S2	WET	24.2	36.10	1953	0.043	7	8	15	0.08
SA-1	771	P	DRY	23.3	19.73	3327	0.027	13	14	27	0.09
SA-1	771	S1	DRY	23.3	35.03	2054	0.027	5	9	14	0.08
SA-1	771	S2	DRY	23.3	35.29	2014	0.039	7	9	15	0.09
SA-1	771	P	WET	23.3	19.59	3396	0.023	12	15	26	0.08
SA-1	771	S1	WET	23.3	36.63	1801	0.033	5	8	12	0.07
SA-1	771	S2	WET	23.3	36.33	1849	0.039	6	8	14	0.08
SA-1	774	P	DRY	22.2	18.78	3663	0.019	11	16	28	0.07
SA-1	774	S1	DRY	22.2	33.73	2208	0.018	4	10	14	0.04
SA-1	774	S2	DRY	22.2	33.59	2246	0.021	5	10	15	0.04
SA-1	779	P	DRY	24.3	18.84	3967	0.018	11	16	28	0.08
SA-1	779	S1	DRY	24.3	33.83	2390	0.021	5	10	15	0.06
SA-1	779	S2	DRY	24.3	34.02	2353	0.024	6	10	15	0.05
SA-1	780	P	DRY	24.6	19.98	3382	0.016	8	14	21	0.06
SA-1	780	S1	DRY	24.6	35.40	2095	0.016	3	9	11	0.04
SA-1	780	S2	DRY	24.6	35.58	2069	0.026	4	8	13	0.06
SA-1	782	P	DRY	24.2	19.28	3683	0.024	13	15	29	0.08
SA-1	782	S1	DRY	24.2	34.34	2264	0.037	8	9	17	0.11
SA-1	782	S2	DRY	24.2	34.53	2233	0.028	6	9	15	0.06
SA-1	783	P	DRY	23.8	18.69	3980	0.060	41	17	57	0.22
SA-1	783	S1	DRY	23.8	33.63	2386	0.052	13	10	23	0.13
SA-1	783	S2	DRY	23.8	33.40	2451	0.062	16	10	26	0.17

Table 4.2 Precision of ultrasonic data – Tor formation (continued).

Well	Plug no.	Wave type	Satu-ration	Length mm	First arrival 10-6 sec	Velocity m/s	Error-picking 10-6 sec	Error-picking m/s	Error-length m/s	Error-total m/s	Uncertainty Value: 0 -1
System	Alu1	P	DRY	14.9	15.07	6346	0.012	33	42	75	0.04
System	Alu1	S1	DRY	14.9	28.50	3094	0.028	18	21	39	0.08
System	Alu1	S2	DRY	14.9	28.55	3083	0.019	12	21	33	0.05
System	Alu2	P	DRY	24.9	16.64	6365	0.011	19	26	44	0.03
System	Alu2	S1	DRY	24.9	31.84	3051	0.042	16	12	28	0.18
System	Alu2	S2	DRY	24.9	31.87	3052	0.034	13	12	25	0.08
System	Alu3	P	DRY	35.9	18.31	6417	0.014	16	18	34	0.04
System	Alu3	S1	DRY	35.9	35.24	3103	0.034	9	9	18	0.12
System	Alu3	S2	DRY	35.9	35.24	3112	0.016	4	9	13	0.04
System	Transducer	P	DRY	0	12.70	-	0.012	-	-	-	0.04
System	Transducer	S1	DRY	0	23.65	-	0.030	-	-	-	0.08
System	Transducer	S2	DRY	0	23.67	-	0.012	-	-	-	0.03
System	ALU-6061	P	DRY	25.4	16.69	6399	0.011	18	25	44	0.04
System	ALU-6061	S1	DRY	25.4	31.91	3083	0.038	14	12	26	0.14
System	ALU-6061	S2	DRY	25.4	31.91	3096	0.030	12	12	24	0.07
System	Acrylic	P	DRY	25.4	22.07	2721	0.018	5	11	16	0.06
System	Acrylic	S1	DRY	25.4	41.99	1389	0.028	2	5	8	0.06
System	Acrylic	S2	DRY	25.4	42.01	1390	0.030	2	5	8	0.06

5. Results of special core analysis

The results of the special core analysis are shown in the following tables and figures:

The dry ultrasonic velocities from the EKOFISK formation are presented in table 5.1
The saturated ultrasonic velocities from the EKOFISK formation are presented in table 5.2.
The dry ultrasonic velocities from the TOR formation are presented in table 5.3
The saturated ultrasonic velocities from the TOR formation are presented in table 5.4
The data from the partial saturated plugs are presented in table 5.5

The ultrasonic velocity have been plotted as follows:

- P,S1,S2-wave velocity on DRY plugs vs. Porosity
- P,S1,S2-wave velocity on WET plugs vs. Porosity
- P-wave velocity vs. S-wave velocity for all plugs
- P and S-waves measured dry vs. saturated measurements

All presented data can also be found in the CD-ROM.

5.1 Data tabulation.

Table 5.1: Ultrasonic velocities measured on DRY plugs from the South Arne field – Ekofisk formation.

Well name	plug no.	Depth feet or meter	Porosity %	Gr. Dens g/cc	P-waves Velocity m/s	Error m/s	S1-waves Velocity m/s	Error m/s	S2-waves Velocity m/s	Error m/s	P/S
Rigs-1	3	9111.00	13.81	2.705	3020	26	2192	15	2192	17	1.38
Rigs-1	7	9114.00	14.09	2.705	2659	18	1863	13	1873	13	1.42
Rigs-1	8	9114.32	14.03	2.707	3452	22	-	-	2155	14	1.60
Rigs-1	10	9116.30	14.93	2.704	3746	34	2374	17	2376	19	1.58
Rigs-1	11	9117.00	14.33	2.711	-	-	1991	14	2016	14	-
Rigs-1	12	9117.32	14.76	2.726	3556	82	2279	33	2234	29	1.58
Rigs-1	36	9137.51	16.64	2.727	3029	18	2138	13	2136	15	1.42
Rigs-1	54	9153.20	19.45	2.709	4024	23	-	-	2486	13	1.62
Rigs-1	55	9154.00	24.73	2.710	3620	20	2252	13	2248	12	1.61
Rigs-1	82	9176.00	34.47	2.706	2893	15	1837	9	1850	12	1.57
Rigs-1	102	9193.00	14.61	2.714	4070	32	2590	18	2590	22	1.57
Rigs-1	122	9210.00	28.07	2.710	3350	24	2121	17	2127	16	1.58
Rigs-1	130	9216.00	23.93	2.717	3361	28	2171	15	2180	13	1.54
Rigs-1	146	9230.00	34.67	2.703	3035	28	1892	25	1888	22	1.61
Rigs-1	170	9250.39	30.90	2.704	3187	23	1972	18	-	-	1.62
Rigs-1	196	9273.50	18.79	2.711	4117	33	2525	18	2532	19	1.63
Rigs-1	213	9287.32	20.43	2.716	4296	45	2585	19	2609	25	1.65
Rigs-2	15	2800.00	41.55	2.696	2304	30	-	-	1622	22	1.42
Rigs-2	22	2802.00	25.62	2.700	3576	6	2265	13	2262	13	1.58
Rigs-2	37	2806.00	38.74	2.692	2578	16	1695	11	1710	12	1.51
Rigs-2	62	2814.15	39.75	2.700	2546	14	1643	10	1646	9	1.55
Rigs-2	74	2818.04	43.86	2.709	2386	23	1536	15	1547	15	1.55
Rigs-2	93	2824.00	25.18	2.685	3408	20	2234	13	2231	13	1.53
Rigs-2	100	2826.00	20.29	2.695	4230	27	2610	16	2612	15	1.62

Table 5.2: Ultrasonic velocities measured on WET plugs from the South Arne field – Ekofisk formation.

Well name	plug no.	Depth feet or meter	Porosity %	Gr. Dens g/cc	P-waves Velocity m/s		S1-waves Velocity m/s		S2-waves Velocity m/s		P/S
Rigs-1	3	9111.00	13.81	2.705	3132	26	1528	20	1543	22	2.04
Rigs-1	7	9114.00	14.09	2.710	-	-	-	-	-	-	-
Rigs-1	8	9114.32	16.16	2.700	-	-	-	-	-	-	-
Rigs-1	10	9116.30	14.93	2.704	3791	30	1956	22	1786	29	2.03
Rigs-1	11	9117.00	14.33	2.711	3378	33	1698	20	1706	20	1.98
Rigs-1	12	9117.32	14.76	2.726	-	-	-	-	-	-	-
Rigs-1	36	9137.51	15.81	2.704	3565	27	1908	14	1899	15	1.87
Rigs-1	54	9153.20	19.45	2.709	4051	22	2193	15	2226	15	1.83
Rigs-1	55	9154.00	24.73	2.710	3619	21	2019	12	2011	12	1.80
Rigs-1	82	9176.00	34.47	2.706	2993	16	1602	8	1627	9	1.85
Rigs-1	102	9193.00	14.61	2.714	4230	31	2415	19	2410	18	1.75
Rigs-1	122	9210.00	28.07	2.710	3413	23	1880	13	1877	14	1.82
Rigs-1	130	9216.00	23.93	2.717	3521	21	1923	15	1927	16	1.83
Rigs-1	146	9230.00	34.58	2.694	3051	26	1648	15	1632	15	1.86
Rigs-1	170	9250.39	30.90	2.704	3213	22	1774	16	1755	33	1.82
Rigs-1	196	9273.50	18.79	2.711	4197	30	2371	14	2384	16	1.77
Rigs-1	213	9287.32	20.43	2.716	4437	39	2501	22	2471	21	1.78
Rigs-2	15	2800.00	41.55	2.696	2506	26	1394	29	-	-	1.80
Rigs-2	22	2802.00	25.62	2.700	3574	21	2043	12	2047	13	1.75
Rigs-2	37	2806.00	38.74	2.692	2680	16	1445	8	1448	9	1.85
Rigs-2	62	2814.15	39.75	2.700	2662	14	1387	8	1404	8	1.91
Rigs-2	74	2818.04	43.86	2.709	2506	23	1289	13	1297	15	1.94
Rigs-2	93	2824.00	24.67	2.670	3509	45	2007	12	2014	12	1.75
Rigs-2	100	2826.00	20.29	2.695	4291	26	2451	13	2453	15	1.75

Table 5.3: Ultrasonic velocities measured on DRY plugs from the South Arne field – Tor formation.

Well name	plug no.	depth meter or feet	Porosity %	Gr. Dens g/cc	P-waves Velocity m/s		S1-waves Velocity m/s		S2-waves Velocity m/s		P/S
Rigs-1	216	9291.00	14.09	2.731	4305	66	2576	35	2629	32	1.65
Rigs-1	220	9294.00	31.66	2.703	3331	19	2072	10	2066	10	1.61
Rigs-1	236	9307.00	36.42	2.710	3152	44	-	-	2045	19	1.54
Rigs-1	240	9311.00	37.71	2.715	2571	17	1674	8	1687	8	1.53
Rigs-1	244	9314.00	37.58	2.715	2865	19	1785	11	1828	14	1.59
Rigs-1	260	9326.00	40.78	2.710	2448	21	1604	9	1635	13	1.51
Rigs-1	264	9329.00	40.01	2.713	2433	14	1578	9	1589	11	1.54
Rigs-1	274	9337.74	36.58	2.710	2683	18	1759	12	1765	13	1.52
Rigs-2	121	2832.00	41.80	2.707	2086	17	1401	8	1431	9	1.47
Rigs-2	128	2834.00	42.53	2.707	2064	16	1365	11	1383	10	1.50
Rigs-2	136	2836.00	41.20	2.706	2072	13	1382	8	1390	9	1.49
Rigs-2	151	2840.12	43.44	2.717	2198	14	1413	8	1460	8	1.53
Rigs-2	162	2843.12	43.03	2.706	2323	18	-	-	1511	10	1.54
Rigs-2	176	2847.00	40.39	2.714	2704	27	1744	15	1709	16	1.57
Rigs-2	200	2854.00	44.94	2.673	1979	19	1300	12	1296	10	1.52
Rigs-2	204	2855.00	41.13	2.689	1959	11	1345	7	1326	8	1.47
Rigs-2	212	2857.00	42.30	2.697	2063	10	1397	7	1387	8	1.48
SA-1	755	3389.24	24.21	2.714	4048	43	2428	15	2415	16	1.67
SA-1	759	3399.20	27.43	2.729	3586	30	2151	13	2140	13	1.67
SA-1	760	3401.20	28.80	2.713	3485	37	2160	12	2162	18	1.61
SA-1	761	3403.52	30.50	2.719	-	-	-	-	-	-	-
SA-1	763	3407.31	26.56	2.702	3518	33	2175	14	2175	19	1.62
SA-1	767	3414.60	29.71	2.703	3466	28	2121	14	2118	14	1.64
SA-1	771	3419.96	31.42	2.714	3327	27	2054	14	2014	15	1.64
SA-1	774	3426.25	27.75	2.721	3663	28	2208	14	2246	15	1.65
SA-1	779	3436.36	23.18	2.710	3967	28	2390	15	2353	15	1.67
SA-1	780	3437.35	30.69	2.717	3382	21	2095	11	2069	13	1.62
SA-1	782	3440.70	27.65	2.717	3683	29	2264	17	2233	15	1.64
SA-1	783	3441.68	18.62	2.718	3980	57	2386	23	2451	26	1.65

Table 5.4: Ultrasonic velocities measured on WET plugs from the South Arne field – Tor formation.

Well name	plug no.	Depth Meter or feet	Porosity %	Gr. Dens g/cc	P-waves Velocity m/s		S1-waves Velocity m/s		S2-waves Velocity m/s		P/S
Rigs-1	220	9294.00	31.66	2.703	3335	20	1820	10	1830	10	1.83
Rigs-1	260	9326.00	40.78	2.710	2632	33	1373	10	-	-	1.92
Rigs-1	264	9329.00	40.01	2.713	2577	15	1344	9	1340	10	1.92
Rigs-2	121	2832.00	41.80	2.707	2441	14	1248	8	1250	13	1.95
Rigs-2	128	2834.00	42.53	2.707	2366	20	1134	10	1136	14	2.08
Rigs-2	136	2836.00	41.20	2.706	2429	15	1224	8	1221	11	1.99
Rigs-2	151	2840.12	43.44	2.717	2480	16	1249	8	1278	10	1.96
Rigs-2	200	2854.00	44.94	2.673	2311	18	1136	12	1103	11	2.06
Rigs-2	204	2855.00	41.13	2.689	2364	14	1186	8	1191	10	1.99
Rigs-2	212	2857.00	42.30	2.697	2429	13	1229	7	1232	9	1.97
SA-1	755	3389.24	24.21	2.714	4079	29	2242	20	2242	15	1.82
SA-1	760	3401.20	28.80	2.713	3597	21	1981	25	1987	24	1.81
SA-1	761	3403.52	30.50	2.719	3466	24	1855	19	1859	34	1.87
SA-1	763	3407.31	26.56	2.702	3598	23	1981	23	1976	17	1.82
SA-1	767	3414.60	29.71	2.703	3529	21	1961	12	1953	15	1.80
SA-1	771	3419.96	31.42	2.714	3396	26	1801	12	1849	14	1.86

Table 5.5: Ultrasonic velocities measured at varied saturations on 2 plugs.

Well name	plug no.	Sat. %	Porosity %	P-waves Velocity m/s	Error m/s	S1-waves Velocity m/s	Error m/s	S2-Waves Velocity m/s	Error m/s	Vp/Vs
Rigs-2	62	0.2	39.75	2546	14	1643	10	1646	9	1.55
Rigs-2	62	25.2	39.75	2361	14	1523	7	1508	8	1.56
Rigs-2	62	49.9	39.75	2304	12	1468	8	1477	8	1.56
Rigs-2	62	75.0	39.75	2310	14	1433	7	1438	8	1.61
Rigs-2	62	99.3	39.75	2662	14	1387	8	1404	8	1.91
Rigs-2	100	0.8	20.29	4230	27	2610	16	2612	15	1.62
Rigs-3	100	25.0	20.29	4155	22	2541	15	2543	14	1.63
Rigs-2	100	50.0	20.29	4157	29	2507	13	2509	15	1.66
Rigs-2	100	75.0	20.29	4195	23	2476	14	2478	14	1.69
Rigs-2	100	98.5	20.29	4291	26	2451	13	2453	15	1.75

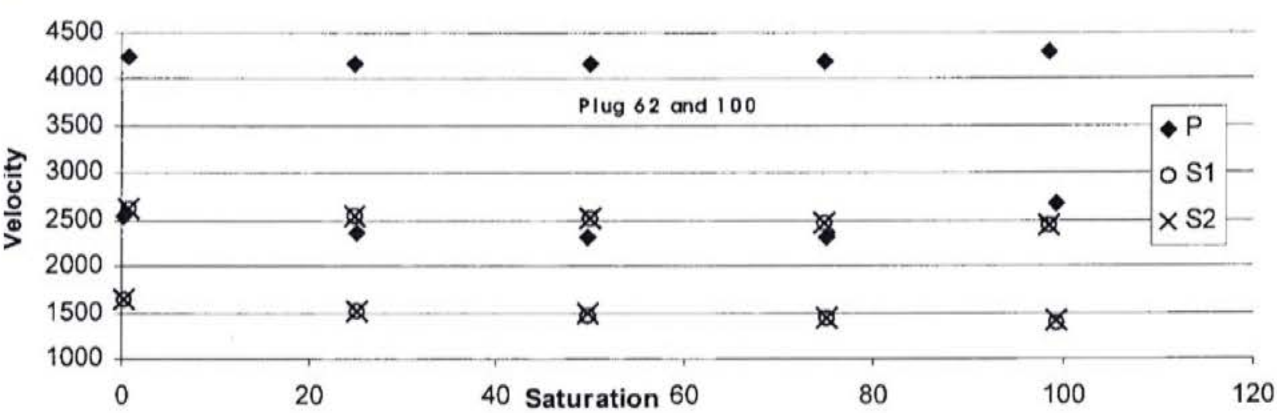

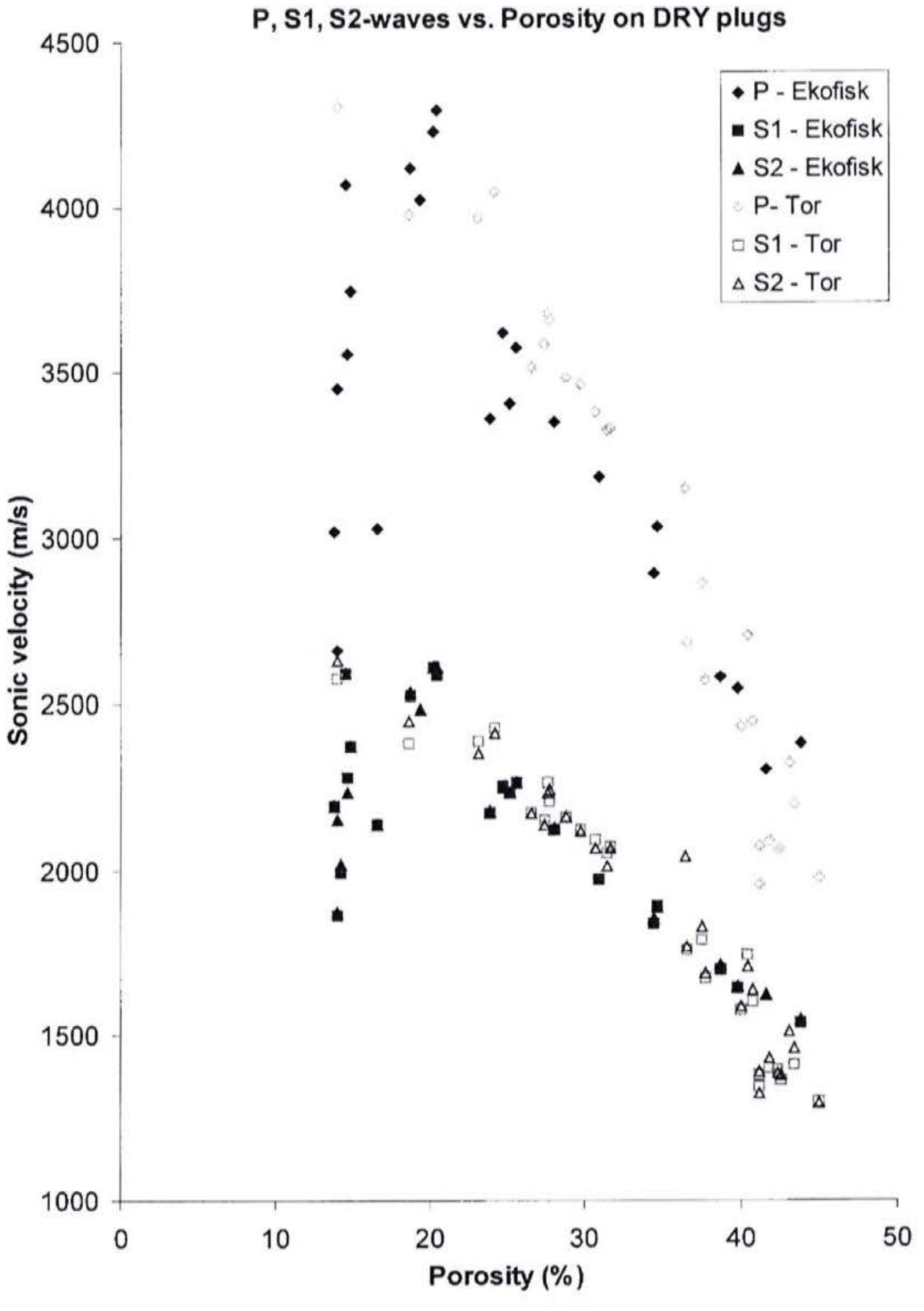

Figure 5.1: P,S1,S2 waves vs. porosity on DRY plugs from the Ekofisk and Tor formation.

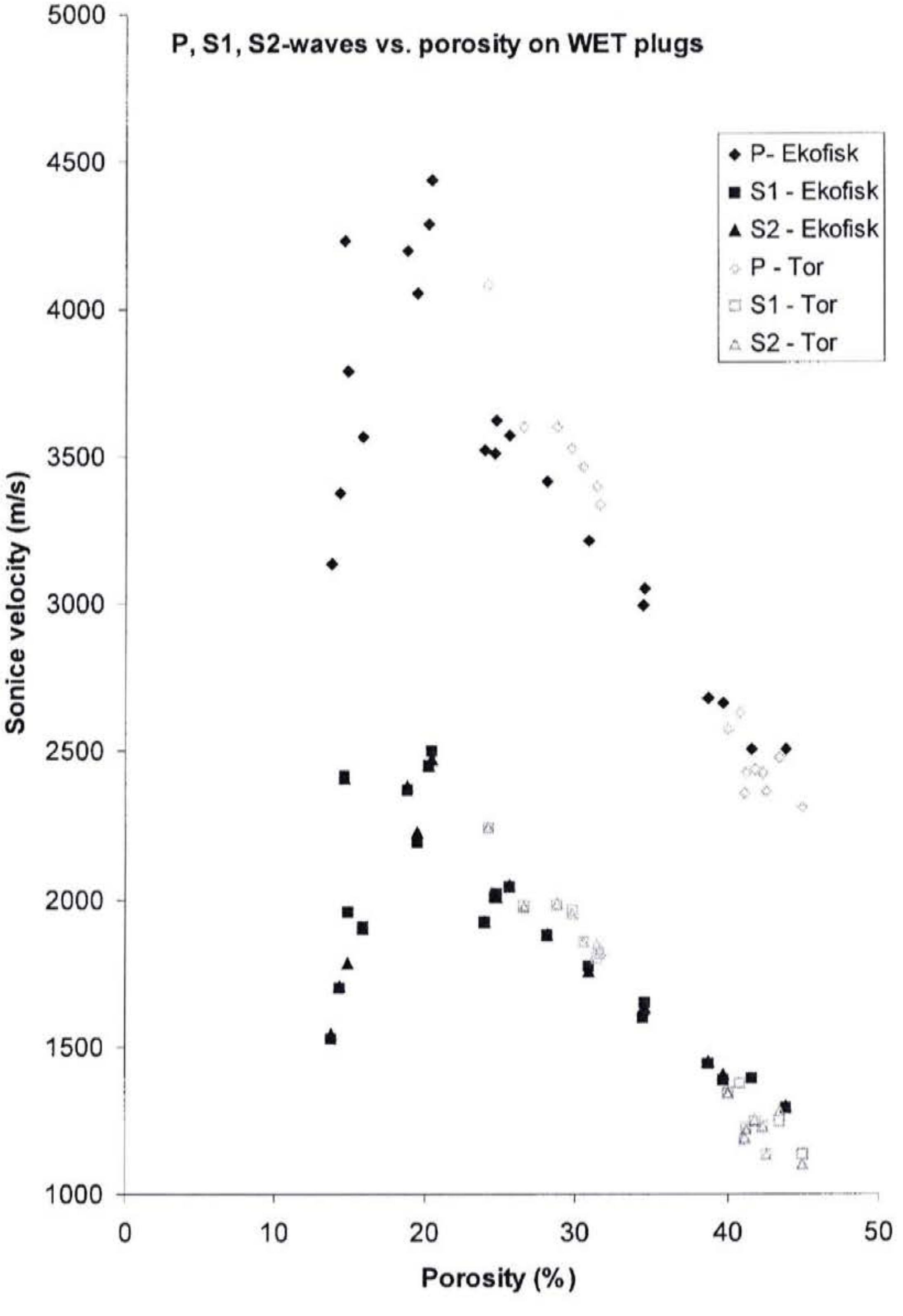

Figure 5.2: P,S1,S2 waves vs. porosity on WET plugs from the Ekofisk and Tor formation.

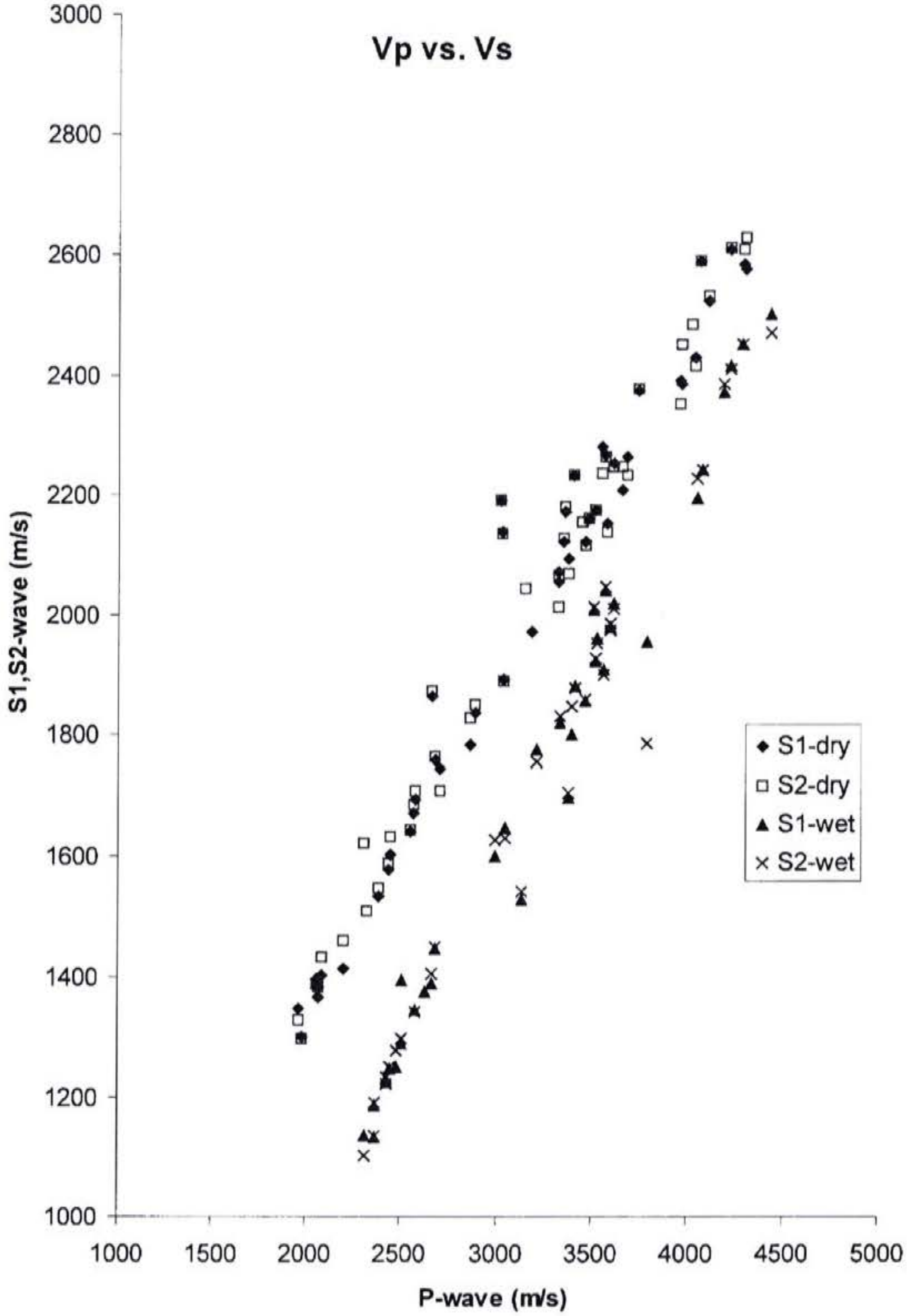

Figure 5.3: Vp vs Vs on DRY and WET plugs from the Ekofisk and Tor formation.

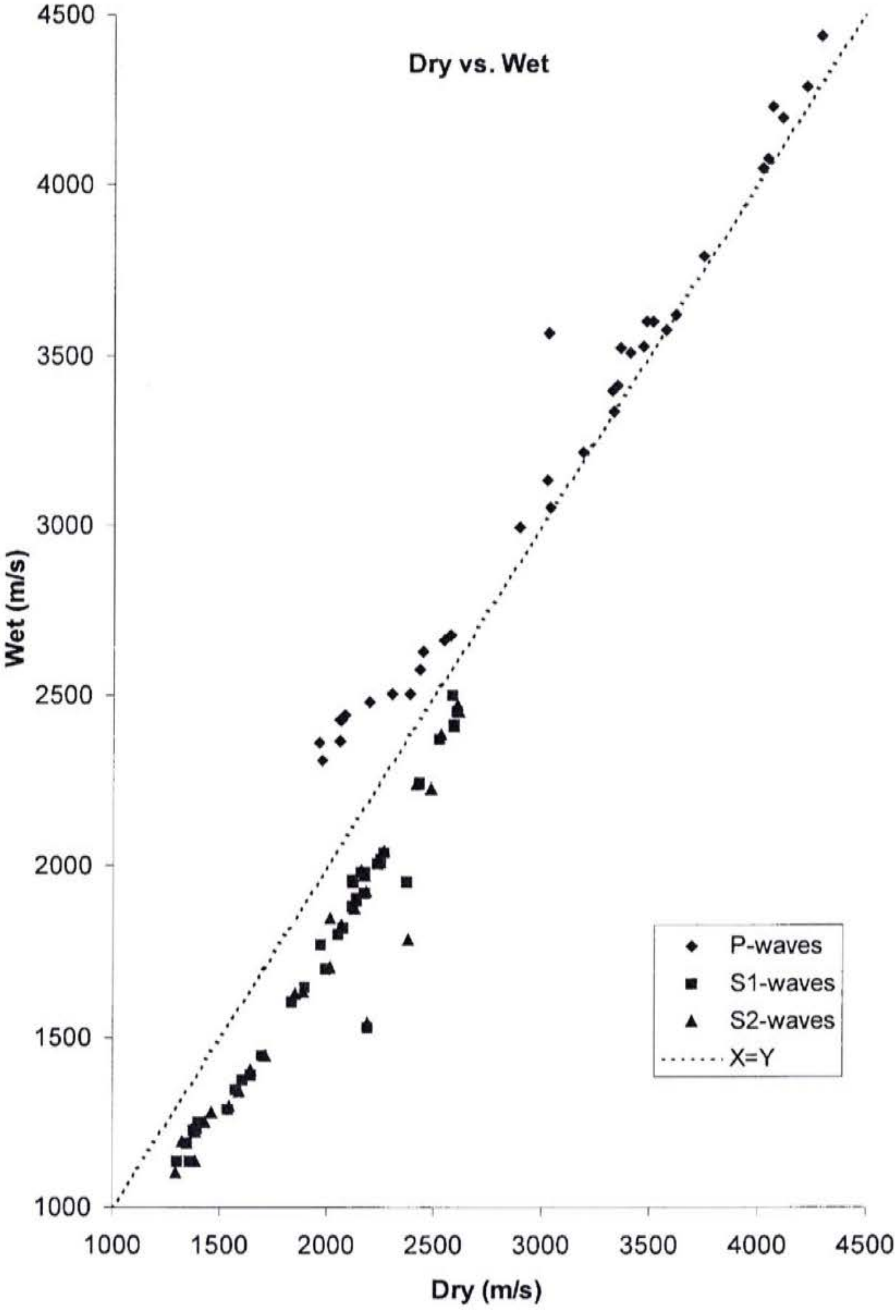

Figure 5.4: DRY vs. WET on plugs from the Ekofisk and Tor formation.

6. Documentation of data.

All the ultrasonic measurements were saved digitally and are stored on the CD-ROM. The data can be found in the "Measured sonic data" folder. The data is stored as a comma separated value file (*.csv) and as a screenshot of the oscilloscope in gif format (*.gif)

The picked maximum by the arrival picker is shown in the "plots" folder. The picked maximum is marked by a blue line.

The analysed of data can be seen in the "Tor.xls" and "Ekofisk.xls" excel97 files.

The filename convention of the files from Ekofisk is the following:
The well name is given by **R1** (Rigs-1) or **R2** (Rigs-2). The plug number is listed as the **number**. The type of velocity measurement is given as **p** (P-wave) or **s1** (S1-wave) or **s2** (S2-wave) and then the conditions of the plug is given as **d** (dry) or **s** (saturated).

E.g. "R13s1s.csv" is the data file from: well: Rigs-1 , plug 3 , S1-wave , saturated plug.

The filename convention for the files from Tor is the following:
The plug number is given as a **number.** The type of velocity measurement is given as **P** (P-wave) or **S1** (S1-wave) or **S2** (S2-wave). The applied hydrostatic pressure is given as **75** (75 bar) and then the conditions of the plug is given as **W** (Wet) or not marked if is a dry measurements.

E.g. "759S275.csv" is the data from: plug 759 , S2-wave , 75 bar hydrostatic sleeve pressure , dry plug.

Seismic AVO inversion of 2D seismic data for use in the EFP 2001 Rock Physics Of Impure Chalk project using the ISIS Software Package

Ødegaard A/S

Ødegaard A/S

A Company in the Ødegaard & Danneskiold-Samsøe Group

Report 02.24017.01

Seismic AVO inversion of 2D seismic data for use in the EFP 2001 Rock Physics Of Impure Chalk project using the ISIS Software Package

EFP 2001

March 2003

Prepared by

Anders Bruun

Bruun, Anders

Seismic AVO inversion of 2D seismic data for use in the EFP 2001 Rock Physics Of Impure Chalk project using the ISIS Software Package

Report 02.24017.01
2002.

Summary

The work described in this report is a part of the EFP 2001 Rock Physics of Impure Chalk project.

2D lines (near and far offset) extracted from a 3D seismic survey covering the South Arne in the Danish part of the North Sea were inverted for calculation of AVO attributes. The inversion was carried out for the time window 1.900–3.600 and was targeted on the chalk interval.

Well log data were provided for the wells Rigs-1, Rigs-2, I-1x and Sa-1 by the project. The well logs comprise sonic, shear, density, porosity, gamma ray logs check shots and deviation data. The wells Rigs-1, Rigs-2 and I-1x are near vertical and were treated as such. The well Sa-1 are treated as deviated.

Using a least squares wavelet estimation method with constrain on the phase, wavelets were estimated for each of the two offset stacks. The wavelets were estimated from well I-1x.

Low-frequency components of the acoustic impedance variations are not present in the seismic data. Since this information is essential to the interpretation, it should be accounted for in the seismic inversion. Simple low-frequency impedance models for use in the offset stack inversions were constructed by extrapolating the angle impedance well logs through the 3D volume by using seismic horizons, followed by low-pass filtering.

The final inversions model 93.7 % of the seismic energy for the near offset stack and 93.4 % for the far offset stack.

The offset stack inversions are both generally rated as good in terms of match with the acoustic impedance logs from the wells.

The AVO attributes were computed from the near and far offset stack angle impedance inversions with low-frequency information. The resulting AVO attributes values where extracted at well positions and delivered as ASCII tables. The results delivered where from the wells Rigs-1, Rigs-2, I-1x and Sa-1.

The avo results consist of:

1. Acoustic impedance.
2. Shear impedance.
3. Poisson's ratio.

The AVO results are generally rated as good in terms of match with the logs from the wells.

Low values of Poisson ratio indicates the presence of oil clearest in the high-porous chalk at the well Rigs-2.

Contents

List of Figures

List of Tables

CHAPTER 1

Introduction

This report describes the results of an ISIS global seismic inversion requested by EFP2001 and carried out by Ødegaard A/S. Near and far offset stacks were inverted for calculation of AVO attributes in the interval Top Chalk to Base Chalk.

1.1 Seismic data

Near and far offset 2D inlines were extracted from a 3D seismic survey covering the South Arne field in the Danish North Sea.

The seismic inversions were targeted on the interval Top Chalk to Base Chalk. Figure 1.1 shows the outline of the seismic data and the inverted 2D inlines.

1.2 Well data

Sonic, density, porosity and gamma ray logs and check shots plus deviation data were supplied for the six wells Rigs-1, Rigs-2, I-1x and Sa-1. Shear sonic logs were available for all wells except well Sa-1. For the wells Rigs-1, Rigs-2 and Sa-1 fluid substituted logs was generated by GEUS using a MUHS approach (Walls et al. (1998)). The surface locations of the wells are given in Table 1.1.

Well	UTM-X(m)	UTM-Y(m)
Rigs-1	575581	6216839
Rigs-2	575835	6217754
I-1x	577802	6212763
Sa-1	576617	6215654

Table 1.1: *The surface locations of the wells.*

1.3 Horizon data

Four interpreted horizons were available for the seismic data cube. These were Top Chalk, Top Tor, Base Tor and Base Chalk.

1.4 Goal of the project

The goal of the AVO inversions was to calculate AVO attributes at well locations and compare them with estimated and MUHS corrected well logs in the Top Chalk - Base Chalk interval. This is to test the possibility of light oil detection in chalk reservoirs by AVO inversion.

1.5 Seismic inversion approach

The near and far offset 2D lines were processed separately and were performed in the following steps:

- The far offset seismic data were aligned to the near offset using a statistical alignment method (See Section B.8).
- Logs from the wells were evaluated and calibrated against the near and far offset 2D seismic data (Sections A.1 and 2.1).
- Suites of wavelets were estimated from the wells using a least squares estimation method and wavelets for the near and far offset stack inversions chosen (Sections A.3 and 2.2 and 2.2.1).
- Two 3D low-frequency angle impedance models were calculated using the well logs and the interpreted horizons (Sections B.5 and 3.2). These low-frequency models were used for the near and far offset stack inversions.
- For each of the offset stacks, the optimum inversion parameters were determined (Sections B.3 and 3.3), and the seismic 2D inlines were inverted for near and far angle impedance with low-frequency information (Section 3.4).
- AVO attributes, Poisson's ratio, acoustic impedance and shear impedance were calculated at the well location from the near and far offset inversion results with the low-frequency information (Section 3.5).

References

Walls, J. D., Dvorkin, J. & Smith, B. A. 1998. Modeling seismic velocity in Ekofisk Chalk. SEG 68th annual conference. 1016-1019.

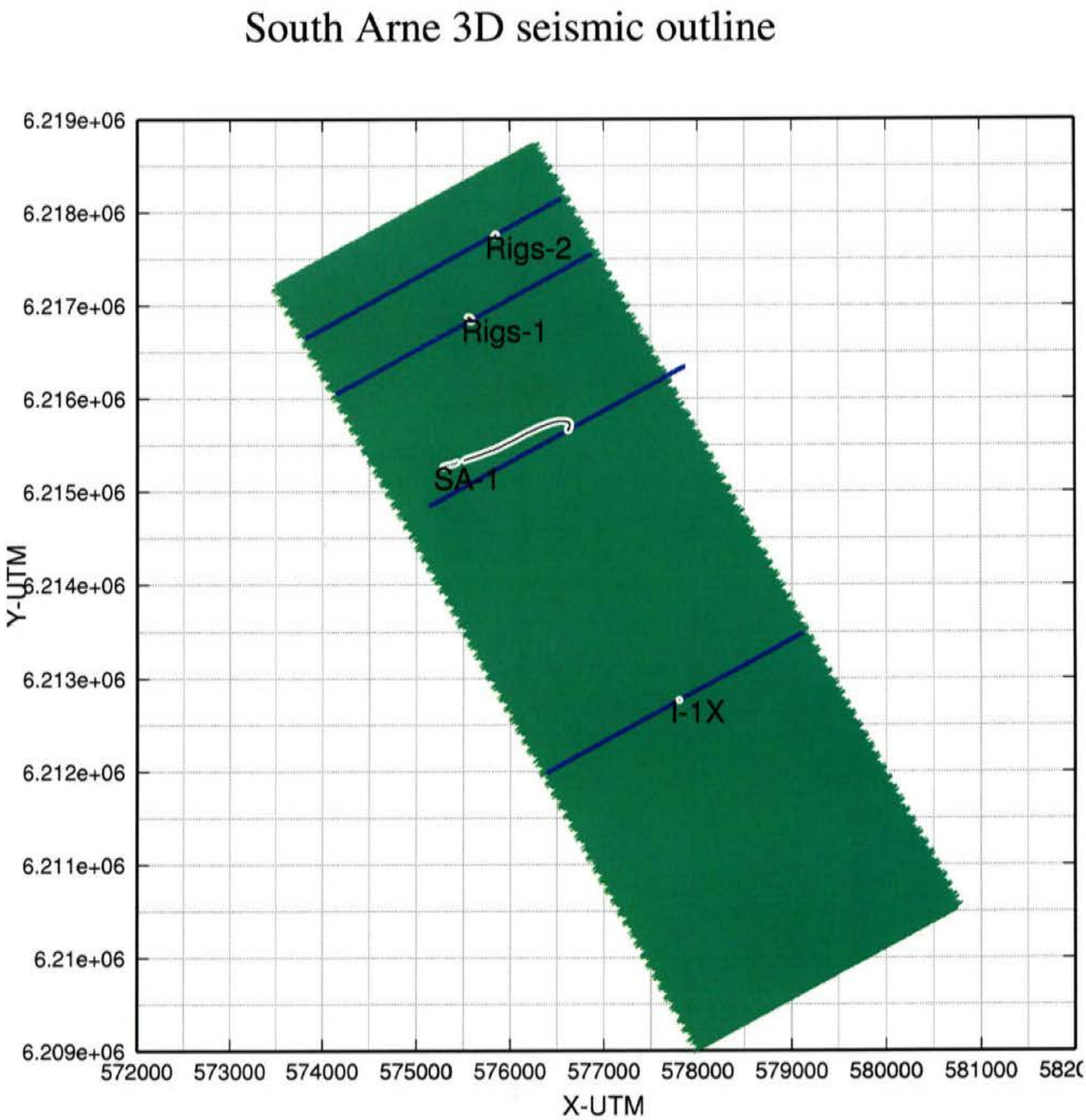

Figure 1.1: *Outline of the seismic data cube (green rectangle), and well paths. Blue lines are the path of the extracted 2D lines used for the AVO inversions*

CHAPTER 2

Wavelet estimation results

This chapter describes the log calibration and the wavelet estimation.

2.1 Log alignment

Once the optimum wavelets have been found for the seismic inversions of the offset stacks (see Section 2.2), the logs from the other wells were calibrated using the optimal wavelet (see Section A.1). Where necessary, visual ties between the logs and the closest seismic trace were applied in order to stretch, squeeze or shift the logs. The visual ties for each well were found by comparing the seismic trace at the well location with the synthetic seismic trace obtained by convolving the optimum wavelet for the inversion with the angle reflectivity log from the well. The visual ties for each well are listed in Table 2.1.

Rigs-1	Rigs-2	I-1x	Sa-1
2.000→2.020	1.900→1.912	2.500→2.504	2.600→2.608
		2.600→2.604	
		2.900→2.904	
		3.040→3.048	

Table 2.1: *Visual ties applied to the well logs during calibration with the offset stacks using the optimum near-stack and far-stack wavelets derived from well I-1x. All numbers are in s TWT.*

Figures D.1 to D.8 in Appendix D shows the raw well log data and the final calibrated and resampled logs for each well at target level.

2.2 Least squares wavelet estimation

Wavelet estimation was carried out for the two offset stacks (see Sections C.5 to C.7) at all the well locations using the least squares estimation method described in Section A.3.

A number of different estimation windows were tested for each well. The wavelet experiments were performed for wavelet lengths from 40 to 176 ms using a step length of 4 ms. The main criteria for selecting the optimum wavelet are described in Section A.3. The wavelet was constrained to a constant phase.

The estimated wavelets were taken forward to test inversions. The results of the test inversions indicated that wavelets estimated in well I-1x had the better inversions capabilities.

The optimum offset stack wavelets from well I-1x are specified in Table 2.2 and shown in Figures 2.1 and 2.2.

Well	Estimation window on log [s TWT]	Wavelet length [ms]	Relative misfit energy	Cross-correlation
I-1x (near)	2.536–3.004	144	0.3943	0.779
I-1x (far)	2.600–3.000	44	0.3415	0.814

Table 2.2: *Specification of the optimum wavelets from well I-1x and their fitting properties.*

Figures 2.1 and 2.2 show the suites of wavelets estimated from well I-1x which contain the optimum wavelets for the near and far offset stacks. The following is also presented: Curves of Akaike's FPE and the relative misfit energy; the phase and amplitude spectra of the optimum wavelets; the amplitude spectra in the wavelet estimation window of the seismic traces at the well locations and the synthetic seismic traces. The near offset stack wavelet is zero phase-like and the far offset wavelet is minimum phase-like. Both wavelets have SEG normal polarity (a positive reflection coefficient corresponds to a white trough on the seismic data). The wavelets estimated from well I-1x are considered good and stable wavelets for inversion purposes.

2.2.1 Wavelet validation

Figures 2.3 – 2.4 show, the synthetic seismic traces obtained from all wells using the optimum wavelets estimated in well I-1x for the near and far offset stacks.

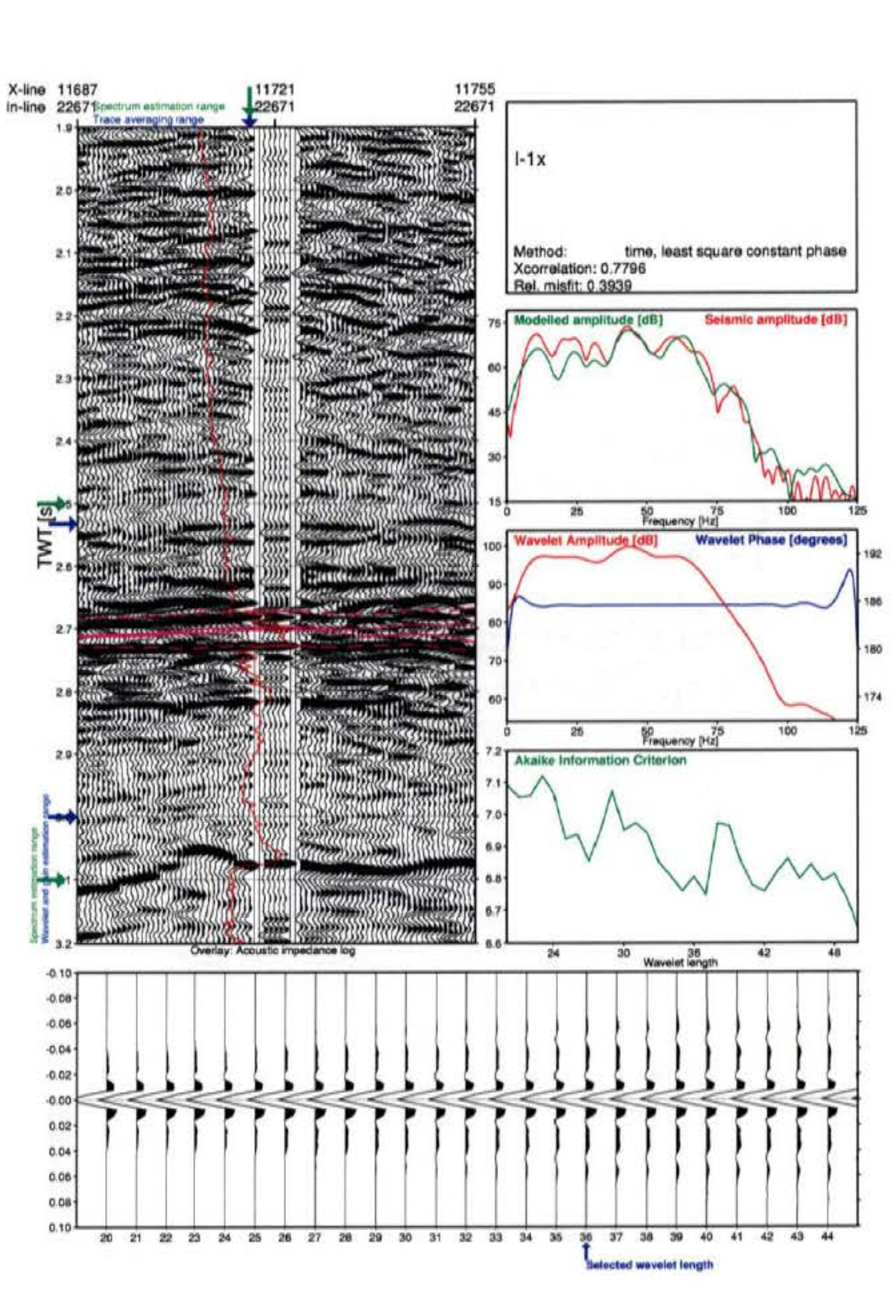

Figure 2.1: *Near offset stack: Least squares wavelet estimation in well I-1x.* **Bottom**: *Wavelet suite. The lengths of the predicted wavelets range from 20 samples to 44 samples (80 ms to 176 ms, horizontal axis).* **Left**: *Synthetic seismic trace obtained by convolution of the optimum wavelet (length 36 samples) with the near offset angle reflectivity log from the well inserted into the seismic data.* **Top right**: *Amplitude spectra in the wavelet estimation window of the seismic trace at the well location and the synthetic seismic trace.* **Middle right**: *Phase and amplitude spectra of the optimum wavelet.* **Bottom right**: *Relative misfit energy, Akaike's FPE, cross-correlation and relative number of parameters for the wavelet suite. Left-hand axis refers to the curves of relative misfit energy and Akaike's FPE. Right-hand axis refers to the curves of cross-correlation and relative number of parameters.*

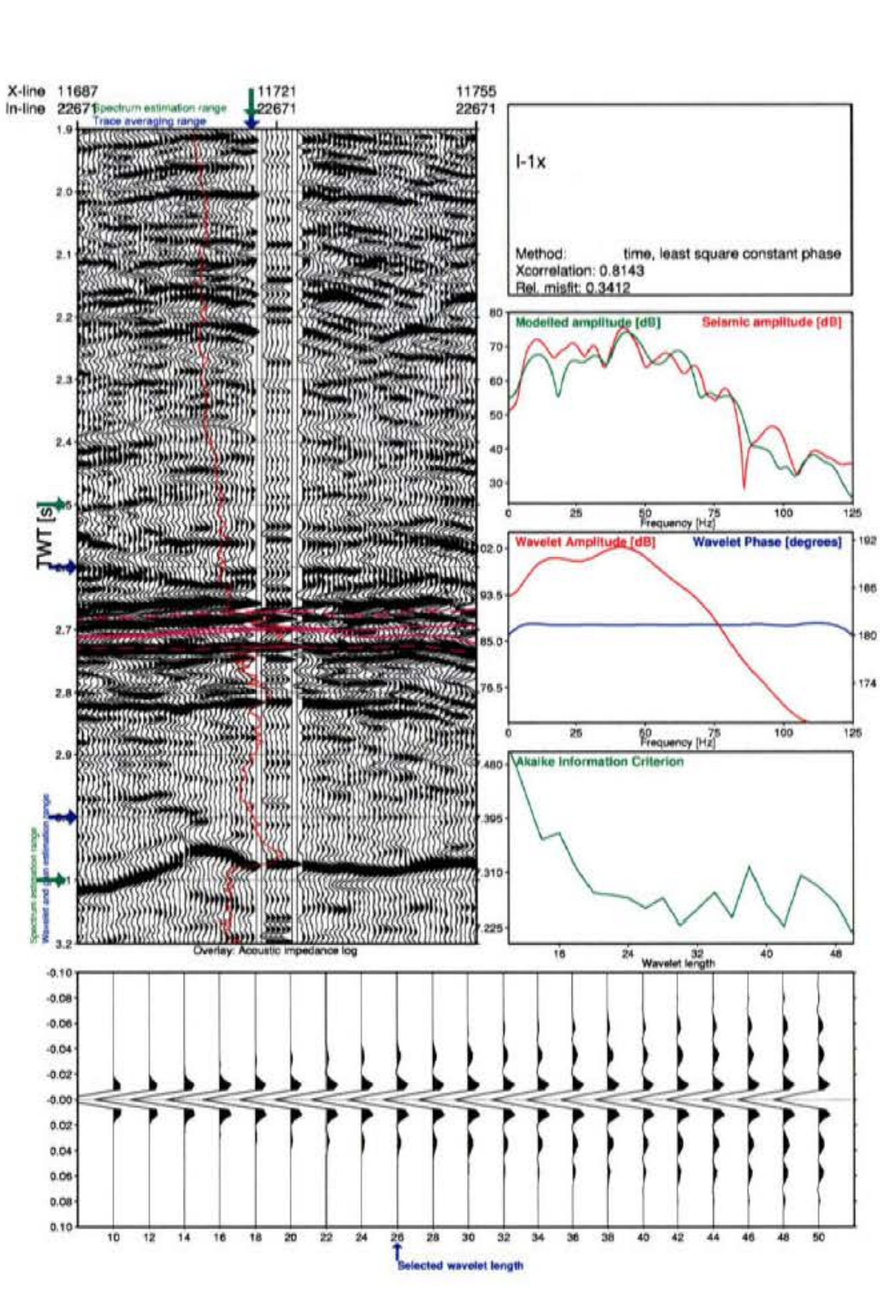

Figure 2.2: *Near offset stack: Least squares wavelet estimation in well I-1x.* **Bottom***: Wavelet suite. The lengths of the predicted wavelets range from 10 samples to 55 samples (80 ms to 176 ms, horizontal axis).* **Left***: Synthetic seismic trace obtained by convolution of the optimum wavelet (length 25 samples) with the near offset angle reflectivity log from the well inserted into the seismic data.* **Top right***: Amplitude spectra in the wavelet estimation window of the seismic trace at the well location and the synthetic seismic trace.* **Middle right***: Phase and amplitude spectra of the optimum wavelet.* **Bottom right***: Relative misfit energy, Akaike's FPE, cross-correlation and relative number of parameters for the wavelet suite. Left-hand axis refers to the curves of relative misfit energy and Akaike's FPE. Right-hand axis refers to the curves of cross-correlation and relative number of parameters.*

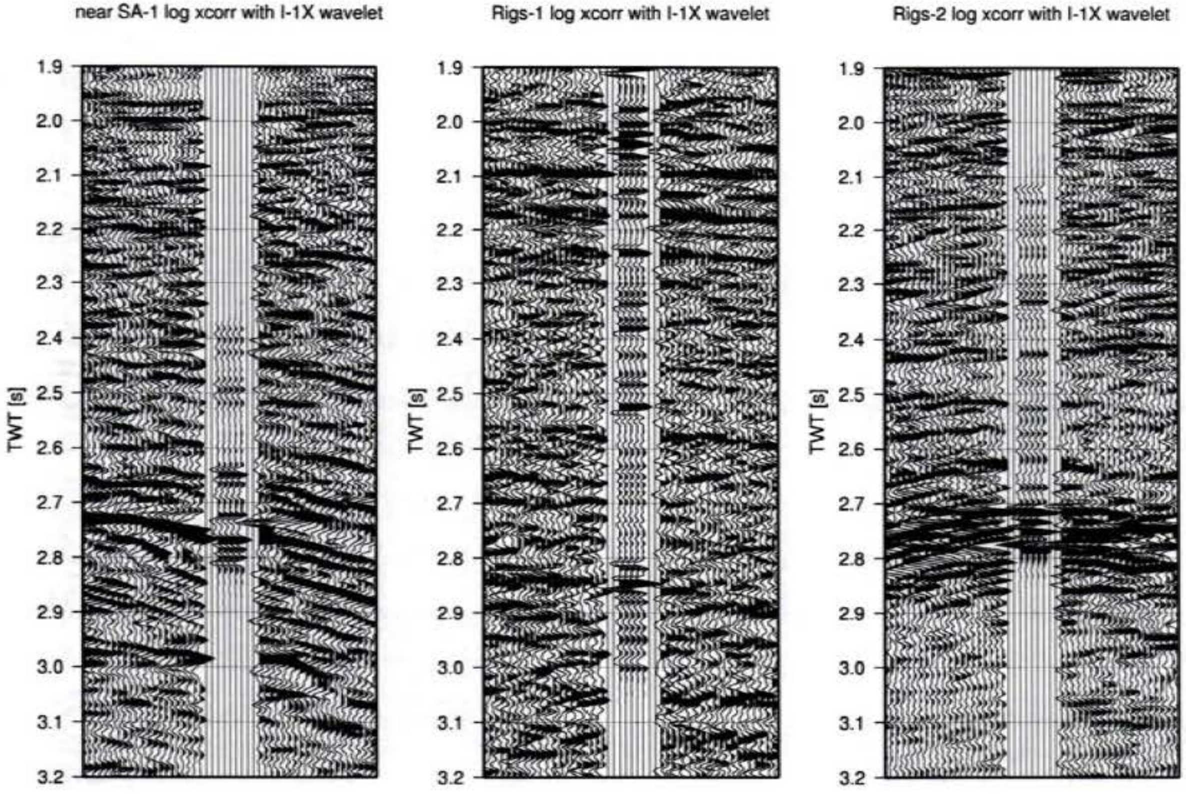

Figure 2.3: *Crossvalidation near offset: Synthetic seismic trace from well Rigs-1, Rigs-2 and Sa-1 inserted into the seismic at well position. The synthetic traces are obtained by convolution of the optimum near stack wavelet from well I-1x with the near stack angle reflectivity log for the wells.*

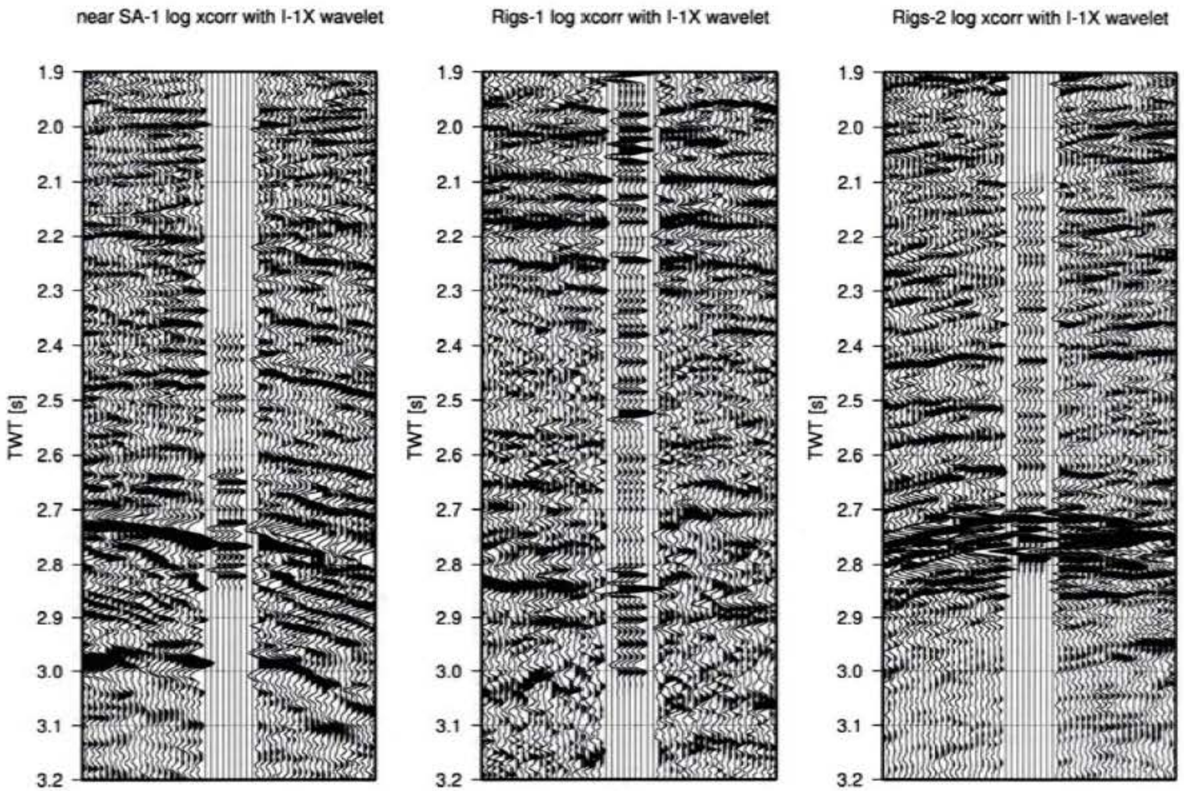

Figure 2.4: *Crossvalidation far offset: Synthetic seismic trace from well Rigs-1, Rigs-2 and Sa-1 inserted into the seismic at well position. The synthetic traces are obtained by convolution of the optimum near stack wavelet from well I-1x with the near stack angle reflectivity log for the wells.*

CHAPTER 3

Seismic AVO inversion results

This chapter describes the inversion parameters used for the final seismic inversions and the results delivered to EFP2001.

3.1 Inversion window

Near and far offset 2D inlines passing trough the wells were inverted for angle impedance between 1.900 and 3.200 s TWT.

3.2 Prior knowledge

For the absolute angle impedance inversion results, i.e. the inversion results including low-frequency information, a low-frequency angle impedance model was created for each offset-stack. The low-frequency angle impedance model was constructed using the calibrated angle impedance logs from the four wells and the four interpreted horizons available, Top Chalk, Top Tor, Base Tor, and Base Chalk (see Sections B.5 and C.7).

A suite of tests was performed to find the optimum low-pass filter for construction of the low-frequency models for use in the final near and far offset stack inversions. The low-pass filter used to build the final low-frequency models is shown in Figure 3.1.

3.3 Determination of inversion parameters

Table 3.1 shows the values of the seismic inversion parameters (see Section B.3) which were determined by a parameter study and used in the final inversions. The inversion results are stable in the neighborhood of the selected parameter values.

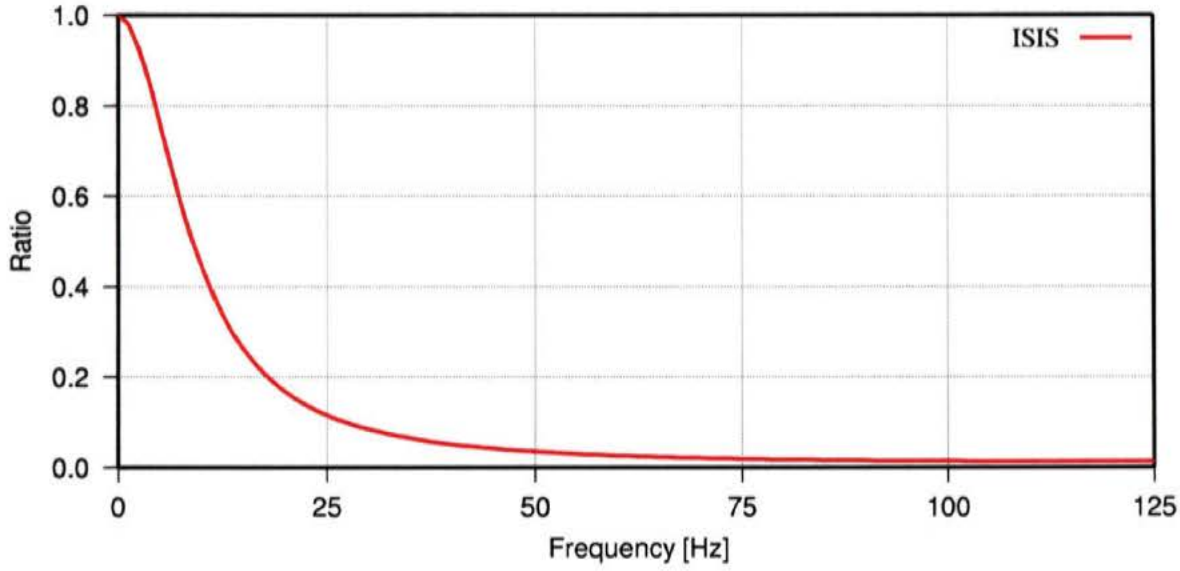

Figure 3.1: *The low-pass filter used for generating the angle impedance low-frequency models.*

Inversion parameter	Value	Value
	Near stack	Far stack
Signal-to-noise ratio, RSNR	4.000	4.000
Horizontal continuity, RALPHA	0.120	0.080
Deviation of prior model, RSIGMA	0.150	0.100
Threshold for reflection coeff., R1	0.02	0.015

Table 3.1: *Seismic inversion parameter values used for the ISIS global seismic inversions.*

3.4 Inversion results

Table 3.2 shows the amount of energy of the seismic volumes modelled by the final inversions.

Data	Energy modelled [%]
Near stack	93.7
Far stack	93.4

Table 3.2: *The amount of energy modelled in the final seismic inversions.*

Extracts from the seismic data and the final inversion results are presented in Figures 3.3 to 3.9. The presentation consists of:

- Near and far offset stack seismic data extracted along part of in-line 23097 (see Figures 3.2 and 3.6).
- Near and far offset stack seismic data, synthetic seismic traces and residual traces

extracted along part of in-line 23097 (see Figures 3.3 and 3.7). The synthetic seismic traces are derived by convolution between the wavelet and the reflectivity volume determined from the angle impedance inversion result with low-frequency information. The residual traces are equal to the difference between the seismic data and the synthetic seismic traces.

- Angle impedance inversion result with low-frequency information extracted along part of in-line 23097 for the near and far offset stack data (see Figures 3.4 and 3.8).
- Angle impedance inversion result with low-frequency information, angle impedance inversion result without low-frequency information and the low-frequency model extracted along part of in-line 23097 for the near and far offset stack data (see Figures 3.5 and 3.9).
- Angle impedance logs from well Rigs-2 for the near and far offset stack data inserted into the angle impedance inversion results with low-frequency information (see Figures 3.10 and 3.11). Similar plots for wells Rigs-1, I-1x and Sa-1 are presented in Appendix E.

3.5 Estimated Poisson's ratio, acoustic impedance and shear impedance volumes

Figures 3.12–3.14 show the Poisson's ratio log, the acoustic impedance log and the shear impedance log of well Rigs-2 inserted into the corresponding volume estimated from the near and far offset stack inversion results with low-frequency information. Similar plots for wells Rigs-1, I-1x and Sa-1 in Appendix F.

3.6 Conclusions on AVO results

The estimated AVO attributes are generally validated as good to acceptable. Their quality reflects the quality of the angle stack inversion results and thereby the quality of the input offset stack.

The AVO results shows that is is possible to detect light oil in the chalk reservoir by AVO inversion.

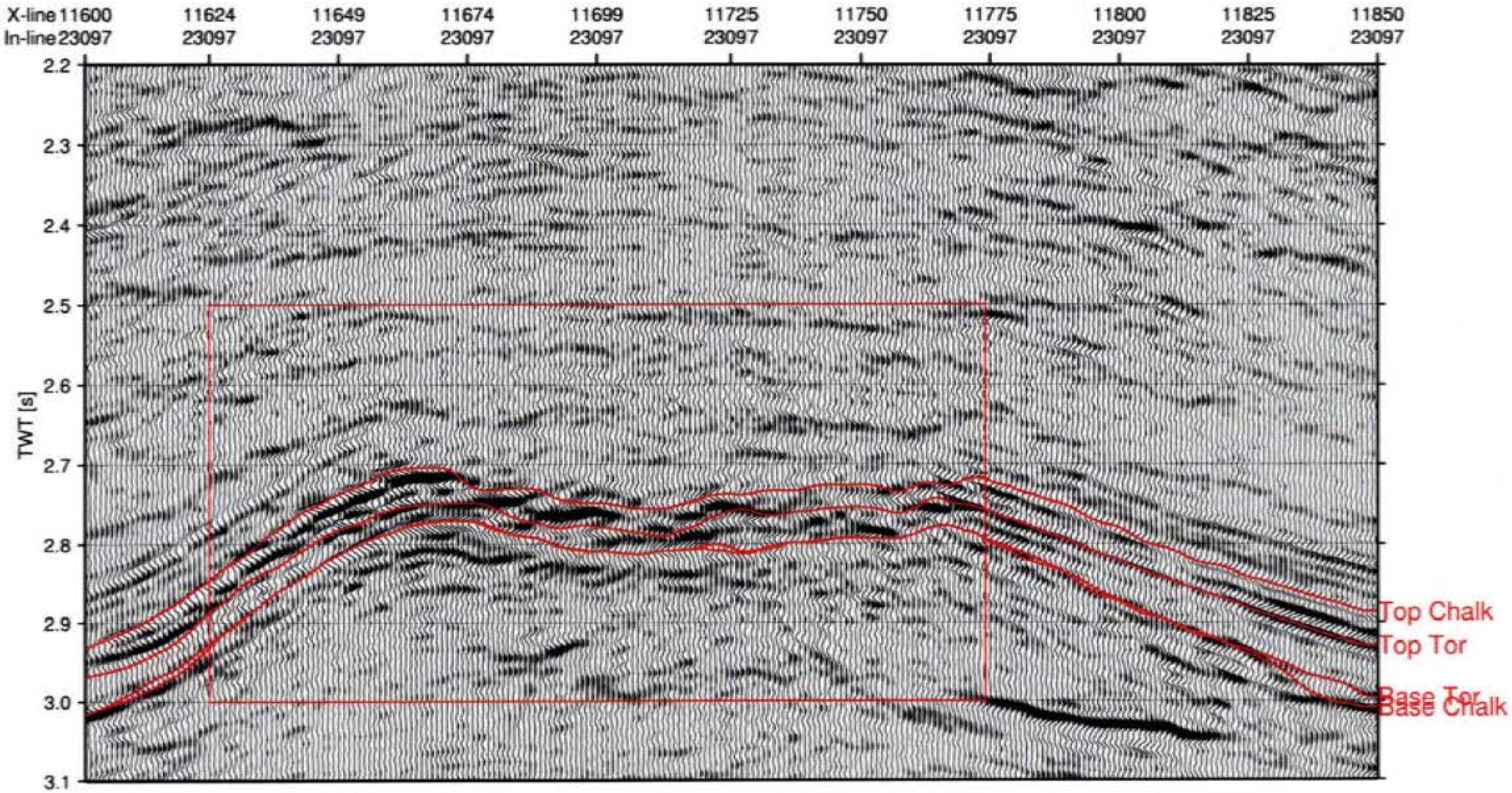

Figure 3.2: *Near offset stack: Seismic data extracted along in-line 23097. The horizons are shown in green. The box marks the outline of the sections shown in Figure 3.3.*

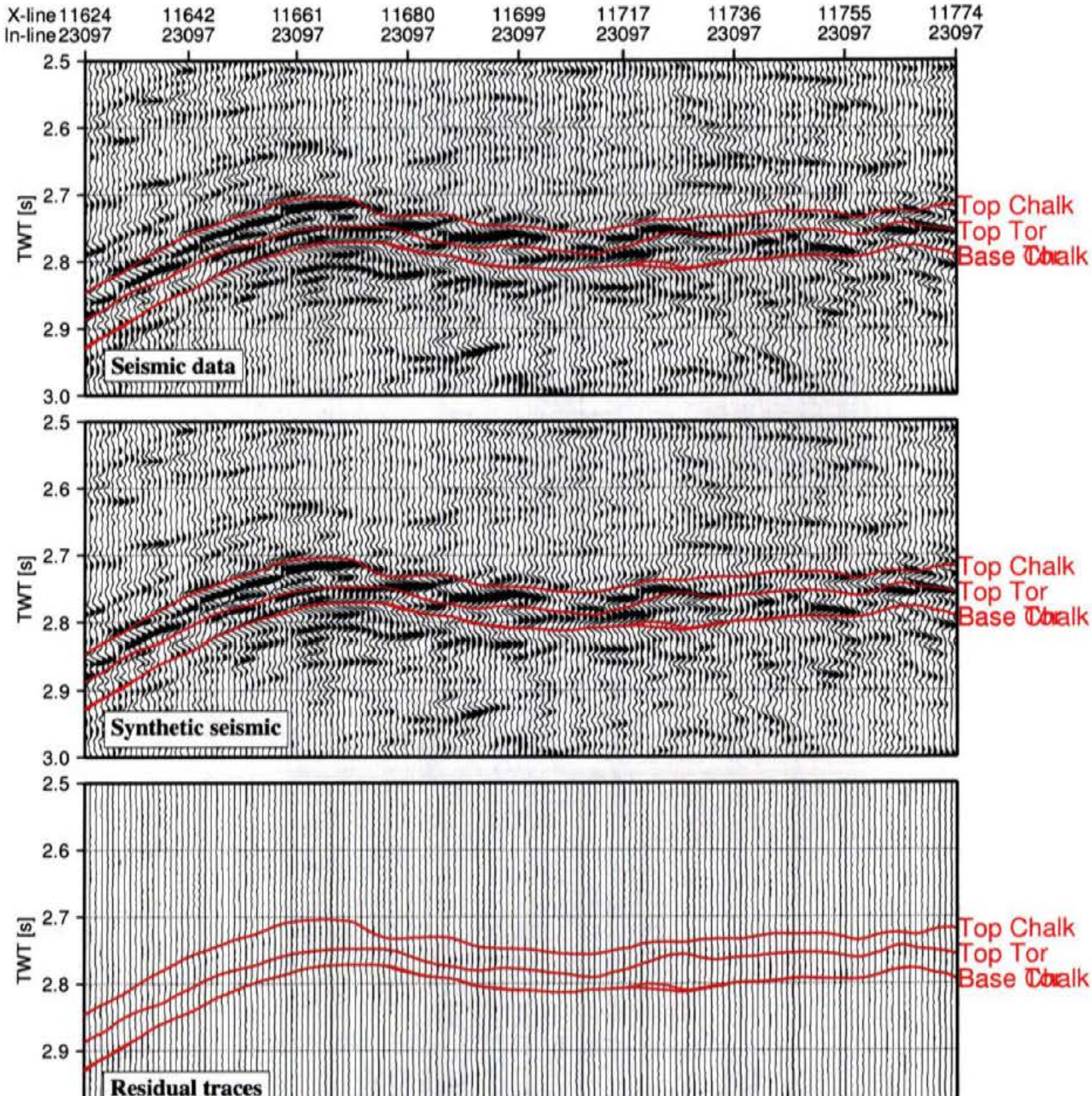

Figure 3.3: *Near offset stack: Seismic data (top), synthetic seismic (centre) and residual traces (bottom) extracted along part of in-line 23097. The horizon are shown in green.*

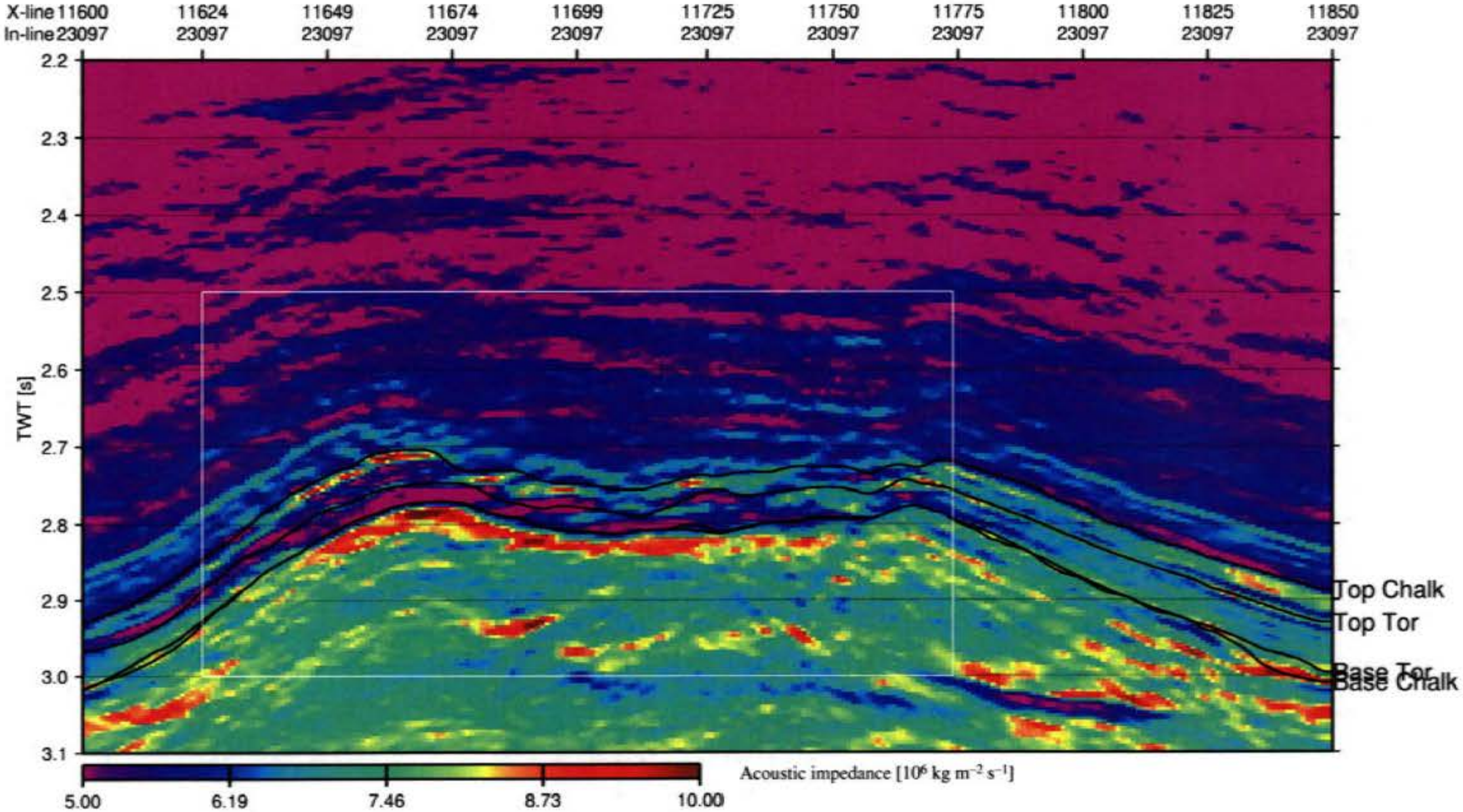

Figure 3.4: *Near offset stack: Angle impedance inversion result with low-frequency information from in-line 23097. The horizons are shown in black. The box marks the outline of the sections shown in Figure 3.5.*

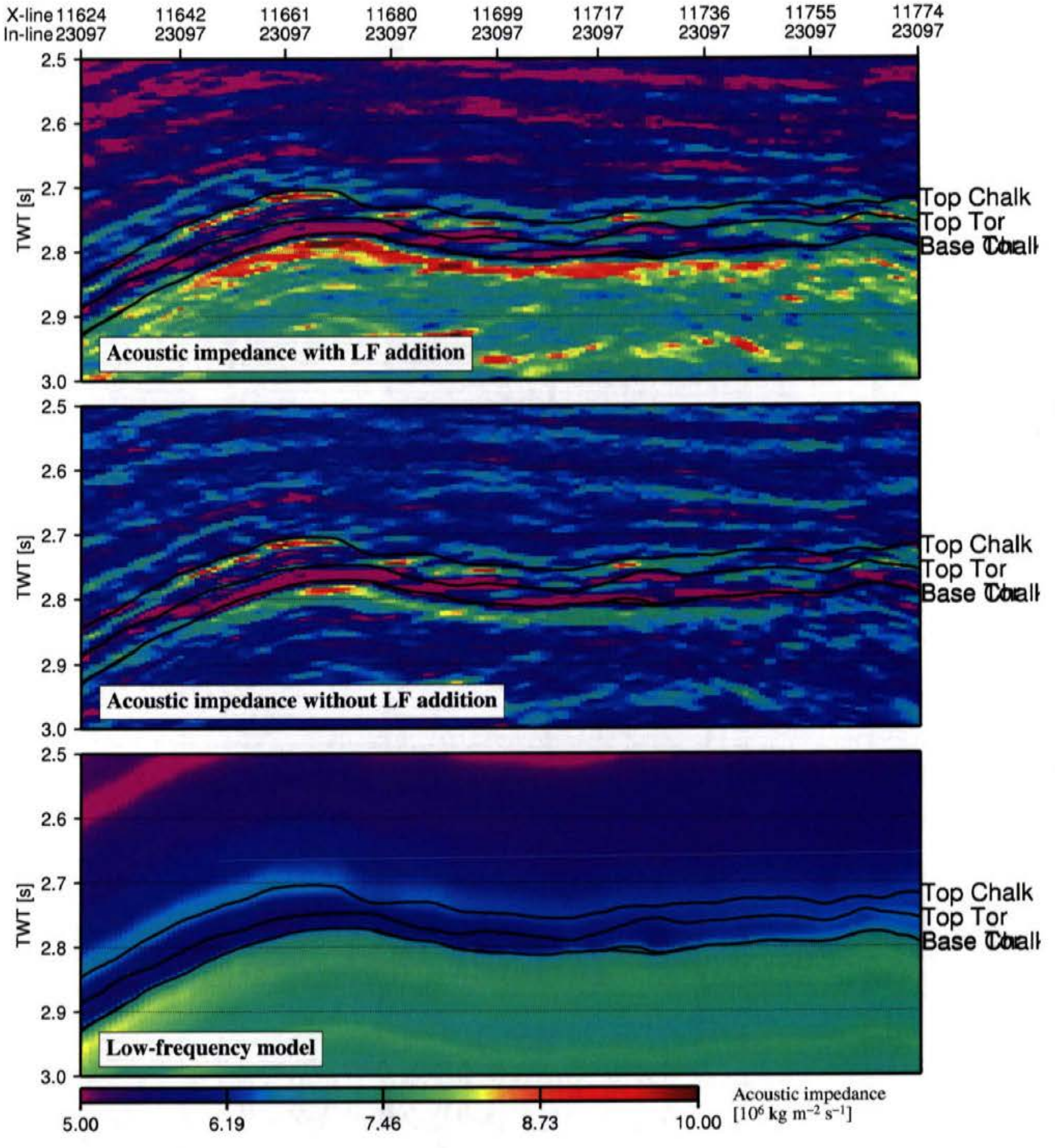

Figure 3.5: *Near offset stack: Angle impedance inversion result with low-frequency information (top), inversion result without low-frequency information (centre) and the low-frequency model (bottom) extracted along part of in-line 23097. The horizons are shown in black.*

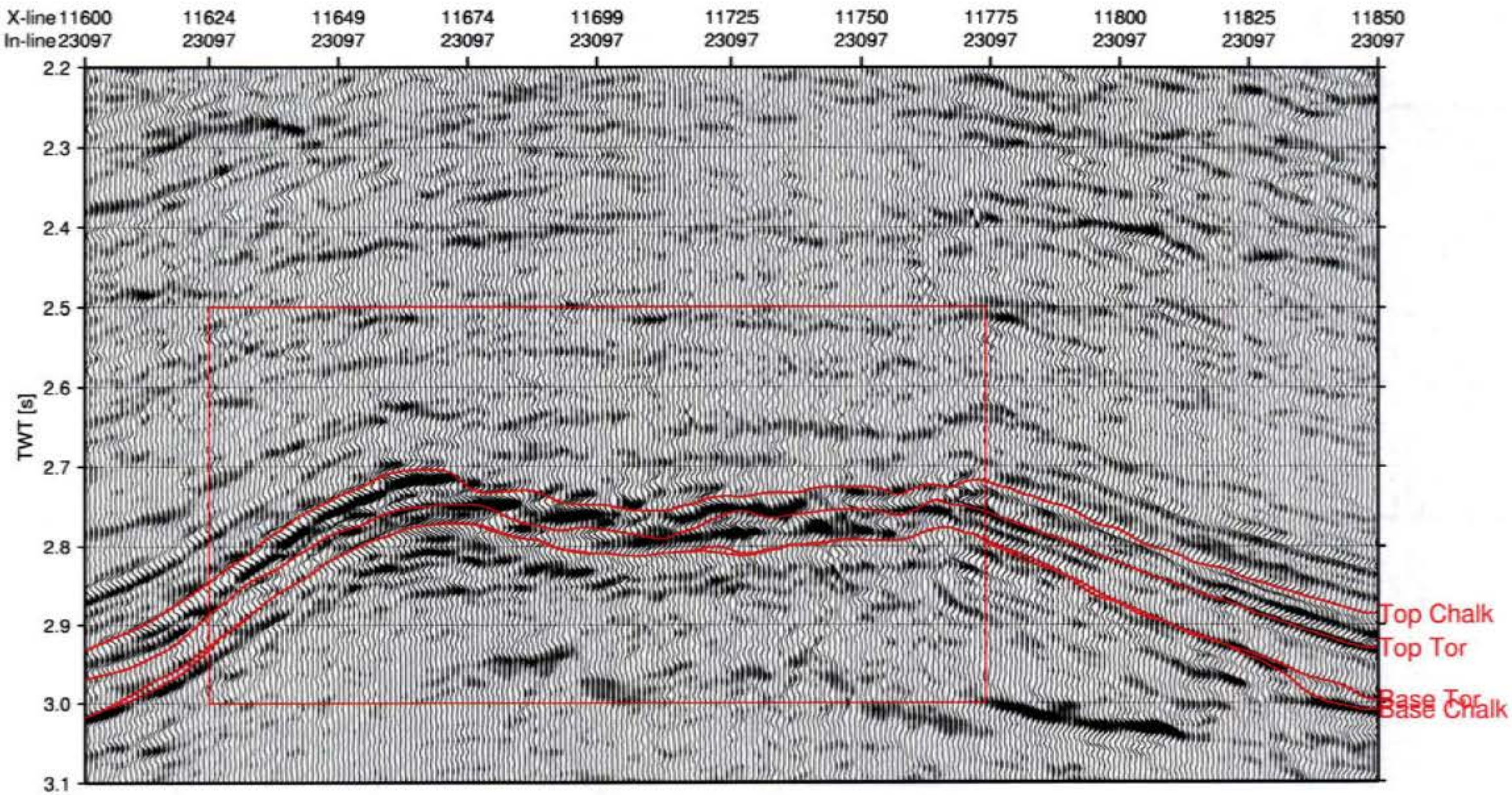

Figure 3.6: *Far offset stack: Seismic data extracted along in-line 23097. The horizons are shown in green. The box marks the outline of the sections shown in Figure 3.7.*

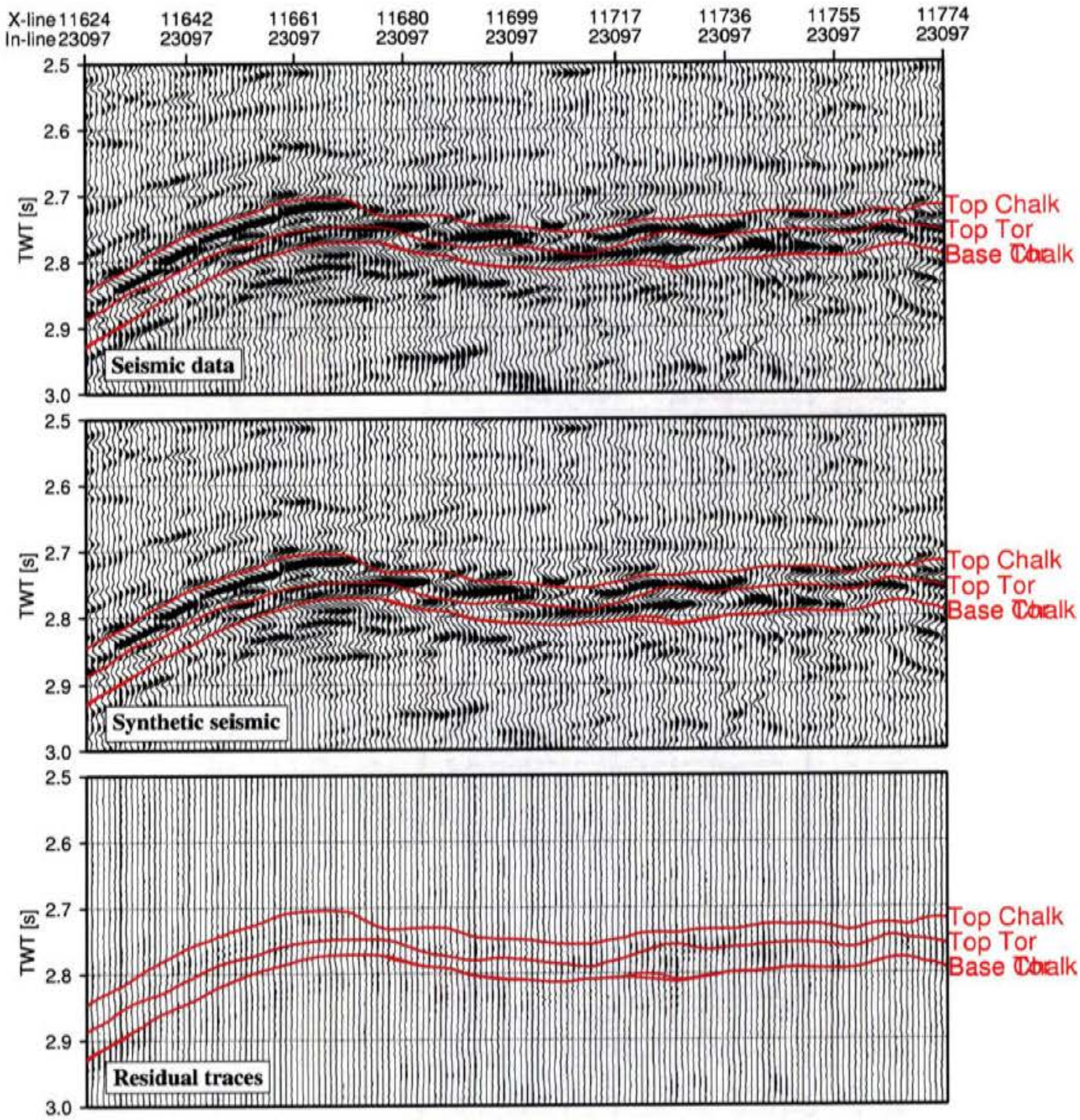

Figure 3.7: *Far offset stack: Seismic data (top), synthetic seismic (centre) and residual traces (bottom) extracted along part of in-line 23097. The horizons are shown in green.*

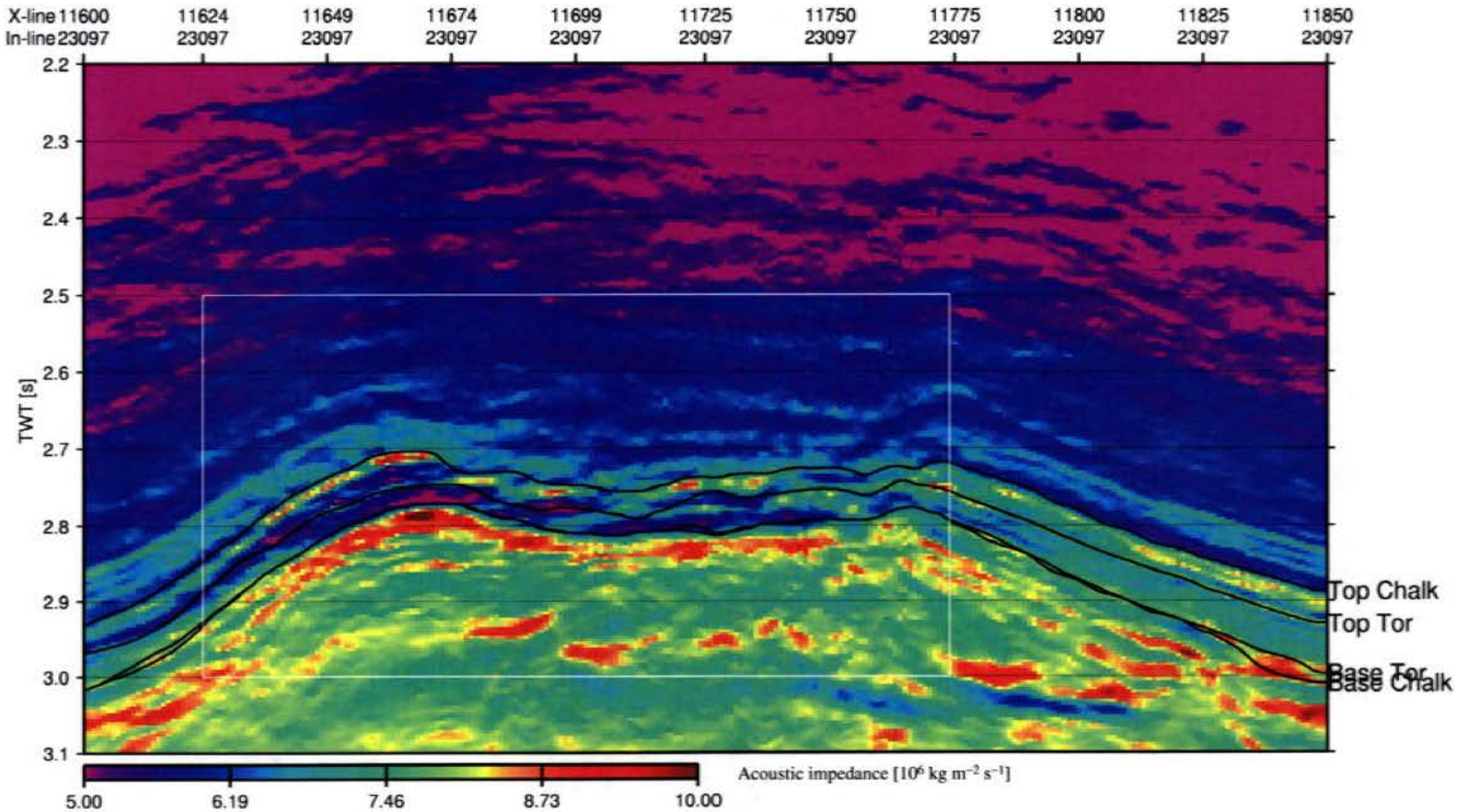

Figure 3.8: *Far offset stack: Angle impedance inversion result with low-frequency information from in-line 23097. The horizons are shown in black. The box marks the outline of the sections shown in Figure 3.9.*

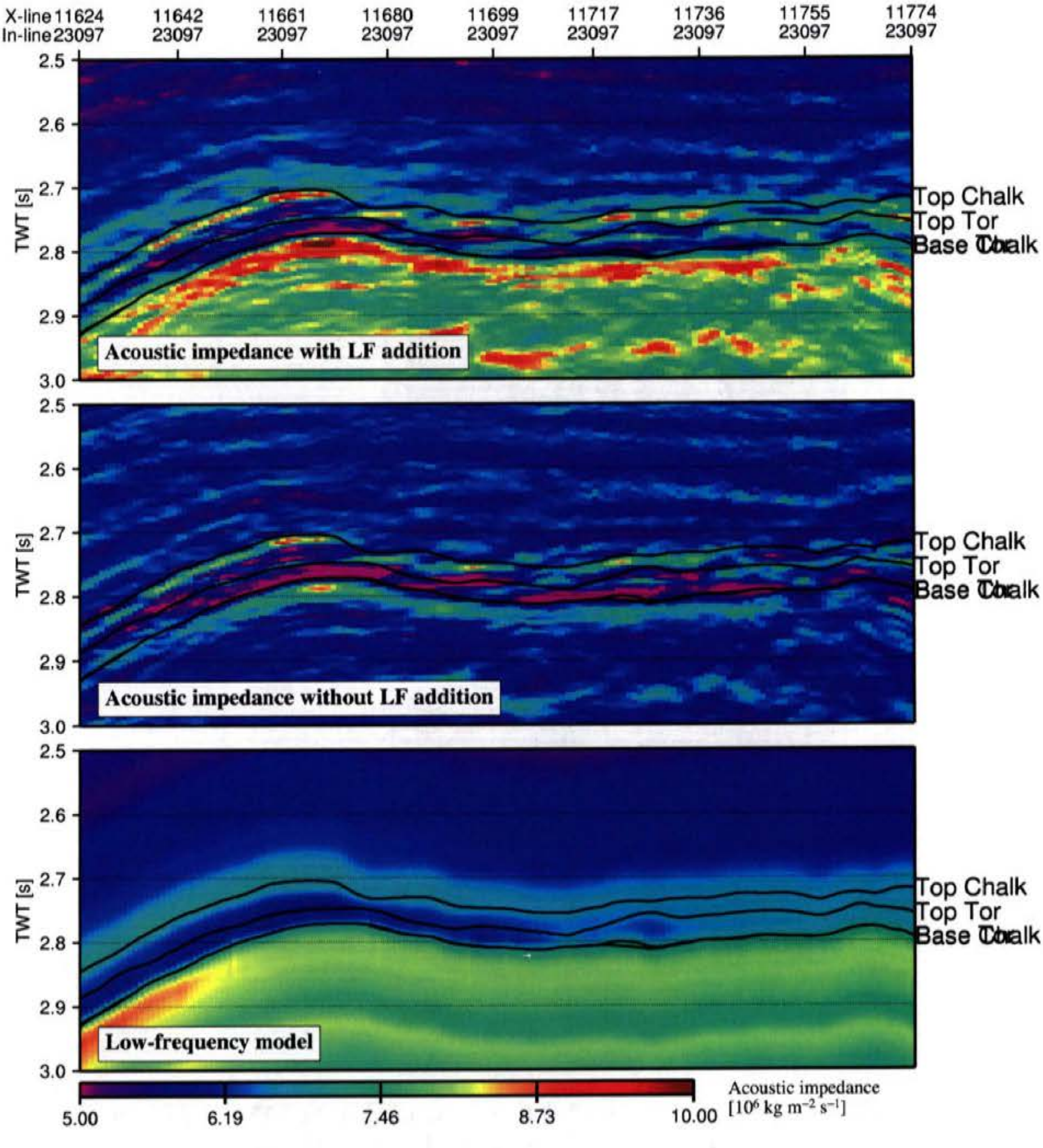

Figure 3.9: *Far offset stack: Angle impedance inversion result with low-frequency information (top), inversion result without low frequency information (centre) and the low-frequency angle impedance model (bottom) extracted along part of in-line 23097. The horizons are shown in black.*

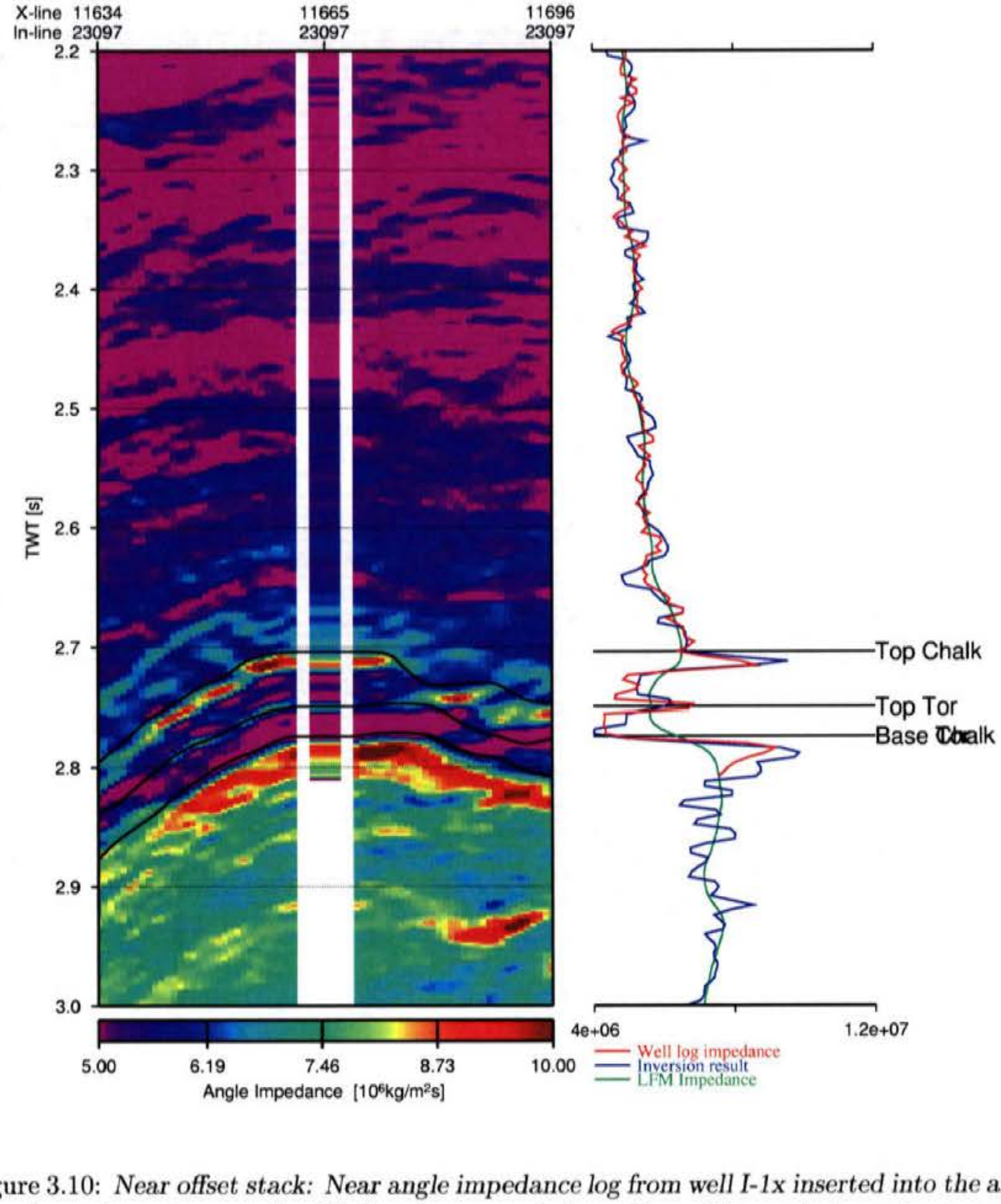

Figure 3.10: *Near offset stack: Near angle impedance log from well I-1x inserted into the angle impedance inversion result with low-frequency information. The angle impedance section shown has been extracted along part of in-line in-line 23097. The log is repeated five times. To the right of the angle impedance section, curves of the following are plotted: the calibrated angle impedance log, the low-frequency angle impedance model at the well location and the angle impedance trace estimated by the inversion at the well location.*

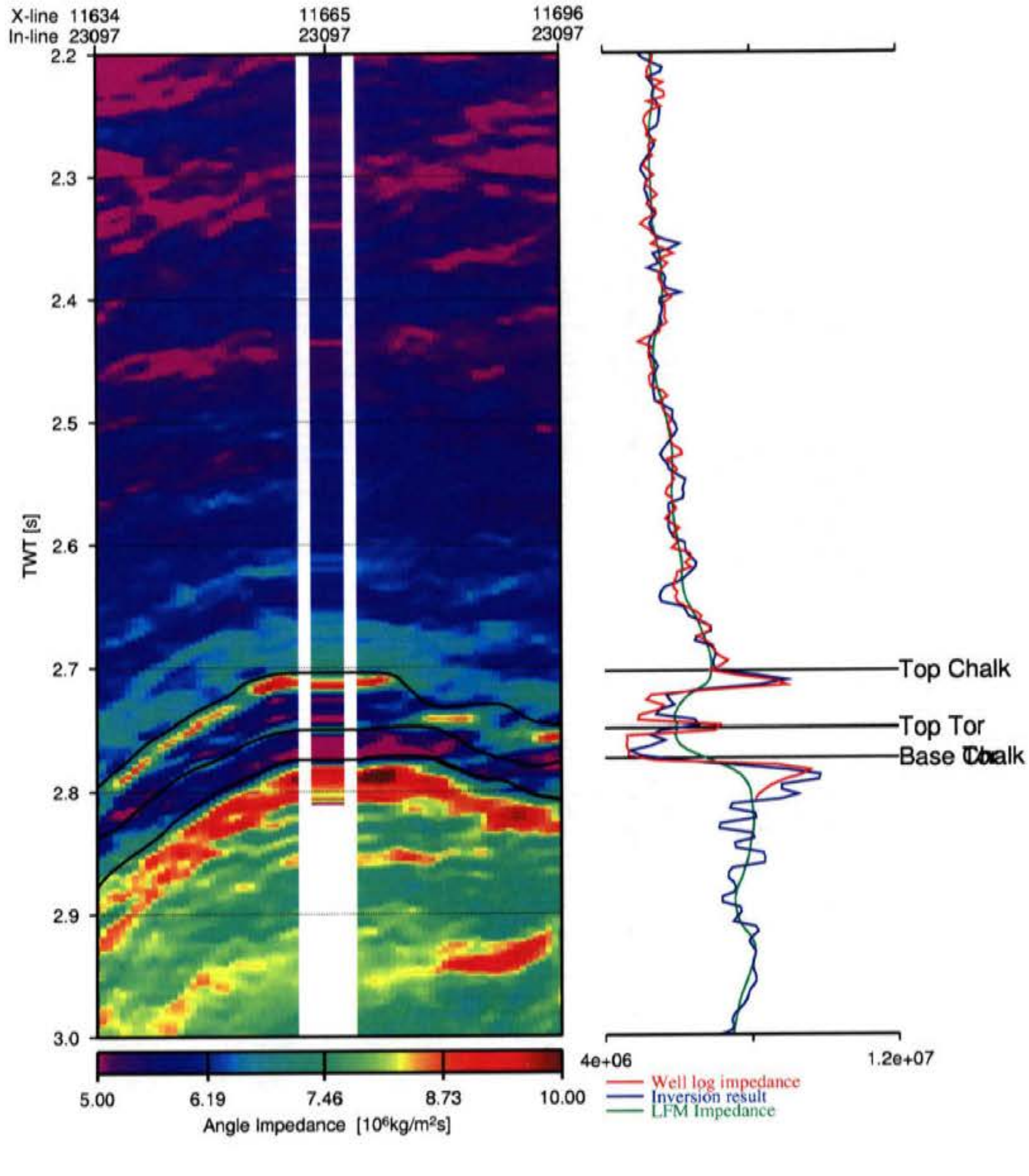

Figure 3.11: *Far offset stack: Far angle impedance log from well Rigs-2 inserted into the angle impedance inversion result with low-frequency information. The angle impedance section shown has been extracted along part of in-line 3066. The log is repeated five times. To the right of the angle impedance section, curves of the following are plotted: the calibrated angle impedance log, the low-frequency angle impedance model at the well location and the angle impedance trace estimated by the inversion at the well location.*

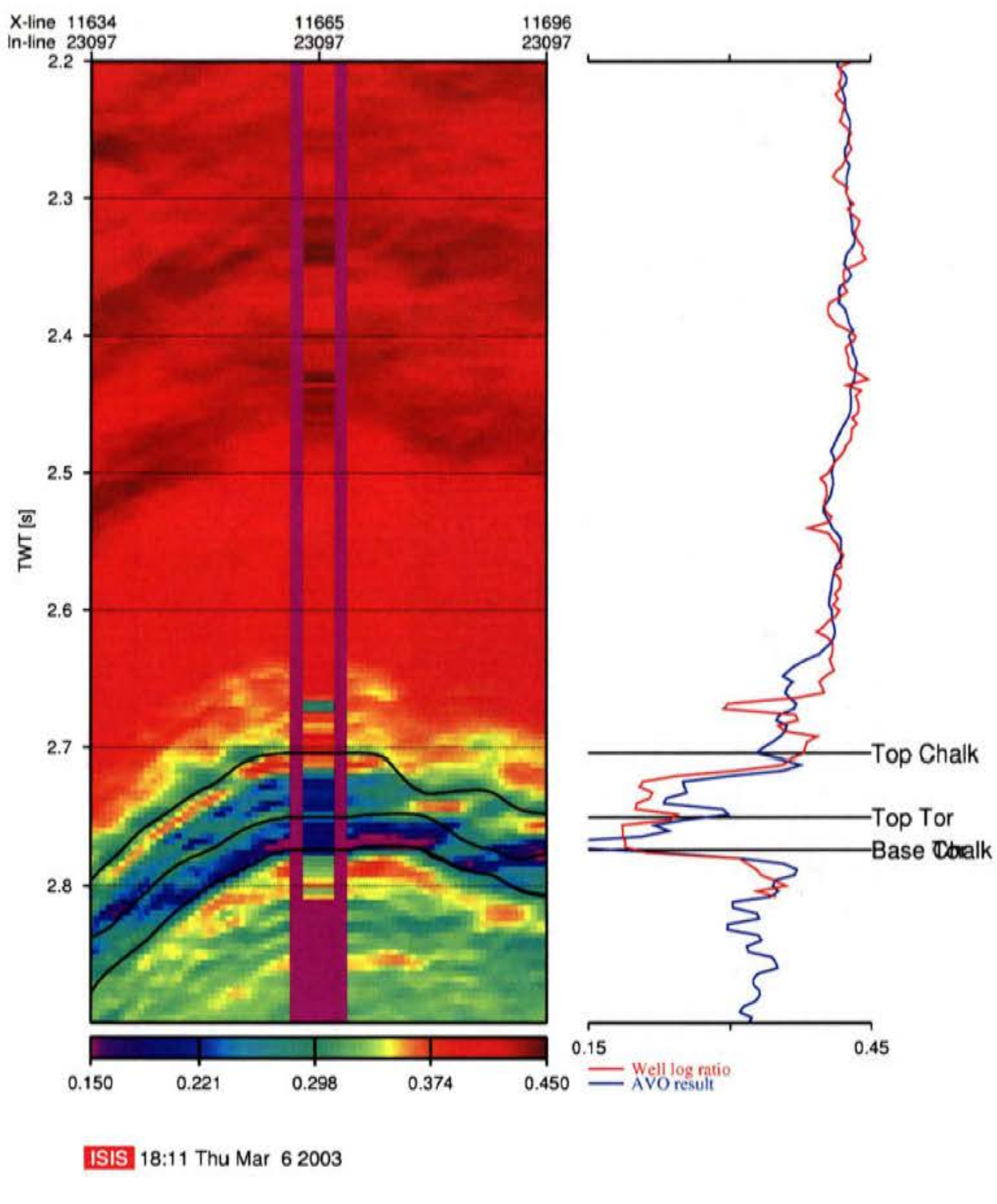

Figure 3.12: *Poisson's ratio estimated from the offset stack inversion results: Poisson's ratio log from well Rigs-2 inserted into estimated Poisson's ratio with low-frequency information. The Poisson's ratio section shown has been extracted along part of in-line in-line 23097. The log is repeated five times. To the right of the Poisson's ratio section, curves of the following are plotted: the calibrated Poisson's ratio log and the Poisson's ratio trace estimated at the well location.*

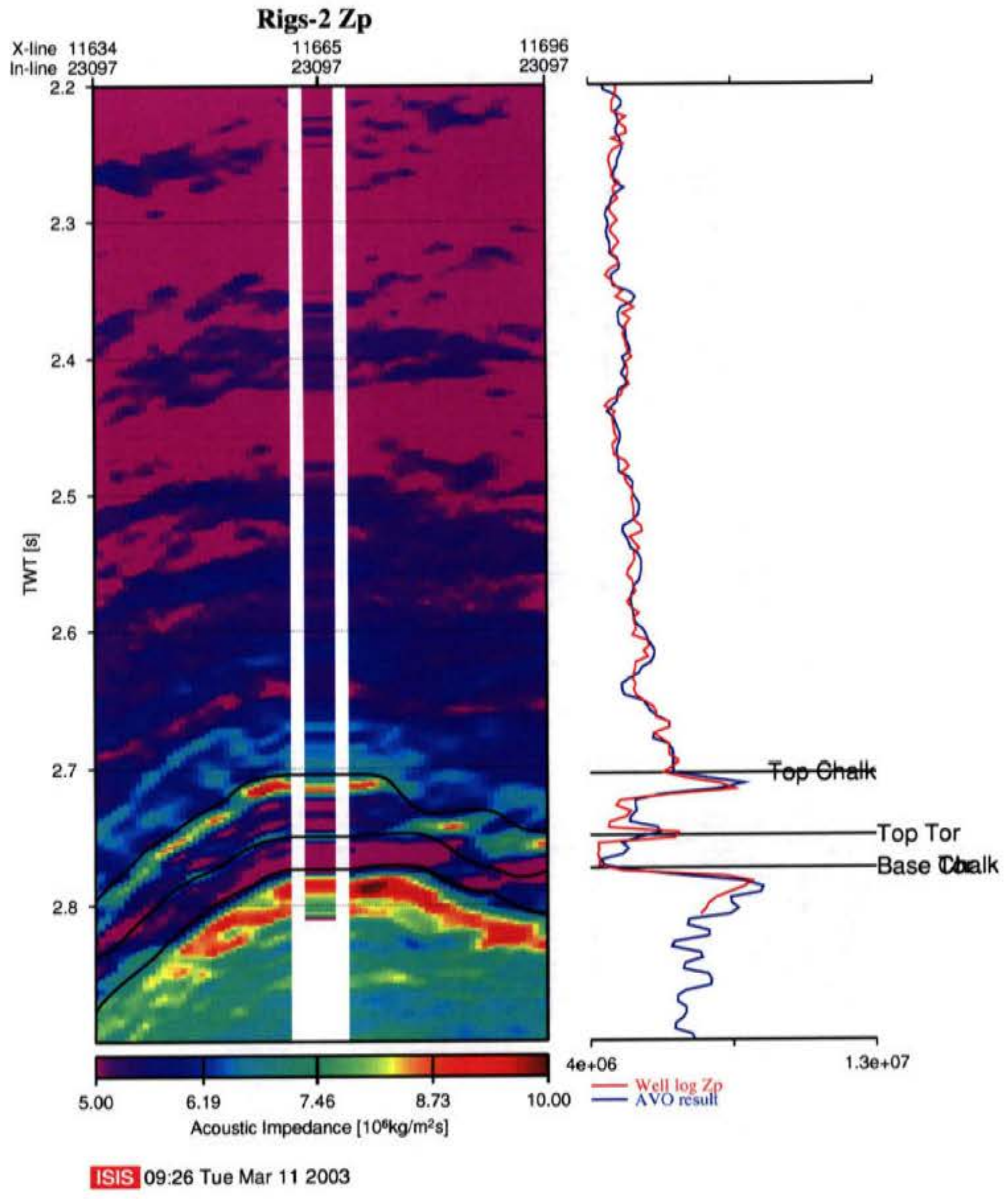

Figure 3.13: *Acoustic impedance estimated from the offset stack inversion results: Acoustic impedance log from well Rigs-2 inserted into estimated acoustic impedance with low-frequency information. The acoustic impedance section shown has been extracted along part of in-line in-line 23097The log is repeated five times. To the right of the acoustic impedance section, curves of the following are plotted: the calibrated acoustic impedance log and the acoustic impedance trace estimated at the well location from the angle stack inversion results.*

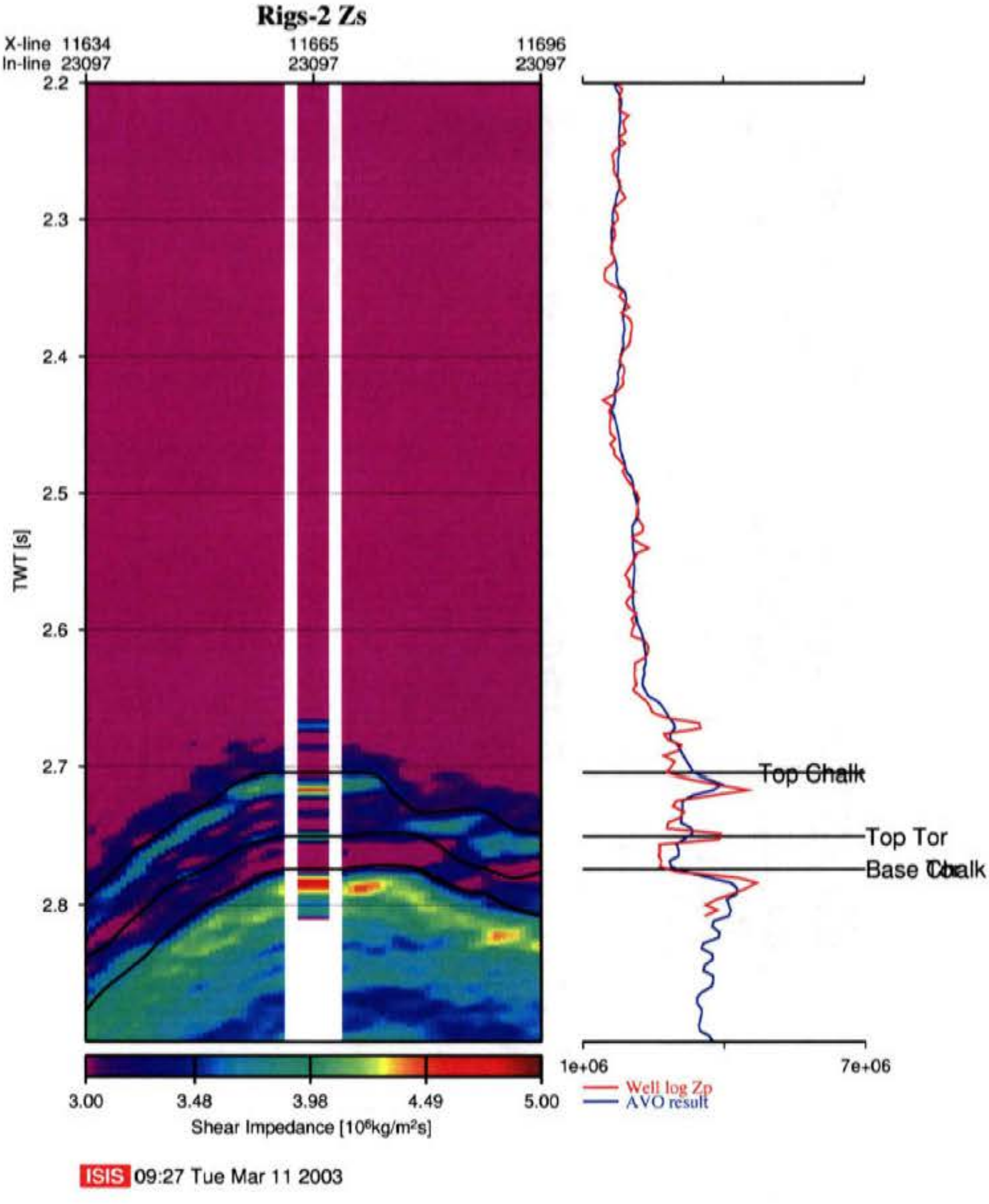

Figure 3.14: *Shear impedance estimated from the offset stack inversion results: Shear impedance log from well Rigs-2 inserted into estimated shear impedance with low-frequency information. The shear impedance section shown has been extracted along part of in-line in-line 23097. The log is repeated five times. To the right of the shear impedance section, curves of the following are plotted: the calibrated shear impedance log and the shear impedance trace estimated by the inversion at the well location from the angle stack inversion results.*

Chapter 4

List of final products delivered

Report 02.24017.01: Seismic AVO inversion of 2D seismic data for use in the EFP 2001 Rock Physics Of Impure Chalk project using the ISIS Software Package Report delivered to EFP2001	March 2003
Final results of ISIS AVO inversion In total, three ASCII tables, containing the AVO inversion results trough the chalk interval were delivered to EFP2001. **The files rigs-1.avo.data, rigs-2.avo.data and sa-1.avo.data contains** • MD • TVDSS • Poisson ratio. • Acoustic impedance. • Shear impedance. Results delivered	March 2003

Appendix A

Wavelet estimation theory

This chapter outlines the theory behind the log calibration and the wavelet estimation.

A.1 Log calibration

The purpose of the log calibration is usually to create:

1. A reflectivity series with the same sampling rate as the seismic data for use in the wavelet estimation.
2. An acoustic impedance series for use in construction of the low-frequency model.

Using available check-shots, the sonic and density logs are converted from the depth domain to the two-way travel-time domain. The acoustic impedance series is computed by multiplication of the calibrated density log and the velocity log derived from the calibrated sonic log. The reflectivity series is then derived by differentiating the acoustic impedance series. If necessary, visual ties are added to shift, stretch or squeeze the logs. Visual ties are determined by comparing the calibrated logs directly with the seismic data, or by comparing the seismic trace at the well location with the synthetic seismic trace derived by convolving a wavelet with the calibrated reflectivity log. Visual ties may be required for the following reasons:

1. The well logs are measured at much higher frequencies than the seismic data. Consequently, the well log velocities can be up to 10% higher than the reflection seismic velocities. This error is largely compensated for by using check-shots.
2. The filters used in the seismic processing may introduce a static time shift into the seismic data. It is therefore sometimes necessary to apply a compensatory static shift using the visual ties.
3. The seismic migration does not perfectly move the reflectors back to their correct position as the migration velocities and the migration algorithms are imperfect. This will introduce a varying time shift dependent on depth and dip of the reflectors.

4. The normal move-out correction for the check-shots is imperfect, particularly for deep and dipping reflectors.

Once the optimum wavelet for the inversion has been chosen, synthetic seismic traces are calculated by convolving the wavelet with the reflectivity series derived from the well logs. The resulting synthetic traces are compared with the seismic traces at the well locations. The well logs are then finally calibrated (stretched and squeezed) for optimum match.

A.2 Deviated wells

In order to compare logs from a deviated well with the seismic data, the seismic data along the well trajectory are extracted from the seismic cube. The resulting seismic trace is called a super-trace.

In order to evaluate the significance of individual events in a super-trace, a super-section passing through the super-trace is also extracted from the seismic data. For plotting, super-traces and super-sections are projected onto vertical lines or planes.

For a deviated well, whenever the depth-to-time relationship is changed by applying a visual tie, the deviation of the well needs to be adjusted. Hence, after applying a visual tie, a new super-trace must be extracted from the seismic data along the new well trajectory. Hence, the calibration of deviated wells involves considerably more steps than the calibration of vertical wells.

For deviated wells, the super-trace along the well trajectory is used for wavelet estimation, rather than the trace at the well-head location. The deviation of wells is also fully utilized when constructing 3D low-frequency impedance models.

A.3 Least squares wavelet estimation in the time domain

The time domain based least squares wavelet estimation process is divided into two parts. A least squares method is first used to estimate a suite of wavelets with different lengths. The optimum wavelet length is then determined by using Akaike's Final Prediction Error (FPE) criterion (Ljung, 1987) in combination with visual inspection of the wavelet and synthetic seismic. Vertical variations of the wavelet (see Section ??) can be specified as part of the least squares estimation.

The least squares method in the time domain minimizes the sum of squared differences (the misfit) between the seismic trace and a synthetic trace obtained by convolution of the well log reflectivity series and a wavelet. Wavelets are estimated using the least squares method for a range of lengths and a range of initial delays. For each wavelet length, the best initial delay is determined by using the misfit criterion.

Akaike's FPE is a function of the misfit, which decreases as a function of wavelet length, and the relative number of parameters, which increases as a function of wavelet length. The relative number of parameters is equal to the length of the wavelet divided by the length of the window within which the misfit between the synthetic trace and the seismic data is calculated. The optimum wavelet length, and thereby the optimum wavelet, is determined by finding the minimum value for the wavelet suite of Akaike's FPE. The wavelet with the minimum value of Akaike's FPE models as much of the coherent signal as is possible without modelling a significant amount of the local noise. Wavelets, which are too long and model large amounts of local noise, are unlikely to be representative of the seismic data away from the well location.

A.4 Zero-phasing

Zero-phasing seismic data can be implemented by first estimating a wavelet using one of the methods described elsewhere in this report. The phase spectrum of the wavelet is then subtracted from the phase spectrum of the seismic data. The amplitude spectrum of the seismic data is left untouched. The main advantage of zero-phased seismic data is that the events are compressed as much as possible without modifying the amplitude spectrum and thereby potentially, but not necessarily, decreasing the signal to noise ratio.

References

Ljung, L., 1987. *System Identification: Theory for the User.* Prentice-Hall.

Oppenheim, A. V. and Schafar, R. W., 1989. *Discrete-Time Signal Processing.* Prentice-Hall.

Welch, P. D., 1970. *The Use of the Fast Fourier Transform for Estimation of Power Spectra.* IEEE Trans. Audio Electroacoustics, Vol. AU-15.

Appendix B

Seismic inversion theory

B.1 Introduction

The ISIS seismic inversion algorithm is based on a unique combination of an advanced global search algorithm and a non-linear cost function. A global search algorithm is employed in order not to get trapped in sub-optimum models close to the starting model which local methods frequently are. ISIS inversion uses the convolutional model for generating the synthetic seismic data that are compared with the original seismic data. ISIS inversion can consequently be implemented on migrated full-stack, offset-stack, or angle-stack reflection seismic data. The wavelet in the convolutional forward model can be varied both horizontally and vertically.

ISIS seismic inversion improves the resolution as the wavelet includes both amplitude and phase spectrum information. Further improvement in the resolution is due to the spectral expansion caused by the non-linear inversion (Cooke & Schneider, 1983).

The inversion can be constrained by a so-called prior model. In the simplest case, the prior model consists of one constant background impedance value. For such a prior model, the inversion gives an unbiased result called the plain ISIS result. The prior model may also consist of the low-frequency components of the impedance variations, which cannot be resolved from the seismic data. These low-frequency components can be determined by extrapolating the impedance logs using horizons and faults as a guide followed by low-pass filtering. Seismic velocities, e.g. stacking velocities, and dip information from the seismic data can also be used to constrain the prior model.

B.2 ISIS seismic inversion algorithm

The ISIS seismic inversion algorithm uses an advanced global search algorithm to estimate the impedance subsurface model that minimizes a non-linear cost function containing the following terms:

- Penalty for differences between the seismic data and the synthetic seismic determined from the estimated impedance model by convolutional forward modelling.

- Penalty for horizontal variations in the estimated impedance model.
- Penalty for deviation of the estimated impedance model from the prior model.
- Penalty for the presence of significant reflectors. Significant reflectors are places in the estimated impedance model where the reflection coefficient exceeds a predefined threshold.
- Penalty for vertical changes in impedance between the significant reflectors.

The inversion algorithm therefore finds a subsurface impedance model which gives synthetic seismic that approximates the seismic data while also satisfying the other constraints in the cost function which provide damping of random noise, incorporation of the prior model and correct location of significant reflectors.

B.3 ISIS seismic inversion input

The inversion algorithm requires as input: the migrated seismic data, a wavelet, a prior model and values for four inversion parameters that appear in the cost function. These four inversion parameters are:

- **Signal-to-noise ratio (RSNR)**: controls to what degree differences between the synthetic seismic and the seismic data are penalized. The greater RSNR, the greater the penalty, so the inversion algorithm models more of the seismic energy.
- **Horizontal continuity (RALPHA)**: controls to what degree horizontal variations in the impedance model are penalized. RALPHA is the standard deviation of neighbouring impedance traces. The greater the value given to RALPHA, the lesser the penalty, so the inversion algorithm imposes less horizontal continuity.
- **Relative standard deviation of the prior model (RSIGMA)**: controls to what degree deviation of the estimated impedance model from the prior model is penalized. The greater RSIGMA, the lesser the penalty, so the further the estimated acoustic impedance model is allowed to deviate from the prior model.
- **Threshold for reflection coefficient (R1)**: all points in the estimated impedance model with a reflection coefficient greater than R1 are interpreted as significant reflectors. The penalty for the presence of significant reflectors is strongly influenced by the value of R1. The greater R1, the greater the penalty for each significant reflector present in the model, but the lesser the probable total number of significant reflectors.

Values for the above inversion parameters are estimated initially using available information. To find the best set of values, a parameter study is conducted. The value of each parameter is varied and each result evaluated by inspection of the inversion result and by statistical analysis.

The allowed ranges of the four inversion parameters are given in Table B.1.

Parameter	Lower limit	Upper limit
Signal-to-noise ratio, RSNR	>0	∞
Horizontal continuity, RALPHA	>0	1
Deviation of prior model, RSIGMA	>0	1
Threshold for reflection coeff., R1	>0	1

Table B.1: *Permitted ranges of the seismic inversion parameter values.*

B.4 Horizon interpolation

In order to generate the prior model it is necessary that the original horizons are interpolated and extrapolated such that the whole section, which is to be inverted, is covered.

The horizons are interpolated in succession based on their degree of coverage and starting with the one with the highest degree of coverage. The linear interpolation of each horizon is guided by the nearest horizon above and the nearest horizon below that already have been wholly interpolated if such horizons are available. Pinching-out of horizons is handled by letting them follow the horizons on which they truncated.

B.5 Addition of low-frequency information

For a constant prior model, the ISIS inversion result lacks the very low-frequency components as they also are missing in the seismic data. These components can only be introduced into the inversion result by using a non-constant prior model. Such a prior model can be constructed by extrapolating laterally the calibrated impedance logs using a number of interpreted horizons and faults as a guide and then by low-pass filtering the resulting model. Each well log is weighted by one divided by the distance squared to the well plus a constant. The prior model is also called the low-frequency model due to the low-pass filtering that in most cases is applied.

The extrapolation of the well log values can be modified by a depth trend. It is done by multiplying the well log values before the weighted averaging by $\exp(\mathbf{RDEPTH}\Delta T/t_s)$ where the depth trend constant **RDEPTH** denotes the relative increase per sample, ΔT denotes the increase in two-way travel time when going away from the well along horizon slices, and t_s denotes the sample period. The depth trend is applied only in between the two horizon slices that intersect the top and bottom of the well log.

In the present implementation, the depth trend constant is allowed to change when crossing a horizon as long as it is constant in between the horizons. Proper depth trend constants can be estimated by performing a statistical analysis of the depth trends of the available well logs. This, of course, requires that at least two well logs with significant depth differences between the layers when going from one well to the other are available.

Seismic velocity data can also be used to constrain the low-frequency model. Velocity values are computed for each trace by linear interpolation using the nearest defined grid points.

The resulting 3D velocity model is low-pass filtered laterally parallel to the interpreted horizons and vertically to remove anomalies. The velocity model is finally transformed to acoustic impedance using Gardner's relation. In the case of multiple crossing 2D lines, sometimes referred to as the 2.5D case, the velocity data is treated as 3D and only at the very end, 2D lines are extracted. This procedure ensures that incompatible information is not introduced where two 2D lines crosses.

The acoustic impedance well log information, extrapolated along the interpreted horizons, is then used in combination with the velocity-derived low-frequency acoustic impedance model to generate a detailed acoustic impedance model, which is then low-pass filtered to produce the final low-frequency model. The velocity-derived low-frequency acoustic impedance model is used to guide the acoustic impedance changes between the well locations. This guidance is such that only lateral variations in the seismic velocities have an influence on the final low-frequency model between the wells. The degree of guidance is specified by a parameter, RGUIDE, for which the value zero corresponds to no guidance by the velocity-derived low-frequency acoustic impedance model and the value 1 corresponds to proportional or full guidance. The absolute level of the velocity-derived acoustic impedance model has no influence between the well logs.

Dip information from the seismic data can also be used to help guide the extrapolation of the well logs. Dips estimated from the seismic data are converted to horizon like information called a layer sequence field. The layer sequence field is then used to guide the extrapolation of the well logs either with or without interpreted horizons and faults and seismic velocity information (Rasmussen, 1999).

The degree to which the resulting impedance model is low-pass filtered is represented by a filter constant: the higher the value of the constant, the greater the degree of filtering. If the filter constant is too high, the final inversion result will not contain variations with frequencies between the lowest frequency resolvable from the seismic data and the very low frequencies introduced by the prior model. However, if the filter constant is too low, the frequency content of the prior model will overlap significantly with that of the seismic and the detail in the inversion result will not be independent of the well log information.

B.6 ISIS seismic inversion results

The primary results produced by the ISIS seismic inversion are two impedance models; one with and one without low-frequency information.

The impedance result without low-frequency information enables the interpreter to carry out an interpretation of a fully unbiased result as neither well logs nor seismic horizons have been utilized. However, only the relative impedance level can be interpreted. In the inversion result with low-frequency information, the absolute impedance level may also be interpreted.

B.7 ISIS seismic inversion for porosity

Inversion of the seismic data for porosity is performed in exactly the same way as the inversion for acoustic impedance. The inputs to the ISIS seismic inversion algorithm are, however, different. Rather than the normal acoustic impedance wavelet, a porosity wavelet is used, and the prior model consists of a low-frequency porosity model. The method is described in more detail in Rasmussen & Maver (1996).

B.8 Alignment

Misalignment of events in a number of different areas can to the degree that it is representing errors in the different simplified models used in the seismic processing have a degrading influence on the results and extracting the displacement information can to the degree that it is not representing the above mentioned errors be valuable in itself. The areas that this concerns are:

- **Well log calibration**: Misalignment between synthetic and original seismic data at the well position due to for instance migration inaccuracies can lead to loss of especially the high frequency components in the least square wavelet. An alignment should therefore be performed either manually or automatically.
- **Time lapse**: Misalignment between the different seismic vintages can be due to a number of reasons: acquisition and processing inaccuracies, changed layer thicknesses due to compaction, changed wave velocities due to compaction, fluid, temperature, and/or pressure changes. The different seismic vintages should be aligned before sample by sample differencing. The displacement information could furthermore be a valuable attribute in itself.
- **AVO**: Due to inaccurate NMO, DMO, and/or migration some misalignment in depth is often present between the events in the different angle- or offset-stacks. The misalignment is less, but still present, in the inverted data as separate wavelets have been used for the different angle- or offset-stacks. The misalignment can degrade the results that are obtained by combining the different separate angle- or offset-stacks inversion results, e.g. Poisson's ratio and Shear impedance, and to a lesser degree the computed Acoustic Impedance. An alignment should therefore be performed if the misalignment is not due to that acoustic and shear reflection coefficients simply are not fully correlated.
- **4C**: Misalignment of the PP and PS seismic data due to for instance inaccurate estimated Poisson's ratio can degrade the results obtained by combining the two data sets. An alignment as in the AVO case should therefore be performed.

If it for some technical or economic reason is not possible to correct the misalignment using an improved deterministic seismic processing scheme then one is left with the less reliable statistical approaches. Statistical approaches work by modifying one of the two data sets by a constrained mathematical transformation such that the data set in some mathematical sense becomes more like the other data set. The reason why statistical approaches are less reliable than deterministic approaches is that they cannot directly distinguish between misalignment due to the simplified models used and misalignment bearing useful information. The way they attempt to distinguish the two contributions is by using a very constrained mathematical transformation.

Our implementation of statistical alignment is a pure single trace algorithm meaning that the data is stretched and squeezed vertically only, and that there is no requirements with respect to horizontal continuity of the vertical displacement. Furthermore are the amplitudes not modified. Our algorithm is fully automatic in the sense that the only interaction required by the user is to choose a parameter describing how much vertical displacement that is allowed in the search for maximum cross-correlation.

B.9 Spectral balancing

When comparing two signals visually or arithmetically as for instance in statistical alignment algorithms, it is in some cases advantageous that they have approximately identical amplitude spectra. This amplitude spectra has to be the common frequency interval of the two input signals of the spectral balancing in order not to introduce noise in either of the two output signals. Denoting the amplitude spectrum as a function of the frequency f before spectral balancing of signal 1 as $A_1(f)$ and of signal 2 as $A_2(f)$, one way to obtain spectral balancing is to compute the filter $H_1(f)$, which is to be applied to signal 1, and the filter $H_2(f)$, which is to be applied to signal 2, as follows

$$H_1(f) = \frac{A_2(f)}{\sqrt{A_1(f)^2 + A_2(f)^2}} \tag{B.1}$$

$$H_2(f) = \frac{A_1(f)}{\sqrt{A_1(f)^2 + A_2(f)^2}} \tag{B.2}$$

The common amplitude spectrum $A(f)$ after the spectral balancing is simply

$$A(f) = \frac{A_1(f)A_2(f)}{\sqrt{A_1(f)^2 + A_2(f)^2}} \tag{B.3}$$

which means that the common power spectrum is the harmonic mean of the two input power spectra.

References

Cooke, D.A. & W.A. Schneider, 1983. Generalized linear inversion of reflection seismic data. *Geophysics*, **48**, 665–676.

Rasmussen, K. B. & K.G. Maver, 1996. Direct inversion for porosity of post stack seismic data. **SPE35509**. *Society of Petroleum Engineers.*

Rasmussen, K. B. 1999. Use of dip in seismic inversion. *61th Mtg.: Eur. Assoc. Expl. Geophys., Session 4049.*

Appendix C

AVO inversion theory

This chapter describes how seismic Amplitude Versus Offset (AVO) attribute data are used in the ISIS seismic inversion. It is also described how Poisson's ratio and other petrophysical and direct hydrocarbon indicators are computed from the AVO inversion results.

C.1 AVO attribute data

The analysis of seismic AVO variation provides the possibility of obtaining both acoustic and shear information from acoustic data and thus obtaining information regarding pore fluid variation for a more detailed reservoir description.

The implementation of inversion methods in the analysis of AVO attribute data provides the ability to derive estimates of the real physical parameters which control the AVO, acoustic impedance and shear impedance which can be compared directly with well log data. Not only do the volumes derived in the inversions have real physical meaning, they also benefit from the removal of the effect of the wavelet and damping of random noise.

The following AVO attribute data can be inverted:

- Intercept and gradient data. (Section C.3).
- Angle stack data. (Section C.5).
- Offset stack data. (Section C.6).

The acoustic, shear and angle impedance inversion results (Z_P, Z_S and Z_θ) can be interpreted directly and direct comparison of the inversion results with well log values is possible.

C.2 Calculation of intercept and gradient data

The AVO attributes, intercept and gradient are commonly used to quantify the variation of amplitude with offset. The attributes are calculated on the basis of the Shuey's approximation (Equation (C.1)) to the full Zoeppritz equations [Shuey, 1985].

$$R_P(\theta) \;=\; I + G\sin^2(\theta) \qquad \text{(C.1)}$$

where R_P is the acoustic reflection coefficient, θ is the angle of incidence, and I and G are the intercept and gradient as defined in Equations (C.2) and (C.3).

The I and G attributes are calculated using the NMO-corrected, true amplitude processed and pre-stack migrated data in conjunction with an interpreted interval velocity model which is used to convert offset to angle.

C.3 AVO inversion of intercept and gradient data

The intercept and gradient data are used to calculate acoustic and shear reflection seismic (R_P and R_S) (see Section C.4). These seismic data are then inverted for acoustic and shear impedance (Z_P and Z_S). For the inversion of the shear reflection seismic the wavelet is derived using a shear reflectivity log rather than the normal acoustic reflectivity log, and the low-frequency model is derived using shear impedance logs rather than acoustic impedance logs. The same depth-to-time relationship is used for the acoustic and shear logs from each well.

The acoustic impedance (Z_P) and shear impedance (Z_S) inversion results can be interpreted directly, or supplementary physical properties such as V_P/V_S, Poisson's ratio and fluid factor can be calculated from them (see Section C.8). In all cases, direct comparison of the inversion results with well log data is possible, and use of cross-plotting techniques enables quantitative lithological and pore fluid determination.

C.4 Calculation of shear reflectivity seismic

When inverting intercept and gradient data using the ISIS global seismic inversion package, a shear reflection volume (R_S) is calculated by implementing a variant of Shuey's approximation [Shuey, 1985; Castagna and Backus, 1993; Smith and Gidlow, 1987], which takes into account a slowly varying V_S/V_P ratio and an estimated exponential constant for Gardner's relationship. The intercept and gradient can be expressed as:

$$I \;=\; R_P \qquad \text{(C.2)}$$

$$G \;=\; \frac{R_P}{1+a} - 2\left(\frac{2V_S}{V_P}\right)^2 \left(R_S - \frac{a}{2}\frac{R_P}{1+a}\right) \qquad \text{(C.3)}$$

where a is Gardner's exponential constant. It should be noted that V_S/V_P in Equation (C.3) refers to the low-frequency content only of the V_S/V_P variation.

From Equations (C.2) and (C.3) the following equations for acoustic reflection seismic (R_P) and shear reflectivity seismic (R_S) in the acoustic time domain can be derived.

$$R_P = I \tag{C.4}$$

$$R_S = \frac{\frac{I}{1+a} - G}{2\left(\frac{2V_S}{V_P}\right)^2} + \frac{a}{2}\frac{I}{1+a} \tag{C.5}$$

C.5 AVO inversion of angle stack data

A frequently used method for examining AVO effects is to compute angle stacks and analyze them qualitatively. In order to perform a quantitative analysis, the angle stacks can be inverted using the concept of the effective impedance at a constant angle of incidence. This impedance we have called angle impedance (see Section C.7).

The implementation of angle impedance in ISIS, makes it possible to invert angle stacks as if the data were ordinarily stacked seismic data. Using angle reflectivity and angle impedance logs computed for the effective angle of the angle stack makes the application of the convolution model valid for inversion of the angle stacks. The angle reflectivity logs are used for the wavelet estimation (see Appendix A). The angle impedance logs are used in the prior model generation (see Section B.5) and for quality-control of the inversion result. The same depth-to-time relationship is used for all logs from each well.

The effective angle of the angle stack is the single angle corresponding to the arithmetic mean of the reflection coefficient over the traces in the angle stack. Using an unweighted mean, of course, assumes that the traces in the angle stack have been equally weighted. As the reflection coefficient according to Shuey's approximation (Equation (C.1)) is approximately linear related to $\sin^2(\theta)$, the effective angle, θ_{eff}, is given by

$$\sin^2(\theta_{\text{eff}}) = \frac{\sin^2(\theta_{\text{min}}) + \sin^2(\theta_{\text{max}}) + \sin(\theta_{\text{min}})\sin(\theta_{\text{max}})}{3} \tag{C.6}$$

where θ_{min} and θ_{max} denote the minimum and maximum angle of the angle stack, respectively. The effective angle can be up to 16% larger than the arithmetic mean of the minimum and maximum angle of the angle stack.

Estimating a separate wavelet for each angle stack decreases the influence of many kinds of errors. Effects of NMO stretch, frequency variation with offset and energy variation with offset can be compensated for by using separate wavelets in the inversions.

The angle impedance inversion results can either be interpreted directly, for example for differentiation of sands and shales, or can be combined to derive more classical AVO indicators, for instance V_P/V_S and Poisson's ratio (see Section C.8).

C.6 AVO inversion of offset stacks

A variation of angle stacks is offset stacks. Offset stacks are generated by stacking receivers according to offset rather than angle of incidence. For offset stacks the angle of incidence is a function of depth and horizontal position. Angle stacks are therefore preferred to offset stacks. However, it is possible to invert offset stacks using the ISIS global seismic inversion package. Inversion of offset stacks is done by computing the variation of the angle with depth and using it instead of a constant angle in all the equations originally developed for angle stacks.

The effective offset, x_{eff}, of an offset stack is computed in a similar way as the effective angle of an angle stack:

$$x_{\mathrm{eff}}^2 = \frac{x_{\mathrm{min}}^2 + x_{\mathrm{max}}^2 + x_{\mathrm{min}} x_{\mathrm{max}}}{3} \tag{C.7}$$

where x_{min} and x_{max} denote the minimum and maximum offset of the offset stack, respectively . The effective offset can be up to 16% larger than the arithmetic mean of the minimum and maximum offset of the offset stack.

Neglecting formation dip, the angle of incidence, θ can be computed by

$$\sin(\theta) = \frac{v_{\mathrm{int}} x}{v_{\mathrm{rms}} \sqrt{(v_{\mathrm{rms}} t)^2 + x^2}} \tag{C.8}$$

where v_{int} is the interval velocity, v_{rms} is the root-mean-square velocity, x is the source-receiver offset, and t is the zero-offset two-way travel-time [Castagna and Backus, 1993].

C.7 Logs for angle stacks and offset stacks

Angle impedance (Z_θ) is a function of the acoustic impedance (Z_P), the shear impedance (Z_S) and the angle of incidence (θ).

The angle impedance is based on the Shuey's approximation and is defined as

$$Z_\theta = Z_p \exp\left([\log(Z_p) - 2\log(Z_s) + \log(5.0 \cdot 10^6)] \sin^2(\theta) \right) \tag{C.9}$$

The constant $5.0 \cdot 10^6$ in Equation C.9 above could be replaced by any other arbitrary constant and the equation would still possess the following properties:

- The angle impedance is identical to the acoustic impedance for normal incidence.
- The reflection coefficient, derived in the same way as for normal incidence but using angle impedance instead of acoustic impedance, is identical to the reflection coefficient for a P-P reflection at the given angle.

In the derivation of Equation C.9, it has been assumed that:

- The low-frequency V_S/V_P ratio is approximately 0.5, and that density variations are small.
- The angle of incidence is reasonably low (less than about 33°).

C.8 Calculation of supplementary physical properties

Acoustic impedance (Z_P) and shear impedance (Z_S) inversion results can be converted to Poisson's ratio, V_P/V_S and fluid factor:

$$Poisson's\ ratio = \frac{\frac{(Z_P)^2}{2} - (Z_S)^2}{(Z_P)^2 - (Z_S)^2} \tag{C.10}$$

where Z_P and Z_S are the acoustic impedance and shear impedance inversion results with low-frequency information.

$$V_P/V_S = \frac{Z_P}{Z_S} \tag{C.11}$$

where Z_P and Z_S are the acoustic impedance and shear impedance inversion results with low-frequency information.

$$Fluid\ factor = Z_S - Z_P \tag{C.12}$$

where Z_P and Z_S are the acoustic impedance and shear impedance inversion results with the same constant low-frequency value (see Appendix B). Fluid factor as defined here highlights changes in fluid properties, without adding any empirical relations between shear and acoustic velocities as in the conventional fluid factor calculation.

From angle stack and offset stack inversion results, acoustic impedance, shear impedance, V_P/V_S and Poisson's ratio can be derived by estimating the optimum linear relation in the $(\log(Z_\theta), \sin^2(\theta))$-domain using all angle impedance inversion results. The V_P/V_S and Poisson's ratio estimates are calculated from the angle impedance at $\theta = 90°$ computed using the estimated optimum linear relation. In order to obtain reliable V_P/V_S and Poisson's ratio volumes it is therefore essential to use angle stacks with large differences between the effective angles. The estimation of V_P/V_S, Poisson's ratio and shear impedance can be additionally constrained by low-frequency angle impedance models calculated for $\sin^2(\theta) = 1$ and $\sin^2(\theta) =$ -1. The constraints are introduced to avoid unphysical fluctuations appearing in the estimated V_P/V_S values, Poisson's ratio and shear impedance values.

C.9 Lithological identification by cross-plotting

Cross-plotting of the well log data can be used to aid interpretation of the inversion results. The well log data can be used to establish relationships between lithology and the physical parameters determined in the seismic inversions, e.g. acoustic impedance and Poisson's ratio. These relationships can then be used to predict lithology from the inversion results.

Figure C.1 shows a cross-plot of acoustic velocity versus density with general curves for some common lithologies [Castagna, 1993]. Contours of acoustic impedance are drawn on the plot. The plot shows the following:

- Acoustic impedances of sand and shale is similar.
- Limestone and sand-shale lithologies can be separated in acoustic impedance.
- Low porosity lithologies tend to have a large acoustic impedance while high porosity lithologies have low values of acoustic impedance.

Figure C.2 shows a cross-plot of acoustic impedance versus Poisson's ratio. Empirical sand and shale lines are plotted, and general trends of varying pore-fluid and compaction are indicated. Poisson's ratio is, generally, very sensitive to sand-shale and pore-fluid variations, while the acoustic impedance is sensitive to porosity and pore-fluid variations (see Section C.1). The plot also indicates that by using a combination of acoustic impedance and Poisson's ratio gas sands can be separated from water filled sands and sands can be separated from shales.

Identification of lithologies using cross-plots of log data and subsequent correlation to the inversion results makes it possible to make regional lithology interpretations and increase confidence in hydrocarbon detection.

References

Castagna, John P. and Backus, Milo M., 1993, Offset-dependent reflectivity - Theory and practice of AVO analysis. *Society of Exploration Geophysicists.*

Shuey, R.T., 1985. A simplification of the Zoeppritz equations. *Geophysics*, **50**, 609–614.

Smith, G.C. & Gidlow, P.M., 1987. Weighted Stacking for Rock Property Estimation and Detection of Gas. *Geophysical Prospecting*, **35**, 993–1014.

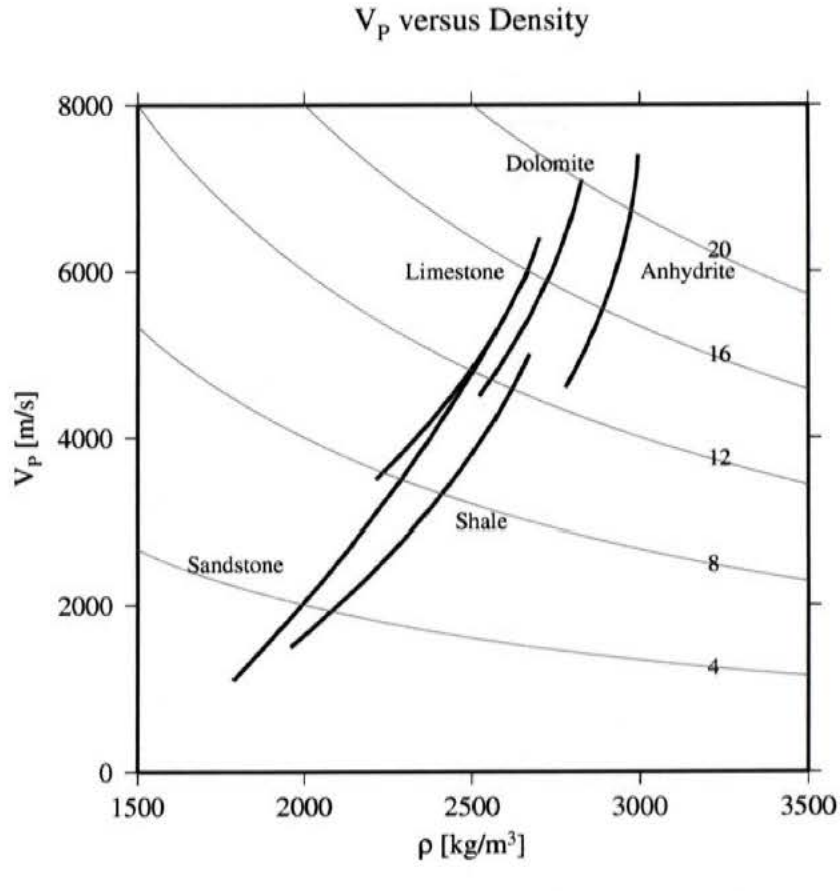

Figure C.1: *Empirical relations between acoustic velocity and density for major lithologies [Castagna, 1993]. Contours of acoustic impedance ($\times 10^6$) have been plotted on top.*

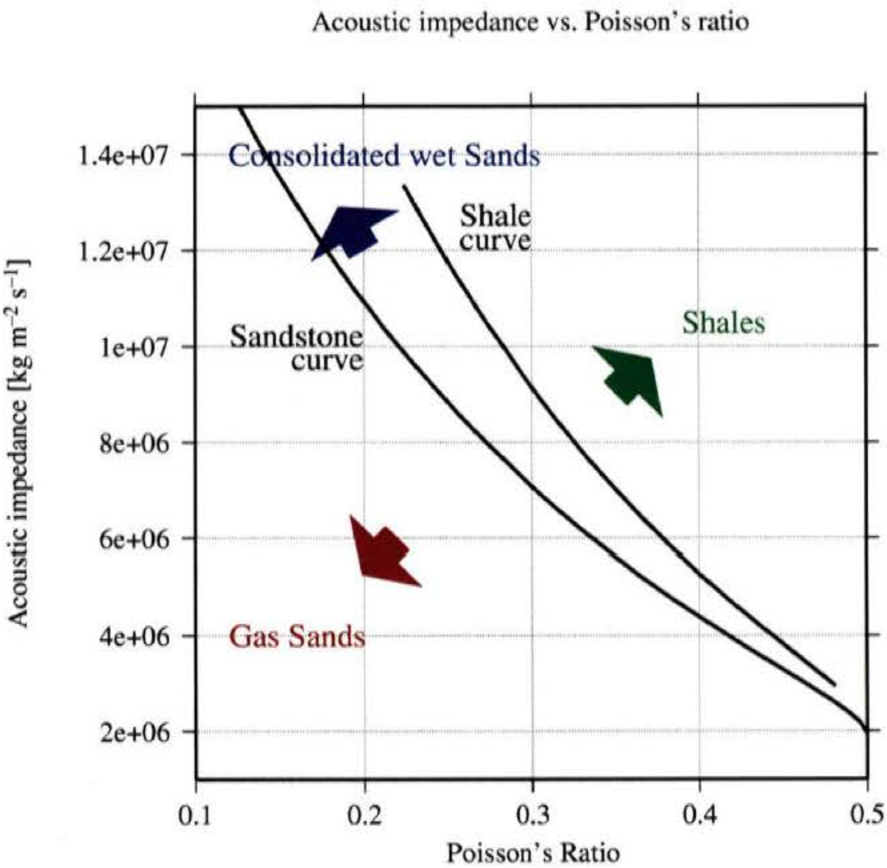

Figure C.2: *Empirical relations between acoustic impedance and Poisson's ratio for sand and shale. Poisson's ratio is generally highly sensitive to sand-shale and pore-fluid variations, while the acoustic impedance is sensitive to porosity and pore-fluid variations.*

Appendix D

Raw and calibrated log data

This appendix documents the log calibrations.

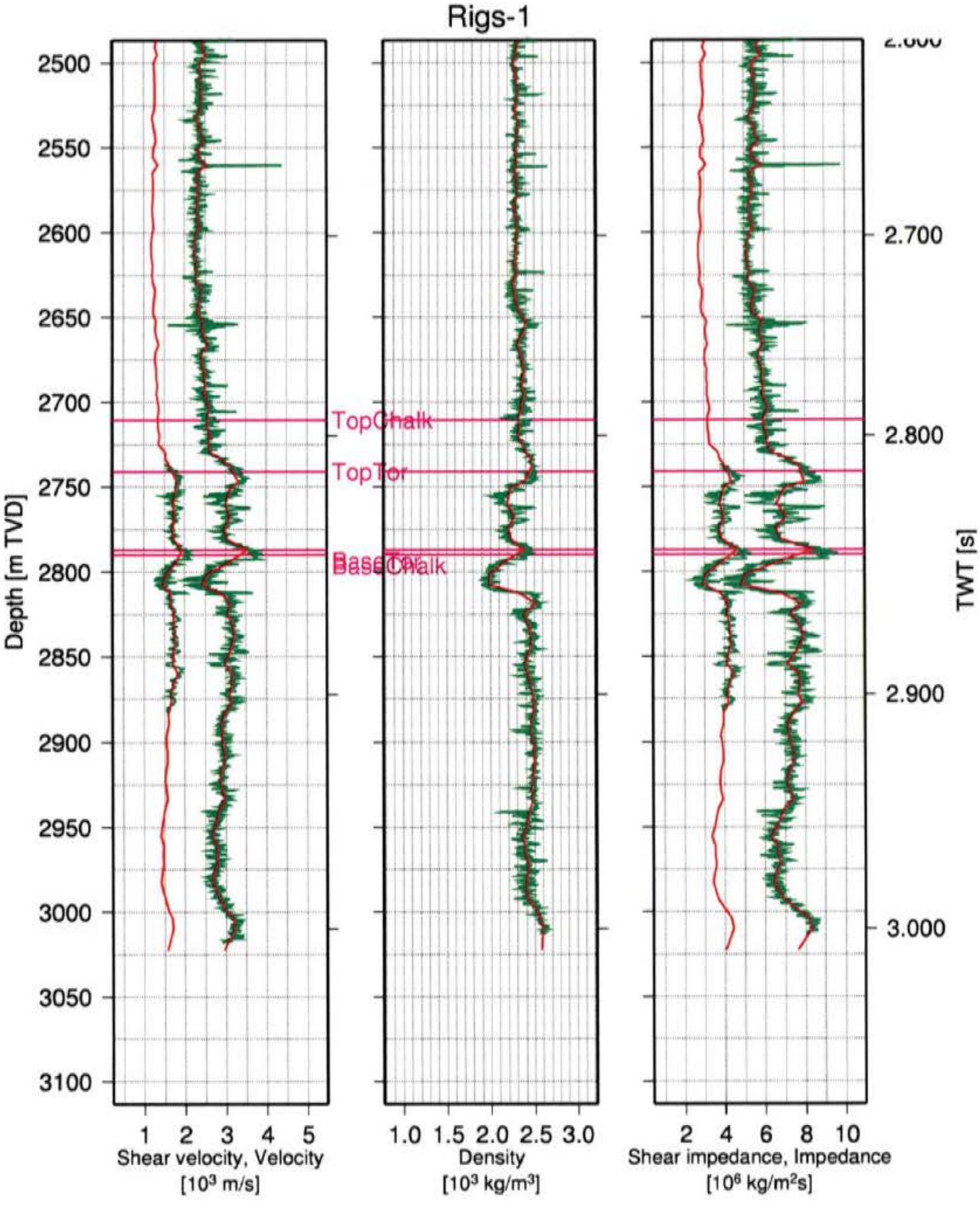

Figure D.1: *The shear velocity, acoustic velocity and density well log data available for well Rigs-1. The raw well log data are shown in green and the resampled well logs in red. The left hand axis is annotated in depth in metres. The right hand axis is annotated in depth in s TWT. The right hand axis is annotated in depth in s TWT after application of the visual ties in Table 2.1. Formation tops are shown in blue. The horizons are shown in purple.*

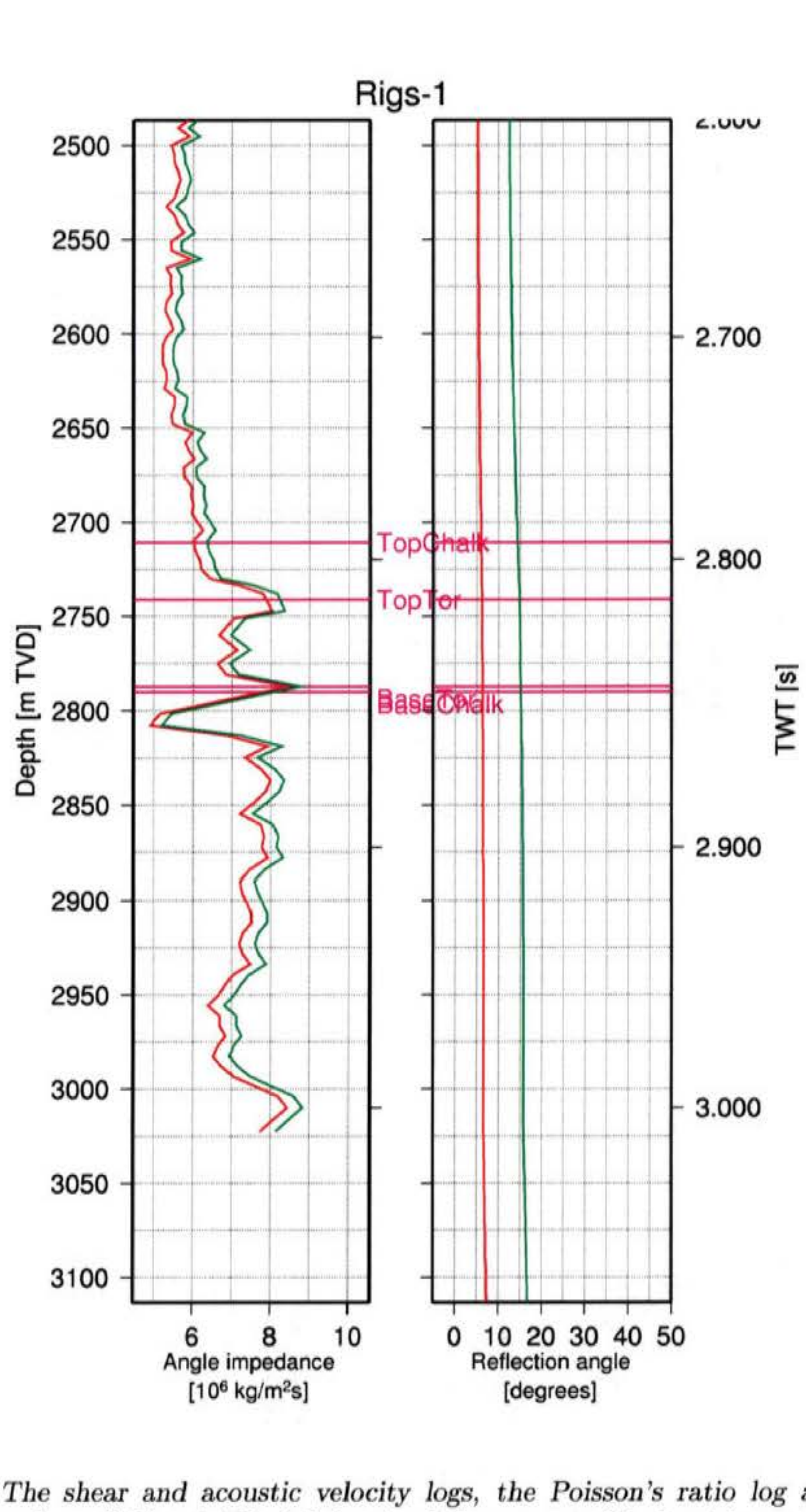

Figure D.2: *The shear and acoustic velocity logs, the Poisson's ratio log and the angle impedance logs for well Rigs-1. The left hand axis is annotated in depth in metres. The right hand axis is annotated in depth in s TWT. The right hand axis is annotated in depth in s TWT after application of the visual ties in Table 2.1. Formation tops are shown in blue. The horizons are shown in red.*

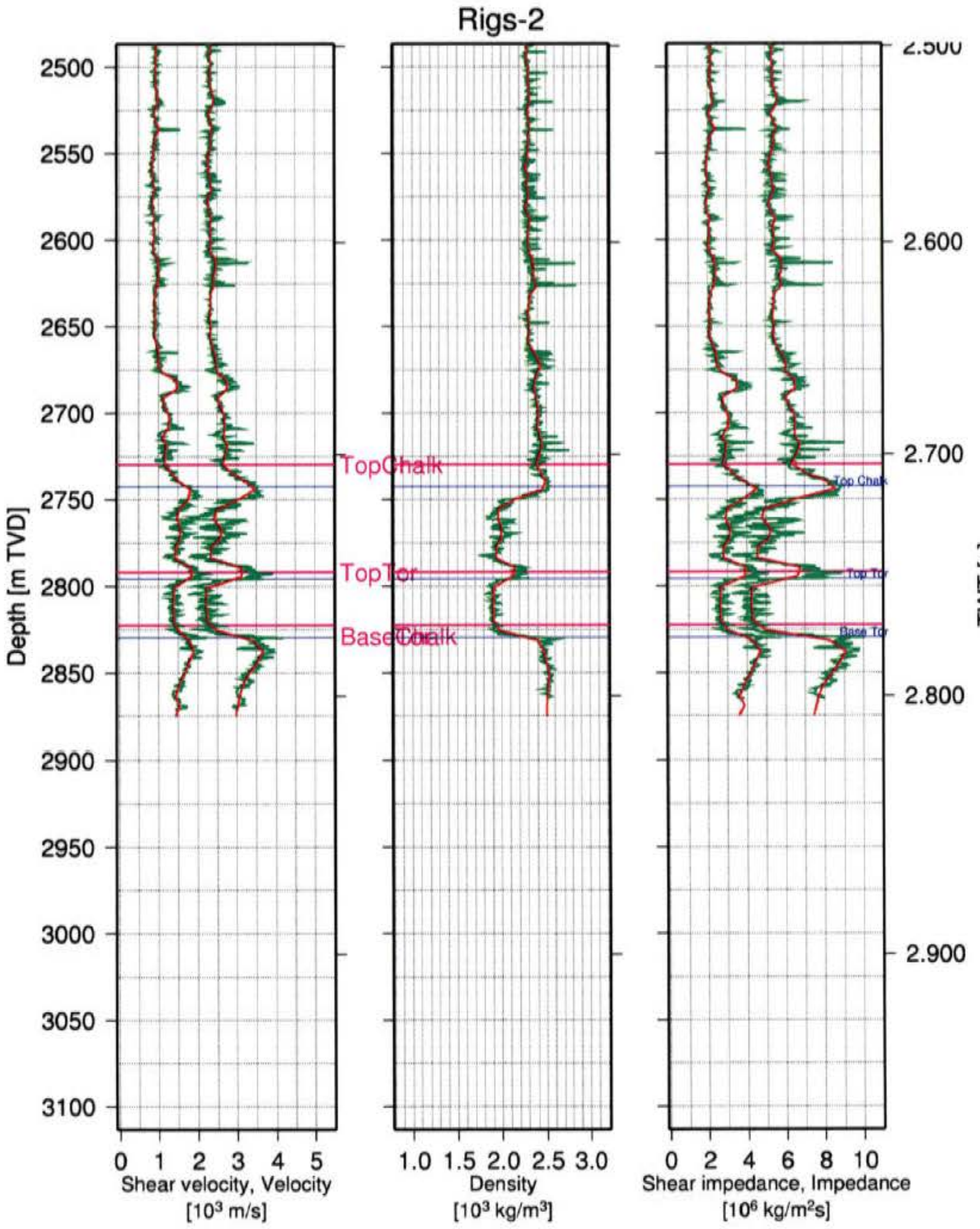

Figure D.3: *The shear velocity, acoustic velocity and density well log data available for well Rigs-2. The raw well log data are shown in green and the resampled well logs in red. The left hand axis is annotated in depth in metres. The right hand axis is annotated in depth in s TWT. The right hand axis is annotated in depth in s TWT after application of the visual ties in Table 2.1. Formation tops are shown in blue. The horizons are shown in purple.*

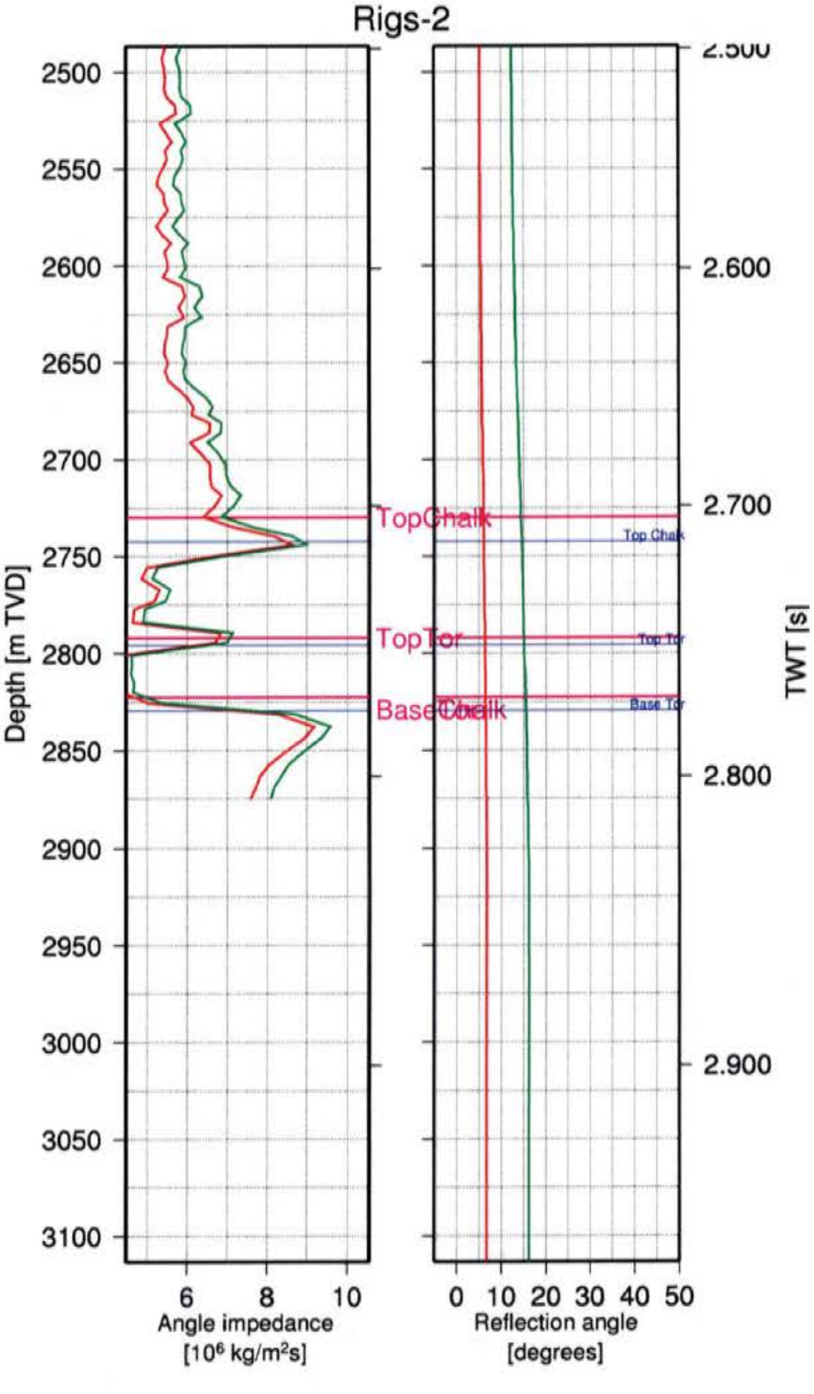

Figure D.4: *The shear and acoustic velocity logs, the Poisson's ratio log and the angle impedance logs for well Rigs-2. The left hand axis is annotated in depth in metres. The right hand axis is annotated in depth in s TWT. The right hand axis is annotated in depth in s TWT after application of the visual ties in Table 2.1. Formation tops are shown in blue. The horizons are shown in red.*

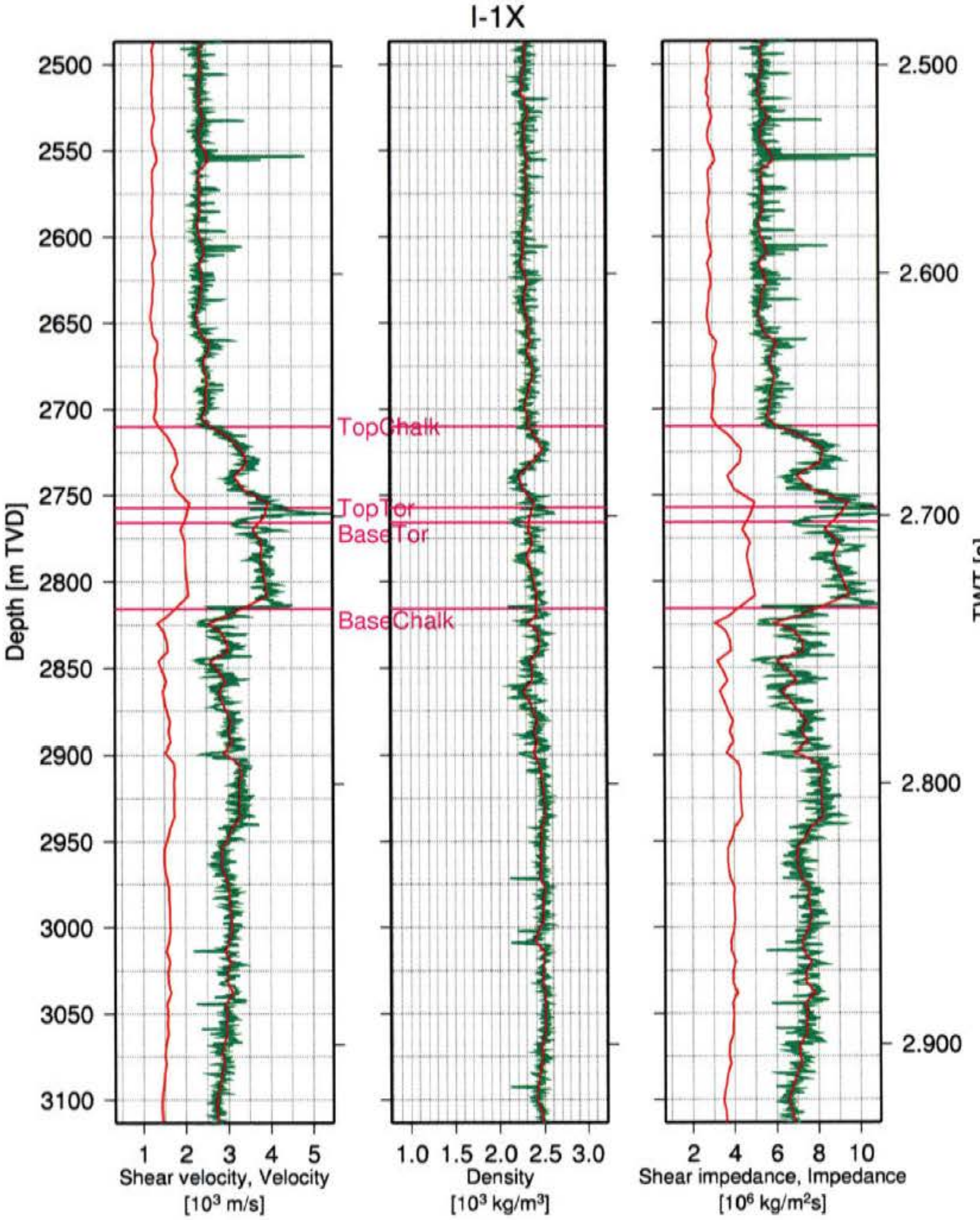

Figure D.5: *The shear velocity, acoustic velocity and density well log data available for well I-1x. The raw well log data are shown in green and the resampled well logs in red. The left hand axis is annotated in depth in metres. The right hand axis is annotated in depth in s TWT. The right hand axis is annotated in depth in s TWT after application of the visual ties in Table 2.1. Formation tops are shown in blue. The horizons are shown in purple.*

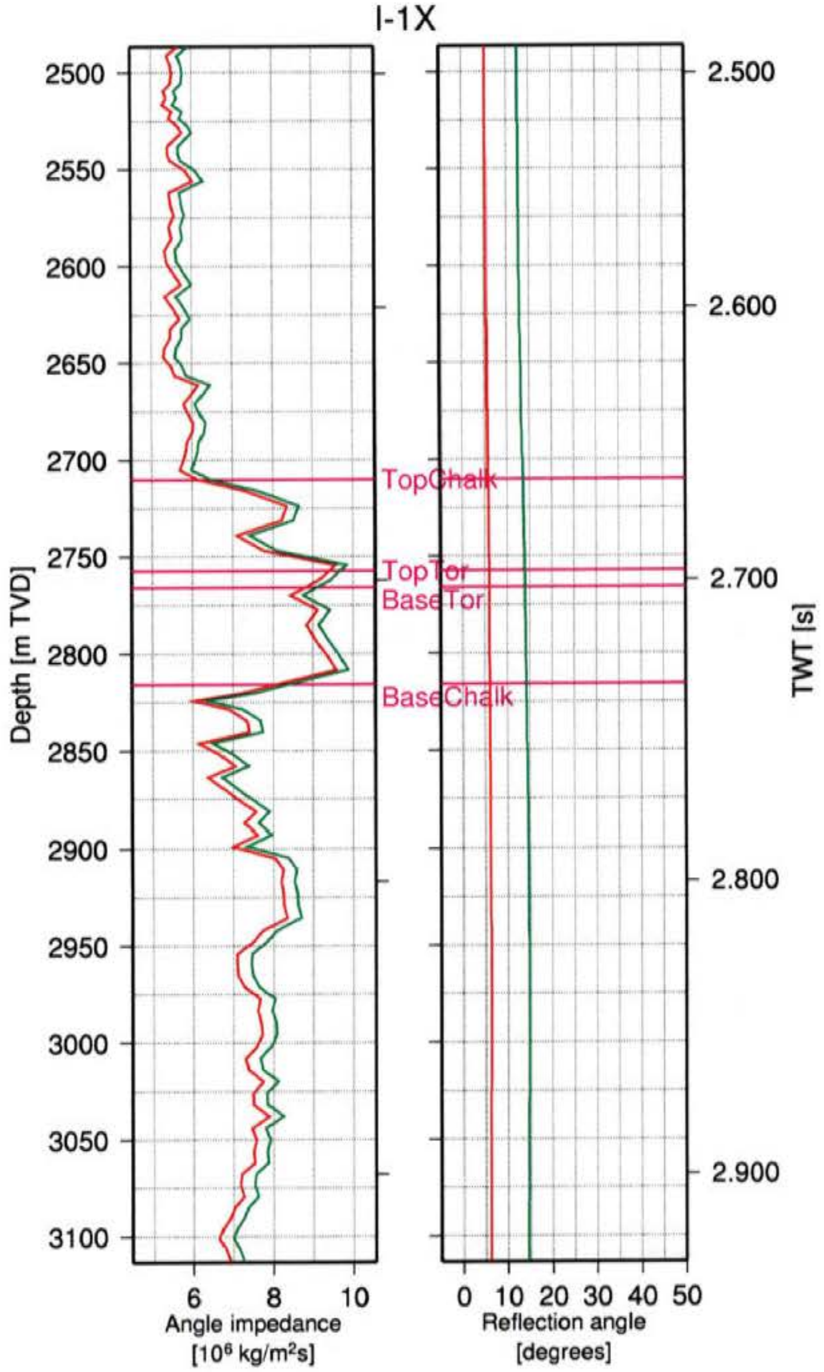

Figure D.6: *The shear and acoustic velocity logs, the Poisson's ratio log and the angle impedance logs for well I-1x. The left hand axis is annotated in depth in metres. The right hand axis is annotated in depth in s TWT. The right hand axis is annotated in depth in s TWT after application of the visual ties in Table 2.1. Formation tops are shown in blue. The horizons are shown in red.*

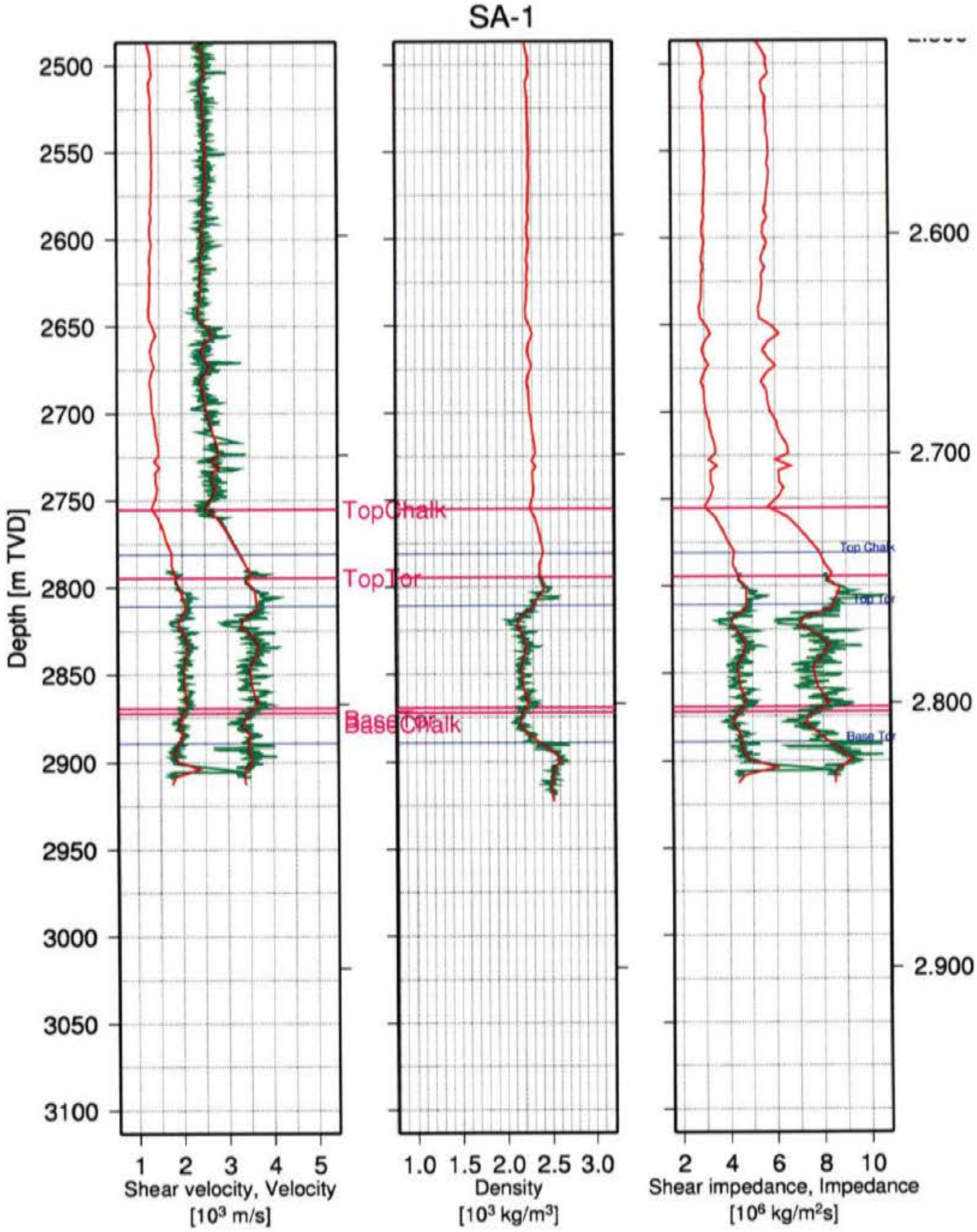

Figure D.7: *The shear velocity, acoustic velocity and density well log data available for well Sa-1. The raw well log data are shown in green and the resampled well logs in red. The left hand axis is annotated in depth in metres. The right hand axis is annotated in depth in s TWT. The right hand axis is annotated in depth in s TWT after application of the visual ties in Table 2.1. Formation tops are shown in blue. The horizons are shown in purple.*

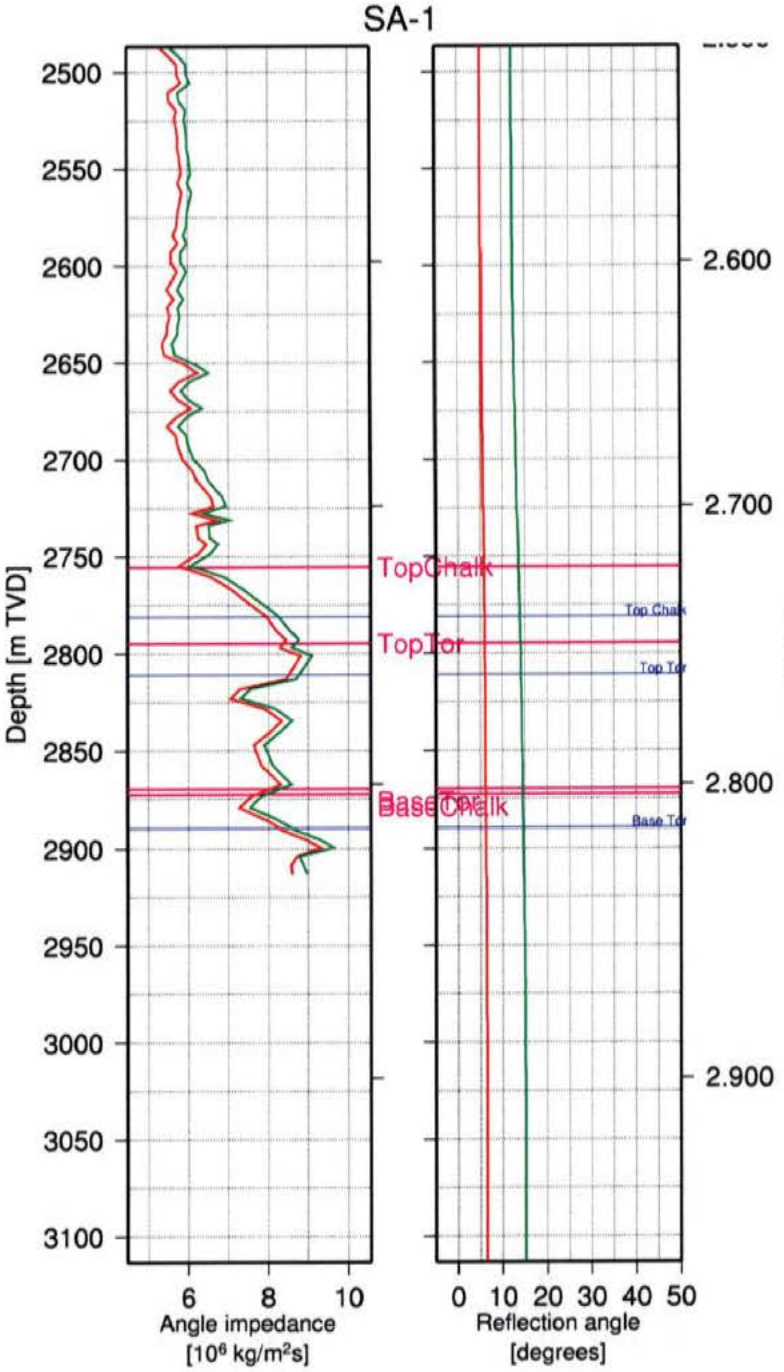

Figure D.8: *The shear and acoustic velocity logs, the Poisson's ratio log and the angle impedance logs for well Sa-1. The left hand axis is annotated in depth in metres. The right hand axis is annotated in depth in s TWT. The right hand axis is annotated in depth in s TWT after application of the visual ties in Table 2.1. Formation tops are shown in blue. The horizons are shown in red.*

APPENDIX **E**

Seismic inversion results at the well locations

Plots showing the angle impedance logs at the wells inserted into the final inversion results are presented on the following pages.

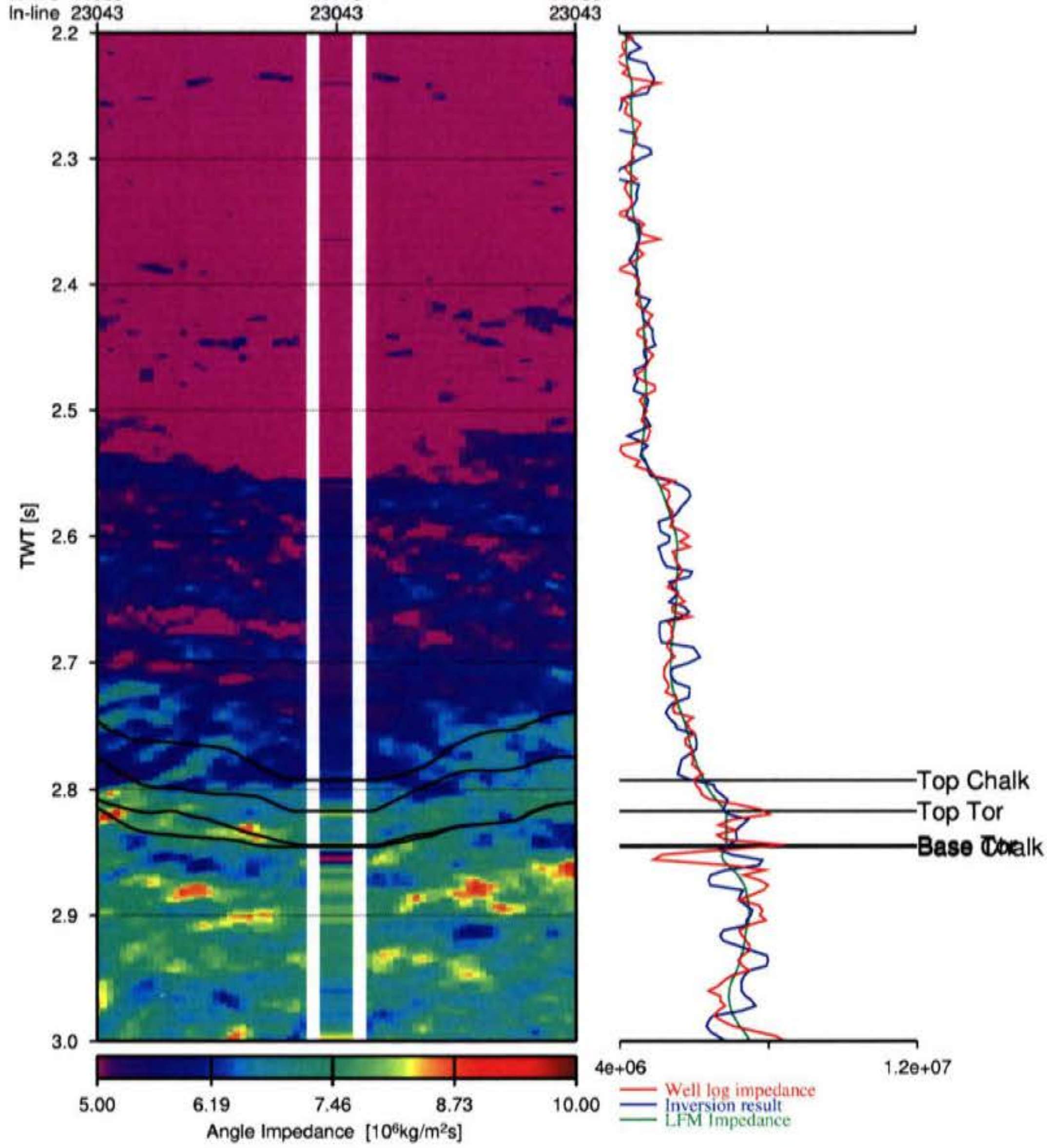

Figure E.1: *Near offset stack: Near angle impedance log from well Rigs-1 inserted into the angle impedance inversion result with low-frequency information. The angle impedance section shown has been extracted along part of in-line in-line 23043. The log is repeated five times. To the right of the angle impedance section, curves of the following are plotted: the calibrated angle impedance log, the low-frequency angle impedance model at the well location and the angle impedance trace estimated by the inversion at the well location.*

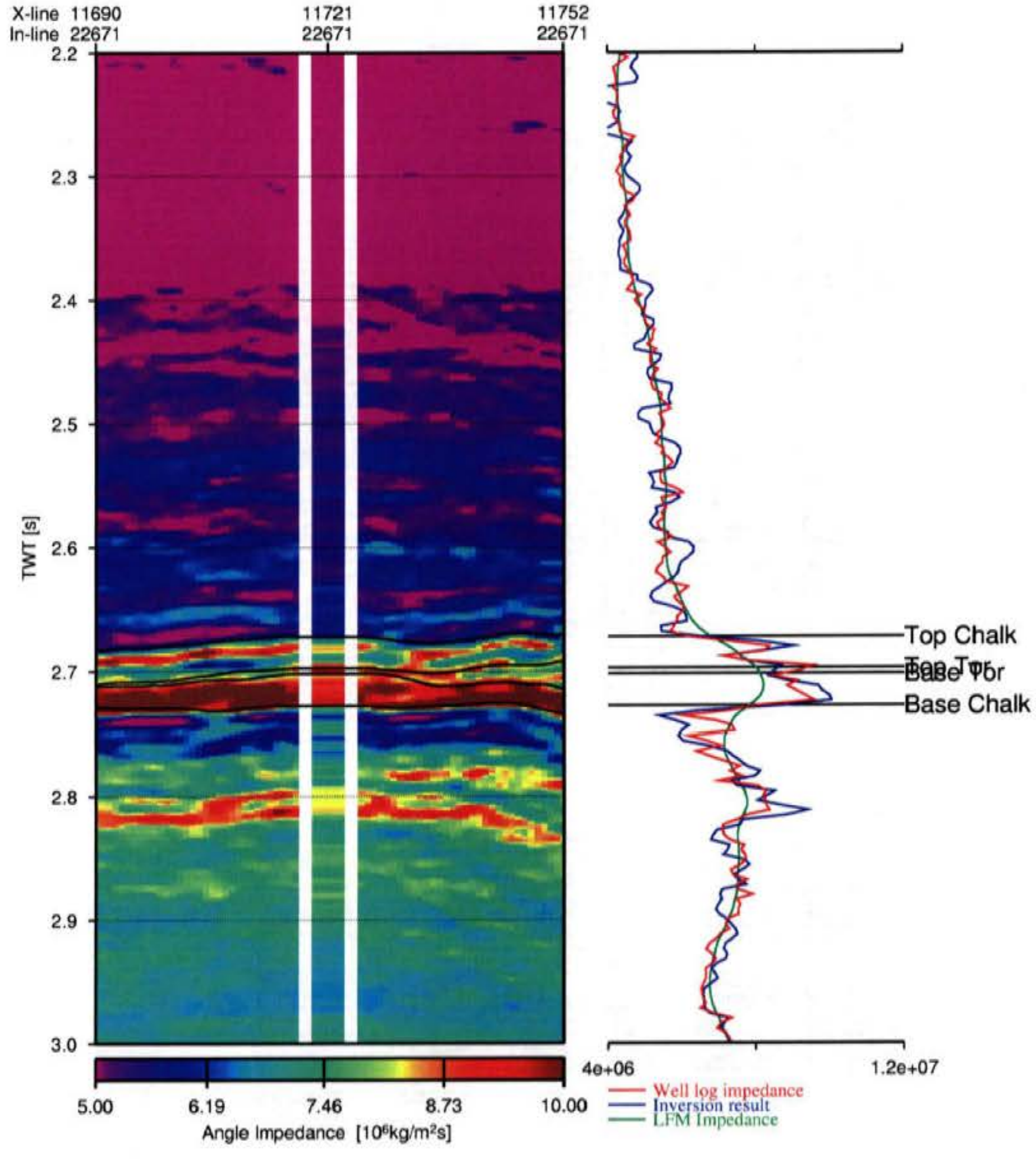

Figure E.2: *Near offset stack: Near angle impedance log from well I-1x inserted into the angle impedance inversion result with low-frequency information. The angle impedance section shown has been extracted along part of in-line in-line 22920. The log is repeated five times. To the right of the angle impedance section, curves of the following are plotted: the calibrated angle impedance log, the low-frequency angle impedance model at the well location and the angle impedance trace estimated by the inversion at the well location.*

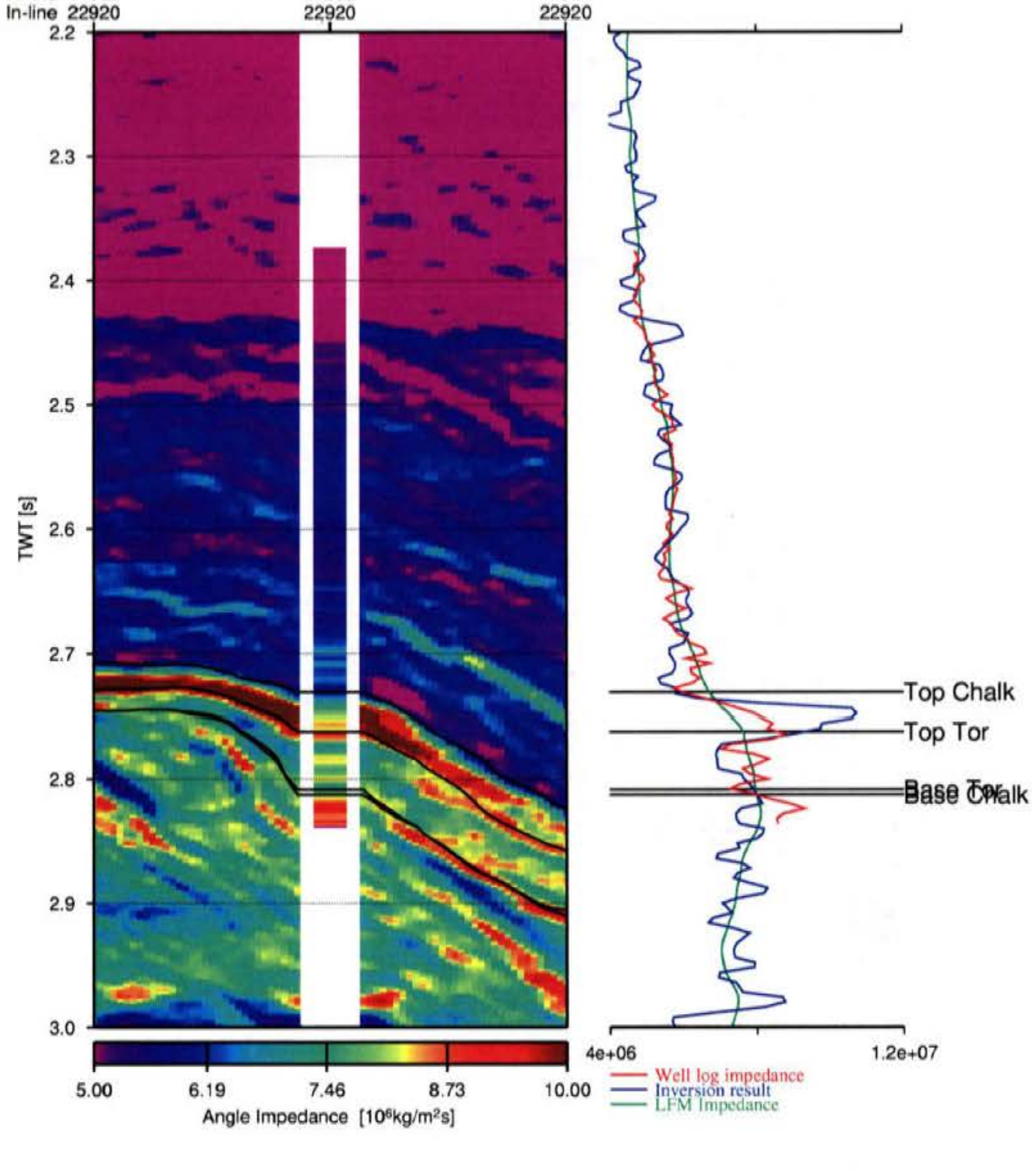

Figure E.3: *Near offset stack: Near angle impedance log from well Sa-1 inserted into the angle impedance inversion result with low-frequency information. The angle impedance section shown has been extracted along part of in-line in-line 22671. The log is repeated five times. To the right of the angle impedance section, curves of the following are plotted: the calibrated angle impedance log, the low-frequency angle impedance model at the well location and the angle impedance trace estimated by the inversion at the well location.*

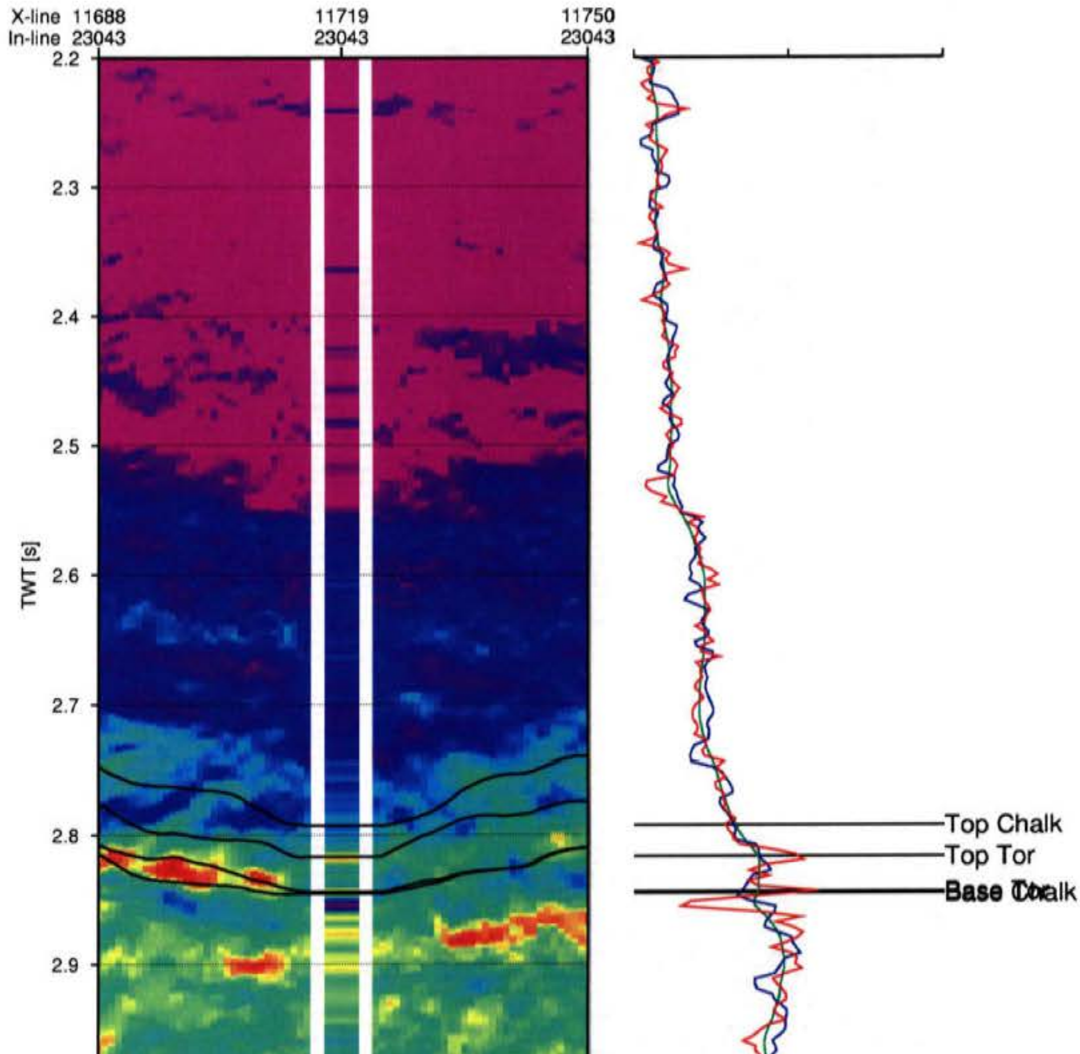

Figure E.4: *Far offset stack: Far angle impedance log from well Rigs-1 inserted into the angle impedance inversion result with low-frequency information. The angle impedance section shown has been extracted along part of in-line in-line 23043. The log is repeated five times. To the right of the angle impedance section, curves of the following are plotted: the calibrated angle impedance log, the low-frequency angle impedance model at the well location and the angle impedance trace estimated by the inversion at the well location.*

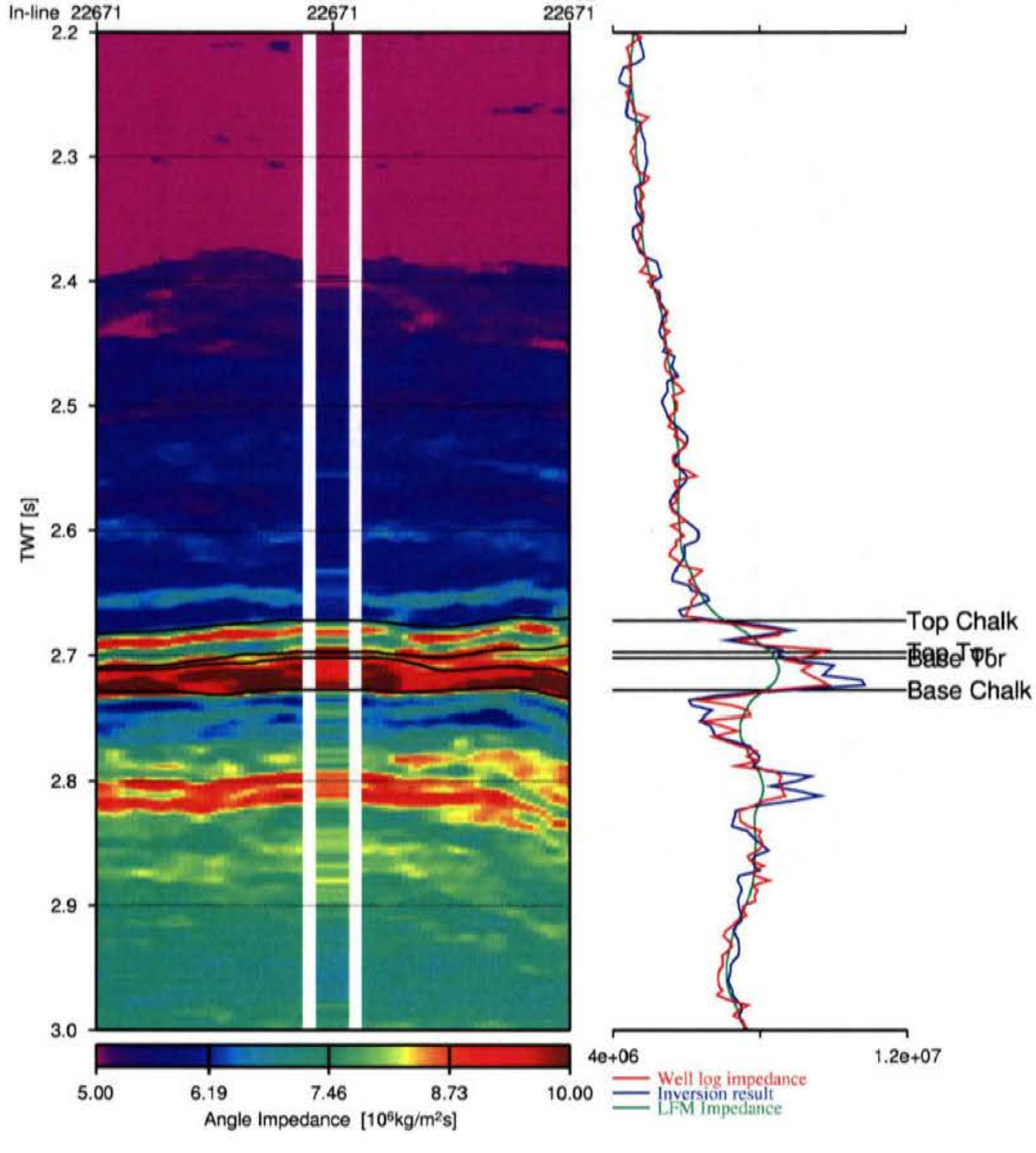

Figure E.5: *Far offset stack: Far angle impedance log from well I-1x inserted into the angle impedance inversion result with low-frequency information. The angle impedance section shown has been extracted along part of in-line in-line 22920. The log is repeated five times. To the right of the angle impedance section, curves of the following are plotted: the calibrated angle impedance log, the low-frequency angle impedance model at the well location and the angle impedance trace estimated by the inversion at the well location.*

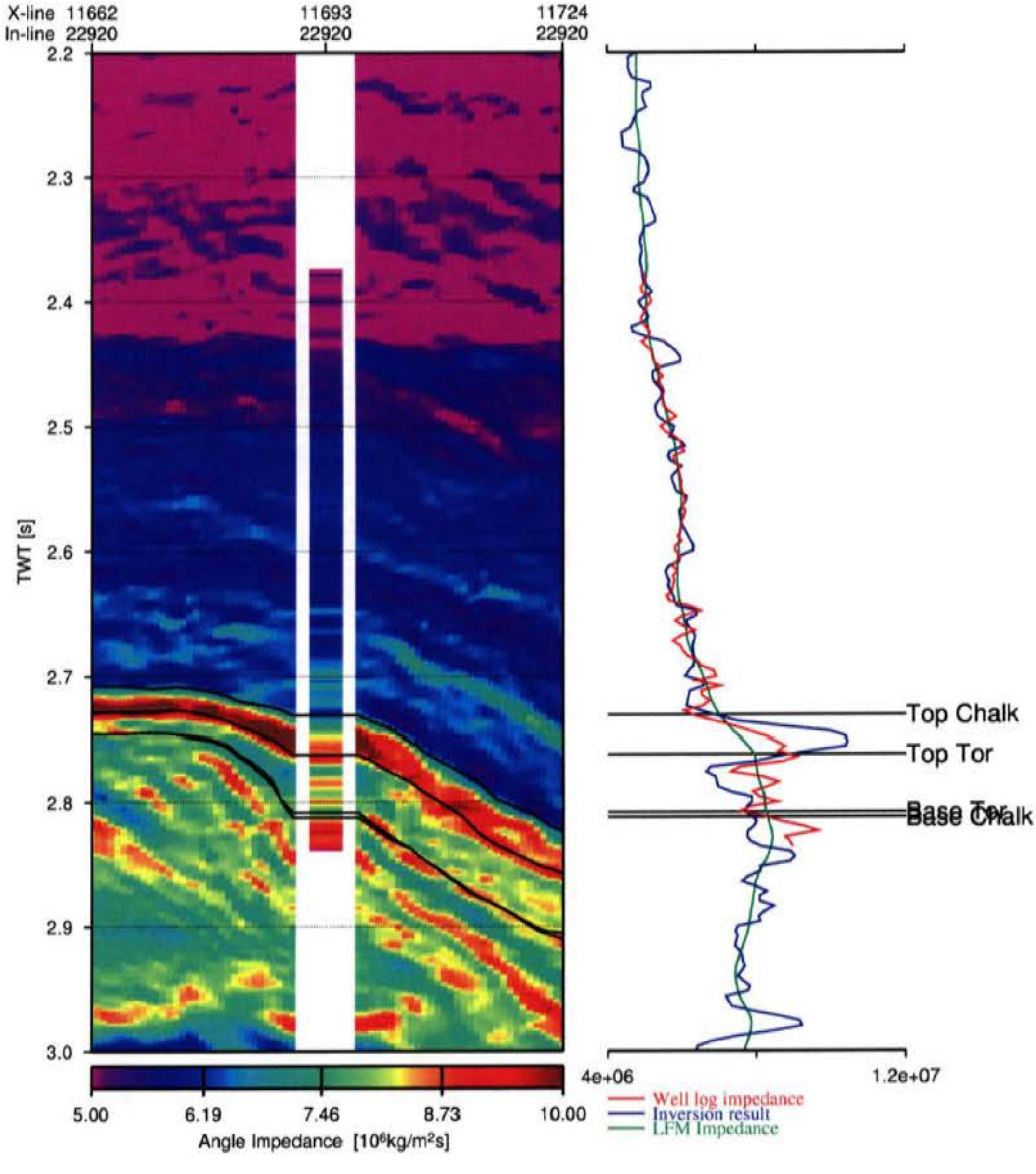

Figure E.6: *Far offset stack: Far angle impedance log from well Sa-1 inserted into the angle impedance inversion result with low-frequency information. The angle impedance section shown has been extracted along part of in-line in-line 22671. The log is repeated five times. To the right of the angle impedance section, curves of the following are plotted: the calibrated angle impedance log, the low-frequency angle impedance model at the well location and the angle impedance trace estimated by the inversion at the well location.*

APPENDIX **F**

AVO attributes at the well locations

Extracts from the estimated AVO attributes are presented on the following pages

The presentation consists of the following:

AVO attributes estimated from the near and far offset stack inversion results:

- Figures F.1–F.3 show the Poisson's ratio logs of wells Rigs-1, I-1x and Sa-1 inserted into the estimated Poisson's ratio with low-frequency information.
- Figures F.4–F.6 show the acoustic impedance logs of wells Rigs-1, I-1x and Sa-1 inserted into the estimated acoustic impedance with low-frequency information.
- Figures F.7–F.9 show the shear impedance logs of wells Rigs-1, I-1x and Sa-1 inserted into the estimated shear impedance with low-frequency information.

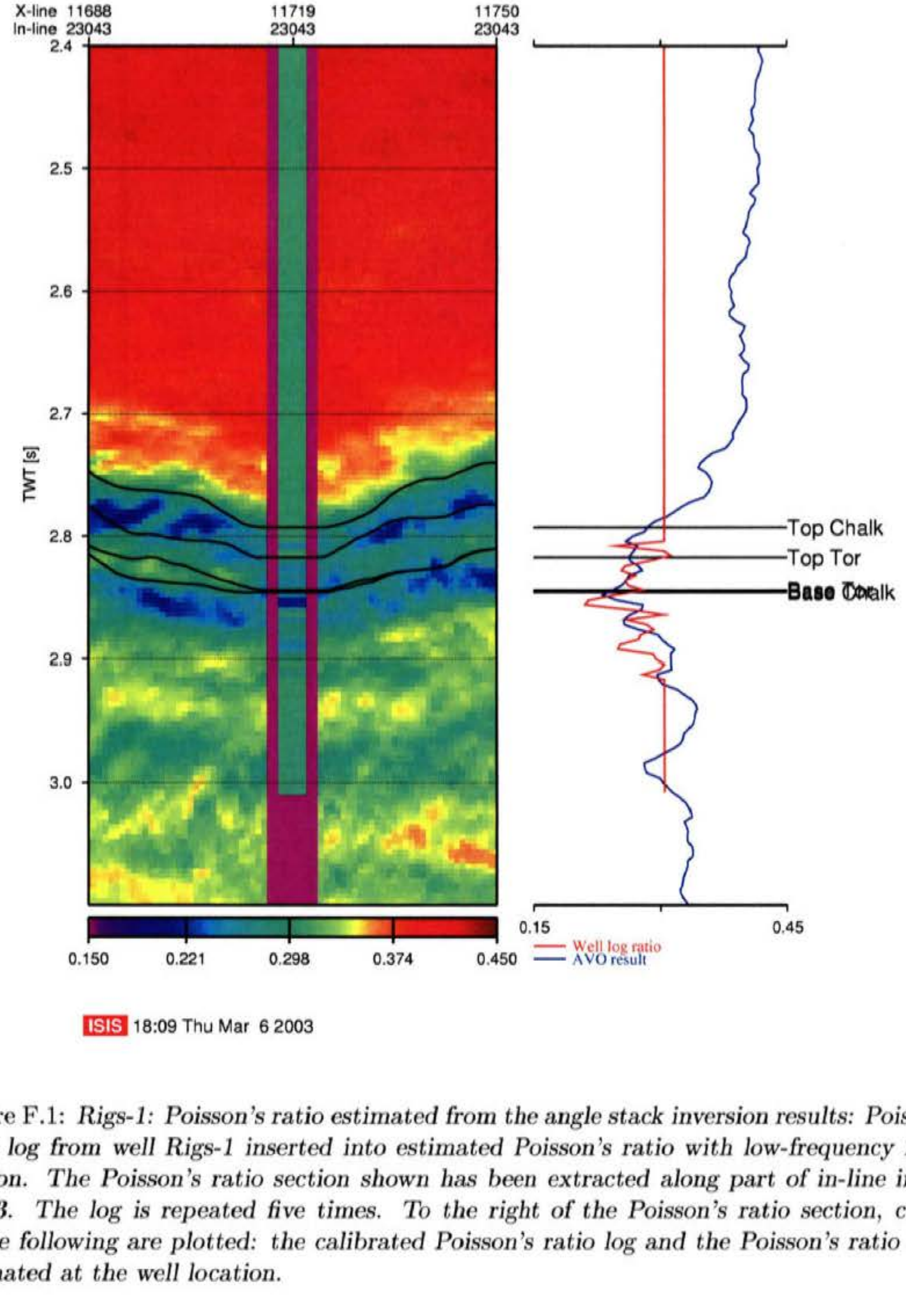

Figure F.1: *Rigs-1: Poisson's ratio estimated from the angle stack inversion results: Poisson's ratio log from well Rigs-1 inserted into estimated Poisson's ratio with low-frequency information. The Poisson's ratio section shown has been extracted along part of in-line in-line 23043. The log is repeated five times. To the right of the Poisson's ratio section, curves of the following are plotted: the calibrated Poisson's ratio log and the Poisson's ratio trace estimated at the well location.*

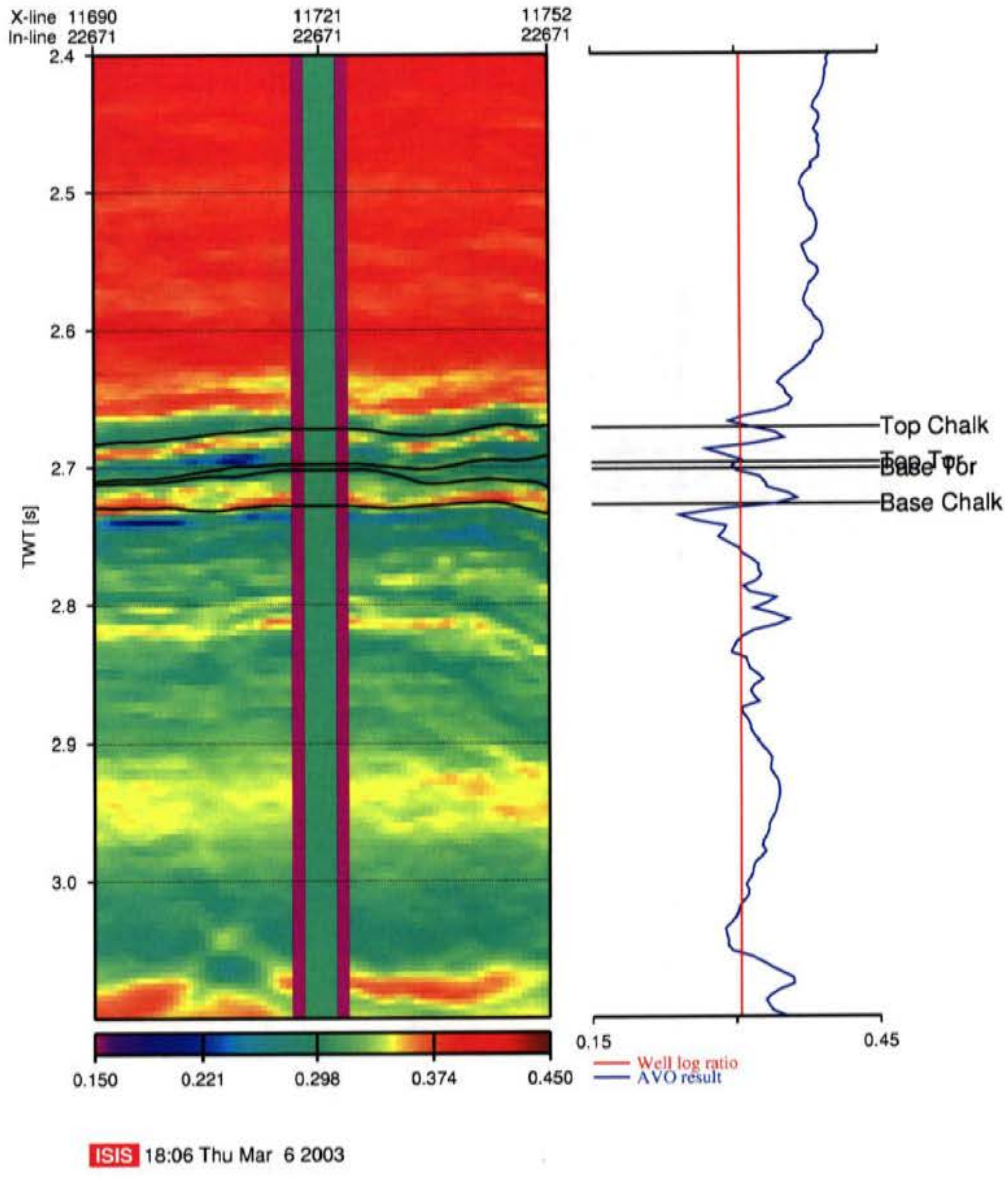

Figure F.2: *I-1x: Poisson's ratio estimated from the angle stack inversion results: Poisson's ratio log from well I-1x inserted into estimated Poisson's ratio with low-frequency information. The Poisson's ratio section shown has been extracted along part of in-line in-line 22920. The log is repeated five times. To the right of the Poisson's ratio section, curves of the following are plotted: the calibrated Poisson's ratio log and the Poisson's ratio trace estimated at the well location.*

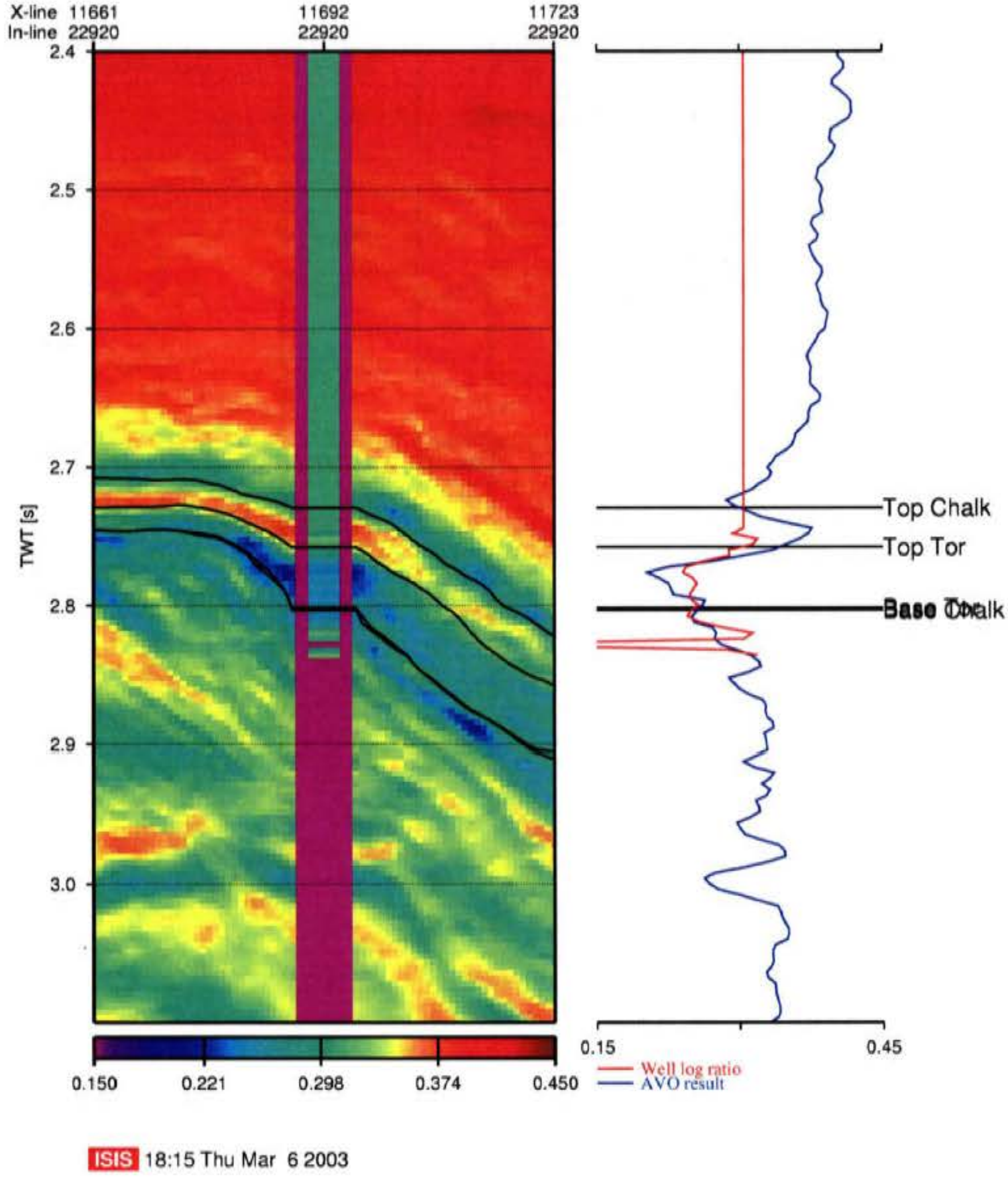

Figure F.3: *Sa-1: Poisson's ratio estimated from the angle stack inversion results: Poisson's ratio log from well Sa-1 inserted into estimated Poisson's ratio with low-frequency information. The Poisson's ratio section shown has been extracted along part of in-line in-line 22671. The log is repeated five times. To the right of the Poisson's ratio section, curves of the following are plotted: the calibrated Poisson's ratio log and the Poisson's ratio trace estimated at the well location.*

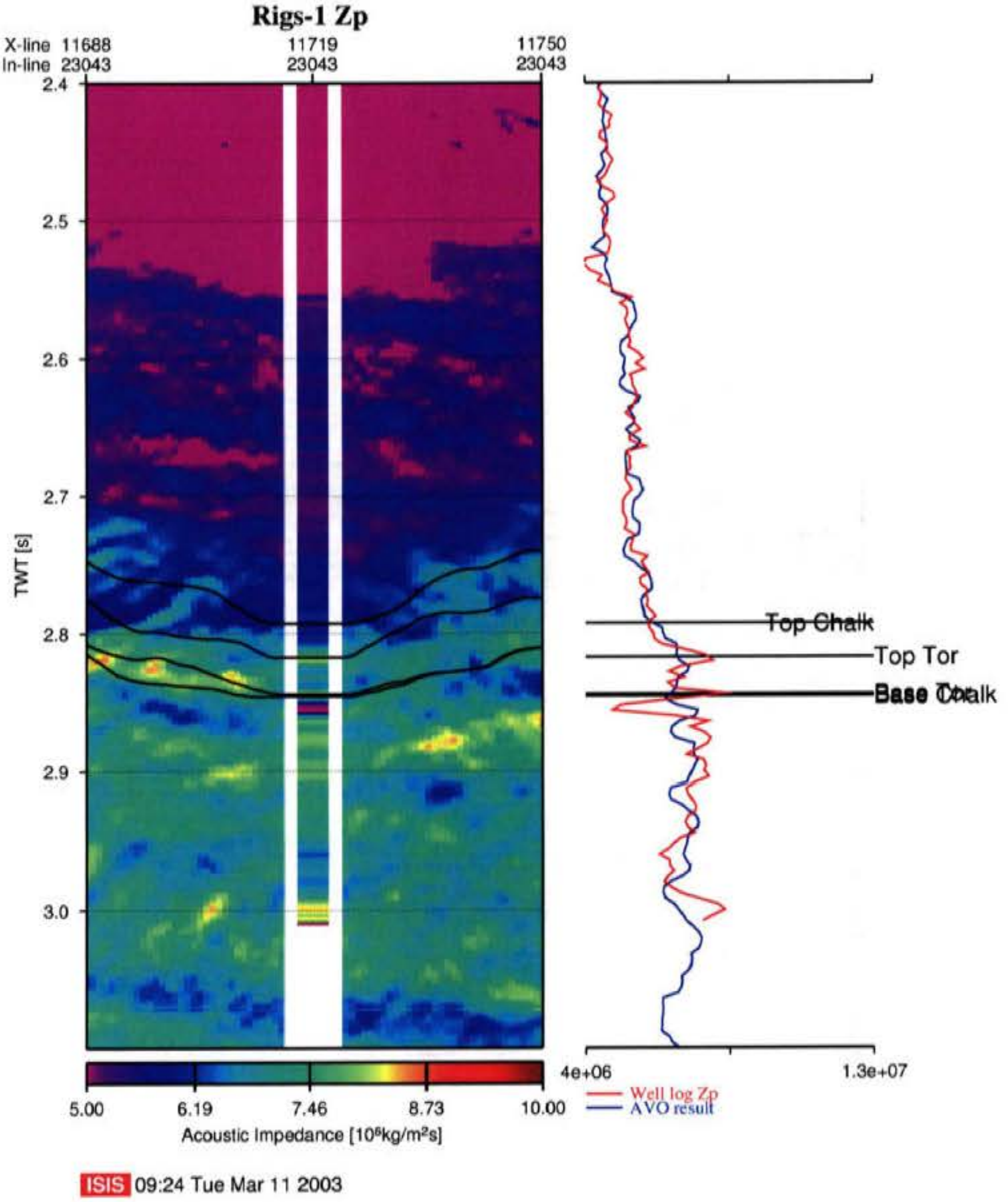

Figure F.4: *Rigs-1: Acoustic impedance estimated from the angle stack inversion results: Acoustic impedance log from well Rigs-1 inserted into estimated acoustic impedance with low-frequency information. The acoustic impedance section shown has been extracted along part of in-line in-line 23043. The log is repeated five times. To the right of the acoustic impedance section, curves of the following are plotted: the calibrated acoustic impedance log and the acoustic impedance trace estimated at the well location from the angle stack inversion results.*

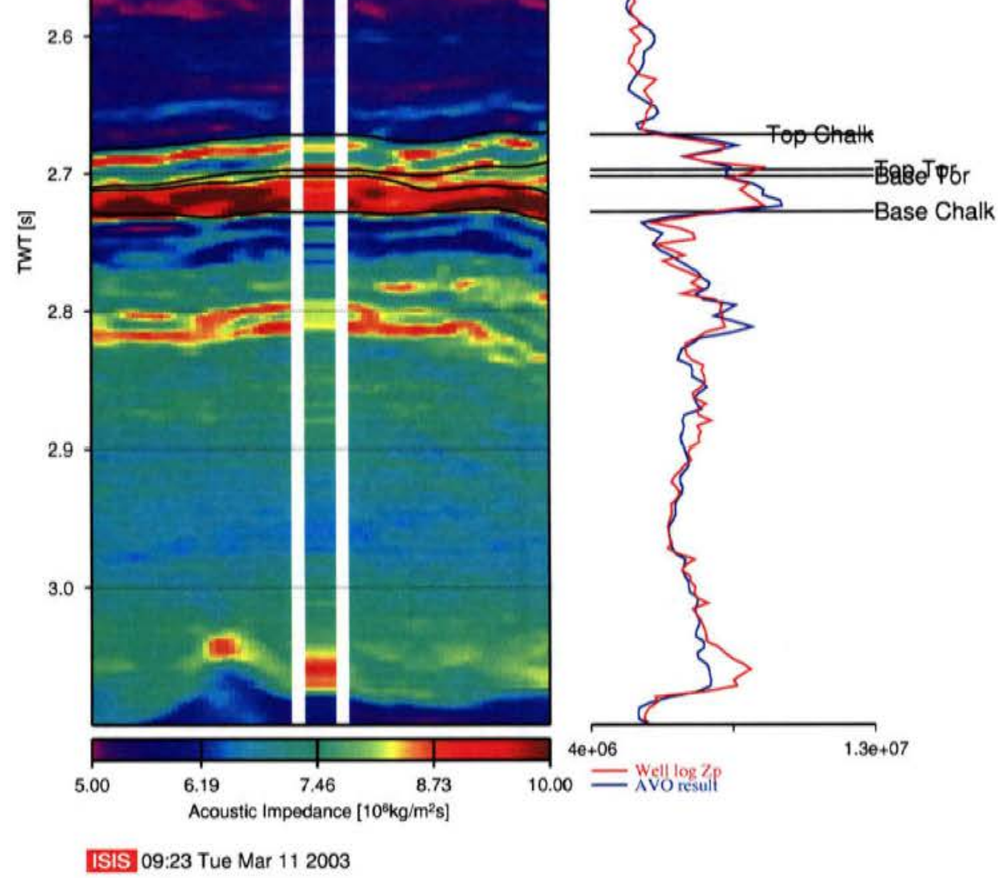

Figure F.5: *I-1x: Acoustic impedance estimated from the angle stack inversion results: Acoustic impedance log from well I-1x inserted into estimated acoustic impedance with low-frequency information. The acoustic impedance section shown has been extracted along part of in-line in-line 22920. The log is repeated five times. To the right of the acoustic impedance section, curves of the following are plotted: the calibrated acoustic impedance log and the acoustic impedance trace estimated at the well location from the angle stack inversion results.*

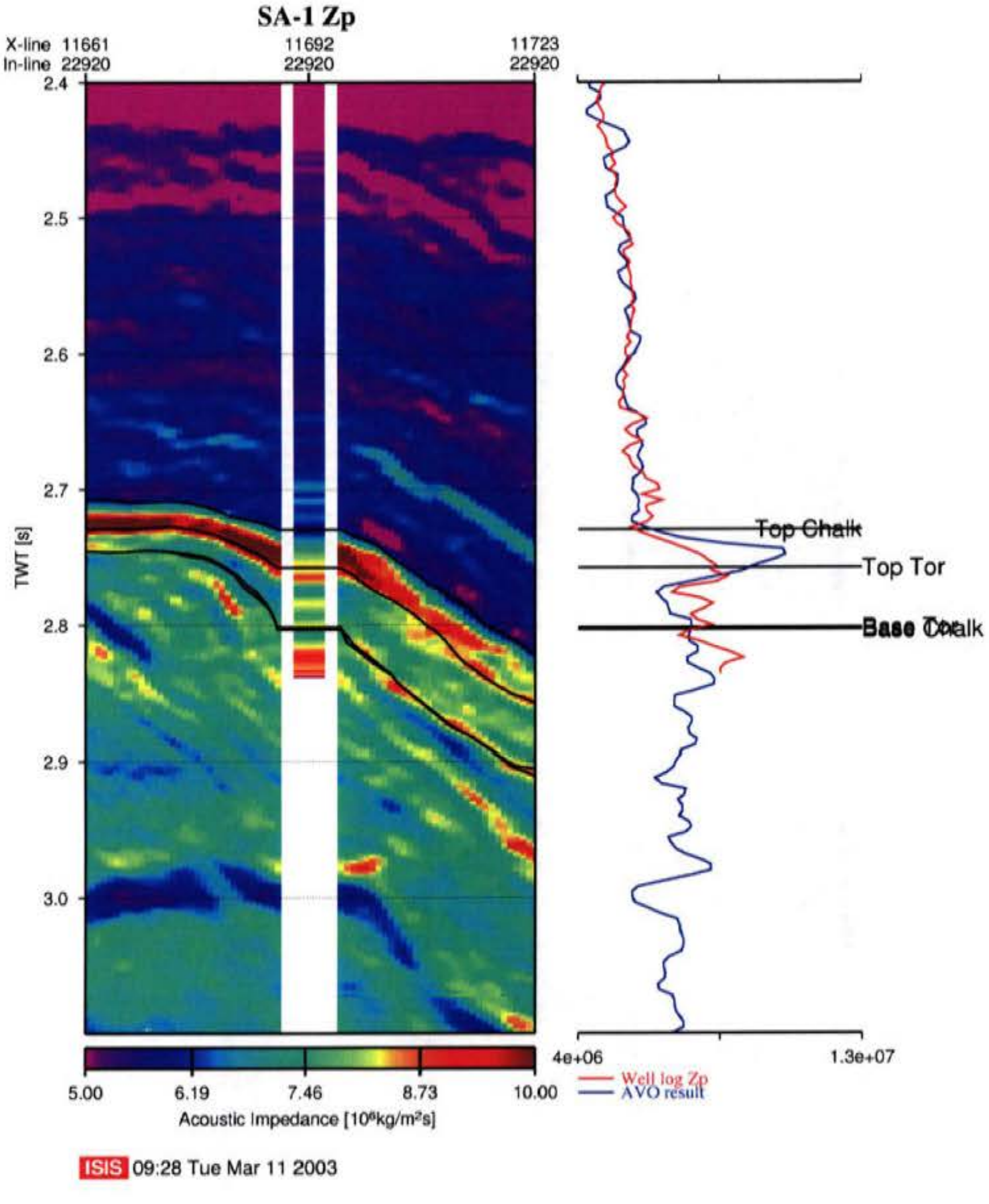

Figure F.6: *Sa-1: Acoustic impedance estimated from the angle stack inversion results: Acoustic impedance log from well Sa-1 inserted into estimated acoustic impedance with low-frequency information. The acoustic impedance section shown has been extracted along part of in-line in-line 22671. The log is repeated five times. To the right of the acoustic impedance section, curves of the following are plotted: the calibrated acoustic impedance log and the acoustic impedance trace estimated at the well location from the angle stack inversion results.*

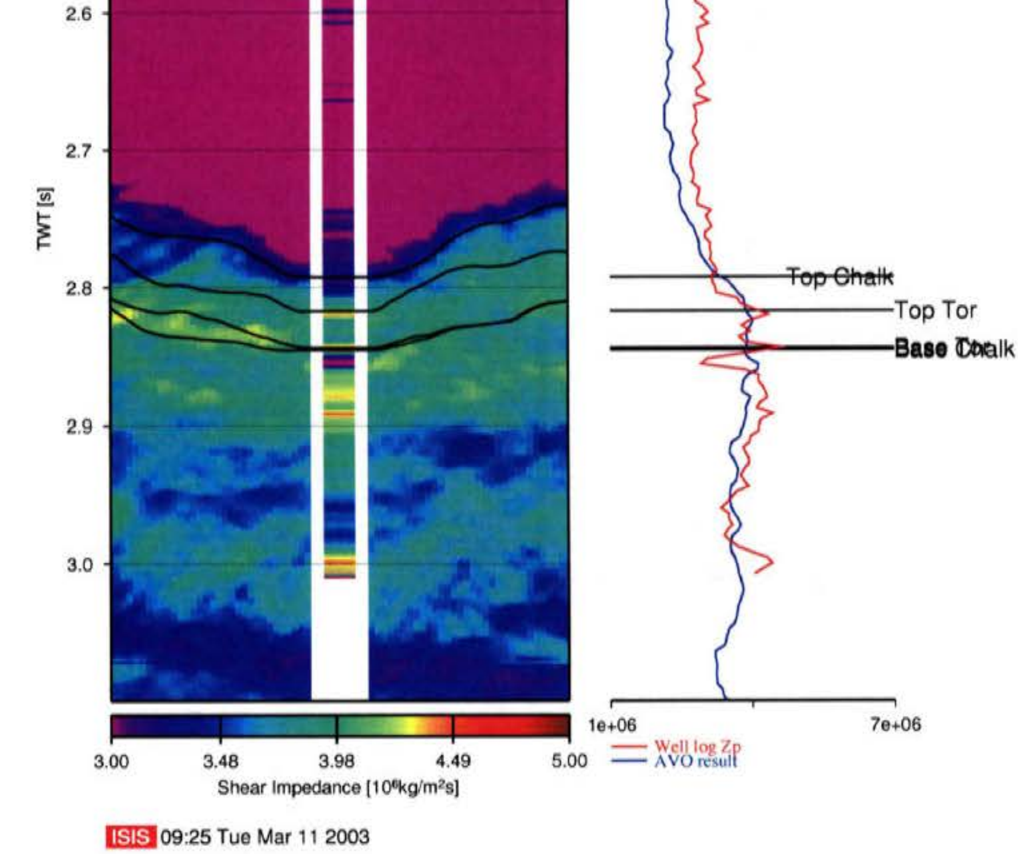

Figure F.7: *Rigs-1: Shear impedance estimated from the angle stack inversion results: Shear impedance log from well Rigs-1 inserted into estimated shear impedance with low-frequency information. The shear impedance section shown has been extracted along part of in-line in-line 23043. The log is repeated five times. To the right of the shear impedance section, curves of the following are plotted: the calibrated shear impedance log and the shear impedance trace estimated at the well location from the angle stack inversion results.*

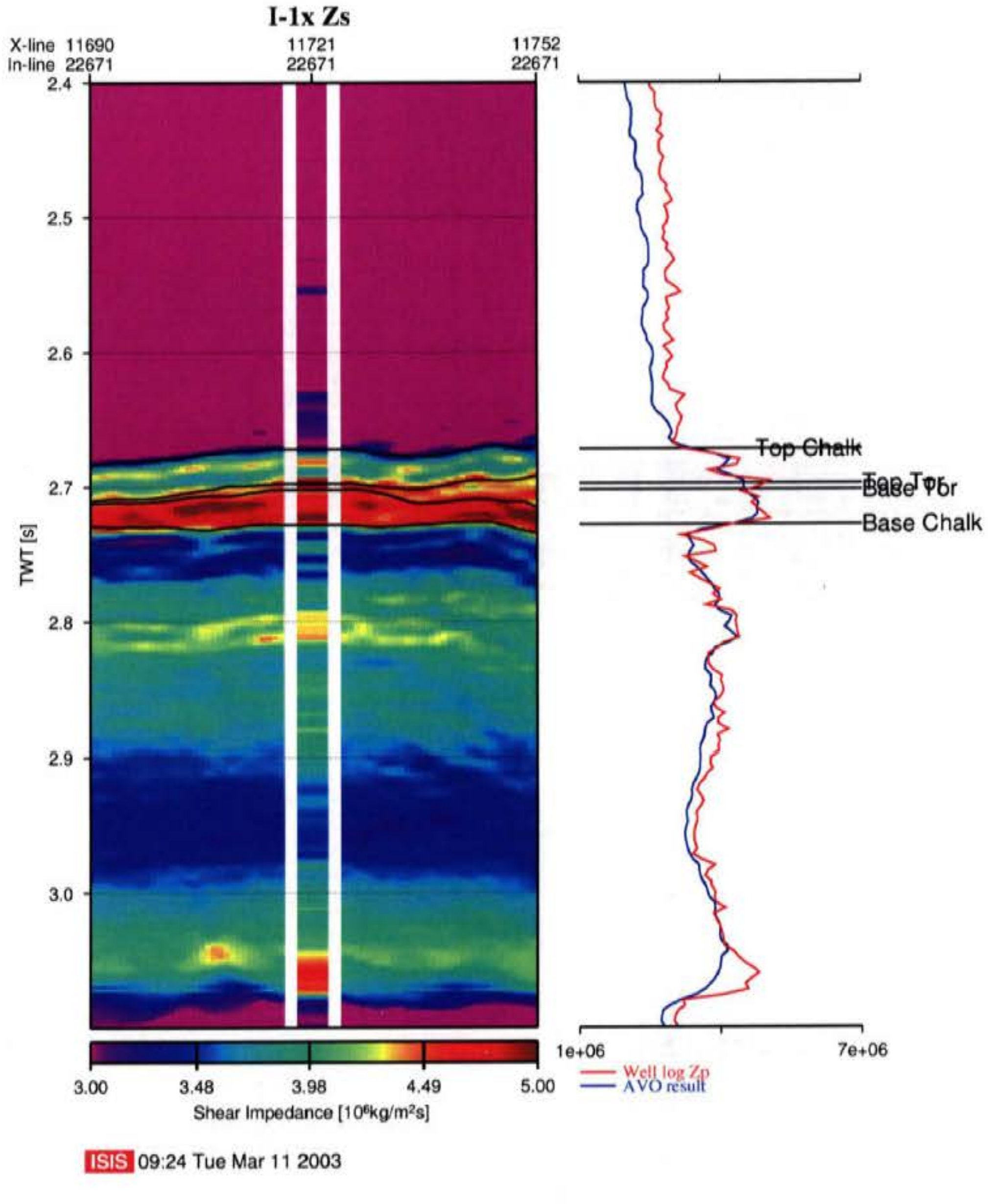

Figure F.8: *I-1x: Shear impedance estimated from the angle stack inversion results: Shear impedance log from well I-1x inserted into estimated shear impedance with low-frequency information. The shear impedance section shown has been extracted along part of in-line in-line 22920. The log is repeated five times. To the right of the shear impedance section, curves of the following are plotted: the calibrated shear impedance log and the shear impedance trace estimated at the well location from the angle stack inversion results.*

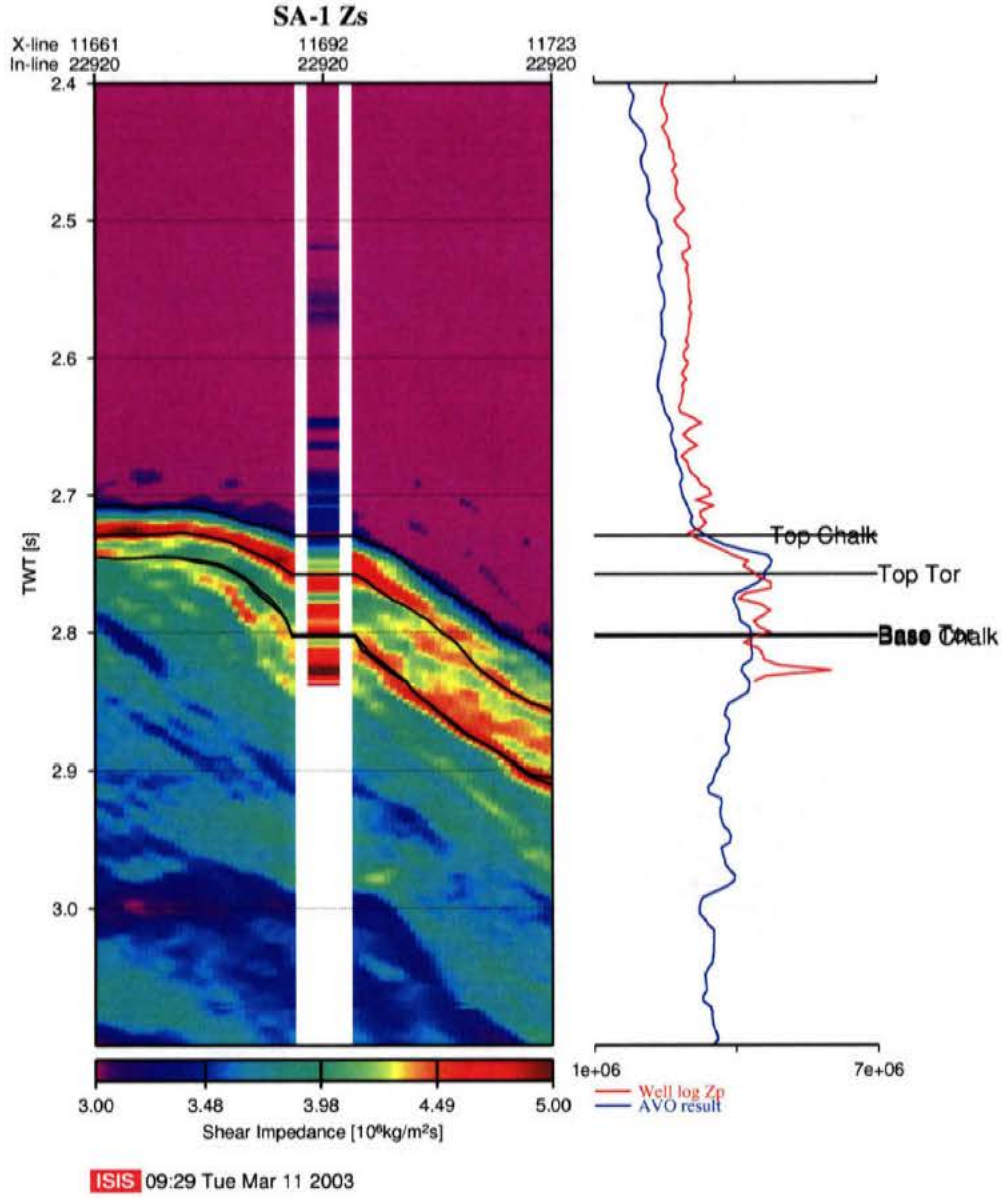

Figure F.9: *Sa-1: Shear impedance estimated from the angle stack inversion results: Shear impedance log from well Sa-1 inserted into estimated shear impedance with low-frequency information. The shear impedance section shown has been extracted along part of in-line in-line 22671. The log is repeated five times. To the right of the shear impedance section, curves of the following are plotted: the calibrated shear impedance log and the shear impedance trace estimated at the well location from the angle stack inversion results.*

Ødegaard A/S

A Company in the Ødegaard & Danneskiold-Samsøe Group

Titangade 15
DK-2200 Copenhagen N
Denmark
Telephone: +45 35 31 10 10
Telefax: +45 35 31 10 11

EFP 2001: Quality control of well log data from the South Arne Field

Ødegaard A/S and DTU

Ødegaard A/S and DTU

EFP-2001 Rock Physics of Impure Chalk

Report 01.1031

EFP 2001: Quality control of well log data from the South Arne Field

Danish Energy Agency
44 Amaliegade
DK – 1256 Copenhagen K
Denmark

September 2002

Prepared by

Christian Mogensen (Ødegaard A/S) and Ida Fabricius (DTU)

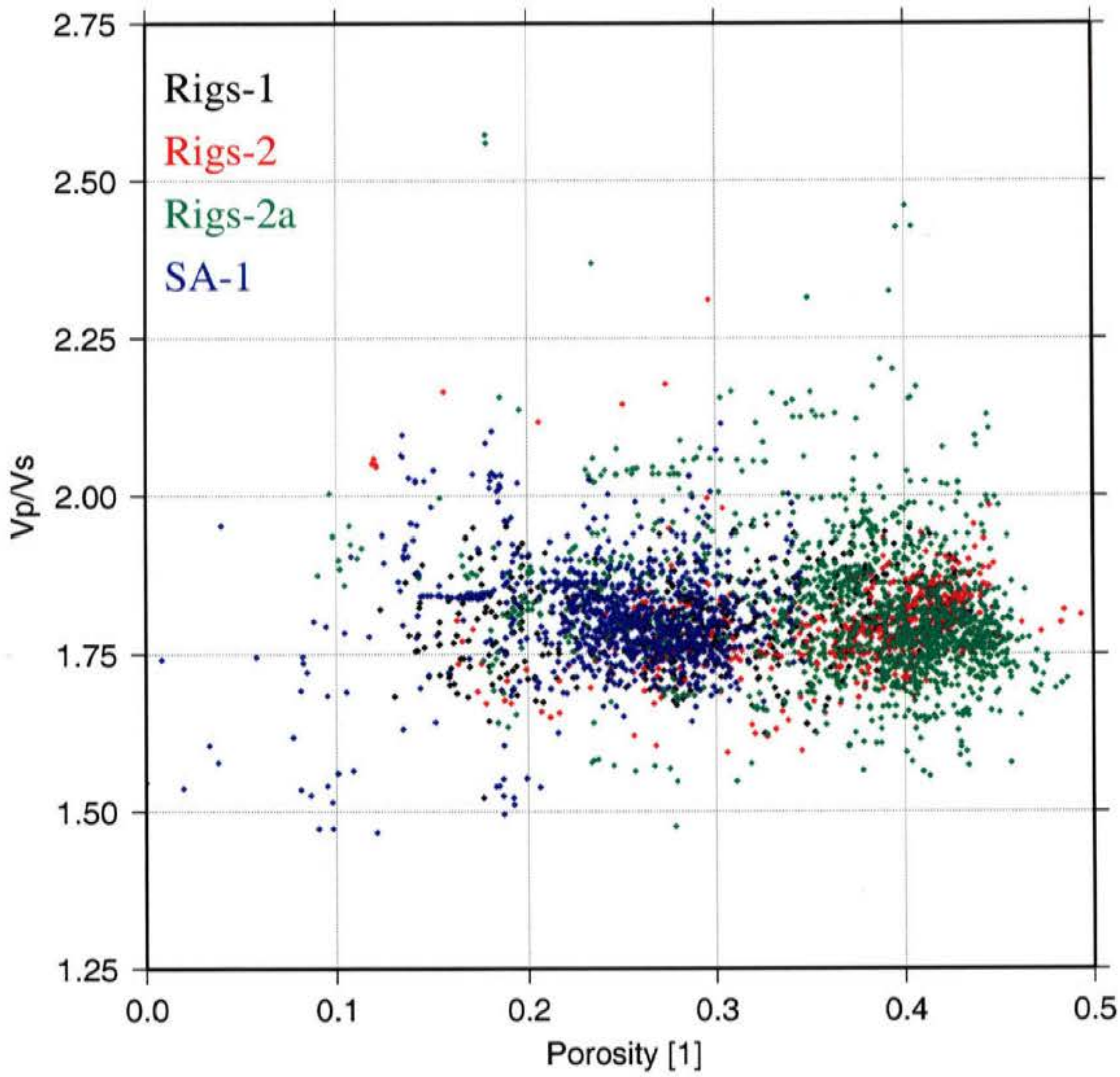

Figure 1.16: *Wells Rigs-1, Rigs-2, Rigs-2a and SA-1:* V_p/V_s *plotted against porosity* PHI_{rho}.

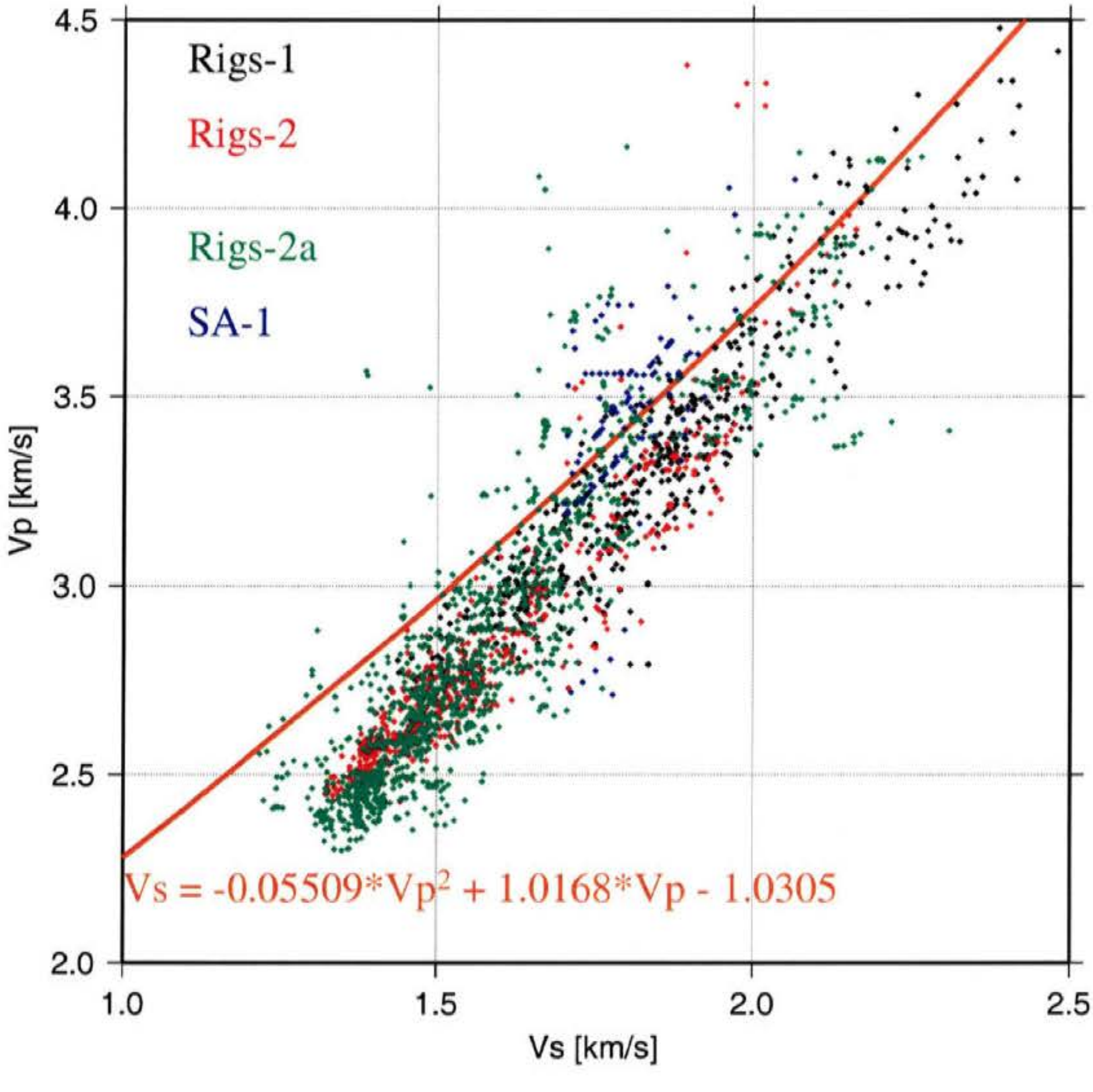

Figure 1.15: *Wells Rigs-1, Rigs-2, Rigs-2a and SA-1: Compression velocity* V_p *plotted against shear velocity* V_s. *An imperical relation between* V_p *and* V_s *for limestone is also shown (from Castagna et al, 1993).*

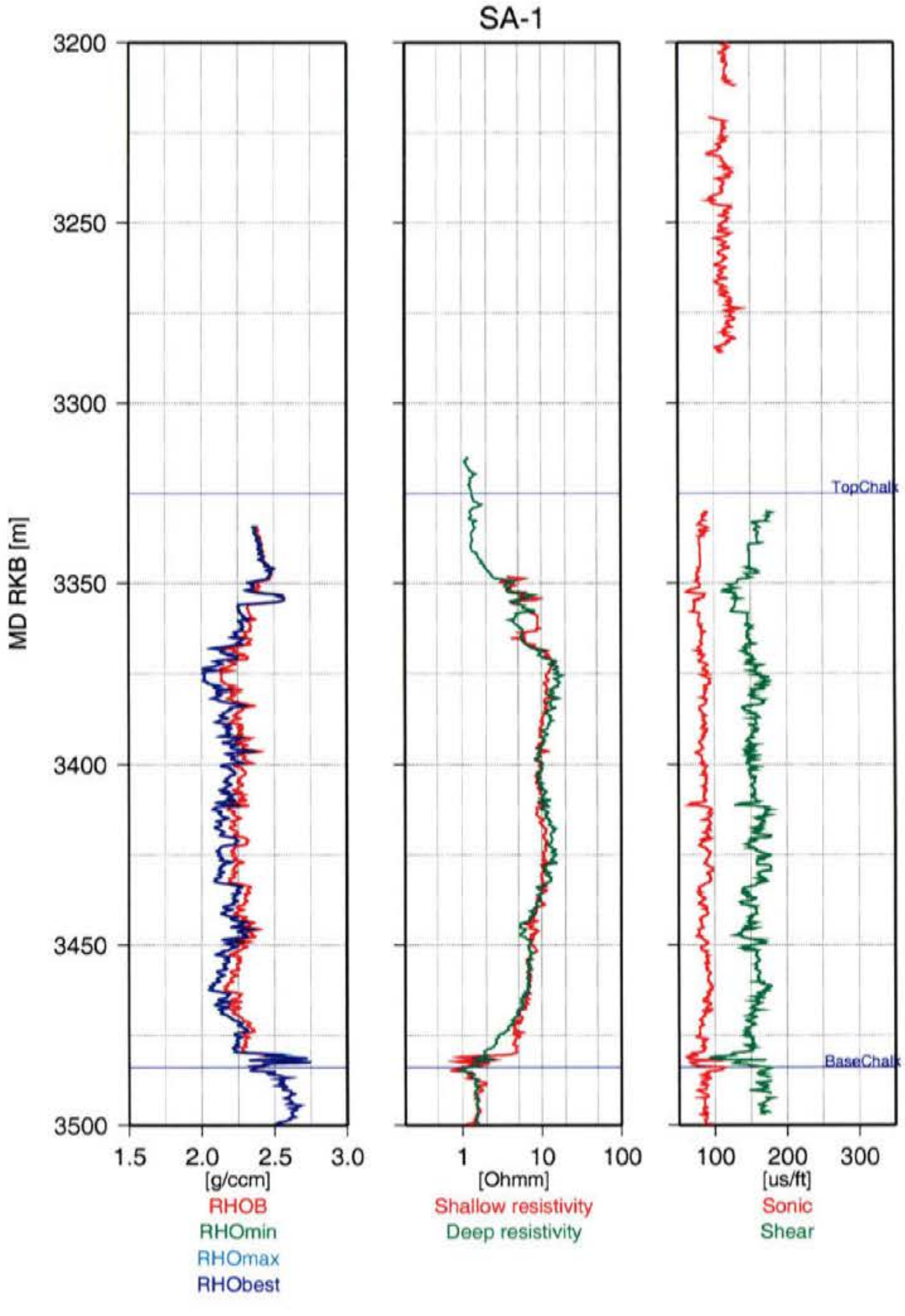

Figure 1.14: *Well SA-1: Density, resistivity, sonic and shear logs.*

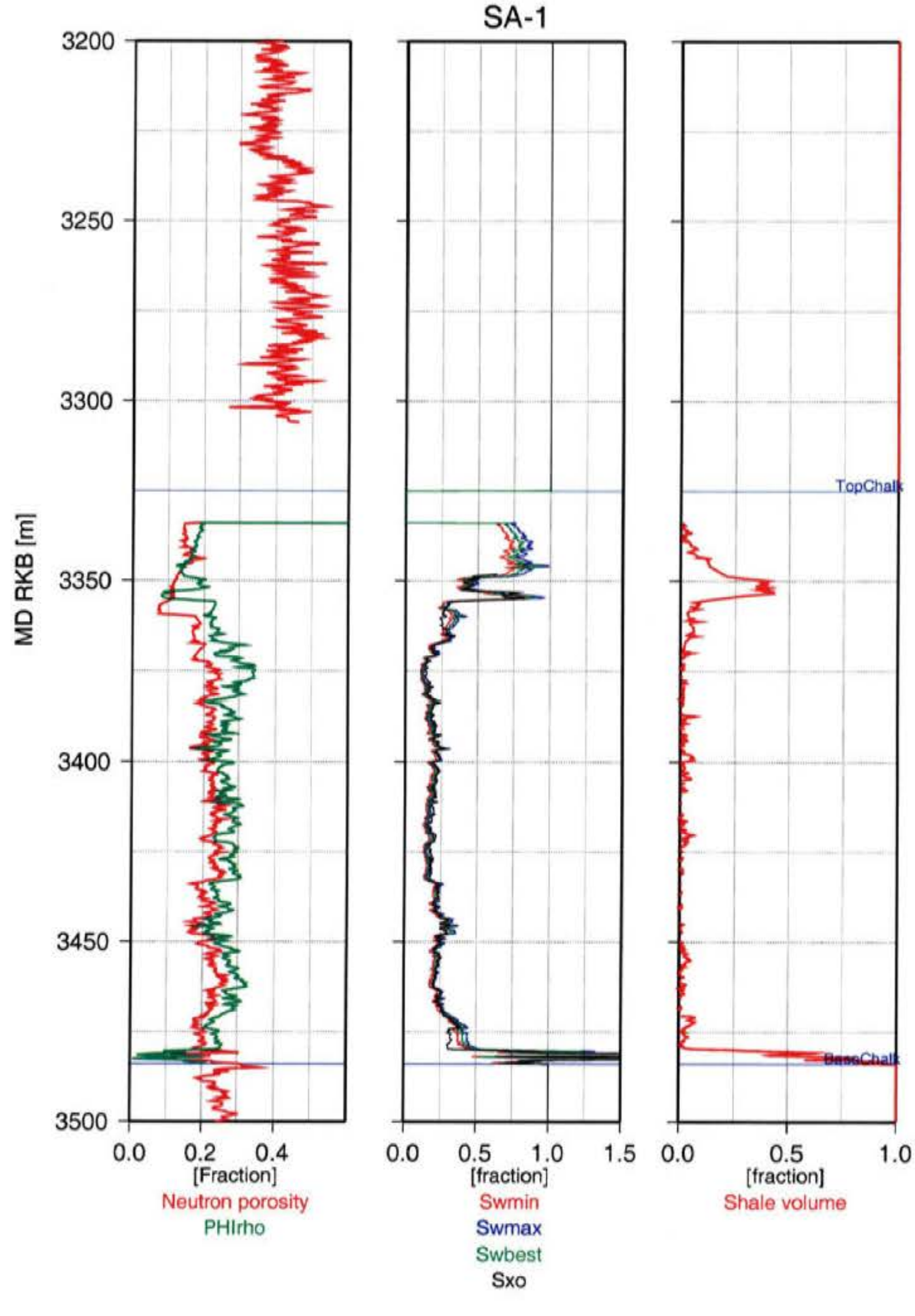

Figure 1.13: *Well SA-1: Porosity, water saturation and shale volume logs.*

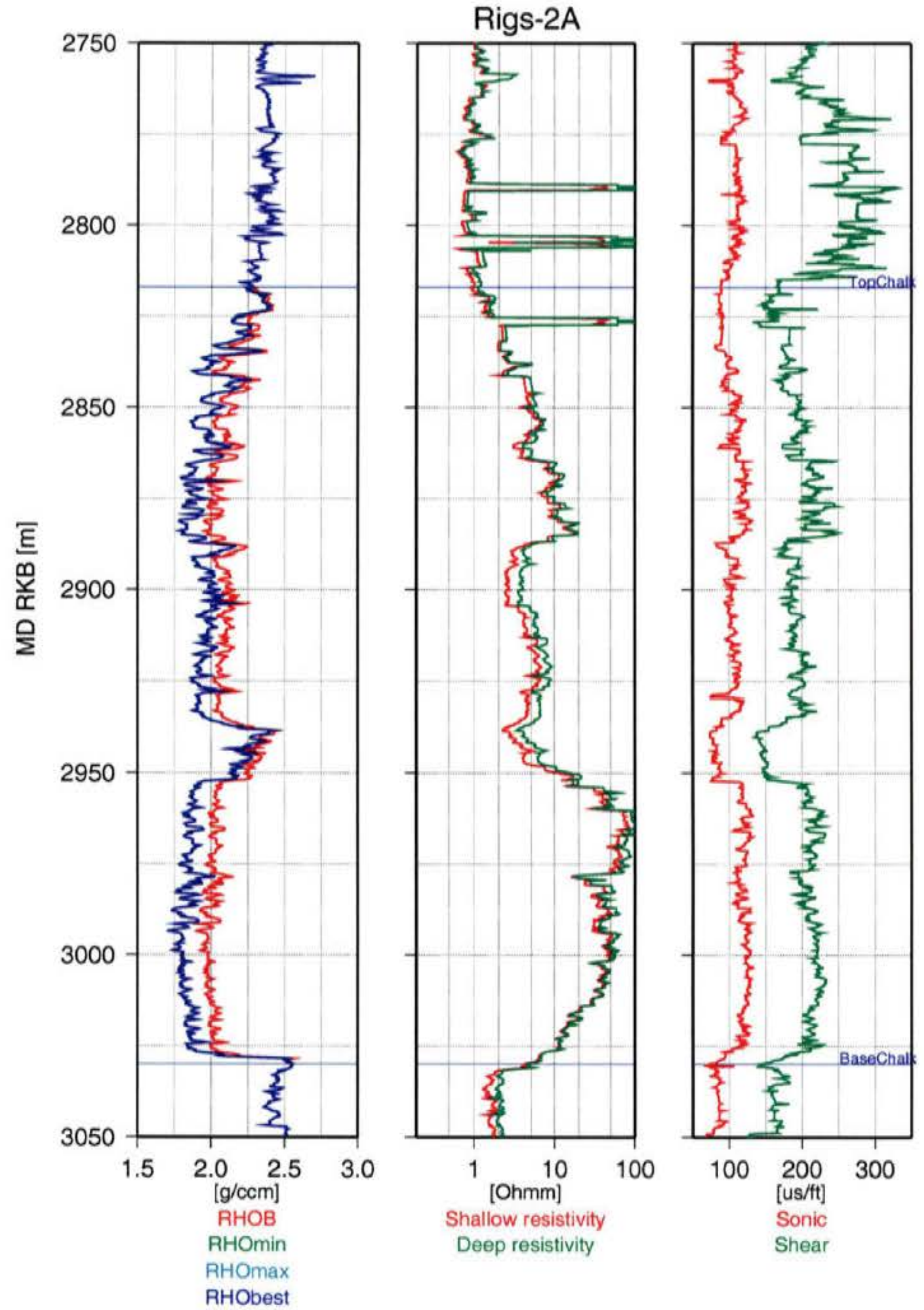

Figure 1.12: *Well Rigs-2a: Density, resistivity, sonic and shear logs.*

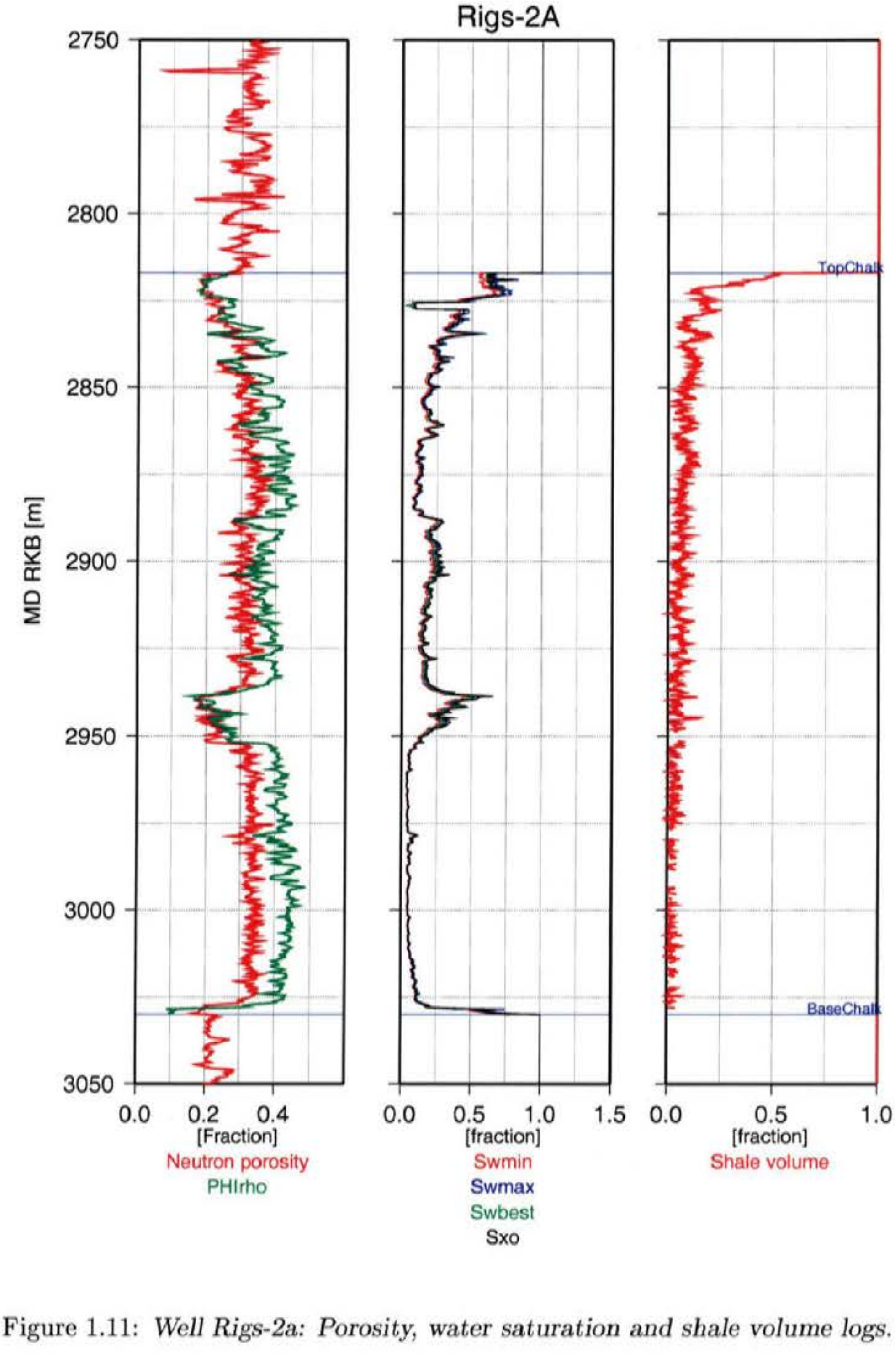

Figure 1.11: *Well Rigs-2a: Porosity, water saturation and shale volume logs.*

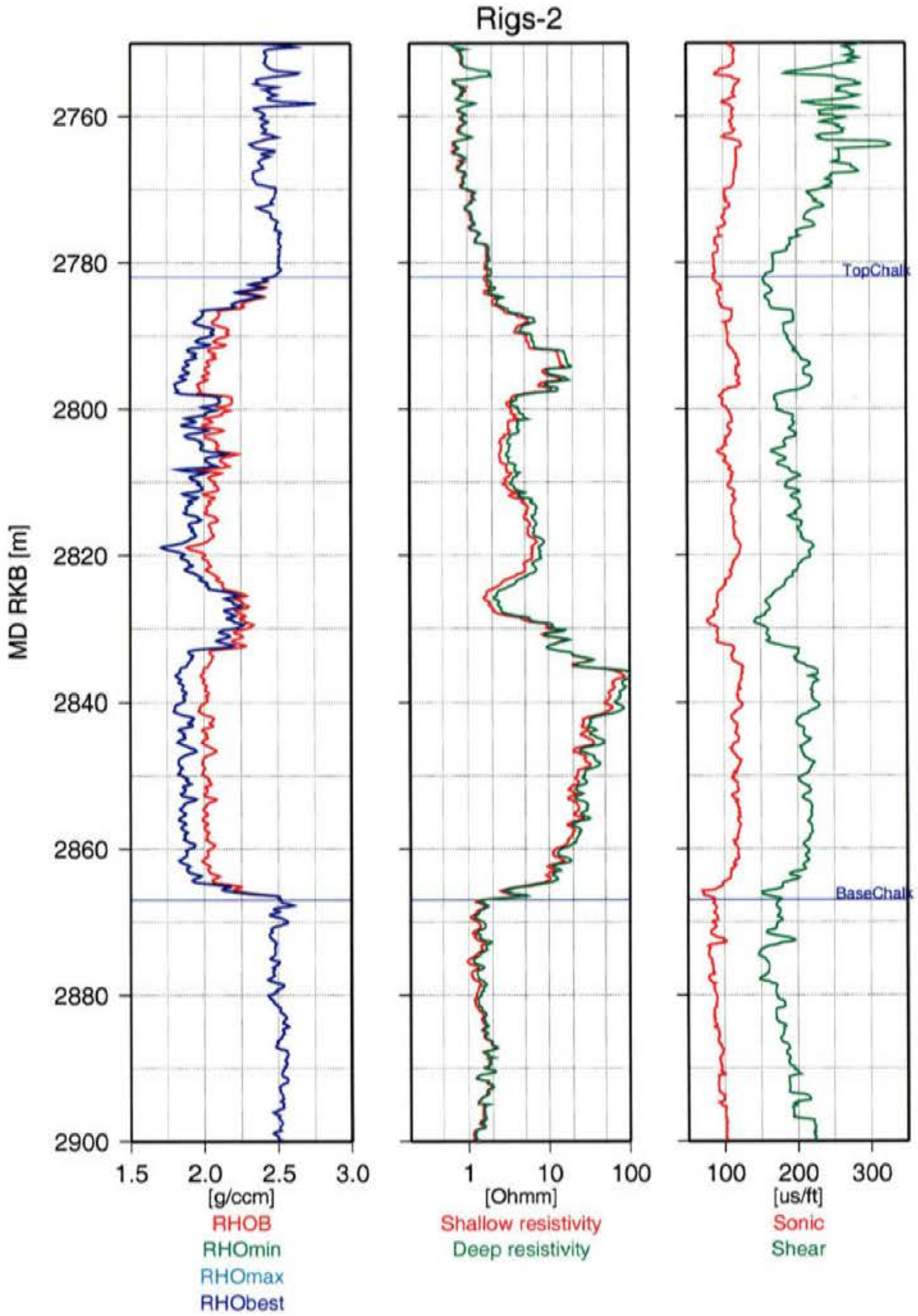

Figure 1.10: *Well Rigs-2: Density, resistivity, sonic and shear logs.*

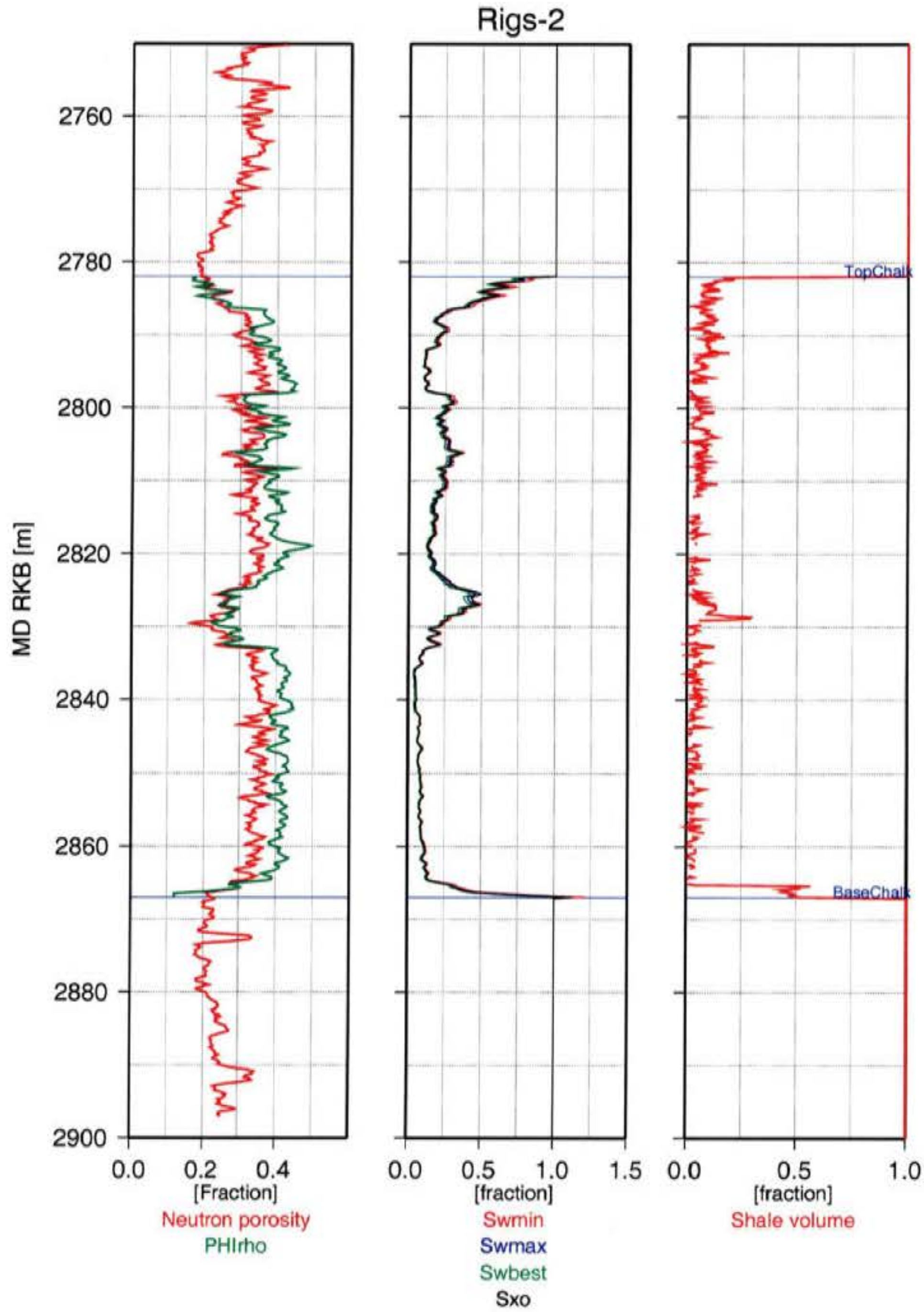

Figure 1.9: *Well Rigs-2: Porosity, water saturation and shale volume logs.*

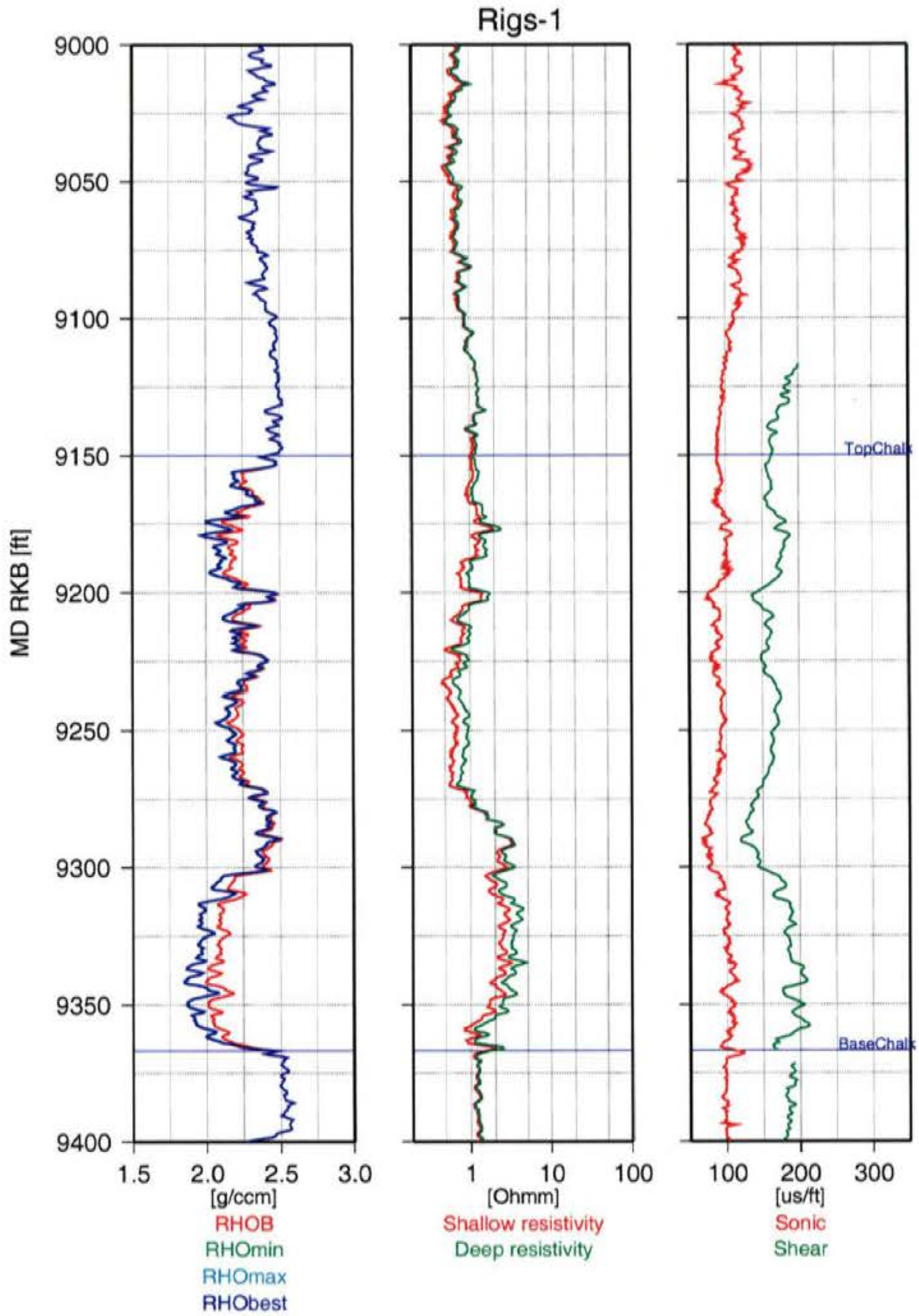

Figure 1.8: *Well Rigs-1: Density, resistivity, sonic and shear logs.*

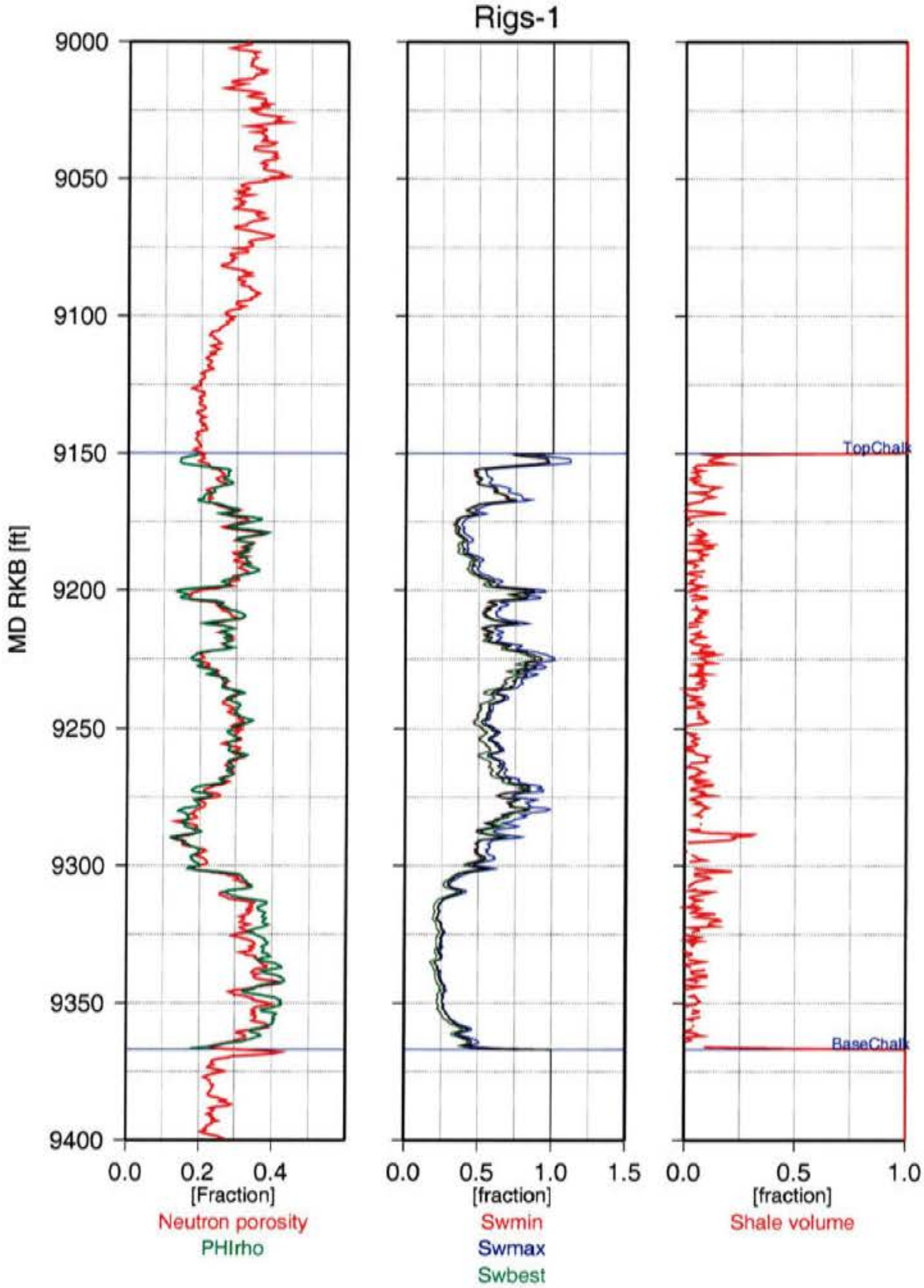

Figure 1.7: *Well Rigs-1: Porosity, water saturation and shale volume logs.*

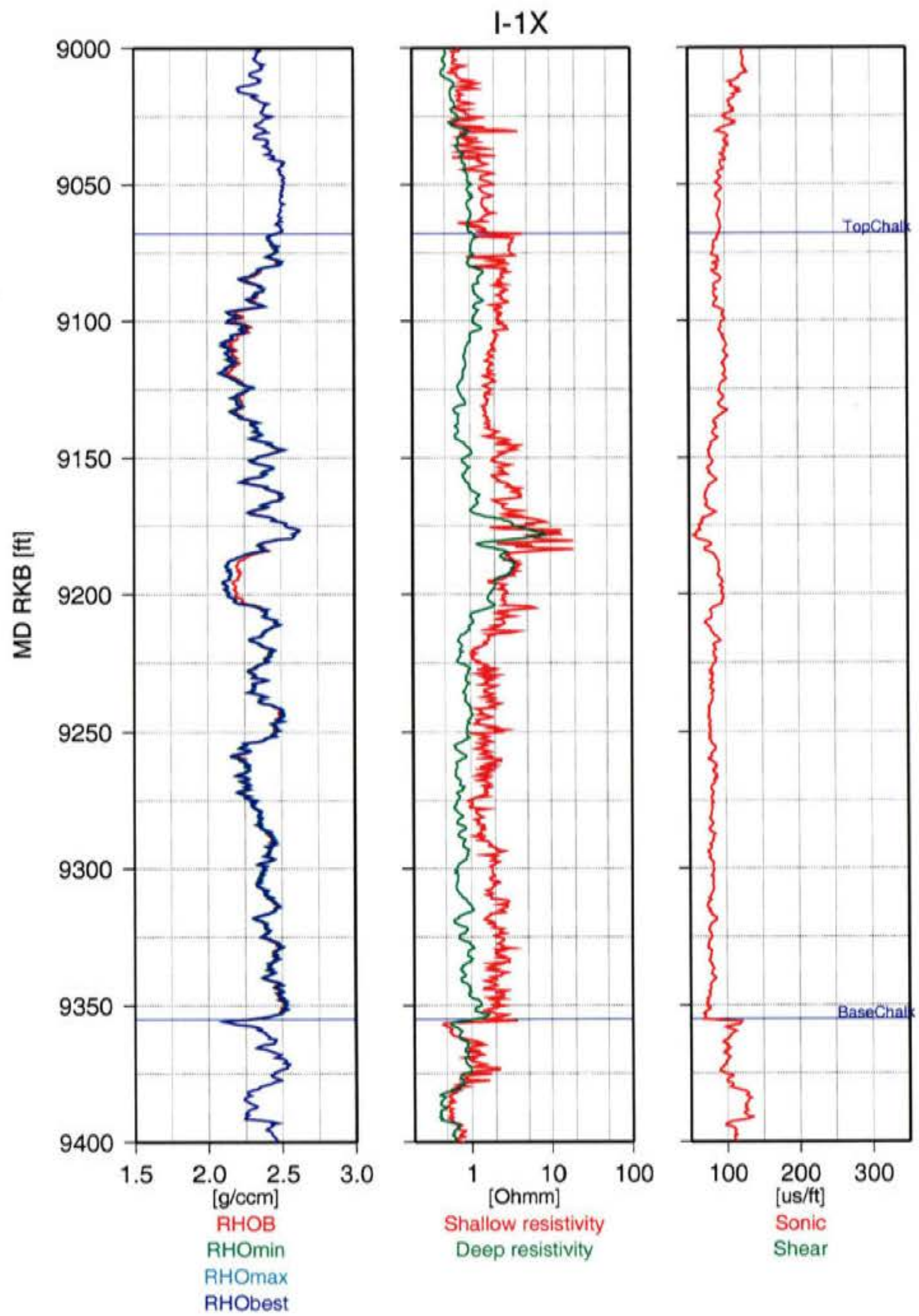

Figure 1.6: *Well I-1X: Density, resistivity and sonic logs.*

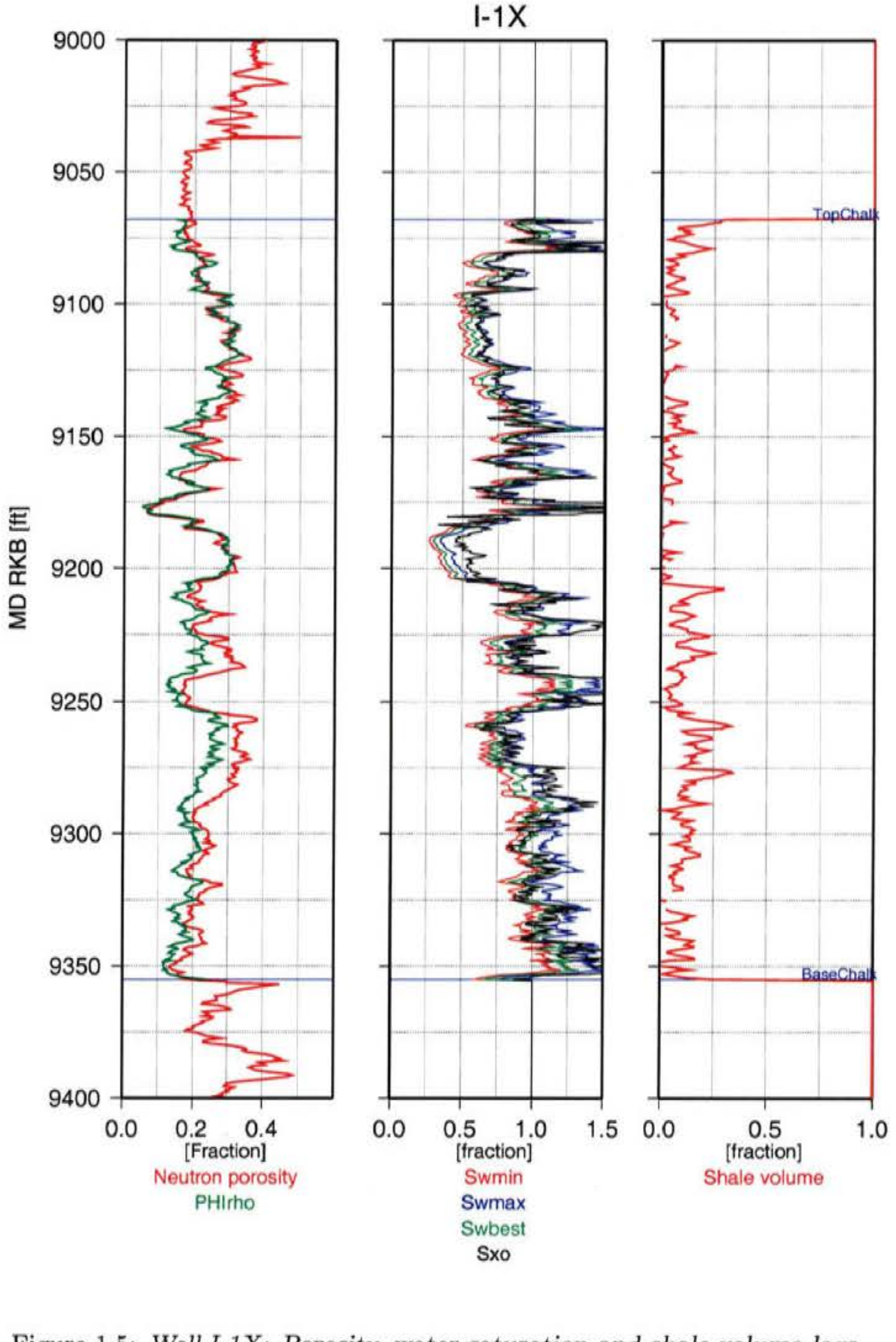

Figure 1.5: *Well I-1X: Porosity, water saturation and shale volume logs.*

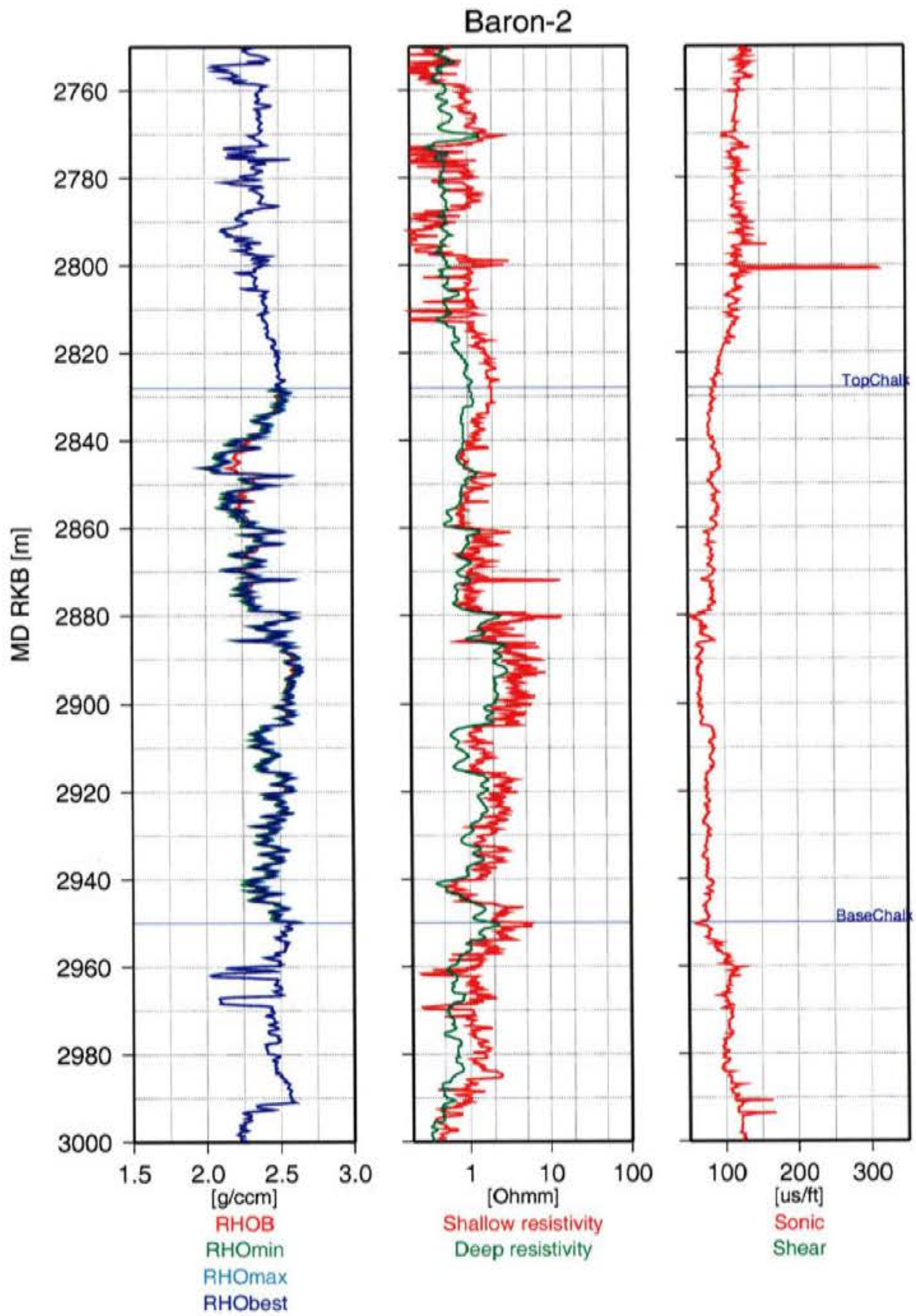

Figure 1.4: *Well Baron-2: Density, resistivity and sonic logs.*

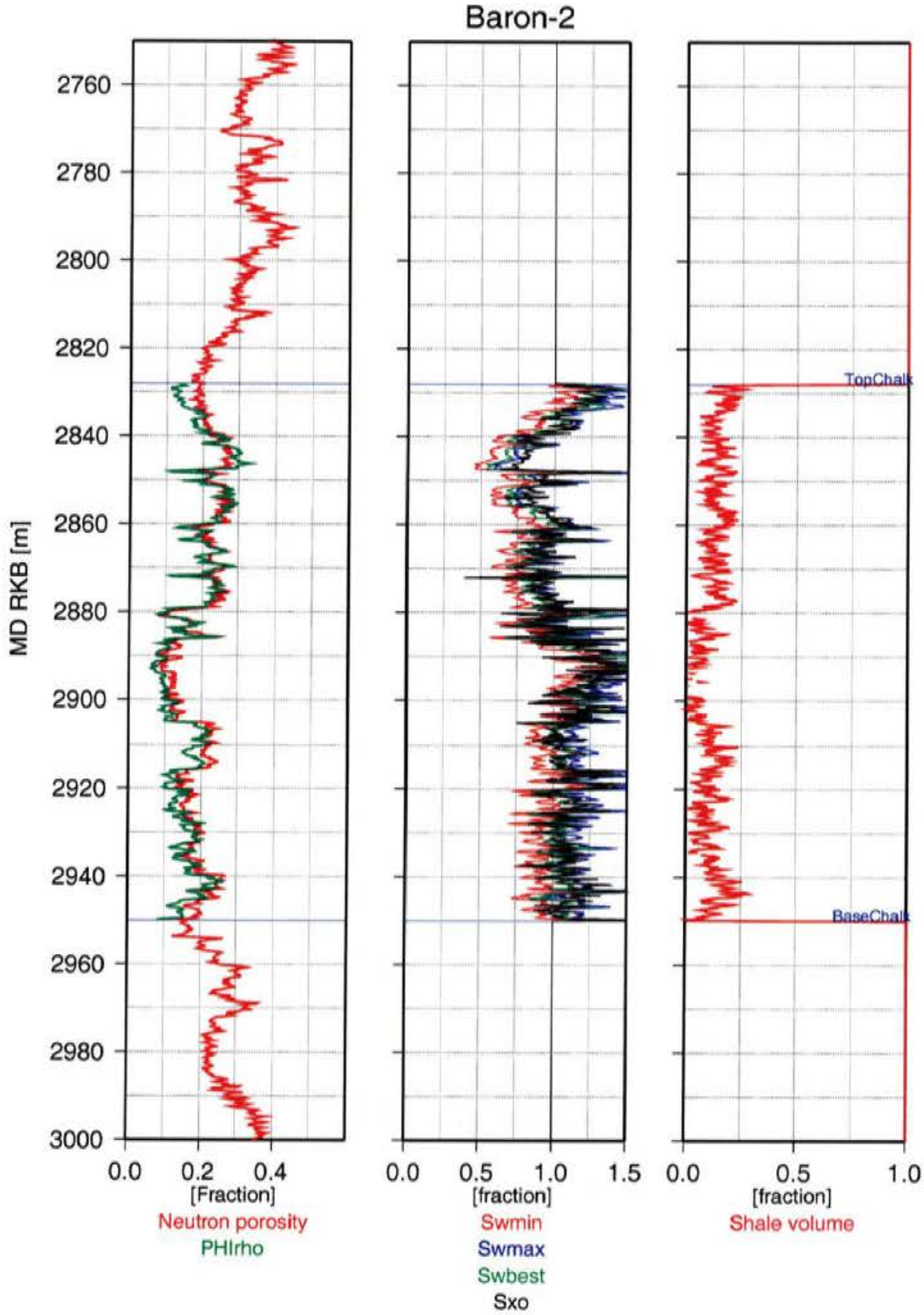

Figure 1.3: *Well Baron-2: Porosity, water saturation and shale volume logs.*

References

Mavko, G., Mukerji, T. and Dvorkin, J. 1998: The rock Physics Handbook. Cambridge University Press.

Batzle, M.L., and Wang, Z. 1992: Seismic Properties of Pore Fluids, Geophysics, 57, 1396-1408.

Castagna, J.P., Batzle, M.L. and Kan, T.K. 1992: Rock Physics - The Link Between Rock Properties and AVO Response. In : Offset-dependent reflectivity - Theory and Practice of AVO analysis. Investigations in Geophysics no. 8. Society of exploration geophysics.

1.5 Density calculation

The variability of water saturation in the rock results in a variability in the bulk density of the undisturbed rock given by

$$\mathrm{RHO} = \mathrm{RHO_{min}} * (1 - \mathrm{PHI}) + \mathrm{RHO_{hc}} * \mathrm{PHI} * (1 - \mathrm{S_w}) + \mathrm{RHO_w} * \mathrm{S_w} * \mathrm{PHI}$$

where

RHO = Rock bulk density.

$\mathrm{RHO_{min}}$ = Rock mineral density. Kept constant at 2.71 g/ccm.

$\mathrm{RHO_{hc}}$ = Hydrocarbon density.

PHI = Porosity $\mathrm{PHI_{rho}}$ as described in Section 1.3.

$\mathrm{S_w}$ = Water saturation as described in Section 1.3.

The resulting density curves ($\mathrm{RHO_{min}}$, $\mathrm{RHO_{best}}$ and $\mathrm{RHO_{max}}$) are plotted together with the raw bulk density curve RHOB.

1.6 Sonic and shear measurements

Sonic and shear measurements were compared in wells Rigs-1, Rigs-2, Rigs-2a and SA-1. As seen in Figure 1.15 the trends for the wells are consistent. The overall trend of the plotted data is slightly steeper than the relation from Castagna et al (1993).

$\mathrm{V_p/V_s}$ plotted against porosity $\mathrm{PHI_{rho}}$ is shown in Figure 1.16.

1.7 Notes

In places the neutron porosity is seen to exceed the density based porosity $\mathrm{PHI_{rho}}$ (e.g. Baron-2 2890–2950 m, I-1X 9125–9350 ft, see Figures 1.3 and 1.5). This is probably due to shale-bound water in the rock. The corrected density logs show in general lower values than the raw bulk density log. This is due to the successful correction for mud filtrate invasion and also due to the presence of hydrocarbons.

The pore water resistivity variation and the resulting variation in water saturation and density indicate the extremes within which the true rock properties should be found.

1.8 Acknowledgements

We would like to thank Jørgen Jensenius from Amerada Hess ApS for supplying information as input to derivation of petrophysical parameters and for general comments on the work flow.

For the calculation of water saturation of the uninvaded zone, pore water resistivity values R_w were delivered by Amerada Hess ApS and Mærsk Olie og Gas AS. A range of pore water resistivity values were given as R_w (minimum), R_w (best) and R_w (maximum) (see Table 1.5).

Well	R_w (minimum) [ohmm]	R_w (best) [ohmm]	R_w (maximum) [ohmm]
Baron-2	0.022	0.030	0.036
I-1X	0.022	0.027	0.036
Rigs-1	0.022	0.023	0.030
Rigs-2	0.022	0.026	0.030
Rigs-2a	0.022	0.026	0.030
SA-1	0.022	0.026	0.030

Table 1.5: *Water resistivity at reservoir level.*

The variability seen among the water saturation curves (Swmin, Swbest and Swmax) is given by the variation in chosen pore water resistivity values.

1.4 Shale volume

The shale volume was calculated from

$$V_{sh} = (GR - GR_{ma})/(GR_{sh} - GR_{ma})$$

where

GR = Measured gamma ray.

GR_{ma} = Gamma ray level in pure matrix, i.e. chalk.

GR_{sh} = Gamma ray level in shale intervals, i.e. Tertiary sequence.

GR_{ma} and GR_{sh} were estimated visually from the gamma ray log. The levels are given in Table 1.6.

Well	GR_{sh} [API]	GR_{ma} [API]
Baron-2	65	27
I-1X	50	12
Rigs-1	100	35
Rigs-2	115	41
Rigs-2a	135	41
SA-1	95	5

Table 1.6: GR_{ma} *and* GR_{sh} *estimated in all wells.*

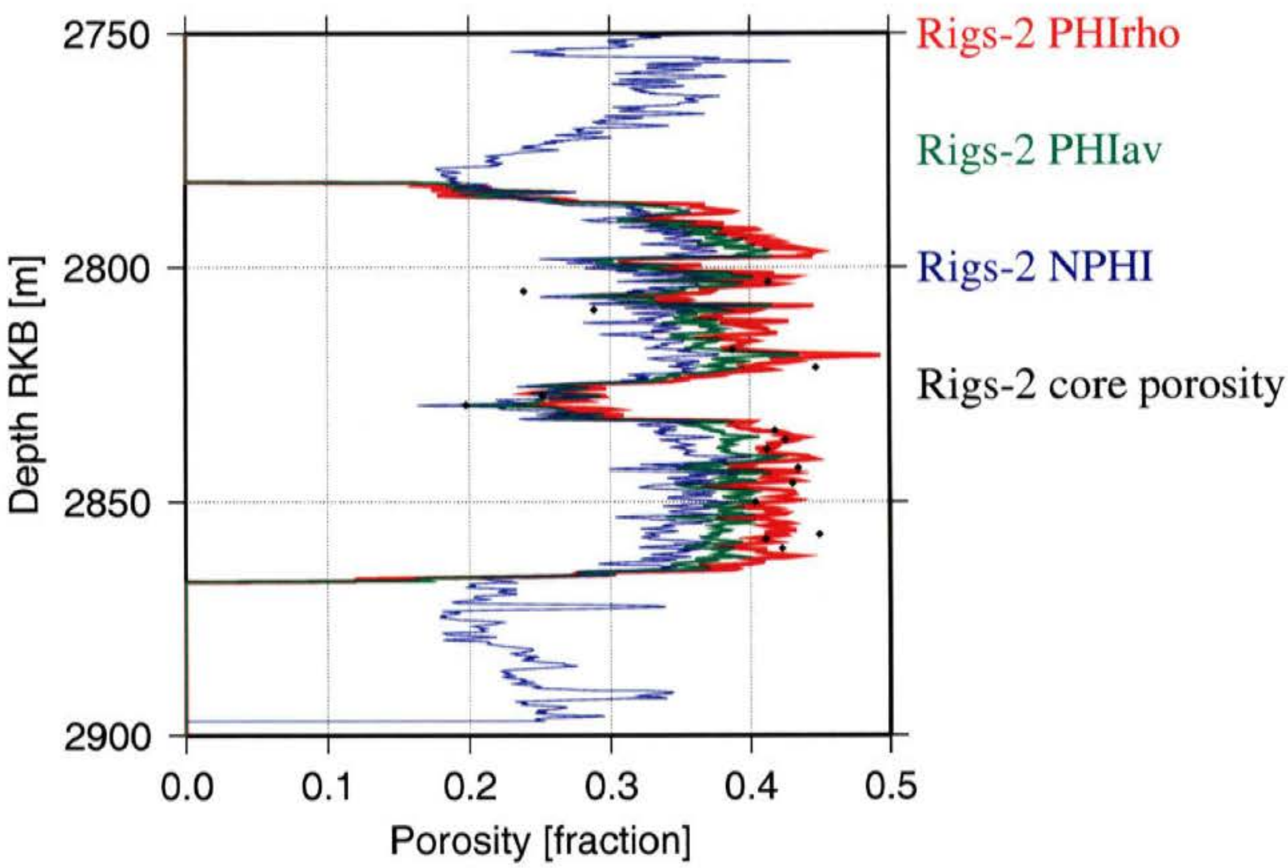

Figure 1.2: *Well Rigs-2:* NPHI, PHI_{rho}, PHI_{av} *and core porosity.*

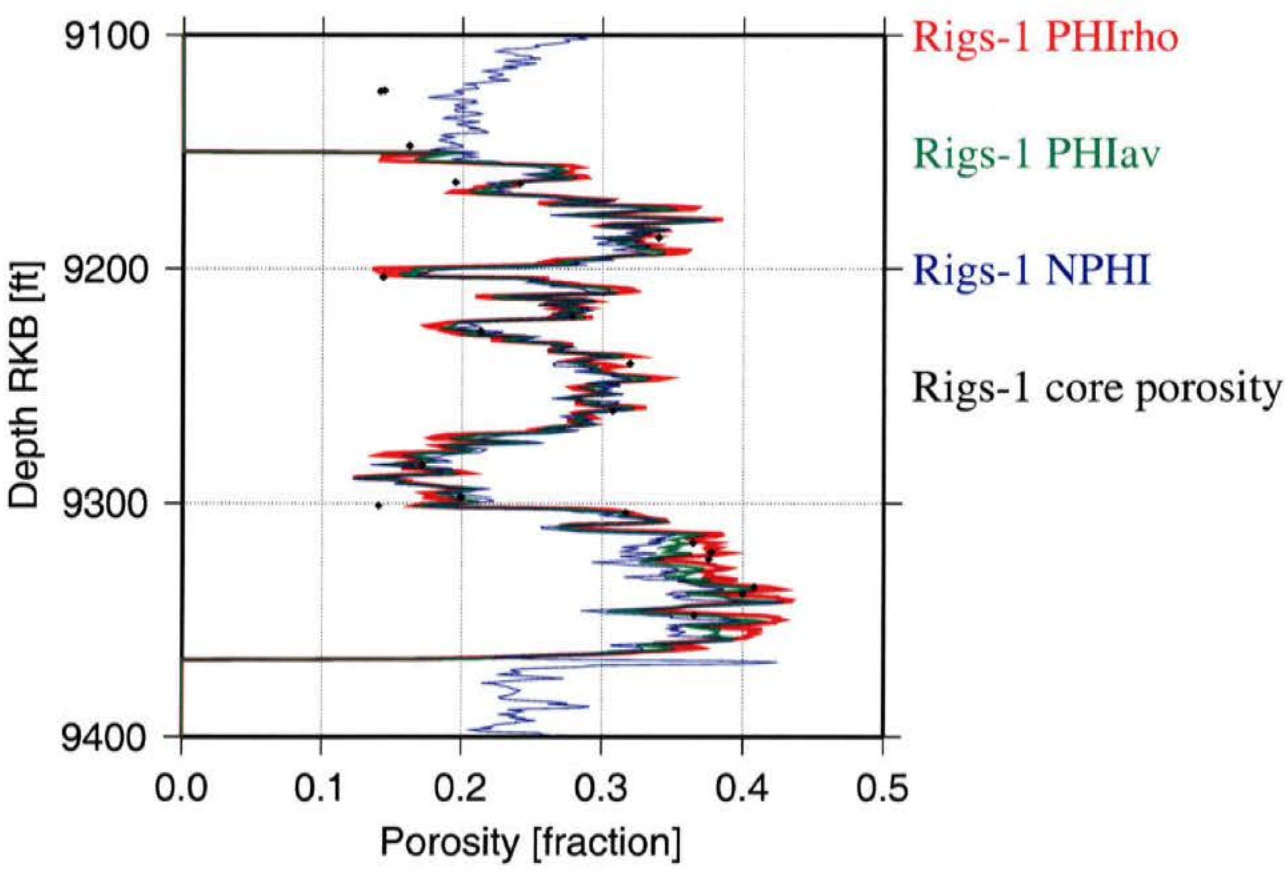

Figure 1.1: *Well Rigs-1:* NPHI, PHI_{rho}, PHI_{av} *and core porosity.*

$PHI_{rho} = (RHO_{min} - RHOB)/(RHO_{min} - RHO_{mf})$

where

RHO_{min} = Rock mineral density. Kept constant at 2.71 g/ccm.

RHOB = Rock bulk density.

RHO_{mf} = Mud filtrate density.

Assuming full invasion RHO_{mf} was chosen as listed in Table 1.3.

An average porosity PHI_{av} was calculated from PHI_{rho} and the neutron logs using

$PHI_{av} = (PHI_{rho} - NPHI)/2 + NPHI$

For wells Rigs-1 and Rigs-2 the following logs were compared with core porosity measurements: NPHI, PHI_{rho} and PHI_{av} (see Figures 1.1 and 1.2).

Comparison between the core porosity measurements and the given curves indicates that PHI_{rho} obtains the best match in terms of absolute porosity values. Hence, it was decided to use PHI_{rho} in the following calculations.

Water saturations were calculated for both the invaded zone and the uninvaded zone. Initially, the water saturation for the invaded zone S_{xo} was calculated using Archie's equation

$S_{xo} = \sqrt{(R_{mf}/(R_{shallow} * (PHI_{rho})^2))}$

PHI_{rho} is for this purpose calculated on the basis of the RHO_{mf} values given in Table 1.3. A suite of mud filtrate resistivity (R_{mf}) values was then tested in order to obtain a realistic mud filtrate saturation estimate. The chosen R_{mf} values were used as input to Batzle & Wang (1992) (in Mavko et al, 1998) to calculate an improved mud filtrate density RHO_{mf}, which was then used to calculate a new PHI_{rho}. This was then used in the final calculation of S_{xo}.

The water saturation in the uninvaded zone S_w was found with

$S_w = \sqrt{(R_w/(R_{deep} * (PHI_{rho})^2))}$

S_{xo} should generally always be larger or equal to S_w.

The improved RHO_{mf} and PHI_{rho} values are given in Table 1.4 together with pore water density RHO_w for the uninvaded zone.

Well	R_{mf} [ohmm]	RHO_{mf} [g/ccm]	RHO_w [g/ccm]
Baron-2	0.050	1.02	1.02
I-1X	0.070	0.99	1.03
Rigs-1	0.020	1.06	1.05
Rigs-2	0.026	1.03	1.04
Rigs-2a	0.023	1.05	1.04
SA-1	0.028	1.03	1.04

Table 1.4: *Updated fluid properties at reservoir level.*

Well	Year	Company
Baron-2	1992	Schlumberger
I-1X	1969	Schlumberger
Rigs-1	1995	Schlumberger
Rigs-2	1996	Schlumberger
Rigs-2a	1996	Schlumberger
SA-1	1998	Schlumberger

Table 1.2: *Year of completion and logging company for each of the wells.*

1.2 Calculation of supplementary properties

For quality control purposes, and to illustrate the potential variability of the input data, supplementary properties were calculated from the available well log data. The supplementary properties were calculated only for the target interval. The supplementary properties are listed below:

- Porosity and water saturation (Section 1.3).
- Shale volume (Section 1.4).
- Density (Section 1.5).

Plots of the raw well log data and supplementary properties are shown in Figures 1.3–1.14. General fluid properties available and reservoir interval depths are given in Table 1.3.

Well	RHO_{mf} [g/ccm]	RHO_{hc} [g/ccm]	Top Chalk [depth RKB]	Base Chalk [depth RKB]
Baron-2	1.06	0.63	2828 m	2950 m
I-1X	0.98	0.63	9068 ft	9355 ft
Rigs-1	1.08	0.63	9150 ft	9367 ft
Rigs-2	1.08	0.63	2782 m	2867 m
Rigs-2a	1.10	0.63	2817 m	3030 m
SA-1	0.98	0.63	3325 m	3484 m

Table 1.3: *Available fluid density data at reservoir level.* RHO_{mf} = *Mud filtrate density and* RHO_{hc} = *Hydrocarbon density.*

1.3 Porosity and water saturation

A detailed analysis was performed in wells Rigs-1 and Rigs-2 to find the best method for calculation of porosity.

Density based porosities were derived from

Chapter 1

Log QC

This chapter describes the selection of well logs from six wells in the South Arne field and calculation of supplementary properties.

1.1 Selection of well logs

Well log data were supplied by GEUS and Amerada Hess ApS for the following wells : Baron-2, I-1X, Rigs-1, Rigs-2, Rigs-2a and SA-1. Neutron, density, gamma ray, sonic, shear, as well as shallow and deep resistivity were selected for the well log quality control study. Table 1.1 summarizes the selected well log data. No shear logs were available for wells Baron-2 and I-1X.

Well	Neutron [fraction]	Density [g/ccm]	Gamma ray [API]	Sonic [us/ft]	Shear [us/ft]	Shallow res. [ohmm]	Deep res. [ohmm]
Baron-2	NPHI	RHOB	GR	DTLF	-	MSFL	ILD
I-1X	SNP	RHOB	GR	DT	-	MLL	LL7
Rigs-1	NPHI	RHOB	SGR	DTLF	DTSM	LLS	LLD
Rigs-2	NPHI	RHOB	SGR	DT4P	DTSM	LLS	LLD
Rigs-2a	NPHI	RHOB	SGR	DT4P	DT2	LLS	LLD
SA-1	NPHI	RHOZ	GR	DTCO	DTSM	HLLS	AT90

Table 1.1: *Well log data.*

For all well logs the study was initiated with a visual inspection. The inspection was focused on the Chalk interval. The logs were inspected for missing intervals, spikes, etc. Alignment of the well log data was controlled by doing a visual comparison of all logs with the sonic log. For all the wells the alignment of the well logs was found to be satisfactory.

List of Tables

List of Figures

Contents

This document is confidential.

This document was typeset using LaTeX. It is published by Ødegaard A/S, Titangade 15, DK–2200 Copenhagen N, Denmark.

TeX is a trademark of the American Mathematical Society.

Christian Mogensen (Ødegaard A/S) and Ida Fabricius (DTU)

EFP 2001: Quality control of well log data from the South Arne Field

Report 01.1031
2002.

EFP-01 ROCK PHYSICS OF IMPURE CHALK – TECHNICAL NOTE 2001/1 MAY, CONFIDENTIAL

Well data summary, South Arne field

Peter Japsen
pj@geus.dk, Geological Survey of Denmark and Greenland (GEUS)

This is a summary of available samples, logs and reports for wells on the South Arne Field where cores have been taken plus the Modi-1 well. Some formation tops are also included. The following wells are included:

*Baron-2 (released)
*I-1 (released)
Modi-1 (24-06 2004)
*Rigs-1 (released)
*Rigs-2 (release date 29-07 2001)
*SA-1 (release date 29-11 2004)

* Spliced logs available (CD included).

Information for the released wells are taken from GEUS web site whereas information on the remaining well are from confidential reports prepared by Danop or Amerada Hess.

The Ekofisk Formation was encountered in the following intervals according to various sources.

(MD)	Top	Base	Thickness	~core
Baron-2	2826 m	2886 m	60 m	60 m
I-1	9070 '	9181 '	34 m	18 m
Modi-1	3065 m	3128 m	63 m	0 m
Rigs-1	9132 '	9291 '	48 m	48 m
Rigs-2	2782 m	2829 m	47 m	24 m
SA-1	3317 m	3361 m	44 m	30 m

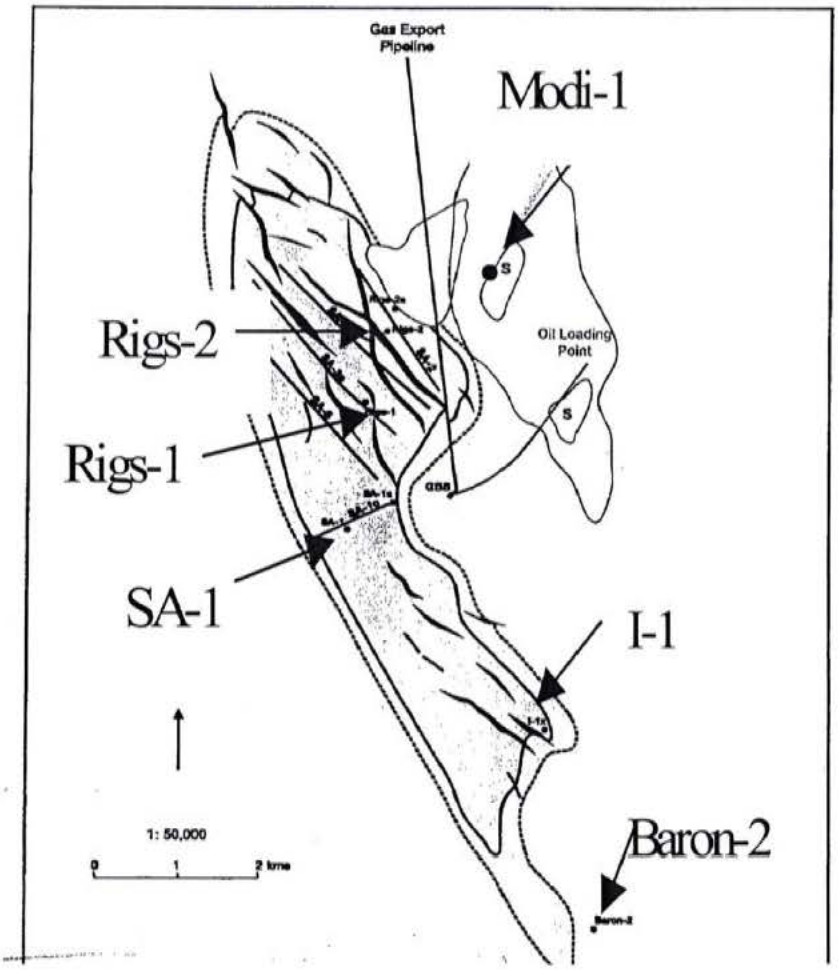

Figure 1. South Arne field, well location sketch.

WELL BARON-2

Contents

Technical and administrative data

Location	Offshore
Longitude	04°15'29".43
Latitude	56°01'43".68
UTM Zone	31
UTM Easting (x)	578412.8 (m)
UTM Northing (y)	6210137.0 (m)
Well block no.	5604/30-3
Reference point	KB 23 m above MSL.
Water depth	56 m below MSL.
TD drill	5232 m below KB.
The well is	Deviated.
Structure:	South-Arne
Spudded	01/08-1991.
Completed	13/01-1992
Spud classification	Exploration
Status (completion)	Plugged And Abandoned .
License	7/89
Operator	Norsk Hydro
Contractor	Mærsk Drilling
Rig	Mærsk Jutlander

Casing

top depth		shoe depth		diameter	
ft	m	ft	m	inch	inch (decim)
0.0	0.0	0.0	0.0	10 3/4"	10.750
0.0	0.0	3152.9	961.0	18 5/8"	18.625
0.0	0.0	8503.9	2592.0	13 3/8"	13.375
0.0	0.0	11033.5	3363.0	9 5/8"	9.625
275.6	84.0	534.8	163.0	30"	30.000
10393.	3168.0	14983.6	4567.0	7" LINER	7.000

Lithostratigraphy (Groups)

Top	Bottom	Unit
m. below ref. level.		
79.0	2826.0	Post Chalk Group
2826.0	2953.5	Chalk Group
2953.5	3424.0	Cromer Knoll Group
3424.0	5232.0	Jurassic units

Chronostratigraphy (Periods)

Top	Bottom	Unit
m. below ref. level.		
79	2886	Tertiary And Quaternary
2886	2954	Cretaceous
2954	5233	Jurassic

Cores

core	top	bottom	recovery
no.	m. below ref. level		
1	2821.00	2847.30	100.0
2	2847.30	2872.50	96.0
3	2872.50	2899.50	100.0
4	2899.50	2926.50	100.0
5	3085.00	3096.00	87.0

Cuttings

from	to	distance
m. below ref. level		bt cuttings
976.00	980.00	4.00
980.00	1410.00	10.00
1420.00	2530.00	10.00
2540.00	2600.00	10.00
2600.00	5232.00	2.50

Sidewall Cores

79 samples recovered from interval 2726.0 - 5124.0 m. below ref.level

Available well logs

Company: Schlumberger

File no.	Log type, interval, suite no., run no., scale
1290	AMS , 2592.00-3214.00m , , 1A , 1:500
1296	AMS , 3150.00-3350.00m , , 2B , 1:500
3763	AMS , 4567.00-5224.00m , , 5D , 1:500
1292	CBL-VDL-GR , 2222.00-2546.00m , , 1A , 1:200
3761	CBL-VDL-GR , 2743.00-3163.00m , , 3B , 1:200
3755	CST , 3391.00-4593.00m , , 3B , 1:0
3765	CST , 4597.00-5115.00m , , 5D , 1:200
3764	CST , 4597.00-5124.00m , , 5C , 1:200
1297	CST-GR , 3050.00-3150.00m , , 2A , 1:200
3746	DIL-LSS-GR-SP , 2875.00-3323.00m , , 2B , 1:200
1302	DIL-LSS-GR-SP , 3150.00-3350.00m , , 2B , 1:500
3754	DIL-LSS-GR-SP , 3360.00-4610.00m , , 3D , 1:500
3753	DIL-LSS-GR-SP , 3360.00-4610.50m , , 3D , 1:200
3768	DIL-LSS-GR-SP , 4567.00-5230.00m , , 5E , 1:200
3769	DIL-LSS-GR-SP , 4567.00-5230.00m , , 5E , 1:500
3772	DIL-LSS-GR-SP - Composite Playback , 2592.00-5230.00m , , 1A , 1:500
3773	DIL-LSS-GR-SP- Composite Playback - TVD , 2592.00-5232.00m , , 1A , 1:500
1287	DIL-MSFL-LSS-GR-SP , 2592.00-3214.00m , , 1A , 1:200
1289	DIL-MSFL-LSS-GR-SP , 2592.00-3214.00m , , 1A , 1:500
3752	FMS-4 , 3360.00-4613.00m , , 3B , 1:200
3751	FMS-4 - Cyberdip , 3360.00-4613.00m , , 3B , 1:500
3762	FMS-4-GR-AMS , 4567.00-5233.00m , , 5C , 1:200
1294	FMS4-GR , 2592.00-3329.00m , , 2A , 1:200
1295	FMS4-GR - Caliper , 2592.00-3329.00m , , 2A , 1:200
1291	LDL-CNL-GR , 2592.00-3188.00m , , 1A , 1:200
1288	LDL-CNL-GR , 2592.00-3188.00m , , 1A , 1:500
1300	LDL-CNL-GR , 3149.00-3305.00m , , 2B , 1:200
1301	LDL-CNL-GR , 3149.00-3305.00m , , 2B , 1:500
3756	LDL-CNL-GR , 3660.00-4593.00m , , 3C , 1:200
3757	LDL-CNL-GR , 3660.00-4593.00m , , 3C , 1:500
3767	LDL-CNL-GR , 4567.00-5224.00m , , 5D , 1:200
3766	LDL-CNL-GR , 4567.00-5224.00m , , 5D , 1:500
3771	LDL-CNL-GR - Composite Playback , 2592.00-5232.00m , , 1A , 1:500
1298	LSS-GR , 3130.00-3312.00m , , 2B , 1:200
1299	LSS-GR , 3130.00-3312.00m , , 2B , 1:500
1285	MWD Log , 150.00-4200.00m , , , 1:500
1293	RFT-HP-GR , 2840.00-3147.00m , , 1A , 1:0
3758	VDL Survey , 3108.00-3348.00m , , 3A , 1:200

Available Reports

File no.	Author, company, title, publication date
2133	NORSK HYDRO : Final Well Report, June 1992.
2372	SCHLUMBERGER : Directional survey report - Tabulations - Depth interval: 77.28m - 4360.72m, August 1991.
2375	SCHLUMBERGER : Formation micro scanner (FMS) Precessing report - (Logged 15. Sept. 1991, processed 18. Sept. 1991) - MSD Tabulation, October 1991.
2378	SCHLUMBERGER : Stratigraphic High Resolution Dipmeter (3360m-4613m) - 4-pad FMS tool-processing no.1 (Logged 07 Nov 1991, Processed 25 Nov 1991), November 1991.
2379	NORSK HYDRO : Sidewall core description - run 5c - Depth Interval: 4597m-5124m, December 1991.
2380	NORSK HYDRO : Sidewall core description - run 5d - Depth Interval: 4597m-5112m, December 1991.
2384	THE GEOCHEM GROUP/CORE ANALYSIS DIVISION : Special Core Analysis study - Final report, January 1992.
2385	ANADRILL-SCHLUMBERGER : End of well report - MWD logging report - Depth interval: 79m - 4611m, November 1991.
2386	SCHLUMBERGER : Dipmeter Processing Report - MSD and LOC results - Depth interval: 4567,1m - 5232,9m, January 1992.
2387	EXLOG : End of well report - Mud logging report (text and enclosure), January 1991.
2388	READ WELL SERVICES : VSP REPORT, May 1992.
2389	THE ROBERTSON GROUP : Biostratigraphy of the interval 980m - 5232m TD, March 1992.
2390	NORSK HYDRO : Petroleum Geochemistry, April 1992.
2391	Kim Zink-Jørgensen, Dan Olsen, Niels Springer , DGU : Conventional Core analysis - for Norsk Hyrdro - Core 1-5 - Plug Description - Core Photos -, January 1992.

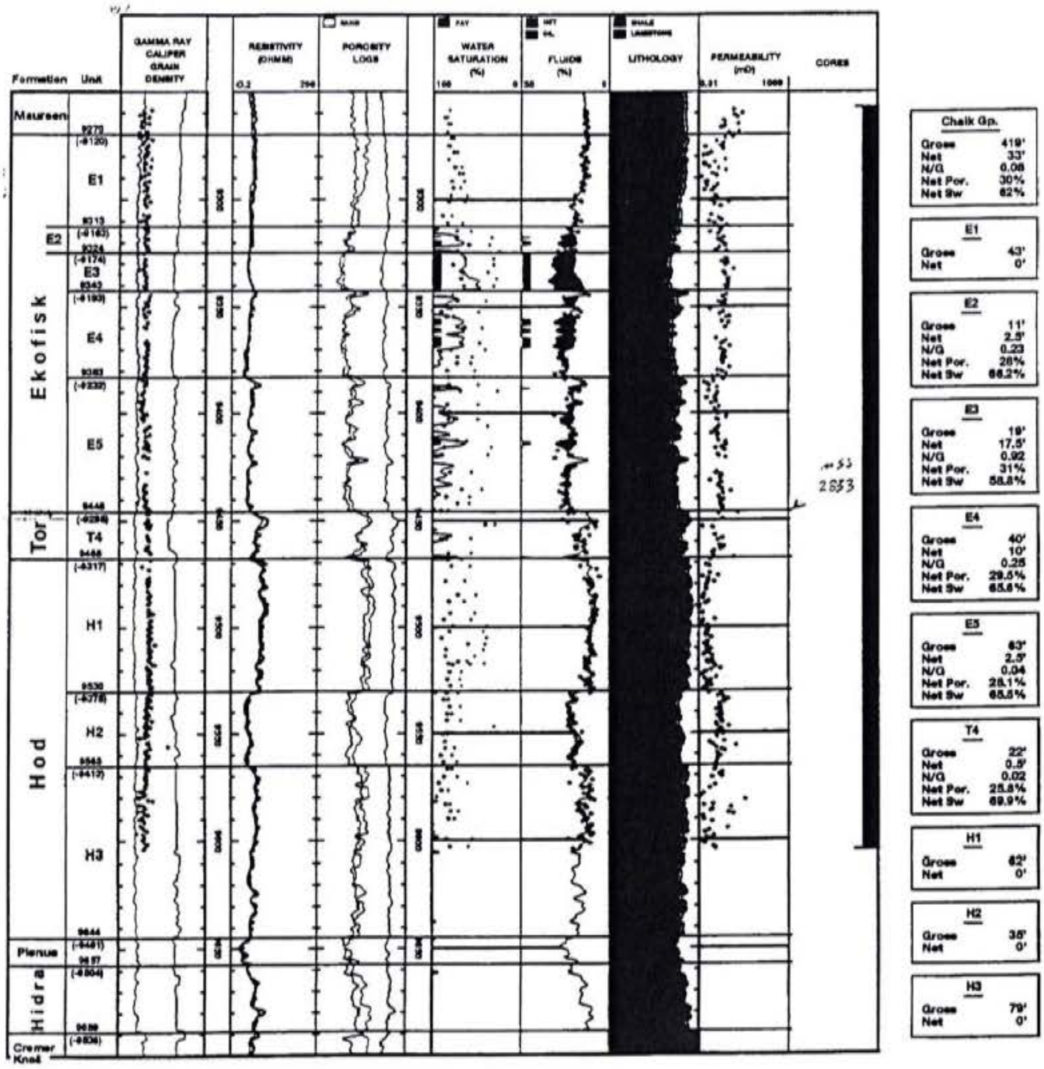

Figure 2. Petrophysical analysis, Baron-2 (Amerada Hess, 1996).

WELL I-1X

Contents

Technical and administrative data

Location	Offshore
Longitude	04°14'59".5
Latitude	56°03'10".
UTM Zone	31
UTM Easting (x)	577846.3 (m)
UTM Northing (y)	6212795.0 (m)
Well block no.	5604/29-1
Reference point	KB 122 ft above MSL.
Water depth	187 ft below MSL.
TD log	12848 ft below KB.
TD drill	12823 ft below KB.
The well is	Vertical.
Structure:	South-Arne
Spudded	12/02-1969.
Completed	09/04-1969
Spud classification	Exploration
Status (completion)	Plugged And Abandoned .
License	Duc Eneret 1962 A-Sv
Operator	Gulf
Contractor	Zapata North Sea
Rig	Zapata Explorer

Casing

top depth		shoe depth		diameter	
ft	m	ft	m	inch	inch (decim)
324.1	98.8	371.1	113.1	42"	42.000
324.1	98.8	736.9	224.6	20"	20.000
324.1	98.8	4028.9	1228.0	13 3/8"	13.375
324.1	98.8	10874.0	3314.4	9 5/8"	9.625

Lithostratigraphy(Groups)

Top	Bottom	Unit
f. below ref. level.		
310.0	9069.9	Post Chalk Group
9069.9	9354.9	Chalk Group
9354.8	11017.8	Cromer Knoll Group

Chronostratigraphy (Periods)

Top	Bottom	Unit
f. below ref. level.		
310	1901	Quaternary
1901	9181	Tertiary
9181	11540	Cretaceous
11540	12848	Jurassic

Cores

core	top	bottom	recovery
no.	f. below ref. level		
1	9091.00	9121.00	57.0
2	9121.00	9153.00	100.0
3	9188.00	9218.00	100.0
4	9218.00	9276.00	58.0
5	9493.00	9541.00	92.0

Cuttings

from	to	distance
f. below ref. level		bt cuttings
433.00	450.00	17.00
450.00	6990.00	30.00
6990.00	7011.00	21.00
7011.00	7020.00	9.00
7020.00	9000.00	30.00
9000.00	9090.00	10.00
9090.00	9160.00	70.00
9160.00	9180.00	20.00
9180.00	9188.00	8.00
9188.00	9200.00	12.00
9200.00	9490.00	10.00
9490.00	9493.00	3.00
9493.00	9510.00	17.00
9510.00	10000.00	10.00
10000.00	10020.00	20.00
10020.00	10310.00	10.00
10310.00	10313.00	3.00
10313.00	10320.00	7.00
10320.00	10370.00	10.00
10370.00	10810.00	20.00
10810.00	10970.00	10.00
10970.00	10976.00	6.00
10976.00	10980.00	4.00
10980.00	12200.00	10.00
12200.00	12220.00	20.00
12220.00	12820.00	10.00

Well Tests

Top	Bottom	Test type
f. below ref. level		
9185	9203	DST 1

Available well logs

Company: Schlumberger

File no.	Log type, interval, suite no., run no., scale
2659	Borehole compensated sonic log (Gamma ray) , 738.00-4052.00ft , , 1 , 1:200
2660	Borehole compensated sonic log (Gamma ray) , 738.00-4052.00ft , , 1 , 1:1000
2635	Borehole compensated sonic log (Gamma ray) , 4031.00-9546.00ft , , 2 , 1:200
2636	Borehole compensated sonic log (Gamma ray) , 4031.00-9546.00ft , , 2 , 1:1000
2637	Borehole compensated sonic log (Gamma ray) , 9450.00-10986.00ft , , 3 , 1:200
2638	Borehole compensated sonic log (Gamma ray) , 9450.00-10986.00ft , , 3 , 1:1000
2639	Borehole compensated sonic log (Gamma ray) , 10887.00-12838.00ft , , 4 , 1:200
2640	Borehole compensated sonic log (Gamma ray) , 10887.00-12838.00ft , , 4 , 1:1000
2645	Continuous dipmeter , 7000.00-10990.00ft , , 1 , 1:0
2641	Formation density log , 7500.00-9554.00ft , , 1 , 1:200
2642	Formation density log , 7500.00-9554.00ft , , 1 , 1:1000
2643	Formation density log , 9450.00-10994.00ft , , 2 , 1:200
2644	Formation density log , 9450.00-10994.00ft , , 2 , 1:1000
2646	Gamma ray , 8800.00-9800.00ft , , 1 , 1:0
2647	Induction electrical log , 738.00-3963.00ft , , 1 , 1:200
2648	Induction electrical log , 738.00-3963.00ft , , 1 , 1:1000
2649	Induction electrical log , 4031.00-9555.00ft , , 2 , 1:200
2650	Induction electrical log , 4031.00-9555.00ft , , 2 , 1:1000
2651	Induction electrical log , 9450.00-10955.00ft , , 3 , 1:200
2652	Induction electrical log , 9450.00-10995.00ft , , 3 , 1:1000
2653	Induction electrical log , 10887.00-12847.00ft , , 4 , 1:200
2654	Induction electrical log , 10887.00-12847.00ft , , 4 , 1:1000
2655	Laterolog , 8550.00-9552.00ft , , 1 , 1:0
2656	Microlaterolog , 8500.00-10995.00ft , , 1 , 1:0
2657	Sidewall neutron porosity log , 8550.00-9555.00ft , , 1 , 1:0

Available Reports

File no.	Author, company, title, publication date
2859	FLOPETROL : Drill stem test no. 1 (4.-8. April 1969). , April 1969.
2860	GEOPETROLE : PVT an analysis on oil and gas samples. , May 1969.
2863	ROBERTSON RESEARCH : The micropalaeontology and stratigraphy , May 1969.
2864	GULF OIL : Completion report , June 1969.
2870	SCHLUMBERGER : Continuous dipmeter - tabulated - Depth: 7000'-10990' , March 1969.
2881	SEISMOGRAPH SERVICES : Well Velocity Survey , April 1969.

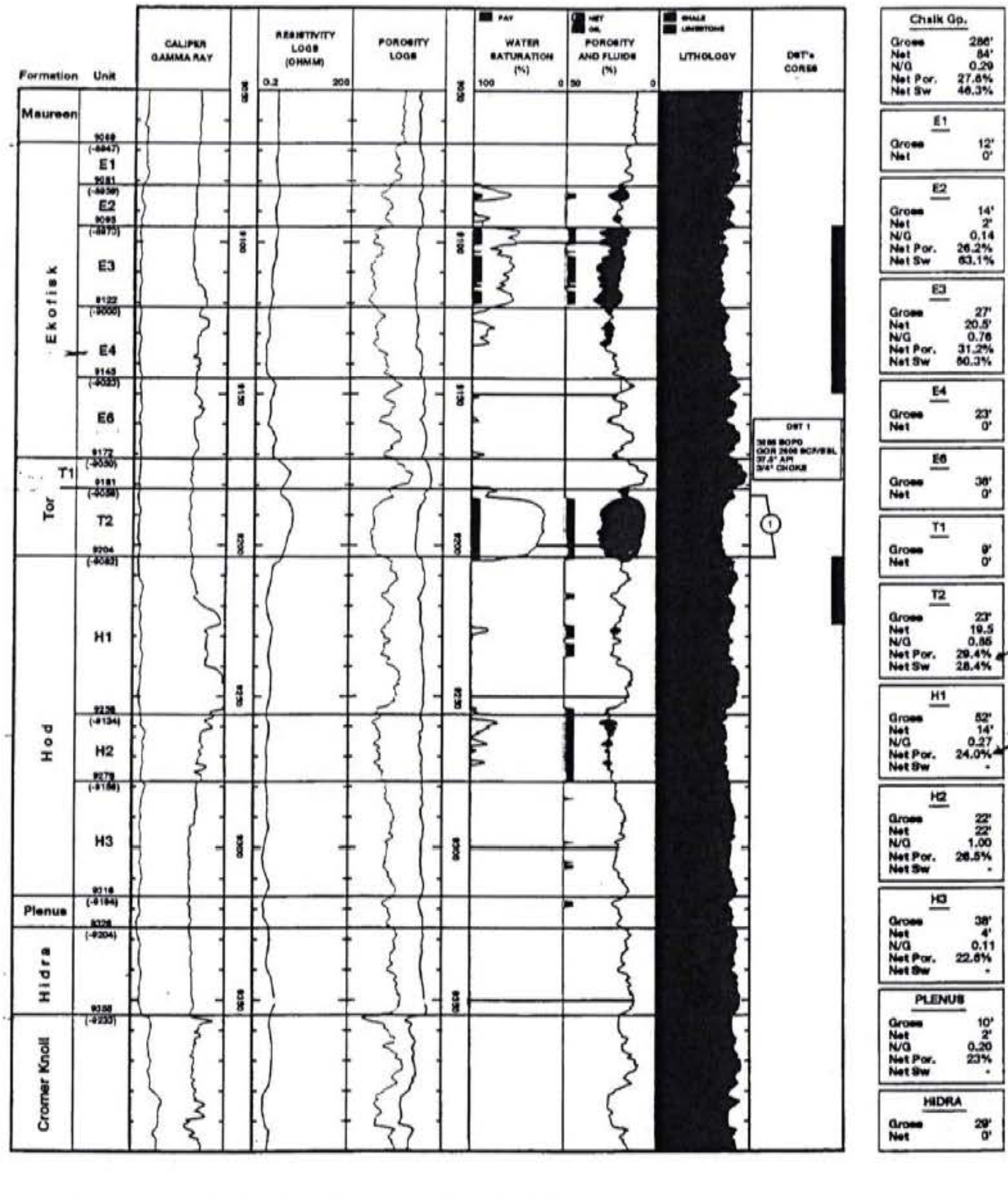

Figure 3. Petrophysical analysis, I-1 (Amerada Hess, 1996).

WELL MODI-1

Techinical and administrative data

Location	Offshore
Longitude	04 14´15´.75
Latitude	56 06´11´.87
UTM Zone	31
UTM Easting (x)	576988.6 (m)
UTM Northing (y)	6218404.0 (m)
Well block no.	5604/29-6
Reference point	RT 38 m above MSL
Water depth	61 m
Spudded	17 May 1999
Completed	30 June 1999

Available well logs

Company: Schlumberger

File no.	Log type, interval, suite no., run no., scale
18122	Vision475 LWD Triple Combo Log, 2402.00-3118. 00m,3 4, 1:500 200
18123	Vision475 LWD Triple Combo Log, 2402.00-3229. 00m, 3 4 5 6 7, 1:500 200
18121	Vision475 LWD Resistivity Log, 2402.00-3118. 00m, 3 4, 1:500 200
18124	Vision475 LWD Resistivity Log, 2402.00-3229. 00m, 3 4 5 6 7, 1:500 200

Available Reports

File No.	Author, company, title, publication date
16829	Amerada Hess A/S : Drilling programme. Well: Modi-1. License 7/89, 5604/29-6, May 1999
17114	Gardline Surveys Ltd. : Site survey report. South Arne Location. Danish sector 5604/29, March 1999
17562	Amerada Hess A/S; Dansk Operatørselvskab I/S : Final well report. Well Modi-1A. License 7/89, December 1999.
18176	Network Stratigraphic Consulting Litimed : Biostratigraphy of the intervals 1000m – 3124.5m and 2997m- 3237m. Wells: Modi-1 and Modi-1A, December 2000.

WELL RIGS-1

Contents

Technical and administrative data

Location	Offshore
Longitude	04°12'52".73
Latitude	56°05'22".05
UTM Zone	31
UTM Easting (x)	575581.3 (m)
UTM Northing (y)	6216839.0 (m)
Well block no.	5604/29-4
Reference point	KB 130.0 ft above MSL.
Water depth	198.2 ft below MSL.
TD drill	10136.0 ft below KB.
The well is	Deviated
Field:	Syd Arne
Structure:	South-Arne
Spudded	26/12-1994
Completed	25/02-1995
Spud classification	Exploration
Status (completion)	Plugged And Abandoned
License	7/89
Operator	Amerada Hess
Contractor	Mærsk Drilling
Rig	Mærsk Giant

Casing

top depth		shoe depth		diameter	
ft	m	ft	m	inch	inch (decim)
0.0	0.0	559.1	170.4	30"	30.000
0.0	0.0	3305.1	1007.4	13 3/8"	13.375
0.0	0.0	8049.9	2453.6	9 5/8"	9.625
0.0	0.0	10130.9	3087.9	7" LINER	7.000

Lithostratigraphy (Groups)

Top	Bottom	Unit
f. below ref. level.		
328.0	9132.0	Post Chalk Group
9132.0	9367.0	Chalk Group
9367.0	10136.0	Lower Cretaceous

Chronostratigraphy (Periods)

Top	Bottom	Unit
f. below ref. level.		
328.0	9291.0	Tertiary - Quaternary
9291.0	10136.0	Cretaceous

Cores

core	top	bottom	recovery
no.	f. below ref. level		
1	9107.0	9169.0	100.0
2	9169.0	9269.6	100.0
3	9260.0	9352.0	100.0
4	9352.0	9381.0	86.0

Cuttings

from	to	distance
f. below ref. level		bt. cuttings
3360.0	7980.0	30.0
7980.0	8000.0	20.0
8000.0	9140.0	10.0
9140.0	9300.0	160.0
9300.0	9380.0	20.0
9380.0	10130.0	10.0

Available well logs

Company: Halliburton

File no.	Log type, interval, suite no., run no., scale
12185	Gamma-Ray Resistivity memory log, 559.00-10136.00ft, 1:200
12184	Gamma-Ray Resistivity memory log, 559.00-10136.00ft, 1:500
12183	Gamma-Ray Resistivity memory log, 559.00-10136.00ft, 1:1000

Company: Schlumberger

File no.	Log type, interval, suite no., run no., scale
12168	AS-GR-AMS, 458.00-3288.00ft, 1A, 1:200
12167	AS-GR-AMS, 458.00-3288.00ft, 1A, 1:500
12201	Bottom hole sampling CPLT/Press/Temp/Gradio, 9250.00-9470.00ft, 1
12202	Bottom hole sampling CPLT/Press/Temp/Gradio - (plot sample 1 and 2), 9250.00-9470.00ft, 1
12188	CSAT-GR-AMS, 4700.00-10050.00ft, 3B
12198	Cement bond log GR-CCL, 7400.00-9836.00ft, 1, 1:200
12199	Cement evaluation GR-CCL, 7400.00-9836.00ft, 1, 1:200
12169	FMI-GR-AMS (Field transmitted print - not edited), 8052.00-9957.00ft, 3E, 1:40
12187	FMI-GR-AMS (MSDIP), 8052.00-9957.00ft, 3E, 1:200
12182	HP-RFT-GR-AMS, 4647.00-6560.00ft, 2B
12192	HP-RFT-GR-AMS, 9174.00-9400.00ft, 3C
12196	Junk Basket Bridge plug, 0.00-8500.00ft, 1
12180	LDL-CNL-NGS-AMS, 8052.00-10088.00ft, 3A, 1:200
12190	LDL-CNL-NGS-AMS, 8052.00-10088.00ft, 3A, 1:500
12166	MSFL-DLL-AS-NGS-AMS, 3300.00-8028.00ft, 2A, 1:200
12165	MSFL-DLL-AS-NGS-AMS, 3300.00-8028.00ft, 2A, 1:500
12181	MSFL-DLL-AS-NGS-AMS, 8052.00-10088.00ft, 3A, 1:200
12186	MSFL-DLL-AS-NGS-AMS, 8052.00-10088.00ft, 3A, 1:500
12164	NGS Ratios, 3300.00-8028.00ft, 2A, 1:200
12163	NGS Ratios, 3300.00-8028.00ft, 2A, 1:500
12191	NGS Ratios, 8052.00-10088.00ft, 3A, 1:200
12189	NGS Ratios, 8052.00-10088.00ft, 3A, 1:500
12200	Perforating record 1 11/16" enerjet, 9190.00-9500.00ft, 1, 1:200
12195	Production log - CPLT - Press/Temp/Spin/Gradio, 8800.00-9599.00ft, 1
12193	Production log - CPLT - Press/Temp/Spin/Gradio - (Ver.1), 8880.00-9599.00ft, 1
12194	Production log- CPLT - Press/Temp/Spin/Gradio - (Ver.2), 8880.00-9599.00, 1
12203	Rt-Rxo (resistivity computation), 9100.00-9700.00ft, 3A, 1:200
12197	TCP Gun correlation GR-CCL, 8200.00-8789.00ft, 1, 1:200

Available Reports

File no.	Author, company, title, publication date
11683	SCHLUMBERGER : Array-sonic waveform processing. Interval: 9050' - 9650'. Job ref.: UKJ.12290SK. Processed date: 09/03 1995. Well: Rigs-1, March 1995.
11685	SCHLUMBERGER; GEOQUEST : Walkaway seismic profile. WSP processing report. Vol. 1 (2). Well: Rigs-1, March 1995.
11686	SCHLUMBERGER; GEOQUEST : Walkaway seismic profile. WSP processing report. Vol. 2 (2). Well: Rigs-1, March 1995.
11687	SCHLUMBERGER : Interactive FMI image analysis of a Cretaceous rock sequence. Processed interval: 9050' - 9600'. Run 3E. Well: Rigs-1, March 1995.
11688	SCHLUMBERGER : MSRT / LINC with PCT. DST 1, 1A. Well: Rigs-1, February 1995.
11689	EXAL : Well site test report. DST 1, 1A. Perforation interval: 9155' - 9270' and 9270' - 9370' MDBRT. Well: Rigs-1, February 1995.
11690	EXPLORATION AND PRODUCTION SERVICES (NORTH SEA) LTD. : Welltest field report. DST 1A. Perforation: 9155' - 9270' and 9270' - 9370'. Well: Rigs-1, February 1995.
11691	EXPLORATION AND PRODUCTION SERVICES (NORTH SEA) LTD. : DST 1. Perforation: 9155' - 9270'. Well: Rigs-1, February 1995.
11692	OILPHASE : Oil sampling report. DST 1A. Well: Rigs-1, February 1995.
11693	CORE LABORATORIES [U.K.] LIMITED : Wellsite oil and gas analysis. DST 1 and 1A. Well: 5604/29-4, Rigs-1, February 1995.
11694	CORE LABORATORIES [U.K.] LIMITED : Produced water analysis. Well: 5604/29-4, Rigs-1, May 1995.
11695	Laier, T., DGU : Chemical and isotopic analyses of gas (cores). Well: Rigs-1, May 1995.
11696	Jutson, D. , DGU : Wellsite biostratigraphy interval: 8100' - 9397'(MDRT). Well: 5604/29-4, Rigs-1, January 1995.
11697	EXAL : Black oil PVT study. DST 1. Perforation: 9155'-9270'. Well: Rigs-1, June 1995.
11698	EXAL : Black oil PVT study. DST 1A. Perforation: 9155' - 9270', 9270' - 9370', June 1995.
11699	PRODUCTION LOG SOFTWARE LTD. : Production log interpretation. PLT run 1. Well: Rigs-1, June 1995.
11700	EXAL : Fluid analysis. 5604/29-4, Rigs-1, February 1995.
12891	SCHLUMBERGER : Borehole seismic processing report. Well: Rigs-1, January 1995.
12896	Burgess, C., GEOLAB UK LIMITED : A geochemical evaluation of the DKCS. Well: 5604/29-4 (Rigs-1), June 1995.
12897	AMERADA HESS : Well test interpretation. DST 1, 1A. Well: 5604/29-4 (Rigs-1), June 1995.
12898	Laier, T., DGU : Analysis of pore water and mud filtrate and calculation of formation water chemistry. Rigs-1, July 1995.
12899	Krogsbøll, A.; Jacobsen, F.; Nielsen, Å., DGU : Conventional Core Analysis, June 1995.
12900	AMERADA HESS A/S : Geodetic survey listing, (MSL and RKB). Well: Rigs-1, August 1995.
12902	SIMON PETROLEUM TECHNOLOGY : Biostratigraphy - interval: 3390'-10130' TD, August 1995.
12904	AMERADA HESS A/S : Final well report. Rigs-1, (5604/29-4), August 1995.
12905	Laier, T., DGU : Chemical and Isotopic analysis of gas from DST-1A. Well: Rigs-1, August 1995.
12906	DANISH GEOTECHNICAL INSTITUTE : Rock mechanical and compaction tests and core material. Brazil tests. Unconfined compression tests. Triaxial tests. Unixial

compaction tests. Well: Rigs-1, September 1995.

12907 SGR REDWOOD (U.K.) LTD. : Test report. Crude oil assay. DST 1A. Well 5604/29-4, Rigs-1, February 1995.

12911 SCHLUMBERGER; GEOQUEST : South Arne well test analysis. Rigs-1, February 1996.

12913 CORE LABORATORIES [U.K.] LIMITED : Produced water analysis. Well: 5604/29-4, Rigs-1, September 1995.

12914 SCHLUMBERGER; GEOQUEST : Fullbore formation microImager processing and analysis final report. Interval: 8.054' - 9.050'. Well: 5604/29-4, Rigs-1, January 1995.

13181 Springer, N., GEUS : Special core analysis, September 1996.

14713 SCHLUMBERGER; arry sonic waveform processing. Interval: 9000´- 10090´, run 3. Well: Rigs-1, February 1997.

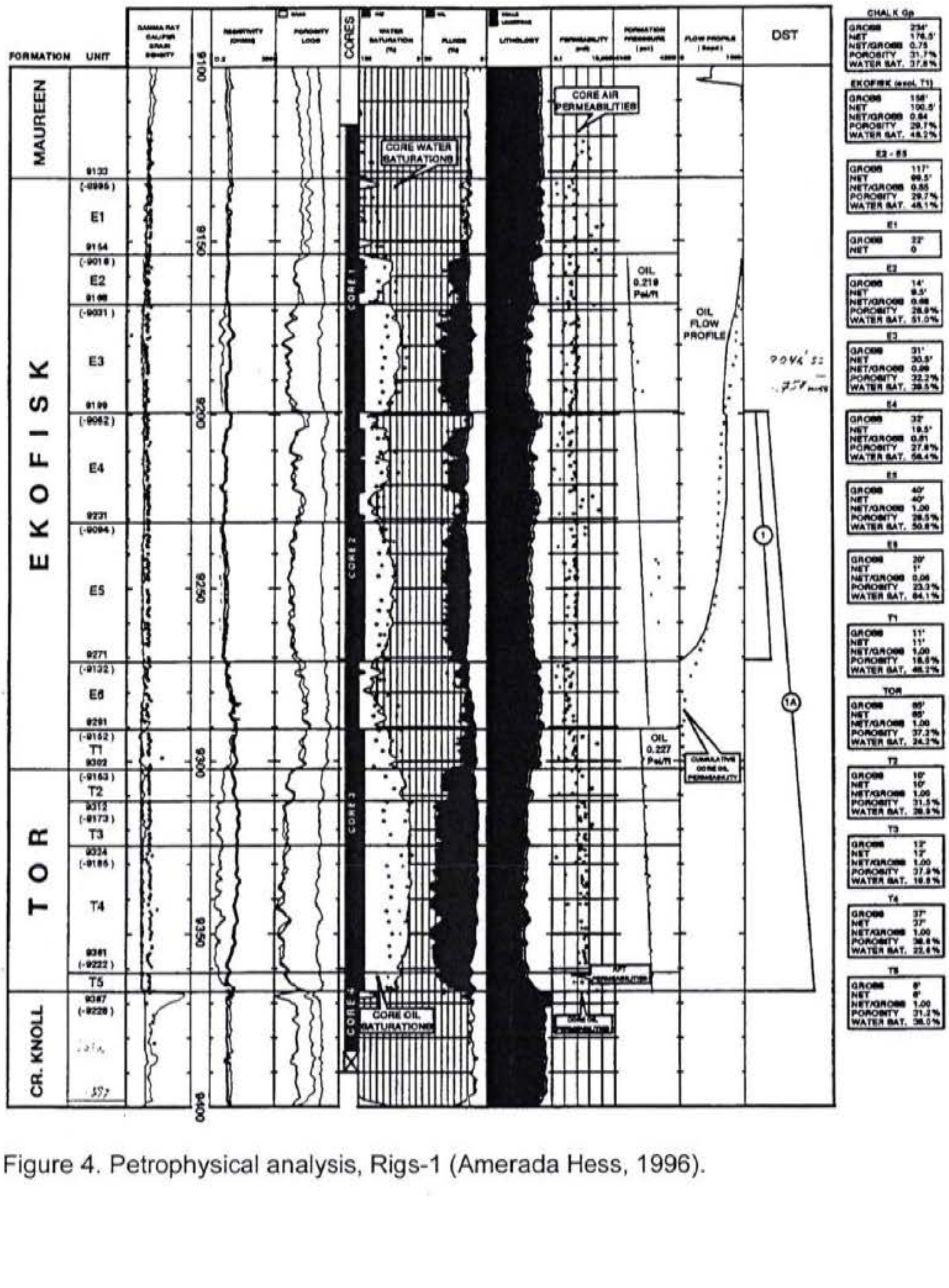

Figure 4. Petrophysical analysis, Rigs-1 (Amerada Hess, 1996).

WELL RIGS-2

Techinical and administrative data

Location	Offshore
Longitude	04 13´08´. 91
Latitude	56 05´51´. 55
UTM Zone	31
UTM Easting (x)	575844.8 (m)
UTM Northing (y)	6217756.0 (m)
Well block no.	5604/29-6
Water depth	60,6 m
	TD drill
Structure	South Arne

Available well logs

Company: Baker Hughes Inteq

File no.	Log type, interval, suite no., run no., scale
17828	Drilling Engineering Plot, 150.00-3000.00m,,, 1:2500
17829	Formation Evaluation Log, 176.00-2925.00m,,, 1:500
17827	Pressure Data Plot, 250.00-3000.00m,,, 1:2500
17826	Temperature Data Plot, 100.00-3000.00m,,, 1:2500

Company: Schlumberger

File no.	Author, company, title, publication date
15668	DLL- DSI- MSFL- NGS- AMS- SP, 97.00-2463.40m,, 1, 1:200
15670	DLL- DSI- MSFL- NGS- AMS- SP, 97.00-2463.40m,, 1, 1:500
15669	DLL- DSI- MSFL- NGS- AMS- SP, 2456.00-2922.00m,, 2, 1:200
15671	DLL- DSI- MSFL- NGS- AMS- SP, 2456.00-2922.00m,, 2, 1:500
15660	LDL-CNL-AMS, 97.00-2440.00,,1, 1:200
15662	LDL-CNL-AMS, 97.00-2440.00,, 2, 1:500
15661	LDL-CNL-AMS, 2456.00-2900.00m,, 2, 1:200
15673	LDL-CNL-AMS, 2456.00-2900.00m,, 2, 1:500
15663	LDL-CNL-AMS, 2456.00-2927.00m,, 2, 1:500
15665	NGS- AMS, 97.00-2423.50m,, 1, 1:200
15666	NGS- AMS, 97.00-2423.50m,, 1, 1:500
15664	NGS- AMS, 2456.00-2884.00m,, 2 , 1:200
15667	NGS- AMS, 2456.00-2884.00m,, 2 , 1:500

Cores

core	top	bottom	length
no.	m. below ref. level		
1	2789.00	2789.50	0.50
2	2797.00	2808.00	11.00
3	2809.00	2822.00	13.00
4	2832.00	2868.00	36.00

Available Reports

File no.	Author, company, title, publication date
13185	Bidgood, M.D., G.S.S. – Grampian Stratigraphic Services : High resolution biostratigraphic zonation of Rigs-2, Rigs-2A and Rigs-2B wells; South Arne Field (with additional comments on Rigs-1 and I-1 wells, March 1997.
13213	Dansk Operatørselskab I/S : Drilling Programme. Well: Rigs-2. Licence 7/87, April 1996.
13214	Seateam : Site survey final report. Well: Rigs-2, April 1996
13215	Corelab, wellsite analysis -DST-1/1A. Well: Rigs-2, July 1996
13216	Oilphase : Operations report – DST- 1/1A. Well: Rigs-2, July 1996
12217	Andrews Hydrographics : Well: Rigs-2. Survey Report, June 1996
12218	Schlumberger : Rigs-2. Dipol Sonic – DSI Sonic Waweform Processing – interval: 300m – 324m, September 1996.
13220	Robertson : Biostratigraphy (cores), intervals: 2828m-2867m (Rigs-2 – 2971m – 2980m (Rigs-2A))
13221	Hansen, H.C.S, Danmarks og Grønlands Geologiske Undersøgelse (GEUS) : Rigs-2. Core Analysis Tabulation, core 1, 2, 3, 4, September 1996
13222	Dahl, R., Reservoir Laboratories A/S : Rigs-2. Capillary pressure measurements by mercury injection – chalk samples, October 1996.
13223	The Expro Group : MDT Fluid analysis. Well: Rigs-2, August 1996.
13225	Høier, C.; Jakobsen, F., Danmarks og Grønlands Geologiske Undersøgelse (GEUS), Conventional Core Analysis, December 1996.
13226	The Expro Group : Black Oil PVT study – DST 1- Perforation: 2818-2934m. Well: Rigs-2, October 1996
13227	The Expro Group : Black Oil PVT study – DST 1A - Perforation: 2818-2934m MDBRT, 2953-3026m MDBRT. Well: Rigs-2, September 1996.
13228	Amerada Hess A/S; Dansk Operatørselskab A/S : Final well report. Well: Rigs-2, January 1997
13229	Schlumberger/GeoQuest : Vertical Seismic Profile Processing report. Well: Rigs-2. Volume 2 (2), July 1997.
13230	Schlumberger/GeoQuest : Vertical Seismic Profile Processing report. Well: Rigs-2. Volume 2 (2), July 1997.
13270	Schlumberger/Amerada Hess A/S : Rigs-2. Verification Listing, May 1996.
13978	Jutson, D.; Bidgood, M., Danmarks og Grønlands Geologiske Undersøgelse (GEUS), High resolution biostratigraphic study of the Danian /Late Cretaceous Chalks from the Rigs-1, 2A and 2B wells, South Arne field, May 1997.
14711	Oilfield Chemical Technology Ltd. : Properties of SOUTH ARNE crude samples wax and asphaltene studies. Well: Rigs-2, April 1997.
15189	Mærsk Olie og Gas : Daily drill report – 7/5-96 – 6/6-1996, May 1996.
15263	Baker Hughes Inteq : Final well report – vol. 1 (enclosure) – Rigs-2, 2A, 2B, June 1996.
16113	Bojesen-Koefod, J.A; Nytoft, H.P., Danmarks og Grønlands Geologiske Undersøgelse (GEUS) : SA-1A petroleum geochemistry, May 1999.
16120	Andersen, G.; Springer, N., Danmarks og Grønlands Geologiske Undersøgelse (GEUS) : Special core analysis for Amerada Hess A/S, June 1999

17324 Høier, C., Core Laboratory, Danmarks og Grønlands Geologiske Undersøgelse (GEUS) : Special core Analysis for The Rock Physics Project (EFP-98) ENS j.nr. : 1313/98-0007, April 2000.

17782 Nielsen, E.B., Danmarks og Grønlands Geologiske Undersøgelse (GEUS) : EFP-98 Rock Physics of Chalk: Sedimentoligical evaluation of the Tor Formation in the South Arne wells SA-1, Rigs-1 and Rigs-2, December 2000.

18059 Normann, H.P., Reservoir Laboratories A/S : Capillary pressure measurements by mercury injection on SA-1, Rigs-1 and Rigs-2 rock samples (Report: 30186732-00), June 1996.

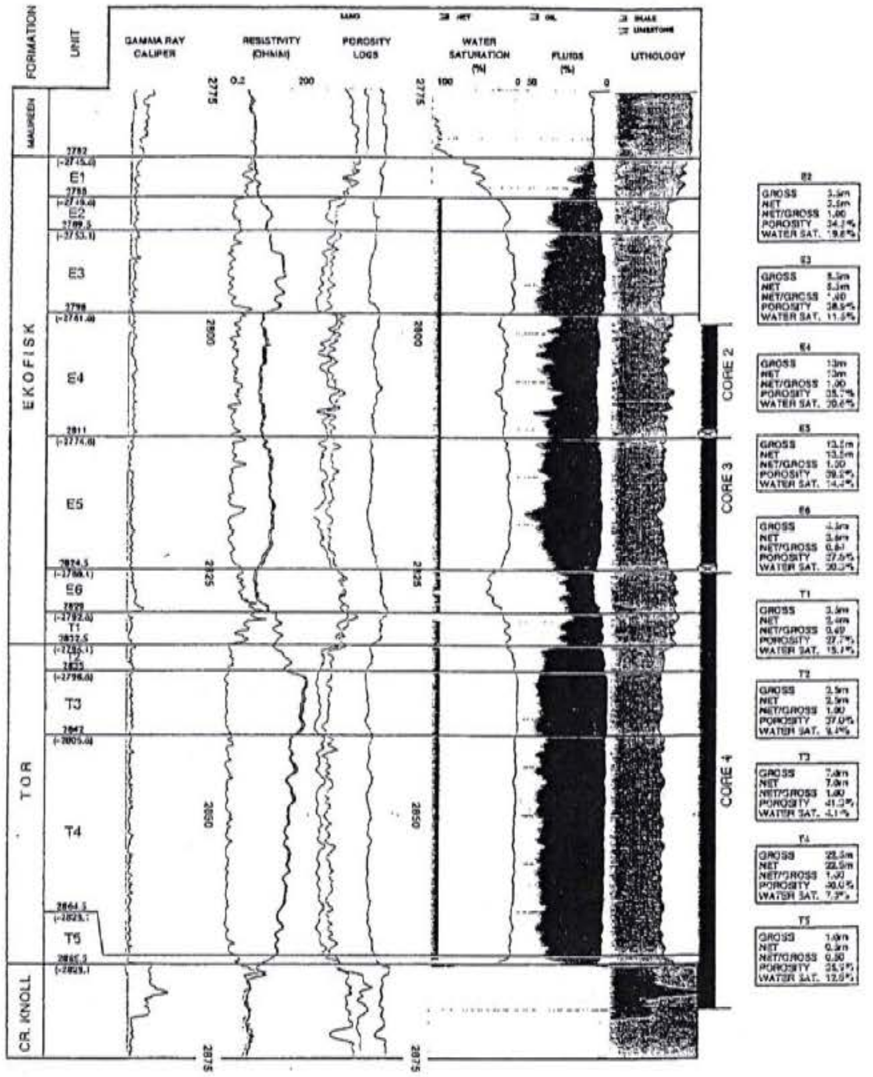

Figure 5. Petrophysical analysis, Rigs-2 (Danop, 1998).

15740 Stringfellow, R., Oilphase Sampling Services Ldt. : FPE report. Chamber MPSR-BA-0775. Well: SA-1 (Flank Pilot Hole), September 1998.

16113 Bojesen-Koefod, J.A.; Nytoft, H.P., Danmarks og Grønlands Geologiske Undersøgelse (GEUS) : SA-1A petroleum geochemistry, May 1999.

16115 Gommesen, L.; Japsen, P., Danmarks og Grønlands Geologiske Undersøgelse (GEUS) : EFP-98 Rock physics of chalk: Analysis of acoustic lig data from the well SA-1 South Arne field, April 1999.

16120 Andersen, G.; Springer, N., Danmarks og Grønlands Geologiske Undersøgelse (GEUS) : Special core analysis for Amerada Hess A/S, June 1999.

16130 Høier, C., Danmarks og Grønlands Geologiske Undersøgelse (GEUS) : Conventional core analysis for Rock physics project, June 1999.

16174 Amerada Hess A/S / Dansk Operatørselskab I/S : Final well report, vol. (1/2). Well: SA-1, SA-1A, SA-1B, SA-1C, December 1998.

16175 Amerada Hess A/S / Dansk Operatørselskab I/S : Final well report, vol. (1/2). Well: SA-1, SA-1A, SA-1B, SA-1C, December 1998.

16629 Christensen, C.L., Danish Geotechnical Institute : South Arne, SA-1. Rock mechanics test on liw porosity Tor and Ekofisk. Report no. 1, March 1999.

16980 Compagnie Generale de Geophysique : Vertical seismic profile, log calibration and syntetic seismogram report (VSP). Well: SA-1 (hell pilot), Sa-1C, January 1999.

17017 Schlumberger : SA-1 tape summary. Logtape file no. 30000 to 30005, November 1999.

17324 Høier, C., Danmarks og Grønlands Geologiske Undersøgelse (GEUS) : Special core analysis for The Rock Physics Project (EFP-98) ENS. J.nr. 1313/98-0007, April 2000.

17782 Nielsen, E. B. , Danmarks og Grønlands Geologiske Undersøgelse (GEUS) : EFP-98 Rock Physics of Chalk: Sedimentologival evaluation of the Tor Formation in the South Arne wells SA-1, Rigs-1 and Rigs-2.

18059 Normann, H.P., Reservoir Laboratories A/S : Capillary pressure measurements by mercury injection on SA-1, Rigs-1 and Rigs-2 rock samples (Report: 30186732-00), June 2000.

Available well logs

Company: Baker Hughes Inteq

File no.	Log type, interval, suite no., run no., scale
17817	MWD. Dual Propagation Resistivity, Gamma Ray (DPR-GR). 9 7/8" Pilot Hole, 258.00-642.00m,,,1:500
17818	MWD. Gamma Ray (GR) In 16" and 12 ¼ Hole, 642.00-996.00m,,, 1:500

Company: Schlumberger

File no.	Log type, interval, suite no., run no., scale
17608	DSI-GR (P and S), 2100.003510.50m, 2,1, 1:200 500
17619	DSI-PS/UD, 1000.00-1590.20m, 1,1,1:200 500
17609	FMI-GR image and MSD, 55.00-3530.60m, 2, 2, 1:40 200
17611	MDT-GR Pretests and sampling, 331.2050m, 2,6, 1:0
17612	MDT-GR Stress testing and sampling, 3355.40-3472.00m, 2,7, 1:0
17620	NGT Ratios, 1000.00-1590.20m, 1, 1, 1:200
17610	PEx-AITH, 3307.40-3528.60m, 2, 3, 1:200 500
17607	PEx-HALS-DSI, 2100.00-3528.70m, 2, 1, 1:200 500
17618	PI-DSI-LDL-NGS, 1000.00-1590.20m, 1, 1, 1:200 500

Available Reports

File no.	Author, company, title, publication date
14861	Dansk Operatørselskab I/S / Amerada Hess A/S : Licence 7/89. Development well SA-1. Drilling Programme, October 1997
14990	Andersen, G.; Høier, C.; Springer, N.; Stentoft, N., Danmarks og Grønlands Geologiske Undersøgelse (GEUS), May 1998.
15463	Nicoll, A., Oilphase : PVT Laboratory study report. South Arne-1 (Flank Pilot Hole), June 1998.
15580	Hansen, C.F., Danish Geotechnical Institute : South Arne, Standard rock mechanics test of Maureen, E1, E6 and Cromer Knoll Formations. Report 1.
15588	Havmøller, O., Danish Geotechnical Institute : South Arne, Compaction, Waterfloding and standard rock mechanics tests of E3, E5, T3 and T4 formations. Well: SA1, May 1998.
15620	Baker Hughes Inteq : Final report, South Arne 1-1A -1B-1C. Offshore Denmark. December 1997 – May 1998. Volume 1 (2): Text, May 1998.
15621	- : Final well report. South Arne 1-1A-1B-1C. Offshore Denmark. December 1997-May 1998. Volume 2(2): 16 log enclosures, May 1998.
15649	Dahl, R., Reservoir Laboratories A/S : Capillary pressure measurements by mercury injection on South Arne samples. Report. Well: South Arne-1, July 1998.
15738	Oilfield Chemical Technology Ltd. : Connate wateranalysis. Well: SA-1, August 1998.
15739	Stringfellow, R., Oilphase Sampling Services Ldt. : FPE report. Chamber MPSR-BA-0770. Well: SA-1 (Flank Pilot Hole), September 1998.

WELL SA-1

Technical and administrative data

Location	Offshore
Longitude	04 13´51´´. 4
Latitude	56 04´43´´.2
UTM Zone	31
UTM Easting (x)	576616.8 (m)
UTM Northing (y)	6215656.0 (m)
Well block no.	5604/29-0
Reference point	KB 40 m above MSL
Water depth	60 m
The well is	Deviated
Structure	South Arne
Spudded	8 December 1997

Cores

core	top	bottom	recovery	length
no.	f. below ref. level			
1	9091.00	9121.00	88.2	9.00
2	9121.00	9153.00	56.0	9.00
3	9188.00	9218.00	97.0	11.60
4	9218.00	9276.00	11.0	3.10
5	9493.00	9541.00	99.3	26.80
6	3407.00	3424.00	96.0	16.30
7	3424.00	3440.00	100.0	16.30
8	3440.00	3446.00	77.0	4.60

Ødegaard A/S

A Company in the Ødegaard & Danneskiold-Samsøe Group

Titangade 15
DK-2200 Copenhagen N
Denmark
Telephone: +45 35 31 10 10
Telefax: +45 35 31 10 11

Some Comments on Upscaling Rock Physics Relations in North Sea Chalks

Gary Mavko, Stanford University
mavko@stanford.edu

INTRODUCTION

In this note we discuss some issues of upscaling of rock physics relations in chalks. An important motivation for understanding upscaling is for comparing diverse geophysical measurements, for example, ultrasonic velocities on laboratory core plugs, sonic velocities in well logs, and 3D seismic in the field. For elastic (seismic) waves, we encounter scale differences in both frequency and wavelength. Frequencies range from 10^6 Hz in the lab to 10 Hz in the field; and wavelengths vary from ~ 10^{-3} m in the lab to ~10^2 m in the field. We often derive or calibrate seismic-to-rock properties transforms from cores and logs, and apply them for the interpretation of 3D seismic cubes. It is critical to understand when these transforms can be "exported" to the field, and when they need to be modified.

Although frequency, *f*, and wavelength, λ, vary together,

$$\lambda = V / f$$

(where V is the velocity), their impact on scaling can be fundamentally different. Frequency variations tend to change the physical phenomena governing wave propagation in rocks (e.g. Mavko et al., 1998). For example, at very low frequencies, Gassmann's (1951) relations describe the quasi-static effect of pore fluids, when wave-induced pore fluid pressures are equilibrated throughout the pore space. At higher frequencies, wave-induced fluid motion starts to be influenced by viscous and inertial stresses, wave attenuation increases, and the rock appears viscoelastic. At very high frequencies, inertially immobile pore fluids can make the rock stiffer and more elastic (Biot, 1956; Mavko and Jizba, 1991). Reviews of many frequency-dependent phenomena in rocks can be found in Knopoff, 1964; and Mavko et al, 1979. Our separate report "Fluid Substitution In Chalks: Effects Of Saturation Scales," by

Mavko and Japsen, illustrates the importance of saturation scaling when analyzing the effects of saturation on velocities.

Spatial scaling involves issues of both spatial averaging and changing physical phenomena. Waves propagate with speeds determined by rock properties averaged over roughly a wavelength. Therefore, ultrasonic waves "see" tremendous spatial heterogeneity in elastic moduli, while 3D seismic waves miss many of the details. Lucet (1989), for example, observed geometric velocity dispersion in laboratory measurements of heterogeneous carbonates. Mukerji et al (1997) review some of the wavelength-dependent velocity dispersion.

In this report we illustrate a few examples of upscaling of seismic and rock properties in chalks of the rigs-2 well. We find the expected result that measurements at the 3D seismic scale "see" less reservoir variability than those at the log or core scale. What determines this is the correlation length (or scale of spatial variability) relative to the scale of measurement (seismic wavelength). At the rigs-2 well, the correlation length is on the order of 1 meter, so the cores and logs see similar porosities, while porosities at the seismic scale are significantly different. We also show some examples of rock physics relations at two different scales. Linear relations (such as Vp vs porosity or Vp vs. Vs) tend to be scale invariant. While non-linear relations can change from the core to log scale.

SPATIAL SAMPLING AND SMOOTHING

Figure 1 shows a comparison of laboratory helium porosity and log-derived porosity, taken from logs in the rigs-2 well. At the top, the data are compared at their measurement scales. The data indicate considerable vertical heterogeneity in the reservoir, with a 5-10 porosity unit variation over a few meters. The correlation length of porosity as indicated by the log appears to be roughly 1 m. Hence, there is a reasonable agreement between the log and core porosities, even though core porosities are measured on the scale of 1-2 cm , while log densities (from which porosity is derived) are measured on the scale of tens of cm.

At the bottom of Figure 1, we superimpose a (blue) curve representing a 10m running average of the log porosities. This is a rough estimate of the porosity scale that might be inferred from 3D seismic inversion for porosity, when the seismic wavelength is about 40m. Because the spatial correlation length is so much finer than the seismic wavelength, the "upscaled" porosity does capture the true porosity heterogeneity in the reservoir.

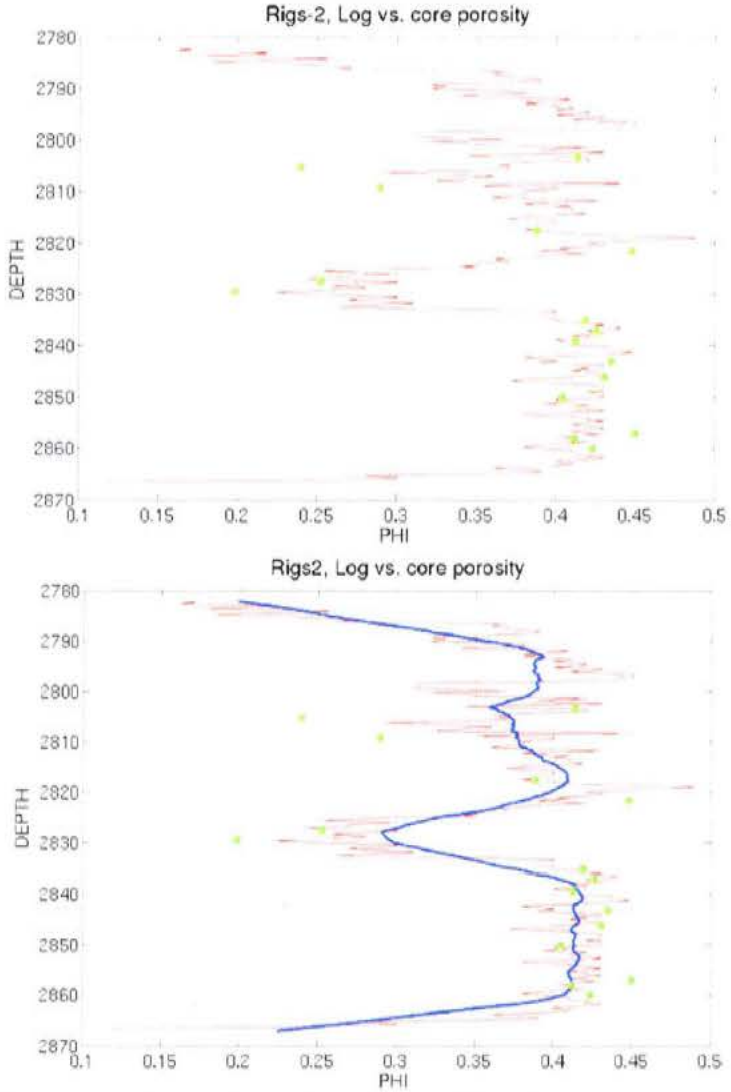

Figure 1. Comparison of log and core porosities at well rigs-2. Depth is in meters. Top: helium porosities with unsmoothed log density porosity. Bottom: additional (blue) curve showing a 10-m running average of the log-derived porosity.

Figure 2 shows histograms of the porosity from Figure 1, along with sonic Vp from the rigs2 well. While the means in Vp and porosity stay essentially unchanged, the upscaling has the reduced the standard deviation of porosity from .07 to .05 porosity units, and the standard deviation of velocity from 296 to 225 m/s.

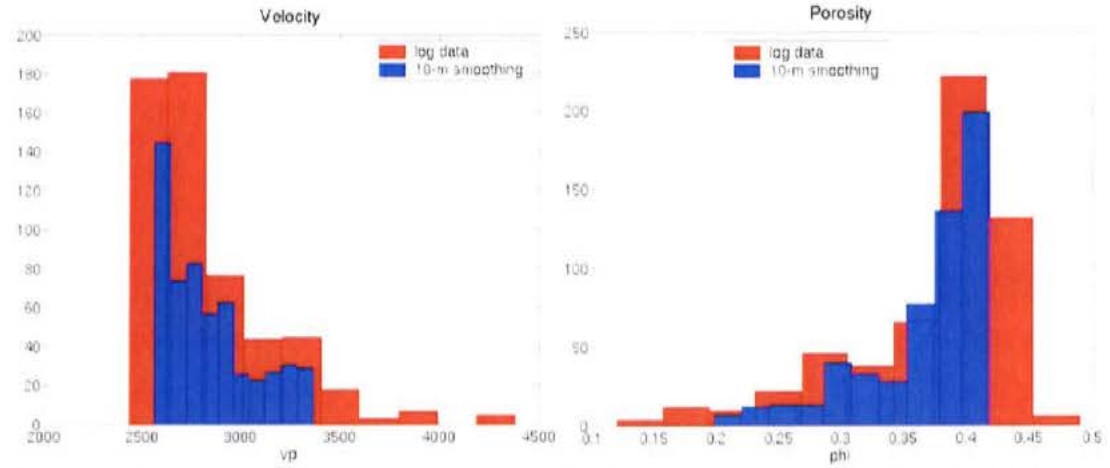

Figure 2. Histograms of Vp and porosity in the rigs2 well before (red) and after (blue) 10m smoothing.

UPSCALING OF LINEAR ROCK PHYSICS RELATIONS

A common goal in rock physics is to determine seismic-to-rock properties transforms that can be used to interpret 3D seismic. Since these are often determined or calibrated at the log or core scale, an obvious question is whether or not the rock physics equation actually changes with scale.

A simple criterion is whether or not the rock physics relation is linear. Figure 3 shows a plot of sonic Vp vs. porosity from the rigs-2 well. Although there is considerable scatter, we see the usual nearly-linear decrease of Vp with increasing porosity. Strictly speaking, a modified upper Hashin-Shtrikman bound is a better model (Walls et al, 1998), though over a small porosity range, a linear approximation is adequate. The red line is a least-squares fit to the trend, given by:

$$Vp = 4450 - 3780\phi$$

where Vp is in units of (m/s). The blue dots show the velocity-porosity relation after 10m smoothing, with a least squares linear fit (blue line) that is only slightly different:

$$Vp = 4390 - 3640\phi$$

The near invariance of the trend is a consequence of the nearly linear relation, combined with a linear smoothing operator. Consider any linear relation between *X* and *Y* of the form:

$$Y = aX + b$$

Also, consider any linear operator <>. Applying the operator to the X-Y relation gives:

$$\langle Y \rangle = \langle aX + B \rangle$$
$$= a\langle X \rangle + B$$

Hence, a simple smoothing (upscaling) operation leaves the relation unchanged. If $Y = f(X)$, then $\langle Y \rangle = f(\langle X \rangle)$. Therefore, we would expect our linear seismic-to-rock properties transform to remain relatively scale independent.

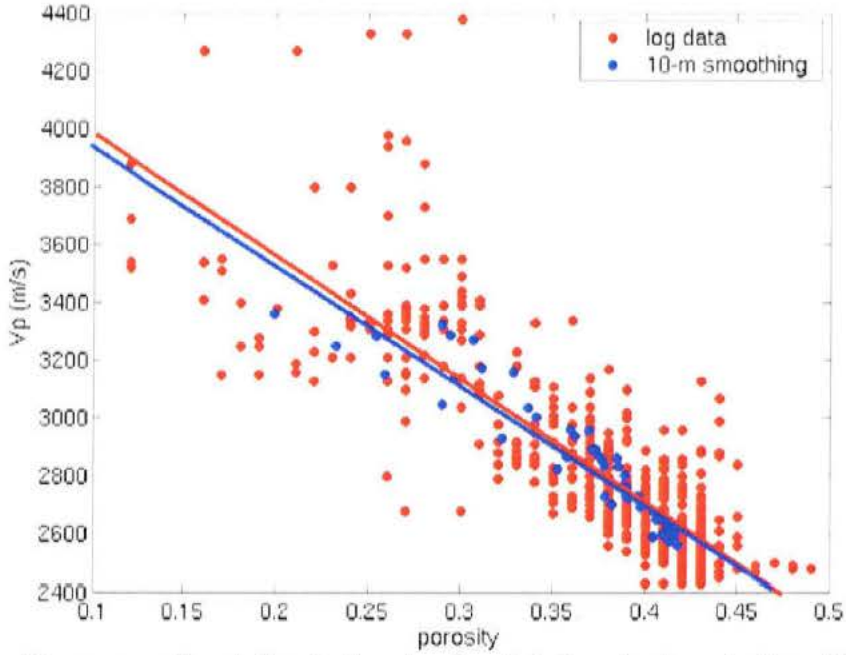

Figure 3. Vp vs. porosity relation in the rigs-2 well before (red) and after (blue) 10m smoothing.

FLUID SUBSTITUTION: A NONLINEAR RELATION

One of the most common rock physics relation is the Gassmann (1951) equation for fluid substitution:

$$\frac{K_{sat}}{K_{mineral} - K_{sat}} = \frac{K_{dry}}{K_{mineral} - K_{dry}} + \frac{K_{fluid}}{\phi\left(K_{mineral} - K_{fluid}\right)}; \quad \mu_{sat} = \mu_{dry}$$

where K_{dry}, K_{sat}, and $K_{mineral}$ are the bulk moduli of the saturated rock, the dry rock and the mineral; μ_{dry} and μ_{sat} are dry and saturated rock shear moduli; and ϕ is the porosity. Since the relation between dry and saturated moduli is nonlinear, then its application is non scale-invariant.

Figure 4 shows a plot of Vp vs. Vs for the rigs-2 well. The red dots are brine saturated data at the log scale, and the blue dots are oil saturated data, computed from the brine data, point by point at the log scale (labeled fine-scale Gassmann to oil). The magenta data are the result of applying a 10m smoothing to the blue points. In contrast, the green points are the result of first smoothing the input brine data (red points) and then applying Gassmann fluid substitution to the smoothed result. (Kwater = 2.96 Gpa; Rhowater = 1.35 g/cc; Koil = 0.44 Gpa; Rhooil = 0.67 g/cc;).

In Figure 4 we see that applying fluid substitution and then smoothing is not the same as smoothing first and then applying fluid substitution. This is a direct result of the nonlinearity of the Gassmann equation. It is generally recommended that Gassmann be applied at the fine (log) scale. This also means that applying fluid substitution to the results of a seismic inversion will suffer some scale artifacts.

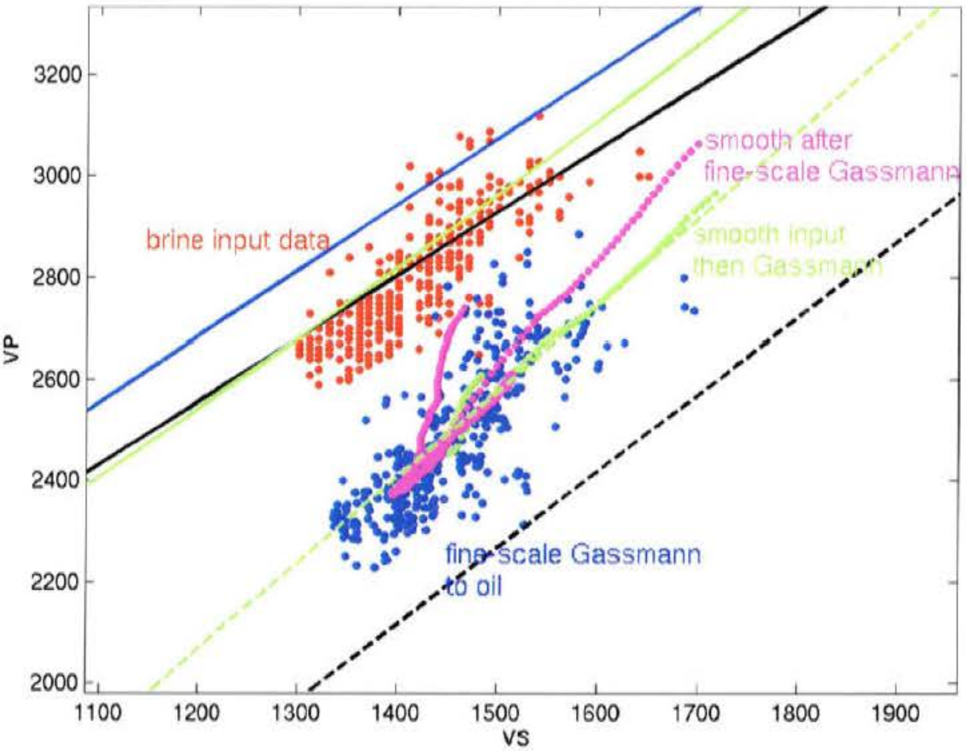

Figure 4. The invariance of fluid substitution. Red dots: input water saturated data at the log scale. Blue dots: input data fluid substituted to oil at the log scale. Magenta dots: 10 m smoothing of the fine-scale oil data (blue). Green dots: result of first smoothing the input (red) data and then applying fluid substitution. Solid curves are Greenberg-Castagna (1992) lines: blue=shale: solid green=water carbonate; dashed green=dry carbonate; solid black=water sand; dashed black=dry sand.

SUMMARY

We find the expected result that 3D seismic scale measurements "see" less reservoir variability than the logs or cores. What determines this is the correlation length (or scale of spatial variability) relative to the scale of measurement (seismic wavelength). At rigs-2 the correlation length is on the order of 1 meter, so the cores and logs see similar porosities, while porosities at the seismic scale are significantly different. We also show some examples of rock physics relations at two different scales. Linear relations (such as Vp vs porosity or Vp vs. Vs) tend to be scale invariant, while non-linear relations, such as fluid substitution can change from the core to log scale.

REFERENCES

Biot, M. A., 1956, Theory of propagation of elastic waves in a fluid saturated porous solid I. Low-frequency range, *J. Acoust. Soc. Amer.*, 28, 168-178.

Gassmann, F., 1951, Uber die elastizitat poroser medien, *Vier. der Natur Gesellschaft:* 96, 1-23.

Greenberg, M.L. and Castagna, J.P., 1992, Shear-wave velocity estimation in porous rocks: theoretical formulation, preliminary verification and applications, *Geophysical Prospecting*, 40, 195-209.

Knopoff Knopoff, L., 1964, Q, *Reviews of Geophysics*, 2, 625-660.

Lucet, N., 1989, *Vitesse et attenuation des ondes elastiques soniques et ultrasoniques dans les roches sous pression de confinement*, Ph.D. dissertation, University of Paris.

Mavko, G., and Jizba, D., 1991, Estimating grain-scale fluid effects on velocity dispersion in rocks, *Geophysics*, 56, 1940-1949.

Mavko, G., Mukerji, T., and Dvorkin, J., 1998, *The Rock Physics Handbook*, Cambridge University Press.

Mavko, 1979, G., E. Kjartansson, and K. Winkler, Seismic wave attenuation in rocks, *IUGG Quadrennial Report, American Geophysical Union.Reviews of Geophysics and Space Physics.*, 17, (6), 1155-1164.

Mukerji, T., Mavko, G., and Rio, P., 1997, Scales of reservoir heterogeneities and impact of seismic resolution on geostatistical integration, *Mathematical Geology*, 29, 933-950

Walls, J., Dvorkin, J., and Smith, B., 1998, Modeling seismic velocity data in Ekofisk chalk, *SEG Extended Abstracts*, 1016-1019.

Extrapolation of the modified upper Hashin-Shtrikman model of Walls et al. (1998)

Peter Japsen, Geological Survey of Denmark and Greenland (GEUS)
pj@GEUS.dk

The modified upper Hashin-Shtrikman model of Walls et al. (1998) is defined from log data for the Ekofisk Formation on the Ekofisk Fied with porosities less than 40%. The following parameters were estimated for that data set:

ϕ_{max} *=40%,* $K_{\phi max}$ *= 4 GPa,* $\mu_{\phi max}$ *=4 GPa,* K_0*=65 GPa and* μ_0*=27 GPa.*

Ultrasonic measurements on core samples from the South Arne field are good agreement with the model of Walls et al. However, chalk porosities between 40% and 45% occur on the South Arne field as estimated from both log data and core samples. Consequently, it is useful to extrapolate the range of the MUHS model of Walls et al. from 40% to 45% to be able to e.g. model the effect of porosity variations on the acoustic properties of the chalk.

The following high-porosity end-member moduli at 45% represent an extrapolation of the MUHS model of Walls et al:

$K_{\phi max}$ = 1.5 GPa, $\mu_{\phi max}$ =2.5 GPa,

Furthermore, the extrapolated model is agreement with the acoustic properties of the south Arne samples with porosities between 40% and 45% (Figs 1–3).

It was tested to extrapolate the MUHS model to 50% porosity, but even with $K_{\phi max}$ as low as 0.2 GPa the V_P-prediction was above that of the Walls et al. model (Fig. 4).

Legend

Blue:	saturated conditions
Circles:	Ekofisk Formation
Dots:	Tor Formation
Crosses:	outlying values (plug numbers B003, B0010, B0036)

Full line, blue: MUHS model of Walls et al (1998)
Dashed line, red: Extrapolation of MUHS model of Walls et al (1998)

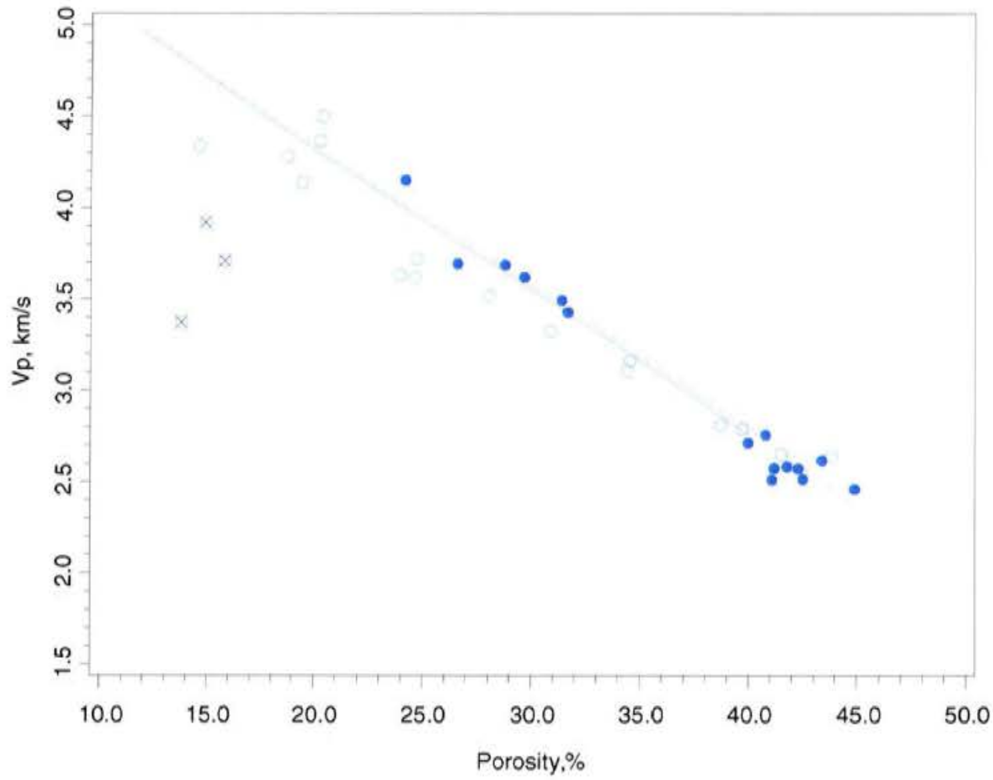

Figure 1. V_p versus porosity, ϕ. Saturated samples at Rigs-2 reference conditions.

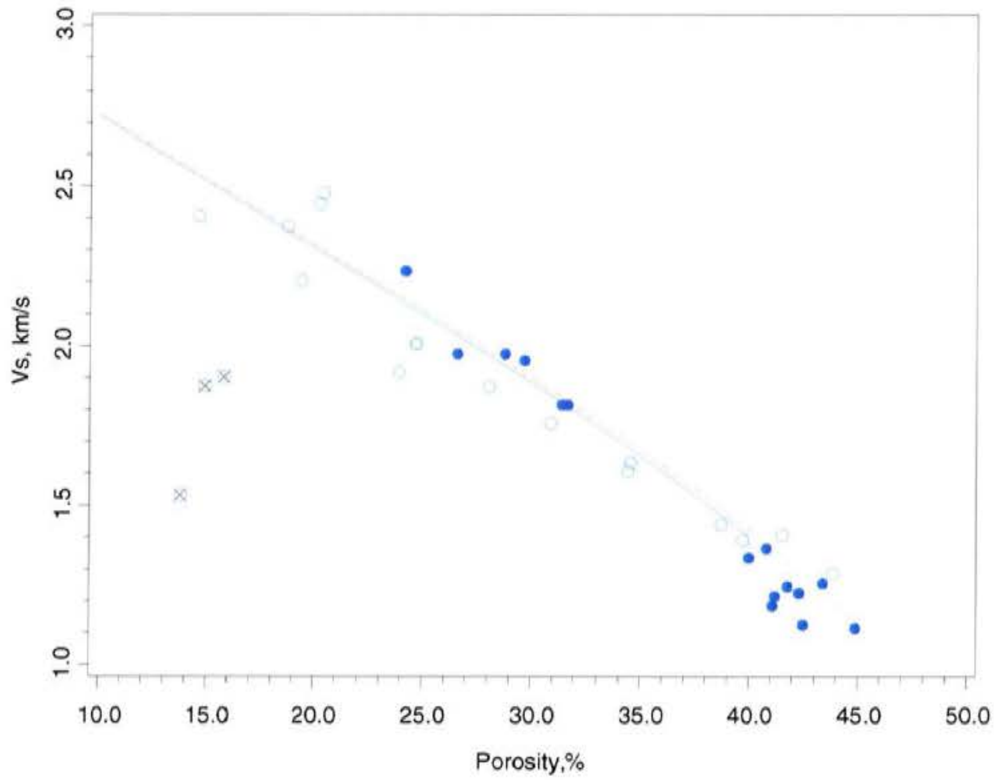

Figure 2. V_S versus porosity, ϕ. Saturated samples at Rigs-2 reference conditions.

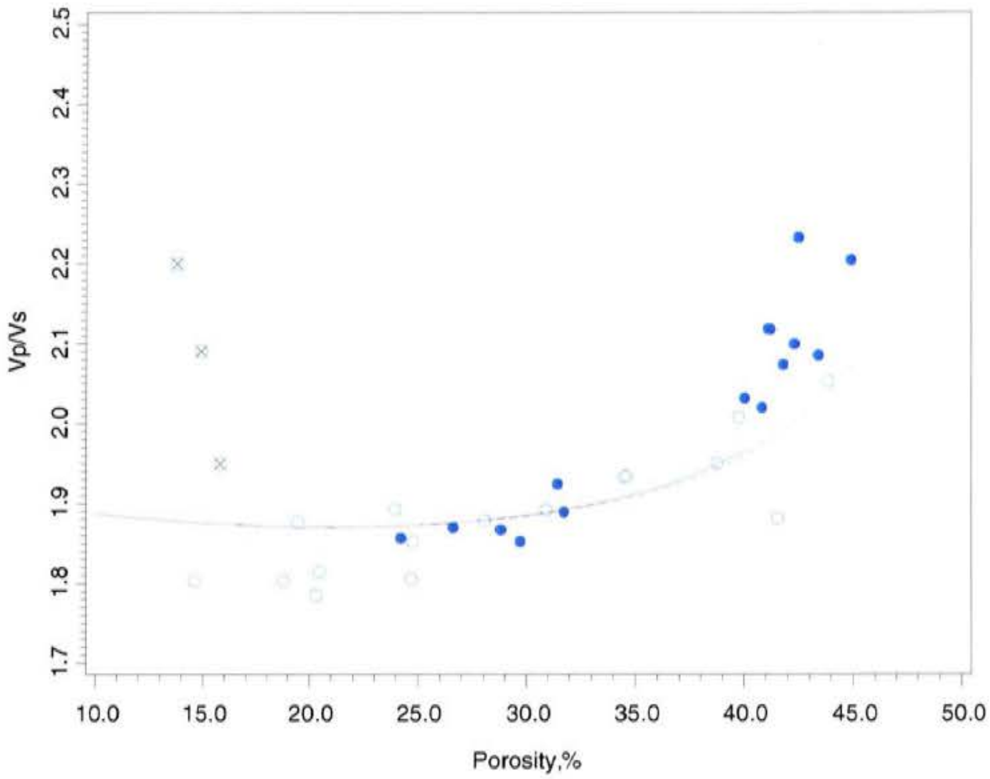

Figure 3. V_P -V_S ratio versus porosity, ϕ. Saturated samples at Rigs-2 reference conditions.

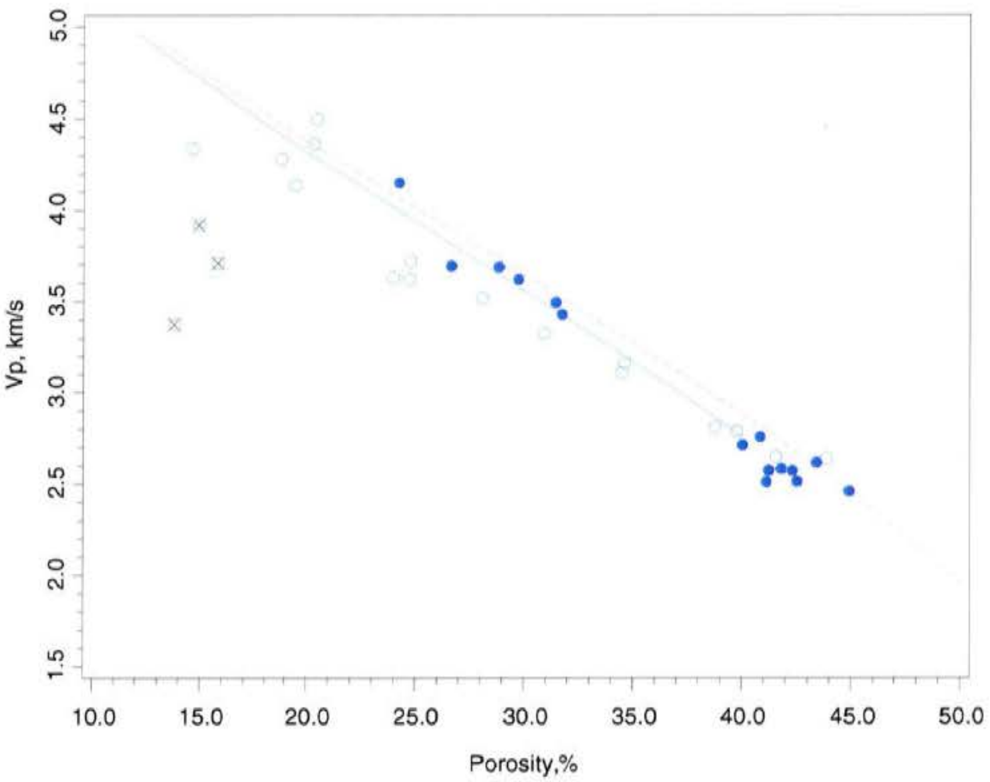

Figure 4. V_P versus porosity, ϕ. Saturated samples at Rigs-2 reference conditions. The tested model does not fit the original Walls et al. model nor the data.
Red, dashed curve: Extrapolated MUHS model with 50% porosity as the high-porosity end-member and $K_{\phi max}$ = 0.2 GPa

Compilation of ultrasonic data for chalk plugs from the South Arne field, Tor and Ekofisk formations

Peter Japsen, Geological Survey of Denmark and Greenland (GEUS)
pj@GEUS.dk

P- and S-wave velocities have been estimated at 75 bar for dry plugs and plugs saturated with tap water. Measurements were carried out on South Arne plug samples from the Tor Formation (Høier 2000) and from the Ekofisk Formation (Høier 2002) as part of the EFP-98 Rock Physics of Chalk and the EFP-01 Rock Physics of Impure Chalk projects, respectively. All readings of travel times have been done by the First Arrival Picker developed by Ødegaard. The results from the saturated samples are transformed to the reservoir conditions of the South Arne field to make comparison with down-hole log data possible. The fluid substitution is carried out using Gassmann's equations with parameters from the Rigs-2 well as reference. Reuss fluid mix is found to be valid for correcting almost dry samples to Sw=0% whereas Voigt fluid mix is valid for correcting for patchy saturation in almost fully saturated samples to Sw=100%

This report presents a compilation of the data at the Rigs-2 reference conditions and a number of derived parameters with cross plots of the parameters, but only for the 34 samples measured only at dry and saturated conditions (Figures 1 to 10). Tables of the data at Rigs-2 conditions sorted by plug number and porosity are given in Tables 1 and 2, respectively, and the original data set is given in Table 3.

Very good agreement is observed between the data set at Rigs-2 conditions and the modified upper Hashin-Shtrikman model of Walls et al. (1998) calculated at the same conditions (see Japsen 2002). Similar agreement is observed with the V_p-V_s relation for water-saturated limestone of Castagna et al. (1993), whereas the MUHS model of Japsen et al. (2000) based on Dan field data results in variations of the V_p-V_s ratio as a function of porosity that are not observed for the present data set.

Data

Ultrasonic measurements have been carried out on 50 dry and 37 saturated chalk samples from the South Arne field (Høier 2000, 2002). The measurements were carried out under both dry and saturated conditions on 34 of these samples, and out of these samples 19 were from the Ekofisk Formation and 15 from the Tor Formation. Values of density, ρ [g/cm^3], grain density, ρ_{gr}, porosity, ϕ [-] and permeability, k [Darcy] were determined.

Each plug is labelled by an ID of the form AXXX where A is a well reference and XXX a unique plug number for the well. The three South Arne wells SA-1, Rigs-1 and Rigs-2 are referenced A, B and C.

Three dry Ekofisk samples had a higher than normal residual water saturation (Sw=7%–12%; plug numbers B003, B0010, B0036). This may be an indication of high shale content and data points for these three plugs are thus marked as outliers in the plots in this report.

Measurements were furthermore carried out under partially saturated conditions on two samples (Sw=25%, 50%, 75%; plug numbers C062, C100).

Fluid substitution using Gassmann' equations

Fluid substitutions to the brine at reservoir conditions in the Rigs-2 well were carried out for the 34 plugs for which measurements on both dry and saturated plugs were available. The data for the dry and saturated plugs were corrected to water saturation of either 0 or 1, respectively, because these ideal conditions were not always met in the lab.

Previous studies have shown that the difference between the properties of the dry and the saturated samples deviates considerably from the difference predicted by Gassmann's relations (Japsen 2002). The difference between the properties of the partially saturated samples are, however, in agreement with Gassmann theory and the properties of the dry samples are consequently found to be unrepresentative for the samples saturated with different fluids.

The acoustic properties of two chalk samples were investigated for during draingage (Fig. 0). The measured bulk modulus falls between the Gassmann prediction for fluid properties based on Voigt and Reuss averages for air and water using the measured bulk modulus at 100% and calcite matrix as input. The maximum saturations of the two samples are, however, only 98% and 99% respectively, so the bulk modulus at 100% saturation was estimated. We found that the extrapolation to 100% saturation could be done by calculating the fluid properties of the almost saturated samples as a Voigt average and thus assuming patchy saturation. In contrast, the extrapolation along a Reuss bound predicted high bulk moduli that do not agree with the measured moduli at low saturations. The measured bulk moduli plot on the Reuss bound for low water saturations but depart from the bound at an intermediate value due to patchy saturation as it has been found in studies of other rock types.

The shear modulus is almost unaffected by the degree of water saturation in the partially saturated plugs as predicted by Gassman's relations. But the modulus increases by c. 0.5 GPa for S_W=0 relative to the non-zero saturations for both samples due to some over-dry effect which has been observed for other rock types as well.

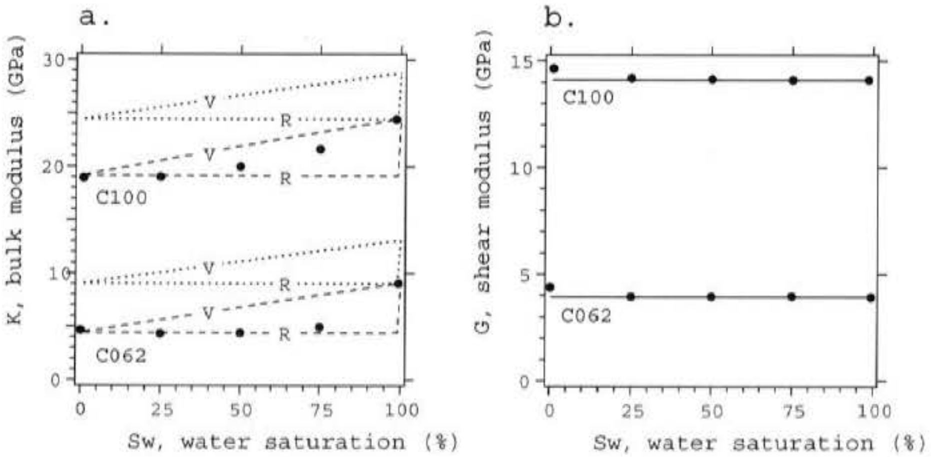

Figure 0. Elastic moduli versus water saturation, S_W, for two chalk samples; a. Bulk modulus, b. Shear modulus.
The measured moduli agree with Gassmann-prediction based on the properties at 100% saturation estimated from those measured at the maximum saturation (98% and 99%): Bulk modulus agree if fluid properties are calculated as a Reuss average for low saturation but as a Voigt average at maximum saturation. The shear modulus is almost constant for non-zero saturations.
Legend:

Dots:	*Measured values (K, G)*
Lines:	*Gassmann predictions from measured value with maximum saturation*
Dashed line:	*Prediction for full fluid mixing; Sw 98% – 100% (Reuss average)*
Split line:	*Prediction for patchy fluid mixing; Sw 98% – 100% (Voigt average)*

Initial fluid properties

Ultrasonic velocities in the chalk plugs were measured under both dry and saturated conditions. However, dry samples did not always have S_w=0 but S_w<0.34, probably due to water bound to clay particles and saturated plugs did not always have S_w=1 but S_w>0.93. The initial fluid properties during the measurement were thus calculated by considering the pore fluid occupying the pore space of the plug as a mixture of air and water. The effective density of the pore fluid, ρ_{fl1} was calculated as:

$$\rho_{fl1} = S_w \cdot \rho_w + (1 - S_w)\rho_{air} \approx S_w \cdot \rho_w$$

where the measured density of water, ρ_w=0.998 g/cm^3 at room temperature and the density of air is taken to 0 GPa.

The effective bulk modulus, K_{fl1}, of the pore fluid was calculated as a Voigt average for the almost fully saturated samples:

$$K_{fl1\_V} = S_w \cdot K_w + (1 - S_w)K_{air} \approx S_w \cdot K_w$$

and as a Reuss average for the almost dry samples:

$$K_{fl1\_R} = 1/(S_w / K_w + (1 - S_w)/K_{air})$$

Where the bulk modulus of water, K_w=2.20 GPa and the bulk modulus of air is taken to 0.000131 GPa.

Brine properties at Rigs-2 reservoir conditions

The brine properties of the Rigs-2 well at reservoir condition are chosen as the reference for comparing the elastic properties of chalk based on ultrasonic measurement on plug samples from the three South Arne wells:

$$K_{fl2} = 2.96 \text{ GPa}$$

$$\rho_{fl2} = 1.035 \text{ g/cm}^3$$

Estimated for 110 ppm salinity at 116°C and a fluid pressure of 44 Mpa.

Fluid substitution to Rigs-2 reservoir conditions

We can predict the moduli of the sample at Rigs-2 reservoir conditions (K_{sat2}, μ_{sat2}) from the moduli of the sample with initial fluid saturation (K_{sat1}, μ_{sat1}) using Gassmann's relations (see Mavko et al. 1998, p. 169):

$$\mu_{sat2} = \mu_{sat1}, \quad K_{sat2} = K_0 \tfrac{\Gamma}{1+\Gamma}$$

where

$$\Gamma = \frac{K_{sat1}}{K_0 - K_{sat1}} - \frac{K_{fl1}}{\phi(K_0 - K_{fl1})} + \frac{K_{fl2}}{\phi(K_0 - K_{fl2})}$$

and the properties of the calcite matrix are taken to be

$$K_0 = 71\,\text{GPa}, \quad \mu_0 = 30\,\text{GPa}\,.$$

The density of the sample at Rigs-2 conditions is

$$\rho_{sat2} = (1-\phi)\rho_{gr} + \phi \cdot \rho_{fl2}$$

where ρ_{gr} is the measured grain density for the sample.

For the dry plugs for which the water saturation, S_w, was non-zero the data were corrected to Sw=0, also using Gassmann's equations.

Parameters

We can calculate the elastic moduli and related parameters in terms of the estimated values of V_P, V_S [km/s] and ρ (Mavko et al. 1998). The bulk modulus, K [GPa] is calculated as:

$$K = \rho \cdot (V_P^{\,2} - \tfrac{4}{3} V_S^{\,2}),$$

the P-wave modulus, P [GPa]:

$$M = \rho \cdot V_P^{\,2},$$

the shear modulus, μ [GPa] (also referred to as G):

$$\mu = \rho \cdot V_S^{\,2},$$

Poisson's ratio, ν [-]:

$$\nu = \frac{(V_P / V_S)^2 - 2}{2(V_P / V_S)^2 - 2},$$

Young's modulus, *E* [GPa]:

$$E = 2\rho \cdot V_S^{\ 2}(1+\nu),$$

Lamé's coefficient, λ [GPa]:

$$\lambda = \rho(V_P^{\ 2} - 2V_S^{\ 2})$$

and finally, the P- and S-impedances, Z_P and Z_S [kg/m^2/s]:

$$Z_P = \rho \cdot V_P, \qquad Z_S = \rho \cdot V_S.$$

Reference models

We can compare the results of the ultrasonic measurements with some reference models:

- The Castagna V_p-V_s relation estimated from ultrasonic measuremetns on water-saturated limestone is shown in Figs 6 and 9 (Castagna er al. 1993):
  $V_S = -0.055V_P^{\ 2} + 1.017V_P - 1.031 \quad \text{(km/s)}$
- The modified upper Hashin-Shtrikman model (MUHS) with the parameters found from log data for the Ekofisk field is shown in all figures (Walls et al 1998):
  ϕ_{max} =40%, $K_{\phi max}$ = 4 GPa, $\mu_{\phi max}$ = 4 GPa, K_0=65 GPa and μ_0=27 Gpa,
  and its extension to 45% porosity (Japsen 2002):
  ϕ_{max} =45%, $K_{\phi max}$ = 1.5 GPa, $\mu_{\phi max}$ = 2.5 Gpa.
  The latter trend is shown in the plots but the two models are almost identical for 10%–40% porosity.
- The MUHS model with parameters estimated from log data from the Tor Formation at the Dan field is shown in Fig. 6 (Japsen et al. 2000):
  ϕ_{max} =45%, $K_{\phi max}$ = 2.6 GPa, $\mu_{\phi max}$ 3.0 GPa, K_0=62 GPa and μ_0=20 GPa.

The elastic properties of the rock at Rigs-2 fluid conditions can be estimated from the MUHS models using Gassmann's relations. The V_p-V_s relation corresponding to the Castagna trend is calculated for $V_P(\phi)$ as estimated from MUHS model of Walls et al. (1998).

Results

Both P- and S-wave velocities are slighly higher for the saturated Tor samples than for the Ekofisk samples in the porosity interval around 25%-30%, whereas there is no clear discrimination for porosities above 40% (Figs 1a, 2a). The resulting V_p-V_s ratio is about equal at intermediate porosities (Fig. 6).

The properties of the three samples with high residual water content at dry conditions are found to be clearly outlying, also for the saturated samples, e.g. low P- and S-velocities (Figs 1, 2; plug number B003, B010, B036). The resulting V_p-V_s ratio is high for the saturated samples and low for the dry samples (Fig. 6). Poisson's ratio is negative or zero for two of the three outlying dry samples at original conditions and Poisson's ratio is even smaller at reference conditions for these samples (B003, B036 in Tables 1b, 3b). The properties of sample B102 are outlying for the dry measurements, but not clearly for the saturated measurements (e.g. Vp/Vs versus porosity, Fig. 6).

Overall agreement is observed between the data for saturated plugs and the MUHS model of Walls et al. (1998) (porosities<40%), e.g. in the plots of V_p and V_s versus porosity (Figs 1a, 2a). This agreement is furthermore seen for V_s versus V_p and for V_p-V_s ratio versus porosity (Figs 6, 9), but the extended MUHS model is seen to predict Vp-Vs-ratios that are rather low compared to the data at 45% porosity.

Agreement between the MUHS model of Walls et al. (1998) and the Castagna V_p-V_s relation for limestone can also be noted (Figs 6, 9). However, the V_p-V_s ratio predicted the MUHS model is a bit high for small porosities relative to the data (c. 1.9 compared to 1.8) and the extrapolation above 40% porosity appears to be a bit low (the MUHS model is not defined above this porosity).

The Castagna line is shifted more in the direction of the data points in this plot (Fig. 6). Note, however, that Castagna's line is based on lab measurements of undifferentiated limestone samples saturated with tap water. The agreement between Castagna's line and the present data set may thus be accidental; e.g. the agreement is less convincing if the properties of the samples are calculated for tap water.

The MUHS model of Japsen et al. (2000) does not agree well with the present data set (Figs 6, 9). Note, that this model was developed for log data from the Dan field where results from the previous Chalk project showed that porosity was c. 5% smaller for Dan field than for South Arne samples for a velocity of 3 km/s.

The disagreement between the properties of the dry sample and the MUHS model is obvious for small porosities, e.g. in the plots of V_s versus V_p and of V_p-V_s ratio versus porosity (Figs 6, 9), but not immediately visible in the plots of V_p and V_s versus porosity (Figs 1b, 2b). However, the shear modulus of the dry samples is relatively high at low porosity (Fig. 3b), whereas the bulk modulus and Lamé's constant are relatively low (Figs 4b, 5b). Consequently, the deviation between the MUHS model and the properties of the dry samples are particularly evident in the plot of shear modulus versus Lamé's constant (Fig. 8). The non-Gassmann behavior of the dry samples have previously been noted (Japsen et al. 2002) .

References

Castagna, J.P., Batzle, M.L. & Kan, T.K. 1993: Rock physics – The link between rock properties and AVO response. In: Offset-Dependent Reflectivity –Theory and practice of AVO Analysis. J.P. Castagna & M. Backus (Eds): Investigations in Geophysics, **8**, Society of Exploration Geophysicists. Tulsa, Oklahoma, 135-171.

Høier, C. 2000: Special core analysis for the rock physics project (EFP-98) ENS J.nr.: 1313/98-0007. Ultrasonic velocity measured on plugs from the South Arne Field. Geological Survey of Denmark and Greenland Report 2000/19, 71 pp.

Høier, C. 2002: Special core analysis for the rock physics project (EFP-2001). GEUS rapport 2002/23. 26 pp, 1 CD.

Japsen, P., Wagner, H., Gommesen, L. & Mavko, G., 2000: Rock physics of Chalk: modeling the sonic velocity of the Tor Formation, Danish North Sea. 62nd EAGE Meeting, Glasgow 2000, 4 pp.

Japsen, P. 2002: Extrapolation of the modified upper Hashin-Shtrikman model of Walls et al. (1998). EFP-01 Rock Physics of Impure Chalk – Technical Note, November 2002/5, 4 pp.

Japsen 2002 Japsen, P., Høier, C., Rasmussen, K. B., Fabricius, I., Mavko, G., & Pedersen, J. M. 2002: Effect of fluid substitution on ultrasonic velocities in chalk plugs, South Arne field, North Sea. SEG 2002 Annual Meeting. 4 pp.

Mavko, G., Mukerji, T. & Dvorkin, J. 1998: The Rock Physics Handbook. Cambridge: Cambridge University Press.

Walls, J., Dvorkin, J., and Smith, B., 1998, Modeling seismic velocity data in Ekofisk chalk, SEG Extended Abstracts, 1016-1019.

Figures of data points for 34 samples measured at both dry and saturated conditions

Legend

Blue:	saturated conditions
Red:	dry conditions
Circles:	Ekofisk Formation
Dots:	Tor Formation
Crosses:	outlying values (plug numbers B003, B0010, B0036)
Full line:	MUHS model of Walls et al (1998)
Dashed line:	Castagna's V_p-V_s relation for water-saturated limestone limestone
Dotted Line:	MUHS model of Japsen et al. (2000)

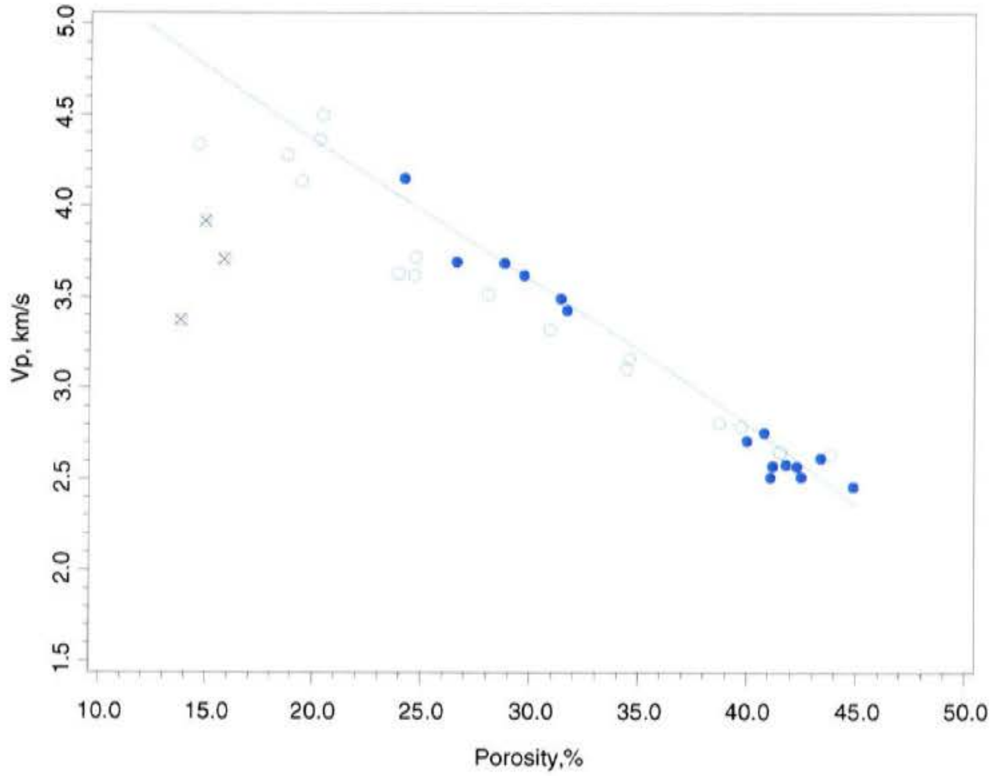

Figure 1a. V_p versus porosity, ϕ. Saturated samples at reference conditions (Table 1a).

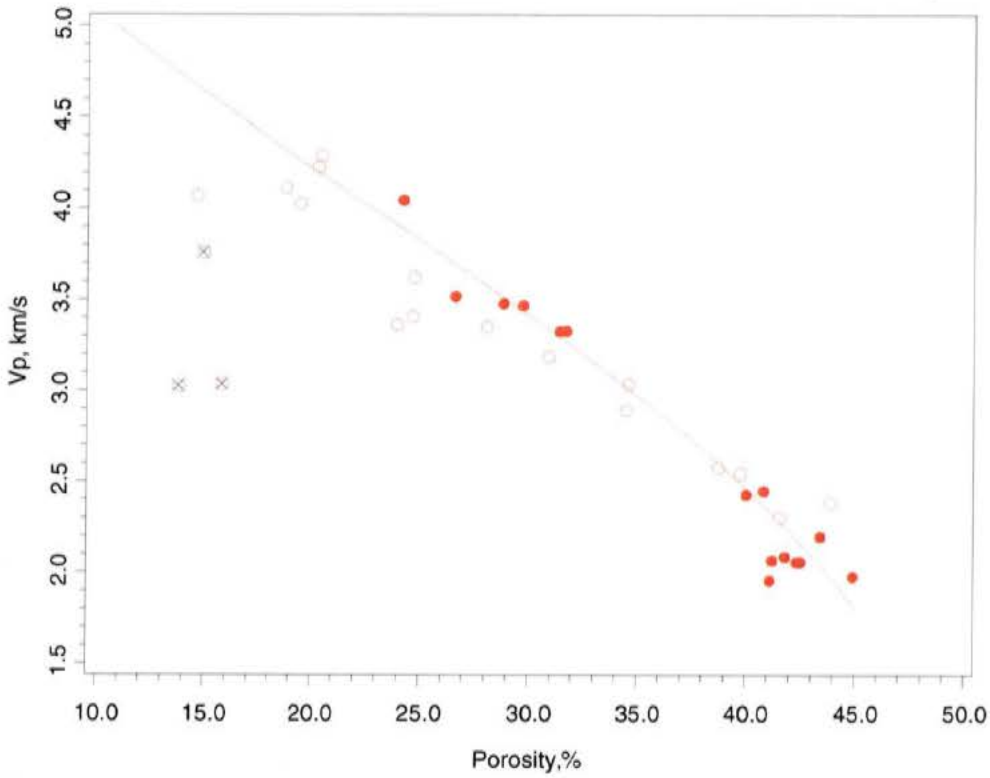

Figure 1b. V_P versus porosity, ϕ. Dry samples at reference conditions (Table 1b).

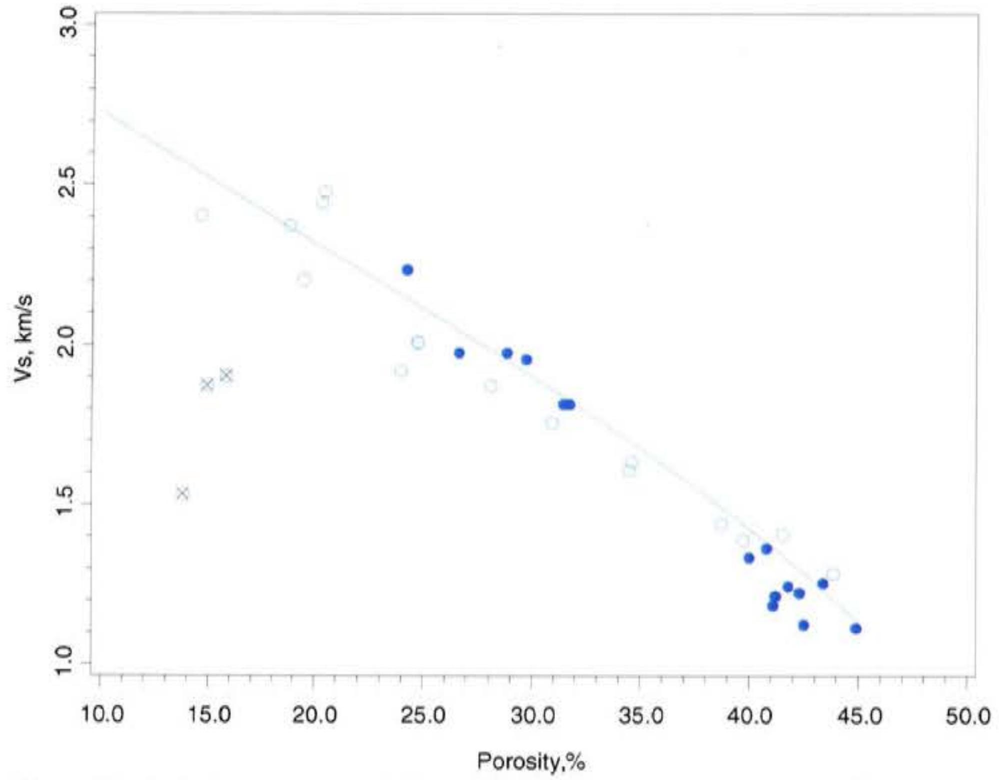

*Figure **2a**. V_S versus porosity, ϕ. Saturated samples at reference conditions (Table 1a).*

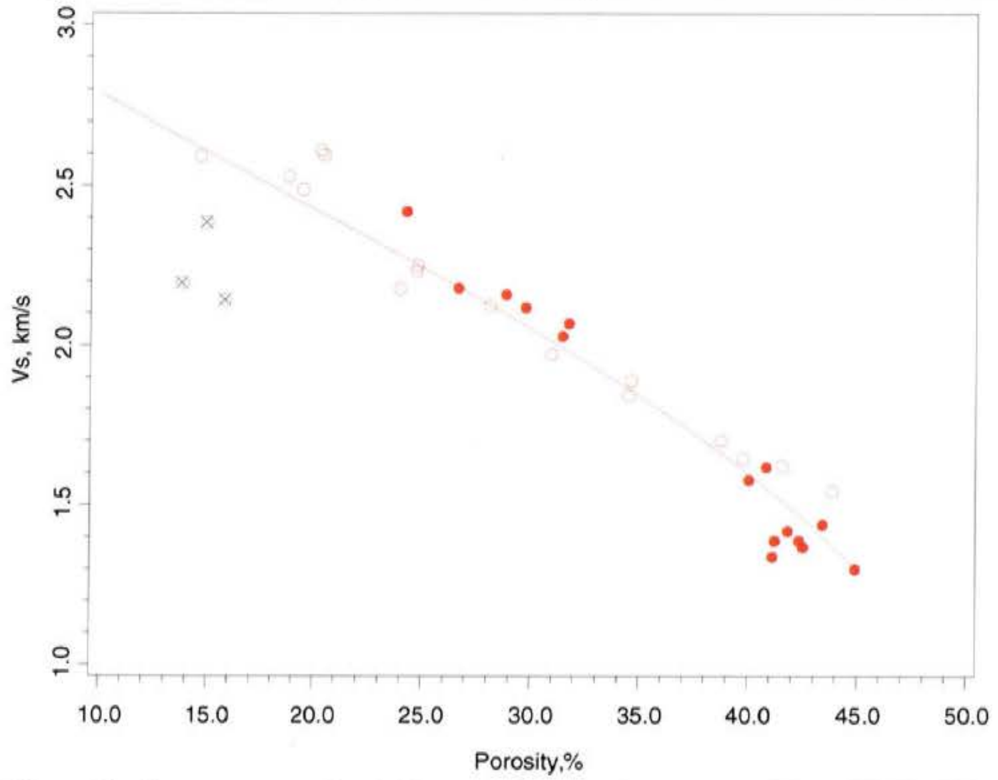

Figure 2b. V_s versus porosity, ϕ. Dry samples at reference conditions (Table 1b).

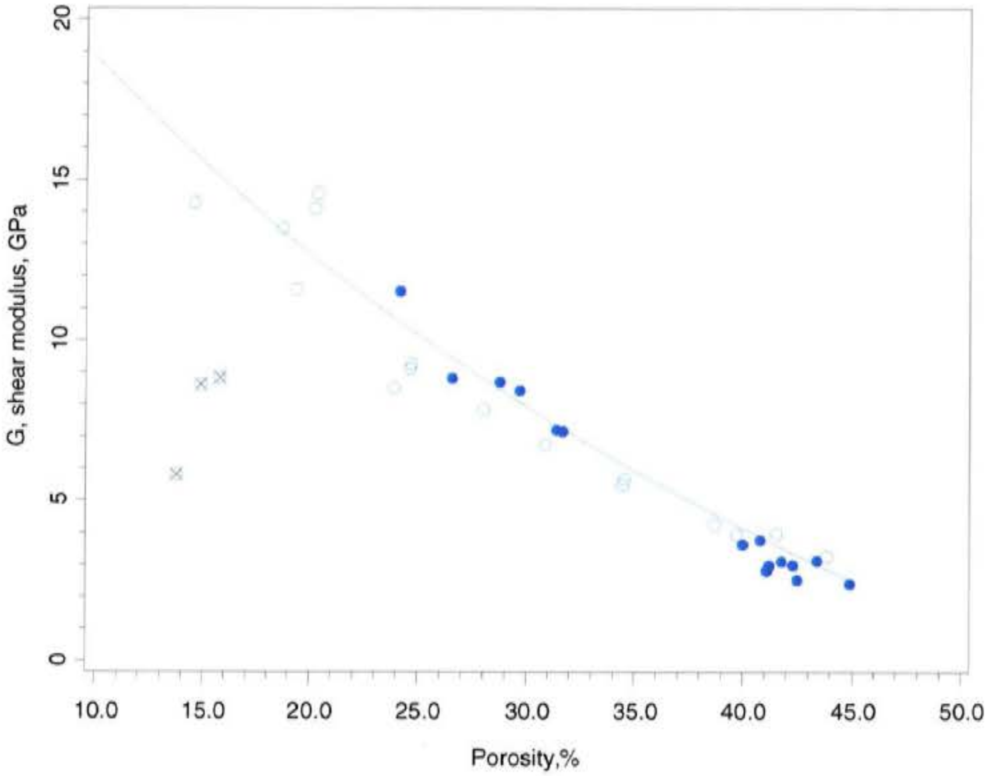

Figure 3a. Shear modulus, G versus porosity, ϕ. Saturated samples at reference conditions (Table 1a).

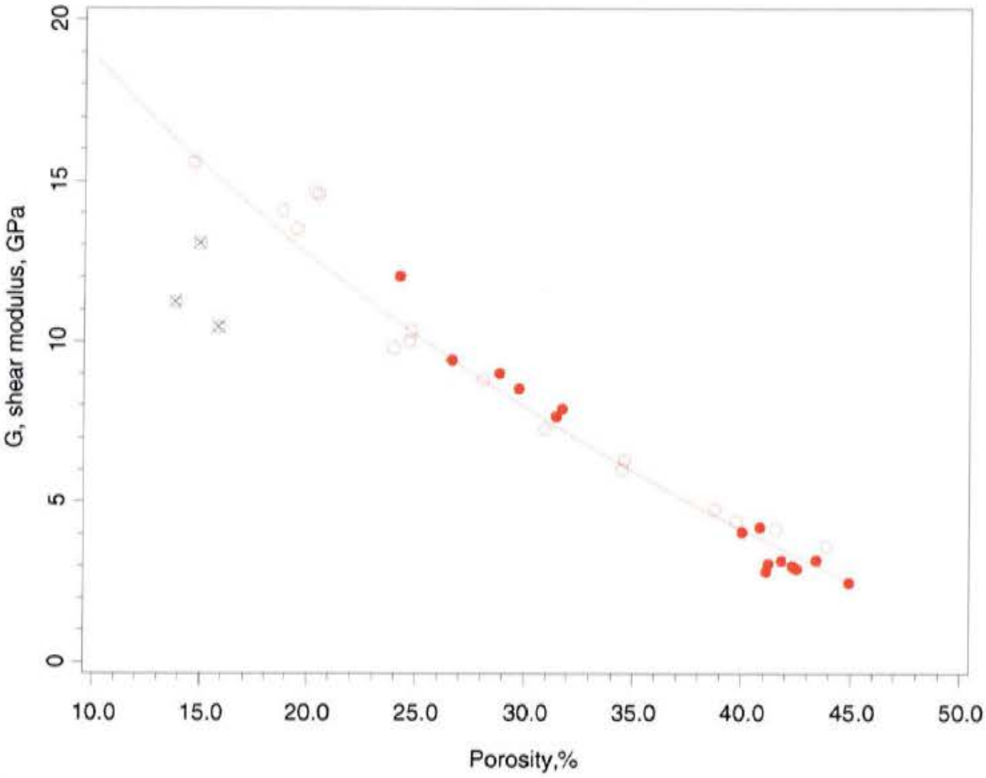

Figure 3b. Shear modulus, G versus porosity, ϕ. Dry samples at reference conditions (Table 1b).

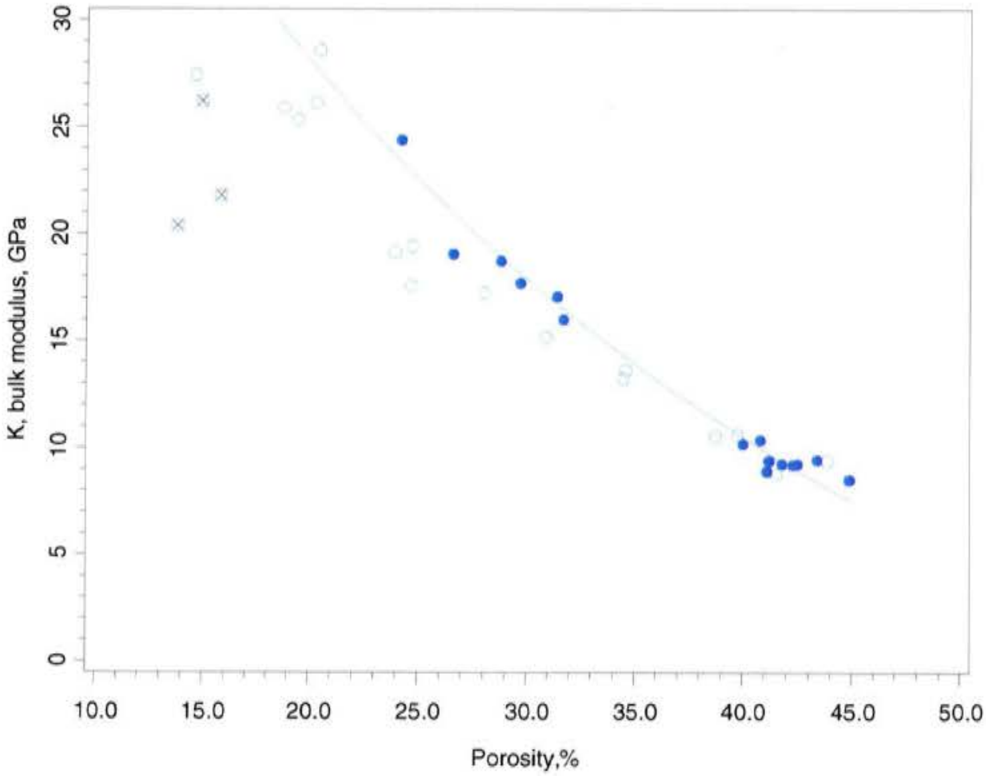

Figure 4a. Bulk modulus, K versus porosity, ϕ. Saturated samples at reference conditions (Table 1a).

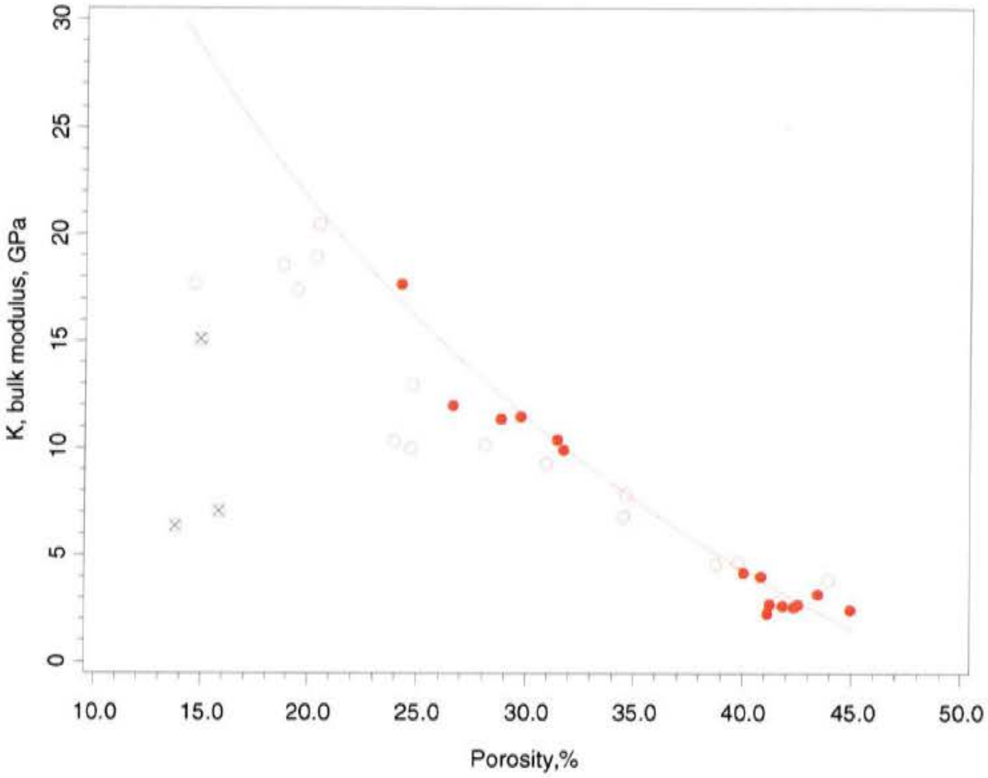

Figure 4b. Bulk modulus, K versus porosity, ϕ. Dry samples at reference conditions (Table 1b).

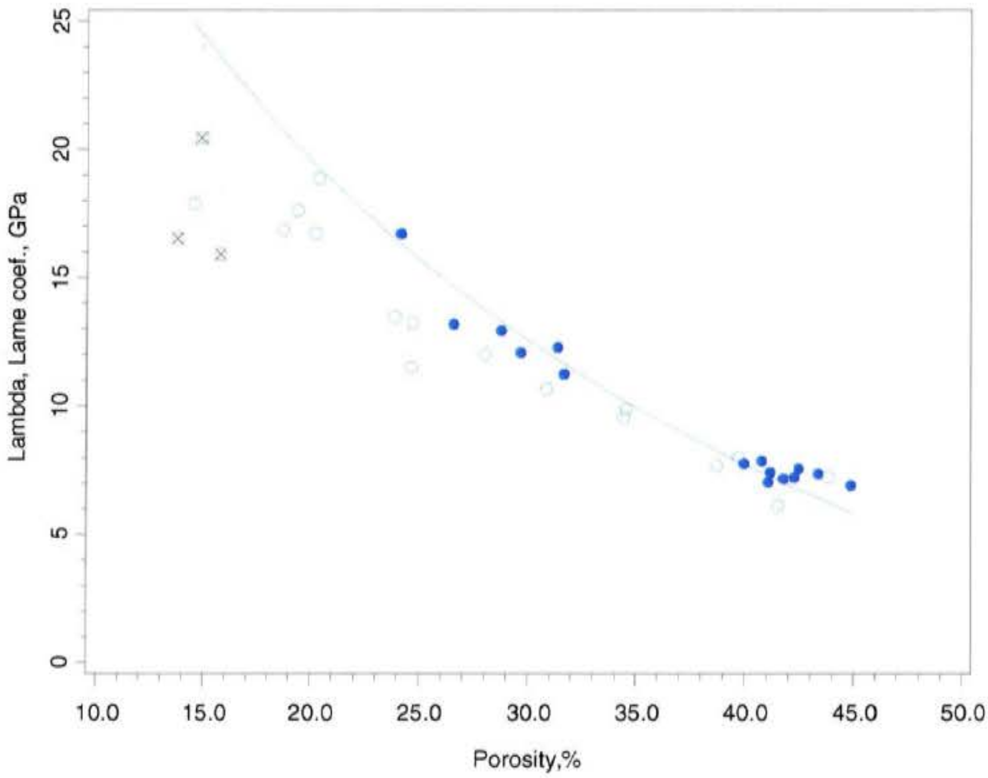

Figure 5a. Lamé's coefficient, λ versus porosity, ϕ. Saturated samples at reference conditions (Table 1a).

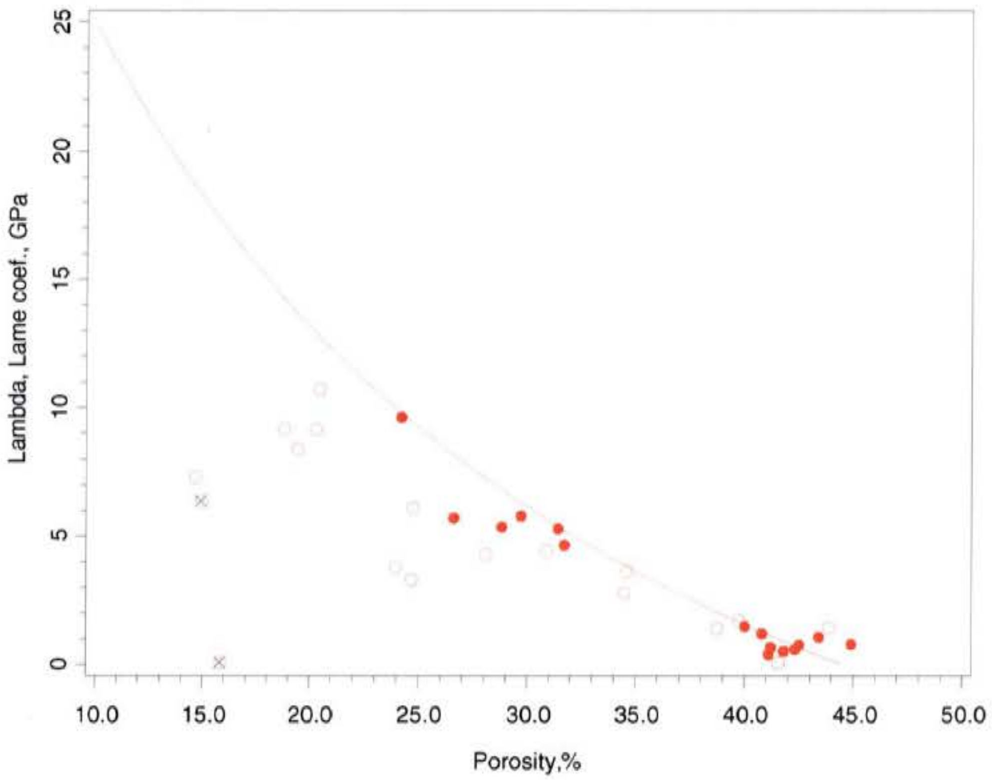

Figure 5b. Lamé's coefficient, λ, versus porosity, ϕ. Dry samples at reference conditions (Table 1b). Sample B003 has λ<0).

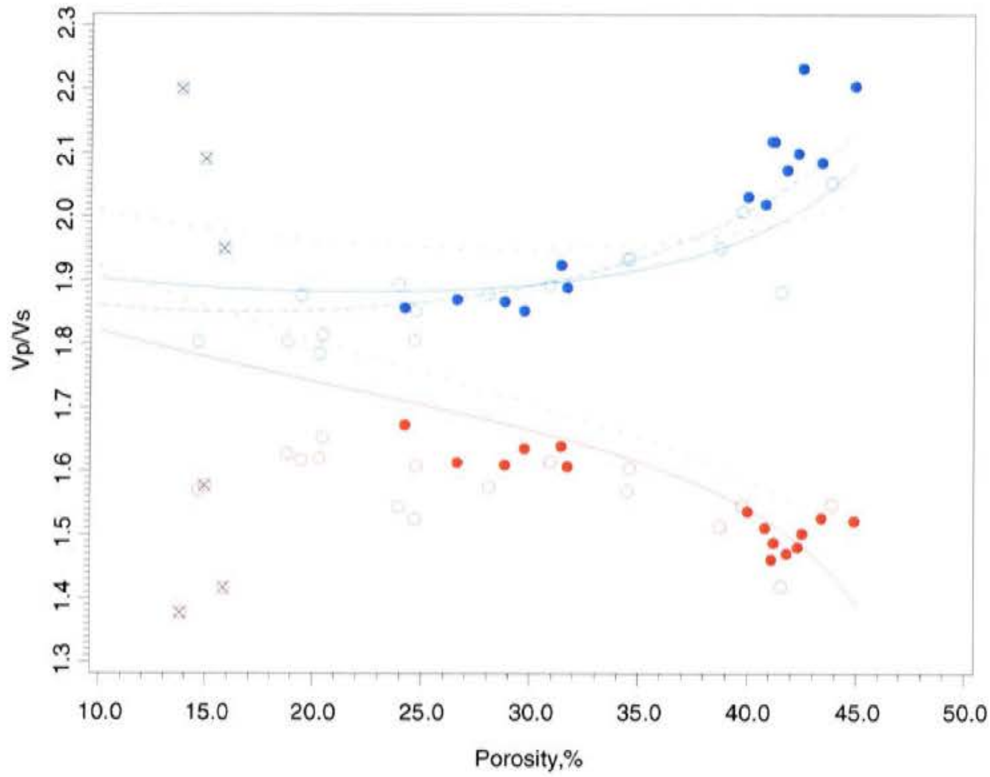

Figure 6. V_p-V_s ratio versus porosity, ϕ. Samples at reference conditions (Tables 1a,b). Dashed line: Castagna's V_p-V_s relation calculated for $V_p(\phi)$ based on the MUHS model of Walls et al. (1998).

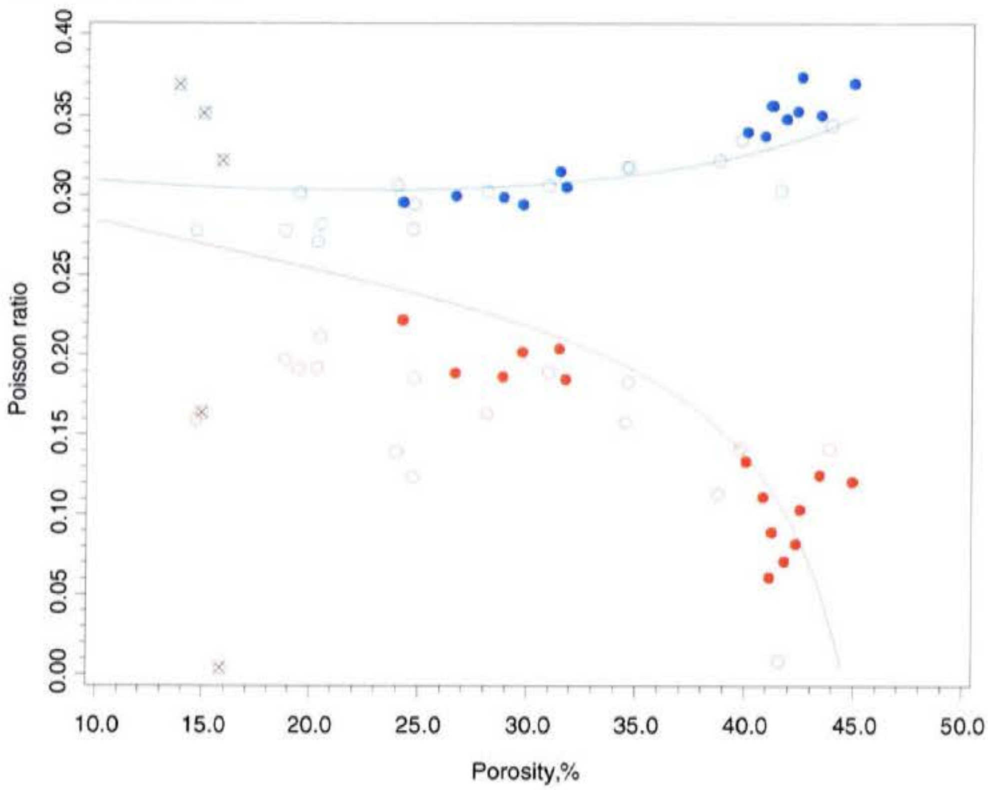

Figure 7. Poisson's ratio, ν versus porosity, ϕ. Samples at reference conditions (Tables 1a,b). Sample B003 has λ<0 at dry conditions.

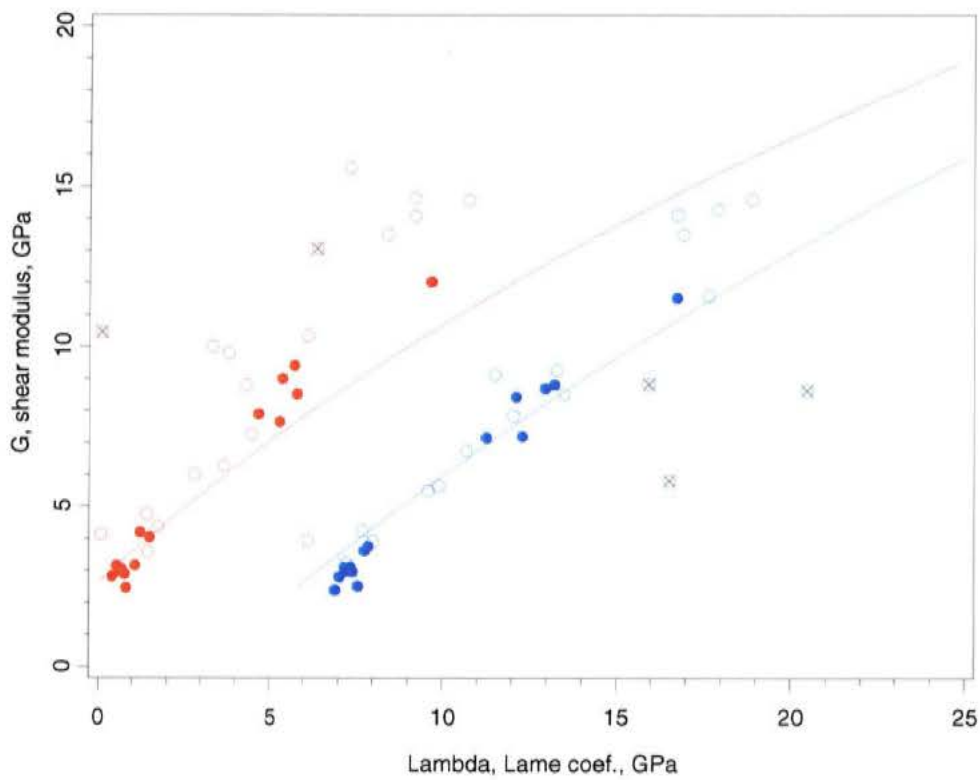

Figure 8. Shear modulus, G versus Lamé's coefficient, λ. Samples at reference conditions (Tables 1a,b). Sample B003 has λ<0 at dry conditions.

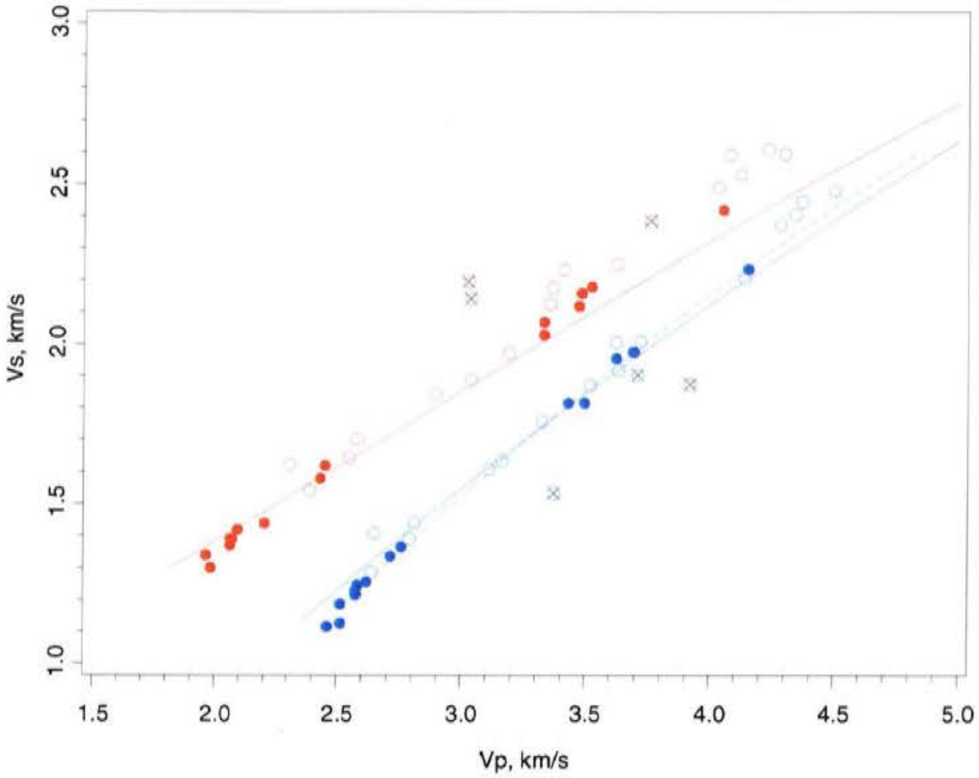

Figure 9. V_s versus V_p. Samples at reference conditions (Tables 1a,b).

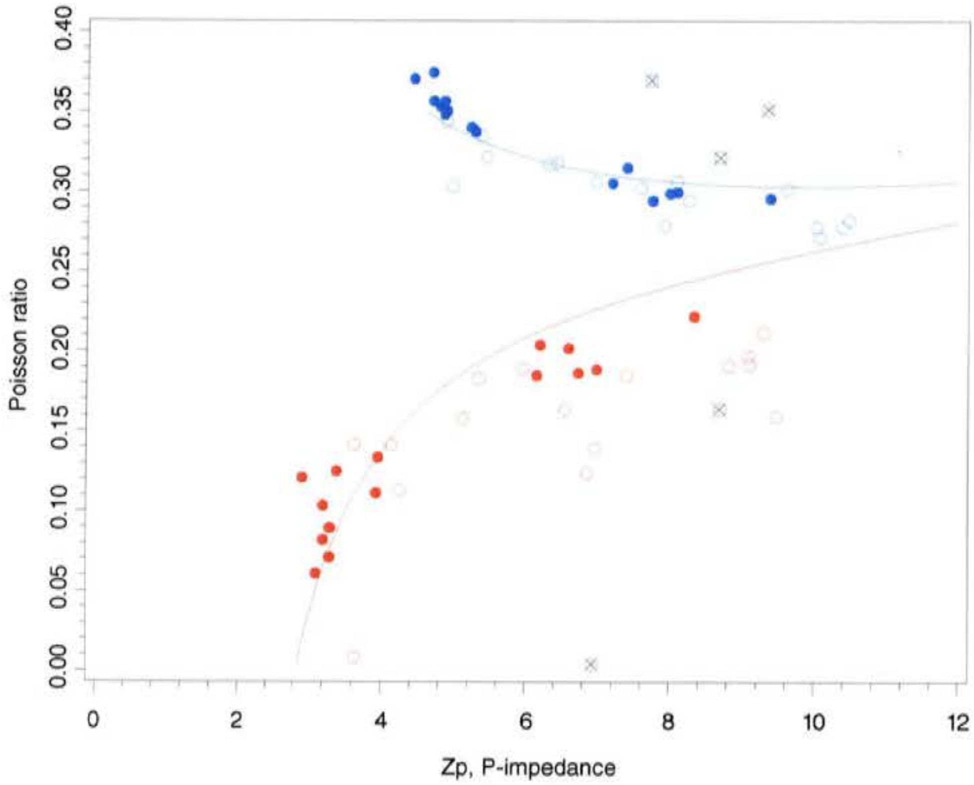

Figure 10. Possoin's ratio, ν versus P-impedance. Samples at reference conditions (Tables 1a,b). Sample B003 has λ<0 at dry conditions.

Table 1. Plug data corrected to reference conditions, sorted by plug number

Only plugs with measurement at both dry and saturated condititions.
Form: Tor = Tor Formation, Eko= Ekofisk Formation

Table 1a. Saturated samples at reference conditions, sorted by plug number

Data corrected to Sw=1 and brine at Rigs-2 reservoir conditions using Gassmann's equations and Voigt fluid mix.

Plug	Form	ϕ	V_P	V_S	V_P/V_S	ν	K	μ	M	E	λ	Z_P	Z_S
A755	Tor	0.24	4.15	2.24	1.86	0.30	24.42	11.54	39.80	29.90	16.73	9.38	5.15
A760	Tor	0.29	3.69	1.98	1.87	0.30	18.75	8.70	30.36	22.61	12.95	7.99	4.40
A761	Tor	0.31	3.57	1.86	1.92	0.31	17.91	7.59	28.04	19.96	12.85	7.62	4.08
A763	Tor	0.27	3.70	1.98	1.87	0.30	19.09	8.82	30.85	22.92	13.21	8.10	4.45
A767	Tor	0.30	3.62	1.96	1.85	0.29	17.73	8.44	28.98	21.85	12.10	7.76	4.31
A771	Tor	0.31	3.49	1.82	1.92	0.32	17.10	7.21	26.71	18.96	12.29	7.40	3.96
B003	Eko	0.14	3.37	1.53	2.20	0.37	20.42	5.82	28.18	15.95	16.54	7.73	3.79
B010	Eko	0.15	3.92	1.87	2.09	0.35	26.21	8.63	37.72	23.32	20.46	9.34	4.61
B011	Eko	0.14	3.56	1.71	2.08	0.35	21.65	7.19	31.23	19.42	16.86	8.38	4.22
B036	Eko	0.16	3.71	1.90	1.95	0.32	21.82	8.83	33.60	23.35	15.93	8.69	4.64
B054	Eko	0.19	4.14	2.21	1.88	0.30	25.37	11.59	40.82	30.18	17.64	9.62	5.25
B055	Eko	0.25	3.72	2.01	1.85	0.29	19.45	9.26	31.81	23.98	13.28	8.26	4.60
B082	Eko	0.34	3.11	1.61	1.93	0.32	13.26	5.51	20.61	14.52	9.59	6.33	3.41
B102	Eko	0.15	4.34	2.41	1.80	0.28	27.44	14.29	46.49	36.54	17.91	10.39	5.93
B122	Eko	0.28	3.52	1.87	1.88	0.30	17.26	7.85	27.73	20.46	12.02	7.59	4.18
B130	Eko	0.24	3.63	1.92	1.89	0.31	19.18	8.52	30.54	22.26	13.50	8.10	4.43
B146	Eko	0.35	3.16	1.63	1.93	0.32	13.66	5.66	21.21	14.93	9.88	6.43	3.45
B170	Eko	0.31	3.33	1.76	1.89	0.31	15.19	6.76	24.20	17.66	10.68	6.97	3.83
B196	Eko	0.19	4.28	2.37	1.80	0.28	25.92	13.50	43.92	34.52	16.92	10.03	5.68
B213	Eko	0.20	4.50	2.48	1.82	0.28	28.60	14.59	48.05	37.40	18.88	10.47	5.87
B220	Tor	0.32	3.43	1.82	1.89	0.31	16.03	7.16	25.58	18.71	11.25	7.20	3.94
B260	Tor	0.41	2.76	1.37	2.02	0.34	10.38	3.78	15.42	10.10	7.86	5.29	2.76
B264	Tor	0.40	2.71	1.34	2.03	0.34	10.18	3.64	15.04	9.76	7.76	5.23	2.72
C015	Eko	0.42	2.65	1.41	1.88	0.30	8.78	3.97	14.08	10.35	6.13	4.98	2.81
C022	Eko	0.26	3.69	2.03	1.81	0.28	18.35	9.40	30.87	24.08	12.08	8.03	4.60
C037	Eko	0.39	2.81	1.44	1.95	0.32	10.53	4.26	16.20	11.25	7.69	5.45	2.94
C062	Eko	0.40	2.79	1.39	2.01	0.34	10.63	3.94	15.88	10.51	8.00	5.38	2.82
C074	Eko	0.44	2.64	1.29	2.05	0.34	9.41	3.26	13.76	8.77	7.23	4.89	2.52
C093	Eko	0.25	3.62	2.01	1.81	0.28	17.59	9.12	29.75	23.33	11.51	7.92	4.54
C100	Eko	0.20	4.37	2.45	1.79	0.27	26.16	14.11	44.98	35.88	16.75	10.07	5.76
C121	Tor	0.42	2.58	1.25	2.07	0.35	9.25	3.11	13.40	8.40	7.17	4.86	2.49
C128	Tor	0.43	2.51	1.13	2.23	0.37	9.25	2.53	12.62	6.96	7.56	4.70	2.24
C136	Tor	0.41	2.58	1.22	2.12	0.36	9.41	2.98	13.38	8.09	7.42	4.87	2.44
C151	Tor	0.43	2.62	1.26	2.09	0.35	9.45	3.13	13.62	8.46	7.36	4.89	2.48
C200	Tor	0.45	2.46	1.12	2.21	0.37	8.51	2.41	11.73	6.61	6.91	4.44	2.15
C204	Tor	0.41	2.51	1.19	2.12	0.36	8.92	2.83	12.69	7.67	7.04	4.71	2.37
C212	Tor	0.42	2.57	1.23	2.10	0.35	9.21	2.99	13.20	8.10	7.22	4.81	2.43

Table 1b. Dry samples at reference conditions, sorted by plug number

Data corrected to Sw=0 using Gassmann's equations and Reuss fluid mix.

Plug	Form	ϕ	V_P	V_S	V_P/V_S	ν	K	μ	M	E	λ	Z_P	Z_S
A755	Tor	0.24	4.05	2.42	1.67	0.22	17.68	12.05	33.74	29.45	9.65	8.33	4.98
A759	Tor	0.27	3.59	2.15	1.67	0.22	13.32	9.15	25.52	22.34	7.21	7.11	4.26
A760	Tor	0.29	3.48	2.16	1.61	0.19	11.38	9.01	23.40	21.39	5.37	6.72	4.17
A763	Tor	0.27	3.52	2.18	1.61	0.19	12.01	9.43	24.58	22.42	5.72	6.98	4.33
A767	Tor	0.30	3.47	2.12	1.64	0.20	11.49	8.54	22.88	20.53	5.80	6.59	4.03
A771	Tor	0.31	3.33	2.03	1.64	0.20	10.41	7.67	20.64	18.47	5.30	6.20	3.78
A774	Tor	0.28	3.66	2.23	1.64	0.20	13.30	9.78	26.34	23.56	6.78	7.20	4.38
A779	Tor	0.23	3.97	2.37	1.68	0.22	17.22	11.69	32.81	28.61	9.43	8.27	4.93
A780	Tor	0.31	3.38	2.08	1.63	0.20	10.65	8.15	21.51	19.47	5.22	6.36	3.92
A782	Tor	0.28	3.68	2.25	1.64	0.20	13.35	9.95	26.62	23.92	6.72	7.23	4.42
A783	Tor	0.19	3.98	2.42	1.64	0.21	17.77	12.95	35.04	31.26	9.13	8.80	5.35
B003	Eko	0.14	3.03	2.20	1.38	-0.06	6.35	11.25	21.35	21.22	-1.15	7.07	5.13
B007	Eko	0.14	2.68	1.89	1.42	0.01	5.72	8.26	16.73	16.73	0.21	6.29	4.42
B008	Eko	0.14	3.49	2.18	1.60	0.18	13.60	11.03	28.31	26.05	6.25	8.20	5.12
B010	Eko	0.15	3.76	2.38	1.58	0.16	15.10	13.08	32.55	30.46	6.38	8.69	5.51
B012	Eko	0.15	3.57	2.27	1.58	0.16	13.71	11.93	29.61	27.74	5.76	8.33	5.29
B036	Eko	0.16	3.04	2.14	1.42	0.00	7.05	10.46	20.99	20.99	0.08	6.93	4.89
B054	Eko	0.19	4.03	2.49	1.62	0.19	17.41	13.53	35.45	32.24	8.39	8.81	5.44
B055	Eko	0.25	3.62	2.25	1.61	0.19	13.00	10.35	26.79	24.53	6.10	7.40	4.60
B082	Eko	0.34	2.89	1.84	1.57	0.16	6.81	6.03	14.86	13.97	2.79	5.14	3.27
B102	Eko	0.15	4.08	2.59	1.57	0.16	17.71	15.60	38.51	36.17	7.31	9.46	6.02
B122	Eko	0.28	3.35	2.13	1.58	0.16	10.17	8.82	21.93	20.52	4.30	6.55	4.15
B130	Eko	0.24	3.36	2.18	1.54	0.14	10.33	9.80	23.40	22.34	3.79	6.96	4.51
B146	Eko	0.35	3.04	1.89	1.61	0.18	7.84	6.30	16.24	14.91	3.65	5.35	3.33
B170	Eko	0.31	3.19	1.97	1.62	0.19	9.29	7.28	18.99	17.31	4.44	5.96	3.69
B196	Eko	0.19	4.12	2.53	1.63	0.20	18.58	14.10	37.38	33.76	9.18	9.08	5.58
B213	Eko	0.20	4.30	2.60	1.65	0.21	20.46	14.59	39.91	35.36	10.73	9.29	5.62
B216	Tor	0.14	4.30	2.60	1.65	0.21	22.23	15.86	43.38	38.44	11.66	10.09	6.10
B220	Tor	0.32	3.33	2.07	1.61	0.19	9.93	7.91	20.48	18.76	4.65	6.15	3.82
B236	Tor	0.36	3.15	2.05	1.54	0.13	7.44	7.24	17.10	16.40	2.61	5.43	3.53
B240	Tor	0.38	2.57	1.68	1.53	0.13	4.81	4.77	11.17	10.76	1.62	4.35	2.84
B244	Tor	0.38	2.86	1.81	1.58	0.17	6.46	5.55	13.86	12.95	2.76	4.85	3.07
B260	Tor	0.41	2.45	1.62	1.51	0.11	4.02	4.21	9.63	9.36	1.21	3.93	2.60
B264	Tor	0.40	2.43	1.58	1.54	0.13	4.19	4.06	9.61	9.22	1.48	3.96	2.57
B274	Tor	0.37	2.68	1.76	1.52	0.12	5.25	5.32	12.35	11.94	1.70	4.61	3.03
C015	Eko	0.42	2.31	1.62	1.42	0.01	2.84	4.15	8.38	8.37	0.07	3.64	2.56
C037	Eko	0.39	2.58	1.70	1.51	0.11	4.59	4.78	10.97	10.65	1.40	4.26	2.81
C062	Eko	0.40	2.55	1.65	1.55	0.14	4.67	4.40	10.55	10.05	1.74	4.14	2.68
C074	Eko	0.44	2.39	1.54	1.55	0.14	3.84	3.62	8.66	8.26	1.43	3.63	2.35
C093	Eko	0.25	3.41	2.23	1.53	0.12	9.99	10.03	23.36	22.54	3.31	6.86	4.49
C100	Eko	0.20	4.23	2.61	1.62	0.19	18.94	14.65	38.47	34.94	9.17	9.09	5.61
C121	Tor	0.42	2.09	1.42	1.47	0.07	2.65	3.18	6.88	6.80	0.53	3.29	2.24
C128	Tor	0.43	2.06	1.37	1.50	0.10	2.71	2.92	6.60	6.45	0.76	3.21	2.13
C136	Tor	0.41	2.07	1.39	1.49	0.09	2.72	3.07	6.82	6.70	0.67	3.29	2.21
C151	Tor	0.43	2.20	1.44	1.53	0.13	3.19	3.19	7.44	7.17	1.06	3.38	2.21
C162	Tor	0.43	2.32	1.51	1.54	0.13	3.61	3.52	8.30	7.96	1.27	3.58	2.33
C176	Tor	0.40	2.70	1.73	1.56	0.15	5.34	4.84	11.80	11.15	2.11	4.37	2.80
C200	Tor	0.45	1.98	1.30	1.52	0.12	2.45	2.49	5.77	5.58	0.80	2.91	1.91
C204	Tor	0.41	1.96	1.34	1.46	0.06	2.29	2.84	6.08	6.03	0.40	3.10	2.12
C212	Tor	0.42	2.06	1.39	1.48	0.08	2.59	3.01	6.60	6.51	0.59	3.21	2.16

Table 2. Plug data corrected to reference conditions, sorted by porosity

Only plugs with measurement at both dry and saturated conditions.
Form: Tor = Tor Formation, Eko= Ekofisk Formation

Table 2a. Saturated samples at reference conditions, sorted by porosity

Data corrected to Sw=1 and brine at Rigs-2 reservoir conditions using Gassmann's equations and Voigt fluid mix.

Plug	Form	ϕ	V_P	V_S	V_P/V_S	ν	K	μ	M	E	λ	Z_P	Z_s
B003	Eko	0.14	3.37	1.53	2.20	0.37	20.42	5.82	28.18	15.95	16.54	7.73	3.79
B011	Eko	0.14	3.56	1.71	2.08	0.35	21.65	7.19	31.23	19.42	16.86	8.38	4.22
B102	Eko	0.15	4.34	2.41	1.80	0.28	27.44	14.29	46.49	36.54	17.91	10.39	5.93
B010	Eko	0.15	3.92	1.87	2.09	0.35	26.21	8.63	37.72	23.32	20.46	9.34	4.61
B036	Eko	0.16	3.71	1.90	1.95	0.32	21.82	8.83	33.60	23.35	15.93	8.69	4.64
B196	Eko	0.19	4.28	2.37	1.80	0.28	25.92	13.50	43.92	34.52	16.92	10.03	5.68
B054	Eko	0.19	4.14	2.21	1.88	0.30	25.37	11.59	40.82	30.18	17.64	9.62	5.25
C100	Eko	0.20	4.37	2.45	1.79	0.27	26.16	14.11	44.98	35.88	16.75	10.07	5.76
B213	Eko	0.20	4.50	2.48	1.82	0.28	28.60	14.59	48.05	37.40	18.88	10.47	5.87
B130	Eko	0.24	3.63	1.92	1.89	0.31	19.18	8.52	30.54	22.26	13.50	8.10	4.43
A755	Tor	0.24	4.15	2.24	1.86	0.30	24.42	11.54	39.80	29.90	16.73	9.38	5.15
C093	Eko	0.25	3.62	2.01	1.81	0.28	17.59	9.12	29.75	23.33	11.51	7.92	4.54
B055	Eko	0.25	3.72	2.01	1.85	0.29	19.45	9.26	31.81	23.98	13.28	8.26	4.60
C022	Eko	0.26	3.69	2.03	1.81	0.28	18.35	9.40	30.87	24.08	12.08	8.03	4.60
A763	Tor	0.27	3.70	1.98	1.87	0.30	19.09	8.82	30.85	22.92	13.21	8.10	4.45
B122	Eko	0.28	3.52	1.87	1.88	0.30	17.26	7.85	27.73	20.46	12.02	7.59	4.18
A760	Tor	0.29	3.69	1.98	1.87	0.30	18.75	8.70	30.36	22.61	12.95	7.99	4.40
A767	Tor	0.30	3.62	1.96	1.85	0.29	17.73	8.44	28.98	21.85	12.10	7.76	4.31
A761	Tor	0.31	3.57	1.86	1.92	0.31	17.91	7.59	28.04	19.96	12.85	7.62	4.08
B170	Eko	0.31	3.33	1.76	1.89	0.31	15.19	6.76	24.20	17.66	10.68	6.97	3.83
A771	Tor	0.31	3.49	1.82	1.92	0.32	17.10	7.21	26.71	18.96	12.29	7.40	3.96
B220	Tor	0.32	3.43	1.82	1.89	0.31	16.03	7.16	25.58	18.71	11.25	7.20	3.94
B082	Eko	0.34	3.11	1.61	1.93	0.32	13.26	5.51	20.61	14.52	9.59	6.33	3.41
B146	Eko	0.35	3.16	1.63	1.93	0.32	13.66	5.66	21.21	14.93	9.88	6.43	3.45
C037	Eko	0.39	2.81	1.44	1.95	0.32	10.53	4.26	16.20	11.25	7.69	5.45	2.94
C062	Eko	0.40	2.79	1.39	2.01	0.34	10.63	3.94	15.88	10.51	8.00	5.38	2.82
B264	Tor	0.40	2.71	1.34	2.03	0.34	10.18	3.64	15.04	9.76	7.76	5.23	2.72
B260	Tor	0.41	2.76	1.37	2.02	0.34	10.38	3.78	15.42	10.10	7.86	5.29	2.76
C204	Tor	0.41	2.51	1.19	2.12	0.36	8.92	2.83	12.69	7.67	7.04	4.71	2.37
C136	Tor	0.41	2.58	1.22	2.12	0.36	9.41	2.98	13.38	8.09	7.42	4.87	2.44
C015	Eko	0.42	2.65	1.41	1.88	0.30	8.78	3.97	14.08	10.35	6.13	4.98	2.81
C121	Tor	0.42	2.58	1.25	2.07	0.35	9.25	3.11	13.40	8.40	7.17	4.86	2.49
C212	Tor	0.42	2.57	1.23	2.10	0.35	9.21	2.99	13.20	8.10	7.22	4.81	2.43
C128	Tor	0.43	2.51	1.13	2.23	0.37	9.25	2.53	12.62	6.96	7.56	4.70	2.24
C151	Tor	0.43	2.62	1.26	2.09	0.35	9.45	3.13	13.62	8.46	7.36	4.89	2.48
C074	Eko	0.44	2.64	1.29	2.05	0.34	9.41	3.26	13.76	8.77	7.23	4.89	2.52
C200	Tor	0.45	2.46	1.12	2.21	0.37	8.51	2.41	11.73	6.61	6.91	4.44	2.15

Table 2b. Dry samples at reference conditions, sorted by porosity

Data corrected to Sw=0 using Gassmann's equations and Reuss fluid mix.

Plug	Form	ϕ	V_P	V_S	V_P/V_S	ν	K	μ	M	E	λ	Z_P	Z_s
B003	Eko	0.14	3.03	2.20	1.38	-0.06	6.35	11.25	21.35	21.22	-1.15	7.07	5.13
B008	Eko	0.14	3.49	2.18	1.60	0.18	13.60	11.03	28.31	26.05	6.25	8.20	5.12
B007	Eko	0.14	2.68	1.89	1.42	0.01	5.72	8.26	16.73	16.73	0.21	6.29	4.42
B216	Tor	0.14	4.30	2.60	1.65	0.21	22.23	15.86	43.38	38.44	11.66	10.09	6.10
B102	Eko	0.15	4.08	2.59	1.57	0.16	17.71	15.60	38.51	36.17	7.31	9.46	6.02
B012	Eko	0.15	3.57	2.27	1.58	0.16	13.71	11.93	29.61	27.74	5.76	8.33	5.29
B010	Eko	0.15	3.76	2.38	1.58	0.16	15.10	13.08	32.55	30.46	6.38	8.69	5.51
B036	Eko	0.16	3.04	2.14	1.42	0.00	7.05	10.46	20.99	20.99	0.08	6.93	4.89
A783	Tor	0.19	3.98	2.42	1.64	0.21	17.77	12.95	35.04	31.26	9.13	8.80	5.35
B196	Eko	0.19	4.12	2.53	1.63	0.20	18.58	14.10	37.38	33.76	9.18	9.08	5.58
B054	Eko	0.19	4.03	2.49	1.62	0.19	17.41	13.53	35.45	32.24	8.39	8.81	5.44
C100	Eko	0.20	4.23	2.61	1.62	0.19	18.94	14.65	38.47	34.94	9.17	9.09	5.61
B213	Eko	0.20	4.30	2.60	1.65	0.21	20.46	14.59	39.91	35.36	10.73	9.29	5.62
A779	Tor	0.23	3.97	2.37	1.68	0.22	17.22	11.69	32.81	28.61	9.43	8.27	4.93
B130	Eko	0.24	3.36	2.18	1.54	0.14	10.33	9.80	23.40	22.34	3.79	6.96	4.51
A755	Tor	0.24	4.05	2.42	1.67	0.22	17.68	12.05	33.74	29.45	9.65	8.33	4.98
C093	Eko	0.25	3.41	2.23	1.53	0.12	9.99	10.03	23.36	22.54	3.31	6.86	4.49
B055	Eko	0.25	3.62	2.25	1.61	0.19	13.00	10.35	26.79	24.53	6.10	7.40	4.60
A763	Tor	0.27	3.52	2.18	1.61	0.19	12.01	9.43	24.58	22.42	5.72	6.98	4.33
A759	Tor	0.27	3.59	2.15	1.67	0.22	13.32	9.15	25.52	22.34	7.21	7.11	4.26
A782	Tor	0.28	3.68	2.25	1.64	0.20	13.35	9.95	26.62	23.92	6.72	7.23	4.42
A774	Tor	0.28	3.66	2.23	1.64	0.20	13.30	9.78	26.34	23.56	6.78	7.20	4.38
B122	Eko	0.28	3.35	2.13	1.58	0.16	10.17	8.82	21.93	20.52	4.30	6.55	4.15
A760	Tor	0.29	3.48	2.16	1.61	0.19	11.38	9.01	23.40	21.39	5.37	6.72	4.17
A767	Tor	0.30	3.47	2.12	1.64	0.20	11.49	8.54	22.88	20.53	5.80	6.59	4.03
A780	Tor	0.31	3.38	2.08	1.63	0.20	10.65	8.15	21.51	19.47	5.22	6.36	3.92
B170	Eko	0.31	3.19	1.97	1.62	0.19	9.29	7.28	18.99	17.31	4.44	5.96	3.69
A771	Tor	0.31	3.33	2.03	1.64	0.20	10.41	7.67	20.64	18.47	5.30	6.20	3.78
B220	Tor	0.32	3.33	2.07	1.61	0.19	9.93	7.91	20.48	18.76	4.65	6.15	3.82
B082	Eko	0.34	2.89	1.84	1.57	0.16	6.81	6.03	14.86	13.97	2.79	5.14	3.27
B146	Eko	0.35	3.04	1.89	1.61	0.18	7.84	6.30	16.24	14.91	3.65	5.35	3.33
B236	Tor	0.36	3.15	2.05	1.54	0.13	7.44	7.24	17.10	16.40	2.61	5.43	3.53
B274	Tor	0.37	2.68	1.76	1.52	0.12	5.25	5.32	12.35	11.94	1.70	4.61	3.03
B244	Tor	0.38	2.86	1.81	1.58	0.17	6.46	5.55	13.86	12.95	2.76	4.85	3.07
B240	Tor	0.38	2.57	1.68	1.53	0.13	4.81	4.77	11.17	10.76	1.62	4.35	2.84
C037	Eko	0.39	2.58	1.70	1.51	0.11	4.59	4.78	10.97	10.65	1.40	4.26	2.81
C062	Eko	0.40	2.55	1.65	1.55	0.14	4.67	4.40	10.55	10.05	1.74	4.14	2.68
B264	Tor	0.40	2.43	1.58	1.54	0.13	4.19	4.06	9.61	9.22	1.48	3.96	2.57
C176	Tor	0.40	2.70	1.73	1.56	0.15	5.34	4.84	11.80	11.15	2.11	4.37	2.80
B260	Tor	0.41	2.45	1.62	1.51	0.11	4.02	4.21	9.63	9.36	1.21	3.93	2.60
C204	Tor	0.41	1.96	1.34	1.46	0.06	2.29	2.84	6.08	6.03	0.40	3.10	2.12
C136	Tor	0.41	2.07	1.39	1.49	0.09	2.72	3.07	6.82	6.70	0.67	3.29	2.21
C015	Eko	0.42	2.31	1.62	1.42	0.01	2.84	4.15	8.38	8.37	0.07	3.64	2.56
C121	Tor	0.42	2.09	1.42	1.47	0.07	2.65	3.18	6.88	6.80	0.53	3.29	2.24
C212	Tor	0.42	2.06	1.39	1.48	0.08	2.59	3.01	6.60	6.51	0.59	3.21	2.16
C128	Tor	0.43	2.06	1.37	1.50	0.10	2.71	2.92	6.60	6.45	0.76	3.21	2.13
C162	Tor	0.43	2.32	1.51	1.54	0.13	3.61	3.52	8.30	7.96	1.27	3.58	2.33
C151	Tor	0.43	2.20	1.44	1.53	0.13	3.19	3.19	7.44	7.17	1.06	3.38	2.21
C074	Eko	0.44	2.39	1.54	1.55	0.14	3.84	3.62	8.66	8.26	1.43	3.63	2.35
C200	Tor	0.45	1.98	1.30	1.52	0.12	2.45	2.49	5.77	5.58	0.80	2.91	1.91

Table 3. Original plug data, sorted by plug number

All plug data

Form: Tor = Tor Formation, Eko= Ekofisk Formation

Table 3a. Saturated samples at original conditions, sorted by plug number

Plug	Sw	Form	ϕ	V_P	V_S	V_P/V_S	ν	K	μ	M	E	λ	Z_P	Z_S
A755	0.99	Tor	0.24	4.08	2.24	1.82	0.28	22.89	11.54	38.27	29.63	15.20	9.38	5.15
A760	1.00	Tor	0.29	3.60	1.98	1.82	0.28	17.17	8.70	28.77	22.34	11.36	7.99	4.40
A761	0.99	Tor	0.31	3.47	1.86	1.87	0.30	16.30	7.59	26.43	19.72	11.24	7.62	4.08
A763	1.00	Tor	0.27	3.60	1.98	1.82	0.28	17.39	8.82	29.15	22.63	11.51	8.10	4.45
A767	1.00	Tor	0.30	3.53	1.96	1.80	0.28	16.12	8.44	27.38	21.56	10.50	7.76	4.31
A771	1.00	Tor	0.31	3.40	1.82	1.87	0.30	15.54	7.21	25.15	18.73	10.74	7.40	3.96
B003	0.92	Eko	0.14	3.13	1.54	2.04	0.34	16.45	5.82	24.21	15.62	12.57	7.73	3.79
B010	1.03	Eko	0.15	3.79	1.87	2.03	0.34	23.92	8.63	35.42	23.10	18.17	9.34	4.61
B011	1.03	Eko	0.14	3.38	1.70	1.98	0.33	18.73	7.19	28.31	19.12	13.93	8.38	4.22
B036	1.02	Eko	0.16	3.57	1.90	1.87	0.30	19.21	8.83	30.99	22.98	13.32	8.69	4.64
B054	0.99	Eko	0.19	4.05	2.21	1.83	0.29	23.51	11.59	38.96	29.86	15.78	9.62	5.25
B055	0.98	Eko	0.25	3.62	2.02	1.80	0.28	17.54	9.26	29.89	23.63	11.36	8.26	4.60
B082	0.99	Eko	0.34	2.99	1.61	1.85	0.29	11.59	5.51	18.94	14.27	7.92	6.33	3.41
B102	0.95	Eko	0.15	4.23	2.41	1.75	0.26	24.90	14.29	43.96	35.99	15.37	10.39	5.93
B122	0.98	Eko	0.28	3.41	1.88	1.82	0.28	15.45	7.85	25.92	20.15	10.22	7.59	4.18
B130	0.97	Eko	0.24	3.52	1.92	1.83	0.29	17.14	8.52	28.50	21.92	11.46	8.10	4.43
B146	1.00	Eko	0.35	3.05	1.64	1.86	0.30	12.05	5.66	19.61	14.69	8.28	6.43	3.45
B170	0.98	Eko	0.31	3.21	1.76	1.82	0.28	13.39	6.76	22.40	17.35	8.88	6.97	3.83
B196	1.00	Eko	0.19	4.20	2.38	1.77	0.26	24.08	13.50	42.09	34.13	15.08	10.03	5.68
B213	0.98	Eko	0.20	4.44	2.49	1.78	0.27	27.03	14.59	46.48	37.09	17.30	10.47	5.87
B220	1.00	Tor	0.32	3.33	1.82	1.83	0.29	14.43	7.16	23.99	18.44	9.66	7.20	3.94
B260	1.00	Tor	0.41	2.63	1.37	1.92	0.31	8.88	3.78	13.92	9.92	6.36	5.29	2.76
B264	1.01	Tor	0.40	2.58	1.34	1.93	0.32	8.64	3.64	13.50	9.58	6.22	5.23	2.72
C015	0.99	Eko	0.42	2.51	1.41	1.77	0.27	7.17	3.97	12.47	10.06	4.53	4.98	2.81
C022	0.93	Eko	0.26	3.57	2.04	1.75	0.26	16.17	9.40	28.70	23.62	9.91	8.03	4.60
C037	0.99	Eko	0.39	2.68	1.45	1.85	0.29	8.93	4.26	14.60	11.02	6.09	5.45	2.94
C062	0.99	Eko	0.40	2.66	1.40	1.91	0.31	9.07	3.94	14.32	10.32	6.45	5.38	2.82
C074	0.98	Eko	0.44	2.51	1.29	1.94	0.32	7.90	3.26	12.25	8.60	5.73	4.89	2.52
C093	1.00	Eko	0.25	3.51	2.01	1.75	0.26	15.63	9.12	27.79	22.91	9.55	7.92	4.54
C100	0.98	Eko	0.20	4.29	2.45	1.75	0.26	24.42	14.11	43.23	35.49	15.01	10.07	5.76
C121	1.00	Tor	0.42	2.44	1.25	1.95	0.32	7.71	3.11	11.87	8.23	5.64	4.86	2.49
C128	1.00	Tor	0.43	2.37	1.13	2.10	0.35	7.76	2.53	11.13	6.85	6.07	4.70	2.24
C136	0.99	Tor	0.41	2.43	1.22	1.99	0.33	7.85	2.98	11.83	7.94	5.86	4.87	2.44
C151	0.99	Tor	0.43	2.48	1.26	1.97	0.33	7.95	3.13	12.13	8.30	5.87	4.89	2.48
C200	0.99	Tor	0.45	2.31	1.12	2.06	0.35	7.04	2.41	10.26	6.49	5.43	4.44	2.15
C204	1.00	Tor	0.41	2.36	1.19	1.98	0.33	7.34	2.83	11.11	7.51	5.46	4.71	2.37
C212	1.00	Tor	0.42	2.43	1.23	1.98	0.33	7.69	2.99	11.69	7.95	5.70	4.81	2.43

Table 3b. Dry samples at original conditions, sorted by plug number

Plug	Sw	Form	ϕ	V_P	V_S	V_P/V_S	ν	K	μ	M	E	λ	Z_P	Z_S
A755	0.00	Tor	0.24	4.05	2.42	1.67	0.22	17.68	12.05	33.74	29.45	9.65	8.33	4.98
A759	0.00	Tor	0.27	3.59	2.15	1.67	0.22	13.32	9.15	25.52	22.34	7.21	7.11	4.26
A760	0.00	Tor	0.29	3.48	2.16	1.61	0.19	11.38	9.01	23.40	21.39	5.37	6.72	4.17
A763	0.00	Tor	0.27	3.52	2.18	1.61	0.19	12.01	9.43	24.58	22.42	5.73	6.98	4.33
A767	0.00	Tor	0.30	3.47	2.12	1.64	0.20	11.49	8.54	22.88	20.53	5.80	6.59	4.03
A771	0.00	Tor	0.31	3.33	2.03	1.64	0.20	10.41	7.67	20.64	18.47	5.30	6.20	3.78
A774	0.00	Tor	0.28	3.66	2.23	1.64	0.20	13.30	9.78	26.34	23.56	6.78	7.20	4.38
A779	0.00	Tor	0.23	3.97	2.37	1.68	0.22	17.22	11.69	32.81	28.61	9.43	8.27	4.93
A780	0.00	Tor	0.31	3.38	2.08	1.63	0.20	10.65	8.15	21.51	19.47	5.22	6.36	3.92
A782	0.00	Tor	0.28	3.68	2.25	1.64	0.20	13.35	9.95	26.62	23.92	6.72	7.23	4.42
A783	0.00	Tor	0.19	3.98	2.42	1.64	0.21	17.77	12.95	35.04	31.26	9.13	8.80	5.35
B003	0.07	Eko	0.14	3.02	2.19	1.38	-0.06	6.35	11.25	21.35	21.22	-1.15	7.07	5.13
B007	0.30	Eko	0.14	2.66	1.87	1.42	0.01	5.72	8.26	16.73	16.73	0.21	6.29	4.42
B008	0.34	Eko	0.14	3.45	2.16	1.60	0.18	13.60	11.03	28.31	26.05	6.25	8.20	5.12
B010	0.12	Eko	0.15	3.75	2.38	1.58	0.16	15.10	13.08	32.55	30.46	6.38	8.69	5.51
B012	0.12	Eko	0.15	3.56	2.26	1.58	0.16	13.71	11.93	29.61	27.74	5.76	8.33	5.29
B036	0.08	Eko	0.16	3.03	2.14	1.42	0.00	7.05	10.46	20.99	20.99	0.08	6.93	4.89
B054	0.04	Eko	0.19	4.02	2.49	1.62	0.19	17.41	13.53	35.45	32.24	8.39	8.81	5.44
B055	0.02	Eko	0.25	3.62	2.25	1.61	0.19	13.00	10.35	26.79	24.53	6.10	7.40	4.60
B082	0.01	Eko	0.34	2.89	1.84	1.57	0.16	6.81	6.03	14.86	13.97	2.79	5.14	3.27
B102	0.05	Eko	0.15	4.07	2.59	1.57	0.16	17.71	15.60	38.51	36.17	7.31	9.46	6.02
B122	0.02	Eko	0.28	3.35	2.12	1.58	0.16	10.17	8.82	21.93	20.52	4.30	6.55	4.15
B130	0.02	Eko	0.24	3.36	2.18	1.54	0.14	10.33	9.80	23.40	22.34	3.79	6.96	4.51
B146	0.00	Eko	0.35	3.04	1.89	1.61	0.18	7.85	6.30	16.24	14.91	3.65	5.35	3.33
B170	0.01	Eko	0.31	3.19	1.97	1.62	0.19	9.29	7.28	18.99	17.31	4.44	5.96	3.69
B196	0.02	Eko	0.19	4.12	2.53	1.63	0.20	18.58	14.10	37.38	33.76	9.19	9.08	5.58
B213	0.01	Eko	0.20	4.30	2.60	1.65	0.21	20.46	14.59	39.91	35.36	10.73	9.29	5.62
B216	0.00	Tor	0.14	4.30	2.60	1.65	0.21	22.23	15.86	43.38	38.44	11.66	10.09	6.10
B220	0.00	Tor	0.32	3.33	2.07	1.61	0.19	9.93	7.91	20.48	18.76	4.65	6.15	3.82
B236	0.00	Tor	0.36	3.15	2.05	1.54	0.13	7.44	7.24	17.10	16.40	2.61	5.43	3.53
B240	0.00	Tor	0.38	2.57	1.68	1.53	0.13	4.81	4.77	11.17	10.76	1.62	4.35	2.84
B244	0.00	Tor	0.38	2.86	1.81	1.58	0.17	6.46	5.55	13.86	12.95	2.76	4.85	3.07
B260	0.00	Tor	0.41	2.45	1.62	1.51	0.11	4.02	4.21	9.63	9.36	1.21	3.93	2.60
B264	0.00	Tor	0.40	2.43	1.58	1.54	0.13	4.19	4.06	9.61	9.22	1.48	3.96	2.57
B274	0.00	Tor	0.37	2.68	1.76	1.52	0.12	5.25	5.32	12.35	11.94	1.70	4.61	3.03
C015	0.00	Eko	0.42	2.30	1.62	1.42	0.01	2.84	4.15	8.38	8.38	0.07	3.64	2.56
C037	0.00	Eko	0.39	2.58	1.70	1.51	0.11	4.59	4.78	10.97	10.65	1.40	4.26	2.81
C062	0.00	Eko	0.40	2.55	1.64	1.55	0.14	4.67	4.40	10.55	10.05	1.74	4.14	2.68
C074	0.00	Eko	0.44	2.39	1.54	1.55	0.14	3.84	3.62	8.66	8.26	1.43	3.63	2.35
C093	0.00	Eko	0.25	3.41	2.23	1.53	0.12	9.99	10.03	23.36	22.54	3.31	6.86	4.49
C100	0.01	Eko	0.20	4.23	2.61	1.62	0.19	18.94	14.65	38.47	34.94	9.17	9.09	5.61
C121	0.00	Tor	0.42	2.09	1.42	1.47	0.07	2.65	3.18	6.88	6.80	0.53	3.29	2.24
C128	0.00	Tor	0.43	2.06	1.37	1.50	0.10	2.71	2.92	6.60	6.45	0.76	3.21	2.13
C136	0.00	Tor	0.41	2.07	1.39	1.49	0.09	2.72	3.07	6.82	6.70	0.67	3.29	2.21
C151	0.00	Tor	0.43	2.20	1.44	1.53	0.13	3.19	3.19	7.44	7.17	1.06	3.38	2.21
C162	0.00	Tor	0.43	2.32	1.51	1.54	0.13	3.61	3.52	8.30	7.96	1.27	3.58	2.33
C176	0.00	Tor	0.40	2.70	1.73	1.56	0.15	5.34	4.84	11.80	11.15	2.11	4.37	2.80
C200	0.00	Tor	0.45	1.98	1.30	1.52	0.12	2.45	2.49	5.77	5.58	0.80	2.91	1.91
C204	0.00	Tor	0.41	1.96	1.34	1.46	0.06	2.29	2.84	6.08	6.03	0.40	3.10	2.12
C212	0.00	Tor	0.42	2.06	1.39	1.48	0.08	2.59	3.01	6.60	6.51	0.59	3.21	2.16

Table 3c. Partly saturated samples at original conditions

Plug	Sw	Form	ϕ	V_P	V_S	V_P/V_S	ν	K	μ	M	E	λ	Z_P	Z_S
C062	0.25	Eko	0.40	2.36	1.52	1.56	0.15	4.34	3.96	9.62	9.11	1.70	4.08	2.62
C062	0.50	Eko	0.40	2.30	1.47	1.56	0.15	4.41	3.95	9.69	9.14	1.78	4.20	2.69
C062	0.75	Eko	0.40	2.31	1.44	1.61	0.19	4.98	3.97	10.27	9.40	2.33	4.44	2.76
C100	0.25	Eko	0.20	4.16	2.54	1.63	0.20	19.02	14.21	37.96	34.12	9.55	9.14	5.59
C100	0.50	Eko	0.20	4.16	2.51	1.66	0.21	20.00	14.15	38.87	34.35	10.57	9.35	5.64
C100	0.75	Eko	0.20	4.19	2.48	1.69	0.23	21.65	14.11	40.47	34.78	12.25	9.65	5.70

EFP-01 ROCK PHYSICS OF IMPURE CHALK – TECHNICAL NOTE 2002/2 JANUARY

Discussion on the elastic properties of wet and dry chalk samples

Klaus Bolding Rasmussen, Ødegaard A/S
Peter Japsen, GEUS
Gary Mavko, Stanford University
kbr@oedegaard.com, pj@geus.dk, mavko@stanford.edu

Fra: Klaus Bolding Rasmussen
Sendt: 3. januar 2002 14:13

It is well known that the Gassmann theory predicts that the wet and dry shear moduli are identical in the low frequency limit. Some of you, especially Peter Japsen, have for some time asked about my arguments for that the wet shear modulus theoretical should be larger than or equal to the dry shear modulus for higher frequencies. I have to admit that I have not found a unquestionable proof in the literature, but below I have described a number of indications that support the hypothesis. Anyway, if the hypothesis is not correct then I would like to know where the mistakes are in the indications. And if the hypothesis is indeed correct then I would like an explanation of why the wet shear modulus is significant smaller the dry shear modulus for the GEUS core measurements.

Indication 1:

Any modulus quantity is defined as the ratio of some stress component to some strain component. Adding fluid to the dry rock frame and keeping the strain component unchanged requires that a larger or equal stress component is applied because now the fluid in addition to rock frame has to be moved. Consequently, any modulus quantity, including the shear modulus, has a wet value that is larger than or equal to the dry value.

Indication 2:

Biot's relation for the frequency dependent shear velocity on page 164 in RPH (The Rock Physics Handbook, 1998, Gary Mavko et. al.) can be written as
WetShearModulus = DryShearModulus / (1-FluidDensity^2/(Density*q))
The high-frequency limiting solution on page 162 in RPH can be written as
WetShearModulus = DryShearModulus / (1-porosity*FluidDensity/(Density*alpha))
The definitions of the constants q and alpha are given in RPH, but it should be remarked that 1/q is zero for zero frequency or zero porosity. For all frequencies, the wet shear modulus is consequently larger than or equal to the dry shear modulus.

Indication 3:
The squirt or local flow model, see Section 6.7 and 6.8 in RPH, predicts that the change in the shear modulus has the same sign as the change in the so-called "wet frame bulk modulus", see the equations with 4/15 on page 185 and 188 in RPH. It follows from the other equations in RPH that the "wet frame bulk modulus" has a wet value that is larger than or equal to the dry value. Consequently, the wet shear modulus is larger than or equal to the dry shear modulus. They are only equal for zero porosity.

Indication 4:
The wet and dry shear moduli are identical at zero frequency according to Gassmann. The difference between the two shear moduli can at all other frequencies be found using Kramers-Kronig, see Section 3.7 in RPH. The wet shear modulus is larger than or equal to the dry shear modulus because the (shear) attenuation for all frequencies is larger in the wet case than in the dry case due to the viscous movement between the fluid and the rock frame.

In order to illustrate the potential problem with the GEUS shear core measurements I have attached a plot representing the 18 DAN plugs that have had performed both wet and dry measurements. It shows the difference in travel time in the wet case as predicted by Gassmann and as measured. A value of zero corresponds to identical dry and wet measured shear modulus, a positive value corresponds to a larger wet than dry measured shear modulus, and a negative value corresponds to a larger dry than wet measured shear modulus. It is seen that only a single plug (no. 2) has a positive value. Does anybody know if that plug is special in any way ? The other plugs all take negative values in the order of magnitude of -1us corresponding to approximately a half period of the ultrasonic pulse. By the way, the EFP-98 measurements show a similar behaviour. It is consequently much more than what can be explained by the inaccuracy by arrival picking, being manual or automatic. Neither does the explanation seem to be the porosity and grain density measurements as they both seem to be very accurate and trustworthy. My best explanation so far is that the saturation of the plugs introduces some extra system delay time for shear waves of at least 1us as compared to the dry case. That would also explain why the problem did not occur for the reference plugs. So that is the background for why I proposed Christian Høier to determine the system delay time for shear waves by using a wet porous material cut in different lengths.

Any comments on the above text would be appreciated. I really consider this to be very important with respect to the trustworthiness of the shear measurements because 1us error in the system delay time corresponds to approximately 10% error in the velocities !
Regards, Klaus

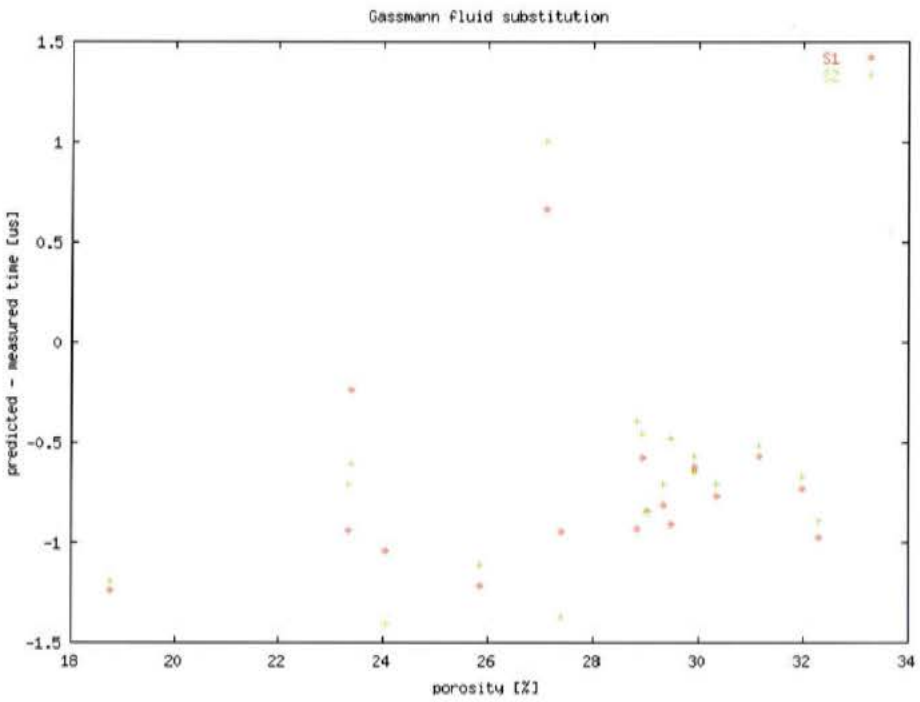

Figure 1. Plot of data for 18 DAN plugs with both wet and dry ultrasonic data. The difference in travel time in the wet case as predicted by Gassmann and as measured. A value of zero corresponds to identical dry and wet measured shear modulus, a positive value corresponds to a larger wet than dry measured shear modulus, and a negative value corresponds to a larger dry than wet measured shear modulus. It is seen that only a single plug (no. 2) has a positive value.

From: pj@geus.dk
Date: Sun, 6 Jan 2002 14:41:34

Hi Klaus and everybody else
Thank you for your response on the differences of moduli of dry and wet chalk samples.
It is certainly worth discussion that the core measurements generally

- give a higher shear modulus for dry than for wet samples (whereas Gassmann predict these moduli to be identical).
- give a relatively higher bulk modulus for dry than for wet samples (the wet-dry difference is less than gassmann prediction)
- that these effects are most pronounced for samples with moderate porosities (20-30%),
- whereas samples high porosities give results corresponding to Gassmann prediction.
- for the samples with moderate porosity these effects are more pronounced for samples from the Dan field than from the SA field.

Take Dan sample M003 (phi=23%) as an example

	Vp	Vs	K	G		
dry	3,39	2,12	11,37	9,35	data	
wet	3,52	1,89	17,59	8,29	data	
data:d-w	-0,13	0,23	-6,21	1,06	data	dry - wet
Gass:d-w	-0,26	0,10	-6,58	0	Gassm., dry-wet(predicted from dry)	
Deviation	-0,13	-0,12	-0,36	-1,06		

What we see is that both K and G are less for the wet sample than predicted by Gassmann (from dry data) (last two numbers in the table: -0,36 and -1,06). Without fully understanding your four 'indications' based on RPH, I agree that it seems unlikely that removal of water should make the sample stiffer, but what about looking at it the other way round: that adding water to the dry sample makes the framework softer (both K and G).
Like this we would have two effects:

- the pure substitution of fluids from the pore volume (surrounded by passive frame)
- a change of the grain contacts due to the presence of water.

This might even explain why the deviation from Gassmann theory is stronger for moderate porosities. Comments are more than welcome, Peter

PS. Regarding the outlying values for Dan sample M002, Christian and I judged the shear wave measurements for the wet sample to be too uncertain (it was not included in the final EFP-98 report).

Fra: Klaus Bolding Rasmussen
Sendt: 8. januar 2002 14:57

Hi, I do not see any significant dependence on porosity in the plot I attached to my email dated 3 Jan 2002. The samples with high porosity do NOT give results corresponding Gassmann prediction (constant shear modulus). I have attached a similar plot for the re-analysed (i.e. picked with the new auto picker and approved by Christian Hoeier) SA data, and it shows the SA data, including the high porosity data (>40%), do not have constant shear modulus. My conclusion is still that there is a problem somewhere in the data, for all porosities and for both the DAN and the SA field !

In the lack of a better explanation I have previously proposed that the reason could be some extra system delay time for shear waves in the wet case as compared to the dry case. The physical reason for this could be a tiny fluid layer between the plug and the transducers. I admit that it seems as a highly unlikely explanation because of the high pressure of
75Bar. I have therefore also now abandoned that explanation for the one below which makes a lot more sense. THIS MEANS THAT THE PROPOSED DETERMINATION OF THE SYSTEM DELAY TIME FOR A POROUS WET SAMPLE COULD BE IRRELEVANT.

The problems can be explained by that the dry samples were TOO DRY, see RPH page 169 and 203. I understand that care have been taken to avoid this problem, but I am afraid

the precautions has not been sufficient, at least not with respect to the shear measurements. The velocity drop can be estimated as the difference between the measured dry rock velocities and the Gassmann predicted dry rock velocities. The plot for the 18 DAN plugs using the mineral (tiny porosity) values Vp=6300m/s and Vs=3400m/s is attached. This means that both the P and the S measured dry rock velocities are in the order of magnitude 100 m/s too large ! THAT IS MUCH MORE SEVERE WITH RESPECT TO PREDICTING SEISMIC PROPERTIES THAN THE INACCURACY DUE TO ARRIVAL PICKING ! One way around the problem could be to make measurements at varying saturations as explained in RPH page 203.
Regards, Klaus

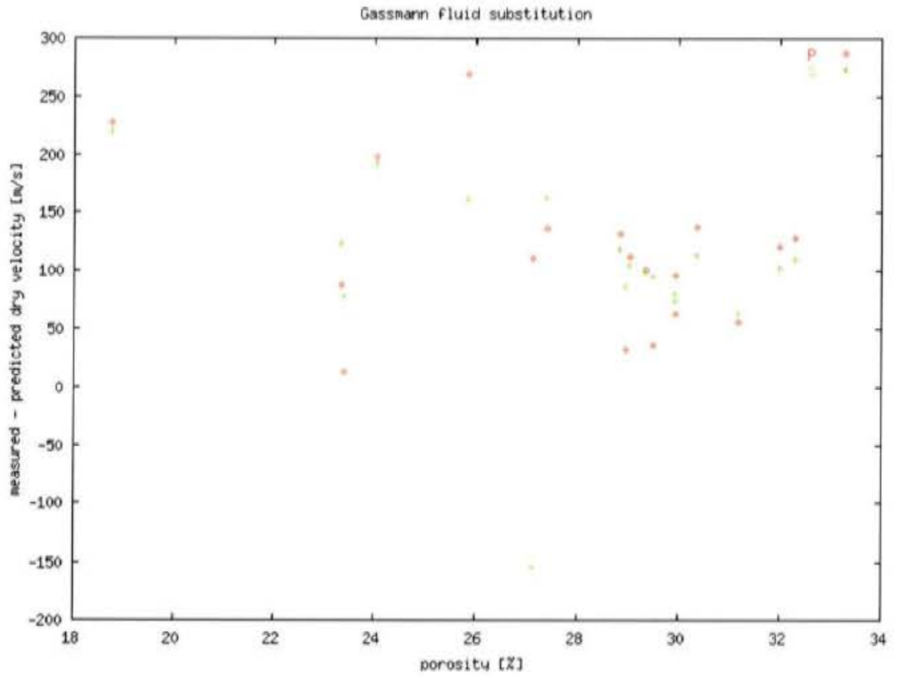

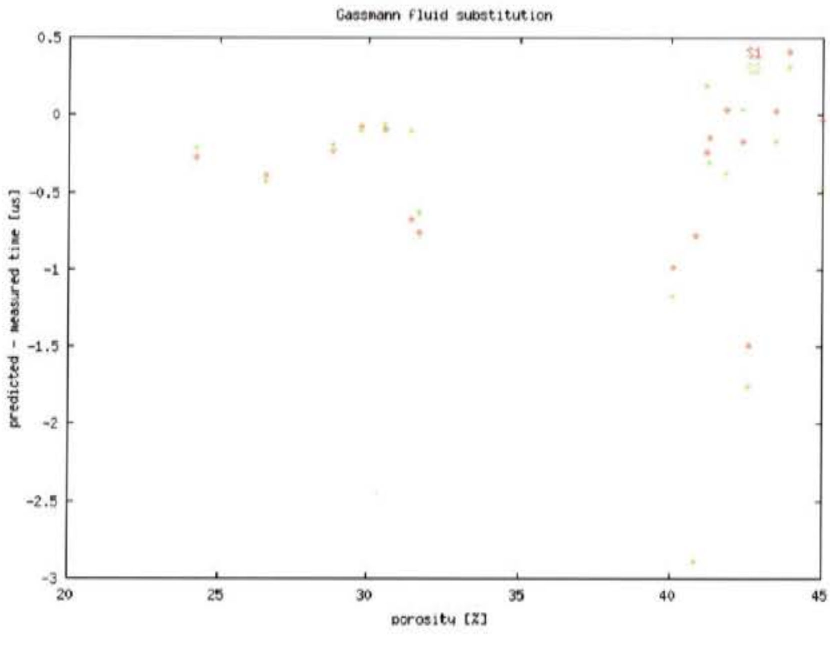

Fra: pj@geus.dk
Sendt: Tue, 8 Jan 2002

Hej Klaus, Tak for din respons - som jeg endnu ikke har set ordentligt igennem. For at gøre vores sammenligninger nemmere kunne du så ikke lave et plot med error=measured - predicted for K og G. Jeg tror problemet er størst i det domæne. - og så synes jeg da der er et porøsitetstrend i dit andet plot.
mvh Peter

Fra: Klaus Bolding Rasmussen
Sendt: 8. januar 2002 16:17

Hej Peter, Der er 2 grunde til, at jeg i første omgang lavede sammenligningen i løbetidsdomænet:

1) Formodningen var på forhånd, at den største usikkerhedsfaktor var picking af løbetider. Det var faktisk en af årsagerne til, at jeg lavede picker programmet ! Ved at teste Gassmann i løbetidsdomænet ses umiddelbart, at usikkerheden i pickingen ikke kan forklare uoverensstemmelsen i Gassmann.
2) Den næste forklaring for uoverensstemmelsen i Gassmann var den eventuelt ekstra dødtid for det våde tilfælde. Det tror jeg nok ikke rigtig på mere, men jeg kan forstå, at Christian Høier er lige på trapperne med nogle målinger, der kan afklare dette emne. Dette emne ville også være mest simpel at analyse i løbetidsdomænet. Problemet med at lave sammenligningen i modulus domænet er, at man ikke umiddelbart har nogen ide om, hvor stor en afvigelse man kan forvente. Hvad er en stor og hvad er en lille afvigelse i modulus domænet ? I øvrigt er grunden til, at jeg i første omgang koncentrerede mig om shear modulusdelen af Gassmann, at den er meget simplere end bulk modulus delen, hvor P og S hastigheder bliver sammenblandet, og hvor diskuterbare mineral hastigheder skal vælges. Bare for at eksemplificere problemet kan jeg nævne, at hvis du i dit M003 eksempel havde valgt 10% lavere mineral hastigheder, så havde din konklusion mht. bulk modulus været lige omvendt !

Grunden til at jeg derefter lavede sammenligningen i "dry rock velocity" domænet er, at det er hensigtsmæssigt til at undersøge hypotesen om "velocity drop".

Med hensyn til problemets størrelse skal det altid ses i forhold til, hvad data skal bruges til. Det seismiske bølgefelt er primært relateret til de seismiske hastigheder, ikke diverse modulus, og i den forbindelse er 100 m/s i potentiel fejl ikke uvæsentlig !

Der er selvfølgelig altid en trend i nogle givne data, bare man gør signifikansniveauet tilstrækkelig lille. Det væsentlige er imidlertid, at intet i data tyder på, at Gassmann bliver opfyldt for store porøsiteter.
Med venlig hilsen, Klaus

Fra: pj@geus.dk:
Sendt: Tue, 8 Jan 2002

hej igen - det er en fin diskussion det her! Det er en god pointe at valget at matrix-egenskaber spiller ind.

Men jeg vil gerne fastholde at det mest fornuftige domæne at sammenligne substitutions-effekten i er moduli: det er jo på den måde Gassmann er defineret på. Og jo, Gassmann predikterer ændringen i moduli meget fint for høje porøsiteter (men her er den absolutte størrelse af moduli på forhånd lav).
mvh, Peter

Fra: Klaus Bolding Rasmussen
Sendt: 8. januar 2002 17:51

Hej Peter, Jeg vil først lige protestere over dit brug af ordet "defineret". Gassmann er ikke "defineret", men udledt eller bevist om man vil. Desuden kan Gassmann formuleres på en række ligeværdige måder eller domæner om man vil. En række eksempler er givet i RHP side 168-177. En formulering er som (bulk modulus forhold) - (shear modulus) (side 168). Der findes faktisk også en hastigheds form (side 172). Desuden kunne man lave et vilkårlig antal af andre ligeværdige formuleringer. Så dit valg af argumentation måde kunne lige så vel tale for et vilkårlig andet domæne for sammenligning. Absurd !

Jeg tror allerede, at jeg har forklaret problemerne i at sammenligne i moduli i det aktuelle tilfælde, men for kort at opsummere. Når du siger, at de opserverede forskelle i shear modulus er "meget fint" for høje porøsiteter, så har du overhovedet ikke set det i forhold den forskel, der kan forklares vha. f.eks. usikkerheden i pickingen. Med andre ord hvad er din begrundelse for at kalde det "meget fint" ? Som vist i det sidste af mine plots, så dækker dine ord "meget fint" altså over en fejl i tør Vp og Vs af størrelsesordnen 100 m/s. Det er netop en fejl i den størrelsesorden, der opserveres i figuren på side 203 i RPH, og som de i RPH nævnte forskere overhovedet ikke har kunnet acceptere.
Med venlig hilsen, Klaus

Fra: Gary Mavko
Sendt: 10. januar 2002 23:43

I agree with everyone!

I think the reasoning by Klaus is theoretically correct. I also do not see any way that elastic models such as KT, Gassmann, or Biot can predict the shear modulus getting stiffer when dry. Nevertheless, we fairly often observe a lower water saturated shear modulus than dry shear modulus in laboratory measurements.

There are at least two explanations:

1. Measurement uncertainties. Picking shear arrivals is often difficult. One of the things we have seen here is the following: Shear transducers always generate a P-wave which arrives before the S-wave. In dry rocks, the P-wave is sometimes more attenuated. When

the rock is saturated, the P-arrival can be stronger, making accurate picking of the S more difficult.

2. Incompleteness of the models. John W. Tukey, one of the inventors of the FFT, once said that "All models are wrong; but some are useful." Virtually all of the rock physics models that we use are based on two very severe assumptions: linear elasticity and only mechanical effects. There is strong experimental evidence that additional effects are present that are not being modeled. For example, when water is added to a rock, some minerals soften or swell. The most common is clay that swells, which can look a little bit like an increase in pore pressure. A related observation is that very dry rocks are usually elastically stiffer than a rocks exposed to humidity. A number of people have modeled this with electrostatic and surface Van Der Waals forces.

In summary, I think we can have a nice discussion/debate on the topic when we get together. Gary

Fra: Klaus Bolding Rasmussen
Sendt: 11. januar 2002 10:49

Hi Gary, Thank you for answering.

1. As already explained in my previous email the deviations from Gassmann are systematic and in the order of magnitude of one half period of the ultrasound pulse. Therefore, I do no think that measurement uncertainties due to interference from the P-arrival can be the main explanation.
2. I do not know, if you have read my last email dated Tue, 8 Jan 2002 ! But in that email, I argue that the deviations seem to be due to the very dry problem that you also mentioned. Fortunately, Christian Hoeier is just about to finish some measurements on two plugs at varying saturation, such that this hypothesis can be examined.

See you in Copenhagen, Klaus

Analysis of acoustic well log data from the South Arne field

Peter Japsen & Rasmus Rasmussen, Geological Survey of Denmark and Greenland (GEUS)
pj@geus.dk, rr@geus.dk

Fluid substitution based on Gassmann theory has been performed on log data from 4 wells on the South Arne field (Rigs-1, -2, -2a, and SA-1). It is found that the sonic logs reflect conditions that are more affected by invasion of mud filtrate than indicated by the available resistively tools but not affected by complete invasion as the zone registered by the density tool. Furthermore, it is suggested that the MUHS model of Walls et al. (1998) can be used to estimate the bulk and shear moduli of chalk in the South Arne area for given brine properties. Invasion of mud filtrate is found to be almost complete in reservoir sections with porosity above 40%

Deviations between the shear modulus estimated from the data and from the MUHS model correlate with porosity and water saturation, Sw, when the chalk is water-wet and the water saturation irreducible: in the SA-1, Rigs-2. -2a wells but not in the Rigs-1 well where the drilled chalk section is relatively close to the free water level. Sw can thus be used as a measure of the clay content in the chalk when it is well above the free water level (see Fabricius *et al.* 2002).

For a full discussion see Japsen et al. (this report).

Data and parameters

Well log data from the South Arne field were quality controlled and porosity, water saturation, shale volume, and density of virgin zone were estimated for the drilled chalk sections (Mogensen & Fabricius 2002). Fluid substitution procedure based on Gassmann theory is presented here for the wells where shear-wave log data are available (Rigs-1, -2, -2a, and SA-1). Furthermore, the wells Baron-2 and I-1x were analyzed by Mogensen and Fabricius (2002), but as no shear-wave data were recorded in these wells a standard fluid substitution procedure can not be applied. The sonic data from the Rigs-2a well do not appear to be well edited as the resulting Vp/Vs log is noisy, but the general trend of the data is in agreement with data from the other wells.

Porosity, ϕ, was estimated from log-readings of the bulk density, ρ_{bulk}, assuming full invasion of the mud filtrate and thus we converted density to porosity based on mud filtrate densities rather than of mixtures of brine and hydrocarbons. These estimates of porosity were found to match porosity measured on core samples from the Rigs-1 and -2 wells. The effect on density of ignoring residual oil for e.g. Sw=0.1 is marginal (c. 0.02 g/cm^3 for ϕ = 40% and a density contrast between brine and oil of 0.4 g/cm^3).

Gommesen et al. (2002) found that the sonic tool measures the acoustic properties chalk in the mud-invaded zone close to the well bore, rather than the virgin zone saturated with a mixture of brine and hydrocarbon. The water saturation in the invaded zone, S_{x0}, was estimated by Mogensen & Fabricius 2002 based on the shallow resistivity log available. However, this tool does not appear to measure the water saturation in the fully invaded zone. See below. Furthermore, a range of water saturations (Swmin, Swbest and Swmax) were estimated for the univaded zone from a range of pore water resistivity values. The calculations resulted in some values of Sw exceeding 1, an effect probably due to water bound in clay. Here we put Sw =1.

Shale volume was calculated from the gamma log based on a calibration to the measured gamma ray level in the sealing shale sequence relative to the purest chalk interval in each well. However, the relation between the gamma response and the clay content in the chalk may be rather arbitrary and the presence of e.g. smectite and silica are not recorded by the gamma log.

Density, ρ, of chalk for a given water saturation was calculated as a function porosity:

$$\rho = \rho_{oil}(1-S_w)\phi + \rho_{brine} \cdot S_w \cdot \phi + \rho_{matrix}(1-\phi)$$

for the density of oil, brine and chalk matrix in the reservoir of the South Arne field (Table 1).

Table 1. Elastic properties

a. reference values	K [GPa]	G [GPa]	ρ [g/cm³]
Calcite	71	30	2.71
Clay	25	9	2.70
Quartz	37	45	2.65
Brine	2.96**	0	1.035*
Hydrocarbon	0.52**	0	0.633*

b. individual wells	K [GPa]	G [GPa]	ρ [g/cm³]
Brine, SA-1	2.91	0	1.035
Brine, Rigs-1	3.12	0	1.061
Brine, Rigs-2	2.96	0	1.035

Mineral properties after Mavko et al. (1998).

* Densities estimated at reservoir level at the South Arne field (Jensenius pers.comm. cited in Mogensen & Fabricius 2002.

** Values for fluids at the crest of the South Arne field estimated with Batzle-Wang algorithm in PetroTools: T=100°, P=44 Mpa,

Oil gravity=33 API, Gas gravity=0.815 (Alister Colby pers.comm.)

GOR=1685 scf/BBL in order to match the hydrocarbon density.

[GOR=1400 (Jensenius pers.comm.) gives ρ= 0.657 g/cm³, K=0.58 GPa, Vp=0.94 km/s]

Fluid substitution using Gassmann's equations

The bulk and the shear moduli, *K* and *G* [GPa], of a rock are related to Vp and Vs [km/s] and density [g/cm³] by the following expressions:

$$K = \rho(V_p^2 - 4/3 \cdot V_s^2),\ G = \rho V_s^2 .$$

We can transform the moduli of the rock for the initial fluid saturation (fluid 1) to moduli of the rock saturated with a new fluid (fluid 2) using Gassmann's (1951) relations (see Mavko *et al.* 1998):

$$K_{\text{sat}2} = K_{\text{m}} \cdot A/(1+A), \quad G_{\text{sat}1} = G_{\text{sat}2} \quad \text{where}$$

$$A = \frac{K_{\text{sat}1}}{(K_{\text{m}} - K_{\text{sat}1})} - \frac{K_{\text{fl}1}}{\phi(K_{\text{m}} - K_{\text{fl}1})} + \frac{K_{\text{fl}2}}{\phi(K_{\text{m}} - K_{\text{fl}2})} \quad (1)$$

K_{sat1}, K_{sat2} are the bulk modulus of rock with the original and new pore fluid; K_m is the bulk modulus of mineral material making up rock; K_{fl1}, K_{fl2} are the bulk modulus of the original and the new pore fluid; G_{sat1}, G_{sat2} are the shear modulus of rock with the original and the new pore fluid. In particular we see that the shear modulus is predicted to be unaffected by fluid content. Gassmann's equtions are establihsed for homogenous mineral modulus and statistical isotropy. The equations are valid at sufficiently low frequencies such that the pore pressures induced by the sonic wave are equilibrated throughout the pore space. We apply

Gassmann's relations to calculate the effects on the acoustic properties of chalk estimated from logging data when one pore fluid is substituted by another.

Properties of mixed fluids

We calculate the bulk modulus, K_{fl}, of mixtures of fluids, $K_{fl\,1}$, $K_{fl\,2}$ (brine/hydrocarbons or brine/air) as a Reuss average if the fluids form a homogenous mixture:

$$1/K_{fl} = S_{fl1}/K_{fl1} + (1 - S_{fl1})/K_{fl2} \tag{2}$$

where $S_{fl\,1}$ is the relative saturation of fluid 1 (e.g. brine, S_w). Even small amounts of the light component (e.g. hydrocarbon or air) reduce the bulk modulus of the mixed fluid significantly because the average modulus is calculated from the inverse values of the individual moduli.

Modified upper Hashin-Shtrikman (MUHS) model

Walls et al. (1998) found that a modified upper Hashin-Shtrikman model predicts the velocity-porosity behaviour of chalk estimated from well logs from the Ekofisk field (porosities from 10% to 40%). The model describes how the dry bulk and shear moduli, K and G increase as porosity is reduced from a maximum value, ϕ_{max}, to zero porosity. The upper and lower Hashin-Shtrikman bounds give the narrowest possible range on the modulus of a mixture of grains and pores without specifying anything about the geometries of the constituents (Hashin & Shtrikman 1963). The upper bound represents the stiffest possible pore shapes for porosity ranging from 0% to 100%, whereas the modified upper bound is defined for porosity up to a maximum value less than 100%. Here we refer the high-porosity end member as the maximum porosity rather than as the critical porosity which is defined as the porosity limit above which a sedimentary rock can only exist as a suspension (Nur *et al.* 1998). The low-porosity end-members, K_s and G_s, are the moduli of the solid at zero porosity found by extrapolation of the data trend at non-zero porosities. The modified upper Hashin-Shtrikman model, MUHS, is given by the dry-rock bulk and shear modulus, K^{MUHS} and G^{MUHS}:

$$\begin{aligned} K^{MUHS} &= \left[\frac{\phi/\phi_{max}}{K_{\phi max} + \frac{4}{3}G_s} + \frac{1-\phi/\phi_{max}}{K_s + \frac{4}{3}G_s} \right]^{-1} - \tfrac{4}{3}G_s \\ G^{MUHS} &= \left[\frac{\phi/\phi_{max}}{G_{\phi max} + Z_s} + \frac{1-\phi/\phi_{max}}{G_s + Z_s} \right]^{-1} - Z_s, \quad \text{where } Z_s = \frac{G_s}{6} \cdot \frac{9K_s + 8G_s}{K_s + 2G_s} \end{aligned} \tag{3}$$

The end-member moduli of the dry rock found by Walls et al. (1998) were

$$\begin{aligned} &K_{\phi max} = 4 \text{ GPa}, \ G_{\phi max}\ 4 \text{ GPa for } \phi_{max} = 40\%, \text{ and} \\ &K_s{=}65 \text{ GPa and } G_s{=}27 \text{ GPa for } \phi = 0\% \end{aligned} \tag{4}$$

Once these end-member parameters are estimated we can calculate the moduli of the dry rock from the MUHS model and given porosity and estimate moduli for the saturated rock using Gassmann's relations and the appropriate fluid properties, and finally calculate V_P and V_S.

Extended MUHS model based on ultrasonic V-ϕ data

Ultrasonic data from core samples from the South Arne field are in good agreement with the model of Walls et al. (1998), which is defined for porosities less than 40%. However, chalk porosities between 40% and 45% occur on the South Arne field as estimated from both log data and core samples (see Japsen et al. this report). For this reason we extrapolated the range of the MUHS model from 40% to 45% by estimating the high-porosity end-member at 45% porosity while keeping the low-porosity end-member unchanged (equations 3, 4):

$$K_{\phi max} = 1.5 \text{ GPa}, \mu_{\phi max} = 2.5 \text{ GPa for } \phi_{max} = 45\% \quad (5)$$

This extrapolated model is in agreement with the acoustic properties of the south Arne plug samples with porosities between 40% and 45%.

Virgin zone properties estimated from sonic data and Land's equation for residual oil

The water saturation of the flushed zone, Sxo (equivalent to the residual oil content) may be estimated from Land's formula (Land 1968):

$$S_{xo} = 1 - \frac{1 - S_{wir}}{1 + C(1 - S_{wir})} \quad (6)$$

where Sir is the irreducible water saturation and C=2.5 for the South Arne field (Flemming Iff, pers. comm.). We can calculate S_{wir} from the normalised capillary pressure curve method developed for the tight chalk in the North Sea (the equivalent radius method, EQR; Engstrøm 1995):

$$S_{wir} = \left(\frac{A}{\phi}\right)^B$$

where A and B are constants. We compute Sxo for the Rigs-2 well based on these two equations where we distinguish between the Ekofisk and Tor formations where Swir is higher for the Ekofisk Formation; A=0.12641, B=2.45422 (Ekofisk Fm) and A=0.06596, B=2.19565 (Tor Fm) (P. Frykman, pers. comm.). In the case of the Rigs-2 well Swir≈Sw because the drilled chalk section is above the oil-water transition zone and the water saturation in the virgin zone thus represents the irreducible water saturation. However, the increase in Sw over the lower 10 m of the Tor Formation may reflect the transition to the water zone. Based on this estimate of Sxo we can do fluid substitution to any saturation using Gassmann's relations and Reuss fluid mixing law (eqs 1, 2).

Virgin zone properties estimated from the MUHS model with ϕ and Sw as input

Forward modeling may be used to calculate the acoustic response corresponding to the measured porosity and the water saturation, Sw, in the virgin zone. The modeling is done in three steps where step 2 may be included to correct the moduli of the most shaley intervals:

1. Calculate the properties of the dry rock from the MUHS model with the porosity log as input (eq. 5).
2. Correct the moduli in the intervals with impure chalk as estimated by Sw by scaling the low-porosity end-member of the MUHS model (see below; eq. 7).
3. Calculate the properties of the virgin zone where the water saturation is given by Sw using Gassmann's relations and the Reuss mixing law (eqs 1, 2).

Corrected MUHS model

In order to correct the MUHS model (eq. 5) for the effect of clay-softening we have chosen a simplistic approach: We have scaled the low-porosity end-members, M_s, of the MUHS model (eq. 4) by the 'clay' content, cl, taken as cl = Sw – 0.2 (see Japsen et al. this report). Note that this approach only will be valid if the chalk is well above the free water level. For a given value of Sw, we calculated M_s as a kind of Hill average by computing the arithmetic average of the upper and lower Hashin-Shtrikman bounds, HS_U and HS_L (see Mavko et al., 1998):

$$M_s = (HS_U + HS_L)/2 \tag{7}$$

where the bounds are calculated as a mixture defined by cl between the 'no-clay' end-member moduli for pure chalk given by Walls et al. (1998): M_{chalk}=(65 GPa, 27 GPa) and the end-member moduli for pure 'clay' equals those for clay given by Table 1: M_{clay}=(25 GPa, 9 GPa). This procedure effectively scales M_s between M_{chalk} for Sw<0.2 and (30 GPa, 11 GPa) for Sw=1. The correction reduces the too high predictions of G to match the data values in the low-porosity zones where Sw reaches maximum values.

Water saturation estimated from sonic data

The bulk modulus, K_{sat}, of the flushed zone is known from the sonic data whereas the dry-rock modulus, K_{dry}, of the chalk can be estimated from the corrected MUHS model (eq. 7). To avoid erroneous Vs-data we use Vs from the corrected MUHS model to compute K_{sat} for ϕ>40%. We can thus rearrange Gassmann's relations expressed in terms of K_{sat} and K_{dry} to give us the effective bulk modulus, k_{fl}, of the pore fluid in the flushed zone (eq. 1; see Mavko et al. 1998):

$$k_{fl} = \phi K_m \frac{A-B}{1+\phi(A-B)}, \text{ where } A = \frac{K_{sat}}{K_m - K_{sat}}, B = \frac{K_{dry}}{K_m - K_{dry}}$$

Substituting this result into the Reuss equation for fine-scaled fluid mixing in the reservoir (eq. 2), we get the saturation of the flushed zone, Sxo:

$$S_{xo} = \frac{k_{brine}(k_{oil} - k_{fl})}{k_{fl}(k_{oil} - k_{brine})} \tag{8}$$

where k_{oil} and k_{brine} are the bulk moduli of the oil and the brine of the reservoir (Table 1). Only values of Sxo in the interval from 0 to 1 are valid.

Results

- SA-1 (Figs 1–4, 17): The depth-wise pattern of the Poisson ratio is generally found to be the same for both the MUHS and the Land method (Fig. 4). This is because

the Land-prediction of Sw works when the porosity is moderate (<35%) (and because the MUHS-model works as well). There is almost no distinction between Vp in the flushed and in the virgin zone, a distinction is only seen in the plot of Poisson ratio. But the results show that an increase of Sw from 20% to 75% due to invasion is compatible with sonic data because even quite large deviations from Sw=0% creates very small changes in the acoustic properties due to the fine-scaled Reuss-mixing.
There is generally good agreement between the corrected MUHS- and the data-estimate of G (Fig. 3). In the uppermost part of the logged section there is a major discrepancy, but the data quality is dubious. The deviation, ΔG, correlate with porosity and Sw, but hardly with the clay content estimated from the gamma log (Fig. 17).

- Rigs-1 (Figs 5–8, 18): In this well, the drilled chalk section is too close to the free water level for the corrected MUHS model to be applicable. The water saturation is high (generally more than 50% in the Ekofisk Formation) but this is inaccordance with the EQR model for the porosities in this well (Ole Vejbæk, pers. comm.). This results in a major deviation in the Ekofisk Formation between the corrected MUHS- and the data-estimate of G (Fig. 7). The large scatter in the plot of ΔG versus Sw for high values of Sw underlines that the correction to the MUHS model leads to overcorrection. The estimation of Poisson's ratio is, however, less affected by the correction that is applied to both K and G, and hence to both Vp and Vs (Fig. 8). Land's model underestimate the invasion in the Tor Formation and thus overestimate the Poisson ratio. No correlation between ΔG and clay content as estimated by the gamma log (Fig. 18).

- Rigs-2 (Figs 9–12, 19): This data set is discussed in detail in Japsen et al. (in prep.), but the main result is that Land's equation underestimates the invasion in the high-porosity sections and thus overestimates the Poisson ratio in reservoir. Only the corrected MUHS model predicts low values of the Poisson ratio in agreement with the AVO-inversion (Fig. 12).
Deviations between the corrected MUHS- and the data-estimate of G correlates with porosity and Sw (Fig. 19). Sw can be taken as a measure of the clay content in this well because the chalk is water-wet and the water saturation irreducible. No correlation between ΔG and clay content as estimated by the gamma log.

- Rigs-2a (Figs 13–16, 20): The quality of the logs of Vp and Vs is not the best as seen in the large scatter in the Poisson ratio versus depth (Fig. 13, blue curve). The general result is, however, identical to that for the Rigs-2a well: Land's equation underestimates the invasion of the high-porosity zones and does thus lead to too high values of the Poisson's ratio in the virgin zone (Fig. 16). The data-values of G are relatively high in most of the Tor Formation where porosity is high; this could be due to erroneous measurements of the shear velocity where it becomes very low. The Sw-corrected MUHS-estimate of G agrees well with the data-estimate (Fig. 15), and ΔG correlates well with porosity and Sw, but not with the clay content estimated by the gamma log.

References

Engstrøm, F. 1995. A new method to normalise capilary pressure curves. Proceedings from the International Symposium of the Society of Core Analysis. 12 pp.

Fabricius, I. L., Mavko, G., Mogensen, C. & Japsen, P. 2002. Elastic moduli of chalk as a reflection of porosity, sorting, and irreducible water saturation. SEG 72nd annual meeting, Salt Lake City, USA. 4 pp.

Gassmann, F. 1951. Über die Elastizität poröser Medien. Vier. der Natur. Gesellschaft in Zürich, 96, 1-23.

Gommesen L., Mavko G., Mukerji T. & Fabricius I. 2002: Fluid substitution studies for North Sea chalk logging data. 72nd SEG annual meeting pp. 1-4.

Hashin, Z. & Shtrikman, S. 1963. A variational approach to the elastic behavior of multi-phase materials. J. Mech. Phys. Solids, 11, 127-140.

Japsen, P. & Rasmussen, R. 2002: Compilation ultrasonic data for chalk plugs from the South Arne field, Tor And Ekofisk formations. EFP-01 Rock Physics of Impure Chalk – Technical Note, November 2002/1, 21 pp.

Japsen, P., A. Bruun, I. L. Fabricius, Rasmussen, R., Vejbæk, O.V., Pedersen, J. M., Mavko, G. & Mogensen, C. in prep: Influence of porosity and pore fluid on acoustic properties of chalk: AVO-response from oil, South Arne field, North Sea. To be submitted to Petroleum Geoscience.

Land, C. S. 1968. Calculation of imbibition relative permeability for two- and three-phase flow from rock properties. Society of Petroleum Engineers Journal, 1968, 149-156.

Mavko, G., Mukerji, T. & Dvorkin, J. 1998: The rock physics handbook. Cambridge: Cambridge University Press.

Mogensen, C. & Fabricius, I. 2002: EFP 2001: Quality control of well log data from the South Arne field. Ødegaard Report 01.1031, 18 pp.

Nur, A., Mavko, G., Dvorkin, J. & Galmundi, D. 1998. Critical porosity; a key to relating physical properties to porosity in rocks. Leading Edge, 17, 357-362.

Walls, J. D., Dvorkin, J. & Smith, B. A. 1998. Modeling seismic velocity in Ekofisk Chalk. SEG 68th annual conference. 1016-1019.

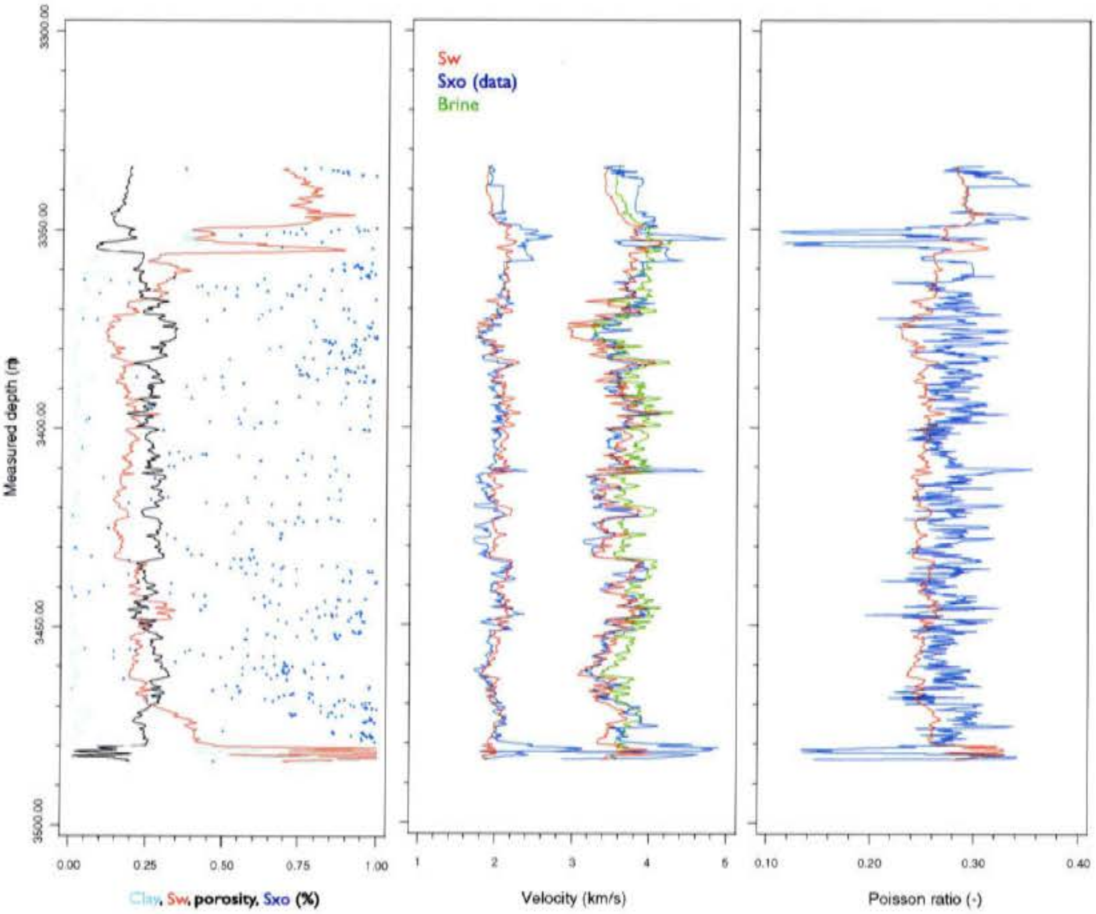

Fig. 1. SA-1: Log data and predictions based on the corrected MUHS model for the chalk section in the Rigs-2 well (eqs 5, 7; Fig. 3).

a. *Clay content (from gamma log), porosity and water saturation, Sw and Sxo. Sxo (dots) is estimated from the relation between the measured sonic data and the corrected MUHS model (eq 8).*
b. *V_P and V_S. Data and predictions of the corrected MUHS model based on porosity and Sw. Brine-estimate for Vs not shown.*
c. *Poisson ratio. Data and predictions of the corrected MUHS model. Brine-estimate not shown.*

In the high-porosity oil zone of the Tor Formation, the oil is predicted to be almost completely flushed as indicated by the closeness of the measured Vp(Sxo) (blue curve) and the predicted Vp(brine) (green curve) whereas Vp(virgin zone, Sw) is predicted to be low. MUHS: Modified Upper Hashin-Shtrikman.

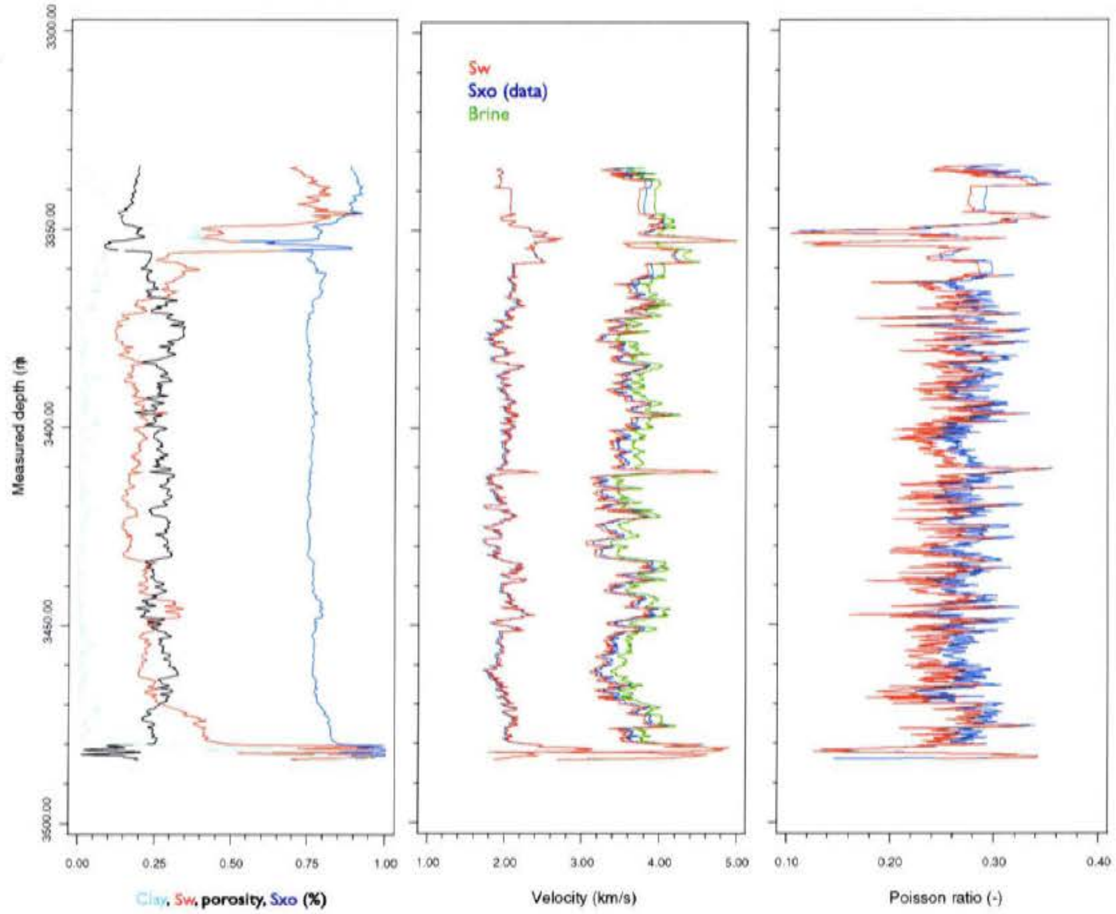

Fig. 2. SA-1: Log data and predictions based on Land's estimate of residual oil for the chalk section in the Rigs-2 well (eqs 5, 7; Fig. 3).

a. Clay content, porosity and water saturation, Sw and Sxo. Sxo is estimated from Land's equation (eq 6).

b. V_P and V_S. Data and predictions based on fluid substitution from Sxo. Brine-estimate for Vs not shown

c. Poisson ratio. Data and predictions of the Land model. Brine-estimate not shown.

In the high-porosity oil zone of the Tor Formation, Sxo is predicted to be reduced to c. 75% and due to the Reuss mixing of the fluids the acoustic properties of invaded zone and of the virgin zone do not differ much. This is indicated by the closeness of the measured Vp(Sxo) (blue curve) and the predicted Vp(virgin zone) (red curve) whereas Vp(brine) (green curve) is predicted to be significantly higher.

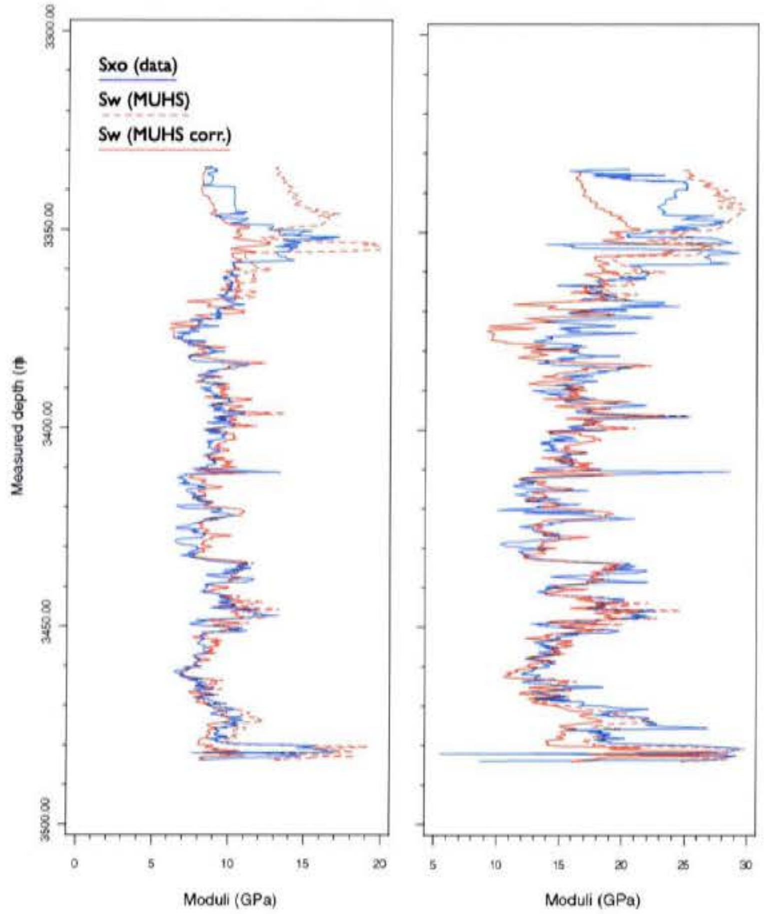

Fig. 3. SA-1: Log response predicted for the virgin zone from the corrected and the uncorrected MUHS-model compared with data from the invaded zone (eqs 5, 7).

a. Shear modulus.

b. Bulk modulus.

Note the good agreement between the shear modulus estimated from data and from the corrected MUHS model. Poor sorting and clay content may explain the difference between the estimated shear modulus from uncorrected MUHS model and from the data in the tight zones (Figs 1, 17). The difference between the two estimates of the bulk modulus is caused by removal of oil by mud invasion in the zone investigated by the sonic log. MUHS: Modified Upper Hashin-Shtrikman.

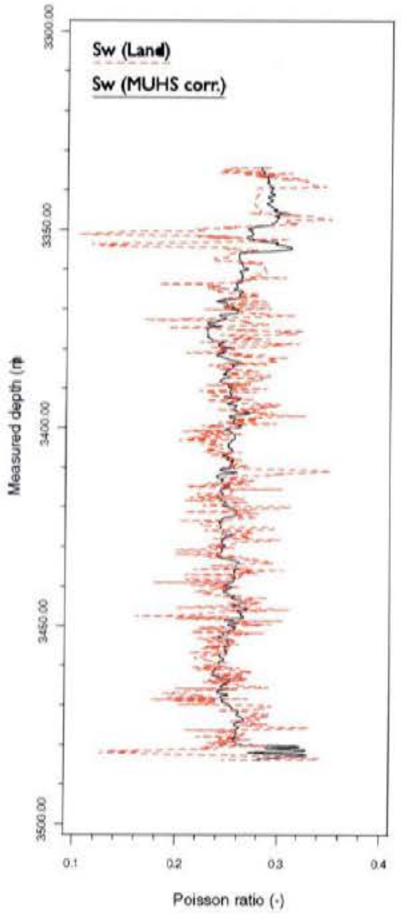

Fig. 4. SA-1: Poisson's ratio versus measured depth estimated for the virgin zone based on Land's equation and on the corrected MUHS model (eqs. 6, 7). Forward modeling based on the MUHS model results in a low ratio in the high-porous Tor reservoir and pronounced peaks at top Ekofisk and top Tor. These features are not captured in the approach based on Land's equation because this model underestimates the flushing of the reservoir.

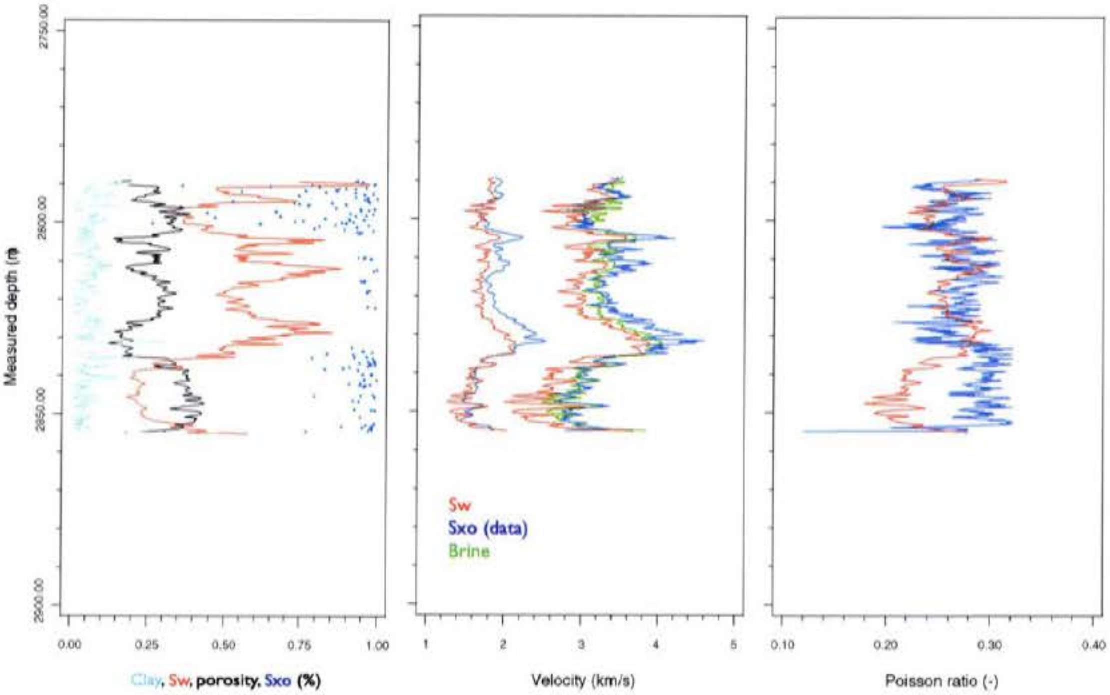

Fig. 5. Rigs-1*: Log data and predictions based on the corrected MUHS model for the chalk section in the Rigs-2 well (eqs 5, 7; Fig. 7).*

d. *Clay content (from gamma log), porosity and water saturation, Sw and Sxo. Sxo (dots) is estimated from the relation between the measured sonic data and the corrected MUHS model (eq 8).*
e. *V_P and V_S. Data and predictions of the corrected MUHS model based on porosity and Sw. Brine-estimate for Vs not shown.*
f. *Poisson ratio. Data and predictions of the corrected MUHS model. Brine-estimate not shown.*

In the high-porosity oil zone of the Tor Formation, the oil is predicted to be almost completely flushed as indicated by the closeness of the measured Vp(Sxo) (blue curve) and the predicted Vp(brine) (green curve) whereas Vp(virgin zone, Sw) is predicted to be low. MUHS: Modified Upper Hashin-Shtrikman.

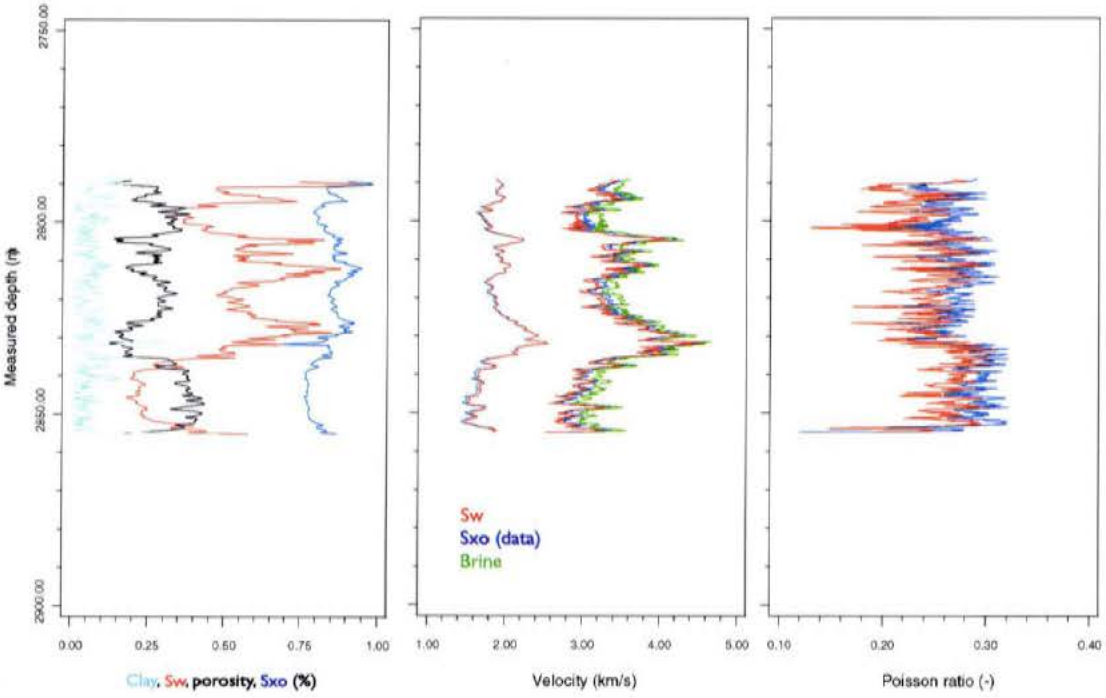

Fig. 6. Rigs-1: Log data and predictions based on Land's estimate of residual oil for the chalk section in the Rigs-2 well (eqs 5, 7; Fig. 7).

a. *Clay content, porosity and water saturation, Sw and Sxo. Sxo is estimated from Land's equation (eq 6).*
b. *V_P and V_S. Data and predictions based on fluid substitution from Sxo. Brine-estimate for Vs not shown*
c. *Poisson ratio. Data and predictions of the Land model. Brine-estimate not shown.*

In the high-porosity oil zone of the Tor Formation, Sxo is predicted to be reduced to c. 75% and due to the Reuss mixing of the fluids the acoustic properties of invaded zone and of the virgin zone do not differ much. This is indicated by the closeness of the measured Vp(Sxo) (blue curve) and the predicted Vp(virgin zone) (red curve) whereas Vp(brine) (green curve) is predicted to be significantly higher.

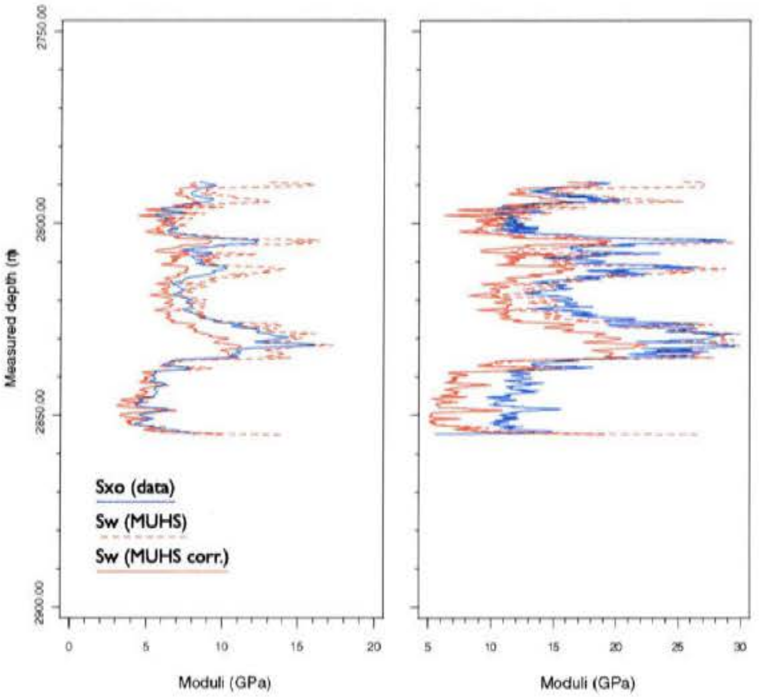

Fig. 7. Rigs-1: Log response predicted for the virgin zone from the corrected and the uncorrected MUHS-model compared with data from the invaded zone (eqs 5, 7).

a. Shear modulus.

b. Bulk modulus.

Note the good agreement between the shear modulus estimated from data and from the corrected MUHS model. Poor sorting and clay content may explain the difference between the estimated shear modulus from uncorrected MUHS model and from the data in the tight zones (Figs 5, 18). The difference between the two estimates of the bulk modulus is caused by removal of oil by mud invasion in the zone investigated by the sonic log. MUHS: Modified Upper Hashin-Shtrikman.

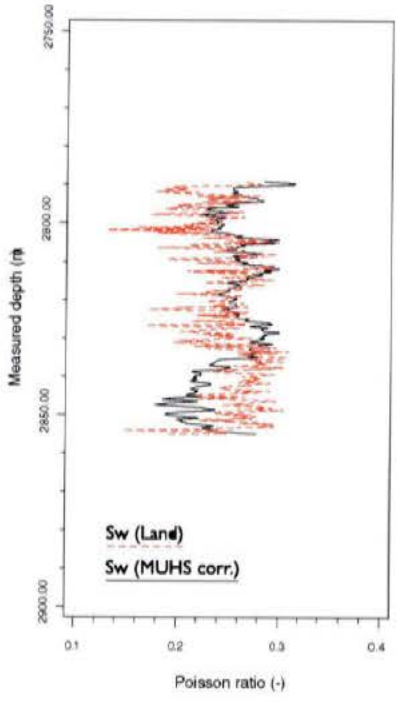

Fig. 8. Rigs-1: Poisson's ratio versus measured depth estimated for the virgin zone based on Land's equation and on the corrected MUHS model (eqs. 6, 7). Forward modeling based on the MUHS model results in a low ratio in the high-porous Tor reservoir and pronounced peaks at top Ekofisk and top Tor. These features are not captured in the approach based on Land's equation because this model underestimates the flushing of the reservoir.

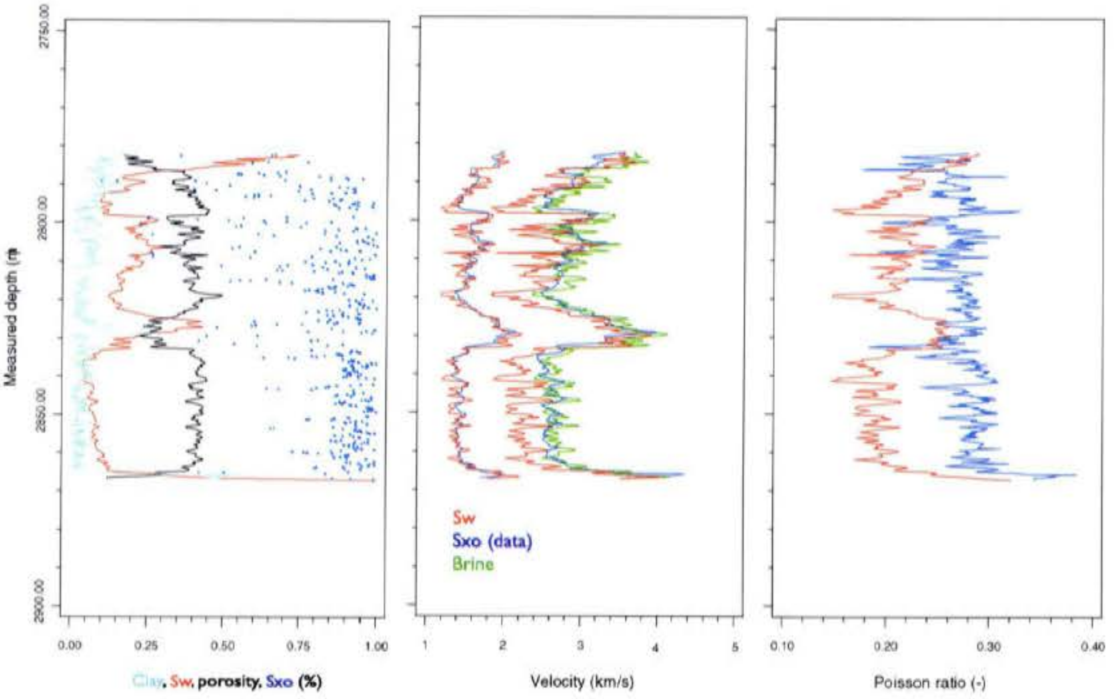

Fig. 9. Rigs-2: *Log data and predictions based on the corrected MUHS model for the chalk section in the Rigs-2 well (eqs 5, 7; Fig. 11).*

- *g. Clay content (from gamma log), porosity and water saturation, Sw and Sxo. Sxo (dots) is estimated from the relation between the measured sonic data and the corrected MUHS model (eq 8).*
- *h. V_P and V_S. Data and predictions of the corrected MUHS model based on porosity and Sw. Brine-estimate for Vs not shown.*
- *i. Poisson ratio. Data and predictions of the corrected MUHS model. Brine-estimate not shown.*

In the high-porosity oil zone of the Tor Formation, the oil is predicted to be almost completely flushed as indicated by the closeness of the measured Vp(Sxo) (blue curve) and the predicted Vp(brine) (green curve) whereas Vp(virgin zone, Sw) is predicted to be low. MUHS: Modified Upper Hashin-Shtrikman.

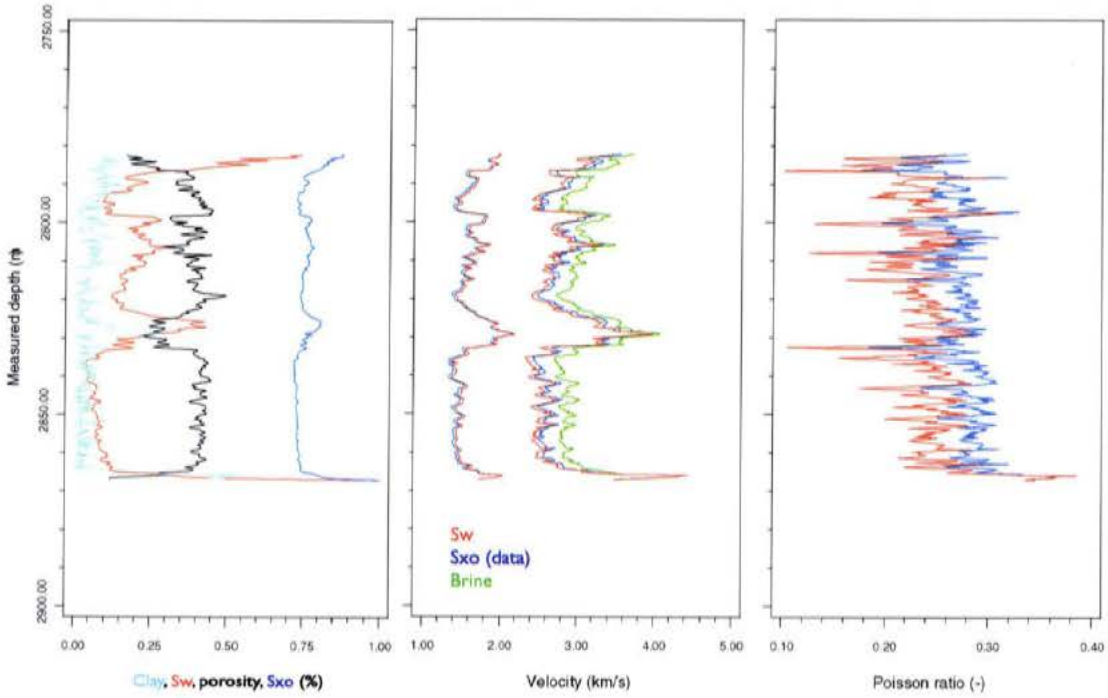

Fig. 10. Rigs-2: Log data and predictions based on Land's estimate of residual oil for the chalk section in the Rigs-2 well (eqs 5, 7; Fig. 11).

- *d. Clay content, porosity and water saturation, Sw and Sxo. Sxo is estimated from Land's equation (eq 6).*
- *e. V_P and V_S. Data and predictions based on fluid substitution from Sxo. Brine-estimate for Vs not shown*
- *f. Poisson ratio. Data and predictions of the Land model. Brine-estimate not shown.*

In the high-porosity oil zone of the Tor Formation, Sxo is predicted to be reduced to c. 75% and due to the Reuss mixing of the fluids the acoustic properties of invaded zone and of the virgin zone do not differ much. This is indicated by the closeness of the measured Vp(Sxo) (blue curve) and the predicted Vp(virgin zone) (red curve) whereas Vp(brine) (green curve) is predicted to be significantly higher.

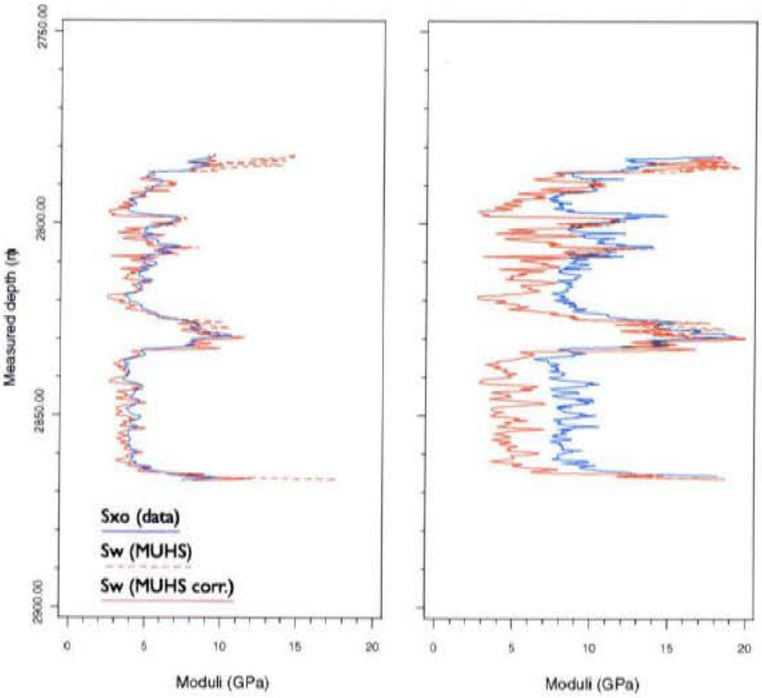

Fig. 11. Rigs-2: Log response predicted for the virgin zone from the corrected and the un-corrected MUHS-model compared with data from the invaded zone (eqs 5, 7).

a. Shear modulus.

b. Bulk modulus.

Note the good agreement between the shear modulus estimated from data and from the corrected MUHS model. Poor sorting and clay content may explain the difference between the estimated shear modulus from uncorrected MUHS model and from the data in the tight zones (Figs 9, 19). The difference between the two estimates of the bulk modulus is caused by removal of oil by mud invasion in the zone investigated by the sonic log. MUHS: Modified Upper Hashin-Shtrikman.

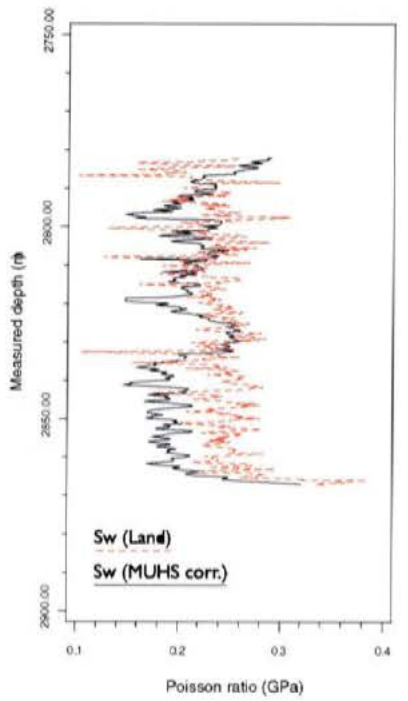

Fig. 12. Rigs-2: Poisson's ratio versus measured depth estimated for the virgin zone based on Land's equation and on the corrected MUHS model (eqs. 6, 7). Forward modeling based on the MUHS model results in a low ratio in the high-porous Tor reservoir and pronounced peaks at top Ekofisk and top Tor. These features are not captured in the approach based on Land's equation because this model underestimates the flushing of the reservoir.

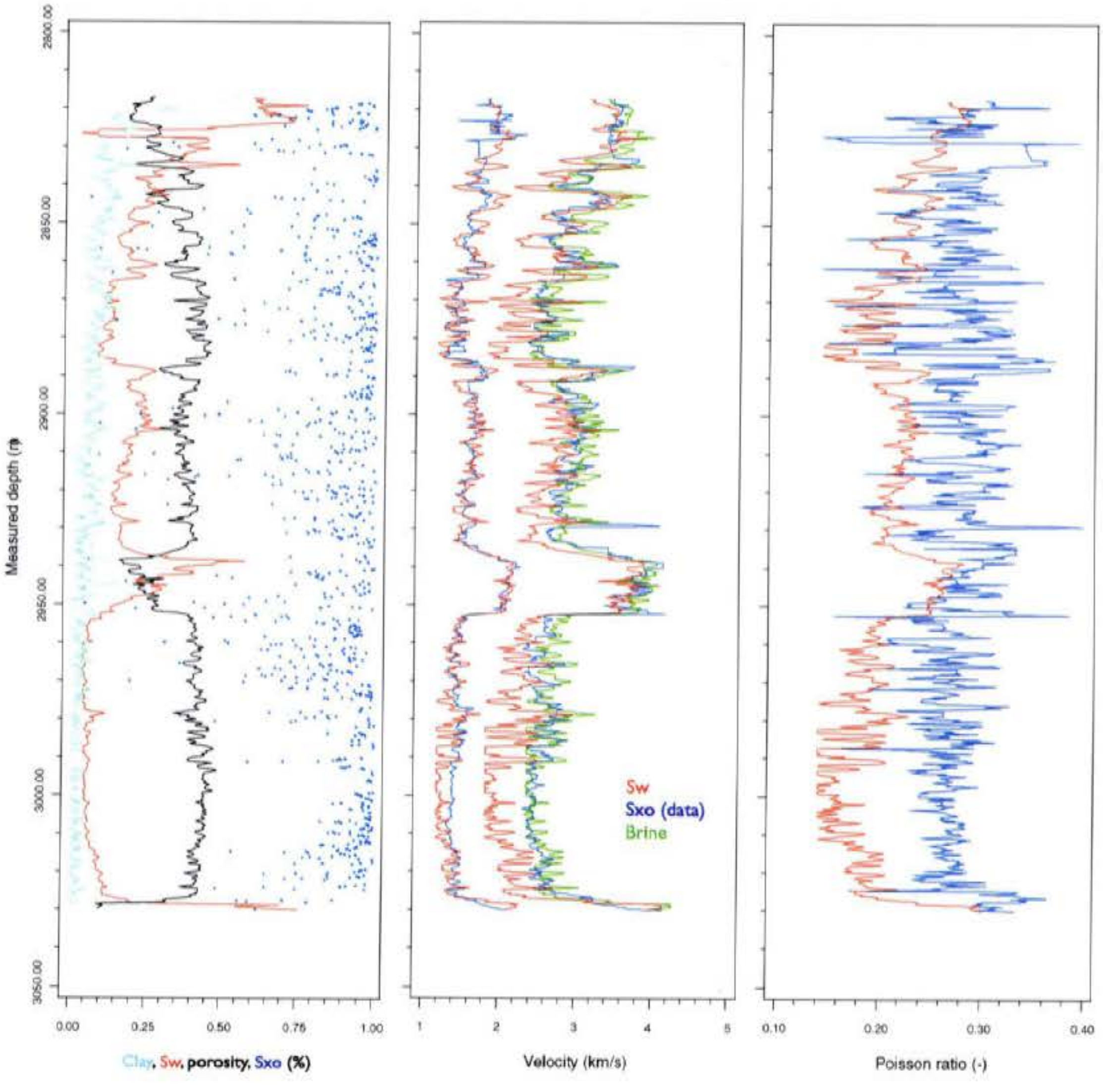

Fig. 13. Rigs-2a*: Log data and predictions based on the corrected MUHS model for the chalk section in the Rigs-2 well (eqs 5, 7; Fig. 15).*

a. *Clay content (from gamma log), porosity and water saturation, Sw and Sxo. Sxo (dots) is estimated from the relation between the measured sonic data and the corrected MUHS model (eq 8).*
b. *V_P and V_S. Data and predictions of the corrected MUHS model based on porosity and Sw. Brine-estimate for Vs not shown.*
c. *Poisson ratio. Data and predictions of the corrected MUHS model. Brine-estimate not shown.*

In the high-porosity oil zone of the Tor Formation, the oil is predicted to be almost completely flushed as indicated by the closeness of the measured Vp(Sxo) (blue curve) and the predicted Vp(brine) (green curve) whereas Vp(virgin zone, Sw) is predicted to be low. MUHS: Modified Upper Hashin-Shtrikman.

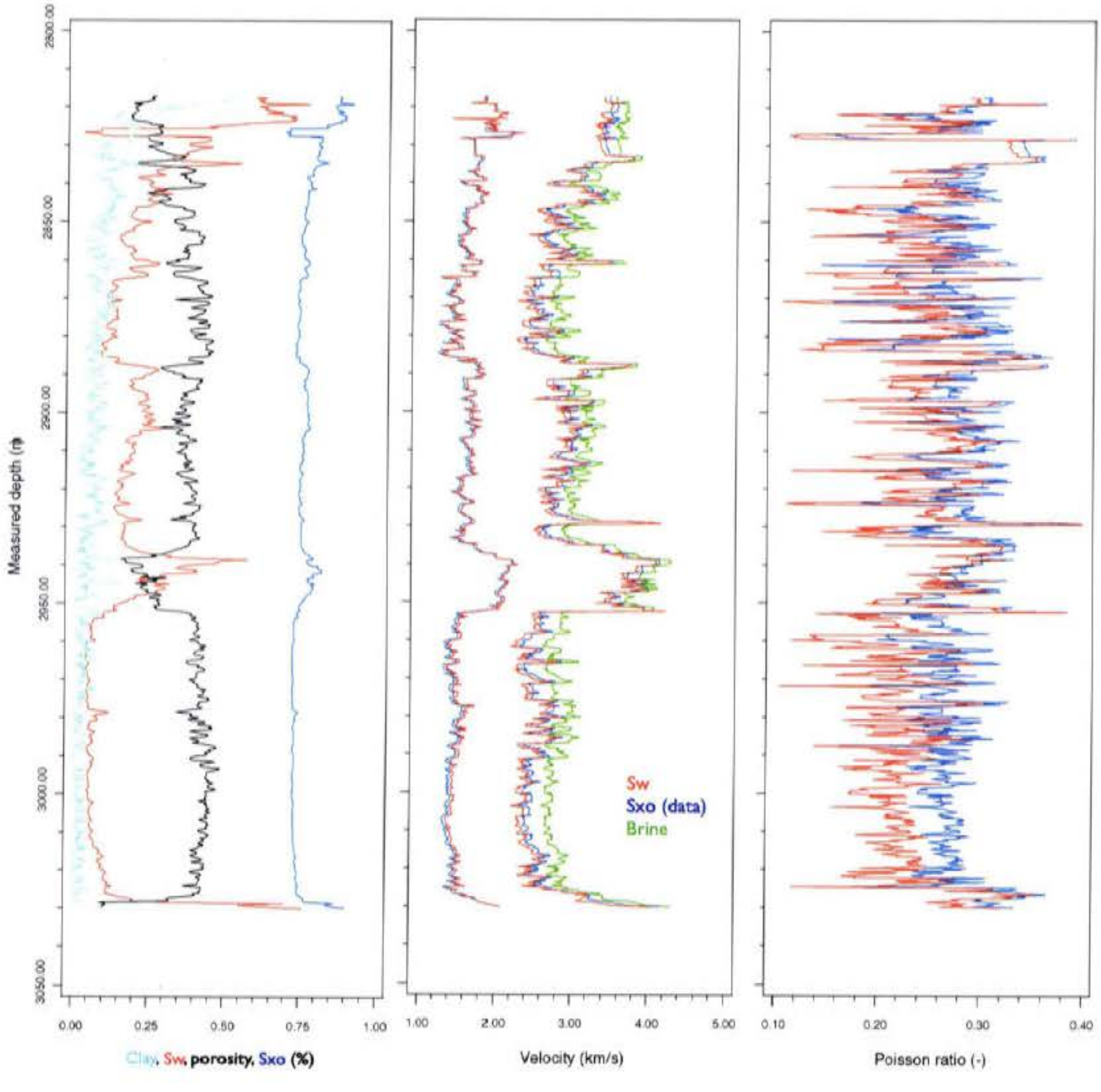

Fig. 14. Rigs-2a: Log data and predictions based on Land's estimate of residual oil for the chalk section in the Rigs-2 well (eqs 5, 7; Fig. 15).

a. *Clay content, porosity and water saturation, Sw and Sxo. Sxo is estimated from Land's equation (eq 6).*
b. *V_P and V_S. Data and predictions based on fluid substitution from Sxo. Brine-estimate for Vs not shown*
c. *Poisson ratio. Data and predictions of the Land model. Brine-estimate not shown.*

In the high-porosity oil zone of the Tor Formation, Sxo is predicted to be reduced to c. 75% and due to the Reuss mixing of the fluids the acoustic properties of invaded zone and of the virgin zone do not differ much. This is indicated by the closeness of the measured Vp(Sxo) (blue curve) and the predicted Vp(virgin zone) (red curve) whereas Vp(brine) (green curve) is predicted to be significantly higher.

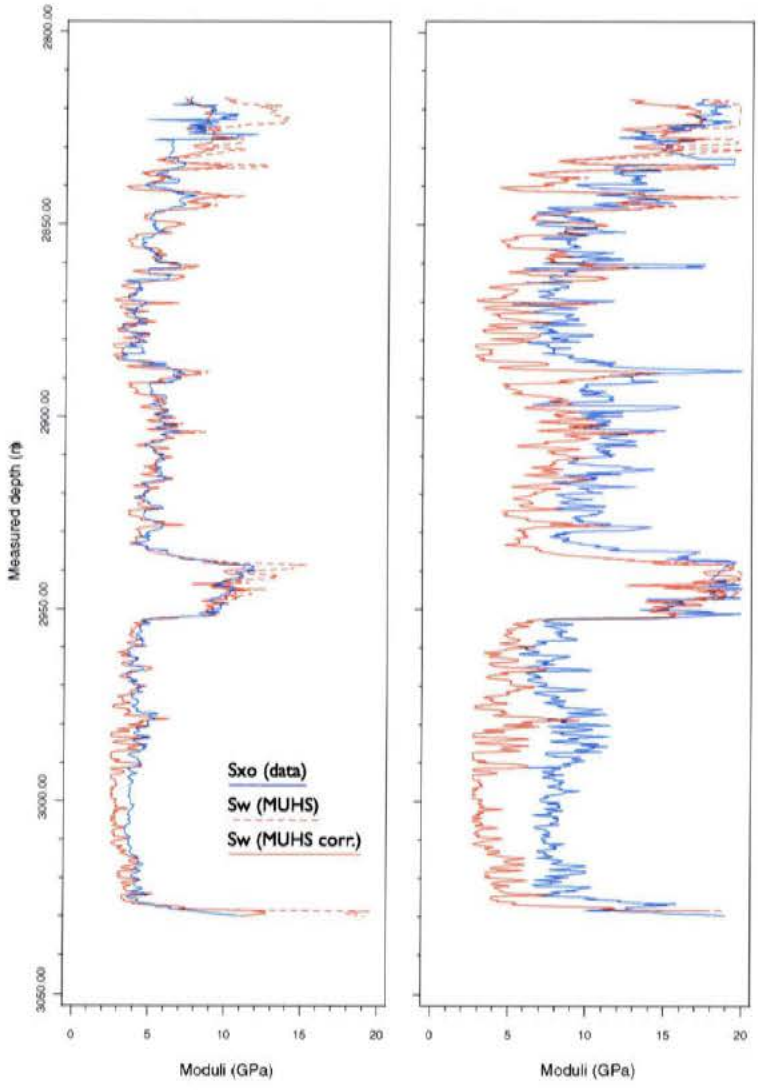

Fig. 15. Rigs-2a: Log response predicted for the virgin zone from the corrected and the uncorrected MUHS-model compared with data from the invaded zone (eqs 5, 7).

a. Shear modulus.

b. Bulk modulus.

Note the good agreement between the shear modulus estimated from data and from the corrected MUHS model. Poor sorting and clay content may explain the difference between the estimated shear modulus from uncorrected MUHS model and from the data in the tight zones (Figs 13, 20). The difference between the two estimates of the bulk modulus is caused by removal of oil by mud invasion in the zone investigated by the sonic log. MUHS: Modified Upper Hashin-Shtrikman.

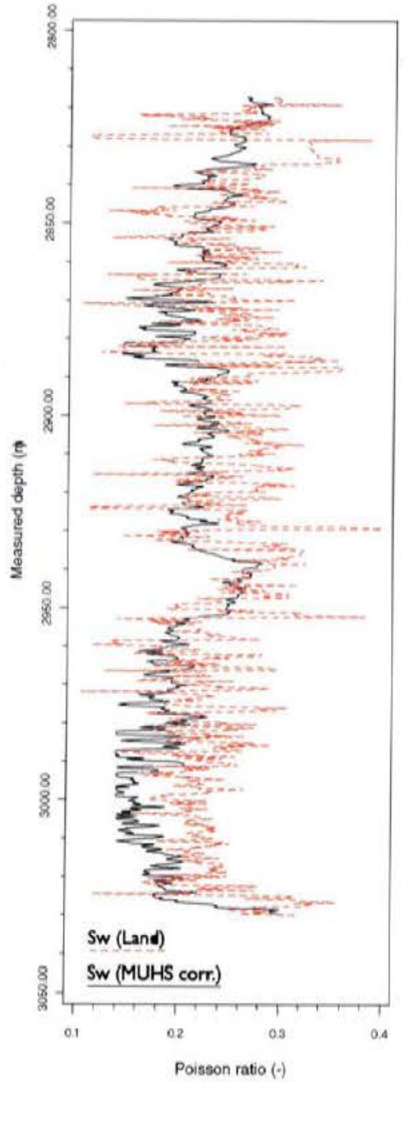

Fig. 16. Rigs-2a: Poisson's ratio versus measured depth estimated for the virgin zone based on Land's equation and on the corrected MUHS model (eqs. 6, 7). Forward modeling based on the MUHS model results in a low ratio in the high-porous Tor reservoir and pronounced peaks at top Ekofisk and top Tor. These features are not captured in the approach based on Land's equation because this model underestimates the flushing of the reservoir.

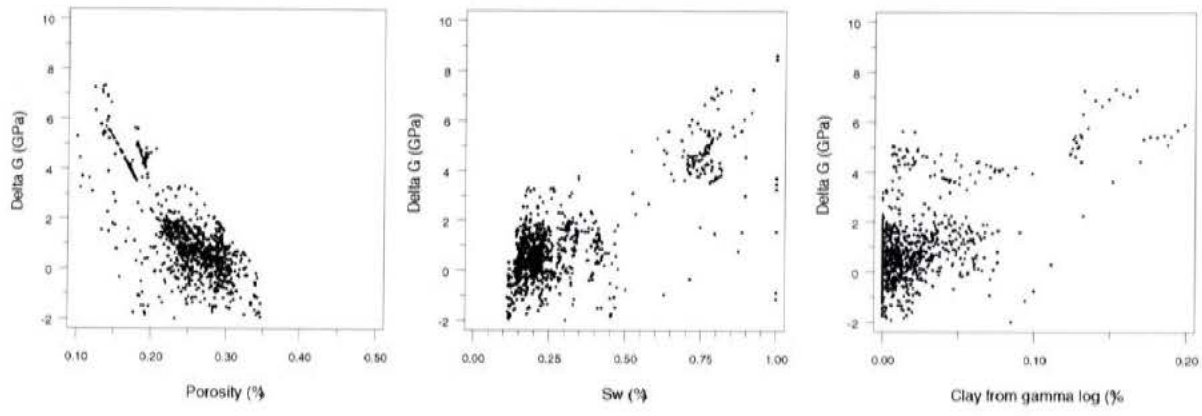

Fig. 17. SA-1: Error in prediction of the shear modulus, $\Delta G = G_{MUHS} - G_{data}$ where G_{MUHS} is estimated from the MUHS model (eq. 5).
ΔG versus porosity, water saturation and clay content estimated from the gamma log.

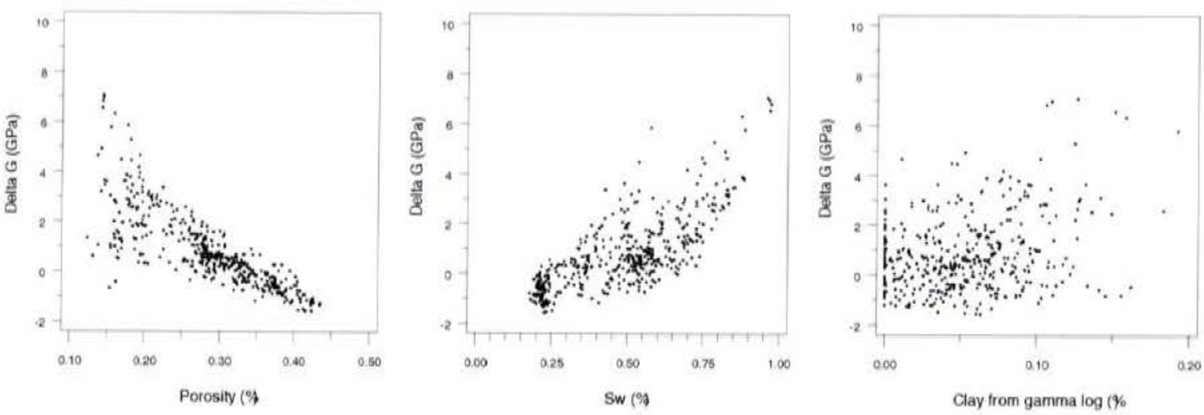

Fig. 18. Rigs-1: Error in prediction of the shear modulus, $\Delta G = G_{MUHS} - G_{data}$ where G_{MUHS} is estimated from the MUHS model (eq. 5).
ΔG versus porosity, water saturation and clay content estimated from the gamma log.

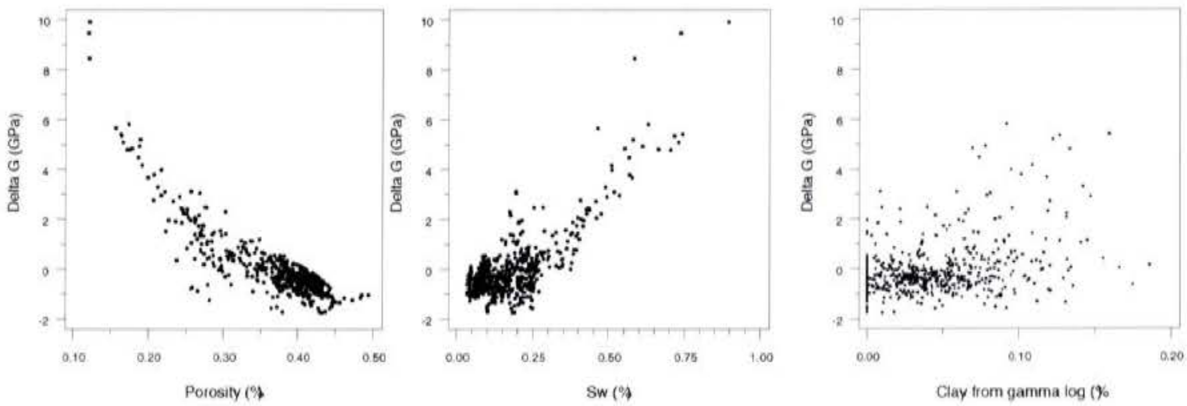

Fig. 19. Rigs-2: Error in prediction of the shear modulus, $\Delta G = G_{MUHS} - G_{data}$ where G_{MUHS} is estimated from the MUHS model (eq. 5).
ΔG versus porosity, water saturation and clay content estimated from the gamma log.

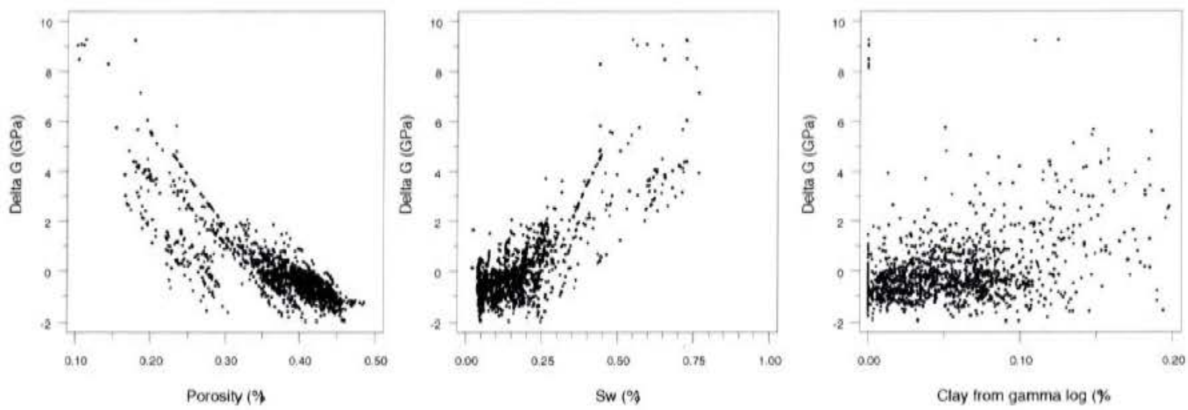

Fig. 20. Rigs-2a: Error in prediction of the shear modulus, $\Delta G = G_{MUHS} - G_{data}$ where G_{MUHS} is estimated from the MUHS model (eq. 5).
ΔG versus porosity, water saturation and clay content estimated from the gamma log.

Some thoughts on upscaling rock physics relations

Gary Mavko
mavko@stanford.edu, Stanford University

We have been most successful finding physically and geologically reasonable rock physics relations at a small scale. For example, Gassmann's fluid substitution is most valid at scales smaller than a few tens of centimeters and at low frequencies. Another example is the relation of velocity-porosity to geologic parameters such as depositional energy and diagenesis. These are often most clear at the core and sonic logging scales. The key is that we have more success when we can focus on a single lithofacies, which tends to be more resolvable at small wavelengths.

The question, of course, is how do these relations look at the seismic scale? When we go from core to log to seismic, we encounter two things: a drastic decrease in frequency, and an increase in spatial sampling as the wavelength increases. Going to lower frequency is beneficial, since we approach the range where Gassmann is more reliable. The longer wavelength means that we have often have to interpret spatial averages, which can look very little like the individual facies below resolution.

We will approach this problem in several ways:

1. Theoretical Upscaling. We will look at a few relevant rock physics equations that relate seismic observables to rock and fluid properties. We will apply smoothing operators directly to the equations to explore the implications. Obviously, linear relations will indicate no change when a linear operator is applied. Nonlinear relations may change completely.

2. Log-based upscaling. This will be a more spatially realistic approach to the above. The idea is to identify relevant rock physics relations at the log scale. Then, smooth the logs over a moving window with a length comparable to the seismic wavelength. Finally, we will repeat the same crossplots to explore if and how they change. Preliminary work has suggested that an important parameter is the ratio of the wavelength to the vertical geologic correlation length.

3. Wave-equation upscaling. We will take a Monte-Carlo approach. We will begin with log data which will reveal the relevant rock physics relations and the spatial statistics of the rock parameters. We will do full-waveform synthetic seismic calculations to get the more realistic prediction of attributes, such as amplitude. We will then repeat the process over many Monte Carlo realizations. The full-waveform synthetics will do the upscaling. The Monte-Carlo simulation will help us to explore the natural variability of the rocks, as indicated in the logs.

DANMARKS OG GRØNLANDS GEOLOGISKE UNDERSØGELSE RAPPORT 2003/15

EFP-01 Rock Physics of Impure Chalks
Final Report

ENS J. nr. 1313/01-0006

Peter Japsen, Anders Bruun, Ida L. Fabricius, Christian Høier,
Gary Mavko, Christian Mogensen, Jacob Mørch Pedersen,
Rasmus Rasmussen and Ole V. Vejbæk

GEUS Report included in this volume: 2002/23

GEOLOGICAL SURVEY OF DENMARK AND GREENLAND
MINISTRY OF THE ENVIRONMENT

G E U S

DANMARKS OG GRØNLANDS GEOLOGISKE UNDERSØGELSE RAPPORT 2003/15

EFP-01 Rock Physics of Impure Chalks
Final Report

ENS J. nr. 1313/01-0006

Peter Japsen[1], Anders Bruun[2], Ida L. Fabricius[3], Christian Høier[1],
Gary Mavko[4], Christian Mogensen[2], Jacob Mørch Pedersen[2],
Klaus Bolding Rasmussen[2], Rasmus Rasmussen[1]
and Ole V. Vejbæk[1]

Released 01.10.2005

[1] Geological Survey of Denmark and Greenland (GEUS)
[2] Ødegaard A/S
[3] Technical University of Denmark (DTU)
[4] Stanford University

GEUS Report included in this volume:
Danmarks og Grønlands Geologiske Undersøgelse Rapport 2002/23:
Speciel Core Analysis for the Rock Physics Project (EFP-2001)
ENS J. nr. 1313/01-006
Ultrasonic velocity measured on plugs from the Ekofisk and Tor Formation. Samples taken from the wells: Rigs-1, Rigs-2 and SA-1, the South Arne Field.

GEUS Core Laboratory
Christian Høier

GEOLOGICAL SURVEY OF DENMARK AND GREENLAND
MINISTRY OF THE ENVIRONMENT

GEUS

GEUS

DTU

LELAND STANFORD JUNIOR UNIVERSITY

ORGANIZED 1891

Summary

We have estimated the elastic properties of chalk at three different scales on the South Arne field, North Sea, by analysing ultrasonic core data, downhole log-readings and results of AVO-inversion based on near- and far-offset stack seismic data (Amplitude Versus Offset). Here we present main results from papers and reports enclosed in this volume.

Fluid substitution in chalks: Effects of saturation scales

We investigated some aspects of ultrasonic fluid substitution in chalks, and we found that Gassmann's relations can be used to understand the variations of velocity with saturation in our samples, even though the velocity data are ultrasonic (high frequency). This suggests that in these samples there are no significant high frequency dispersion effects from the squirt-flow or Biot mechanisms that would invalidate the use of the Gassmann's relations. There is, however, evidence for patchy saturation in the ultrasonic data with a characteristic patch size less than 1/10 mm. This is observed in limited V_p and V_s versus water saturation data (Fig. 1). We also find that fluid substituting to full brine saturation using a modified patchy mixing rule gives velocities more consistent with empirical trends than assuming a fine-scaling mixing rule. It is likely that fine-scale mixing is dominant at logging frequencies in chalks. Another finding is that the dry-rock ultrasonic data tend to be inconsistent, in a Gassmann sense, with data from the water-bearing samples (Japsen et al. 2002). Specifically, the dry-rock velocities are "too fast."
(Mavko & Japsen *this report*)

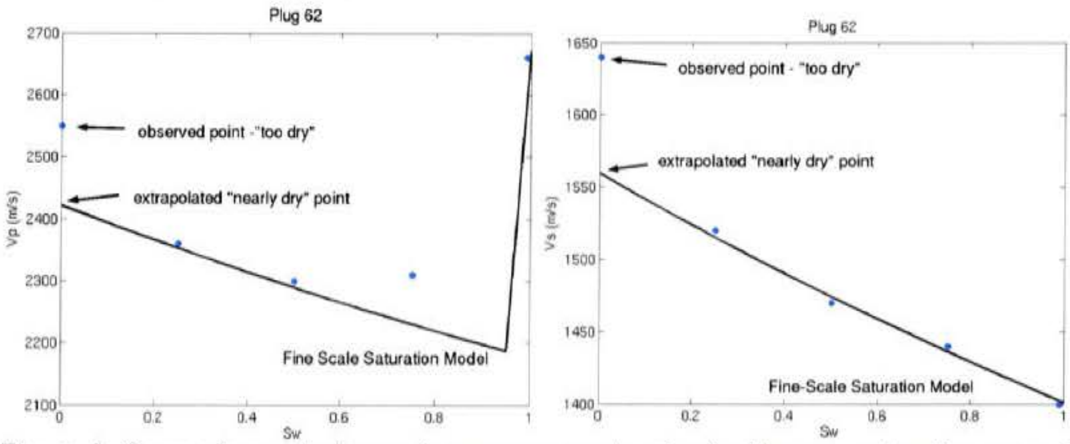

Figure 1. Comparison of ultrasonic measurements of velocities vs. saturation on a South Arne chalk sample, compared with the fine-scale mixing model. Note the departure in V_p *from the fine-scale mixing curve at high saturations. But the characteristic patch size for this sample is only 0,04 mm, and this suggests that fine-scale mixing will be dominant at the lower frequencies used in sonic logging. Core plug 62,* ϕ*=40%, permeability = 1.4 mDarcy.*

Modeling elastic moduli of impure chalk

In impure chalk the elastic moduli are not only controlled by porosity, but also by cementation resulting in relatively large moduli and by admixtures of clay and fine silica which results in relatively small moduli. Based on a concept of framebuilding contra suspended solids (iso-frame values, IF), we model P-wave moduli, *M*, and S-wave moduli, *G*, of dry and wet plug samples by an effective medium model using chemical, mineralogical and textural input ($M = \rho V_p^{\ 2}, G = \rho V_s^{\ 2}$ where ρ is bulk density; Fig. 2). We use a modified upper Hashin Shtrikman mixing-model assuming a critical porosity of 70%. The textural and mineralogical data may potentially be assessed from logging data on spectral gamma radiation, density, acoustic velocity and water saturations in a hydrocarbon zone.

In chalk of reservoir quality, elastic moduli are predictable (Fig. 3): The solid phase has roughly uniform composition, and as porosity decreases from 45% to 25%, the IF-value increases from 0.5 to 0.6. At intermediate porosity (25%–18%) IF-values vary between 0.5 and 0.9: Samples with high IF-values have pore-filling cementation, whereas samples with low IF-values have high amounts of suspended submicron-size quartz in the pore space. Low-porosity samples (13%–16%) have relatively low IF-values (around 0.6) and are packed with pore-filling smectite.
(Fabricius et al. *this report*)

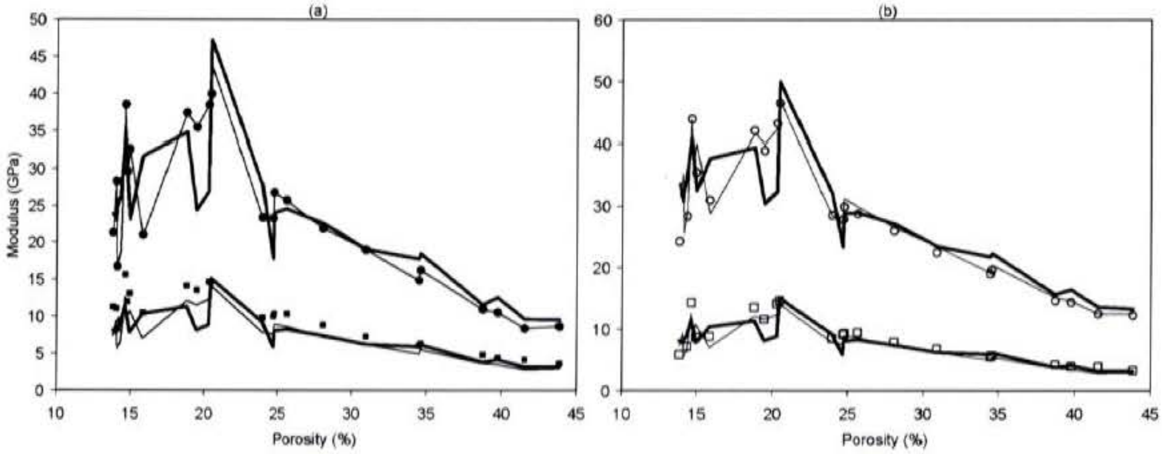

Figure 2. Elastic modulus data and elastic models versus porosity.
a. Dry samples. b. Water saturated samples.
The models fit the wet P-wave modulus data, whereas especially the dry S-wave moduli tend to be higher than predicted. The model based on image analysis has the advantage of being based on petrographic data.
Circles: P-wave modulus data. Squares: S-wave modulus data.
Thin lines: model based on dry P-wave and density data.
Thick lines: model based on image-analysis data calibrated to dry P-wave data.

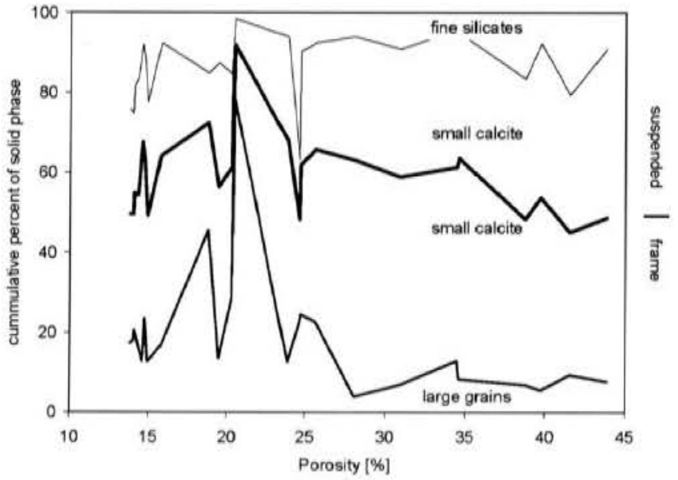

Figure 3. Composition of solid phase of chalk samples versus porosity. The thick line denotes the IF-value of each sample. The area below the thick line represents the solid phase modeled as solid frame with spherical pores, whereas the area above the line represents the solid modeled as being in suspension. Large grains include calcitic microfossils, porfilling carbonate cement, as well as clasts of quartz, feldspar and kaolinite. Fine silicates include smectite, kaolinite and quartz.

Influence of porosity and pore fluid on acoustic properties of chalk: AVO-response from oil

We find that the velocity-porosity relation of the plug data are in agreement with the empirical, modified upper Hashin-Shtrikman (MUHS) model established by Walls et al. (1998) for chalk from the Ekofisk field for porosities between 10% and 40%. In pure chalk intervals, this model furthermore, matches log-estimated values of the shear modulus which are unaffected by fluid content according to Gassmann's relations.

Due to higher porosities in the South Arne field we extend the range of the model to 45% porosity based on the ultrasonic data (Fig. 4). The model predicts the shear modulus to be smaller than observed from logging data for porosities above c. 40%. Erroneous log-determination of Vs may be the cause of this difference when S-wave traveltimes becomes very long.

Variations of the bulk modulus, K, as a function of water saturation are predicted by the model combined with Gassmann's equations, and we find that the sonic log data represent chalk where the oil has been partly flushed by invasion of mud filtrate; $K = \rho(V_p^{\,2} - 4/3 \cdot V_s^{\,2})$. We use the difference between logging data- and model-estimates of the shear modulus to correct the model by scaling it according to clay content as estimated by the water saturation. The water saturation in e.g. the Rigs-2 well can be regarded as a measure of the impurities in the chalk because the chalk is water-wet and the water saturation is close to irreducible saturation (Fabricius et al. 2002).

A characteristic depth-wise pattern of the Poisson ratio, ν, with pronounced peaks at top Ekofisk and top Tor and low values in the high-porous Tor reservoir is derived for the Rigs-2 well from the forward modeling of the acoustic properties of the virgin zone based

on the corrected, modified upper Hashin-Shtrikman model (Fig. 5; $\nu = (V_p^2 / V_s^2 - 2)/(V_p^2 / V_s^2 - 1)/2$). This pattern agrees with the inverted seismic data, whereas these features are not captured if the acoustic properties of the virgin zone are derived from the sonic logs and estimates of residual oil in the flushed zone because of almost complete invasion where porosity is high (Fig. 6). We have thus found AVO-inversion to provide direct evidence for presence of light oil in the high-porous chalk of the South Arne field.
(Japsen et al. *this report*)

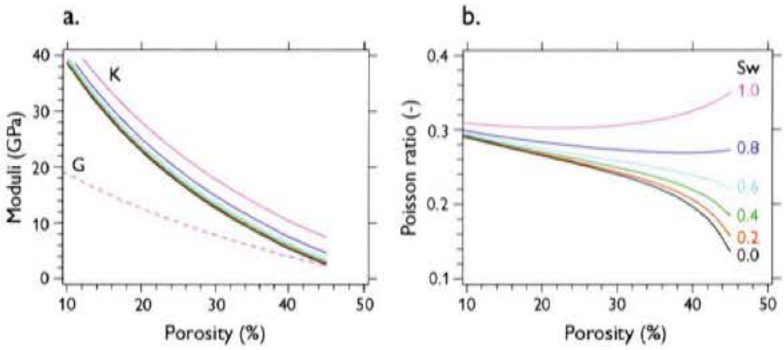

Fig. 4. Acoustic properties of chalk as a function of porosity and water saturation, Sw, predicted from the MUHS model and Gassmann's relations assuming fine-scaled Reuss mixing of the fluids.

a. Bulk and shear modulus, K and G. b. Poisson ratio.

Note the pronounced variation in Poisson ratio for porosities above c. 35% between pure brine and pure oil (density 1.035 and 0.633 g/cm^3). MUHS: Modified Upper Hashin-Shtrikman.

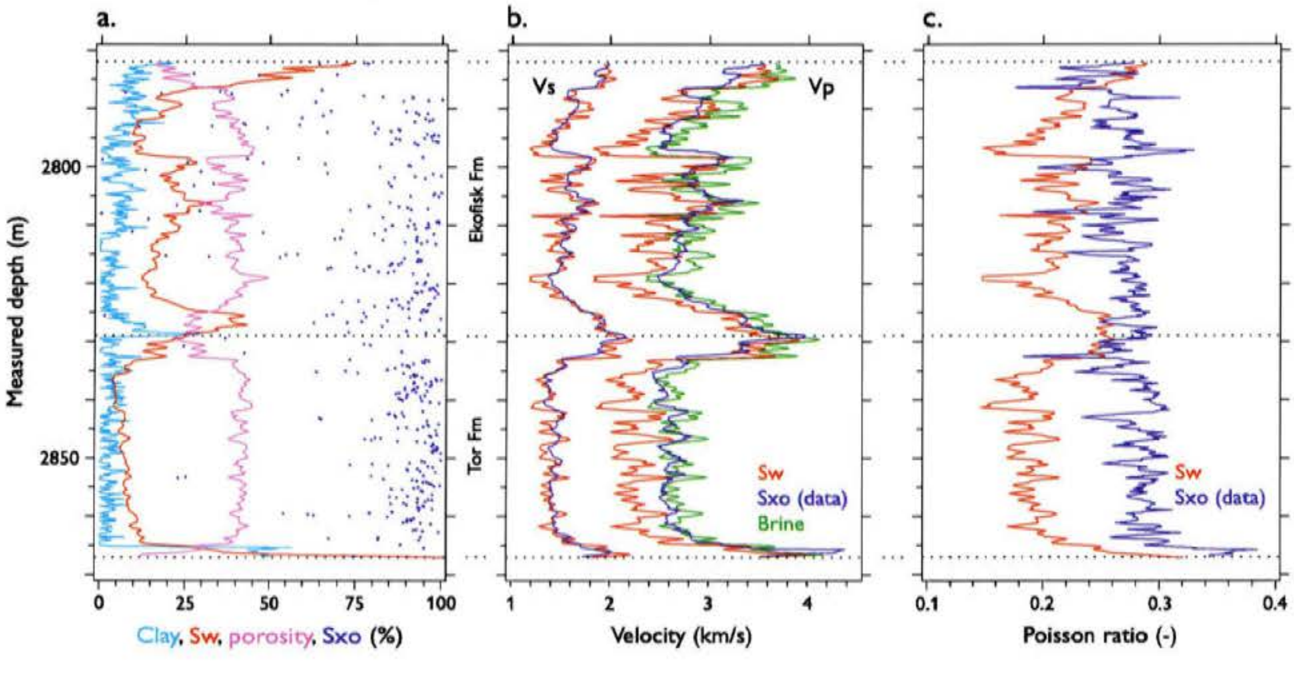

Fig. 5. Log data and predictions based on the corrected MUHS model for the chalk section in the Rigs-2 well.

- *a. Clay content (from gamma log), porosity and water saturation, Sw and Sxo. Sxo (dots) is estimated from the relation between the measured sonic data and the corrected MUHS model.*
- *b. V_P and V_S. Data and predictions of the corrected MUHS model based on porosity and Sw. Brine-estimate for Vs not shown.*
- *c. Poisson ratio. Data and predictions of the corrected MUHS model. Brine-estimate not shown.*

In the high-porosity oil zone of the Tor Formation, the oil is predicted to be almost completely flushed as indicated by the closeness of the measured Vp(Sxo) (blue curve) and the predicted Vp(brine) (green curve) whereas Vp(virgin zone, Sw) is predicted to be low. MUHS: Modified Upper Hashin-Shtrikman.

AVO-inversion of seismic data

AVO attributes were calculated from inverted 2D seismic lines (near- and far-offset data) extracted from the South Arne 3D survey. The inversion was carried out for the two-way time window 1.9–3.6 s and was targeted on the chalk interval. Log data from the I-1x, Rigs-1, -2 and SA-1 wells were used in the inversion process. These data comprise V_p- and V_s-logs based on the corrected, modified upper Hashin-Shtrikman model described above plus density logs, check shot and deviation data. Using a least-squares wavelet estimation method with constrain on the phase, wavelets were estimated for each offset stack and for each of the wells. The wavelet estimated from the I-1x well was preferred based on inversion tests.

Low-frequency components of the acoustic impedance variations with depth are not present in seismic data. Since this information is essential to the interpretation, it should be accounted for in the seismic inversion. Simple low-frequency impedance models were constructed by extrapolation of the angle-dependent impedance well logs through the 3D volume tied to seismic horizons, followed by low-pass filtering. The inversion results are good in terms of match with the angle-dependent impedance well logs.

AVO-attributes were computed from the angle-dependent impedance inversions combined with low-frequency information: Acoustic impedance, shear impedance and Poisson's ratio were extracted at the location of the I-1x, Rigs-1, -2 and SA-1 wells. The AVO-results are good in terms of match with the well log data. Low values of Poisson's ratio at the location of Rigs-2 is in agreement with the presence of light oil in the high-porous chalk of the South Arne field (Fig. 6).
(Bruun *this report*)

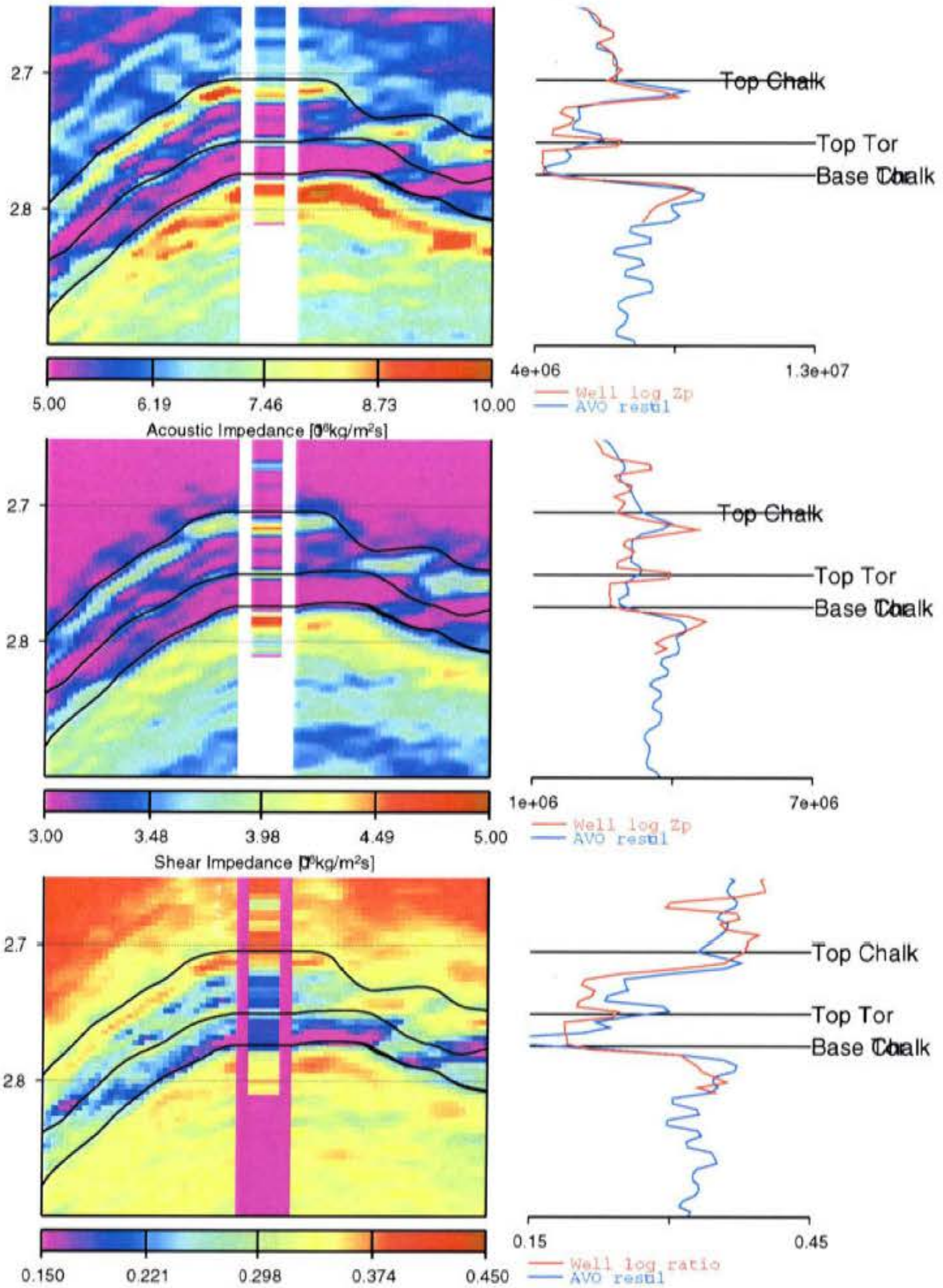

Figure 6. Two-way time section with AVO-inversion of seismic data and inserted log response for the Rigs-2 well computed from forward modeling of the corrected, modified upper Hashin-Shtrikman model NE-SW orented cross section.

a. Acoustic impedance, b. shear impedance, c. Poisson ratio.

Very good agreement is observed for both acoustic and shear impedance. Note the peaks in the tight zones near top chalk and top Tor, There is good agreement between the log- and AVO-pattern of Poisson's ratio, e.g. the peak at top Tor and the low values within the Tor Formation. This pattern cannot be resolved by the log if the acoustic properties are estimated from the sonic log because the water saturation near the well bore is unkown.

Modelling seismic response from chalk reservoirs resulting from changes in burial depth and fluid saturation

We have investigated changes in seismic response caused by changes in degree of compaction and fluid content in North Sea Chalk reservoirs away from a well bore by forward modelling. The investigated seismic response encompasses reflectivity changes, AVO and acoustic impedance based on well data from the South Arne and Dan fields, Danish North Sea and these results are compared to seimic field records. Depth of burial (changes in effective stress) and changes in hydrocarbon saturation are the two main variables to use for seismic response prediction away from the well bore (Fig. <ov-0<). The three main modelling tools used for the modelling are 1) rock physics, 2) saturation modelling and 3) compaction/de-compaction modelling.

1) Rock physics theory is applied to obtain all necessary elastic parameters for the application of the Zoeppritz equations. The challenge is not only to predict the shear velocity, but also to account for the changes in fluid content via application of Gassmann's equations. An approach akin to the one suggested for the Ekofisk Field by Walls et al. (1998) is applied for the prediction of changes in degree of compaction.
2) Hydrocarbon saturation in North Sea Chalk is strongly affected by capillary forces due to the small scale of the pores and transition zones in the order of 50 m are not uncommon. We use the EQR and similar saturation models, which have proved robust for the prediction of saturation profiles in Danish Chalk reservoirs.
3) Compaction modelling relies on a new exponential porosity-depth trend, where abnormal fluid pressures are accounted for. This trend is based on a normal velocity-depth trend established for the North Sea Chalk. The porosity-depth trend appears to be sufficiently fine-tuned to allow fairly precise predictions of abnormal fluid pressures from observed average porosity. Based on this, the relative contribution to porosity preservation by abnormal fluid pressure and early hydrocarbon invasion may be estimated.

Based on these assumptions we find that reflectivity is correlating with porosity, acoustic impedance is more susceptible to porosity variation than to hydrocarbon saturation, and the poisson ratio may be rather sensitive to hydrocarbon saturation.
(Vejbæk et al. *this report*)

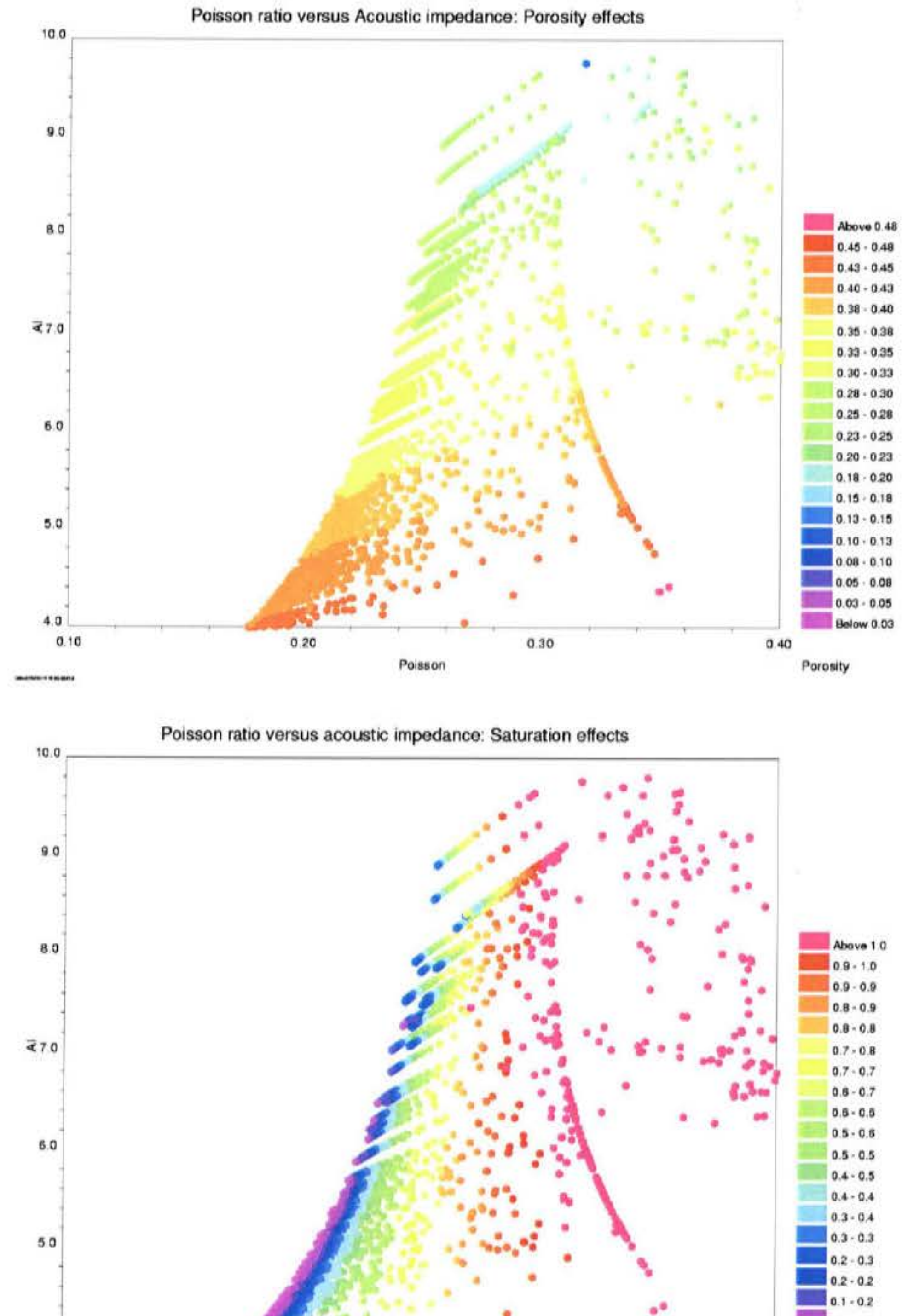

Figure 7. Poisson ratio versus acoustic impedance caused by modelled Sw changes (several free water level positions) in the Rigs-2 well. X- and Y-axis are identical in plot a and b, but colours show porosity and Sw. Points in the upper right are from outside the chalk. Note that acoustic impedance is more sensitive to porosity changes, than to saturation changes whereas the Poisson ratio is more susceptible to saturation changes.

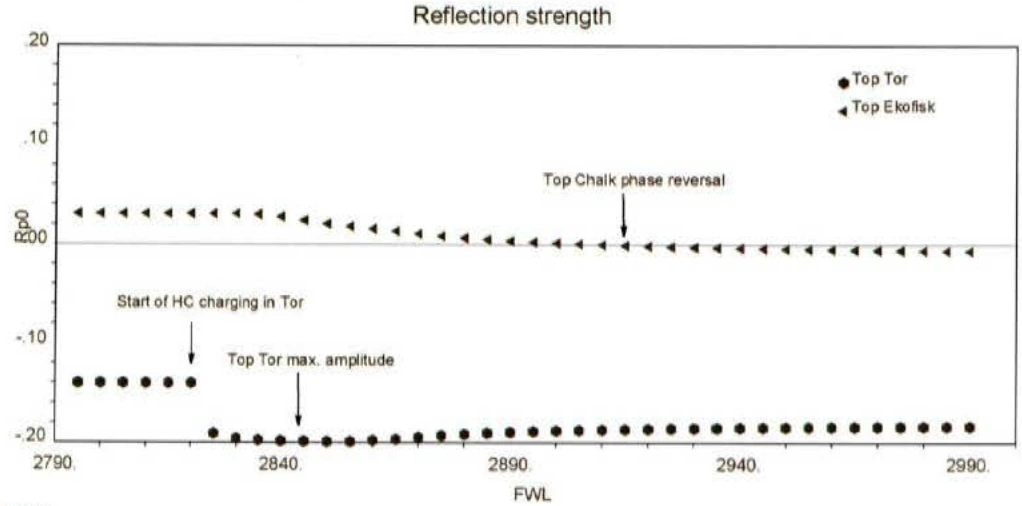

Figure 8. Reflection strength and sign of the Top Chalk and Top Tor reflectors as a function of free water level (or modelled saturation distribution). It is seen that the amplitude of this reflector increases abruptly (more negative) as oil enters the formation. As FWL deepens (saturations increases) it gains amplitude until low to moderate oil saturations. From moderate to high oil saturation it slowly decrease again. The Top Chalk reflector is also affected by increasing oil saturation. It is seen to loose amplitude with increasing oil saturation, and at saturations slightly higher than observed in the well, a reversal is predicted.

References

Bruun, A. *this report*: Seismic AVO inversion of 2D seismic data for use in the EFP 2001 Rock Physics Of Impure Chalk project using the ISIS Software Package. Ødegaard Report 02.24017.01. March 2003. 69 pp.

Fabricius, I. L., Mavko, G., Mogensen, C., & Japsen, P. 2002: Elastic moduli of chalk as a reflection of porosity, sorting, and irreducible water saturation. SEG 2002 Annual Meeting. 4 pp.

Fabricius, I. L, Høier, C., Japsen, P. & Korsbech, U. *this report*: Modeling elastic moduli of impure chalk. *To be submitted to Geophysics.*

Japsen, P., Høier, C., Rasmussen, K. B., Fabricius, I., Mavko, G., & Pedersen, J. M. 2002: Effect of fluid substitution on ultrasonic velocities in chalk plugs, South Arne field, North Sea. SEG 2002 Annual Meeting. 4 pp.

Japsen, P., A. Bruun, I. L. Fabricius, Rasmussen, R., Vejbæk, O.V., Pedersen, J. M., Mavko, G. & Mogensen, C. *this report*: Influence of porosity and pore fluid on acoustic properties of chalk: AVO-response from oil, South Arne field, North Sea. *To be submitted to Petroleum Geoscience.*

Mavko, G. & Japsen, P. *this report*: Fluid substitution in chalks: Effects of saturation scales. *To be submitted to Geophysical Prospecting.*

Vejbæk, O. V., Rasmussen, R., Japsen, P., Pedersen, J. M., Fabricius, I. L., & Marsden, M. *this report*: Modelling seismic response from North Sea Chalk reservoirs resulting from changes in burial depth and fluid saturation. *To be submitted to the Petroleum Geology Conference, London, October 2003.*

Walls, J. D., Dvorkin, J. & Smith, B. A. 1998. Modeling seismic velocity in Ekofisk Chalk. *SEG 68th annual conference*. 1016-1019.

Papers and reports enclosed

Papers

Fabricius, I. L, Høier, C., Japsen, P. & Korsbech, U. *this report*: Modeling elastic moduli of impure chalk. *To be submitted to Geophysics.*

Japsen, P., A. Bruun, I. L. Fabricius, Rasmussen, R., Vejbæk, O.V., Pedersen, J. M., Mavko, G. & Mogensen, C. *this report*: Influence of porosity and pore fluid on acoustic properties of chalk: AVO-response from oil, South Arne field, North Sea. *To be submitted to Petroleum Geoscience.*

Mavko, G. & Japsen, P. *this report*: Fluid substitution in chalks: Effects of saturation scales. *To be submitted to Geophysical Prospecting.*

Vejbæk, O. V., Rasmussen, R., Japsen, P., Pedersen, J. M., Fabricius, I. L., & Marsden, M. *this report*: Modelling seismic response from North Sea Chalk reservoirs resulting from changes in burial depth and fluid saturation. *To be submitted to the Petroleum Geology Conference, London, October 2003.*

Abstracts

Fabricius, I. L., Mavko, G., Mogensen, C., & Japsen, P. 2002: Elastic moduli of chalk as a reflection of porosity, sorting, and irreducible water saturation. SEG 2002 Annual Meeting. 4 pp.

Fabricius, I.L., Høier, C. & Korsbech, U. accepted: Modeling elastic moduli of Danian North Sea chalk from petrographic data. EAGE 65th conference, Stavanger June 2003, 4 pp.

Japsen, P., Høier, C., Rasmussen, K. B., Fabricius, I., Mavko, G., & Pedersen, J. M. 2002: Effect of fluid substitution on ultrasonic velocities in chalk plugs, South Arne field, North Sea. SEG 2002 Annual Meeting. 4 pp.

Vejbæk, O.V., Rasmussen, R., Japsen, P., Pedersen, J.M. & Marsden, G. accepted: Modelling seismic response from North Sea Chalk reservoirs resulting from changes in burial depth and fluid saturation. Petroleum Geology Conference, London, October 2003. 1 p.

Reports and technical notes

DTU E&R report - Fabricius, I. & Høier, C. 2002: Selection of samples. EFP-01 Rock Physics of Impure Chalk, revised January 2002, 12 pp.

DTU E&R report - Fabricius, I. L. in prep: Sample characterization report, EFP-01 Rock Physics of Impure Chalk.

GEUS rapport 2002/23 - Høier, C. 2002: Special core analysis for the rock physics project (EFP-2001), 26 pp.

Ødegaard Report 02.24017.01 - Bruun, A. 2003: Seismic AVO inversion of 2D seismic data for use in the EFP 2001 Rock Physics Of Impure Chalk project using the ISIS Software Package. March 2003, 69 pp.

Ødegaard Report 01.1031 - Mogensen, C. & Fabricius, I. 2002: EFP 2001: Quality control of well log data from the South Arne field. January 2002, 18 pp.

TN 2003/1 - Mavko, G. 2003: Some Comments on upscaling rock physics relations in North Sea chalks. EFP-01 Rock Physics of Impure Chalk – Technical Note, March 2003, 7 pp.

TN 2002/4 - Japsen, P. 2002: Extrapolation of the modified upper Hashin-Shtrikman model of Walls et al. (1998). EFP-01 Rock Physics of Impure Chalk – Technical Note, November 2002, 3 pp.

TN 2002/3 - Japsen, P. & Rasmussen, R. 2002: Compilation ultrasonic data for chalk plugs from the South Arne field, Tor And Ekofisk formations. EFP-01 Rock Physics of Impure Chalk – Technical Note, November 2002, 23 pp.

TN 2002/2 - Rasmussen, K. B., Japsen, P. Mavko, G. 2002: Discussion on the elastic properties of wet and dry chalk samples. EFP-01 Rock Physics of Impure Chalk – Technical Note, January 2002, 8 pp.

TN 2002/1 - Japsen, P. 2002: Analysis of acoustic well log data from the South Arne field. EFP-01 Rock Physics of Impure Chalk – Technical Note, December 2002, March 2003, 29 pp.

TN 2001/2 - Mavko, G. 2001: Some thoughts on upscaling rock physics relations. EFP-01 Rock Physics of Impure Chalk – Technical Note, October 2001, 1 p.

TN 2001/1 - Japsen, P. 2001: Well data summary, South Arne field. EFP-01 Rock Physics of Impure Chalk – Technical Note, May 2001, 25 pp.

Intended for submission to Geophysics

MODELING ELASTIC MODULI OF IMPURE CHALK

by Ida L. Fabricius*, Christian Høier**, Peter Japsen**, and Uffe Korsbech*

*DTU, **GEUS

ABSTRACT

In impure chalk the elastic moduli are not only controlled by porosity, but also by cementation resulting in relatively large moduli and by admixtures of clay and fine silica which results in relatively small moduli. Based on a concept of framebuilding contra suspended solids, we model P-wave and S-wave moduli of dry and wet plug samples by an effective medium model using chemical, mineralogical and textural input. We use a Modified Upper Hashin Shtrikman model assuming a critical porosity of 70%. The textural and mineralogical data may potentially be assessed from logging data on spectral gamma radiation, density, acoustic velocity and water saturations in a hydrocarbon zone.

The studied chalk was interpreted as follows: In chalk of reservoir quality, elastic moduli are predictable. The solid phase has roughly uniform composition, and as porosity decreases from 45% to 25%, IF-value increases from 0.5 to 0.6. At intermediate porosity (25% - 18%) IF-value varies between 0.5 and 0.9. Samples with high IF have pore-filling cementation, whereas samples with low IF-value have high amounts of suspended submicron-size quartz in the pore space. The samples with low porosity (13% - 16%) have relatively low IF-value (around 0.6) and are packed with pore-filling smectite.

INTRODUCTION

We have succeeded in building an effective medium model for impure chalk based on petrographic data. This is not a straightforward task, because the relationship between porosity and elastic moduli of carbonates depends on several factors. According to Marion and Jizba (1997) these factors are mineralogy, pore-shape and fluid type.

The problem of fluid type is in our case probably minor because Gassmanns relations apparently may be used even for ultrasonic data on chalk (Røgen at al. in rev.). The problem of pore shape is related to porosity type. In chalk the porosity is predominantly intergranular. In high-porosity chalk, pores are ill-defined, and may be best described as the irregular continuous space around the irregular but well defined particles. When chalk is subjected to cementation, pores become more and more regular and well defined, while particles fuse to a progressively stiffer frame. During cementation the chalk will thus approach the spherical pore model of an Upper Hashin Shtrikman Bound (Hashin and Shtrikman, 1963).

The question of mineralogy may in our case be simplified to a question of proportion between the dominant low-Mg calcite, quartz, kaolinite, and smectite.

This does not solve the problem, however. Even small amounts of clay may significantly reduce elastic moduli of sandstone (Han et al., 1986), so that the texture (the spatial organization of mineral particles) has significant influence. In a recent study, Avseth et al. (2000) have shown how texture and degree of cementation both control the elastic moduli of sandstone.

In the case of impure chalk we must then find out how the impurities are arranged, are they floating freely in the pore-space or are they part of the solid frame? As we will show below, they may be either. We also need a means of assessing degree of cementation, and thus stiffness of the chalk frame. In order to solve the problem we apply the concept of iso-frame (IF-value), (Fabricius, 2002) which defines to which extent the chalk has achieved a stiff structure with spherical pores as defined by a modified Upper Hashin Shtrikman model (Nur et al., 1998).

We study of the relationship between chalk composition and elastic moduli in 24 plug samples of Danian chalk from the South Arne field in the Danish North Sea (Mackertich and Goulding, 1999). We furthermore demonstrate the use of wire-line logging data to assess composition and degree of cementation.

METHODS

Velocity data

P- and S-wave moduli were measured on dry and water saturated 1½ inch plug samples (Table 1, Figure 1). Samples were dried at 110°C and left to equilibrate at room conditions to constant humidity before dry data were recorded; for smectite bearing samples this resulted in up to 34% water saturation. In order to obtain wet data, smectite poor samples were saturated with calcite-equilibrated tap water. Smectite rich samples were saturated with synthetic formation brine, but contains up to 8% atmospheric air, due to low permeability (Table 1). The ultrasonic measurements were done at a hydrostatic confining pressure of 75 bar in accordance with the procedure described in Røgen et al. (in rev.).

Other physical core data

For all plugs, He-porosity and gas permeability, along with grain density were measured by standard methods.

In order to correlate core data to gamma ray-logs, the concentrations of U, Th and K were measured on powdered samples by a NaI-crystal gamma spectrometer; and in order to interpret the water saturation data, the specific surface of the samples were measured by N_2 adsorption (BET).

Textural and mineralogical data

We estimated the mineralogical and textural composition of each sample. The mineralogical composition was derived from X-ray diffractograms of bulk sample and insoluble residue, carbonate content by titration, Mg, Al, Si, K, Ca, Fe, and Ba by Atomic Adsorption Spectrophotometric analysis of filtrate as well as remanence, P by spectrophotometry (Dr. Lange), and S by combustion in LECO-oven.

Mineralogical and textural data were derived from thin section petrography, backscatter electron microscopy, qualitative energy dispersive microprobe analysis, and petrographic image analysis of electron micrographs at two magnifications (Figure 2). Large grains (more than 2 microns in cross section), and large pores (more than 0.5 microns in cross section) were determined by filtering based on the method of Borre (1998). Specific perimeter of the calcite-pore interface was determined according to the method of Borre et al. (1997). Image analysis included assessment of the amount of silicates in suspension in the pores, as well as assessment of the amount of silicate grains in the solid frame.

Effective medium model

We constructed an effective medium model for the elastic moduli of the samples based on mineralogical and textural data. Large silicate grains, as well as large calcite grains and calcite cement were considered part of the solid frame, whereas small silicate-particles were considered to be suspended in the pore fluid. We modeled the porosity to be spherical holes with part of the solid phase suspended in the pore fluid (air and water), and calculated to which extent the small calcite particles may be modeled as being a part of the solid frame (IF-value for the fine-grained calcite), and to which extent they may be modeled as being in suspension in order to fit dry P-wave modulus data (model (1)). Together with the fraction of large particles this will define the total fraction of solid in the frame or iso-frame (IF) value of a sample (Fabricius, 2002). In order to obtain an IF-value based on petrographic data alone, we correlated the IF-value for the fine-grained calcite to the specific perimeter of the fine-grained calcite as measured by petrographic image analysis. We may now turn around and assess the IF value of the fine-grained calcite from image analysis data and calculate the IF for the total sample from mineralogical and petrographic data alone (model (2), Figure 3, 4).

In order to asses to which extend the IF value applies more generally, the IF-s of model (1) and (2) were used to calculate wet P-wave moduli, as well as S-wave moduli. These predictions fit reasonably well to the measured data (Figure 1).

Model (2) thus involves the following steps when porosity is known: 1) from mineralogical and petrographic analysis assessing amount of large calcite (microfossils and carbonate cement), large silicates (quartz, kaolinite, and feldspar clasts), suspended silicates (quartz, kaolinite, and smectite), as well as specific interface between fine-grained calcite and pores; 2) calculate IF for fine-grained calcite from specific interface, together with large grains this will also define IF for the total sample; 3) calculate elastic modulus for the suspension. For dry samples air, water and suspended solids were mixed according to a homogenous Reuss model. For wet samples, water and suspended solids were mixed according to Reuss model, whereas the air should be mixed with the fluid in accordance with a patchy Voigt model (Figure 5); 4) mixing this suspension with the frame building minerals according to an Upper Hashin Shtrikman bound (Hashin and Shtrikman, 1963) as generalized by Berryman, and by modifying the bound under assumption of a critical porosity (Nur et al., 1998, citations in Mavko et al., 1998). A critical porosity of 70% was in the present case chosen in accordance with ODP data (Fabricius, 2002).

Log-interpretation

The concept of IF-value allows us to model degree of cementation from logging data, alongside a more conventional interpretation of bulk composition (Figure 6).

Solid composition was estimated from spectral gamma-ray Th data and from water saturation data. The Th-log was chosen because it correlates well with core-sample Th-data. We did not use the K and U signal of the spectral gamma-ray log as well as the natural gamma ray log because these logs in the present case have little character and do not correlate with gamma-spectral core-data. The core-sample Th-data correlates roughly to total clay content and to non-carbonate fraction of the core samples.

Fluid saturations were determined by the Archie method by assuming default petrophysical constants for carbonate: $a = 1$, $m = 2$, and $n = 1$. Hydrocarbon density 0.633 g/cm^3, brine density: 1.054 g/cm^3, and brine resistivity of 0.0225 Ohmm and 0.0260 Ohmm respectively for Rigs-1 and Rigs-2 (J. Jensenius pers. comm.). In the presence of more detailed knowledge of the relationship between chalk composition and petrophysical parameters, these may be adjusted accordingly.

For the studied wells, the water saturation gives information on chalk texture because almost the entire logged chalk interval is in the zone of irreducible water saturation. In this case we may assume that in the water wet chalk, the water covers the particle surfaces and rests at particle contacts (Fabricius et al. 2002). The water saturation was recalculated to water volume pr. solid volume, and correlated to specific surface by BET (also recalculated to surface area pr. solid volume). BET correlates to the content of smectite in core samples.

We may thus estimate content of oil, water, smectite, total clay and insoluble residue. In accordance with the petrographic data we assume that smectite is totally in suspension, whereas the remaining clay and insoluble residue are 50% in suspension and 50% in the frame. We may now determine the IF value via adjusting the proportion of calcite in the frame to fit P-wave modulus calculated from density and sonic logging data.

In Rigs-1 water saturations are relatively high, and we may use the logging data directly. In Rigs-2 water saturations are low and invasion may severely affect the sonic signal (Gommesen et al. 2002). Therefore, the sonic velocity of the virgin zone was modeled from porosity and fluid saturation data together with a relationship between porosity and elastic moduli based on core data and in accordance with the relationship for logging data of Walls et al. (1998).

RESULTS

Core data

Elastic moduli calculated from ultrasonic velocities in the chalk core samples may now be given a textural interpretation (Figure 1, 4, Table 1).

In the porosity interval from 45% to 25% elastic moduli show a steady increase. The solid phase does not vary much in composition, but the IF-value increases gradually from around 0.5 to around 0.6. The frame building part of the solid contains a low to moderate amount of large grains of silicates and partially cemented calcitic microfossils (Figure 2a); the suspended part of the solid includes apparently authigenic submicron-size quartz, smectite-illite, and kaolinite.

In the porosity interval from 25% to 18% elastic moduli are more variable but tend to be high. IF value varies between 0.5 and 0.9 with an average around 0.7. Samples with high elastic moduli (and high IF) are characterized by a microfossil-rich texture (Figure 2b) and pore-filling cementation (Figure 2c). Samples with low elastic moduli (and low IF) in this porosity interval are characterized by high amounts of suspended apparently authigenic submicron-size quartz in the pore space (Figure 2f).

For low porosity (13% - 16%), elastic moduli tend to be lower than would be expected by extrapolating the trend from high-porosity chalk; IF is around 0.6. These samples all contain pore-filling, possibly allochtoneous smectite (Figure 2d), accompanied by large kaolinite clasts (Figure 2e). Smectite rich samples have high specific surface as measured by BET.

Logging data

We may now apply the IF model to log interpretation of the chalk interval of Rigs-1 and Rigs-2 (Figure 6).

In both wells the porosity varies considerably, but in general porosity is higher in Rigs-2 than in Rigs 1. The lower porosities in Rigs 1 are accompanied by higher proportions of calcite in the solid frame. The proportion of calcite in the solid frame may be interpreted as degree of cementation, so that Rigs 1 in general appear more cemented than Rigs 2. In clay rich intervals the porosity may be low without the proportion of calcite in frame (i.e. degree of cementation) is correspondingly high.

DISCUSSION AND CONCLUSIONS

We found that elastic P-wave and S-wave moduli calculated from ultrasonic core samples of impure chalk can be modeled from the mineralogical and textural composition of the solid phase as well as the pore fluid composition. The model is the same for S- and P-waves for dry as well as wet samples (Figure 1).

In accordance with petrographic data, a part of the solid is modeled as suspended in the pore fluids. This suspension is then modeled as the soft component in a stiff frame composed of the remaining solid according to a Modified Upper Hashin Shtrikman bound under assumption of a critical porosity of 70%.

Core data

In order to do this, we applied the concept of IF-value which describes to which extent the solid of the sample may be regarded as a frame with spherical pores. In line with this concept, Anselmetti and Eberli (1997) found that carbonate samples with vuggy porosity tend to be stiffer than carbonate samples with other types of porosity. We see IF as a measure of degree of cementation and in accordance with this concept, samples with high IF indeed were seen to be heavily cemented and to have high elastic moduli.

In the studied samples, part of the calcite is modeled as being in suspension although it physically is attached to other particles. A link between the actual pore-shape and the IF model is the specific perimeter of the calcite-pore interface as measured by petrographic image analysis of electron micrographs.

The impurities of the chalk include quartz, kaolinte, and smectite. Quartz and kaolinite occur partly as solid clasts which we consider as part of the frame, partly as suspended pore-filling sub-micron-size particles. The ultra fine-grained quartz is apparently authigenic and may be sourced from dissolved opaline fossils. That these fossils have existed is indicated by the presence of molds. Smectite also occur in two textural ways. High-porosity samples may contain apparently authigenic smectite-illite, whereas low-porosity samples may be packed with apparently allochtoneous smectite. These low porosity smectite rich samples have relatively low IF and relatively low elastic moduli.

Logging data

Sonic logging data have been widely used as an indicator of porosity type, e.g. the velocity–deviation log of Anselmett and Eberli (1999). In the studied chalk the porosity is mainly of intergranular type, although intrafossil porosity and moldic porosity occur frequently but in minor amounts.

Via the IF concept we suggest that the sonic log may be used as an indicator of cementation. This requires that we first assess the mineralogical composition and fluid saturations of the chalk, then estimate to which extent the non-carbonates are in the solid frame and to which extend in suspension (in the present case this was done from studies of core samples), and finally that we by iteration find which IF's fit the elastic modulus-log.

The mineralogical composition was in this case assessed from the spectral gamma Th-log and from the water saturation. The Th log was used for a rough estimate of total clay as well as for total non-carbonate fraction. In the present case the integral gamma and spectral U and K-logs proved of little use, but this may depend logging equipment and on choice of drilling mud. The use of water-saturation log as a smectite indicator is only valid because we could assume that the water saturation is irreducible. In the absence of these specific smectite data, we might have overcome the problem by adjusting the proportion of the total clay that we assume are in suspension.

ACKNOWLEDGEMENTS

Financial support for this study is acknowledged from a Danish Energy Research Program EFP-2001 grant, as well as from Amerada Hess A/S and DONG A/S. For technical support Sinh Hy Nguyen and Hector Diaz, DTU are acknowledged.

REFERENCES

Anselmetti, F. S., and Eberli, G. P., 1997, Sonic velocity in carbonate sediments and rocks, *in* Palaz, I., and Marfurt, K. J., Eds., Carbonate Seismology: Society of Exploration Geophysicists, 53-74.

Anselmetti, F. S., and Eberli, G. P., 1999, The velocity-deviation log: a tool to predict pore type and permeability trends in carbonate drill holes from sonic and porosity or density logs: AAPG Bulletin, **83**, No. 3, 450-466.

Avseth, P., Dvorkin, J., Mavko, G., and Rykkje, J., 2000, Rock physics diagnostic of North Sea sands: link between microstructure and seismic properties: Geophysical Research Letters, **27**, No. 17, 2761-2764.

Borre, M., 1998, Ultrasonic velocity of North Sea Chalk – predicting saturated data from dry, *in* Middleton, M. F., Ed., Nordic Petroleum Series IV, Research in Petroleum Technology: Nordisk Energi Forskningsprogram, 71-98.

Borre, M., Lind, I., and Mortensen, J., 1997, Specific surface as a measure of Burial Diagenesis of Chalk: Zbl. Geol. Paläont. Teil 1, **1995**, 1071-1078.

Fabricius, I. L., 2002, Porosity Loss in Chalk Facies Sediments by Physical Compaction or by Cementation – Consequences for P-wave Modulus: AAPG Ann. Mtg, 2002, Extended Abstracts CD-ROM.

Fabricius, I. L., Mavko, G., Mogensen, C., and Japsen, P., 2002, Elastic Moduli of Chalk as a reflection of porosity, sorting and irreducible water saturation: Soc. Expl. Geophys. Int. Exp. and 72th Ann. Mtg., Paper 445, CD-ROM.

Gommesen, L., Mavko, G., Mukerji, T., Fabricius, I. L. 2002, Fluid Substitution for North Sea Chalk Logging Data: Soc. Expl. Geophys. Int. Exp. and 72th Ann. Mtg., Paper 410, CD-ROM.

Han, D.-h., Nur, A., and Morgan, D., 1986, Effects of porosity and clay content on wave velocities in sandstone: Geophysics, **51**, No. 11, 2093-2107.

Hashin, Z., and Shtrikman, S., 1963, A variational approach to the elastic behavior of multiphase materials: J. Mech. Phys. Solids, **11**, No. 2, 127-140.

Mackertich, D. S., and Goulding, D. R. G., 1999, Exploration and appraisal of the South Arne field, Danish North Sea, *in* Fleet, A. J., and Boldy, S. A. R., Eds., Petroleum Geology of Northwest Europe: Proc. 5th Conf. Geological Society, London, 959-974.

Marion, D., and Jizba, D., 1997, Acoustic properties of carbonate rocks: use in quantitative interpretation of sonic and seismic measurements, *in* Palaz, I., and Marfurt, K. J., Eds., Carbonate Seismology: Society of Exploration Geophysicists, 75-93.

Mavko, G., Mukerji, T., and Dvorkin, J., 1998, The Rock Physics Handbook: Cambridge University Press.

Nur, A., Mavko, G., Dvorkin, J., and Galmudi, D., 1998, Critical porosity: A Key to relating Physical Properties to Porosity in Rocks: The Leading Edge **17**, No. 3, 357-362.

Røgen, B., Fabricius, I. L., Japsen, P., Høier, C., Mavko, G., and Pedersen, J. M., in rev, Ultrasonic velocities of North Sea chalk samples – influence of porosity, fluid content and texture.

Walls, J. D., Dvorkin, J., and Smith, B. A., 1998, Modeling seismic velocity in Ekofisk chalk.: Proc. Soc. Expl. Geophys. Ann. Conf. and Exh., 1016-1019.

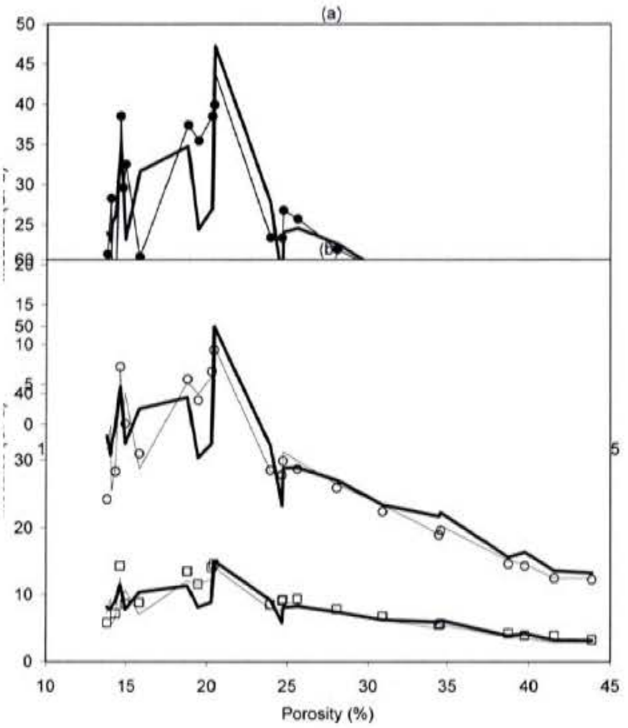

FIG. 1. Elastic modulus data and elastic models. Circles denote P-wave modulus data, squares denote S-wave modulus data. Thin lines: model (1) based on dry P-wave and density data. Thick lines: model (2) based on image analysis data calibrated to model (1). (a) Dry samples (b) Water saturated samples. Model (1) fits the wet P-wave modulus data, whereas especially the dry S-wave moduli tend to be higher than predicted. Model (2) fits less well but has the advantage of being based on petrographic data.

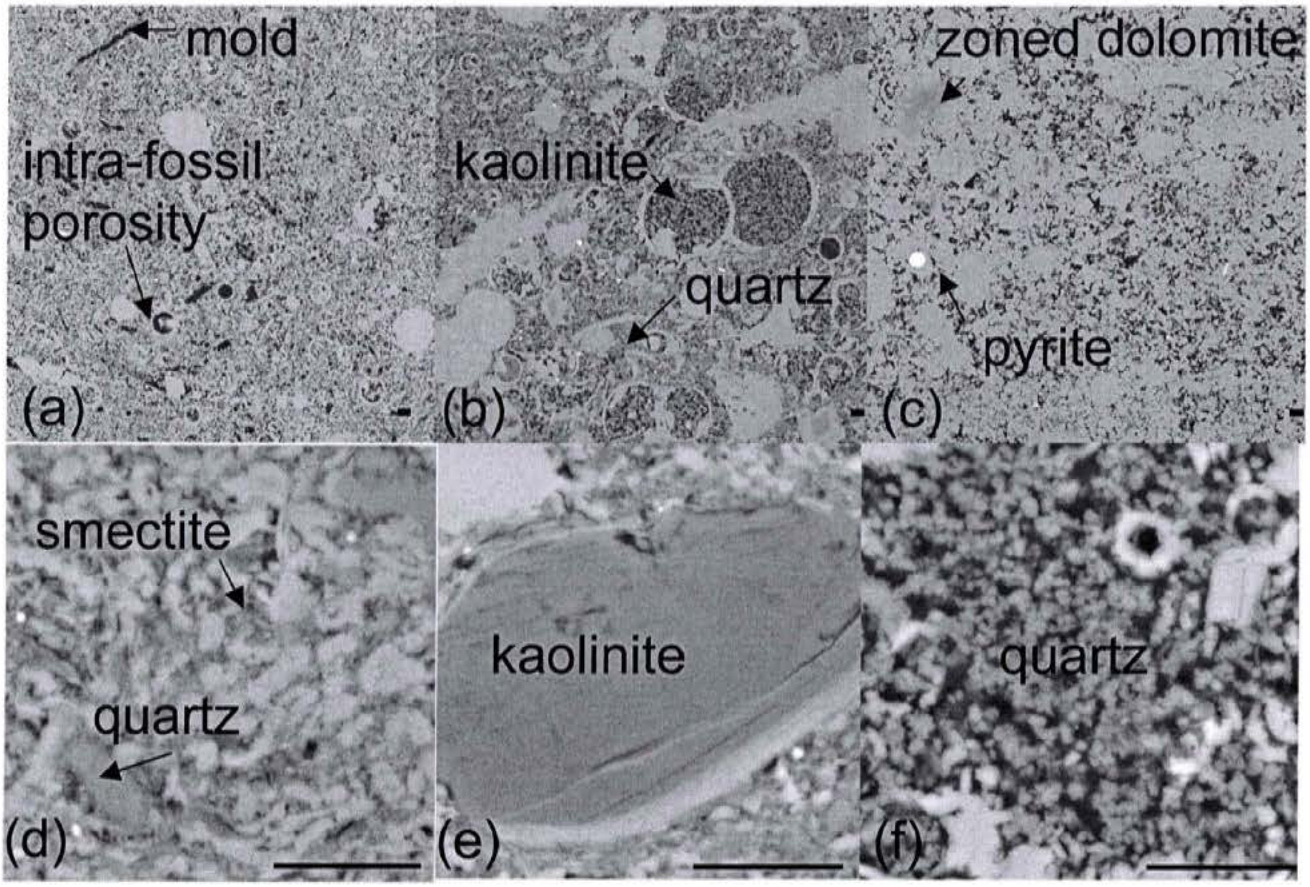

FIG. 2. Backscatter electron micrographs of epoxy-impregnated and polished samples. Black indicates pore-space, various shades of grey reflect densities of the minerals. The black bars measure 10 microns. (a) Rigs 1, 9250.39 ft MD, chalk mudstone with 30.9% porosity. Of the bulk volume 4.8% is large calcite, 4.4% is large intra-fossil porosity and molds. Model (1) and (2) both indicate an IF value of 0.6. (b) Rigs 2, 2824.00 m MD, chalk wackestone with 24.7% porosity. Of the bulk volume 16.2% is large calcite grains and cement, 4.4% is large intra-fossil porosity, 26.2% is disperse sub-micron size pore-filling quartz, and 1.1% is disperse sub-micron size pore-filling kaolinite. Model (1) indicates an IF value of 0.6, model (2) an IF value of 0.5. (c) Rigs 1, 9287.32 ft MD, white chalk wackestone with 20.4% porosity. Of the bulk volume 53.9% is large calcite grains and cement, 9.3% is large intergranular pore space. The calcite cement covers zoned dolomite/ankerite crystals. Model (1) and (2) both indicate an IF value of 0.9. (d) Rigs 1, 9111 ft MD, chalk mudstone with 13.8% porosity. Of the bulk volume 6.1% is clasts of quartz and albite, 5.6% is pore filling smectite. Model (1) indicates an IF value of 0.5, model (2) an IF value of 0.6. (e) Rigs 1, 9114 ft MD. Kaolinite clasts constitute 6.9% of the bulk volume in the chalk mudstone with 14.1% porosity. (f) Rigs 1, 9153.20 ft MD. Disperse sub-micron size pore-filling quartz constitute 9.2% of the bulk volume in the chalk mudstone with 19.5% porosity.

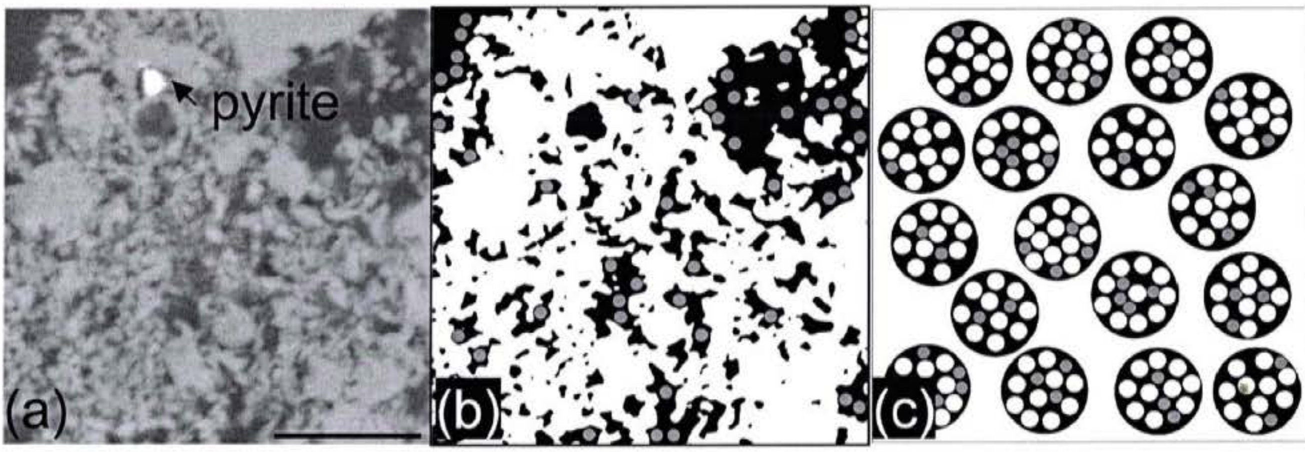

FIG. 3. Iso-frame (IF) model for chalk. (a) Backscatter electron micrograph of the epoxy-impregnated and polished sample Rigs 1, 9210.0 ft MD, chalk mudstone with 28.1% porosity. The black bar measures 10 microns. Of the bulk volume 5.9% is fine grained silicates. (b) By petrographic image analysis the fine-grained calcite (including a pyrite crystal) is marked as white and the pore space as black. The fine grained silicates are symbolized by grey circles. The specific perimeter of the white phase is calculated to be 2.9 micron^{-1}. From correlation with elastic data, this specific perimeter corresponds to an IF value of 0.65 for the fine-grained calcite. When taking large pores and grains (not visible at this magnification) and fine-grained silicates into account, we obtain an IF value of 0.6 for the sample. (c) Model: of the solid phase 70% is forming a frame with spherical pores. The remaining solids are suspended in the fluid within the pores.

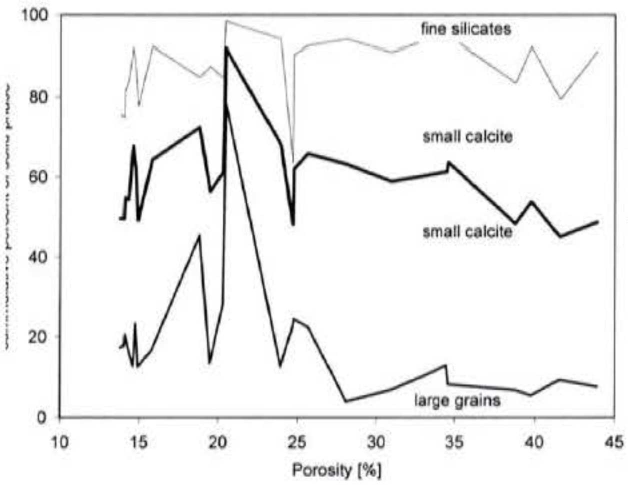

FIG. 4. Composition of solid phase of chalk samples. The thick line denotes the IF value of each sample. The part of the solid phase modeled as a solid frame with spherical pores is below the thick line. The part of the solid modeled as being in suspension is above the thick line. Large grains include calcitic microfossils, as well as clasts of quartz, feldspar and kaolinite. Fine silicates include (apparently athigenic) smectite, kaolinite and quartz.

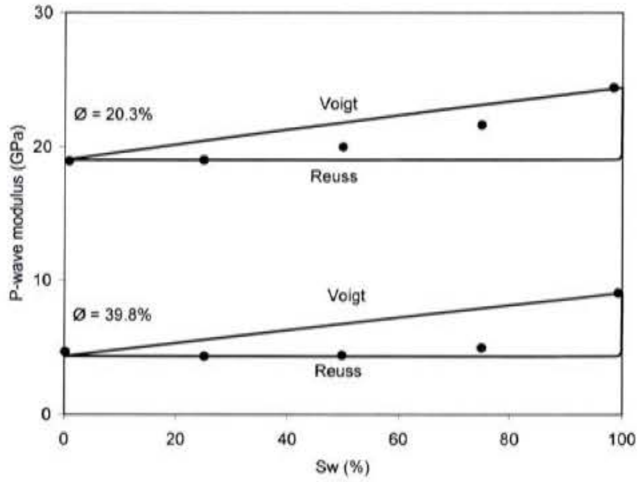

FIG. 5. P-wave modulus of partially water saturated samples compared to modeled moduli. The two models assume water and air to be mixed patchily according to an iso-strain (Voigt) respectively a homogeneous iso-stress (Reuss) model. The modeled data were calculated using Gassmanns equations. The low Sw end point was chosen as a "nearly dry rock" based on extrapolation of data from Sw = 25%. The low Sw end point matches the data for the dry 20.3% porosity sample, whereas the 39.8% porosity sample may stiffen due to superdry-effect at Sw near 0.

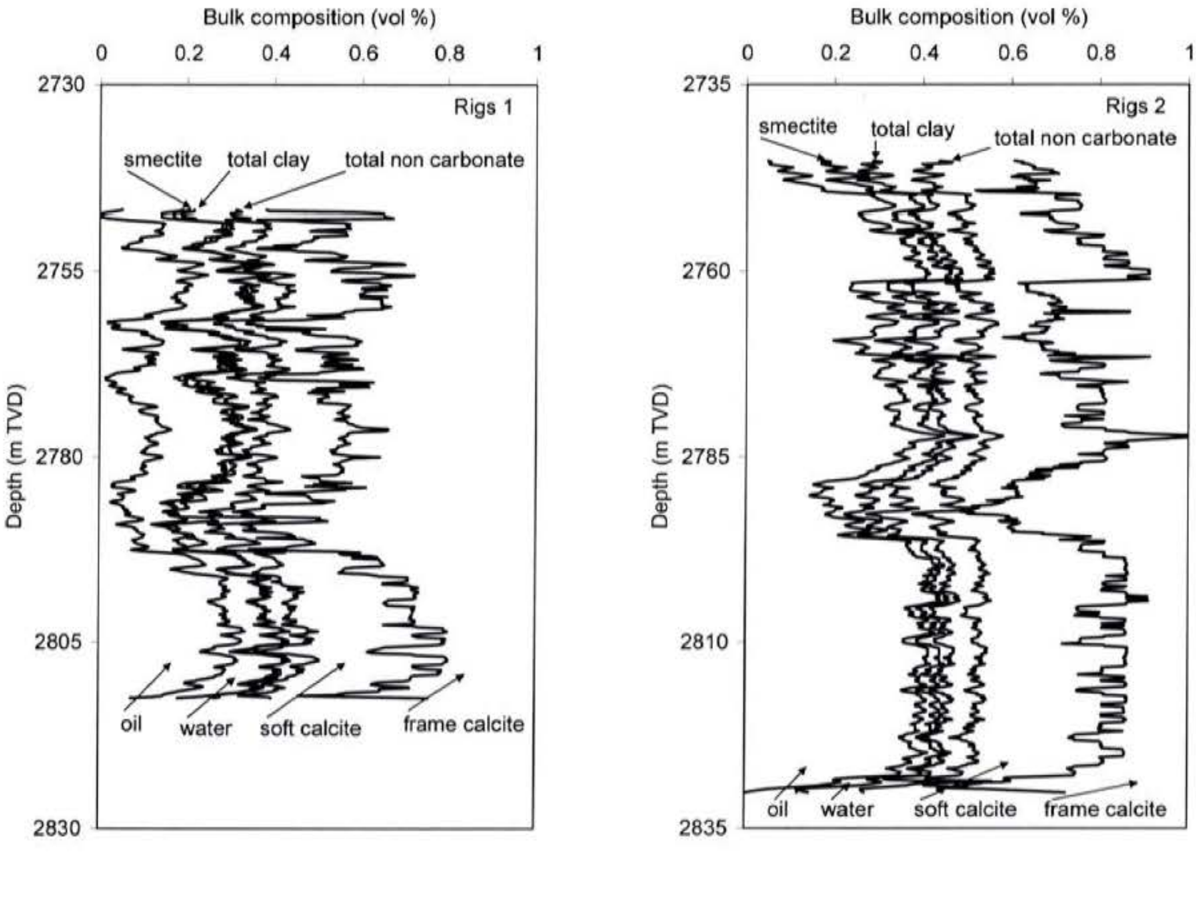

FIG. 6. Bulk composition of chalk interval as interpreted from logging data. The well Rigs 1 has higher water content and smectite content than Rigs 2, where the smectite log disappears in the curve separating water and total clay. Rigs 1 apparently is more cemented as indicated by a higher proportion of the calcite being part of the solid frame.

Core depth	Ø	k	BET	ρ_{grain}	ρ_{fluid}	Dry samples S_w	Dry samples v_P	Dry samples v_S	Wet samples S_w	Wet samples v_P	Wet samples v_S	Composition of solid phase: Non-carb.	Total clay	Smectite	Susp. Quartz	Susp. Kaol.	Silicate gr.	Large Calcite	(1) IF	(2) IF
	%	mD	m^2/g	g/cm^3	g/ml	%	m/s	m/s	%	m/s	m/s	%	%	%	%	%	%	%		
Rigs 1 ft																				
9111	13.8	0.7	12.2	2.71	1.073	6.8	3020	2192	92.2	3132	1536	35.3	16.0	7.2	8.7	6.9	6.2	10.2	0.5	0.5
9114	14.1	0.5	11.6	2.71	0.998	30.4	2659	1868				34.7	15.9	6.7	11.1	0.0	11.0	8.2	0.4	0.5
9114-h	14.0	3.1	12.9	2.71	0.998	34.1	3452	2155				41.4	21.2	8.5	9.2	6.4	9.3	7.2	0.6	0.5
9116-h	14.9	15.0	10.2	2.70	1.073	11.8	3746	2375	102.6	3791	1871	32.6	13.5	5.8	9.6	5.8	5.2	6.8	0.6	0.5
9117	14.3	0.4	10.2	2.71	1.073	12.3		2004	103.0	3378	1702	30.8	14.4	6.0	4.5	5.5	9.3	6.4	0.4	0.5
9117-h	14.8	0.7	10.9	2.73	1.073	11.8	3556	2256				31.7	14.6	6.0	5.6	0.4	12.6	8.8	0.6	0.6
9138	15.8	0.1	7.5	2.70	0.998	7.7	3029	2137	102.4	3565	1904	20.0	9.3	3.3*	3.2	1.4	7.0	9.1	0.5	0.6
9153-h	19.5	0.4	5.8	2.71	0.998	3.6	4024	2486	99.0	4051	2210	23.2	4.1	1.4*	10.6	0.0	6.0	6.9	0.7	0.6
9154	24.7	0.2	3.2	2.71	0.998	1.9	3620	2250	97.9	3619	2015	19.8	2.3	0.8*	8.5	0.0	6.4	17.7	0.7	0.6
9176	34.5	0.8	2.5	2.71	0.998	0.5	2893	1844	98.8	2993	1615	8.8	1.5	0.4*	3.3	0.5	2.5	10.3	0.5	0.6
9193	14.6	0.0	3.3	2.71	0.998	5.0	4070	2590	95.2	4230	2412	21.2	3.7	0.7*	7.1	0.0	9.0	3.0	0.7	0.7
9210	28.1	0.3	4.0	2.71	0.998	1.7	3350	2124	98.3	3413	1879	9.2	3.0	0.6*	3.7	1.6	1.0	2.9	0.6	0.6
9216	23.9	0.2	4.5	2.72	0.998	2.0	3361	2176	97.4	3521	1925	17.5	3.2	0.8*	5.1	0.0	8.2	3.9	0.6	0.7
9230	34.6	0.6	2.7	2.69	0.998	0.3	3035	1890	99.6	3051	1640	12.3	1.6	0.4*	4.0	0.7	4.8	3.2	0.6	0.6
9250	30.9	0.6	2.6	2.70	0.998	0.6	3187	1972	97.8	3213	1765	11.0	1.6	0.6*	7.5	0.6	0.0	6.9	0.6	0.6
9274	18.8	0.1	2.5	2.71	0.998	2.0	4117	2529	99.8	4197	2378	26.2	4.2	1.6*	13.0	0.0	7.2	37.8	0.8	0.7
9287	20.4	0.3	2.5	2.72	0.998	0.9	4296	2597	97.7	4437	2486	14.1	4.7	1.7*	0.0	0.0	10.1	67.7	0.9	0.9
Rigs 2 m																				
2800	41.6	1.9	3.2	2.70	0.998	0.5	2304	1622	98.8	2506	1394	23.6	5.1	0.6*	15.3	3.6	0.0	9.3	0.4	0.5
2802	25.6	0.1	4.0	2.70	0.998	0.9	3576	2264	93.4	3574	2045	23.9	5.6	0.7*	6.5	0.0	12.0	9.7	0.7	0.7
2806	38.7	1.3	3.0	2.69	0.998	0.4	2578	1702	99.4	2680	1447	19.7	2.7	0.4*	13.8	1.6	0.2	6.6	0.5	0.5
2814	39.8	1.4	2.9	2.70	0.998	0.2	2546	1645	99.3	2662	1396	10.8	2.5	0.3*	5.9	1.2	1.1	4.3	0.5	0.5
2818	43.9	3.2	2.7	2.71	0.998	0.2	2386	1541	98.4	2506	1293	11.7	2.3	0.3*	7.1	1.2	0.5	7.2	0.4	0.5
2824	24.7	0.2	3.7	2.67	0.998	0.3	3408	2232	99.8	3509	2010	42.1	4.1	0.7*	30.9	1.3	1.0	21.5	0.6	0.5
2826	20.3	0.2	1.7	2.70	0.998	0.8	4230	2611	98.5	4291	2452	21.7	1.1	0.2*	14.5	0.0	3.3	24.8	0.8	0.6

TABLE. 1. Core plug data. –h indicates a horizontal sample, Ø is He-porosity, k is gas permeability, BET specific surface by N_2 adsorption, ρ is density, S_w is water saturation, v_P and v_S are *P*- and *S*-wave ultrasonic (700 kHz) velocities measured at a hydrostatic confining stress of 75 bar. Experimental errors for v_P is c. ± 25 m/s for v_S c. ±15 m/s. Composition of solid phase is interpreted from X-ray diffraction, chemical analysis, image analysis of backscatter electron micrographs and qualitative energy-dispersive microprobe analysis. IF's are from model (1) and (2). *smectite-illite.

Intended for submission to Petroleum Geoscience

Influence of porosity and pore fluid on acoustic properties of chalk: AVO-response from oil, South Arne field, North Sea

Peter Japsen[1], Anders Bruun[2], Ida L. Fabricius[3], Rasmus Rasmussen[1], Ole V. Vejbæk[1], Jacob Mørch Pedersen[2], Gary Mavko [4] & Christian Mogensen[2]

[1] Geological Survey of Denmark and Greenland (GEUS), [2] Ødegaard A/S, [3] Technical University of Denmark (DTU), [4] Stanford University

Abstract

We have found AVO-inversion to provide direct evidence for presence of light oil in the high-porous chalk of the South Arne field. We estimated the elastic properties of chalk at three different scales on the South Arne field, North Sea, by analysing ultrasonic core data, downhole log-readings and results of AVO-inversion based on near- and far-offset stack seismic data (Amplitude Versus Offset). We find that the velocity-porosity relation of the plug data are in agreement with a modified upper Hashin-Shtrikman model established for chalk from the Ekofisk field and due to higher porosities in the South Arne field we extend the range of the model to 45% porosity. In pure chalk intervals, this model furthermore, matches log-estimated values of the shear modulus which are unaffected by fluid content according to Gassmann's relations. The model thus predicts the variations of the bulk modulus as a function of water saturation. We find that the sonic logging data represent chalk where the oil has been partly flushed by invasion of mud filtrate. We use the difference between logging data- and model-estimates of the shear modulus to correct the model by scaling it according to clay content as estimated by the water saturation that is controlled by silicate content and particle sorting in the zone of irreducible water saturation in water-wet chalk. Forward modeling of the acoustic properties of the virgin zone thus results in a characteristic depth-wise pattern of the Poisson ratio with low values in the high-porosity intervals. This pattern agrees with the inverted seismic data, whereas these features are not captured if the acoustic properties of the virgin zone are derived from the sonic logs and

estimates of residual oil in the flushed zone because of almost complete invasion where porosity is high.

Introduction

Understanding the influence of pore fluids on acoustic properties of sediments is a central issue for evaluating seismic data; e.g. in amplitude versus offset techniques which depend on the discrimination of fluid content from variations in P- and S-velocities (e.g. Castagna & Backus 1993). Much research has been focused on describing such effects in sandstone, whereas few studies have been published on the rock physics of chalk (e.g. Walls *et al.* 1998; Japsen *et al.* 2000; 2002; Fabricius *et al.* 2002; Gommesen *et al.* 2002; Røgen 2002; Gommesen 2003). In the North Sea, chalk is an important reservoir rock and more information could be extracted from seismic data if fundamental physical properties of chalk were better understood. A phase-reversal due to the presence of gas in chalk was documented by Megson (1992), but so far, presence of oil in chalk has not been demonstrated to have effect on surface seismic data. The need for a better link between chalk reservoir parameters and geophysical observables has only increased since the discovery of the Halfdan field proved major reserves outside four-way dip closures (Jacobsen *et al.* 1999, Vejbæk & Kristensen 2000).

We have investigated the acoustic properties of chalk of the Danian Ekofisk Formation and the Maastrichtian Tor Formation in the Danish South Arne field where porosities up to 45% are found in the Tor reservoir at c. 3 km depth due to overpressure caused by compaction disequilibrium (Mackertich & Goulding 1999; Scholle 1978; Japsen 1998). We find that it is possible to describe the velocity-porosity relation for relatively pure chalk in terms of a modified upper Hashin-Shtrikman bound and Gassmann's (1951) relations as suggested by Walls et al. (1998). The model predicts a pronounced change in the relation between P- and S-velocities (and thus a drop in the Poisson ratio) for oil-bearing chalk with porosities above c. 35%. This span in Poisson ratio makes it probable that the light oil in the high-porous chalk of the South Arne field may be detected through AVO-inversion of surface seismic data. But the link between the surface seismic data and the reservoir is hampered by invasion of mud filtrate into the zone where the sonic log is registered (Gommesen et al. 2002). We find that the acoustic properties of the reservoir agree with those estimated from AVO-inversion if we compute a synthetic sonic log from the modified upper Hashin-Shtrikman model with porosity and water saturation of the virgin zone as input.

Data

Measurements on core plugs

Ultrasonic measurements (700 kHz) were carried out on 34 chalk samples from the South Arne field under both dry and saturated conditions; wells SA-1, Rigs-1 and Rigs-2 (Fig. 1; see also Røgen *et al.* 2002; Japsen *et al.* 2002). In order to prevent over-dry conditions, the samples were kept at room-moisture for two months after being dried at 110°C. The water saturation in the saturated plugs was generally between 97% and 103% (related to minor weight errors), but low permeability prevented total saturation in three samples (Sw=92%–95%). Three samples regained high water content after drying, as reflected in high smectite content (Sw=7%–12%; smectite content 3%–7%).

P- and S-wave velocities were determined from measured sample lengths and readings of travel times. The plugs were measured at 75 bar hydrostatic confining pressure corresponding to the magnitude of the effective stress at reservoir conditions. Density, ρ [g/cm^3], grain density, ρ_{gr}, porosity, ϕ [fractions] and permeability, k [Darcy] were also determined. Mineralogical composition of the samples was modelled on the basis of X-ray diffraction data, chemical analysis of insoluble residue and of filtrate after treatment with hydrochloric acid, backscatter electron microscopy of epoxy-impregnated polished samples, as well as qualitative energy dispersive microprobe analysis.

Very good correlation is observed between P- and S-velocity and porosity for saturated samples. Three samples with high clay content have outlying values relative to these trends.

Log data

Well log data from six wells in the South Arne field were quality controlled and for the chalk sections we calculated porosity and shale volume, as well as water saturation and density of the virgin zone. Four wells have readings of compressional and shear velocities, Vp and Vs, and out of these wells data for the near-vertical Rigs-2 well was selected for further analysis because we have good core data for this well and because it is situated outside the "gas cloud" on seismic sections.

Porosity, ϕ, was estimated from log-readings of the bulk density, ρ_{bulk}, assuming full invasion of the mud filtrate and thus we converted density to porosity based on mud filtrate densities rather than of mixtures of brine and hydrocarbons (Fig. 2). These estimates of porosity were found to match porosity measured on core samples from the Rigs-1 and -2 wells.

Water saturation, Sw, was estimated for the virgin zone from a range of pore water resistivity values based on the LLS and LLD logs. A shallow resistivity log was however not available and the saturation, Sxo, in the zone invaded by mud filtrate could thus not be estimated directly.

Shale volume was calculated from the gamma log based on a calibration to the measured gamma ray level in the sealing shale sequence relative to the purest chalk interval in each well. However, the relation between the gamma response and the clay content in the chalk may be rather arbitrary and the presence of e.g. smectite and silica are not recorded by the gamma log.

Bulk density, ρ, of chalk for a given water saturation was calculated as a function porosity:

$$\rho = \rho_{oil}(1-S_w)\phi + \rho_{brine} \cdot S_w \cdot \phi + \rho_{matrix}(1-\phi)$$

for the density of oil, brine and chalk matrix in the reservoir of the South Arne field (Table 1).

Seismic data

Near- and far-offset data were available from a 3D survey covering the South Arne field. The two sub-cubes are generated as partial stacks offset defined.

Theory

Fluid substitution using Gassmann's equations

The bulk and the shear moduli, K and G [GPa], of a rock are related to Vp and Vs [km/s] and density [g/cm^3] by the following expressions:

$$K = \rho(V_p^{\,2} - 4/3 \cdot V_s^{\,2}),\ G = \rho V_s^{\,2}.$$

We can transform the moduli of the rock for the initial fluid saturation (fluid 1) to moduli of the rock saturated with a new fluid (fluid 2) using Gassmann's (1951) relations (see Mavko *et al.* 1998):

$$K_{\mathrm{sat}2} = K_{\mathrm{m}} \cdot A/(1+A), \quad G_{\mathrm{sat}1} = G_{\mathrm{sat}2} \quad \text{where}$$
$$A = \frac{K_{\mathrm{sat1}}}{(K_{\mathrm{m}} - K_{\mathrm{sat1}})} - \frac{K_{\mathrm{fl}1}}{\phi(K_{\mathrm{m}} - K_{\mathrm{fl}1})} + \frac{K_{\mathrm{fl}2}}{\phi(K_{\mathrm{m}} - K_{\mathrm{fl}2})} \tag{1}$$

K_{sat1}, K_{sat2} are the bulk modulus of rock with the original and new pore fluid; K_m is the bulk modulus of mineral material making up rock; K_{fl1}, K_{fl2} are the bulk modulus of the original and the new pore fluid; G_{sat1}, G_{sat2} are the shear modulus of rock with the original and the new pore fluid. In particular we see that the shear modulus is predicted to be unaffected by fluid content. Gassmann's equations are established for homogenous mineral modulus and statistical isotropy. The equations are valid at sufficiently low frequencies such that the pore pressures induced by the sonic wave are equilibrated throughout the pore space. Gommesen et al. (2002) found that Gassmann's theory may be applied to chalk at logging frequencies

and Mavko & Japsen (this report) concluded that Gassmann's relations can be used to understand ultrasonic velocity-variations in chalk samples (cf. Japsen *et al.* 2002). We therefore apply Gassmann's relations to calculate the effects on the acoustic properties of chalk estimated from logging data when one pore fluid is substituted by another.

Properties of mixed fluids and materials

We can calculate the exact bulk modulus, K_{fl}, of mixtures of fluids, $K_{fl\,1}$, $K_{fl\,2}$ (brine/hydrocarbons or brine/air) as a Reuss average if the fluids form a homogenous mixture (Fig. 3):

$$1/K_{fl} = S_{fl1}/K_{fl1} + (1 - S_{fl1})/K_{fl2} \tag{2}$$

where $S_{fl\,1}$ is the relative saturation of fluid 1 (e.g. brine, S_w). Even small amounts of the light component (e.g. hydrocarbon or air) reduce the bulk modulus of the mixed fluid significantly because the average modulus is calculated from the inverse values of the individual moduli.

The properties of mixtures can be estimated as a Voigt average as an approximation to the patchy saturation "upper bound" where the fluids are not evenly distributed:

$$K_{fl} = S_{fl1} \cdot K_{fl1} + (1 - S_{fl1}) \cdot K_{fl2}. \tag{3}$$

Here the average modulus is more dependent on the denser constituents. We assume Reuss mixing to be the best approximation based on the conclusion of Mavko & Japsen (this report) that fine-scale mixing is dominant at logging frequencies in chalk.

Modified upper Hashin-Shtrikman (MUHS) model

Walls et al. (1998) found that a modified upper Hashin-Shtrikman model predicts the velocity-porosity behaviour of chalk estimated from well logs from the Ekofisk field (porosities from 10% to 40%). The model describes how the dry bulk and shear moduli, K and G increase as porosity is reduced from a maximum value, ϕ_{max}, to zero porosity. The upper and lower Hashin-Shtrikman bounds give the narrowest possible range on the modulus of a mixture of grains and pores without specifying anything about the geometries of the constituents (Hashin & Shtrikman 1963). The upper bound represents the stiffest possible pore shapes for porosity ranging from 0% to 100%, whereas the modified upper bound is defined for porosity up to a maximum value less than 100%. Here we refer the high-porosity end member as the maximum porosity rather than as the critical porosity which is defined as the porosity limit above which a sedimentary rock can only exist as a suspension (Nur *et al.* 1998). The low-porosity end-members, K_s and G_s, are the moduli of the solid at zero porosity found by extrapolation of the data trend at non-zero porosities. The modified upper Hashin-Shtrikman model, MUHS, is given by the dry-rock bulk and shear modulus, K^{MUHS} and G^{MUHS}:

$$\begin{aligned} K^{MUHS} &= \left[\frac{\phi/\phi_{max}}{K_{\phi max} + \frac{4}{3}G_s} + \frac{1-\phi/\phi_{max}}{K_s + \frac{4}{3}G_s} \right]^{-1} - \tfrac{4}{3}G_s \\ G^{MUHS} &= \left[\frac{\phi/\phi_{max}}{G_{\phi max} + Z_s} + \frac{1-\phi/\phi_{max}}{G_s + Z_s} \right]^{-1} - Z_s, \quad \text{where } Z_s = \frac{G_s}{6} \cdot \frac{9K_s + 8G_s}{K_s + 2G_s} \end{aligned} \tag{4}$$

The end-member moduli of the dry rock found by Walls et al. (1998) were

$$\begin{aligned} &K_{\phi max} = 4 \text{ GPa}, G_{\phi max} \text{ 4 GPa for } \phi_{max} = 40\%, \text{ and} \\ &K_s\text{=65 GPa and } G_s\text{=27 GPa for } \phi = 0\% \end{aligned} \tag{5}$$

Once these end-member parameters are estimated we can calculate the moduli of the dry rock from the MUHS model and given porosity and estimate moduli for the saturated rock using Gassmann's relations and the appropriate fluid properties, and finally calculate V_P and V_S.

Extended MUHS model based on ultrasonic V-ϕ data

Ultrasonic data from core samples from the South Arne field are in good agreement with the model of Walls et al. (1998), which is defined for porosities less than 40% (Fig. 1). However, chalk porosities between 40% and 45% occur on the South Arne field as estimated from both log data and core samples. For this reason we extrapolated the range of the MUHS model from 40% to 45% by estimating the high-porosity end-member at 45% porosity while keeping the low-porosity end-member unchanged (equations 4, 5):

$$K_{\phi max} = 1.5 \text{ GPa}, \mu_{\phi max} = 2.5 \text{ GPa for } \phi_{max} = 45\% \qquad (6)$$

This extrapolated model is in agreement with the acoustic properties of the south Arne plug samples with porosities between 40% and 45% (Fig. 1). We tried to extrapolate the MUHS model to 50% porosity, but even with $K_{\phi max}$ as low as 0.2 GPa the V_P-prediction was above that of the Walls et al. model and the measured values for the plug samples. The upper Hashin-Shtrikman formalism that reflects stiff pores shapes does thus not apply to the high porosity (45%-70%) pelagic carbonate deposits for which the increase of velocity with porosity reduction is limited (e.g. Urmos & Wilkens 1993).

We can apply the MUHS model to compute elastic moduli and Poisson's ratio for chalk as a function of porosity for the range of water saturations encountered on the South Arne field (Fig. 4), where the Poisson ratio, ν [-], is defined as:

$$\nu = \frac{3K - 2G}{2(3K + G)} = \frac{V_p^2 / V_s^2 - 2}{2(V_p^2 / V_s^2 - 1)}.$$

We see that even minor amounts of oil shift the bulk modulus down as expected from the assumed fine-scale Reuss mixing of the fluids (Fig. 3). The shear modulus is, however, unaffected by fluid properties as predicted by Gassmann's relations and consequently we predict pronounced variations in the Poisson ratio at high porosities. For pure brine, the Poisson ratio is almost constant ≈ 0.31 for $10\% < \phi < 36\%$, but increases along a banana shaped curve to 0.35 for $\phi = 45\%$ (cf. Gommesen 2003). For pure oil, the Poisson ratio decreases to 0.14 for $\phi = 45\%$ and we thus get a pronounced span in Poisson's ratio for porosities above c. 35% between heavy brine and light oil (density 1.035 and 0.633 g/cm^3). This span in Poisson ratio predicted by the MUHS model makes it probable that the light oil in the high-porous chalk on the South Arne field might be detected through AVO inversion of surface seismic data.

Sonic measurements in chalk affected by mud invasion

The acoustic properties of high-porosity chalk depend critically on fluid content, and we expect that the acoustic signal travels in the zone close to the well bore. Because there is no shallow resistivity log available, we cannot follow the procedure of Gommesen et al. (2002) and compare the acoustic signal to a model based on the saturation in the invaded zone. We do, however, not know if invasion was significant, and thus whether the acoustic waves registered by the sonic logs in the Rigs-2 well travelled through the invaded zone where the water saturation, Sw, is known from the deep resistivity log. We will examine the sonic data by comparing them to the MUHS model for brine at reservoir conditions using Gassmann's relations (eq. 6; Table 1). The MUHS model is in agreement with both ultrasonic data from the South Arne field and with the log data from the near-by Ekofisk field.

We find that the logging data are influenced by the presence of hydrocarbons (Fig. 5A): Bulk modulus and Poisson's ratio are low compared to the MUHS model due to presence of low-density oil. The shear modulus (which is unaffected by fluid content according to Gassmann theory) plots close the MUHS trend for $\phi <$ c. 40% (see below). Note that the high-porosity chalk appears to be almost completely flushed as the bulk moduli are close to the MUHS model for ϕ>40%.

If the sonic log data are transformed from water saturation as estimated by S_w to brine conditions assuming no invasion, the result appears to be overcorrected (Fig. 5C): The bulk modulus plots above the MUHS model for high porosities. We therefore find that the sonic logs in the Rigs-2 well are measured in chalk where oil is present but in smaller amounts than indicated by Sw due to invasion of mud filtrate (cf. Gommesen *et al.* 2002).

Erroneous S-velocities from log data for porosities above c. 40%

The S-velocities measured by the dipole log in the Rigs-2 well are almost constant and increasingly higher than those predicted by the extended MUHS model for porosities above c. 40% (Vs less than 1.3 km/s) - and thus higher than Vs measured on the chalk samples (see plot of G versus ϕ, Fig. 5). At 45% porosity, the shear velocity based on lab data is only 1.1 km/s whereas the value from the log data remains c. 1.3 km/s (G=2.4 and 3.5 GPa, respectively). We suggest that this difference is due to erroneous log-determination of Vs when S-wave traveltimes becomes so long that the S-arrivals are masked by minor P-waves or by direct arrivals in the borehole mud.

Acoustic properties of the virgin zone

We want to estimate the acoustic properties of the virgin zone with water saturation Sw to compare with the seismic data that reflect rock properties unaffected by invasion of mud filtrate. We are, however, confronted with two obstacles: First and most importantly, that the sonic log is measured in the mud-invaded zone where we do not know the water saturation, Sxo. Second, that the recording of the shear velocities appear to be erroneous for porosities above c. 40%. Two approaches may be followed:

- Either to estimate Sxo from empirical relations of irreducible water saturation in chalk and transform the sonic data to Sw-conditions using Gassmann's relations (Fig. 6)
- or to estimate the acoustic properties from forward modeling using the MUHS model and Gassmann's relations with ϕ and Sw as input. The bulk moduli estimated from the model and from the data may be used to quantify Sxo using Gassmann's relations (Fig. 7).

Virgin zone properties estimated from sonic data and Land's equation for residual oil

The water saturation of the flushed zone, Sxo (equivalent to the residual oil content) may be estimated from Land's formula (Land 1968):

$$S_{xo} = 1 - \frac{1 - S_{wi}}{1 + C(1 - S_{wir})} \qquad (7)$$

where S_{wi} is the initial water saturation (=Sw, the saturation of the virgin zone), S_{wir} is the irreducible water saturation and C=2.5 for the South Arne field (Flemming Iff, pers. comm.). We can calculate S_{wir} from the normalised capillary pressure curve method developed for the tight chalk in the North Sea (the equivalent radius method, EQR; Engstrøm 1995):

$$S_{wir} = \left(\frac{A}{\phi}\right)^B$$

where A and B are constants. We compute Sxo for the Rigs-2 well based on these two equations where we distinguish between the Ekofisk and Tor formations where S_{wir} is higher for the Ekofisk Formation (Fig. 6); A=0.12641, B=2.45422 (Ekofisk Fm) and

A=0.06596, B=2.19565 (Tor Fm) (P. Frykman, pers. comm.). The mean water saturation is predicted to increase from 17% to 76% in the flushed zone of the Tor Formation and Sxo is seen to mirror Sw so that relatively more oil is removed from the more oil-saturated intervals. Based on this estimate of Sxo we can do fluid substitution to any saturation using Gassmann's relations and Reuss fluid mixing law (eqs 1, 2).

Resulting acoustic response

We assume that the measured Vp- and Vs logging-data (blue curves) reflect the conditions of the flushed zone with Sxo estimated by Land's equation, and do fluid substitution to compute the acoustic properties of the chalk saturated with the fluids of the virgin zone (red curve) and with pure brine (green curve) (Fig. 6b). The P-velocity of the invaded zone and of the virgin zone are not predicted to differ much because the fluid properties are rather identical for medium saturations due to the assumed Reuss mixing of the fluids (Fig. 3). A bigger change in Vp is predicted from the data curve to the brine curve (green). This is to be expected from the assumed Reuss fluid mixing because minor amounts of light fluids reduce the bulk modulus of the brine notably.

Virgin zone properties estimated from the MUHS model with ϕ and Sw as input

Forward modeling may be used to calculate the acoustic response corresponding to the measured porosity and the water saturation, Sw, in the virgin zone (Fig. 7). The modeling is done in three steps where step 2 may be included to correct the moduli of the most shaley intervals:

1. Calculate the properties of the dry rock from the MUHS model with the porosity log as input (eq. 6).
2. Correct the moduli in the intervals with impure chalk as estimated by Sw by scaling the low-porosity end-member of the MUHS model (see below; eq. 8).
3. Calculate the properties of the virgin zone where the water saturation is given by Sw using Gassmann's relations and the Reuss mixing law (eqs 1, 2).

Corrected MUHS model

In Fig. 8 we see the result of the uncorrected MUHS model (steps 1 and 3) and the corrected MUHS model (steps 1 to 3) compared with the measured data. The big difference in the bulk modulus between the model (of the virgin zone) and data (from the flushed zone) is caused by removal of oil by mud invasion. However, the shear modulus is unaffected by fluid content and the model-estimate of G is close to the data-estimate. We compute the difference in the estimates of the shear modulus as $\Delta G = G_{MUHS} - G_{data}$ for the uncorrected MUHS model (Fig. 9). We get large differences expressed as ΔG up to 10 GPa where porosity is low (and moduli large) and where water saturation is high. The clay content estimated from the gamma log reveals, however, no correlation with the mismatch between model and data. Furthermore, we get minor differences expressed as ΔG down to –2 GPa for porosities above 40%.

The too low S-velocities (ΔG<0) modelled at high porosities may be explained by erroneous log-measurements of shear velocities as discussed above. Our interpretation of the too high S-velocities (ΔG>0) modelled at low porosities is that velocity is reduced due to a content of clay, which causes the assumption of a calcite mineral matrix to be too inaccurate. The clay content estimated from the gamma log does however not correlate with ΔG, partly because this log may be erroneous, e.g. due to use of oil-based drilling mud and partly because non-carbonate constituents as quarts and smectite have no or insignificant gamma response. We thus assume that the water saturation can be regarded as a measure of the impurities in the chalk which in this well where the water is irreducible (Fig. 7).

The water saturation may be regarded as irreducible because the water saturation does not increase with depth (apart from the deepest 10 m of the Tor Formation), so that the water saturation reflects the size of the particle-pore interface and amount of particle contacts (Fabricius *et al.* 2002). The controlling factor for the degree of water saturation in the chalk thus becomes clay content and particle sorting. A clear distinction between the Ekofisk and the Tor formations is revealed by Sw but not by the gamma log (Fig. 7). The distinction between these formations is also evident from the well-known lower permeability of the Ekofisk Formation that may be attributed to the higher content of silicates in the Ekofisk formation (Røgen 2003). The relatively low moduli for chalk with high shale content is also evident from the plug data with values of ΔG and ΔK up to –10.5 and -10.0 GPa around 15% porosity (Fig. 1).

In order to correct the MUHS model (eq. 6) for the effect of clay-softening we have chosen a simplistic, but apparently effective approach (Figs 9a2, b2): We have scaled the low-porosity end-members, M_s, of the MUHS model (eq. 5) by the 'clay' content, cl, taken as cl = Sw – 0.2. For a given value of Sw, we calculated M_s as a kind of Hill average by computing the arithmetic average of the upper and lower Hashin-Shtrikman bounds, HS_U and HS_L (see Mavko et al., 1998):

$$M_s = (HS_U + HS_L)/2 \tag{8}$$

where the bounds are calculated as a mixture defined by cl between the 'no-clay' end-member moduli for pure chalk given by Walls et al. (1998): M_{chalk}=(65 GPa, 27 GPa) and the end-member moduli for pure 'clay' equals those for clay given by Table 1: M_{clay}=(25 GPa, 9 GPa). This procedure effectively scales M_s between M_{chalk} for $Sw<0.2$ and (30 GPa, 11 GPa) for Sw=1. The correction reduces the too high predictions of G to match the data values in the low-porosity zones where Sw reaches maximum values (cf. Figs 7, 8).

Water saturation estimated from sonic data

The bulk modulus, K_{sat}, of the flushed zone is known from the sonic data whereas the dry-rock modulus, K_{dry}, of the chalk can be estimated from the corrected MUHS model (eq. 8; fig. 8). To avoid erroneous Vs-data we use Vs from the corrected MUHS model to compute K_{sat} for ϕ>40%. We can thus rearrange Gassmann's relations expressed in terms of K_{sat} and K_{dry} to give us the effective bulk modulus, k_{fl}, of the pore fluid in the flushed zone (eq. 1; see Mavko et al. 1998):

$$k_{fl} = \phi K_m \frac{A-B}{1+\phi(A-B)}, \text{ where } A = \frac{K_{sat}}{K_m - K_{sat}}, B = \frac{K_{dry}}{K_m - K_{dry}}$$

Substituting this result into the Reuss equation for fine-scaled fluid mixing in the reservoir (eq. 2), we get the saturation of the flushed zone, Sxo:

$$S_{xo} = \frac{k_{brine}(k_{oil} - k_{fl})}{k_{fl}(k_{oil} - k_{brine})} \tag{9}$$

where k_{oil} and k_{brine} are the bulk moduli of the oil and the brine of the reservoir (Table 1). Only values of Sxo in the interval from 0 to 1 are valid (234 out of 306 data points for the Rigs-2 well). Sxo is predicted to be 81% in the Tor Formation which is in very good agreement with the 76% obtained by Land's equation (eq. 7). However, Sxo has a large scatter and the indicated mean value includes values above 90% water saturation over much of the Tor reservoir where porosity exceeds 40% (Fig. 7).

Resulting acoustic response

Also in this case we assume that the measured Vp- and Vs-data (blue curve) reflect the conditions of the flushed zone with water saturation given by Sxo, which may be estimated over part of the reservoir by the above equation (Fig. 7). However, we estimate the acoustic properties of the chalk in the virgin zone (red curve) from the corrected MUHS model based on the porosity log and Sw (Fig. 7b). The P-velocity of the flushed zone does not differ much from that predicted for brine (green curve) because of the almost complete mud invasion. A significant difference in Vp is now predicted between the virgin zone and the flushed zone.

AVO-inversion based on logs from the MUHS model

AVO attributes were calculated from inverted 2D seismic lines (near- and far-offset data) extracted from the South Arne 3D survey. The inversion was carried out for the two-way time window 1.9–3.6 s and was targeted on the chalk interval (cf. Cooke & Schneider 2003). Log data from the I-1x, Rigs-1, -2 and SA-1 wells were used in the inversion process. These data comprise Vp- and Vs-data based on the corrected MUHS model described above plus density logs, check shot and deviation data. Using a least-squares wavelet estimation method with constrain on the phase, wavelets were estimated for each offset stack. The wavelet estimations was carried for each of the wells (Fig. 10). The I-1x well has no shear log data so Vp/Vs=2 was used in the calculations. The wavelet estimated from the I-1x well was preferred based on inversion tests.

Low-frequency components of the acoustic impedance variations with depth are not present in seismic data. Since this information is essential to the interpretation, it should be accounted for in the seismic inversion. Low-frequency near- and far-angle impedance models were constructed by extrapolation of the angle-dependent impedance well logs through the 3D volume tied to seismic horizons, followed by low-pass filtering (cf. Castagna & Backus 1993). The final inversion results models 93.7% of the seismic energy for the near-offset stack and 93.4% for the far-offset stack. The inversion results are good in terms of match with the angle impedance well logs.

AVO-attributes were computed from the angle-dependent impedance inversions combined with low-frequency information (Bach *et al.* 2003): Acoustic impedance, shear impedance and Poisson's ratio were extracted at the location of the Rigs-2 well.

The AVO-results are good in terms of match with the well log data. Low values of Poisson's ratio at the location of Rigs-2 is in agreement with the presence of light oil in the high-porous chalk of the South Arne field (Fig. 11).

Discussion and conclusions

We have extended the Modified Upper Hashin-Shtrikman trend established by Walls et al. (1998) for chalk on the Ekofisk field based on log data. This trend describes an empirical relation between porosity and the dry-rock moduli of chalk and hence velocity of saturated chalk through application of Gassmann's relations. Ultrasonic data for relatively pure chalk samples of the Ekofisk and Tor formations from the South Arne field match the trend and due to the higher porosities on the South Arne field we can extend the range of the MUHS model from 10%–40% to 10%–45% (eq. 6). Shaley chalk samples, e.g. with a smectite content of 3%–7% have significantly smaller moduli and a higher Poisson ratio than the general data trend. Modeling of the acoustic properties of chalk as a function of water saturation predicts a pronounced drop in Poisson ratio for oil-bearing chalk with porosities above c. 35%.

Comparison of the MUHS model with sonic data from the South Arne field clearly show that the data records the conditions of a zone close to the well bore where drilling-mud has flushed the reservoir and the water saturation, Sxo, thus is higher than the saturation, Sw, in the virgin zone as estimated from the deep resistivity log. Lacking shallow resistivity data to assess the water saturation in the flushed zone we have investigated two approaches to estimate the acoustic properties of the virgin zone in order to compare the result with inversion of surface seismic data:

1. Estimation of Sxo from Land's (1968) prediction of the irreducible water saturation in chalk followed by transformation of the sonic data to Sw-conditions using Gassmann's relations (eq. 7).
2. Estimation of the acoustic properties from forward modeling using the MUHS model and Gassmann's relations with ϕ and Sw as input. The bulk modulus depend on fluid content and we use differences between the sonic data and the MUHS model to quantify Sxo using Gassmann's relations and Reuss' fine-scale fluid-mixing law. The shear modulus, G, is unaffected by fluid content and we observe good agreement between MUHS model and data in pure chalk. We use the differences between data- and model-estimates of G to establish a corrected

MUHS model where we scale the low-porosity end-member of the MUHS trend according to shale content as estimated by Sw. We do so because the MUHS model predicts too high shear moduli where porosity is low and water saturation is high, whereas we see no correlation with clay content estimated from the gamma log. The water saturation can thus be regarded as a measure of the impurities in the chalk in this well where the chalk is water-wet and the water saturation is irreducible. The controlling factor for the degree of water saturation thus becomes clay content and particle sorting. The MUHS model predicts the shear modulus to be smaller than observed from logging data for porosities above c. 40%. We suggest that this difference is due to erroneous log-determination of Vs when S-wave traveltimes becomes very long.

A characteristic depth-wise pattern of the Poisson ratio with pronounced peaks at top Ekofisk and top Tor and low values in the high-porous Tor reservoir results from forward modeling of the acoustic properties of the virgin zone (Fig. 12). This pattern is in good agreement with the inverted seismic data (Fig. 11), but these features are not captured in the approach based on Land's (1968) equation. We therefore find that Land's equation underestimates the mud-invasion of the high-porous part of the reservoir. We find that the best way to estimate the acoustic properties of the virgin zone is to use the extended Modified Upper Hashin-Shtrikman velocity-porosity relation for chalk presented here. AVO-inversion of the seismic data based on such synthetic sonic logs reveals a zone of very low Poisson ratio that correlates with the oil reservoir in the Tor Formation. AVO-inversion thus provides direct evidence for presence of oil in high-porous chalk saturated with the light oil of the South Arne field.

Acknowledgements

These results are part of the outcome of the energy research project Rock Physics of Impure Chalk which was sponsored by the Danish Energy Research Program (EFP-2001), Amerada Hess A/S and Dong E&P.

References

Bach, T., Espersen, T. B., Pedersen, J. M., Hinkley, R., Pillet, R. P. & Rasmussen, K. B. 2003. Seismic inversion of AVO data. In press for *Inverse methods II, Springer Verlag.*

Castagna, J. P. & Backus, M. M. 1993. *Offset-dependent reflectivity – Theory and practice of AVO analysis.* Society of Exploration Geophysicists, Tulsa.

Cooke, D. A. & Schneider, W. A. 2003. Generalised linear inversion of reflection seismic data. *Geophysics,* **48**, 665-676.

Engstrøm, F. 1995. A new method to normalise capilary pressure curves. *Proceedings from the International Symposium of the Society of Core Analysis*. 12 pp.

Fabricius, I. L., Mavko, G., Mogensen, C. & Japsen, P. 2002. Elastic moduli of chalk as a reflection of porosity, sorting, and irreducible water saturation. *SEG 72nd annual meeting, Salt Lake City, USA*. 4 pp.

Gassmann, F. 1951. Über die Elastizität poröser Medien. *Vier. der Natur. Gesellschaft in Zürich,* **96**, 1-23.

Gommesen, L. 2003. Prediction of porosity and fluid in chalk from acoustic measurements. Technichal University of Denmark (DTU). PhD Thesis.

Gommesen, L., Mavko, G., Mukerji, T. & Fabricius, I. L. 2002. Fluid substitution studies for North Sea chalk logging data. *72nd SEG annual meeting, Salt Lake City, USA*. 4 pp.

Hashin, Z. & Shtrikman, S. 1963. A variational approach to the elastic behavior of multiphase materials. *J. Mech. Phys. Solids,* **11**, 127-140.

Jacobsen, N. L., Engstrøm, F., Uldall, A. & Petersen, N. W. 1999. Delineation of hydrodynamic/geodynamic trapped oil in low permeability chalk (SPE 56514). *SPE annual technical conference*. 10-1.

Japsen, P. 1998. Regional velocity-depth anomalies, North Sea Chalk: a record of overpressure and Neogene uplift and erosion. *AAPG Bulletin,* **82**, 2031-2074.

Japsen, P., Høier, C., Rasmussen, K. B., Fabricius, I. L., Mavko, G. & Pedersen, J. M. 2002. Effect of fluid substitution on ultrasonic velocities in chalk plugs, South Arne field, North Sea. *SEG 72nd annual meeting, Salt Lake City, USA*. 4 pp.

Japsen, P., Wagner, H., Gommesen, L. & Mavko, G. 2000. Rock physics of Chalk: modeling the sonic velocity of the Tor Formation, Danish North Sea. *EAGE 62nd conference, Glasgow, Scotland*. 1-4.

Land, C. S. 1968. Calculation of imbibition relative permeability for two- and three-phase flow from rock properties. *Society of Petroleum Engineers Journal,* **1968**, 149-156.

Mackertich, D. S. & Goulding, D. R. G. 1999. Exploration and appraisal of the South Arne field, Danish North Sea. *In:* Fleet,A.J. & Boldy,S.A.R. (eds) *Petroleum Geology of Northwest Europe: Proceedings of the 5th Conference.* Geological Society, London. 959-974.

Mavko,G. and Japsen,P. *submitted.* Fluid substitution in chalks: Effects of saturation scales. Submitted to Geophysical Prospecting.

Mavko, G., Mukerji, T. & Dvorkin, J. 1998. *The rock physics handbook.* Cambridge University Press, Cambridge.

Megson, J. B. 1992. The North Sea chalk play; examples from the Danish Central Graben. *In:* Hardman,R.F.P. (ed.) *Exploration Britain: Geological insights for the next decade.* Geological Society Special Publication, **67**, 247-25.

Nur, A., Mavko, G., Dvorkin, J. & Galmundi, D. 1998. Critical porosity; a key to relating physical properties to porosity in rocks. *Leading Edge,* **17**, 357-362.

Røgen, B. 2002. North Sea chalk - textural, petrophysical and acoustic properties. Technichal University of Denmark (DTU). PhD Thesis.

----- 2003. Influence of clay and silica on permeability and capillary entry pressure of chalk reservoirs in the North Sea. *Petroleum Geoscience,* **8**, 293.

Røgen, B., Fabricius, I. L., Japsen, P., Høier, C., Mavko, G. & Pedersen, J. M. 2002. Ultrasonic velocities of chalk samples - influence of porosity, fluid content and texture. *In:* Røgen,B. (ed.) *North Sea chalk - textural, petrophysical and acoustic properties.* Technical University of Denmark (DTU), Lyngby.

Scholle, P. 1978. Diagenesis hydrocarbon potential of Upper Cretaceous chalks of Western Interior. 892-892.

Urmos, J. & Wilkens, R. H. 1993. In situ velocities in pelagic carbonates: New insights from Ocean Drilling Program Leg 130, Ontong Java Plateau. *Journal of Geophysical Research,* **98**, 7903-7920.

Vejbæk, O. V. & Kristensen, L. 2000. Downflank hydrocarbon potential identified using seismic inbersion and geostatistics: Upper Maastrichtian reservoir unit, Dan Field, Danish Central Graben. *Petroleum Geoscience,* **6**, 1-13.

Walls, J. D., Dvorkin, J. & Smith, B. A. 1998. Modeling seismic velocity in Ekofisk Chalk. *SEG 68th annual conference.* 1016-1019.

Table 1. Elastic properties. Bulk and shear modulus, K and G, and density, ρ.

	K [GPa]	G [GPa]	ρ [g/cm^3]
Calcite	71	30	2.71
Clay	25	9	2.70
Brine	2.96**	0	1.035*
Hydrocarbon	0.52**	0	0.633*

Mineral properties after Mavko et al. (1998). Fluid properties estimated for the Rigs-2 well.

* Densities estimated at reservoir level at the South Arne field (J. Jensenius pers.comm.)

** Values for fluids at the crest of the South Arne field estimated with Batzle-Wang algorithm FOR T=100°, P=44 MPa, Oil gravity=33 API, Gas gravity=0.815 (Alister Colby pers.comm.). GOR=1685 scf/BBL in order to match the hydrocarbon density.

Figures

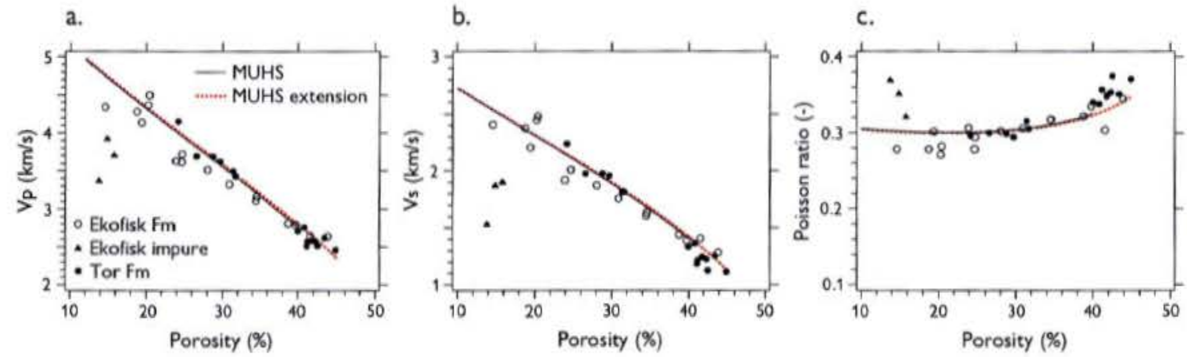

Fig. 1. Acoustic properties of 34 saturated chalk samples versus porosity.

a. P-velocity, V_P.

b. S-velocity, V_S.

c. Poisson's ratio.

Good agreement is observed between the South Arne core data and the MUHS model based on log data from the Ekofisk field (full line; eq. 5; Walls et al. 1998;). We suggest an extrapolation of the model from 40% to 45% porosity that agrees with the plug data (dashed line; eq 6). Both lines for brine at reservoir conditions. Acoustic properties measured on core samples saturated with tap water at 75 bar confining pressure and transformed to the brine properties at reservoir conditions in the South Arne field using Gassmann's relations (Table 1). MUHS: Modified Upper Hashin-Shtrikman.

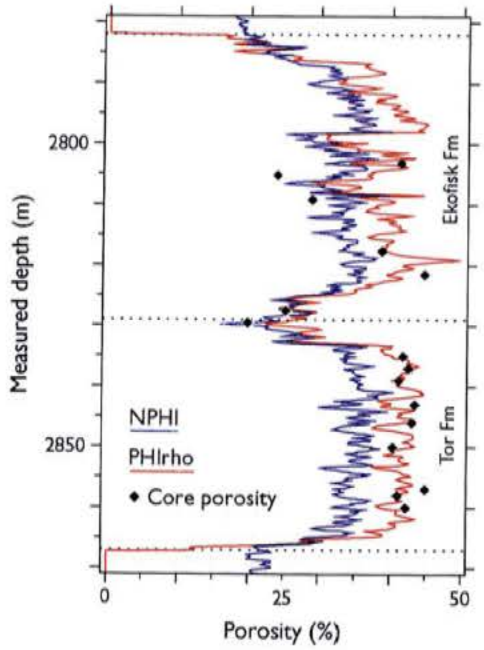

Figure 2. Porosity logs for the Rigs-2 well and data points for core porosity. Note the agreement between core porosity and the density log, PHIrho, which was estimated from log-readings of the bulk density, ρ_{bulk}, assuming full invasion of the mud filtrate. This indicates that ρ_{bulk} measures in the zone fully invaded by mud filtrate. The neutron porosity log, NPHI, underestimates porosity due to the presence of hydrocarbons.

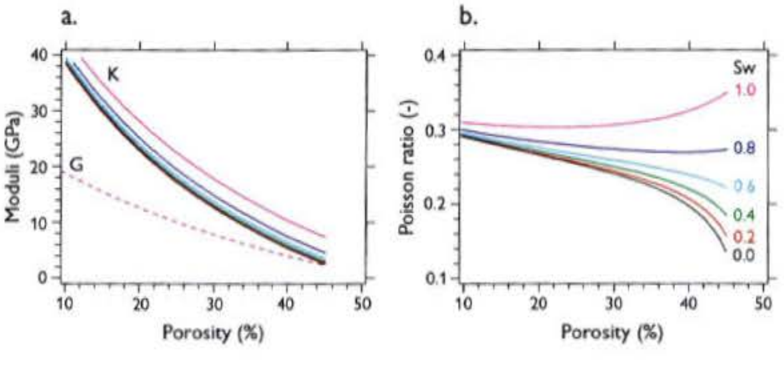

Fig. 4. Acoustic properties of chalk as a function of porosity and water saturation, Sw, predicted from the MUHS model and Gassmann's relations assuming fine-scaled Reuss mixing of the fluids (eqs 6, 1, 2).

a. Bulk and shear modulus, K and G.

b. Poisson ratio.

Note the pronounced variation in Poisson ratio for porosities above c. 35% between pure brine and pure oil (density 1.035 and 0.633 g/cm^3; Table 1). MUHS: Modified Upper Hashin-Shtrikman.

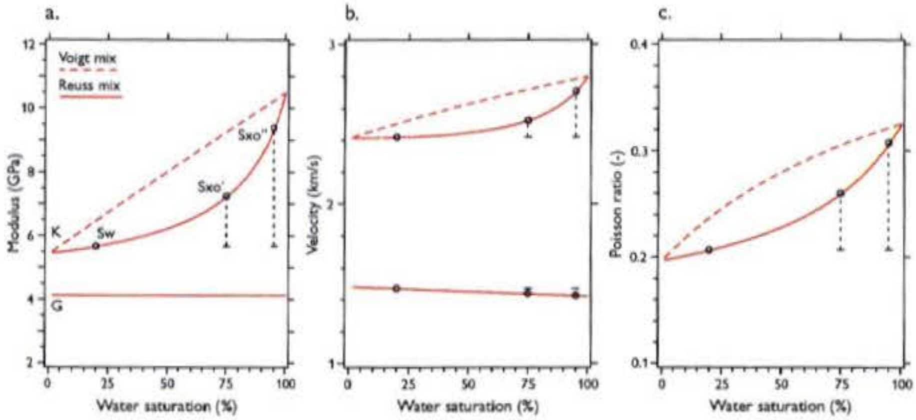

Fig. 3. Acoustic properties as a function of water saturation for chalk with 40% porosity.

a. Bulk and shear modulus, K and G.

b. P- and S- velocities, Vp and Vs,

c. Poisson ratio.

Flushing of the reservoir increases the bulk modulus of the oil-brine mixture along a Reuss curve .

Minor variations in the estimation of Sxo result in major changes in the acoustic properties as indicated by the dashed lines. Dry-rock properties from MUHS model and fluid properties for the South Arne field (eq. 6; Table 1)

Legend:

Sw: Water saturation of the virgin zone.

Sxo': Saturation of the mud-invaded reservoir according to Lands equation for residual oil (eq. 7; Fig. 6).

Sxo'': Saturation of the mud-invaded reservoir estimated from sonic data and the MUHS model (eq. 9; Fig. 7).

Upper bound: Voigt fluid mixture (eq. 3).

Lowert bound: Reuss fluid mixture (eq. 2).

MUHS: Modified Upper Hashin-Shtrikman.

A. Raw data:

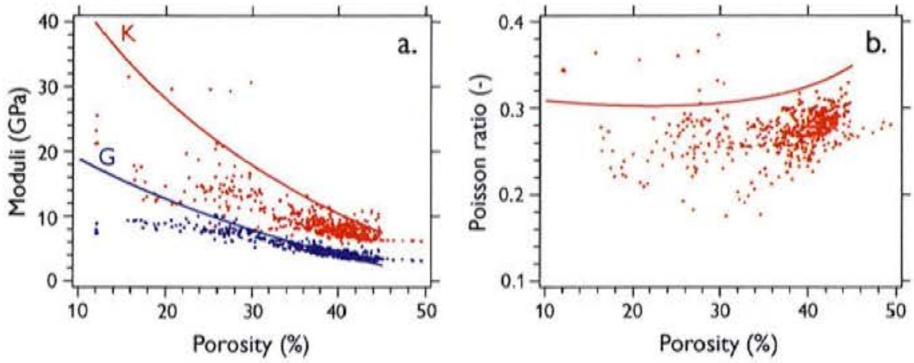

B. Substitution to brine conditions according to land's equation:

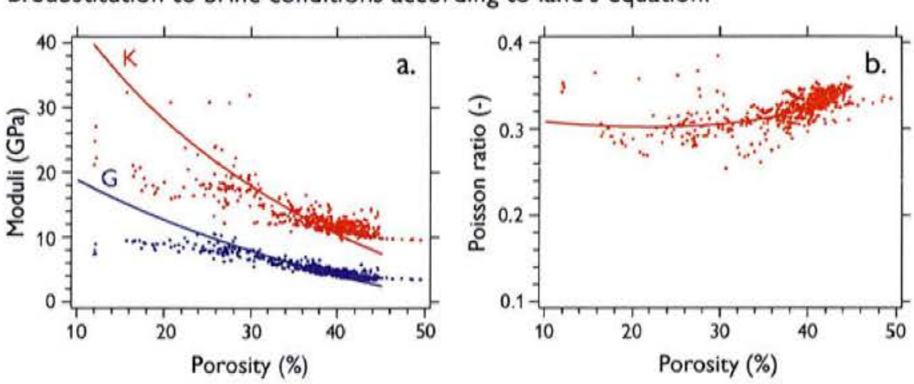

C. Substitution to brine conditions assuming no invasion:

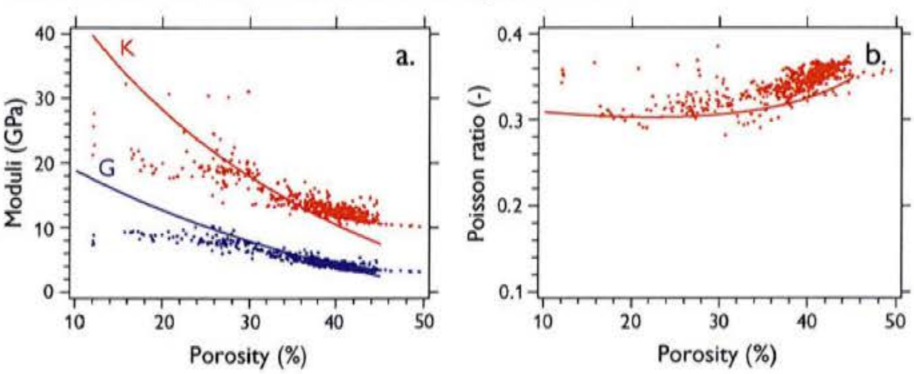

Fig. 5. Acoustic properties of the chalk in the Rigs-2 well versus porosity.

a. Bulk and shear modulus, K and G.

b. Poisson's ratio.

Note that the estimated shear moduli – that are unaffected by fluid content – plot on the MUHS trend for ϕ>40%. This suggests that the MUHS model is valid for log data for the South Arne chalk and that the shear velocity log data probably are erroneous for ϕ>40% where Vs is predicted to be less than 1.4 km/s.

A. Original data. Bulk moduli plot below the MUHS model due to presence of hydrocarbons whereas shear moduli plot on the trend. Note that for ϕ>40% the bulk moduli are close to the MUHS model for brine conditions and this indicates that the high-porosity chalk is almost completely flushed.

B. Substitution to brine conditions assuming invasion according to Land's equation (eq. 7). Bulk moduli plot close to the MUHS model for ϕ up to 40% indicating that Land's equation works well at medium porosities.

C. Substitution to brine conditions assuming no invasion. Bulk moduli plot above the MUHS model indicating that Sw overestimates the oil-content in the flushed zone.

Legend:

Full lines: MUHS model for brine at reservoir conditions (equations 1, 6; Table 1).

MUHS: Modified Upper Hashin-Shtrikman.

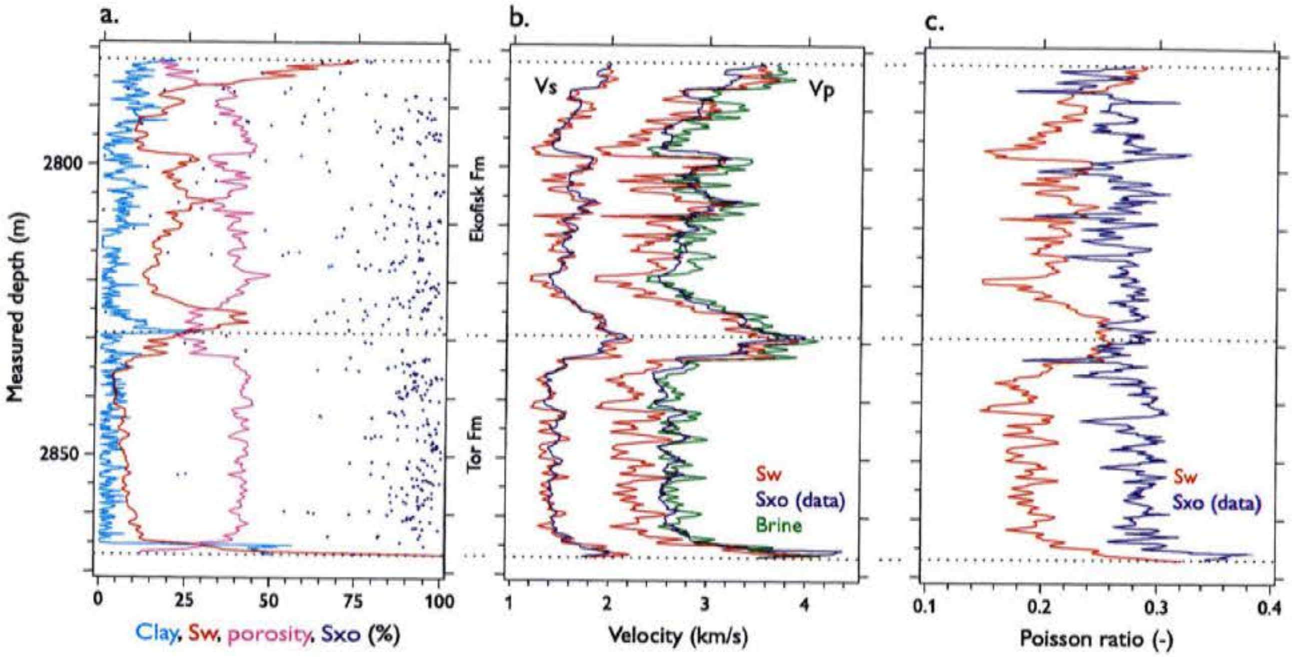

Fig. 7. Log data and predictions based on the corrected MUHS model for the chalk section in the Rigs-2 well (eqs 6, 8; Fig. 8).

a. Clay content (from gamma log), porosity and water saturation, Sw and Sxo. Sxo (dots) is estimated from the relation between the measured sonic data and the corrected MUHS model (eq 9).

b. V_P and V_S. Data and predictions of the corrected MUHS model based on porosity and Sw. Brine-estimate for Vs not shown.

c. Poisson ratio. Data and predictions of the corrected MUHS model. Brine-estimate not shown.

In the high-porosity oil zone of the Tor Formation, the oil is predicted to be almost completely flushed as indicated by the closeness of the measured Vp(Sxo) (blue curve) and the predicted Vp(brine) (green curve) whereas Vp(virgin zone, Sw) is predicted to be low (cf. Fig. 3). MUHS: Modified Upper Hashin-Shtrikman.

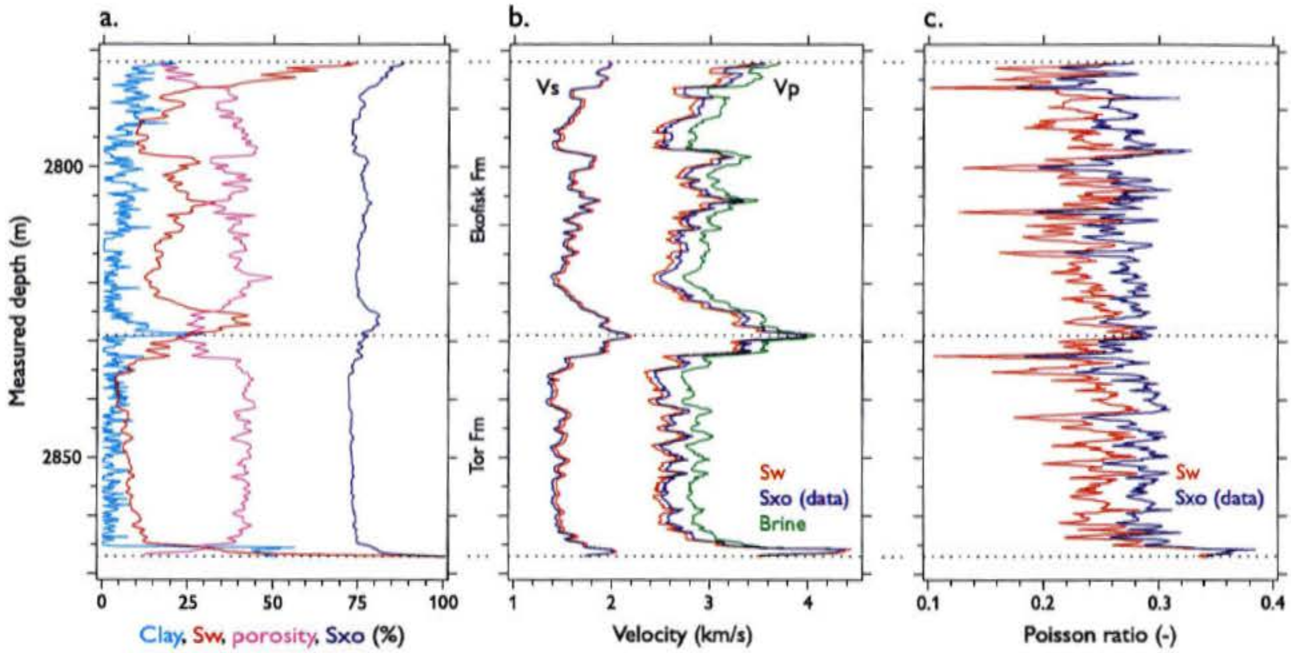

Fig. 6. Log data and predictions based on Land's estimate of residual oil for the chalk section in the Rigs-2 well (eqs 6, 8; Fig. 8).

a. Clay content, porosity and water saturation, Sw and Sxo. Sxo is estimated from Land's equation (eq 7).

b. V_P and V_S. Data and predictions based on fluid substitution from Sxo. Brine-estimate for Vs not shown

c. Poisson ratio. Data and predictions of the Land model. Brine-estimate not shown.

In the high-porosity oil zone of the Tor Formation, Sxo is predicted to be reduced to c. 75% and due to the Reuss mixing of the fluids the acoustic properties of invaded zone and of the virgin zone do not differ much. This is indicated by the closeness of the measured Vp(Sxo) (blue curve) and the predicted Vp(virgin zone) (red curve) whereas Vp(brine) (green curve) is predicted to be significantly higher (cf. Fig. 3).

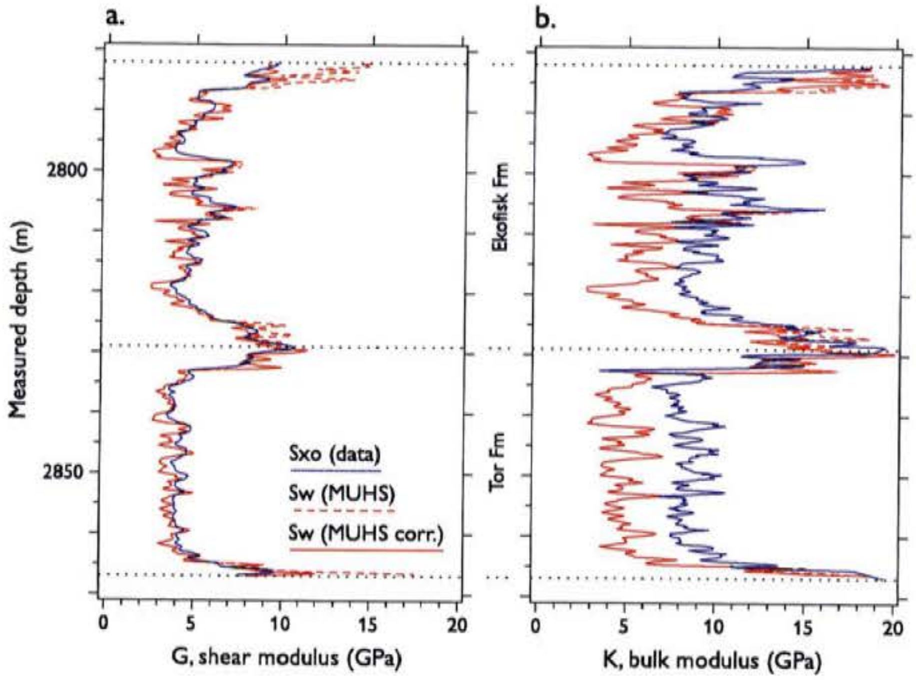

Fig. 8. Log response predicted for the virgin zone from the corrected and the uncorrected MUHS-model compared with data from the invaded zone (eqs 6, 8).

a. Shear modulus.

b. Bulk modulus.

Note the good agreement between the shear modulus estimated from data and from the corrected MUHS model. Poor sorting and clay content may explain the difference between the estimated shear modulus from uncorrected MUHS model and from the data in the tight zones (Figs 7, 9). The difference between the two estimates of the bulk modulus is caused by removal of oil by mud invasion in the zone investigated by the sonic log. MUHS: Modified Upper Hashin-Shtrikman.

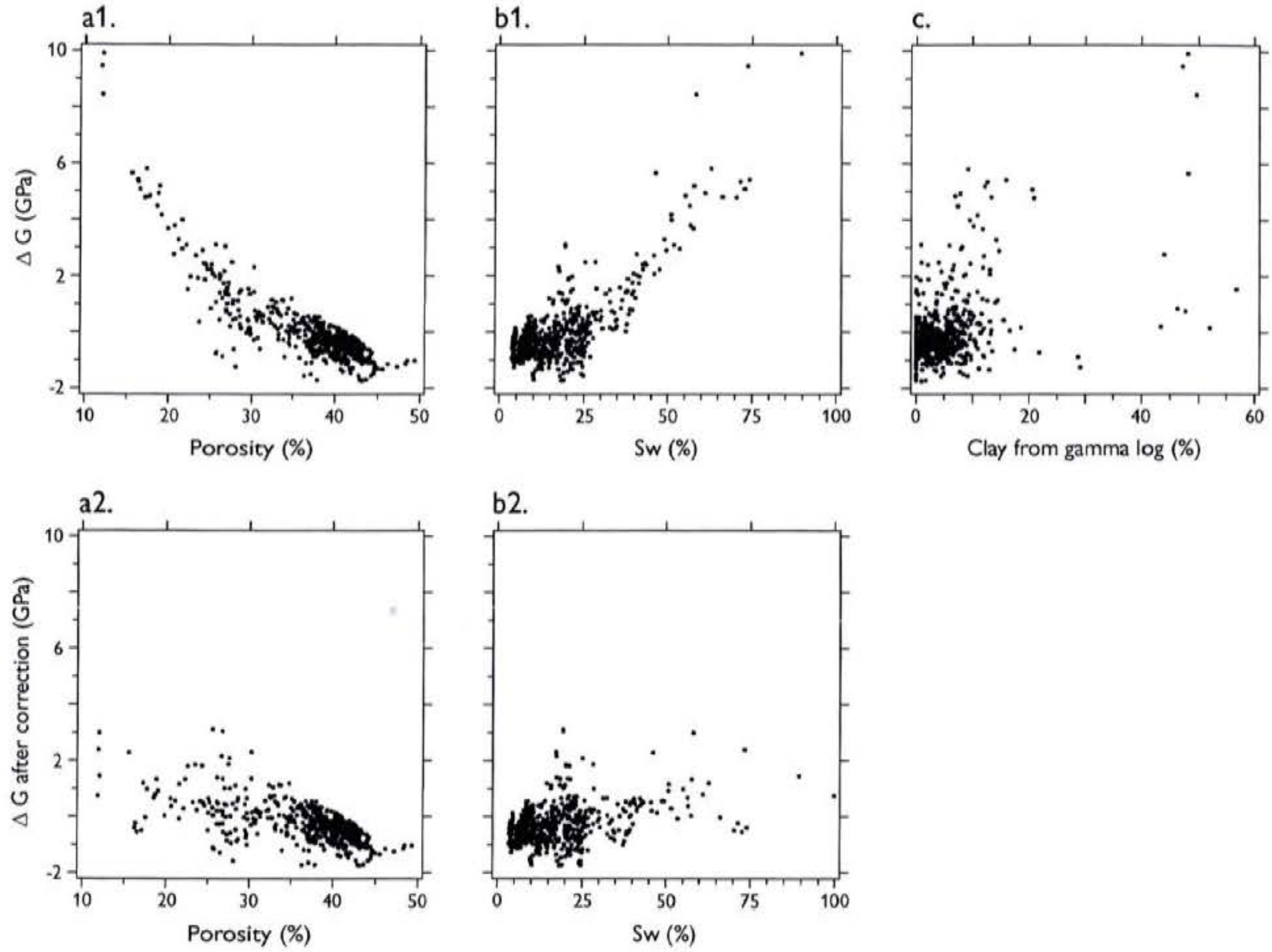

Fig. 9. Error in prediction of the shear modulus, $\Delta G = G_{MUHS} - G_{data}$ and $\Delta G_c = G_{MUHS\_c} - G_{data}$ where G_{MUHS} and G_{MUHS_c} are estimated from the MUHS model and the corrected MUHS model (eqs 6, 8).

a1–c1. ΔG versus porosity, water saturation and clay content estimated from the gamma log.

a2–b2. ΔG_c versus porosity and water saturation.

The error in the MUHS model correlates with Sw and this indicates that the water saturation reflects the degree of impurity of the chalk in this reservoir where the chalk is water wet and the water saturation irreducible (see Fig. 7). The clay content estimated from the gamma log does not correlate with ΔG. MUHS: Modified Upper Hashin-Shtrikman.

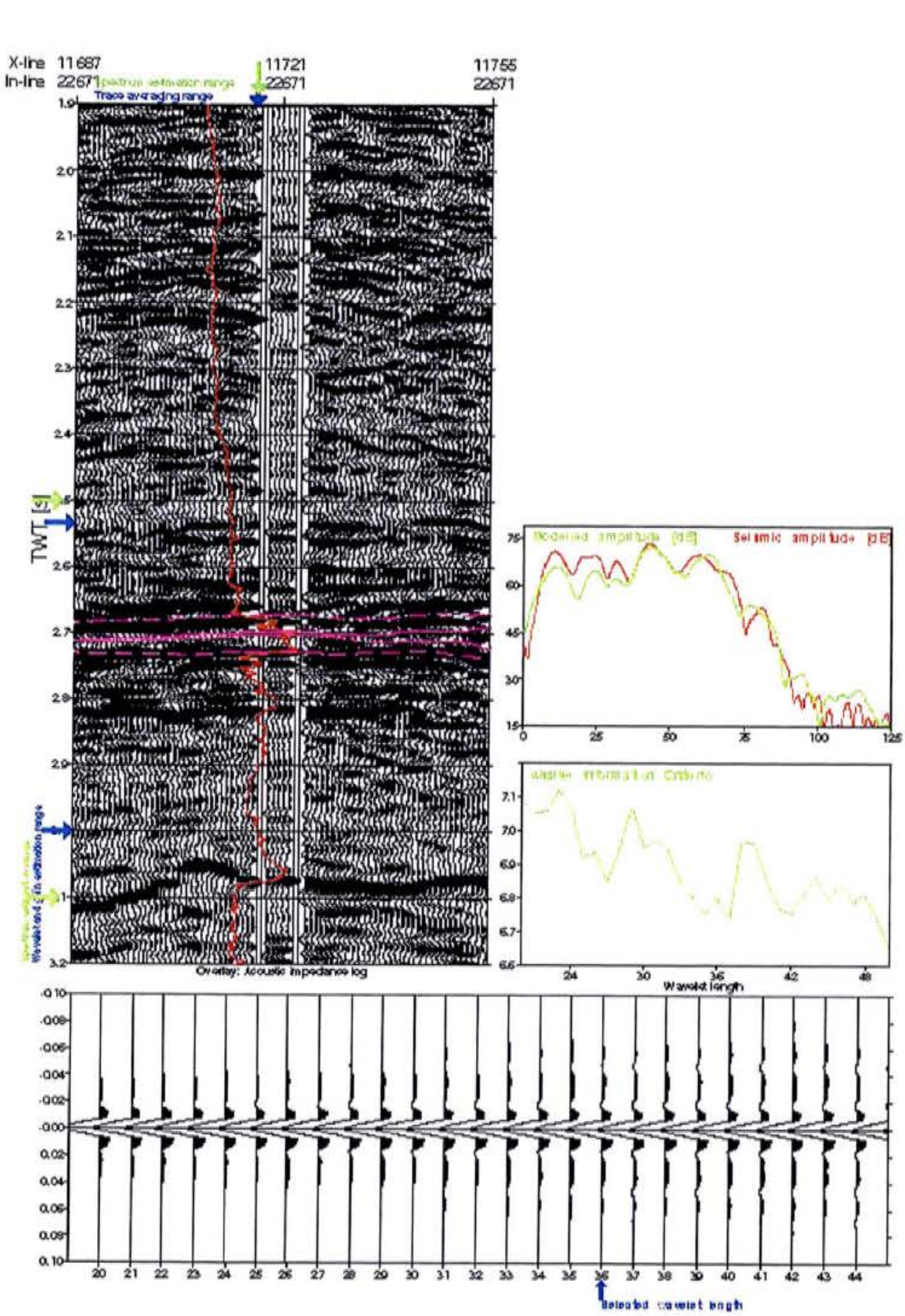

Fig. 10. Near offset stack: Least squares wavelet estimation in well I-1x.

Left: Synthetic seismic trace obtained by convolution of the optimum wavelet (length 36 samples) with the near offset angle reflectivity log from the well inserted into the seismic data.

Top right: Amplitude spectra in the wavelet estimation window of the seismic trace at the well location and the synthetic seismic trace.

Bottom right: Relative misfit energy, Akaike's FPE, cross-correlation and relative number of parameters for the wavelet suite. Left-hand axis refers to the curves of relative misfit energy and Akaike's FPE. Right-hand axis refers to the curves of cross-correlation and relative number of parameters.

Bottom: Wavelet suite. The lengths of the predicted wavelets range from 20 samples to 44 samples (80 ms to 176 ms, horizontal axis).

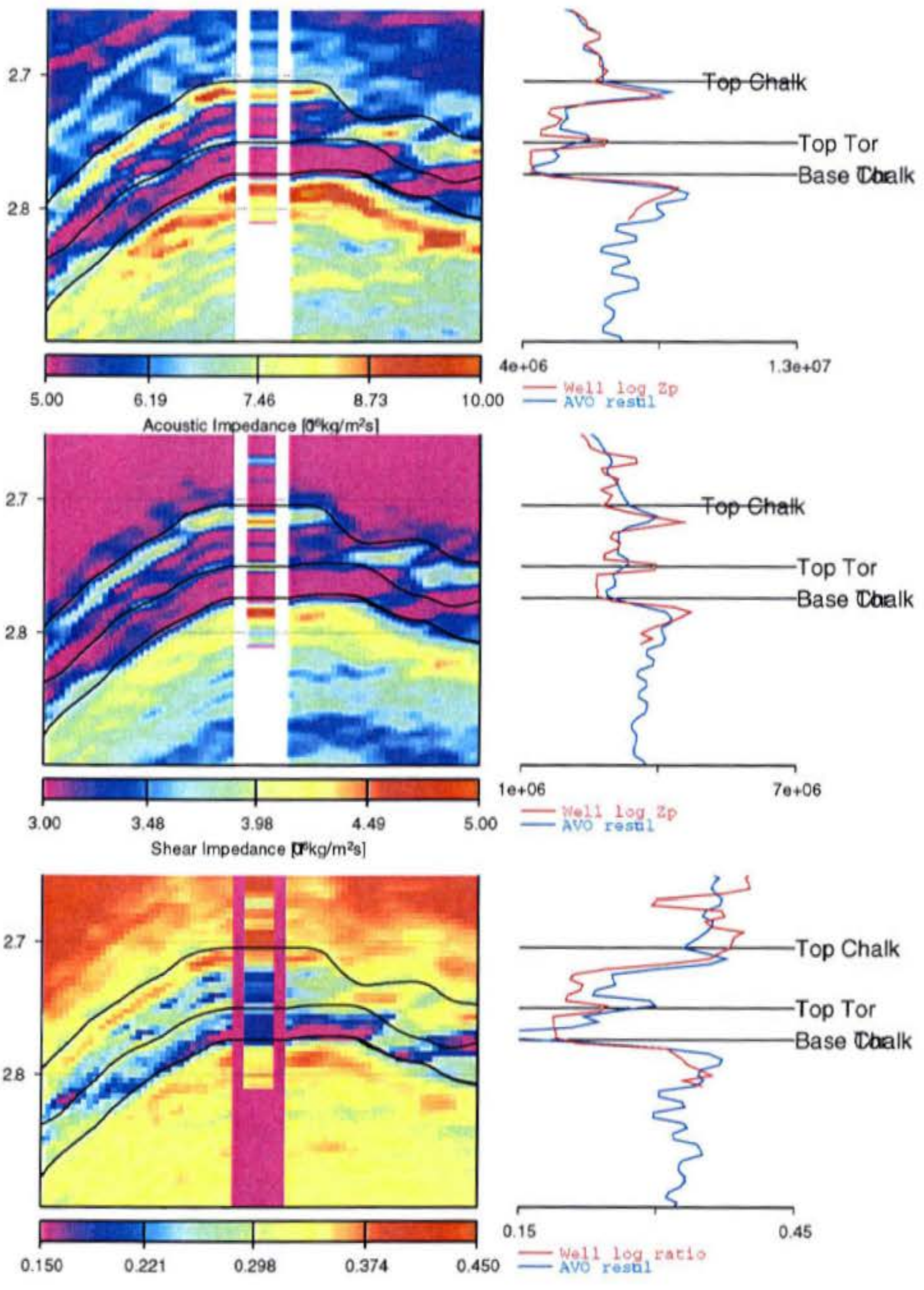

Fig. 11. Two-way time section with AVO-inversion of seismic data and inserted log response for the Rigs-2 well computed from forward modeling of the corrected MUHS model, NE-SW (Fig. 7).

a. Acoustic impedance, b. shear impedance, c. Poisson ratio.

Very good agreement is observed for both acoustic and shear impedance. Note the peaks in the tight zones near top chalk and top Tor, There is good agreement between the log- and AVO-pattern of Poisson's ratio, e.g. the peak at top Tor and the low values within the Tor Formation. This pattern cannot be resolved by the log if the acoustic properties are estimated from the sonic log because the water saturation near the well bore is unkown (Figs 6, 12).

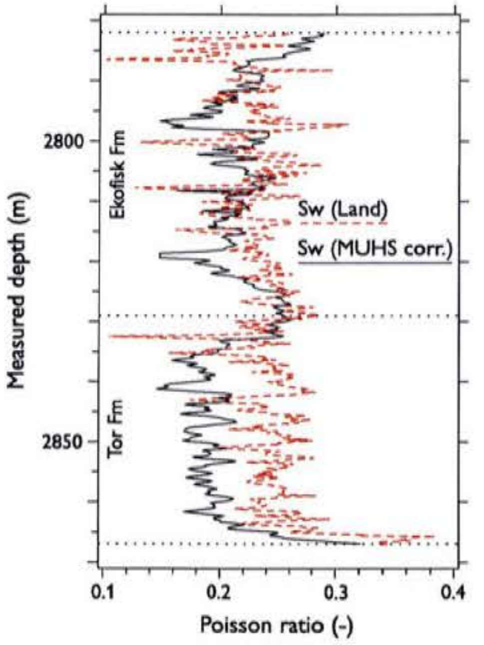

Fig. 12. Poisson's ratio versus measured depth estimated for the virgin zone based on Land's equation and on the corrected MUHS model (eqs. 7, 8). Forward modeling based on the MUHS model results in a low ratio in the high-porous Tor reservoir and pronounced peaks at top Ekofisk and top Tor in agreement with the inverted seismic data (Fig. 11). These features are not captured in the approach based on Land's equation because this model underestimates the flushing of the reservoir.

Intended for submission to Geophysical Prospecting

FLUID SUBSTITUTION IN CHALKS: EFFECTS OF SATURATION SCALES

Gary Mavko and Peter Japsen

ABSTRACT

In this paper we discuss some aspects of ultrasonic fluid substitution in chalks. We find that Gassmann's relations can be used to understand the variations of velocity with saturation in our samples, even though the velocity data are ultrasonic (high frequency). This suggests that in these samples there are no significant high frequency dispersion effects from the squirt-flow or Biot mechanisms that would invalidate the use of the Gassmann's relations. There is, however, evidence for patchy saturation in the ultrasonic data with a characteristic patch size less than 1/10 mm. This is observed in limited Vp and Vs versus Sw data. We also find that fluid substituting to full brine saturation using a modified patchy mixing rule gives velocities more consistent with empirical trends than assuming a fine-scaling mixing rule. It is likely that fine-scale mixing is dominant at logging frequencies in chalks. Another finding is that the dry-rock ultrasonic data tend to be inconsistent, in a Gassmann sense, with data from the water-bearing samples. Specifically, the dry rock velocities are "too fast."

INTRODUCTION

In this paper we discuss some aspects of ultrasonic fluid substitution in chalks. One important finding is that Gassmann's (1951) relations can be used to understand the variations of velocity with saturation in our samples, even though the velocity data are ultrasonic (high frequency). This suggests that in these samples there are no significant high frequency dispersion effects from the squirt-flow (Mavko and Jizba, 1991) or Biot (1956) mechanisms that would invalidate the use of the Gassmann's relations. There is, however, evidence for patchy saturation in the ultrasonic data (Domenico, 1975; Dutta and Odé, 1979; Knight and

Nolen-Hoeksema, 1990; Mavko and Nolen-Hoeksema, 1994; Mavko and Mukerji, 1998). Patchy saturation is another form of velocity dispersion, and its presence means that care must be taken to choose an appropriate mixing law for the air-water mix in the rocks, before applying Gassmann's relations.

Another finding is that the dry-rock ultrasonic data tend to be inconsistent, in a Gassmann sense, with data from the water-bearing samples. Specifically, the dry rock velocities are "too fast," an observation reported by other workers for limestones (Cadoret, 1993) and sandstones (Murphy, 1982; Knight and Dvorkin, 1992; Tutuncu, 1992). Third, we find evidence of patchy saturation during drainage of chalk samples at water saturation above c. 70% and ultrasonic frequencies. This corresponds to a characteristic patch size of much less than 1 mm for the chalk and it is thus likely that fine-scale mixing is dominant at logging frequencies in chalks.

We will begin with short discussions of previous observations of patchy saturation and anomalous dry-rock data. Then, we present evidence for saturation effects in our chalk data.

PREVIOUS OBSERVATIONS OF PATCHY SATURATION BEHAVIOR IN SANDSTONES AND LIMESTONES

It is now well-recognised (e.g. Mavko and Mukerji, 1998) that in rocks with mixed fluid phases, velocities depend not only on saturations but also on the spatial distributions of the phases within the rock. When the gas, oil, and brine phases are mixed uniformly at a very small scale in a rock, the different wave-induced increments of pore pressure in each phase will have time to diffuse and equilibrate during a seismic period. In this case we can replace the mixture of fluids with an average fluid whose bulk modulus, K_{fluid}, is given by the Reuss (1929) iso-stress average:

$$\frac{1}{K_{fluid}} = \frac{S_{water}}{K_{water}} + \frac{S_{oil}}{K_{oil}} + \frac{S_{gas}}{K_{gas}} \tag{1}$$

where $K_{fluid}, K_{oil}, K_{gas}$ are the bulk moduli of the individual phases and $S_{fluid}, S_{oil}, S_{gas}$ are the saturations. This K_{fluid} can, in turn, be substituted into Gassmann's relations to describe the effect of the fluid mix on the overall rock bulk modulus:

$$\frac{K_{sat}}{K_{mineral}-K_{sat}}=\frac{K_{dry}}{K_{mineral}-K_{dry}}+\frac{K_{fluid}}{\phi\left(K_{mineral}-K_{fluid}\right)};\quad \mu_{sat}=\mu_{dry}$$

where K_{dry}, K_{sat}, and $K_{mineral}$ are the bulk moduli of the saturated rock, the dry rock and the mineral; μ_{dry} and μ_{sat} are dry and saturated rock shear moduli; and ϕ is the porosity.

Mavko and Mukerji (1998) showed that equation (1) represents a lower bound; i.e., a fine scale mix of pore fluids gives the lowest possible rock bulk modulus (or P-velocity) for a given rock and given set of saturations. An important assumption of equation (1) is that the pore pressure increments are equal in the gas, oil, and water phases – hence, the name "iso-stress" average.

An approximate upper bound (Mavko and Mukerji, 1998) on velocity (neglecting very high frequency effects such as squirt-flow) can be approximated using a Voigt average fluid mix:

$$K_{fluid}=S_{water}K_{water}+S_{oil}K_{oil}+S_{gas}K_{gas} \tag{2}$$

and putting the resulting K_{fluid} into Gassmann's relations. The Voigt average is sometimes called the "iso-strain" average, which in a pure mixture of fluids is not particularly relevant. However in a porous medium, widely segregated fluid phases can be shown to mimic isostrain behaviour (Mavko and Mukerji, 1998).

What do we mean by a "fine-scale" mix of the fluid phases? A simple diffusion analysis suggests that during a seismic period, pore pressures can equilibrate over spatial scales smaller than $L_c \approx \sqrt{\kappa K_{fluid}/f\eta}$, where f is the seismic frequency, κ is the permeability, and η and K_{fluid} are the viscosity and bulk modulus of the most viscous fluid phase (Mavko and Mukerji, 1998; Sengupta, 2000). If the saturation scales are finer than $\sim L_C$, then diffusion allows the pore pressures in the various phases to be equilibrated, and equation (1) should be valid. In contrast, saturations that are heterogeneous over scales larger than $\sim L_C$ will have wave-induced pore pressure gradients that cannot equilibrate, and equation (1) will fail. We refer to this latter state as "patchy saturation." Table 1 illustrates a few examples of this scaling.

Table 1. Diffusion length or patch size for some values of permeability and seismic frequency (viscosity, η= 1 cPoise ; bulk modulus, K_{fluid} = 2.2 GPa).

Frequency, f	Permeability, κ	L_c
700 kHz	1 mD	0.0004 m
100 Hz	1000 mD	0.3 m
100 Hz	100 mD	0.1 m
100 Hz	1 mD	0.01 m
10 Hz	1000 mD	1.0 m

Examples of Patchy Behaviour

Figure 1 shows low frequency P- and S-wave velocities versus water saturation for Massilon sandstone, measured by Murphy (1982) using the resonant bar technique. The shear velocity V_S was measured in torsional mode at frequencies of 385-653 Hz, and extensional wave velocity V_E was measured at 599-997 Hz. P-wave velocity V_P was calculated from V_S and V_E . Saturations were achieved through drying, beginning with a fully saturated state. These data agree quite well with the fine-scale mixing model, i.e., K_{fluid} from equation (1) into Gassmann's equation, which is shown plotted. Exceptions are the data very close to Sw=0, which we discuss below. Some estimates of the velocities for patchy saturation are plotted for comparison, including the method based on the Voigt average fluid modulus, described above. The curve labelled as the "patchy upper bound" is another approximation, based on the Hill average, and discussed in detail in Mavko and Mukerji (1998) and Sengupta (2000).

Figure 2 shows low frequency P- and S-wave velocities versus water saturation for Estaillades limestone, measured by Cadoret (1993), also using the resonant bar technique, near 1 kHz. The closed circles show data measured during increasing water saturation via an imbibition process combined with pressurisation and depressurisation cycles designed to desolve trapped air. As with Murphy's Massilon sandstone data, these imbibition data fit the fine-scaling mixing (lower bound) model very well, except for the few data points near Sw=0.

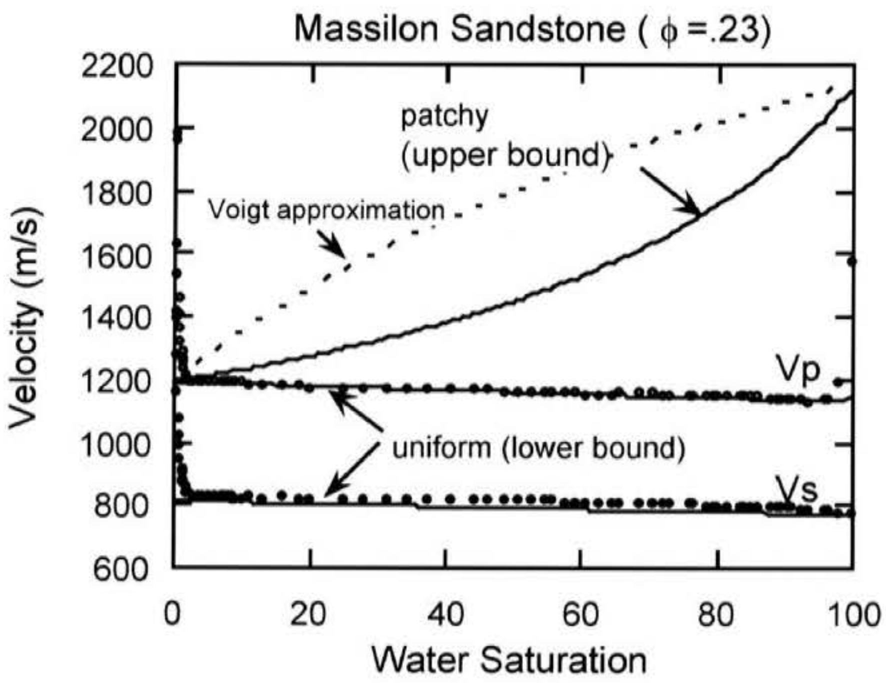

Figure 1. Low frequency data from Murphy (1982), showing excellent agreement with the uniform effective fluid model (lower bound).

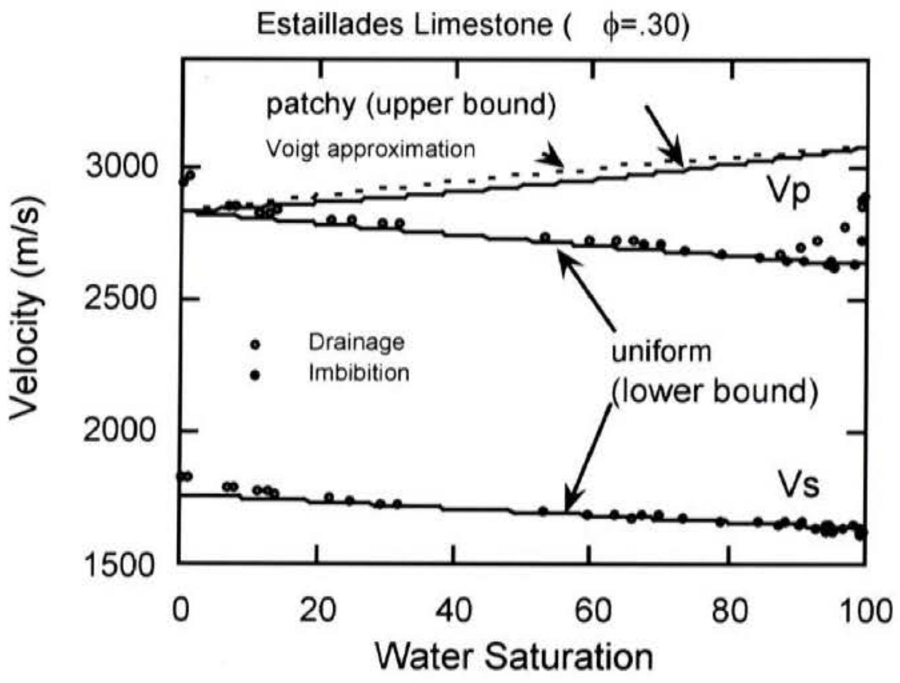

Figure 2. Low frequency data from Cadoret (1993). Closed circles show data during imbibition and are in excellent agreement with the uniform effective fluid model (lower bound). Open circles show data during drainage, indicating heterogeneous or patchy fluid distributions for saturation greater than about 80%. The Voigt approximation does a good job of estimating the patchy upper bound.

The open circles (Figure 2) show data measured during drainage. At saturations greater than 80%, the V_P fall above the uniform saturation line but below the patchy upper bound, indicating a heterogeneous or somewhat patchy fluid distribution. The V_S data fall again on the uniform fluid line, as expected, since patchy saturation is predicted to have no effect on V_S. On the other hand, other sources of dispersion, such as the Biot and squirt mechanisms (Mavko and Jizba, 1991) would cause both V_P and V_S to lie above the uniform saturation lines. Cadoret (1993) used X-ray CAT scans to confirm that, indeed, the imbibition process created saturations uniformly distributed at a fine, sub-millimetre scale, while the drainage process created saturation patches at the several centimetre scale. Using the measured permeability of ~250 mD, we estimate a critical diffusion length $L_c \approx 2$ cm. Thus we believe that during initial drainage, large centimetre-scale patches appeared, causing V_P to fall near the upper bound. With decreasing saturation, the characteristic patch size quickly decreased to less than $L_c \approx 2$ cm, causing V_P to fall near the lower bound at saturations less than 80%.

Figure 3 shows the velocities for Estaillades limestone from Figure 2, with an additional set of velocities measured at 50 kHz. Because the frequency is much higher, we expect the 50 kHz velocities to be contaminated by the ultrasonic dispersion mechanisms; as a result, they exceed the low frequency bounds at saturations > 80%. At 100% saturation, the distinction between patchy and uniform disappears. Hence, using the method of Winkler (1986), we take the difference between the measured V_P and the Gassmann predicted V_P at full saturation as an estimate of the high frequency dispersion, $\Delta V_P \approx 150\ m/s$. Subtracting this 150 *m/s* (~5%) from each of the data leaves a rough estimate of the patchy effect, replotted as the "corrected" values.

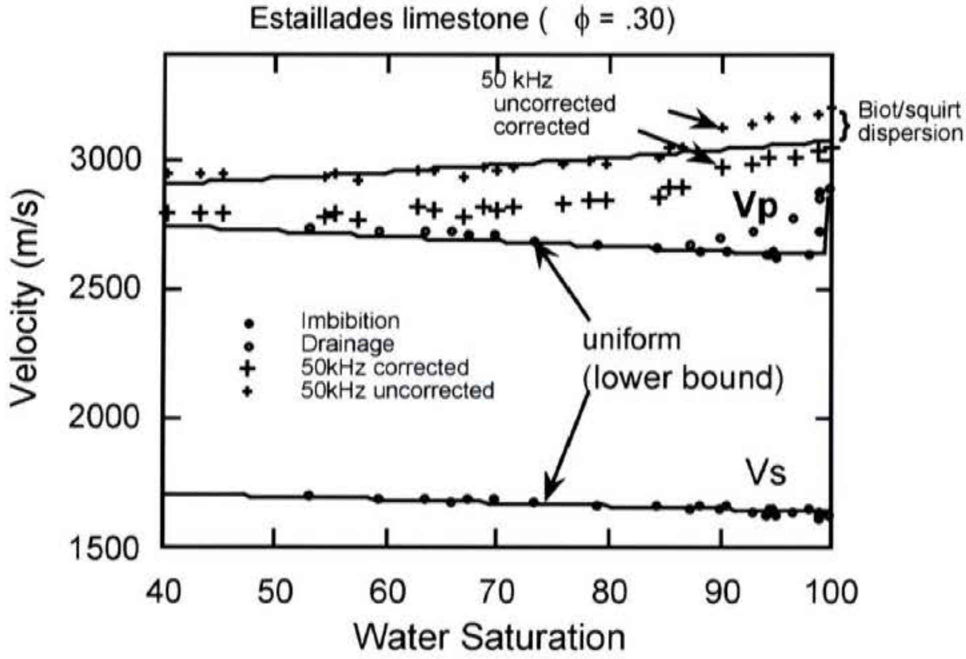

Figure 3. Data from Cadoret (1993). "+" symbols show high frequency data at 50 kHz. The corrected velocities are obtained by removing high frequency dispersion effects estimated from the measured and Gassmann predicted velocities at 100% saturation. Open and closed circles are resonant bar data, near 1 kHz.

In summary, we interpret the three sets of data in Figure 3 as follows: the low frequency imbibition data, falling along the lower bound are consistent with saturations always uniform at scales smaller than $L_c \approx 2$ cm; the low frequency drainage data are consistent with patches comparable to $L_c \approx 2$ cm at water saturations above 80% and smaller than $L_c \approx 2$ cm at lower water saturations; the ultrasonic data are consistent with patches larger than $L_c \approx 0.3$ cm at saturations greater than 60%; furthermore, the ultrasonic data show evidence of high frequency dispersion of the type that might be caused by the squirt-flow or Biot mechanisms.

The Problem With Very Dry Data

Figure 4 illustrates other features of the saturation problem. The data are from the same limestones as in Figures 2 and 3, measured by Cadoret (1993) using the resonant bar technique at 1 kHz. The very dry (dried in a vacuum) rock velocity is approximately 2.95 km/s. Upon initial introduction of moisture (water), the velocity drops by about 4%. This apparent softening of the rock occurs at tiny volumes of pore fluid, equivalent to a few mono-layers of liquid if distributed uniformly over the internal surfaces of the pore space. These amounts are hardly sufficient for a fluid dynamic description as in the Biot-Gassmann theories. Similar behaviour has been reported in sandstones by Murphy (1982), Knight and Dvorkin (1992), and Tutuncu (1992).

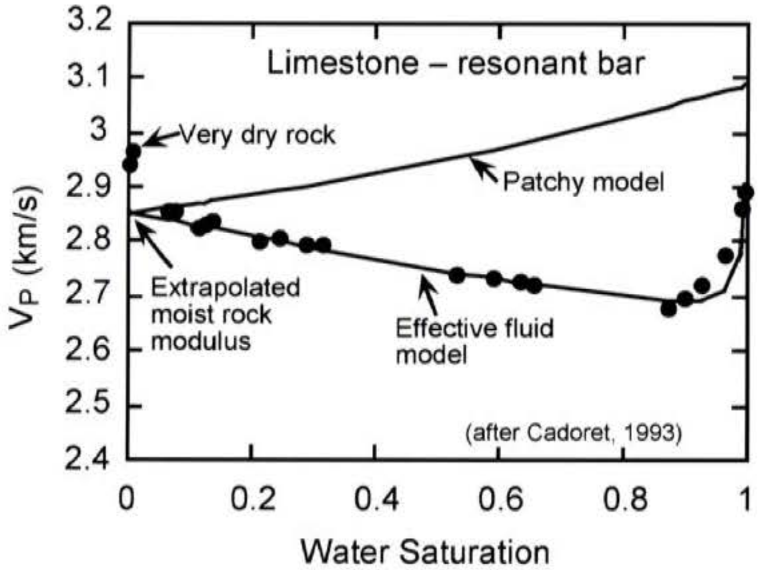

Figure 4. Velocity versus water saturation for a limestone measured at resonant bar frequencies (~1 kHz), from Cadoret (1993). The abrupt change of velocity at very low saturations has been attributed to the disruption of surface forces with the first few monolayers of water.

This velocity drop has been attributed to softening of cements (sometimes called "chemical weakening"), to clay swelling, and to surface effects. In the latter model, very dry surfaces attract each other via cohesive forces, giving a mechanical effect resembling an increase in effective stress. Water or other pore fluids disrupt these forces. A fairly thorough treatment of the subject is found in the papers of Sharma and Tutuncu (Sharma and Tutuncu, 1992; Tutuncu, 1992; Tutuncu and Sharma, 1992; Sharma et al., 1994).

After the first few percent of water saturation, additional fluid effects are primarily elastic and fluid dynamic and are amenable to analysis, for example, by the Biot-Gassmann and squirt models.

A number of authors (Cadoret, 1993; Murphy et al., 1991) have pointed out that classical fluid mechanical models such as the Biot-Gassmann theories perform poorly when the measured very dry rock values are used for the "dry rock" or "dry frame." These models can, however, be fairly accurate if the extrapolated "moist" or "wet" rock modulus (Figures 4 and 5) is used instead. For this reason, and to avoid the artefacts of ultra-dry rocks, it is often recommended to use samples that are at room conditions or that have been prepared in a constant humidity environment as estimates of the Gassmann "dry frame" data, and to not use the vacuum dry data.

Figure 5 shows a similar example for a clean sandstone, from Murphy (1982). Here the jump in velocity at very dry conditions is enormous. Again, using the very dry data in fluid substitution calculations would give nonsense results. However, using the "wet intercept", or measured data at ~ 1% water saturation gives Gassmann-consistent results.

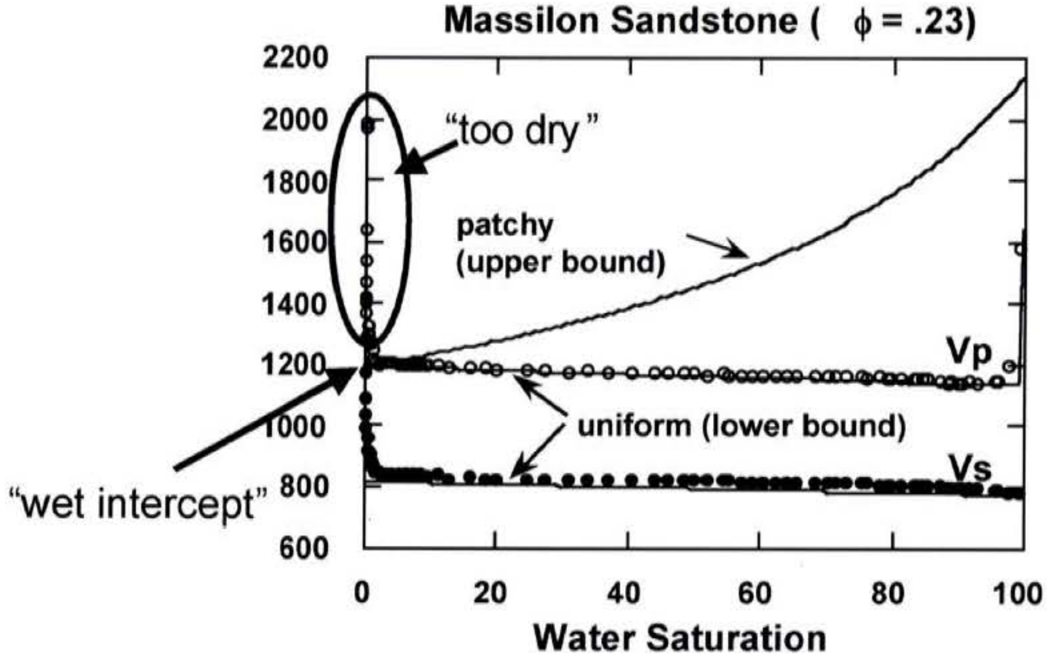

Figure 5. Velocity versus water saturation for a sandstone measured at resonant bar frequencies (~1 kHz), from Cadoret (1982). The abrupt change of velocity at very low saturations has been attributed to the disruption of surface forces with the first few monolayers of water.

Chalk Data

Ultrasonic measurements (700 kHz) were carried out on 77 dry chalk samples and 54 samples saturated with water; out of these 51 samples were investigated under both dry and saturated conditions. The chalk samples were from the Dan and South Arne fields in the Danish North Sea (22 from Danian Ekofisk Formation and 55 from the Maastrichtian Tor Formation. To prevent over-dry conditions, the samples were kept at room-moisture for two months after being dried at 110°C. The water saturation in the saturated plugs was generally between 97% and 103% (related to minor weight errors), but low permeability prevented total saturation in three Ekofisk and one Tor samples (Sw=92%–95%; plug numbers B003, B102, C022). Six Ekofisk samples were characterised by having regained high water content after drying, and this may be indicative of high clay content (Sw=7%–12%, plug numbers B003, B0010, B012 B0036; Sw=30%–34%, plug numbers B007, B008 but these samples fell apart when they were saturated). The remaining 71 dry samples had a mean water saturation of 0.3%. Measurements were also carried out under partially saturated conditions during drainage on two samples (Sw=25%, 50%, 75%; plug numbers C062, C100).

P- and S-wave velocities were determined from measured sample lengths (c. 2 cm) and automated readings of travel times for the maximum amplitude in the first major loop of first arrival events. The maximum amplitude was used rather than the first break because it is less affected by noise. Part of the plugs were measured at 25, 50 and 75 bar hydrostatic confining pressure where 75 bar corresponds to the magnitude of the effective stress at reservoir conditions. The increase of velocity with pressure was found to be limited (*c.* 4% when going from 25 to 75 bar) and velocities were thus only measured at 75 bar for the remaining part of the samples. Values of density, ρ [g/cm^3], grain density, ρ_{gr}, porosity, ϕ [-] and permeability, k [Darcy] were also determined.

Evidence for patchiness On Ultrasonic Chalk Data

Figure 6 shows an example of ultrasonic P- and S-wave velocities vs. water saturation for one of our core plugs. The dots are the ultrasonic measurements, and the solid curves are the predicted velocities assuming fine-scale mixing, equation (1).

For both the P- and S-wave velocities in Figure 6, the measured zero saturation values are "too dry" and "too fast" relative to the other saturation points, similar to what we discussed in for the limestone in Figure 4 and the sandstone in Figure 5. Hence, for our calculations we followed the procedure of Cadoret (1993) and inferred values for "nearly dry" Vp and Vs by extrapolating the data points back to zero saturation. The resulting points are used as the dry frame velocities in Gassmann's relations. We predict the velocities at higher water saturation values relative to the nearly dry values using the fine-scale mixing assumption, using equation (1) to get a K_{fluid} for the air-water mix, and then put K_{fluid} into Gassmann's relations. The results are shown by the solid black curves. Similar to Figure 3 for limestones, we see here that the S-wave velocities are modelled very well using the fine-scale mixing law; the P-wave velocities agree with fine-scale mixing at low saturations, but show evidence of patchiness for Sw greater than about 70%. The characteristic patch size for this sample becomes only 0,04 mm (Table 1), and this suggests that fine-scale mixing will be dominant at the lower frequencies used in sonic logging.

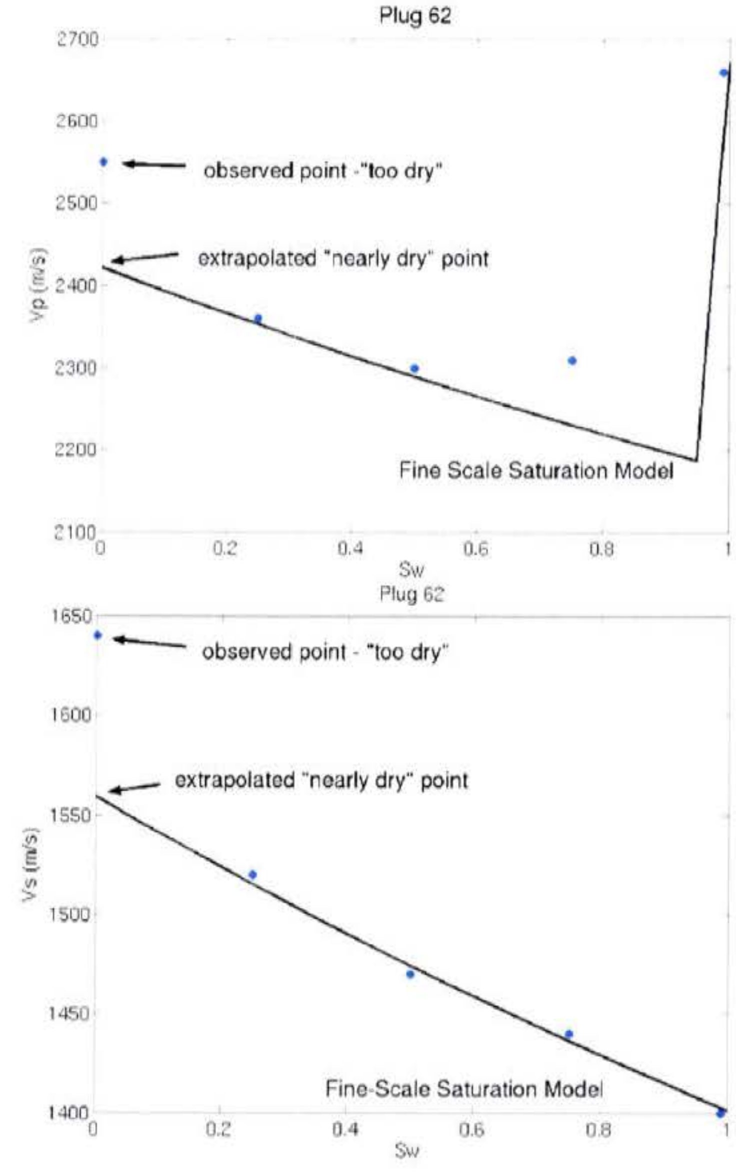

Figure 6. Comparison of ultrasonic measurements of velocities vs. saturation on a North Sea chalk sample, compared with the fine-scale mixing model, for core plug 62. ϕ=40%, permeability = 1.4 mDarcy.

Fluid Substitution to Full Water Saturation

In total, we had ultrasonic data on 77 chalk core plugs. In most cases only two saturations were available, typically Sw near zero or near one, but seldom completely dry or completely saturated. In order to look for systematics in Vp vs. porosity, Vs versus porosity, and Vp versus

Vs, it is desirable to take all measured velocities to a common fluid saturation. In our case, we prefer complete water saturation, since the dry rock velocities are problematic.

Since we have evidence of patchiness in the velocity vs. saturation data (Figure 6), the question is, what fluid mixing law is appropriate for the fluid substitution to full saturation? In this section, we compare the results using the Reuss average fine-scale mixing rule, equation (1), and a "modified patchy" mixing rule, published by Brie et al (1995):

$$K_{fluid} = \left(K_{water} - K_{gas}\right)S_{water}^{e} + K_{gas} \tag{3}$$

where K_{fluid} is the bulk modulus of the gas-water mix, K_{water} and K_{gas} are the moduli of the water and gas phases, and S_{water} is the water saturation. The exponent e is an empirical parameter. When $e=1$, equation (3) reduces to the Voigt model, equation (2) for a patchy gas-water mix. When e becomes very large, $K_{fluid} \rightarrow K_{gas}$, somewhat resembling the behaviour of a Reuss average, equation (1), for a fine-scale gas-water mix. Hence, equation (3) is an interpolation between fine-scale and patchy mixing behaviour. The Brie mixing rule, with a typical value of $e=3$, is plotted in Figure 7, compared with the Voigt and Reuss curves. The Brie mixing model captures some of the behaviour observed in Figures 3 and 6 – essentially fine-scale mixing behaviour at low water saturations, and patchiness at high water saturations.

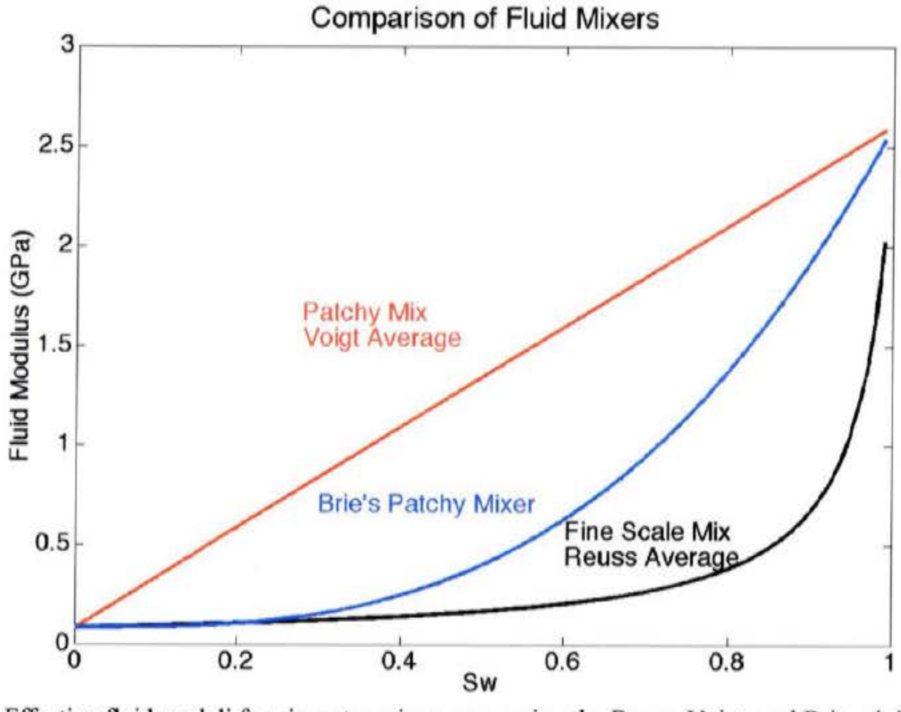

Figure 7. Effective fluid moduli for air-water mixes, comparing the Reuss, Voigt, and Brie mixing laws.

Figure 8 shows results of the fluid substitution calculations. At the top, are the measured ultrasonic Vp vs. Vs relative to Greenberg-Castagna (GC) empirical lines (Greenberg and Castagna, 1992), with the original mixed saturations. The solid green line is the GC empirical trend for water-saturated limestone,, and the dashed green line is for dry carbonates, computed from the GC water-saturated line using the Gassmann relations. The measurements cluster into two trends, mimicking the empirical lines, though at systematically smaller Vp/Vs ratios. The middle plot of Figure 8 shows the results of fluid substitution to 100% water using the Reuss (fine-scale) mixing assumption. We see that all of the nearly dry data are now falling near (slightly below) the empirical trend, though many of the high-Sw data are now overcorrected, falling well above the empirical trend for water-saturated limestone. Effectively, the data still fall along two trends. Finally, the bottom plot in Figure 8 shows the results of fluid substitution to 100% water using the Brie mixing model, with e=3. We see that almost all of the transformed points are now tightly clustered along a very narrow trend, just below the limestone trend. Similar results would have been achieved if had applied Voigt mixing-law to the high-Sw data,

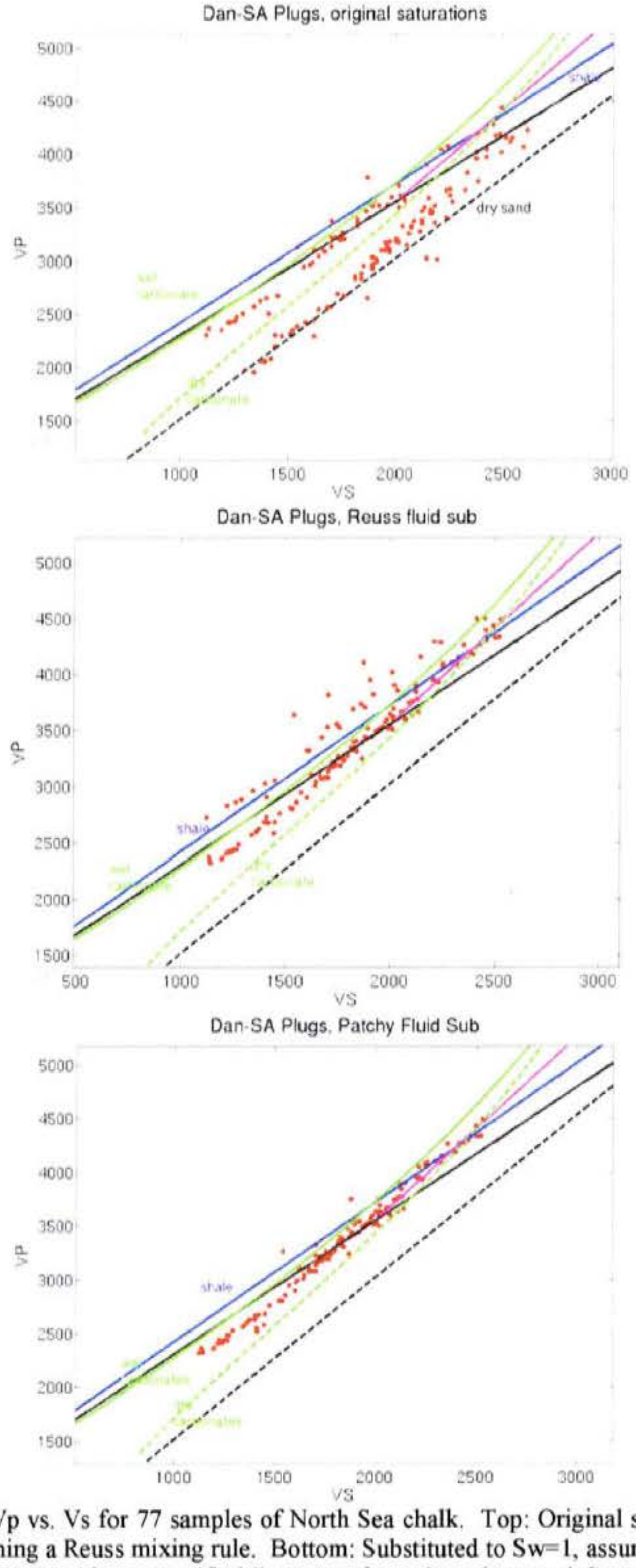

Figure 8. Ultrasonic Vp vs. Vs for 77 samples of North Sea chalk. Top: Original saturations. Middle: Fluid Substituted to Sw=1, assuming a Reuss mixing rule. Bottom: Substituted to Sw=1, assuming a patchy Brie mixing rule with e=3. Empirical relations for unspecified limestone from Greenberg and Castagna (1992). The trend for dry limestone is derived from the Castagna line using Gassmann's relations..

Figure 9 again shows the results of fluid substitution to 100% water using the Brie mixing model, but now comparing two salinities. The red dots are the same as in Figure 8 where the water is assumed to have very low salinity, essentially fresh water. The black dots correspond to reservoir fluids (Kfluid = 2.96 GPa and Rhofluid = 1.35 g/cc). Now we see that the velocities with the representative reservoir fluids fall very close to the GC empirical trend for limestone. The brine salinity and the lithology of the samples studied by Greenberg-Castagna is, however, not known, and the lithology may well be different from the pelagic chalk of the North Sea samples.

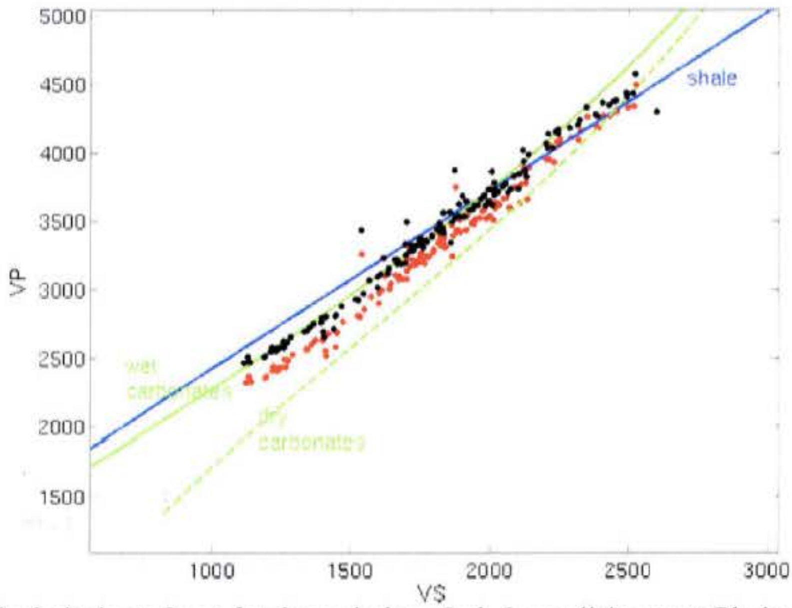

Figure 9. Fluid substitution to Sw=1 for ultrasonic data. Red: Low salinity water; Black: high salinity.

Figure 10 shows results of the same fluid substitution calculations as in Figure 8, but now plotted as Vp/Vs vs. 1/Vp, a typical display for detecting fluids. At the top are the data at original mixed saturations, again relative to Greenberg-Castagna empirical lines. The solid green line is the empirical trend for water-saturated carbonates and the dashed green line is for dry carbonates. Again, the measurements cluster into two trends, corresponding to high and low water saturations. The middle plot of Figure 10 shows the results of fluid substitution to 100% water using the Reuss (fine-scale) mixing assumption. Again, we see that the high-Sw data are overcorrected, falling well above the empirical trend for water. Finally, the bottom plot in Figure 8 shows the results of fluid substitution to 100% water using the Brie mixing model, with e=3. We see that nearly all of the transformed points are tightly clustered along a very narrow trend, below Castagna's limestone trend.

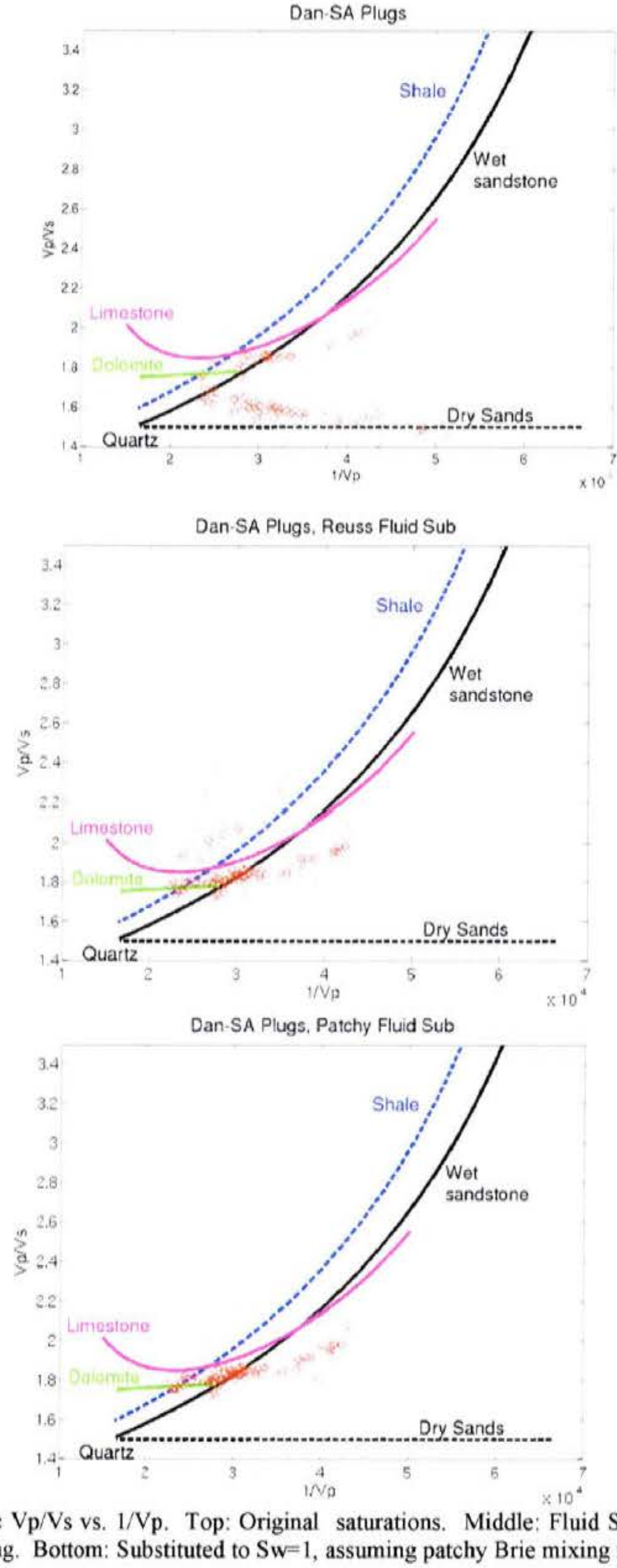

Figure 10. Ultrasonic Vp/Vs vs. 1/Vp. Top: Original saturations. Middle: Fluid Substituted to Sw=1, assuming Reuss mixing. Bottom: Substituted to Sw=1, assuming patchy Brie mixing rule.

SUMMARY

In this paper we discussed some aspects of ultrasonic fluid substitution in chalks. We found that Gassmann's (1951) relations can be used to understand the variations of velocity with saturation in our samples, even though the velocity data are ultrasonic (high frequency). This suggests that in these samples there are no significant high frequency dispersion effects from the squirt-flow or Biot (1956) mechanisms that would invalidate the use of the Gassmann's relations. There is, however, evidence for patchy saturation in the ultrasonic data with a characteristic patch size less than 1/10 mm. This is observed in limited Vp and Vs versus Sw data. We also find that fluid substituting to full brine saturation using a modified patchy mixing rule gives velocities more consistent with empirical trends than assuming a fine-scaling mixing rule. It is likely that fine-scale mixing is dominant at logging frequencies in chalks.

Another finding is that the dry-rock ultrasonic data tend to be inconsistent, in a Gassmann sense, with data from the water-bearing samples. Specifically, the dry rock velocities are "too fast."

ACKNOWLEDGEMENT

These results are part of the outcome of the energy research project Rock Physics of Impure Chalk which was sponsored by the Danish Energy Program (EFP-2001), Amerada Hess A/S and Dong E&P.

REFERENCES

Batzle, M. and Wang, Z., 1992, Seismic properties of pore fluids, *Geophysics*, 57, 1396-1408.

Biot, M. A., 1956, Theory of propagation of elastic waves in a fluid saturated porous solid I. Low-frequency range, *J. Acoust. Soc. Amer.*, 28, 168-178.

Cadoret, T., 1993, *Effet de la Saturation Eau/Gaz sur les Propriétés Acoustiques des Roches*, Ph.D. dissertation, University of Paris, VII.

Domenico, S.N., 1976, Effect of brine-gas mixture on velocity in an unconsolidated sand reservoir, *Geophysics*, 41, 882-894.

Dutta, N. C., and Odé, H., 1979, Attenuation and dispersion of compressional waves in fluid-filled porous rocks with partial gas saturation (White model) – Part 1: Biot theory, Part II: Results, *Geophysics*, 44, 1777-1805.

Gassmann, F., 1951, Über die elastizität poröser medien, *Vier. der Natur Gesellschaft:* 96, 1-23.

Greenberg, M.L. and Castagna, J.P., 1992, Shear-wave velocity estimation in porous rocks: theoretical formulation, preliminary verification and applications, *Geophysical Prospecting*, 40, 195-209.

Knight, R., and Nolen-Hoeksema, R., 1990, A laboratory study of the dependence of elastic wave velocities on pore scale fluid distribution, *Geophys. Res. Lett.*, 17, 1529-1532.

Knight, R., and Dvorkin, J., 1992, Seismic and electrical properties of sandstones at low saturations, *J. Geophys. Res.*, 97, 17425-17432.

Mavko, G., and Jizba, D., 1991, Estimating grain-scale fluid effects on velocity dispersion in rocks, *Geophysics*, 56, 1940-1949.

Mavko, G., and Nolen-Hoeksema, R., 1994, Estimating seismic velocities in partially saturated rocks, *Geophysics*, 59, 252-258.

Mavko, G. and Mukerji, T., 1998, Bounds on low frequency seismic velocity in partially saturated rocks, Geophysics, vol 63., no. 3, pp 918-924.

Murphy, W.F. III, 1982, *Effects of microstructure and pore fluids on the acoustic properties of granular sedimentary materials*, Ph.D. dissertations, Stanford University.

Reuss, A., 1929, Berechnung der Fliessgrense von Mischkristallen, *Zeitschrift fur Angewandte Mathematik und Mechanik*, 9, 49-58.

Sengupta, M. 2000, Integrated rock physics and flow simulation to reduce uncertainties in seismic reservoir characterisation, Ph.D. Dissertation, Stanford University.

Sharma, M.M., and Tutuncu, A.N., 1994, Grain contact adhesion hysteresis: a mechanism for attenuation of seismic waves, *Geophys. Res. Lett.*, 21, 2323-2326.

Sharma, M.M., Tutuncu, A.N., and Podia, A.L., 1994, Grain contact adhesion hysteresis: a mechanism for attenuation of seismic waves in sedimentary granular media, *Extended Abstracts SEG 64th Annual Meeting*, Los Angeles, 1077-1080.

Tutuncu, A.N., 1992, *Velocity Dispersion and Attenuation of Acoustic Waves in Granular Sedimentary Media*, Ph.D. Dissertation, The University of Texas at Austin.

Tutuncu, A.N., and Sharma, M.M., 1992, The influence of grain contact stiffness and frame moduli in sedimentary rocks, *Geophysics*, 57, 1571-1582.

White, J. E., 1975, Computed seismic speeds and attenuation in rocks with partial gas saturation, *Geophysics*, 40, 224-232.

Winkler, K., 1986, Estimates of velocity dispersion between seismic and ultrasonic frequencies, *Geophysics*, 51, 183-189.

Modelling seismic response from North Sea Chalk reservoirs resulting from changes in burial depth and fluid saturation

O. V. Vejbæk[1], R. Rasmussen[1], P. Japsen[1],
J. M. Pedersen[2], I. L. Fabricius[3] and G. Marsden[4]

March 17, 2003

Intended for submission to Petroleum Geology conference, London, 2003.

[1] Geological Survey of Denmark and Greenland, Ministry of the Environment (GEUS), Østervoldgade 10, DK-1350 Copenhagen, Denmark
[2] Ødegaard A/S, Titangade 15, DK-2200 Copenhagen N, Denmark
[3] Technical university of Denmark, (DTU)
[4] Amerada Hess Aps, Østergade 26B, DK-1100 Copenhagen K, Denmark

Abstract

Changes in seismic response caused by changes in degree of compaction and fluid content in North Sea Chalk reservoirs away from a well bore are investigated by forward modelling. The investigated seismic response encompasses reflectivity changes, AVO and acoustic impedance. Synthetic seismic sections, impedance cross sections and AVO response are presented as calculated on the basis of selected wells from the South Arne and Dan Fields, Danish North Sea and compared to field records.

The two main variables to use for seismic response prediction away from the well bore is depth of burial (changes in effective stress) and changes in hydrocarbon saturation (Fig. 0). Three main modelling tools are used for the modelling: 1) Rock physics, 2) Saturation modelling and 3) Compaction/de-compaction modelling.

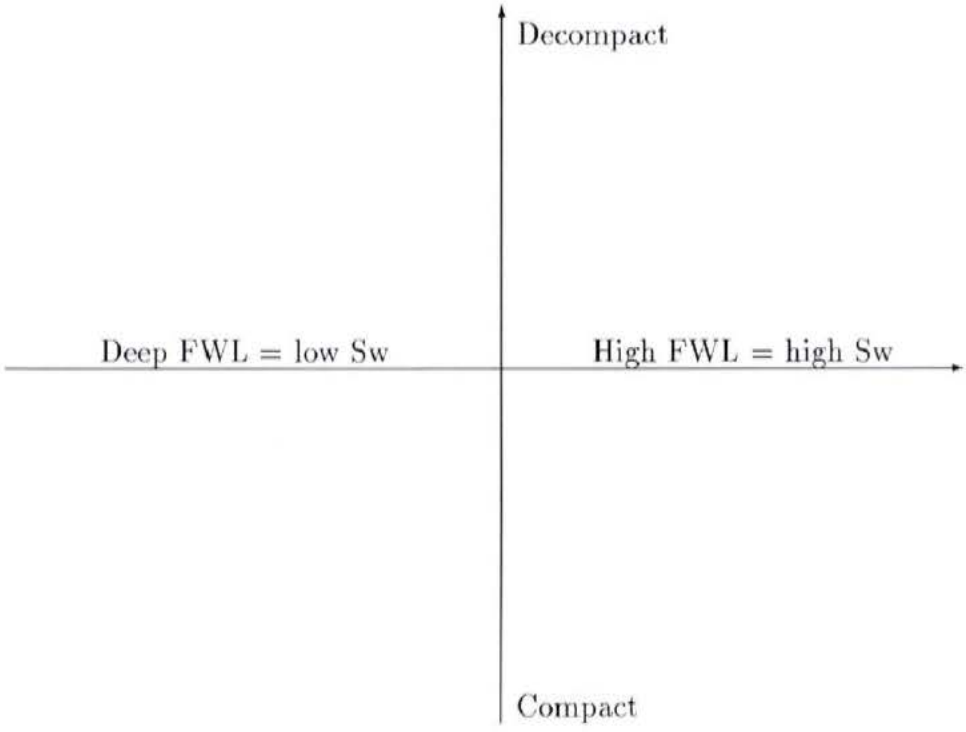

Figure 0: Main variables to investigate away from a well bore are changes in degree of compaction, and changes in HC saturation. The latter is obtained through saturation height modelling via the free water level (FWL)

Rock physics theory is applied to obtain all necessary parameters for the complete set of elastic parameters for the application of the Zoeppritz equations. The challenge is not only to predict the shear velocity, but also to account for the changes in fluid content via application of the Gassmann equation. An approach akin to the one suggested for the Ekofisk Field by Walls et al. (1998) is applied for the prediction of changes in degree of compaction.

Hydrocarbon saturation in North Sea Chalk is strongly affected by capillary forces due to the small scale of the pores and transition zones in the order of 50 m are not uncommon. For this reason, potent saturation modelling is needed in order create realistic input for the seismic modelling. We use saturation height models similar to the EQR model (Engstrøm 1995), which have proved robust for the prediction of

saturation profiles in Danish Chalk reservoirs.

Compaction modelling relies on simple exponential decay of porosity with depth, where abnormal fluid pressures are accounted for. A new set of compaction parameters is presented. These parameters are based on a study on the North Sea Chalk based on some 850 wells. The parameters appear to be sufficiently fine-tuned to allow fairly precise predictions of abnormal fluid pressures from observed average porosity. Based on this, the relative contribution to porosity preservation by abnormal fluid pressure and early hydrocarbon invasion may be estimated.

Some conclusions based on modelling results include: Reflectivity is correlating with porosity, acoustic impedance is more susceptible to porosity variation than to hydrocarbon saturation, and the poisson ratio may be rather sensitive to hydrocarbon saturation.

Introduction

Zero offset seismic response at a well site may be readily modelled provided reliable calibrated sonic and density logs are available. If shear velocity logs are available amplitude versus offset (AVO) response may also be modelled. However, questions may arise as to what cause changes in the response away from the well site. This paper develop methods for creating forward models of the seismic response away from the well site. The models are developed for North Sea Chalk and applied to two wells: Rigs-2 and M-10x drilled in the South - Arne and Dan fields respectively (Fig. 1). The models are aimed at studying effects of hypothetical changes in degree of compaction and hydrocarbon saturation away from a well bore. We aim to use realistic saturation models, which makes it impossible to study changes in compaction without concurrent changes in hydrocarbon saturation. This is because chalk reservoirs are usually strongly affected by capillary forces which vary with porosity. However, this allows us to study more realistic scenarios.

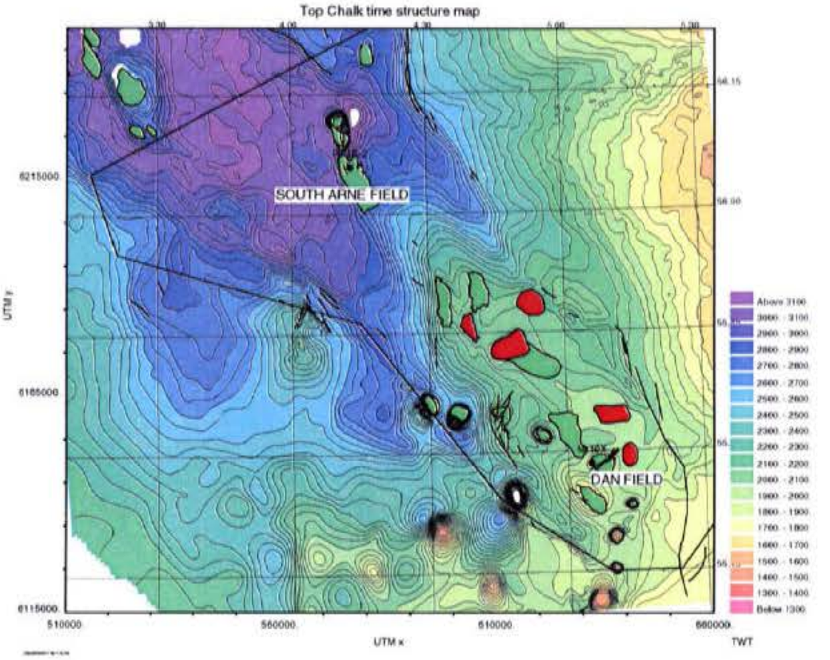

Figure 1: Top Chalk time structure map with locations of wells and fields referred to in this paper.

Compaction modelling

Compaction modelling is done by applying empirical compaction laws where excess fluid pressure is accounted for in a simplistic way. This approach is favoured over deterministic modelling, because pressure development is very hard to model due to inherent uncertainties in the geological development of basinwide hydraulic connectivity.

The goal of the compaction modelling is to calculate porosity logs as a function of changes in burial depth and/or changes in effective stress caused by changes in excess fluid pressure.

Basic assumptions are:

- In the absence of over-pressuring and early diagenesis, porosity decay follows a simple exponential law according to depth.
- Depth is considered a proxy for effective stress in the absence of overpressure.
- Deviations in porosity from the average function are due to very early diagenesis or later over-pressuring for too tight and too porous intervals respectively.
- The overpressure as of today has not dissipated significantly since onset: Overpressure "arrests" porosity as it is at the time of onset.
- Very tight chalk has been cemented shortly after burial, and follows a lower porosity decay curve than standard (This has however proved to be irrelevant for the cases studied here).

The basic approach follows the original proposition by Athy (1930) and is detailed in e.g. Sclater and Christie (1980) and Jensen et al. (1984):

$$\phi = \phi_0 \cdot e^{-a \cdot z} \tag{1}$$

where ϕ_0 is the surface porosity in fractions, z is depth of burial and a is the decay parameter. Some relevant parameters are listed in table 1. This equation can be developed to allow correction of the layer thickness as a function of burial or change in effective stress and thereby preserve rock mass (e.g. Sclater and Christie 1980; Jensen et al. 1984). However, since we are interested in changes away from a well site, and not in what has happened to the succession at the well site, we chose not to change thickness during our compaction/ de-compaction calculations except for the sample subsidence and porosity development curves shown in Figs 3, 4, 5 and 6.

In the case of chalk Sclater and Christie (1980) suggest values of 0.7 for ϕ_0 and $0.00071m^-1$ for a. The reciprocal of the decay parameter, the decay length (reduction to 37% of surface porosity) is equal to 1408.5 m. These values correspond to average normal pressured chalk, but are not consistent with velocity data (Japsen 2000). A compaction trend for North Sea chalk was constructed by transforming the revised normal velocity – depth trend of Japsen (1998, 2000) into a porosity-depth trend. The normal velocity – depth trend for chalk was based on an analysis of data from 845 wells throughout the North Sea Basin and ODP data and burial anomalies relative to the trend were found to agree with estimates of erosion along the basin margins and with measured overpressure in the centre of the basin. The trend was transformed into a porosity – depth trend by converting velocity to porosity via a constructed velocity – porosity trend for chalk (Fig. 2). The velocity – porosity trend was established as a second order polynomial fit to two segments:

a. The modified Hashin – Shtrikman model for chalk with porosities in the range from 10% to 43% suggested by Japsen et al. (2000) and

b. A straight line connecting the endpoint of segment a. at 43% (velocity 2720 m/s) to the parameters corresponding to the critical porosity of chalk at 70% (velocity 1550 m/s).

	ϕ_0	a	$1/a$	source
Neogene	0.56	3.91E-04	2560.2	
Palaeogene	0.71	5.10E-04	1960.0	
Chalk $z < 768.2$	0.70	5.50E-04	1818.2	
Chalk $z > 768.2$	0.97	9.72E-04	1029.3	

Table 1: Compaction constants.

The normal pressure chalk porosity – depth trend derived this way is approximated with a bi-segment exponential model as listed in Table 1.

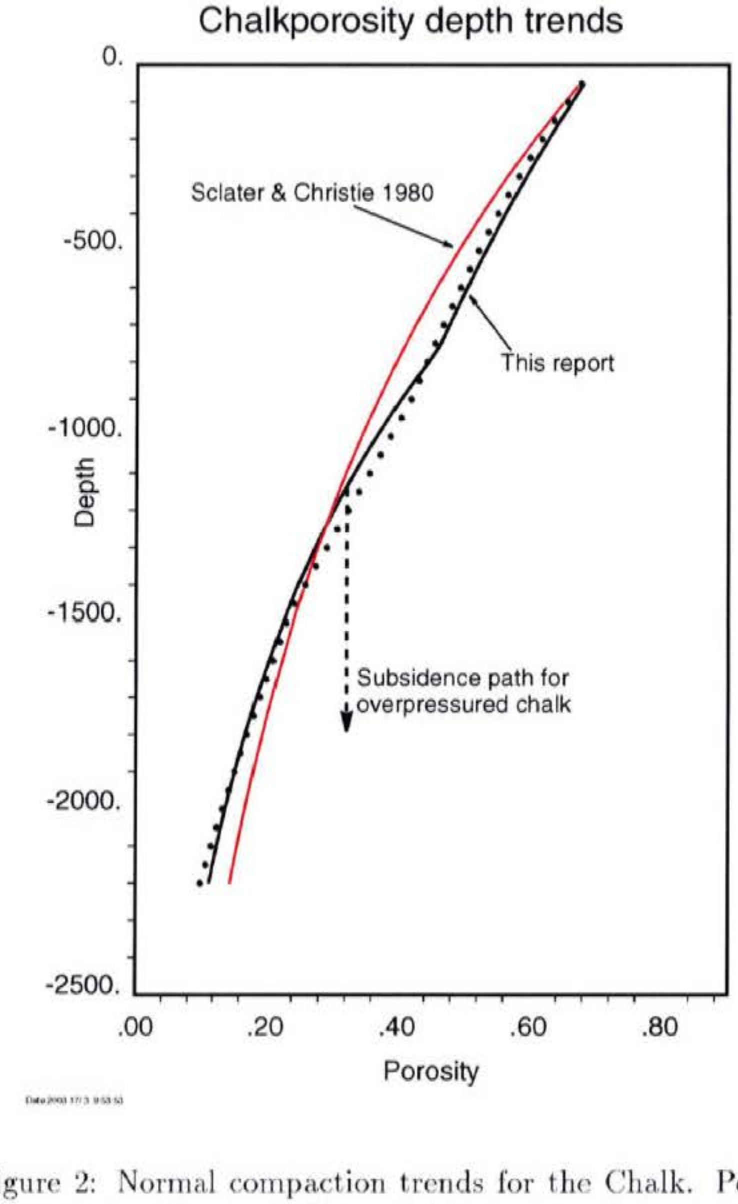

Figure 2: Normal compaction trends for the Chalk. Porosity depth values derived from velocity model is shown as dots, and the fit to this as a black line. Dashed line shows an example porosity – depth path for overpressured chalk.

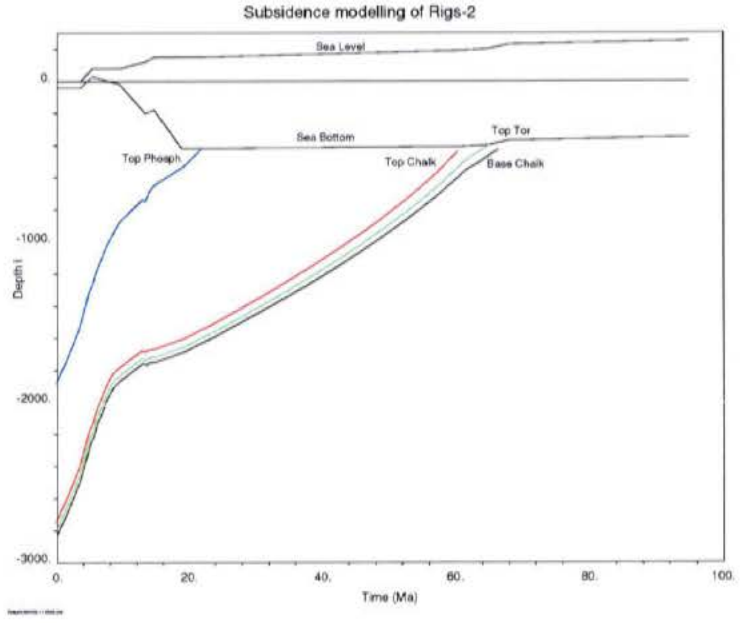

Figure 3: Modelled subsidence at the Rigs-2 well, South Arne Field (see Fig. 1 for location).

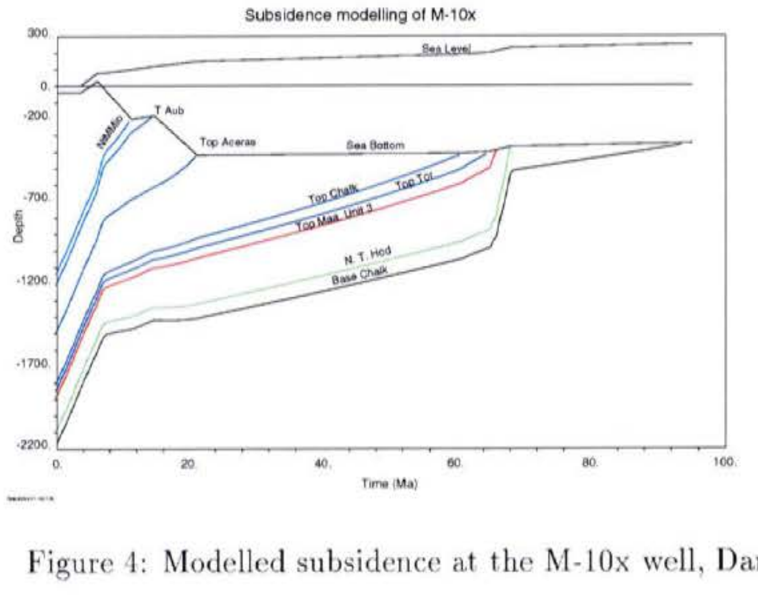

Figure 4: Modelled subsidence at the M-10x well, Dan Field.

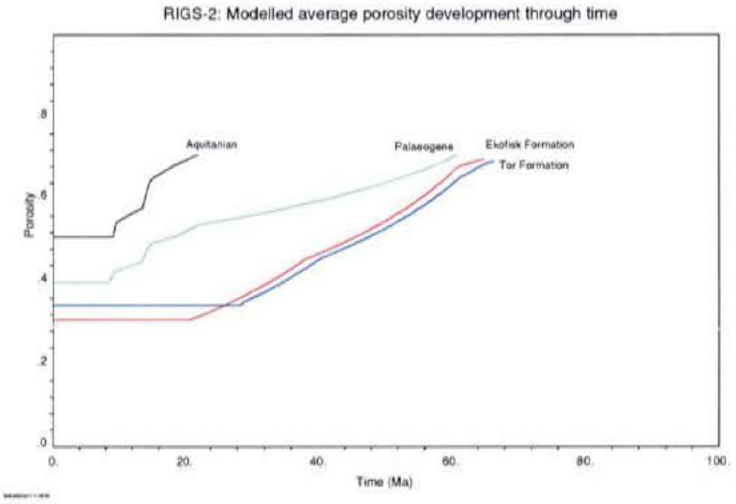

Figure 5: Simplistic porosity development model for the Rigs-2 site. Overpressuring arrests porosity decay in the Palaeogene at ~ 10 Ma, but modelling suggests that HC effects arrest porosity decay in the Chalk much earlier.

Over-pressuring is assumed in depth intervals where the porosity exceeds the porosity expected at the present depth according to the normal compaction trend. It is assumed that excess pore pressure has not dissipated at all since onset. The duration of over-pressuring is the shortest possible with this assumption. This method is hereafter called "pressure preserving de-compaction". An alternative approach would be to assume that overpressure, and thus abnormal porosity, has been building up gradually since deposition, hereafter referred to as "gradual pressure build-up decompaction". The two assumptions may be considered as end-members of possible actual scenarios, but neither handles the case where higher overpressure in the past has dissipated to some extent.

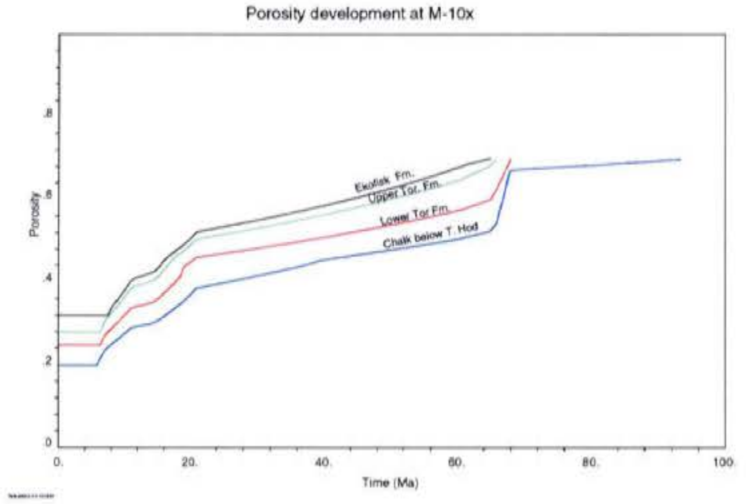

Figure 6: Simplistic porosity development model for the M-10x site. Overpressuring arrests porosity decay at ~ 8 Ma, and HC effects are apparently not important for Chalk porosity preservation.

Burial graphs show rapid burial rates only in the Neogene and very modest burial rates in Cretaceous – Palaeogene times (Figs. 3 and 4). Relative tranquility in Palaeogene times makes it likely that possible earlier over-pressure may have dissipated and present over-pressure to be primarily caused by rapid Neogene deposition. The observed excess pore pressure is therefore assumed to have initiated very late, and only few million years before present. This is further supported by the apparent correspondence between thickness of Neogene deposits and magnitude of overpressure (Japsen 2000). The pressure preserving de-compaction approximation therefore seems to be the best choice as the short time available reduces the problem of modelling pressure dissipation.

In the case of over-pressuring, the average presently observable porosity (ϕ_{obs}) in the interval is higher than predicted by the standard porosity decay function (equation 1). The porosity is assumed to be preserved since onset of over-pressuring. The exact depth where ϕ_{obs} is on the normal compaction curve is given by:

$$z_{obs} = \frac{1}{-a} Log\left(\frac{\phi_{obs}}{\phi_0}\right) \tag{2}$$

where z_{obs} is the depth where the unit left the normal compaction trend. On the basis of the following equation, average burial anomalies (z_{ano}) are computed for each stratigraphic unit where effects of minor lithological is minimized by averaging:

$$z_{ano} = \frac{1}{n}\sum_{n}^{1}\left[z - \frac{1}{-a} Log\left(\frac{\phi_{obs}}{\phi_0}\right)\right] \tag{3}$$

where z is present observation depth and n is the number of porosity log samples in the interval.

During compaction or decompaction a depth shift (Δz) is imposed. The logged porosity is then changed under the assumption that each sample has each their porosity – depth trends. For each sample in the porosity log an individual surface porosity ($\phi_{0'}$)is calculated according to:

$$Log(\phi_{0'}) = a(z - z'_{ano}) + Log(\phi_{obs}) \tag{4}$$

where $z'_{ano} = z_{ano} + \Delta z$ is the depth shift and Δz is the compaction/de-compaction value expressed as a depth shift. It is noted that the surface porosity is corrected according to the depth where the average porosity is on the normally pressured depth trend, and not the present depth. This approach implies that porosity deviations on the log are inherited from surface condition and reflect primary lithological and depositional differences. Diagenetic processes that may add material of cause local redistribution of material are thus neglected.

An example of such depth shifts is discussed below and shown in Fig. 12.

The burial anomalies may be directly converted into an estimated excess pressure as this is the main cause for the porosity anomaly (Japsen 1998). If the overpressure (Δp) is assumed to be caused by Neogene rapid deposition (the burial anomaly), then it is equivalent to the effective stress (σ) exerted by this column:

$$\sigma = \Delta p = (\rho_r - \rho_{br}) \cdot g \cdot z_{ano} \tag{5}$$

where g is the gravity constant. If densities of the rock (ρ_r) and brine (ρ_{br}) are equal to 2000 and $1000 Kg/m^3$, then a burial anomaly of 100 m is roughly equivalent to 1 MPa.

Burial modelling of the Rigs-2 well site

In order to elucidate the conditions at the Rigs-2 well backstripping has been performed. Depths and compaction parameters for this well are listed in table 3. The well encountered excess pressures at 1300 m increasing to app. 7.4 MPa at 1600 m, 12MPa at 2600 m, and 14.8 MPa in the Chalk section (Table 2). In our cases the burial anomalies are calculated as given in table 2 with parameters given in table 3.

Rigs-2	Burial anomaly (m)	Approximate Pressure (MPa)	Observations (MPa)
Below near base Tortonian	381	3.8	-
Below top Aub	730	7.3	-
Below top Aceras	1180	11.8	12
Chalk	1654	16.5	14.8

Table 2: Burial anomalies and excess fluid pressure for the Rigs-2 well. Calculated burial anomalies are converted to over-pressure as described in the text.

The subsidence graph calculated this way (Fig. 3) displays moderate burial rates until approximately 15 Ma b.p., where a considerable increase is noted. At approximately 10 Ma b.p. porosity is arrested in the Palaeogene due to over-pressuring (Fig. 5). Porosity in the Chalk is modelled to be arrested much earlier which reflect early hydrocarbon invasion rather than over-pressuring. A similar modelled porosity development for the M-10x shows no earlier cessation of porosity decay in the chalk reflecting later hydrocarbon charging of the Dan Field as compared to the South Arne Field (Fig. 6).

Rock unit	Base unit TWT Sec.	Base unit m. b.m.s.l.	Surface porosity ϕ_0	Decay length m. $1/a$
Quaternary	na	453.5	0.56	2560.16
Piacenzian	na	794.0	0.56	2560.16
Zanclean	na	809.4	0.56	2560.16
Messinian	na	902.4	0.56	2560.16
Tortonian	1.430	1411.63	0.56	2560.16
Aub	1.805	1772.4	0.71	1960.02
Aceras	2.705	2745.6	0.71	1960.02
Ekofisk Fm.	2.741	2796.1	0.968	1029.34
Tor Fm.	2.766	2829.1	0.968	1029.34

Table 3: Depths and compaction constants for the Rigs-2 well. Note that this listing mode means that for instance Top Chalk is at 2.705 sec.

The observed pressure in the Rigs-2 well is, however, about 10% lower than the estimate based on porosity observations. If the anomalous high porosity in the well is attributed to other factors than over-pressuring, then this other effect may be contributing with 10 % compared to pressures. This other effect may be early hydrocarbon invasion, which frequently has been suggested as a cause for porosity preservation above normal (e.g. Bramwell et al. 1998).

In the Central Graben in general there seem to be roughly the same excess pressure in the water zones of the lower Palaeogene section and the Chalk. As seen in table 2, the calculated excess pressure for the chalk is exceeding the Lower Palaeogene pressure by 3.7 MPa and observed pressure difference is 2.8 MPa. Only 0.74 MPa of this difference is attributable to a direct pressure effect from the hydrocarbons, so the pressure increase in the chalk suggests lateral support from deeper levels.

Within the chalk a difference of 0.9 MPa is seen between observed and calculated excess pressure. It is therefore estimated that the abnormally high porosity is due to a combination of overpressure and preserving effects of the invaded hydrocarbons. It may be estimated that rapid Neogene deposition contributes with 12 MPa, the hydrocarbon column constributes with 0.74 MPa and lateral pressure support contributes 2 MPa to the observed pressures and porosity preservation. The porosity preservation owing to the presence of hydrocarbons could have been replaced by only a further ~ 2 MPa.

Saturation modelling

In order to model the saturation realistically, the strong capillary effects in the chalk must be taken into account. We apply the saturation height model developed by Hess (2001). In this method the saturation is calculated directly from the capillary pressure (P_c) and the capillary entry pressure (P_{ce}):

$$Sw = \left(\frac{P_{ce}}{A \cdot P_c - A \cdot P_{ce} + P_{ce}} \right)^{1/B} \tag{6}$$

where A and B are given by:

$$A = 10^{c_1 + c_2 \cdot \phi} \tag{7}$$

$$B = 0.10 + 1.95 \cdot \phi$$

where ϕ is the porosity (in fractions). Constants c_1 and c_2 differs for the Tor and Ekofisk formations as given in table 4.

The capillary entry pressure is given by an equation of the form:

$$P_{ce} = c_3 \cdot \phi^{c_4} \tag{8}$$

where constants c_3 and c_4 are different for the Tor and Ekofisk Formations as given in table 4.

Formation	c_1	c_2	c_3	c_4
Ekofisk	-0.75	2.70	7.5	-1.2
Tor	-1.10	4.35	7.0	-0.7

Table 4: Constants for the saturation height model.

The capillary pressure is obtained from the height above free water level (FWL):

$$Pc = (FWL - z) \cdot \Delta p \cdot Cap \tag{9}$$

where z is the depth, Δp is the pressure gradient difference between oil and water, and Cap is the conversion factor of interfacial tension in the Hg/air system to the oil/water system at reservoir conditions. In the case of the Rigs-2 well the following values for the parameters are assumed:

$$\Delta p = 0.182 psi/ft = 0.0413 bar/m \tag{10}$$

$$Cap = \frac{\sigma Cos\theta_{ow}}{\sigma Cos\theta_{Hg/air}} = \frac{28}{367} = 0.076 \tag{11}$$

These parameters produce an acceptable fit to observed Sw, if a FWL at 2900 m (b.m.s.l.) is assumed (Fig. 7). During modelling of seismic response to changes in hydrocarbon saturation (Sw), the above saturation height model is applied. Changes in Sw can occur in the model by imposing changes in FWL, such that realistic vertical differences in Sw are calculated. If alternatively the model is aimed at studying changes in compaction the above saturation height model will automatically impose Sw changes due to the porosity dependency.

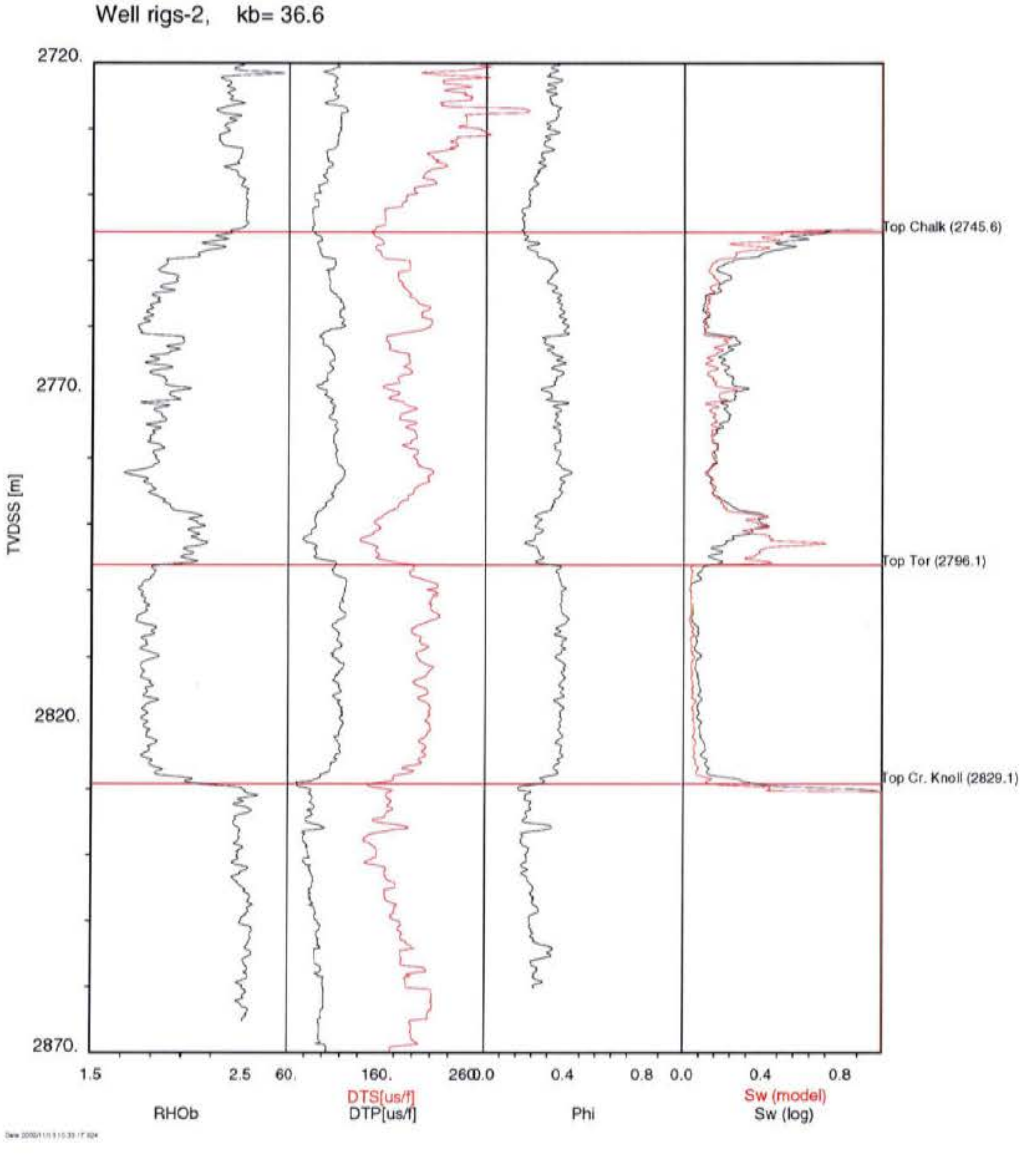

Figure 7: Rigs-2 Log data.

Rock Physics and Fluid substitution

We estimate elastic properties and changes thereof in the chalk as a consequence of changes in hydrocarbon saturation and degree of compaction. The relationships for elastic moduli and velocity versus porosity are described using modified Hashin – Shtrikman bounds and Gassmann's relations in an approach similar to the one suggested by Walls et al (1998).

Fluid substitution

We assume the low-frequency theory for fluid substitution by Gassmann (1951) to be fulfilled for elastic measurements with log tools. It is thus assumed that the chalk is sufficiently permeable to allow pore fluid pressures to equilibrate instantaneously when sound waves propagates through the rock. This is not fulfilled for isolates pores and low permeability rocks at high frequency, but will automatically be fulfilled for seismic data if Gassmann's theory applies to log data. The Gassmann theory gives the following relationship between rock moduli:

$$\frac{K_{sat}}{K_0 - K_{sat}} = \frac{K_{dry}}{K_0 - K_{dry}} + \frac{K_{fl}}{\phi(K_0 - K_{fl}})) \tag{12}$$

and $G_{sat} = G_{dry}$ where K_{dry} ,K_{sat} , K_0 and K_{fl} are bulk moduli of the dry rock, the saturated rock, the mineral components and the pore fluid respectively, G_{sat} and G_{dry} are shear moduli of the saturated and dry rock respectively and ϕ is the porosity. Bulk and shear moduli are related to recorded compressional velocity (V_p), shear velocity (V_s) and density (ρ) according to:

$$K = \rho(V_p^2 - \frac{4}{3}V_s^2) \tag{13}$$

and

$$G = \rho V_s^2$$

We apply this theory for substituting one fluid with another, in which case the Gassmann formula can be develop to:

$$K_{sat2} = \frac{K_0 \cdot A}{1 + A} \tag{14}$$

where

$$A = \frac{K_{sat1}}{K_0 - K_{sat1}} - \frac{K_{fl1}}{\phi(K_0 - K_{fl1})} + \frac{K_{fl2}}{\phi(K_0 - K_{fl2})}$$

and

$$G_{sat1} = G_{sat2}$$

where subscripts $sat1$ and $sat2$ refer to the saturated rock before and after substitution.

Fluid properties (subscripts $fl1$ and $fl2$) are calculated from the properties of formation water and hydrocarbons using Reuss type fluid mixtures:

$$K_{fl} = \frac{1}{Sw/K_w + (1 - Sw)/K_{hc}} \tag{15}$$

where Sw is the water saturation, and subscripts w and hc refer to water and hydrocarbon components respectively. This formula assumes that the two fluids are perfectly mixed considering the influence on wave propagation, which depend on frequency. Laboratory experiments show that this assumption first begin to fail at ultrasonic frequencies (Fabricius et al., this report; Mavco and Japsen, this report). The consequence of the Reuss formulation is that the weak/softer fluid component will dominate the overall acoustic response such that small hydrocarbon saturations will have a large effect.

Effects of compaction/decompation

Changes in rock moduli resulting from changes in porosity are calculated on the basis of a modified Hashin – Shtrikman model similar to the one proposed by Walls et al. (1998) for Ekofisk Field data. The model describes how bulk and shear moduli change with porosity in an interval between zero porosity and a maximum porosity (ϕ_{max}) encompassing the variation in the available data set. Data are allowed to vary between the modified upper Hashin – Shtrikman (MUHS) according to:

$$K_{eff}^{UHS} = \left[\frac{\phi/\phi_{max}}{K_{lim} + \frac{4}{3}G_0} + \frac{1 - \phi/\phi_{max}}{K_0 + \frac{4}{3}G_0}\right]^{-1} - \frac{4}{3}G_0 \tag{16}$$

$$G_{eff}^{UHS} = \left[\frac{\phi/\phi_{max}}{G_{lim} + Z_0} + \frac{1 - \phi/\phi_{max}}{G_0 + Z_0}\right]^{-1} - Z_0$$

where

$$Z_0 = \frac{G_0}{6}\frac{9K_0 + 8G_0}{K_0 + 2G_0}$$

corresponding to the presumably stiffest possible variety, where the subscript lim refer to moduli at the selected maximum porosity. This set of equations can also be developed for the lower bound which, however, is equivalent to the simpler Reuss average as may be developed from:

$$\frac{K_{sat}}{K_0 - K_{sat}} = \frac{K_{dry}}{K_0 - K_{dry}} + \frac{K_R}{K_0 - K_R} \tag{17}$$

where

$$K_R = \left(\frac{\phi_{max} - \phi}{\phi_{max} \cdot K_{lim}} + \frac{1 - (\phi_{max} - \phi)}{\phi_{max} \cdot K_0}\right)^{-1}$$

The upper bound description is applied during changes in porosity, where stratigraphical property differences are accommodated through adjustments of the end members (K_0 and K_{lim}). During decompaction the porosity may exceed ϕ_{max} in which case the further change is set to follow the lower (Reuss) bound.

Seismic model

We obtain zero offset seismic sections and AVO gathers based on the modelled logs as described above. Zero offset synthetic data are obtained from the reflectivity series that are calculated from the P-wave velocity (V_p) and density (ρ) logs as given by equation 22. This reflectivity series is convolved with a Ricker wavelet. A Ricker wavelet with a dominating frequency of 50 Hz was found to produce an acceptable match to field data. P-wave reflectivity for offset gathers ($R(\Theta)$) is calculated on the basis of first order reflectivity equations from the Zoeppritz equations as given by Spratt et al. (1993):

$$R(\Theta) = R_{pp0} + (R_{pp0} - 2' R_{ss0}) Sin^2\Theta + 0' \cdot \frac{\Delta\rho}{\rho_a} Sin^2\Theta \tag{18}$$

where

$$2' = 8\left(\frac{V_s}{V_p}\right)^2$$

and

$$0' = 2\left(\frac{V_s}{V_p}\right)^2 - \frac{1}{2}$$

and R_{pp0} and R_{ss0} are zero offset reflection coefficients for P and S-waves as given by equation 22. ρ_a is average density and $\Delta\rho = \rho_2 - \rho_1$; the density difference across the interface.

Offset calculations are based on an assumed 2500m streamer, which with fairly constant overburden velocities around 2000 m/sec will produce incidence angles (Θ) below 22.5° at top chalk level. Refraction in the chalk overburden is considered negligible due to rather homogeneous velocities and is consequently disregarded.

For standard analyses of amplitude versus offset (AVO) we apply the Shuey (1985 in Castangna 1993) approximation:

$$R_{pp}(\Theta_1) \sim R_{pp0} + \left(A_0 R_{pp0} + \frac{\Delta\sigma}{(1-\sigma^2)^2}\right) Sin^2\Theta_1 + \frac{1}{2}\frac{\Delta V_p}{V_{pa}}(Tan^2\Theta_1 - Sin^2\Theta_1) \tag{19}$$

where

$$A_0 = B_0 - 2(1 + B_0)\left(\frac{1-2\sigma}{1-\sigma}\right) \tag{20}$$

and

$$B_0 = \frac{\frac{\Delta V_p}{V_{pa}}}{\frac{\Delta V_p}{\Delta V_{pa}} + \frac{\Delta \rho}{\Delta \rho_a}} \tag{21}$$

and the zero offset P-wave reflectivity (R_{pp0}) is:

$$R_{pp0} = \frac{I_{p2} - I_{p1}}{I_{p2} + I_{p2}} \tag{22}$$

where the impedance is given by $I_p = V_p \cdot \rho$. Substituting V_p with V_s gives the S-wave reflectivity R_{ss0}. σ is the poisson ratio as given by:

$$\sigma = \frac{\frac{1}{2}(\frac{V_p}{V_s})^2 - 1}{(\frac{V_p}{V_s})^2 - 1} \tag{23}$$

The last term in equation 19 is dropped as it is insignificant for moderate angles of incidence (Θ_1). We use the first two term in equation 19 for the intercept versus slope plots given in Figs xx and xx. We also use the poisson ratio (σ, equation 23) to crossplot with acoustic impedance to illustrate effects of porosity and saturation changes.

Seismic model examples

We exemplify modelling of compaction and saturation changes with data from the Rigs-2 well, South Arne Field (Table 4). Seismic examples are given in the appendix. Input data to the modelling are logs, where key logs like V_p, V_s, and density are restored to virgin conditions. Due to a missing shallow resistivity log, this restoration proved to be most reliably performed using rock physical calculations as described in Japsen et al. (*this report*). This results in an implicid self-consistency that causes modelled property changes calculated in this report to perform somewhat better than if restoration was based on shallow resistivity data (see discussion in Japsen et al. *this report*).

Moduli of the formation components have been estimated during laboratory measurements (Fabricius et al. *this report*) and are listed in Table 4.

Component	Bulk Modulus K	Shear Modulus G	Density ρ
Calcite	71.0	30.0	2.71
Silicates	25.0	9.0	2.70
$lim : \phi = 45$	1.5	2.5	
Brine	2.96	0	1.035
Oil	0.52	0	0.633

Table 5: Moduli and densities of formation components

To demonstrate the capabilities of the modelling tools, two scenarios are tested:

a. The free water level is changed from 2795 m b.m.s.l. over the ideal 2900 m to 2990 in steps of 5 m corresponding to 40 cases (or traces).

b. The present effective stress in the chalk is changed corresponding to depth shifts of -900 m to 900 m in steps of 30 m corresponding to 60 cases (or traces).

Change in free water level

A range of synthetic seismograms are modelled by only changing the free water level and via saturation height modelling change the fluid composition. The range is from 2795 m to 2990 m .b.s.l. corresponding to a change from 100% water saturation to approximately irreducible water saturation (Fig. 8. The best fit FWL relative to logged Sw is in the middle of this range, so maximum modelled hydrocarbon saturation far exceeds observed saturations.

A set of plots illustrating poisson ratio versus acoustic impedance shows that Sw changes affects both of these properties (Fig. 10). However, it is clear that acoustic impedance is more sensitive to porosity changes, than to saturation changes whereas the poisson ratio is more susceptible to saturation changes. These tendencies would be more amplified if gas was used rather than oil in the modelling, and acoustic impedance effects from saturation changes would become more significant. Also is the poisson ration becoming more sensitive to saturation with increasing porosity.

Another interesting effect is seen on the Top Chalk and Top Tor reflectors (at 2.741 sec; table 3; Fig. 9). The Top Tor reflector is characterised by downward decreasing impedance. It is seen that the amplitude of this reflector increases abruptly (more negative) as oil enters the formation. As FWL deepens (saturations increases) it gains amplitude until low to moderate oil saturations. From moderate to high oil saturation it slowly decrease again. This is a consequence of the saturation height model, which causes Tor Formation hydrocarbon saturation to increase faster than in the Ekofisk Formation in spite of lower capillary pressures at low overall hydrocarbon saturation. This is a consequence of lower capillary entry pressures in the Tor Formation.

The Top Chalk reflector is also affected by increasing oil saturation (Fig. 9). It is seen to loose amplitude with increasing oil saturation, and at saturations slightly higher than observed in the well, a reversal is predicted.

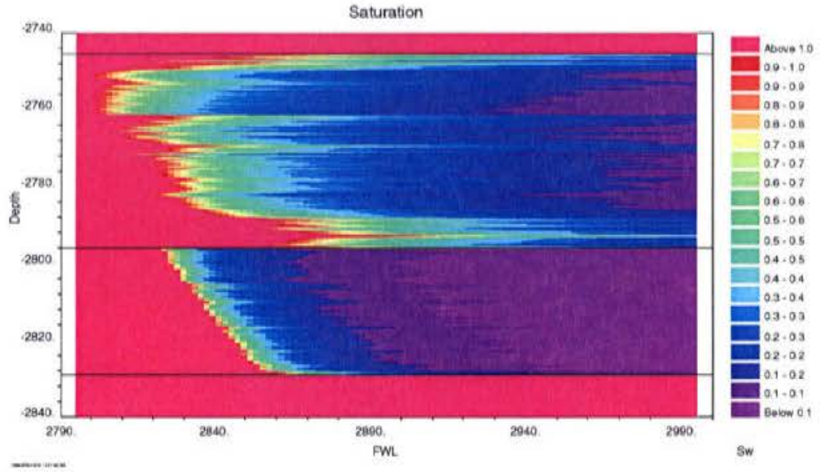

Figure 8: Water saturation profiles calculated by changing the free water level (FWL). Note that different properties in Tor and Ekofisk formations cause the Tor to hold lower saturations for shallow FWL than Ekofisk in spite of lower capillary pressure.

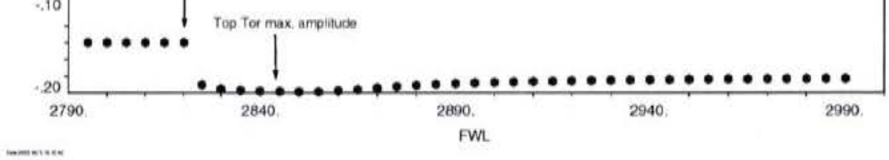

Figure 9: Modelled reflector strength and sign of the Top Chalk and Top Tor reflectors as a function of free water level in the Rigs-2 well(or modelled saturation distribution).

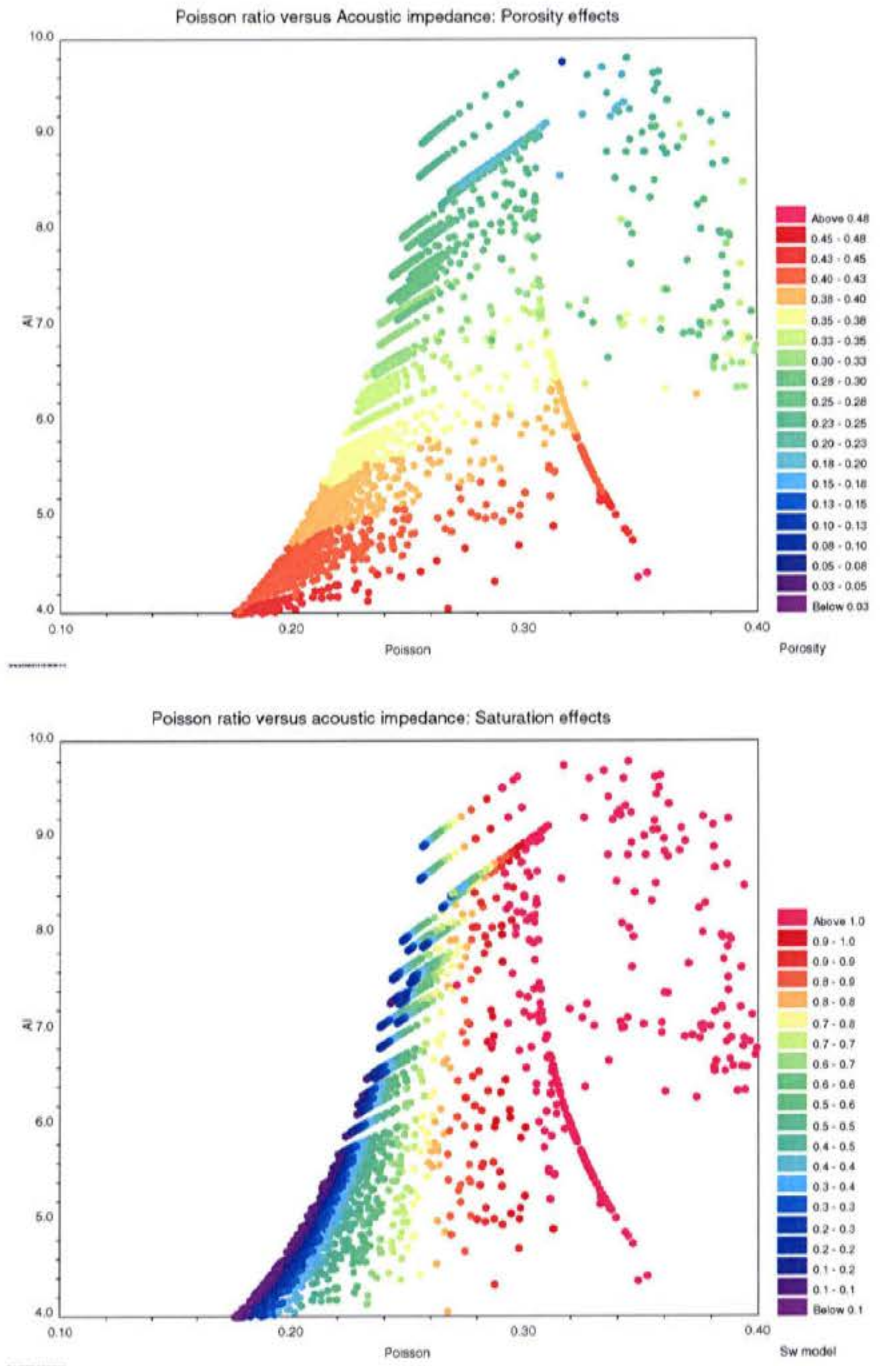

Figure 10: Poisson ratio versus acoustic impedance caused by modelled Sw changes (several free water level positions) in the Rigs-2 well. X and Y are the same, but colours show porosity and Sw. Points in the upper right are from outside the Chalk.

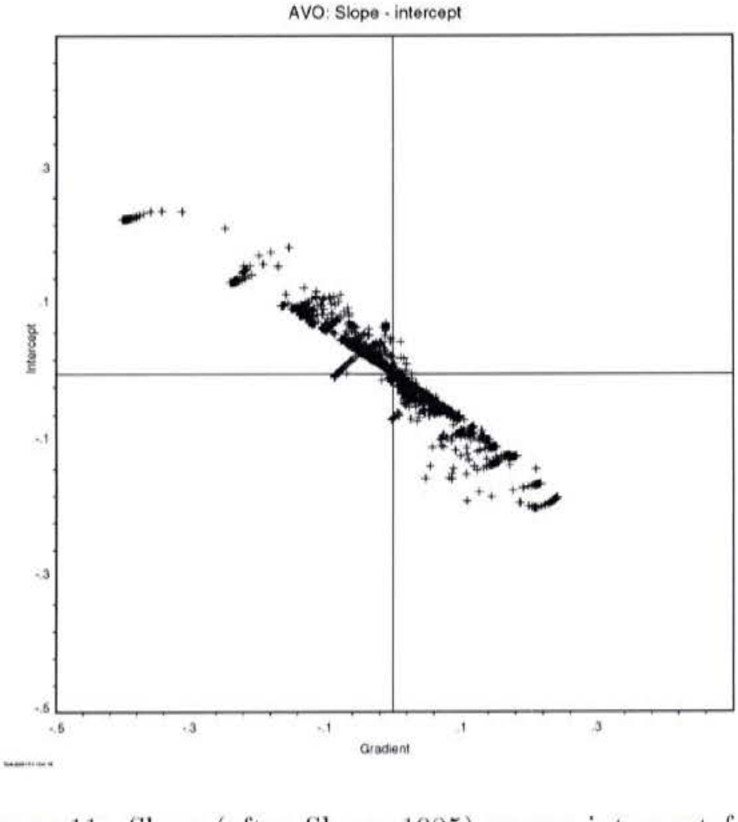

Figure 11: Slope (after Shuey 1985) versus intercept for saturation change models. Chalk interval only.

Change in effective stress

The compaction/de-compaction exercise is illustrated with the porosity logs shown in (Fig. 12). An interesting effect is that the varability in the porosity traces is amplified during de-compaction, and subdued during compaction which is in accordance with observations in seismic data (e.g. Britze et al. 2000). Modelling a change in effective stress inevitably results in saturation changes such that less porosity means higher water saturation. This relationship can be seen to be almost exponential (Fig. 12).

The synthetic porosity and Sw logs also show that the observed Sw is closer to irreducible water saturation in the Tor Formation than in the Ekofisk Formation in spite of lower capillary pressures in Tor. This is seen from the fact that an only negligible reduction in Sw occurs in the Tor although porosity is almost doubled during decompation. The Sw reduction during de-compaction in Ekofisk is more conspicuous. During compaction this diffences, which originates from entry pressure differences, is further amplifed.

Another interesting observation is that amplitudes on the porosity log (as well as the saturation log) are increased during decompation and subdued during compaction. This is a consequence of the design of the compaction/de-compaction model. This effect causes amplitude changes in the seismic model and corresponds to general seismic observations in the Chalk (Britze et al. 2000).

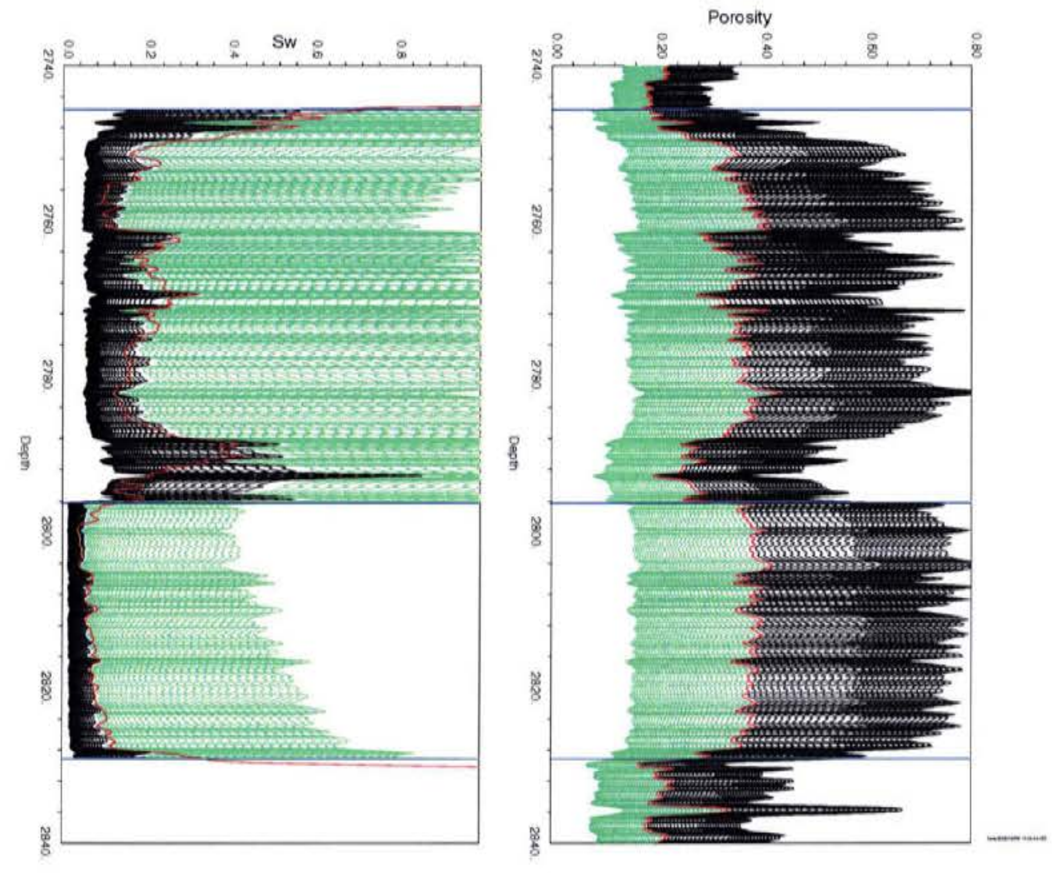

Figure 12: Depth shift of the Rigs-2 well. Right panel shows log traces corresponding to decompaction in black and compaction in green. Corresponding saturation changes resulting from porosity changes are shown to the left in the same colours.

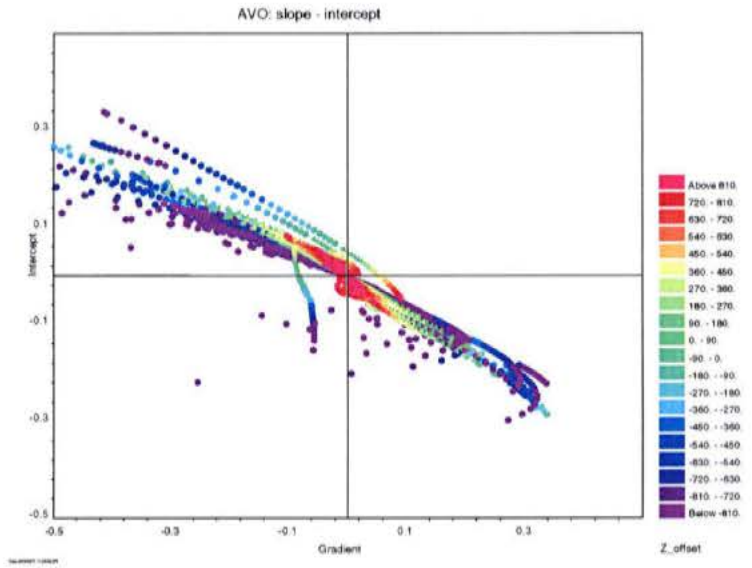

Figure 13: Slope (after Shuey 1985) versus intercept for compaction/de-compaction change models. Chalk interval only. Effective stress changes corresponding to -900 m to +900 m from present position are shown i colour. Very deep burial is seen to subdue reflectivity as well as gradient changes.

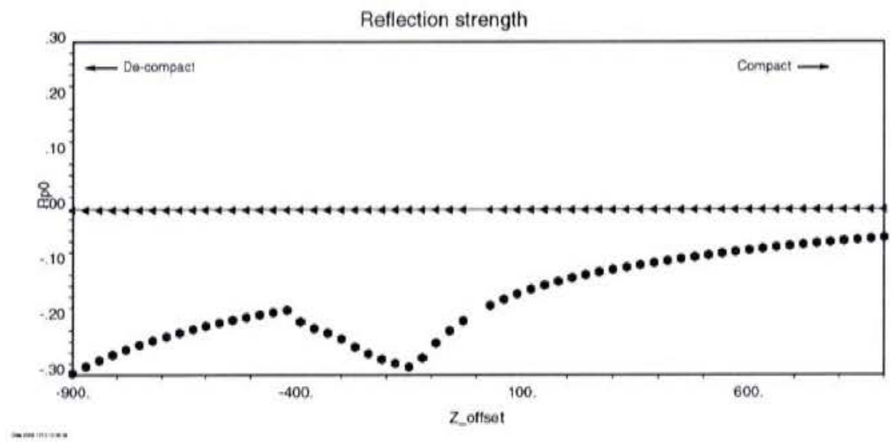

Figure 14: Modelled reflector strength and sign of the Top Chalk and Top Tor reflectors as a function of compaction/decompaction.

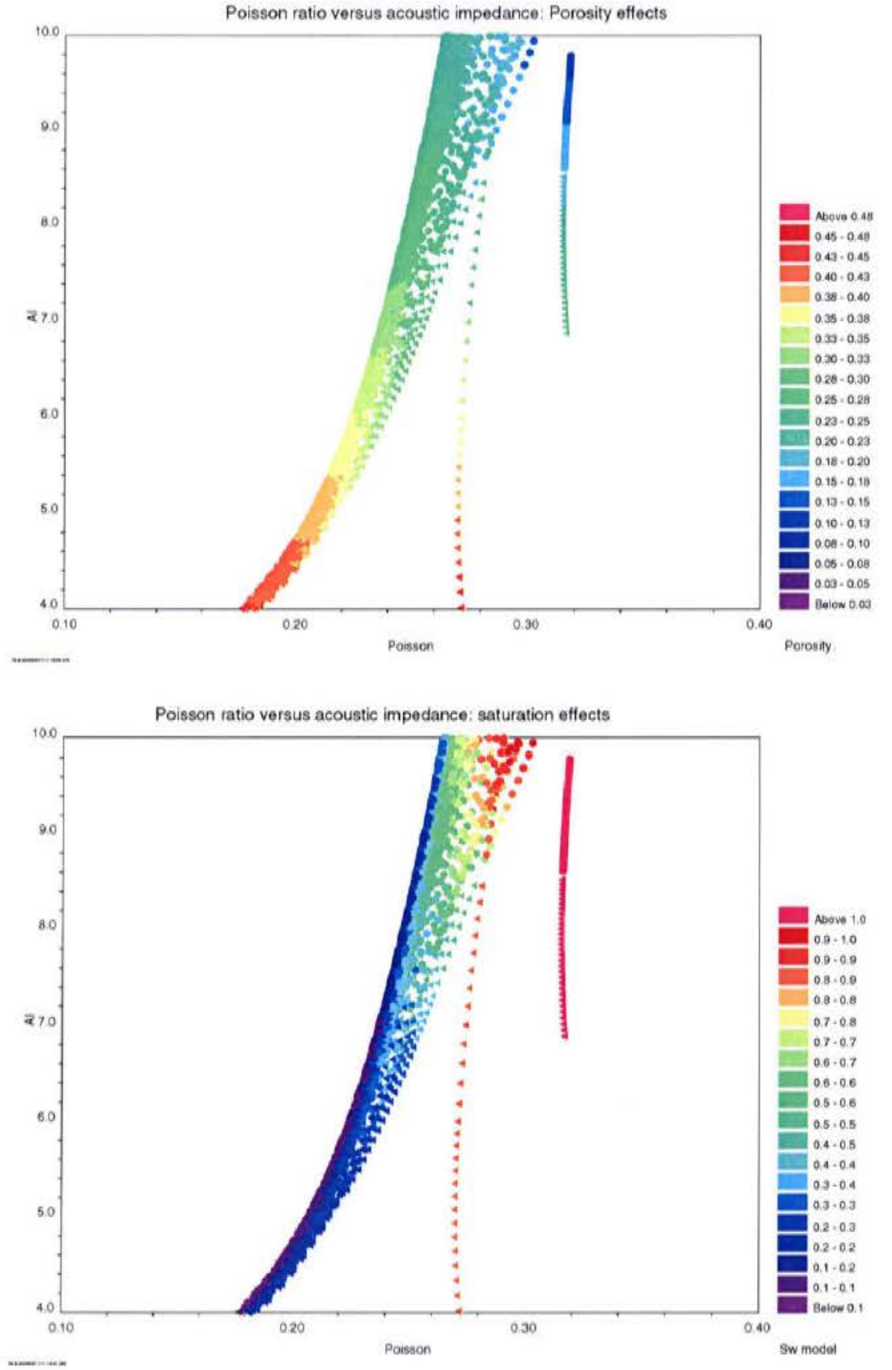

Figure 15: Poisson ratio versus acoustic impedance caused by modelled compaction changes (-900 m to +900 m from present position). Only Chalk from the Rigs-2 well is shown. X and Y are the same, but colours show porosity and Sw.

References

Athy, L. F. 1930: Density, porosity and compaction of sedimentary rocks. Bull. of the American Association of Petroleum Geologists, 14, 1-24.

Bramwell, N. P., Caillet, G., Meciani, L., Judge, N., Green, M. and Adam, P. 1998: Chalk exploration, the search for subtle traps. In Fleet, A. J. & Boldy, S. A. R. (eds.) Petroleum Geology of Northwest Europe: Proceedings of the 5th conference. The Geological society, London, 911-937.

Britze, P., Nielsen, E. B., Dahl, N. and Haug, S., 2000: EAGE, Petrophysics meets Geophysics, Proceedings.

Castagna, J. P. 1993: AVO analysis – Tutorial and review. In J. P. Castagna and M. M. Backus (eds.): Offset-dependent reflectivity – Theory and practice of AVO analysis, Investigations in Geophysics no. 8, Society of Exploration Geophysicists, 3-36.

Engstrøm, F. 1995: A new method to normalize capillary pressure curves. International Symposium of the Society of Core analysts, San Francisco, 1995, SCA no. 9535, 12p.

Fabricius, I. L, Høier, C., Japsen, P. and Korsbech, U. this report: Modeling elastic moduli of impure chalk.

Frederiksen, S., Nielsen, S.B., and Balling, N. 2001: Post-Permian evolution of the Central North Sea: a numerical model. Tectonophysics, 343, 185-203.

Gassmann, F. 1951: Elastic waves through a packing of spheres. Geophysics, 16, 673-685.

Japsen, P. 1998: Regional velocity-depth anomalies, North Sea Chalk; a record of over-pressure and Neogene uplift and erosion. American Association of Petroleum Geologists, Bulletin 82, 2031-2074.

Japsen, P. 1999: Overpressured Cenozoic shale mapped from velocity anomalies relative to a baseline for marine shale, North Sea. Petroleum Geoscience, 5, 321-336.

Japsen, P., 2000: Fra kridthav til Vesterhav, Nordsøbassinets udvikling vurderet ud fra seismiske hastigheder. Geologisk tidskrift, 2, 36 p.

Japsen, P., A. Bruun, I. L. Fabricius, Rasmussen, R., Vejbæk, O.V., Pedersen, J. M., Mavko, G. and Mogensen, C. this report: Influence of porosity and pore fluid on acoustic properties of chalk: AVO-response from oil, South Arne field, North Sea.

Jensen, P. K., Holm, L. and Thomsen, E. 1985: Modelling burial history, temperature and maturation. – In B. M. Thomas et al. (ed.): Petroleum Geochemistry in Exploration of the Norwegian Shelf. Proceedings of a NPF conf. - Graham & Trotman, PP. 145 - 153.

Mavko, G. and Japsen, P. this report: Fluid substitution in chalks: Effects of saturation scales.

Mavko, G., Mukerji, T., and Dvorkin, J. 1998: The rock physics handbook. Tools for seismic analysis in porpus media. Cambridge University Press, 329 p.

Megson, J. and Hardman, R. 2001: Exploration for and development of hydrocarbons in the Chalk of the North Sea: a low permeability system. Petroleum Geoscience, 7, 3-12.

Sclater, J. G. and Christie, P. A. F. 1980: Continental stretching: an explanation of the post-mid-Cretaceous subsidence of the Central North Sea basin. - Jour. of Geoph. Res., vol. 85, no. b7., pp. 3711-3739.

Shuey, R. T. 1985: A simplification of the Zoeppritz equations, Geophysics, 50, 609-614.

Spratt, R. S.m Goins, N. R. and Fitch, T. J. 1993: Pseudo-shear – The analyses of AVO. . In J. P. Castagna and M. M. Backus (eds.): Offset-dependent reflectivity – Theory and practice of AVO analysis, Investigations in Geophysics no. 8, Society of Exploration Geophysicists, 37-56.

Vejbæk, O. V. 2002: Reservoir characterization of the Roar Gas Field, Danish North Sea. Petroleum Geoscience, 2002, 8(1), 71-87.

Walls, J. D., Dvorkin, J., and Smith, B. A. 1998: Modeling SeiSmic Velocity in Ekofisk Chalk. 1998 SEG Expanded abstracts, 4 p.

Appendices

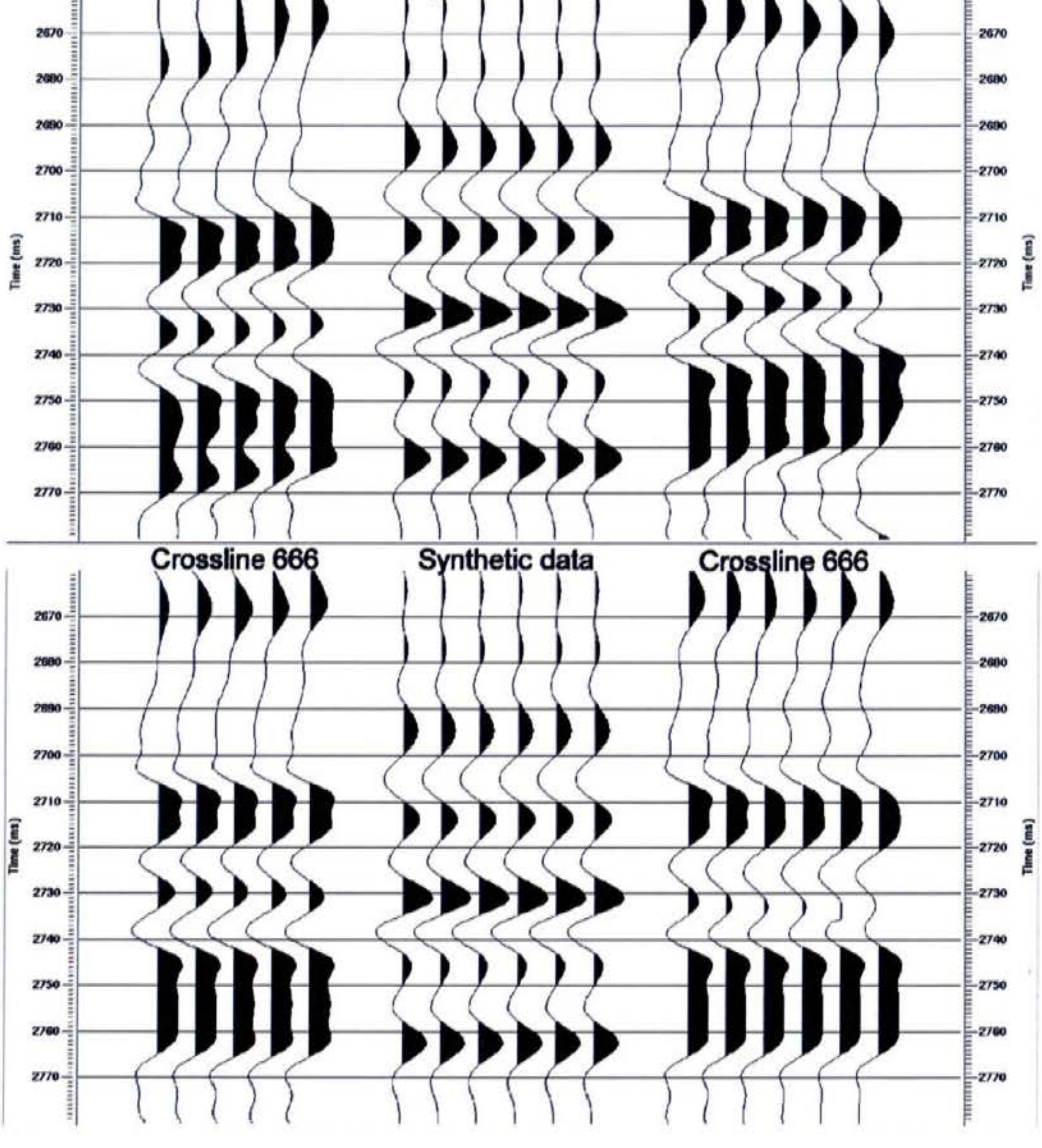

Fig A1: Zero-offset traces based on original log data (no FWL or compaction changes) shown as 6 central traces. Traces to the right and left are field data.

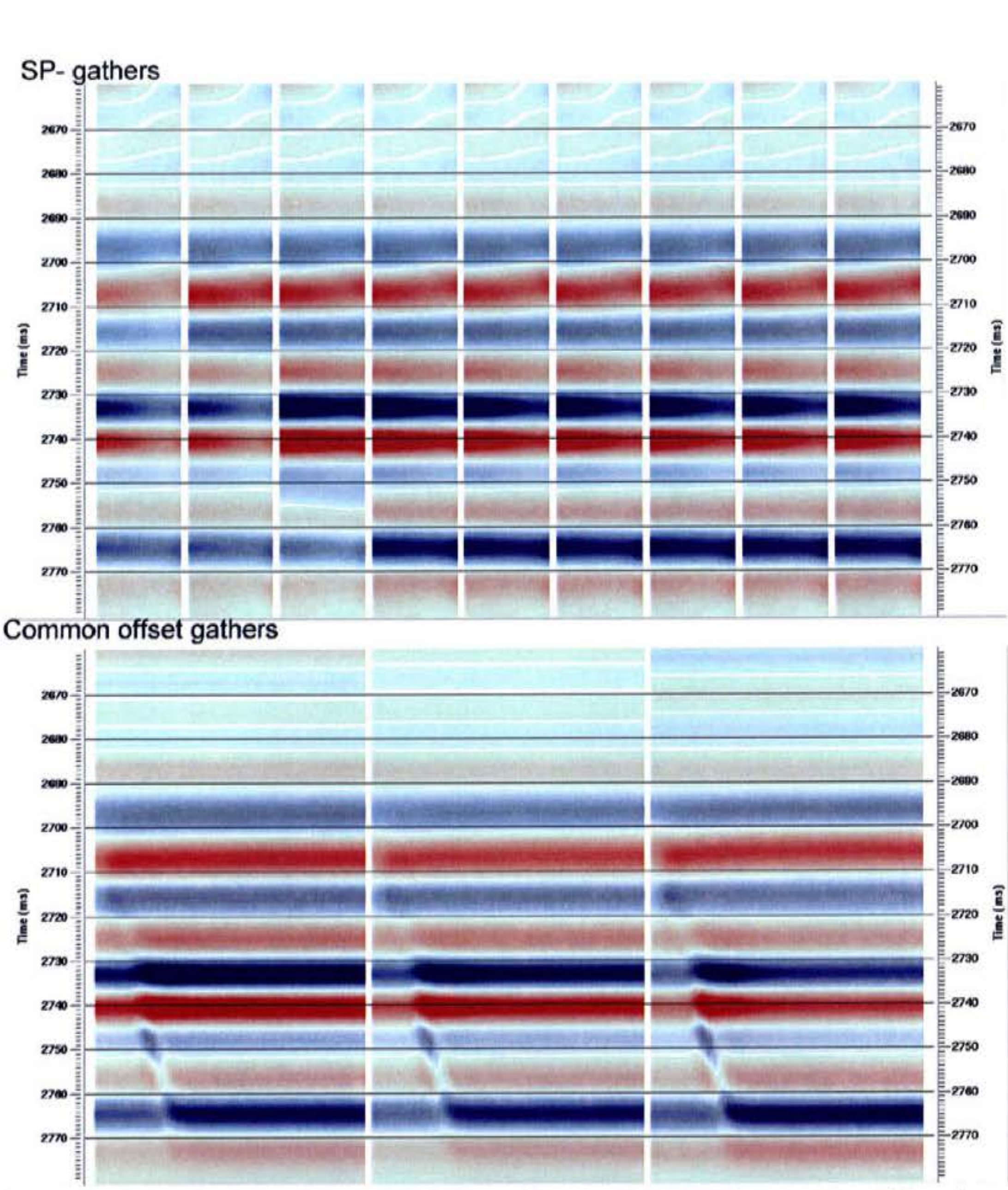

Fig. A2: Synthetic seismic based on modelled changes in saturation. SP-gathers are selected from low saturation models (left) to high saturation models (right). Common offset gathers each display the entire modelled saturation range and represent near offset (left), mid offset and far offset (right). The disturbance in the lower left originates from the modelled oil – water contact.

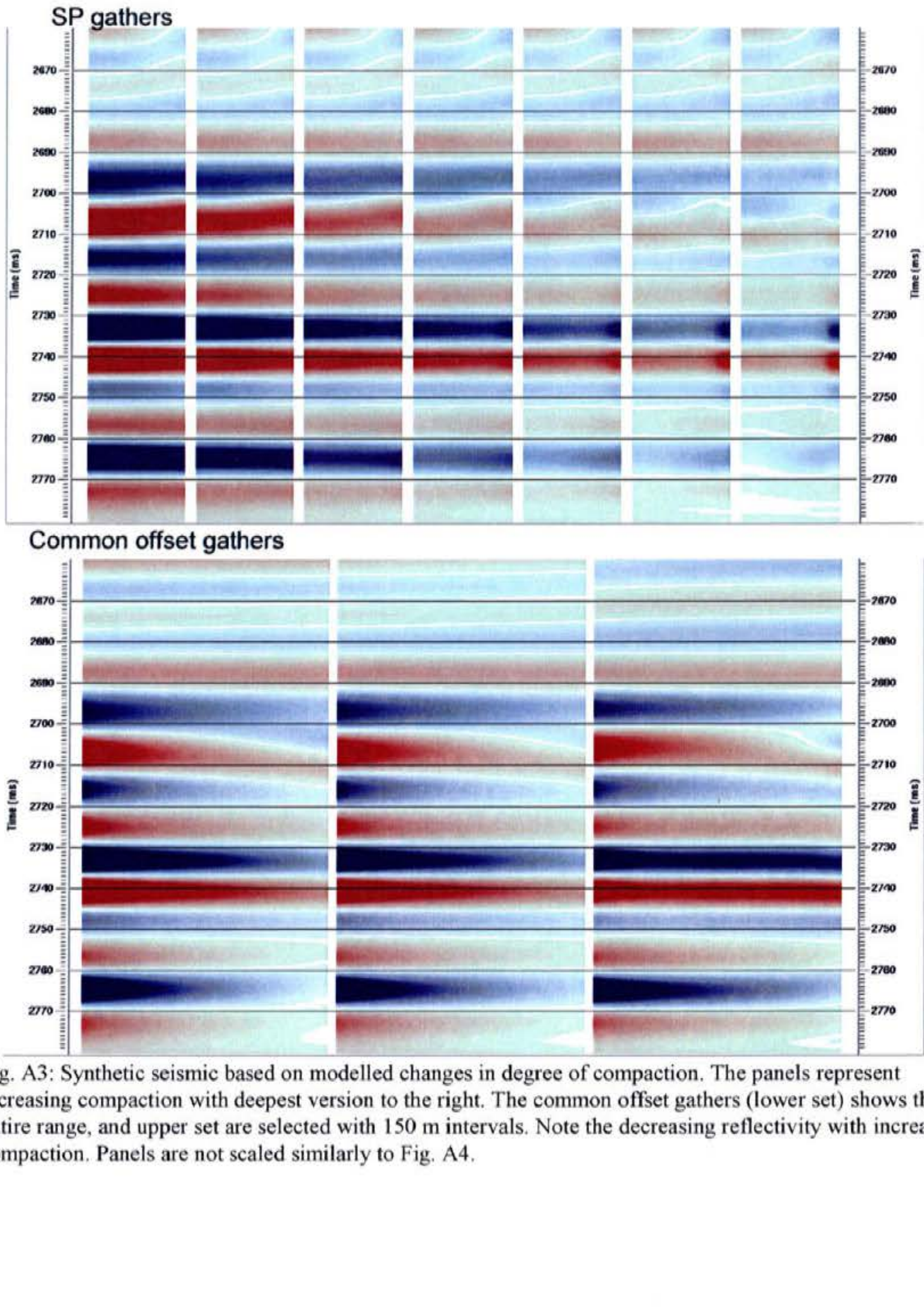

Fig. A3: Synthetic seismic based on modelled changes in degree of compaction. The panels represent increasing compaction with deepest version to the right. The common offset gathers (lower set) shows the entire range, and upper set are selected with 150 m intervals. Note the decreasing reflectivity with increasing compaction. Panels are not scaled similarly to Fig. A4.

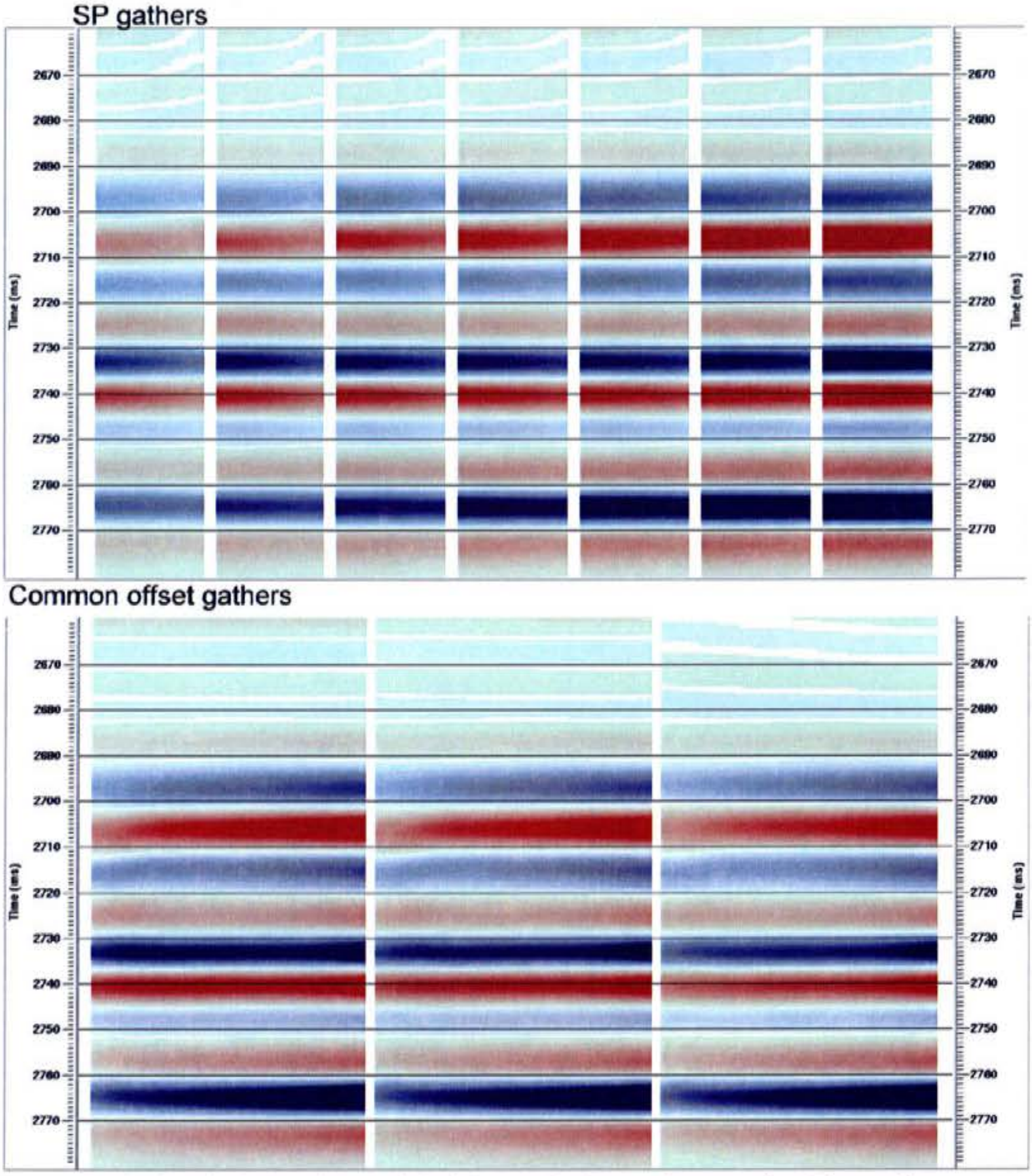

Fig. A4: Synthetic seismic based on modelled changes in degree of compaction. The panels represent decreasing compaction with shallowest version to the right. The common offset gathers (lower set) shows the entire range, and upper set are selected with 150 m intervals. Note the increasing reflectivity with decreasing compaction. Panels are not scaled similarly to Fig. A3.